HEINRICH HEINE
UNIVERSITÄT DÜSSELDORF

Porous Covalent Triazine-Based Frameworks (CTFs): Design, Synthesis and Applications

Dissertation

for the attainment of the title of doctor
in the Faculty of Mathematics and Natural Sciences
at the Heinrich Heine University Düsseldorf

presented by

Subarna Dey

From India

Düsseldorf, September 2016

from the Institute for Anorganische Chemie und Strukturchemie I
at the Heinrich Heine University Düsseldorf

Published by permission of the
Faculty of Mathematics and Natural Sciences at
Heinrich Heine University Düsseldorf

Supervisor: Prof. Dr. Christoph Janiak
Co-supervisor: Prof. Dr. Christian Ganter

Date of the oral examination: 04.10. 2016

To my Parents and Grandparents

Eidesstattliche Erklärung

Ich versichere an Eides statt, dass die Dissertation von mir selbstständig und ohne unzulässige fremde Hilfe unter der Beachtung der „Grundsätze zur Sicherung guter wissenschaftlicher Praxis“ an der Heinrich-Heine-Universität Düsseldorf erstellt worden ist. Die aus fremden Quellen direkt oder indirekt übernommenen Gedanken sind als solche kenntlich gemacht. Die Arbeit wurde bisher weder im Inland noch im Ausland in gleicher oder ähnlicher Form einer anderen Prüfungsbehörde vorgelegt. Es wurden keine früheren erfolglosen Promotionsversuche unternommen.

……………………… ………………………

Ort, Datum Unterschrift

Acknowledgments

First of all, I would like to express my deepest gratitude to my supervisor, Prof. Dr. Christoph Janiak, for giving me the opportunity to work on his group. I am grateful for his excellent guidance, constant encouragement, inspiring motivation and patience throughout the course of investigation. In addition to being a capable, caring, and supportive supervisor, he has been the most influential person in my academic development.

I would also like to thank Prof. Dr. Christian Ganter for being my Co-supervisor.

I would like to thank Mrs. Birgit Tommes for IR measurements.

I sincere thanks goes to Mrs. Claudia Schäfer, Mrs. Annette Ricken, Mr. Dietmar Frunzke and Mr. Axel Mund for their technical assistance and kind help.

I would also like to thank Dr. Nader de Sousa Amadeu for solid state NMR measurements.

I would like to thank Mrs. Fischer, Mr. Jung and Mr. Krebs (glass blowing section).

I would like to thank Janina Dechnik and Dr. Harold Tanh Jeazet for their kind help and explanation for membrane works; Sebastian Glomb, Emrah Hastürk and Niels Tannert for water adsorption measurements; Dennis Dietrich, Annika Herbst and Sandra Nießing for SEM measurements; Karsten Klauke and Ilka Simon for TGA measurements.

I have also received much in the way of support and kind help from my fellow researchers, in particular, Christina Rutz, Hajo Meyer, Anna Christin Kautz and Irina Gruber. My heartfelt thanks to each one of them.

I am grateful to Dr. Sandeep Dey for his suggestions and help for my thesis correction.

My sincere thanks to my family and my family-in-lows for their support.

I would like to thank my aunt Mrs. Krishna Pradhan and uncle Mr. Ahindranath Pradhan for their continuous encouragement. I would like to thank my sister and friend Arijita for her support.

I do not have enough words to express my gratitude to the person behind the whole journey, to my husband, Asamanjoy. Thank you for being with me.

I can never express enough gratitude to my parents, whose love and inspiration has always been strength for me. Without their continuous support and encouragement, neither this dissertation, nor any other achievement could have been possible.

This cumulative thesis was done from October 2012 to September 2016 at the Heinrich-Heine University of Düsseldorf in Institut für Anorganische Chemie und Strukturchemie I under the supervision of Prof. Dr. Christoph Janiak.

Publications

1. Covalent triazine-based frameworks (CTFs) from triptycene and fluorene motifs for CO_2 adsorption.
   Subarna Dey, Asamanjoy Bhunia, Dolores Esquivel and Christoph Janiak*, *J. Mater. Chem. A*, 2016, **4**, 6259-6263. DOI: 10.1039/C6TA00638H.
2. Two linkers are better than one: Enhancing CO_2 capture and separation with porous covalent triazine-based frameworks from mixed nitrile linkers.
   Subarna Dey, Asamanjoy Bhunia and Christoph Janiak*, *J. Mater. Chem. A*, 2016, submitted.
3. A mixed-linker approach towards improving covalent triazine-based frameworks for CO_2 capture and separation.
   Subarna Dey, Asamanjoy Bhunia, Ishtvan Boldog and Christoph Janiak*, *Micropor. Mesopor. Mater.*, 2016, submitted.
4. High adsorptive properties of covalent triazine-based frameworks (CTFs) for surfactants from aqueous solution.
   Asamanjoy Bhunia, **Subarna Dey**, Maria Bous, Chenyang Zhang, Wolfgang von Rybinski* and Christoph Janiak*, *Chem. Commun.*, 2015, **51**, 484-486. DOI: 10.1039/c4cc06393g.
5. Syntheses of two imidazolate-4-amide-5-imidate linker-based hexagonal metal-organic frameworks with flexible ethoxy substituent.
   Suvendu Sekhar Mondal, **Subarna Dey**, Igor A. Baburin, Alexandra Kelling, Uwe Schilde, Gotthard Seifert, Christoph Janiak and Hans-Jürgen Holdt*, *CrystEngComm.*, 2013, **15**, 9394-9399. DOI: 10.1039/c3ce41632a.
6. Microporous La–Metal–Organic Framework (MOF) with Large Surface Area.
   Souvik Pal, Asamanjoy Bhunia, Partha P. Jana, **Subarna Dey**, Jens Mçllmer, Christoph Janiak and Hari Pada Nayek*, *Chem. Eur. J.*, 2015, **21**, 2789-2792. DOI: 10.1002/chem.201405168.
7. A homochiral vanadium–salen based cadmium bpdc MOF with permanent porosity as an asymmetric catalyst in solvent-free cyanosilylation.

Asamanjoy Bhunia, **Subarna Dey**, José María Moreno, Urbano Diaz, Patricia Concepcion, Kristof Van Hecke, Christoph Janiak and Pascal Van Der Voort*, *Chem. Commun.*, 2016, **52**, 1401-1404. DOI: 10.1039/c5cc09459c.

8. A photoluminescent covalent triazine framework: CO_2 adsorption, light-driven hydrogen evolution and sensing of nitroaromatics.
   Asamanjoy Bhunia,* Dolores Esquivel, **Subarna Dey**, Ricardo Fernández-Terán, Yasutomo Goto, Shinji Inagaki, Pascal Van Der Voort and Christoph Janiak*, *J. Mater. Chem. A*, 2016, **4**, 13450-13457. DOI: 10.1039/c6ta04623a.
9. Missing Building Blocks Defects in a Porous Hydrogen-bonded Amide-Imidazolate Network Proven by Positron Annihilation Lifetime Spectroscopy.
   Suvendu Sekhar Mondal, **Subarna Dey**, Ahmed G. Attallah, Asamanjoy Bhunia, Alexandra Kelling, Uwe Schilde, Reinhard Krause-Rehberg, Christoph Janiak, and Hans-Jürgen Holdt*, *ChemistrySelect*, 2016, in revision.

Kurze Zusammenfassung

Die Entwicklung von kovalent gebundenen Triazin-Netzwerken (CTFs) hat in den letzten Jahren aufgrund von verfügbaren, günstigen Ausgangsmaterialien, einfacher Synthese, einer hohen Oberfläche sowie chemischer Stabilität und einer gewissen Hydrophilie zunehmend Beachtung gefunden. Drei Synthesestrategien werden für die Entwicklung der CTFs genutzt: 1. Ionothermale Bedingungen ($ZnCl_2$); 2. Verwendung einer starken Brønsted Säure (CF_3SO_3H); 3. Friedel-Crafts-Reaktionen ($AlCl_3$). CTFs wurden in den Gebieten der Gasspeicherung und Gastrennung, Katalyse, membranbasierten Separationen oder auch der Optoelektronik vielfältig erforscht.

In der vorliegenden Arbeit wird die Synthese neuer CTF-Materialien unter Verwendung verschiedener Synthesebedingungen sowie deren Anwendung in der Gas/Flüssigkeiten/Dampf Adsorption und Trennung beschrieben.

Die porösen Materialien CTF-TPC und CTF-FL wurden unter Verwendung von Triptycen und Fluoren und dem kostengünstigen Katalysator $AlCl_3$ in einer Niedrigtemperatursynthese nach Friedel-Crafts synthetisiert, dabei wurden BET Oberflächen von 1668 m^2/g bzw. 773 m^2/g erreicht. CTF-TPC besitzt die größte Oberfläche aller bekannten CTFs, die mittels einer Friedel-Crafts-Reaktion hergestellt wurden. Es wurden Experimente der Gasadsorption für CO_2, CH_4, H_2 und N_2 bei verschiedenen Temperaturen durchgeführt, die Ergebnisse waren mit denen bekannter CTFs mit großer Oberfläche vergleichbar. CTF-TPC und CTF-FL zeigten eine beachtliche CO_2 Aufnahme von 4.24 und 3.26 mmol/g (95.2 und 73.2 cm^3/g), die auf einer elektrostatischen Wechselwirkung zwischen den stickstoffreichen Triazineinheiten und den CO_2 Molekülen beruht (CO_2 Quadrupolmoment (1.4×10^{-39} C m^2)). Nach der Theorie ideal adsorbierter Lösung (IAST) wurde die CO_2/N_2 Selektivität von CTF-TPC und CTF-FL mit 30 bzw. 48 berechnet.

Um die Aufnahmekapazität von CO_2 zu erhöhen, wurden CTFs auf Basis von gemischten Liganden unter Verwendung von $ZnCl_2$ bei ionothermalen Bedingungen für die Anwendung von CCS synthetisiert. Wir haben dabei erwartet, dass die BET Oberfläche und die CO_2 Aufnahmekapazität der CTFs durch gezielte Wahl der gemischten Linker bei der Synthese der CTFs eingestellt werden kann. Zwei Nitrilgrundgerüste, Tetra(4-cyanophenyl)ethylen (TPE), und Adamantan (Ad), wurden mit 1,4-Terephthalonitril, Tetrafluoroterephthalonitril, 4,4′-Biphenyldicarbonitril und 1,3,5-Benzotricarbonitril in verschiedenen Verhältnissen unter ionothermalen Bedingungen umgesetzt, um neue COFs zu synthetisieren. Vier CTFs wurden

unter Verwendung des TPE Grundgerüstes hergestellt, neun ausgehend von Adamantan, alle CTFs wurden anschließend hinsichtlich ihrer N_2, CO_2 und CH_4 Adsorption untersucht. Die spezifischen BET Oberflächen der auf einem TPE Grundgerüst basierten CTFs (MM1-MM4) betrugen 1800, 1360, 1884 und 1407 m^2/g und zeigten eine hohe CO_2 Aufnahmekapazität bis zu 107 cm^3/g, d.h. 4.73 mmol/g (MM2; bei 273 K und 1 bar), was geringfügig höher als die größter bisher in der Literatur bekannte CO_2 Aufnahme in CTFs, gemessen bei natürlich fluorierten CTFs. Diese CTFs besitzen eine sehr gute CO_2/N_2 (85% N_2: 15% CO_2) Selektivität bis zu 130 bei 273 K und 1 bar unter Verwendung von IAST, die CO_2 Selektivität ist dabei etwa 2-3 mal höher als derzeit bekannte CTF Materialien, die bei 400 °C synthetisiert wurden. Auf der anderen Seite zeigten die auf einem Adamantangrundgerüst basierten CTFs Oberflächen im Bereich von 747-1885 m^2/g. Bei niedrigem Druck (bis zu 1 bar) und 273 K adsorbierten diese CTFs signifikante Mengen an CO_2 (40-76 cm^3/g) und CH_4 (14-26 cm^3/g), was sehr vergleichbar zu vielen literaturbekannten CTFs ist. Bei Verwendung der IAST wurde eine CO_2/N_2 Selektivität im Bereich von 17-30 bei 273 K gefunden.

Die adsorptiven Eigenschaften in wässriger Lösung von CTF-1 gegenüber einem nicht-ionischen und einem anionischen Tensid (Alkylpolyglycolether ($C_{12}EO_7$) bzw. Natriumdodecylsulfat (SDS)) wurden untersucht und mit einem typischen Industrieruß mit einer spezifischen Oberfläche von 150 m^2/g verglichen. CTF-1 ist in der Lage, bis zu 4.0 g/g des Tensids aus wässriger Lösung (c = 8.0 mmol/L) aufzunehmen. Dies ist mehr als die 20-fache Aufnahmekapazität von Industrieruß (Printex L von Evonik).

Der membranbasierte Separationsprozess hat ein beträchtliches Ansehen erlangt, da er eine ökonomisch günstige und energiesparende Methode darstellt. CTFs rein organischer Natur könnten für diesen Zweck von Interesse sein, da sie eine hohe thermische und chemische Stabilität aufweisen. Dafür wurden verschiedene Mixed-Matrix-Membranen (MMMs) hergestellt, wobei eine Mischung aus CTF-1 als Additiv und Polsulfone als Polymermatrix verwendet wurde. Anschließend wurde die Gaspermeabilität unter Standardbedingungen untersucht. Die hergestellten Membranen zeigten eine CO_2 Permeabilität von 9.8 Barrer (bei einer Beladung von 24 wt% CTF-1), was signifikant höher ist als die Permeabilität einer reinen Polysulfonmembran (7.3 Barrer). Ebenso erhöhte sich der Wert der CO_2/N_2 Selektivität (28.6 bei einer Beladung von 8wt% CTF-1) im Vergleich zur reinen Polysulfonmembran (23).

Friedel-Crafts-Alkylierungsreaktionen einiger aromatischer Baueinheiten mit 2-Amino-4,6-dichloro-1,3,5 triazin wurden durchgeführt, um aminfunktionalisierte CTFs zu isolieren. Fünf

CTFs, nämlich AT-FL, AT-TPC, AT-TPB, AT-TPE, AT-TPS, wurden ausgehende von 2-Amino-4,6-dichloro-1,3,5 triazin (AT) und Fluoren (FL) 1,3,5-Triphenylbenzol (TPB), Triptycen (TPC), Tetraphenylethelen (TPE) und Tetraphenylsilan (TPS), katalysiert in einer Friedel-Crafts-Reaktion von $AlCl_3$, synthetisiert. Die so synthetisierten CTFs wurden hinsichtlich ihrer CO_2, N_2, H_2 und CH_4 Adsorption untersucht. Die BET Oberfläche von AT-TPC wurde mit 1174 m^2/g bestimmt und nimmt in der Reihenfolge AT-TPC (1174 m^2/g)> AT-TBP (804 m^2/g)>AT-TPE (594 m^2/g)>AT-FL(572 m^2/g)>AT-TPS (451 m^2/g) ab. Dagegen zeigte AT-TBP die höchste CO_2 Aufnahme (76.7 cm^3/g bei 273 K und 1 bar) im Vergleich zu AT-TPE (66.7 cm^3/g), AT-TPC (60.8 cm^3/g), AT-FL (56.4 cm^3/g), AT-TPS (52 cm^3/g).

Short summary

Development of covalent triazine-based frameworks (CTFs) have gained significant attention in recent years due to readily available cheap starting materials, easy synthesis, high surface area, high thermal and chemical stability and certain hydrophilicity. Three synthetic strategies used for the development of CTFs are, (1) ionothermal condition ($ZnCl_2$) (2) strong Brønsted acid (CF_3SO_3H) condition (3) Friedel-Craft ($AlCl_3$) reaction. CTFs have widely been explored for applications in the field of gas storage and separation, catalysis, membrane based separations and also in optoelectronics.

This thesis describes the synthesis of new CTF materials using different synthetic conditions, and their applications in gas/liquid/vapour adsorption and separation.

Porous CTF-TPC and CTF-FL were synthesized from triptycene and fluorene motif via low temperature and cost-effective $AlCl_3$ catalyzed Friedel-Crafts reaction having a BET surface area of 1668 m^2/g and 773 m^2/g respectively. CTF-TPC has the highest surface area among all reported CTFs synthesized by Friedel-Crafts reaction. Gas adsorption measurements were carried out for CO_2, CH_4, H_2 and N_2 at different temperatures, and the results were comparable with some reported CTFs having high surface areas. CTF-TPC and CTF-FL showed substantial CO_2 uptake capacity of 4.24 and 3.26 mmol/g (95.2 and 73.2 cm^3/g), due to electrostatic interaction between the nitrogen rich triazine units and CO_2 molecules (CO_2 quadrupole moment (1.4×10^{-39} C m^2)). From ideal adsorbed solution theory (IAST), the CO_2/N_2 selectivity of CTF-TPC and CTF-FL were calculated to be 30 and 48, respectively.

Mixed linkers based CTFs were prepared for enhancing the CO_2 uptake capacity of CTFs that are synthesized by $ZnCl_2$ (ionothermal condition) for applications as a CCS materials. We anticipated that, the BET surface area and the CO_2 uptake capacity of CTFs can be fine-tuned with the strategic use of mixed linkers to prepare CTFs. Two main nitrile cores viz, tetra(4-cyanophenyl)ethylene (TPE), and adamantane (Ad) were combined together with 1,4-terephthalonitrile, tetrafluoroterephthalonitrile, 4,4′-biphenyldicarbonitrile, and 1,3,5-benzenetricarbonitrile at different ratios under ionothermal conditions to synthesize several new COFs. Four CTFs were made using the TPE core, whereas nine CTFs were prepared from the adamantane core, and all of them were studied for N_2, CO_2 and CH_4 adsorption. The specific BET surface areas of TPE core based CTFs (MM1-MM4) were 1800, 1360, 1884 and 1407 m^2/g, respectively; and they showed high CO_2 adsorption capacities up to 107 cm^3/g, i.e., 4.73 mmol/g (MM2; at 273 K and 1 bar), which is slightly higher than highest CO_2 uptake in CTFs,

reported until now in native fluorinated CTFs. Even, these CTFs exhibit very good CO_2/N_2 (85% N_2: 15% CO_2) selectivities up to 130 at 273 K and 1 bar using IAST, about 2-3 times more CO_2 selective than presently known CTF materials which were synthesized at 400 ºC. On the other hand, Adamantane core based CTFs showed surface areas in the range of 747-1885 m^2/g. At low pressure (up to 1 bar) and 273 K, these CTFs adsorbed significant amounts of CO_2 (40-76 cm^3/g) and CH_4 (14-26 cm^3/g) which are highly comparable to many reported CTFs. By using IAST the CO_2/N_2 selectivity of these CTFs were found in the range of 17-30 at 273 K.

Adsorptive properties of CTF-1 towards a non-ionic and an anionic surfactant (alkyl polyglycolether, $C_{12}EO_7$ and sodium dodecylsulfate, SDS, respectively) from aqueous solution were investigated and compared with a typical carbon black having a specific surface area of 150 m^2/g. CTF-1 can adsorb up to 4.0 g/g of the surfactants from aqueous solution (c = 8.0 mmol/L) which is more than 20-times the gravimetric uptake capacity of a carbon black (Printex L from Evonik).

Membrane based separation process has attained considerable attention as it is economically friendly and energy saving method. CTFs being purely organic in nature could be of interest for this purpose due to its high thermal and chemical stability. Therefore, several mixed matrix membranes (MMMs) were prepared by using a mixture of CTF-1 (additive) and polysulfone (polymeric matrix) and their gas permeability were studied using standard protocol. The fabricated membranes exhibited higher CO_2 permeability of 9.8 barrer (for 24 wt% of CTF-1 loading), significantly higher than pure polysulfone membrane (7.3 barrer) and also higher CO_2/N_2 selectivity (28.6 for 8 wt% of CTF-1 loading) compared to pure polysulfone membrane (23).

The Friedel-Crafts alkylation reaction of several aromatic building blocks with 2-amino-4,6-dichloro-1,3,5 triazine were carried out to isolate the amine-functionalized CTFs. Five CTFs viz, AT-FL, AT-TPC, AT-TPB, AT-TPE, AT-TPS were synthesized by $AlCl_3$ catalysed Friedel-Crafts reaction of 2-amino-4,6-dichloro-1,3,5 triazine (AT) with fluorene (FL), 1,3,5-triphenylbenzene (TPB), triptycene (TPC), tetraphenylethelene (TPE) and tetraphenyl silane (TPS). The synthesized CTFs were tested for CO_2, N_2, H_2 and CH_4 adsorptions. The BET surface area of AT-TPC was found to be 1174 m^2/g and are in the order AT-TPC (1174 m^2/g)> AT-TBP (804 m^2/g)>AT-TPE (594 m^2/g)>AT-FL (572 m^2/g)>AT-TPS (451 m^2/g). Whereas, AT-TBP exhibited the highest CO_2 uptake (76.7 cm^3/g at 273 K and 1 bar) compared to AT-TPE (66.7 cm^3/g), AT-TPC (60.8 cm^3/g), AT-FL (56.4 cm^3/g), AT-TPS (52 cm^3/g).

List of abbreviations and symbols

1.	B	Benzene
2.	bar	Unit of pressure (1 bar ≙ 100000 Pa ≙ 100 kPa)
3.	BDT	Biphenyl-4,4′-dithiol
4.	BET	Brunauer-Emmett-Teller
5.	BP	Biphenyl
6.	BP	4,4′-Bipiperidine
7.	BT	1,4-Benzenedithiol
8.	BTT	1,3,5-Benzenetrithiol
9.	CCS	Carbon capture and storage
10.	CMP	Conjugated microporous polymer
11.	COF	Covalent organic framework
12.	CTF	Covalent triazine-based framework
13.	DC	1,4-diazacyclohexane
14.	DCA	1,3-bis(4-cyanophenyl)adamantane
15.	DCBP	4,4′-dicyanobiphenyl
16.	DCBPY	5,5′-dicyanobipyridine
17.	DCC	3,6-dicyanocarbazole
18.	DCDE	4,4'-dicyanodiphenyl ether
19.	DCDF	3,6-dicyanodibenzofuran
20.	DCDMP	2,6-dimethylpyridine-3,5-dicarbonitrile
21.	DCDT	3,6-dicyanodibenzothiophene
22.	DCF	9H-Fluorene-2,7-dicarbonitrile
23.	DCMT	1-bis(4-cyanophenyl)methyl-1,2,4-triazole
24.	DCN	2,6-Naphthalenedicarbonitrile
25.	DCP	2,6-dicyanopyridine
26.	DCPM	2,5-dicarbonitrile pyrimidine
27.	DCP-Zn	5,15-bis(4-cyanophenyl)porphyrin Zinc (II)
28.	DCT	2,5-dicyanothiophene
29.	DCTEFB	1,4-dicyanotetrafluorobenzene
30.	DCTP	4,4″-dicyanoterphenyl
31.	DPB	1,4-diphenylbenzene
32.	DPE	*trans*-1,2-diphenylethylene
33.	Fig.	Figure
34.	FL	Fluorene
35.	FT-IR	Fourier transform infrared
36.	h	Hour
37.	HCP	Hyper-crosslinked polymer
38.	IR	Infrared spectroscopy
39.	IUPAC	International Union of Pure and Applied Chemistry
40.	K	Degree Kelvin
41.	mDCB	1,3-dicyanobenzene
42.	mg	Milligram
43.	MMM	Mixed-matrix membrane
44.	mmol	Millimol, unit of amount of substance (1 mol ≙ $6.022\cdot10^{23}$ particles)
45.	MOF	Metal-organic framework
46.	NL-DFT	Nonlocal density functional theory

47.	nm	Nanometer
48.	NMR	Nuclear Magnetic resonance
49.	oDCB	1,2-dicyanobenzene
50.	PAF	Porous aromatic framework
51.	pDCB	1,4-dicyanobenzene
52.	PIM	Polymers of intrinsic microporosity
53.	POP	Porous organic polymer
54.	PPN	Porous polymer network
55.	PSF	Polysulfone
56.	PXRD	Powder X-ray diffraction
57.	PY	Pyrene
58.	SBU	Secondary building unit
59.	SEM	Scanning electron microscopy
60.	TBT	4,4′-Thiobisbenzenethiol
61.	TCA	1,3,5-tris(4-cyanophenyl)adamantane
62.	TCB	1,3,5-tricyanobenzene
63.	TCBPA	Tris(4′-cyanobiphenyl)amine
64.	TCPA	Tris(4-cyanophenyl)amine
65.	TCPA	Tris(4-cyanophenyl)amine
66.	TDCTEPA	Tris(4,4″-dicyanoterphenyl)amine
67.	TECA	1,3,5,7-tetrakis(4-cyanophenyl)adamantane
68.	TECB	1,2,4,5-tetrakis(4-cyanophenyl)benzene
69.	TECPM	Tetrakis(4-cyanophenyl)methane
70.	TECTBPE	Tetrakis[4-(4′-cyanophenyl)phenyl]ethene
71.	TECTPE	Tetra(4-cyanophenyl)ethylene
72.	TETCB	1,2,4,5-Tetracyanobenzene
73.	TGA	Thermogravimetric analysis
74.	TMBP	3,3′,5,5′-tetramethyl-4,4′-bipyrazol
75.	TPA	Triphenylamine
76.	TPB	1,3,5-Triphenylbenzene
77.	TPC	Triptycene
78.	TPE	1,1,2,2-Tetraphenylethylene
79.	TPS	Tetraphenylsilane
80.	wt%	Weight percentage
81.	μm	Micrometer
82.	Å	Ångstrøm
83.	δ	Delta (stands for chemical shift)
84.	λ	Lambda (stands for wavelength)

Table of contents

1 Nanoporous materials

1.1 Introduction

Interest in the field of nanoporous (microporous and mesoporous) materials such as zeolites,[1] metal–organic frameworks (MOFs),[2] covalent organic frameworks (COFs),[3] and porous organic polymers (POPs)[4] have grown enormously during the past two decades because of their broad applications in the field of gas storage and separation, catalysis, energy storage, and optoelectronics. From the chemical point of view, zeolites are purely crystalline inorganic materials composed of $[SiO_4]^{4-}$ and $[AlO_4]^{5-}$ tetrahedral that are connected via oxygen atom to form extended 3D frameworks (Fig. 1a).[5] Due to narrow pore size and lack of functionality-tailoring in the frameworks, zeolites limiting their range of applications.

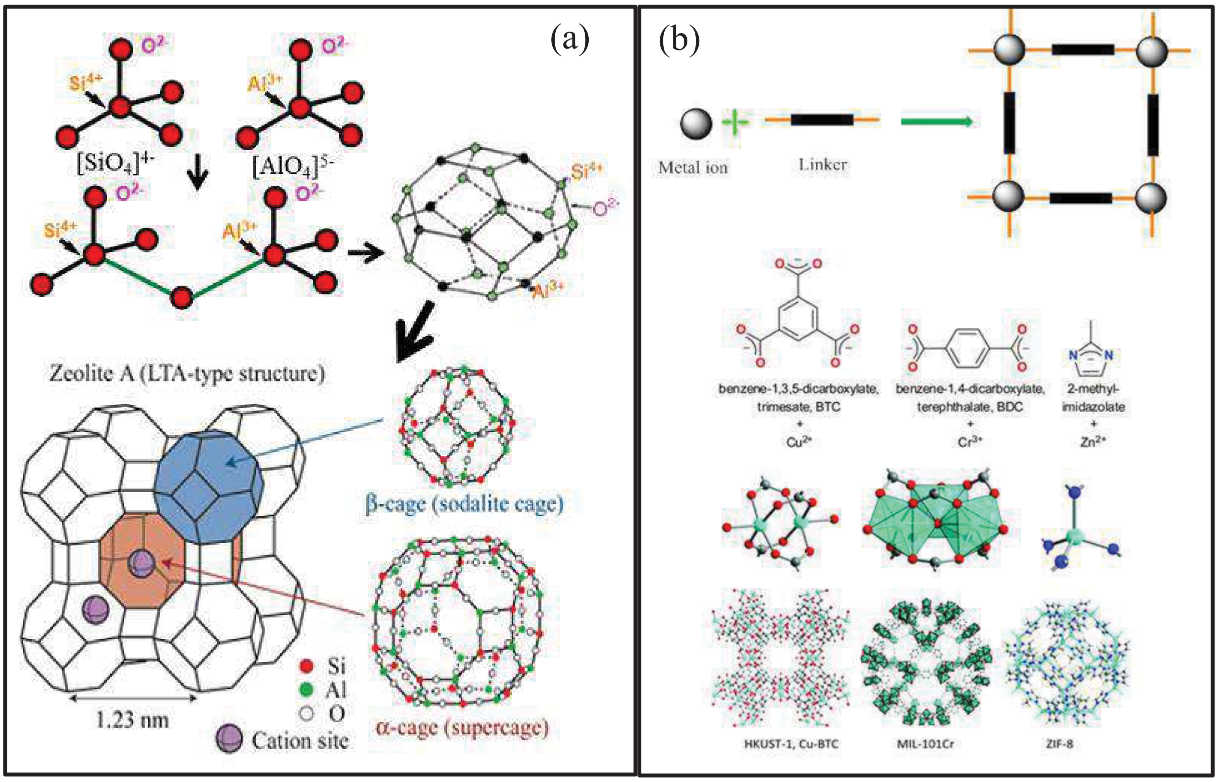

Fig. 1: (a) Schematic representation of formation of zeolites. The structure of zeolite A (IZA code LTA) presenting β-cage and α-cage (redrawn from ref. 5). **(b)** Generic scheme for the synthesis of MOF (top). Prototypical linkers with selected metal nodes and secondary building units in corresponding MOFs (with acronyms). For ZIF-8 the sodalite cage is highlighted (figure taken from ref 2c Published by The Royal Society of Chemistry (RSC) on behalf of the Centre National de la Recherche Scientifique (CNRS) and the RSC).

On the other hand MOFs are hybrid, porous crystalline materials that are comprised of ordered networks formed from organic electron donor linkers and metal cations or clusters (Fig. 1b).[2] However, the concept of reticular chemistry, which uses topologically designed building blocks, has led to the development of metal–organic frameworks (MOFs),[2] and covalent organic frameworks (COFs),[3,6] both first reported by Yaghi *et al.*(Fig. 1-3). Unlike COFs, which are crystalline porous organic polymers with discrete pores, POPs are amorphous porous organic materials with no ordered pore sizes.

Type	Monomer	Repeating unit	Ref.
COF	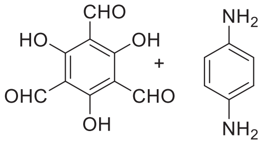	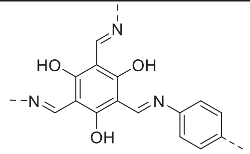	6
HCP	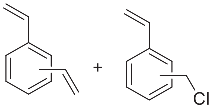	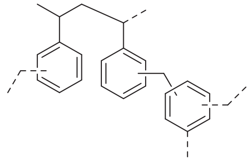	12c
PAF	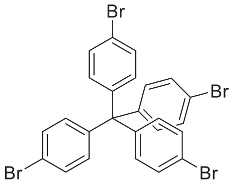	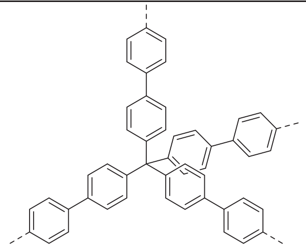	13a
CMP	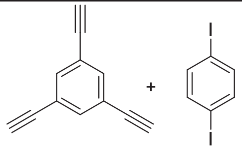	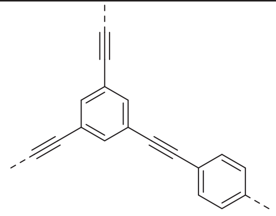	14b
PPN	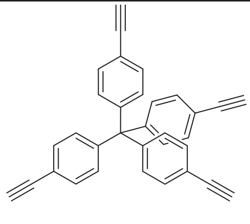	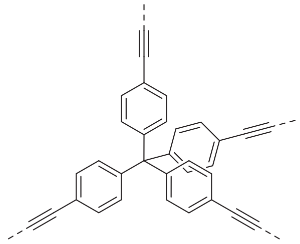	15a

Fig.2: Schematic representation of the synthesis of COFs and POPs from corresponding linkers.

However, both COFs and POPs are formed by the covalent linking of organic molecules and solely composed of light-weight elements (C, H, N, O, B, Si), have low mass densities, possess high thermal stabilities, and provide permanent porosity. It is to be noted that, reversibility in the covalent bond formation is the most important parameter in the synthesis of crystalline COFs (besides adjusting other parameters such as solvent(s), solvent ratio, and reaction time and temperature), whereas, irreversible organic reactions result in amorphous POPs. Several COF materials such as, hydrogen bonded imine-COF[7], β-ketoenamine-COF[8], azine-COF[9] and imide-COF[10] have been tested to be highly water stable and have pronounced stability in acids and bases as well.[11] However MOFs and COFs need to show improvements in stability for industrial applications. In this regards POPs are important. Numerous functional POPs can be synthesized by utilizing a wide variety of organic struts (Fig. 2 and Fig. 3) and following different types of organic reactions, which could led to the formation of porous polymers such as, hyper-crosslinked polymers (HCPs),[12] porous aromatic frameworks (PAFs),[13] conjugated microporous polymers (CMPs),[14] porous polymer networks (PPNs)[15] and polymers of intrinsic microporosity (PIMs)[16].

Covalent triazine-based frameworks (CTFs) is a special class of POP materials which possess some interesting properties, including high surface area, intrinsic basicity and high degree of graphitization which make them attractive candidates for gas storage and separation, and heterogeneous catalysis.

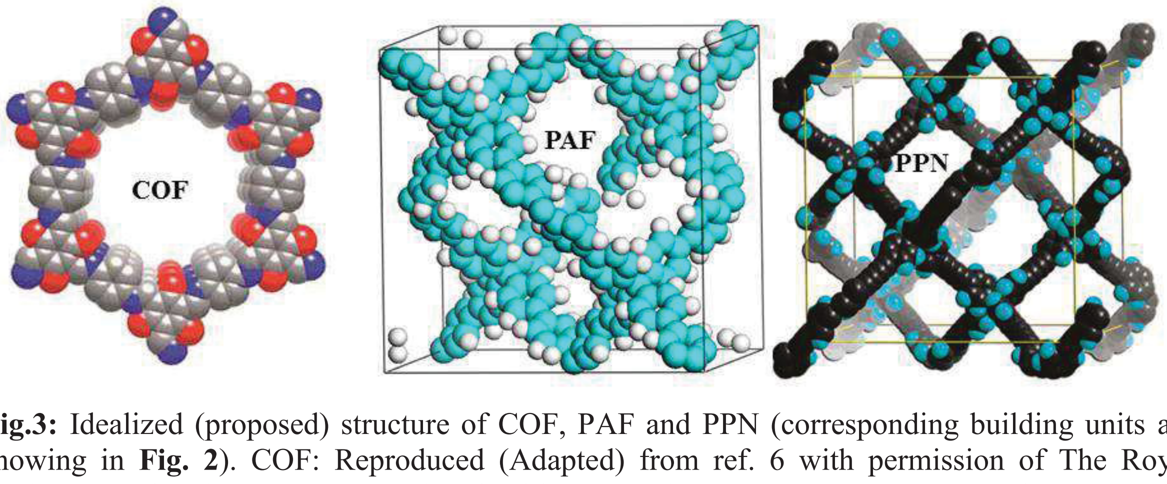

Fig.3: Idealized (proposed) structure of COF, PAF and PPN (corresponding building units are showing in **Fig. 2**). COF: Reproduced (Adapted) from ref. 6 with permission of The Royal Society of Chemistry. PAF: Reprinted with permission from ref. 13a. Copyright 2009 John Wiley and Sons. PPN: Reprinted with permission from ref. 15a. Copyright 2010 American Chemical Society.

CTFs in general are formed by the cyclotrimerization of organic nitriles in which s-triazine cores (1,3,5-triazine) are associated to each other by three conjugated organic struts (Fig. 5a, section 1.3.1). Electron deficiency and spatial coplanarity of the triazine rings provide high stability to CTFs. The following strategies have been adopted for the preparation of porous CTF materials till date: (1) ionothermal conditions ($ZnCl_2$),[17,18,19,20] (2) strong Brønsted acid conditions (CF_3SO_3H),[21,22] (3) Friedel-Crafts ($AlCl_3$) reaction (Fig. 5-6, Scheme 1).[23,24] Kuhn, Antonietti and Thomas *et al.* first developed CTFs with permanent porosity and partial crystallinity (apparent BET surface area as high as 3000 m^2/g) under ionothermal conditions.[18] From their elemental composition, CTFs can be viewed as the class of porous materials placed well between COFs and porous carbon materials. CTFs with moderate to high surface areas (apparent BET surface area as high as 1152 m^2/g) have also been synthesized at room temperature and under microwave irradiations using strong Brønsted acid (CF_3SO_3H) conditions.[21] Strong Brønsted acid conditions usually provide lower surface areas as compared to ionothermal conditions, but they avoid decomposition and condensation reactions such as C–H bond cleavage and carbonization, and thereby result in less structural defects in the frameworks. Recently, anhydrous aluminum chloride ($AlCl_3$) catalyzed Friedel-Crafts reactions have also been used to prepare well-defined CTF materials with moderate to high surface areas (apparent BET surface area as high as 1452 m^2/g).[23,24] Aluminum chloride catalyzed Friedel-Crafts reaction conditions offer the significant advantages of cheap, easy handling, low reaction temperature, facile synthesis conditions and high yield materials with high surface areas.

1.2 Rational design of CTFs

Numerous porous CTF materials with desired topology can be constructed from monomers of different sizes and shapes, with the prerequisite of having at least two reactive functional groups in the monomer (e.g., 1,4-dicyanobenzene) for the polymerization to occur under a suitable reaction condition. Similar to MOFs and COFs, CTFs are prepared using the principle of reticular chemistry, where the topology of the desired framework is largely dictated by the geometry and symmetry of the building block. Three different types of linkers such as ditopic, tritopic and tetratopic molecules (Fig. 4) have been used for the preparation of various CTFs via trimerization reaction and Friedel-Crafts reaction. Depending on the linkers, these materials can be 2D or 3D for which triazine units can act as a secondary building units (SBUs). In 2D CTFs, the framework is generally restricted to 2D sheets, the adjacent sheets are stacked to form a layered eclipsed structure, resulting in accessible pores in one dimension (1D). The porous channels in 2D CTFs could facilitate charge carrier transport in the stacking direction, which implies that 2D CTFs have potential for developing new type π-electronic and photofunctional materials. In contrast, 3D CTFs extending in three dimensions, are ideal candidates for gas storage and separation. As shown in the Fig. 4, three different types of linkers with linear, trigonal planar and tetrahedral geometry were used to make the CTFs materials via trimerization reactions that lead to 2D or 3D frameworks. For example, CTF-1 obtained by polytrimerization of 1,4-dicyanobenzene linker (pDCB). The linear (dicyanobenzene) and triazine (C_3N_3) building units can generate honeycomb-like (hcb) structure, 2D hexagonal plane, with an eclipsed AAA conformation.[17] On the other hand, 3D CTFs have been synthesized by tetrakis(4-cyanophenyl)methane (TECPM) resulting **ctn** and **bor** nets (Fig. 6). Both tetrahedral (tetraphenylmethane) and triangular (C_3N_3 ring) building units on the corresponding nodes can be favored the suggesting structure. Additionally, linker flexibility can create an interpenetration which is also important factor for topology as well as porosity. It is noticeable that the higher penetration in the frameworks for longer length of the monomer was observed compare to shorter length of the monomer, which leads to lower surface area. Thus, the flexibility or rigidity of the frameworks depends on combination of nodal dimensionality, nodal flexibility and strut length.[25]

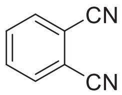
oDCB

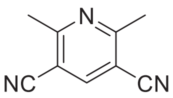
DCDMP

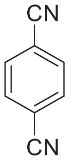
pDCB

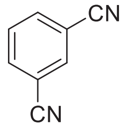
mDCB

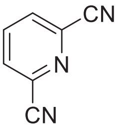
DCP

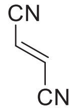
FUM

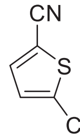
DCT

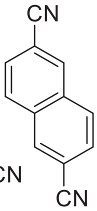
DCN

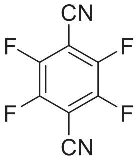
DCTEFB

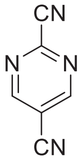
DCPM

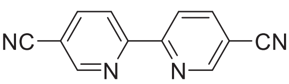
DCBPY

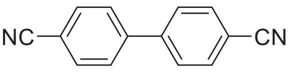
DCBP

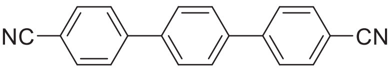
DCTP

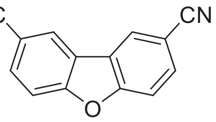
DCDF

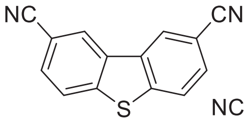
DCDT

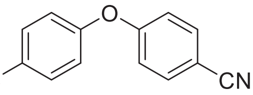
DCDE

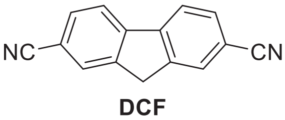
DCF

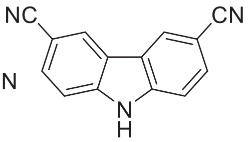
DCC

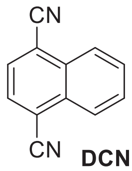
DCN

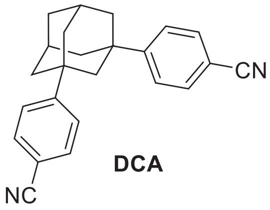
DCA

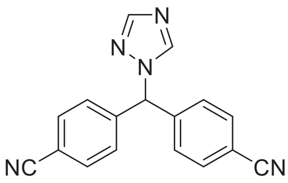
DCMT

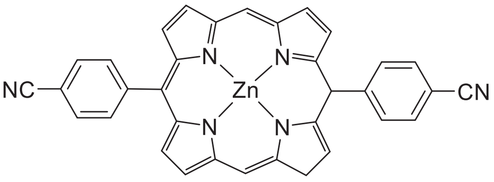
DCP-Zn

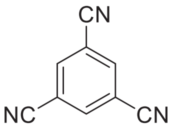
TCB

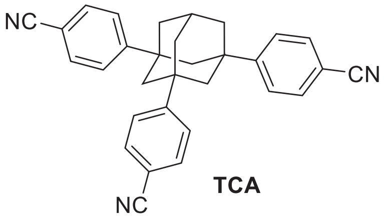
TCA

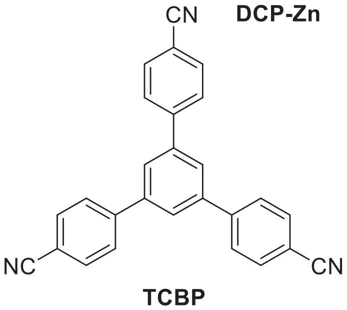
TCBP

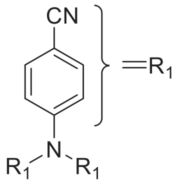
TCPA

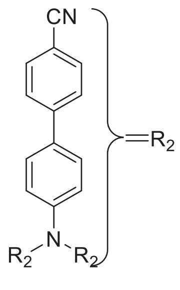
TCBPA

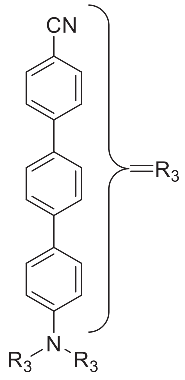
TDCTEPA

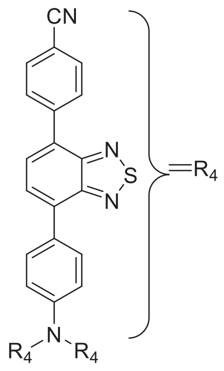
TBCBA

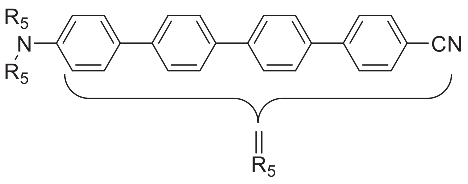
TQPDCA

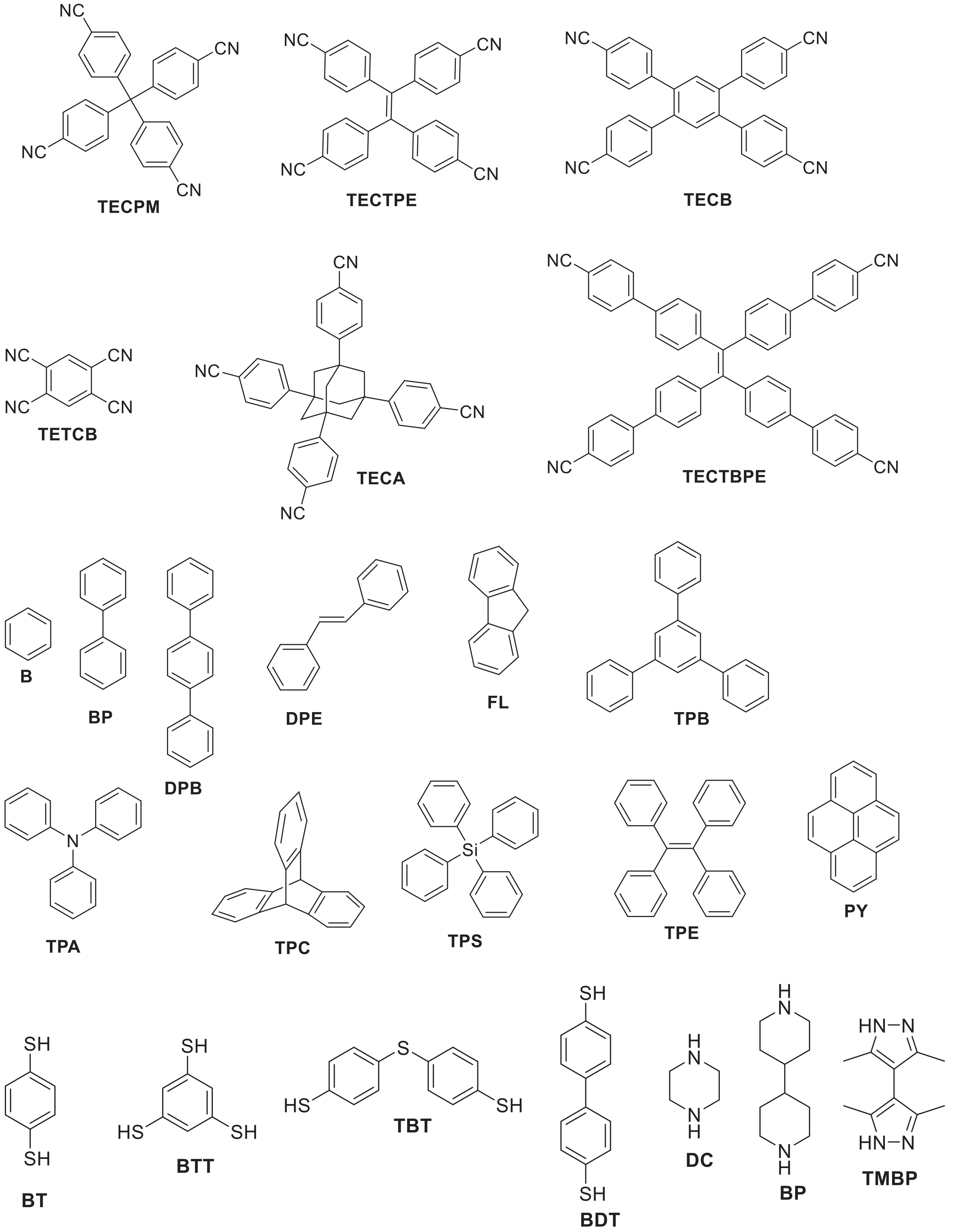

Fig. 4: Schematic illustration of the structures of building units with different geometries, sizes and reactive groups for the synthesis of CTFs.

1.3 Synthesis of CTFs

As mentioned earlier, CTFs were first developed by Kuhn, Antonietti and Thomas *et al.* by the trimerization of aromatic nitriles under ionothermal condition.[17] Different synthetic routes have been adopted by different research groups to expand the synthetic possibilities of developing these porous materials.

1.3.1 Ionothermal conditions ($ZnCl_2$)

Most of the CTFs were synthesized by trimerization of aromatic nitriles under ionothermal conditions at 400-700°C using excess $ZnCl_2$ (Fig. 5). Molten $ZnCl_2$ acts as a Lewis acid catalyst and solvent (porogen) for the polymerization reaction. The porosity of CTFs depends on reaction temperature as well as amount of $ZnCl_2$. For example, CTF obtained from pDCB under ionothermal conditions at 400 °C exhibited a BET specific surface area of 920 m^2/g, while an increase in reaction temperature up to 700 °C can largely enhance the surface area as high as 2530 m^2/g.[18] It has also been reported that increasing the amount of $ZnCl_2$ can also lead to an increase in the BET surface area of CTF at 400 °C (1123 m^2/g), however with reduced crystallinity. The authors argue that the crystallinity of this material was lost for higher amount of $ZnCl_2$. With this processes several organic aromatic nitrile building blocks were employed to prepare the various types of CTFs with different porosity.

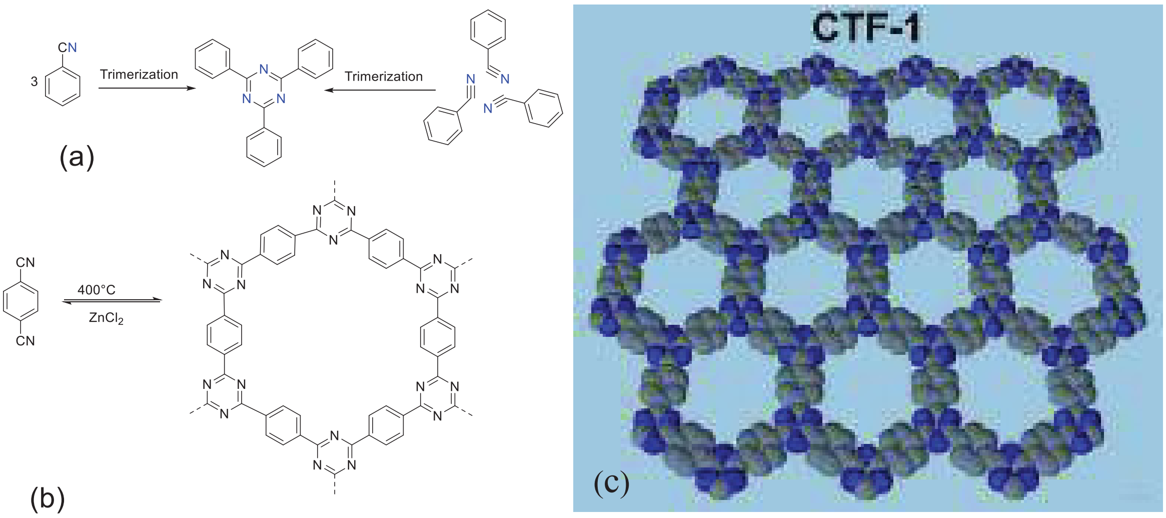

Fig. 5: (a) Schematic representation of trimerization of nitrile group to form triazine ring. (b) Trimerization of pDCB in molten $ZnCl_2$ to a triazine based framework (CTF-1). (c) Idealized extended structure of CTF-1 (dark gray C, blue N). Reprinted with permission from ref. 20. Copyright 2015 American Chemical Society.

1.3.2 Brønsted acid conditions (CF_3SO_3H)

Alternatively, Cooper et al. reported that CTFs can also be synthesized by using aromatic nitriles in presence of strong Brønsted acids, such as trifluoromethanesulfonic acid (CF_3SO_3H), at room temperature and under microwave conditions (Fig. 6).[21] Until now, only a few aromatics nitriles have been used in the Brønsted acid mediated synthesis of CTFs as compared to ionothermal synthesis. These CTFs exhibited moderate BET surface area (above 1000 m^2/g) which limit their applications.

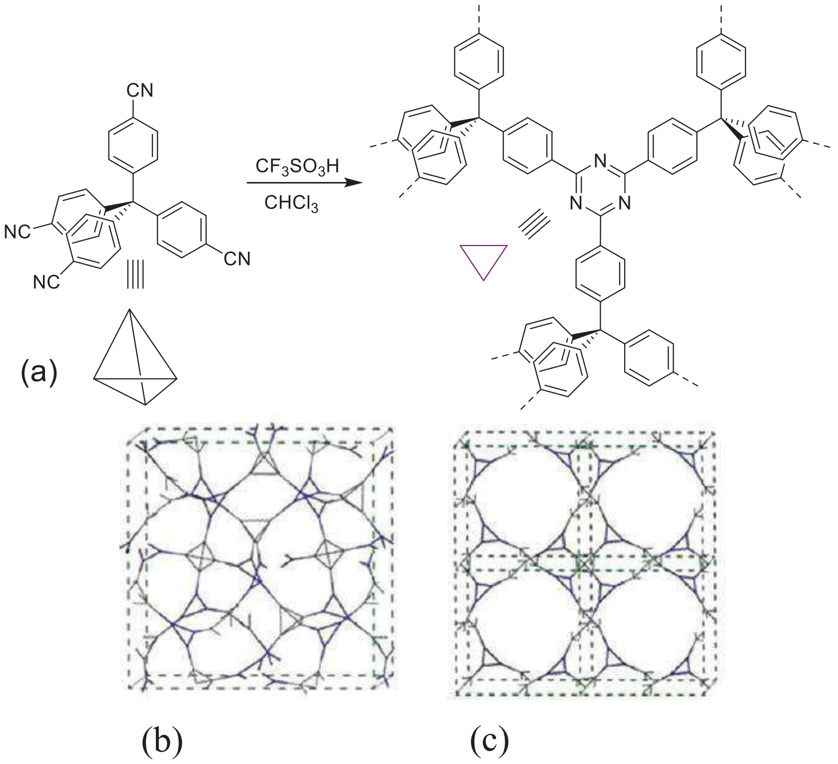

Fig. 6: (a) Schematic representation of synthesis of CTF from TECPM by strong Brønsted acid catalyzed condition[21] and its extended structure (b: **ctn** net and c: **bor** net). Reproduced (Adapted) from ref. 22 with permission of The Royal Society of Chemistry. Similar framework can also be prepared by $ZnCl_2$ condition.[22]

1.3.3 Friedel-Crafts ($AlCl_3$) reaction

Friedel-Crafts reaction between cyanuric chloride and π-electron rich organic linkers using aluminum chloride ($AlCl_3$) as catalyst, can also yield CTFs materials with permanent porosity. Scheme 1 shows the general mechanism for CTFs. In this reaction, $AlCl_3$ acts as a Lewis acid catalyst. This reaction generally performed in presence of DCM at 70°C.[24]

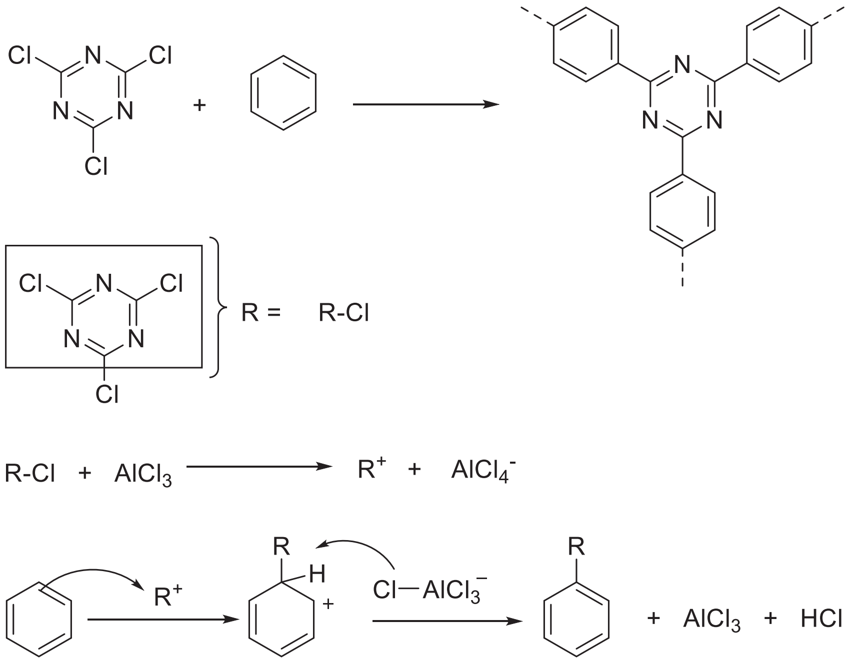

Scheme 1: Schematic representation of synthesis of CTF from cyanuric chloride via Friedel-Crafts acylation reaction.

In the first step, the halide substituted compound reacts with aluminum trichloride and forms an organo-metallic complex in which the carbon attached to the chlorine has a great deal of positive charge character. Afterwards, an aromatic electrophilic substitution results the final product. By using this processes there have been reported several CTFs.[23,24]

1.4 Applications of CTFs

1.4.1 CTFs for gas storage and separation

High surface area, low density, high chemical and thermal stability make CTFs potential candidates for gas storage and separation. CTFs have exhibited high adsorption capacities for important gasses like hydrogen, carbon dioxide and methane.

1.4.1.1 Carbon dioxide storage

With rapid increase in population and industrialization, environment crisis has becomes a challenging issue. Carbon dioxide releases from burning of fossil fuel, as a major greenhouse gas, have a tremendous effect on increasing the average temperature of the earth, sea level increase and ocean acidification.[4,26] CCS (carbon capture and storage) is an efficient method to reduce the CO_2 concentration.[26] Amine scrubbing technology used widely in industry to reduce the CO_2 concentration due to its high CO_2 absorption capacity (up to 98%).[26] However this process has several drawbacks like high energy costs during regeneration, relative instability under the regeneration and corrosive nature of the amine solution.[27] Use of porous solid absorbent in CCS process is an alternative way. Traditional porous materials like zeolite and activated charcoal suffer from drawbacks: (1) lack of functional modification in the network and also the carbon dioxide uptake capacity is very low at high pressure,[27] (2) activated charcoal has limitation like low CO_2/N_2 selectivity.[27] Another class of porous material i.e., metal organic frameworks (MOFs) are also ideal candidates for carbon dioxide capture but sometime suffer difficulty in humid condition. Covalent organic frameworks (COFs) and covalent triazine based frameworks (CTFs) have gained enormous attention in recent years due to their high surface area, structural variety, light weight and excellent thermal and chemical stability.[28,29] The first synthesized CTFs material CTF-1, synthesized from pDCB shows CO_2 uptake 55.33 cm^3/g at 273 K and 1 bar.[29] Zhao *et al.* synthesized FCTF-1 from DCTEFB which shows much higher CO_2 uptake than CTF-1 due to presence of highly electronegative fluorine atoms. FCTF-1 exhibits CO_2 uptake 104.61 cm^3/g at 273 K and 1 bar.[29] Cooper and co-workers have developed a series of CTFs (P1-P6M) based on different nitrile monomers (pDCB, DCBP, DCDE, TCBP, TCPA and TECPM) using trifluoromethanesulfonic acid as catalyst under both room temperature and microwave-assisted conditions.[21] Among P1-P6M, the framework synthesized from TECPM monomer in both room temperature and microwave assisted conditions exhibit highest CO_2 uptake value which are 75.39 cm^3/g and 93.46 cm^3/g respectively.[21] Liu and co-workers developed a series of CTFs (MCTF@300, MCTF@400, MCTF@500) using metalloporphyrin as building block (DCP-Zn) among which MCTF@500 shows highest CO_2 uptake capacity 70.81 cm^3/g.[30] Lotsch and co-workers have synthesized CTFs from fluorene motif (DCF) at different temperature via ionothermal process (fl-CTF300-fl-CTF600).[31] Among the CTFs, fl-CTF350 shows highest CO_2 uptake of 95.87 cm^3/g at 273K and 1 bar.[31] Recently they reported CTFs from DCDMP, DCMP, DCBPY linkers via ionothermal synthesis at different temperatures. The resulted CTFs show CO_2 adsorption values in the range of 41.89-124.99 cm^3/g.[32] Bhunia *et al.* have reported a series of CTFs (PCTF-1 to PCTF-8) synthesized from TECTPE and different adamantane nitrile monomer (DCA, TCA, TECA) via ionothermal as well as Brønsted acid synthetic route.[33,34] PCTF-1 exhibits higher CO_2 uptake which is 73.0 cm^3/g than PCTF-2 at 273 K and 1 bar.[33] Among the CTFs synthesized from different adamantane nitrile monomer via ionothermal reaction as well as via Brønsted acid condition, PCTF-5 shows highest CO_2 uptake value of 58.1 cm^3/g at 273K and 1 bar.[34] Katekomol *et al.* have developed a crystalline CTF from TCBP having CO_2 uptake capacity 94.53 cm^3/g at 273 K and 1 bar.[35] CTFs can also be synthesized by Friedel-Craft reaction between cyanuric chloride with different monomers. Chang and co-workers have showed a batch of CTFs (polymer 2 to polymer 4C) synthesized based on cyanuric chloride and B, BP, and DBP as ligand, among which polymer 4C shows highest CO_2 uptake value of 88 cm^3/g at 298 K and 1 bar.[23] Pan and co-workers synthesized a series of CTFs (NOP-1-NOP-6) from TPA and TPS via trifluoromethane sulfonic acid (CF_3SO_3H) catalyzed Friedel-Craft reaction. NOP-3 exhibits highest CO_2 uptake of 56.15 cm^3/g at 273 K and 1 bar.[30] COP-1 and COP-2 synthesized from PP and BPP as linkers which show CO_2 uptake 30.54 cm^3/g and 20.87 cm^3/g at 298 K respectively.[36] Puthiaraj *et al.* reported MCTP-1, MCTP-2, PCTP-1 and PCTP-2 with CO_2 uptake 104 cm^3/g, 81.75 cm^3/g, 110.21 cm^3/g and 77.48 cm^3/g respectively.[24,37] FUM and DCN based CTFs exhibited CO_2 uptake capacity in the range of 47.5-78.2 cm^3/g.[38] Mu and co-workers reported a metalloporphyrin based microporous CTFs exhibited CO_2 uptake upto 70.81 cm^3/g.[39]

Table 1: Surface area (BET), H_2, CO_2 and CH_4 adsorption values for CTFs at low pressure (1 bar).

CTF	Building unit [a]	Reaction temperature (°C)/ condition	BET (m^2/g)	CO_2 uptake, 273 K (cm^3/g) [b]	CH_4 uptake, 273 K (cm^3/g)	H_2 uptake, 77 K (wt %)	Ref.
CTF-0	TCB	400/600/ $ZnCl_2$	2011	94.53	-	-	35
CTF-1	pDCB	400/$ZnCl_2$	746	55.33	-	1.55	29
CTF-1-600	pDCB	600/$ZnCl_2$	1533	85.57	-	-	29
FCTF-1	DCTEFB	400/$ZnCl_2$	662	104.61	-	-	29

FCTF-1-600	DCTEFB	600/$ZnCl_2$	1535	123.87	-	-	29
CTF-P2	DCBP	RT/ CF_3SO_3H	776	41.78	-	-	21
CTF-P3	DCDE	RT/ CF_3SO_3H	571	50.37	-	-	21
CTF-P4	TCBP	RT/ CF_3SO_3H	867	69.36	-	-	21
CTF-P5	TCPA	RT/ CF_3SO_3H	960	66.79	-	-	21
CTF-P6	TECPM	RT/ CF_3SO_3H	1152	75.39	-	-	21
CTF-P1M	pDCB	MW/ CF_3SO_3H	4	20.95	-	-	21
CTF-P2M	DCBP	MW/ CF_3SO_3H	464	42.46	-	-	21
CTF-P3M	DCDE	MW/ CF_3SO_3H	523	50.17	-	-	21
CTF-P4M	TCBP	MW/ CF_3SO_3H	542	41.48	-	-	21
CTF-P5M	TCPA	MW/ CF_3SO_3H	542	46.15	-	-	21
CTF-P6M	TECPM	MW/ CF_3SO_3H	947	93.46	-	-	21
MCTP-1	TPB	70/$AlCl_3$	1452	104	55.31	-	24
MCTP-2	DPE	70/$AlCl_3$	859	81.75	19.97	-	24
PCTP-1	TPE	70/$AlCl_3$	1200	110.21	35.75	-	37
PCTP-2	TPS	70/$AlCl_3$	523	77.48	28.07	-	37
Polymer 2	B	DCM (reflux)/	--	38(298K)	-	-	23

		$AlCl_3$					
Polymer 3	BP	DCM (reflux)/ $AlCl_3$	646	41(298K)	-	-	23
Polymer 4	DPB	DCM (reflux)/ $AlCl_3$	1266	51(298K)	-	-	23
Polymer 2C	B	400/800	427	73(298K)	-	-	23
Polymer 3C	BP	400/800	1173	75(298K)	-	-	23
Polymer 4C	DPB	400/800	1316	88(298K)	-	-	23
NOP-1	TPA	140/ CH_3SO_3H	978	40.97	-	-	30
NOP-2	TPA	140/ CH_3SO_3H	1055	53.03	-	-	30
NOP-3	TPA	140/ CH_3SO_3H	1198	56.15	-	1.14	30
NOP-4	TPS	140/ CH_3SO_3H	635	38.23	-	-	30
NOP-5	TPS	140/ CH_3SO_3H	913	32.48	-	-	30
NOP-6	TPS	140/ CH_3SO_3H	1130	29.42	-	-	30
MCTF-300	DCP-Zn	300/$ZnCl_2$	640	50.34	-	-	39
MCTF-400	DCP-Zn	400/$ZnCl_2$	1060	52.99	-	-	39
MCTF-500	DCP-Zn	500/$ZnCl_2$	1510	70.81	-	-	39
fl-CTF300	DCF	300/$ZnCl_2$	15	28.45	-	-	31
fl-CTF350	DCF	350/$ZnCl_2$	1235	95.87	-	-	31
fl-CTF400	DCF	400/$ZnCl_2$	2862	92.51	-	4.36	31
fl-CTF500	DCF	500/$ZnCl_2$	2322	73.02	-	-	31
fl-CTF600	DCF	600/$ZnCl_2$	2113	77.95	-	-	31

COP-1	PP	85/DIPEA	168	33.3 (298 K)	-	0.03 (298 K)	36
COP-2	BPP	85/DIPEA	158	22.77 (298 K)	-	0	36
PCTF-1	TECTPE	400/$ZnCl_2$	2235	73.0	23.6	1.86	33
PCTF-2	TECTPE	400/$ZnCl_2$	784	41.5	15.1	0.9	33
PCTF-3	DCA	400/$ZnCl_2$	641	48.7	17.1	1.03	34a
PCTF-4	TCA	400/$ZnCl_2$	1090	51.6	20.2	1.13	34a
PCTF-5	TECA	400/$ZnCl_2$	1183	58.1	20.5	1.24	34a
PCTF-7	TCA	RT/ CF_3O_3H	613	48.9	14.6	1.04	34a
PCTF-8	TECTPE	RT/ CF_3O_3H	625	56	17	1.007	34b
CTF-TPC	TPC	70/$AlCl_3$	1668	95.2	30	1.75	100
CTF-FL	FL	70/$AlCl_3$	773	73.2	24.9	1.31	100
CTF-FUM-350	FUM	350/$ZnCl_2$	230	78.2	-	-	38
CTF-DCN-500	DCN	500/$ZnCl_2$	735	60.4	-	-	38
pym-CTF500	DCPM	500/$ZnCl_2$	208	61.6	-	-	32
pym-CTF600	DCPM	600/$ZnCl_2$	689	74.82	-	-	32
bipy-CTF300-600	DCBPY	300-600/$ZnCl_2$	360-2479	41.89-124.99	-	2.71-4	32
lut-CTF300-600	DCDMP	300-600/$ZnCl_2$	486-2815	81.31-111.78	-	1.79-4.18	32
CTFs	pDCB	MW/$ZnCl_2$	1140-			0.7-1.78	45

			2390					
CTF-PAF-2	TECPM	400/$ZnCl_2$	1109	-	-	-	22	

[a] See Fig. 4.

[b] Transformation into cm^3/g can be done by the given value in mmol/g with the molar gas volume at 1 bar of 22.711 L/mol (or mL/mmol = $cm^3/mmol$) (at 273 K), 24.375 L (at 293 K) and 24.791 L (at 298 K).
Alternatively, transformation from given cm^3/g into mmol/g:
at 273 K: value in (cm^3/g): (22.711 $cm^3/mmol$) = value in (mmol/g)
(22.711 L is the molar volume at 1 bar and 273 K for an ideal gas).
at 293 K: value in (cm^3/g): (24.375 $cm^3/mmol$) = value in (mmol/g) (24.375 L is the molar volume at 1 bar and 293 K for an ideal gas).

1.4.1.2 Methane storage

Due to the environmental issue caused by the carbon dioxide emission by the burning of fossil fuel, development of alternative energy source has become necessary. Methane is a main component of natural gas, which is considered as a good alternative of fossil fuel due to its abundant nature, lower carbon emission (eq. 1), higher hydrogen to carbon ratio.[40] Due to low volumetric energy density of methane under normal condition, which is 0.11% of gasoline, limits its application in various fields, especially onboard applications.[41]

$$CH_4 + 2O_2 \longrightarrow CO_2 + 2H_2O \quad (\Delta H = -891\ kJ/mol)............(1)$$

Many porous materials including zeolite and activated carbon have been studied as a potential media for methane storage. Zeolite shows methane uptake value less than 100 cm^3/g, whereas most of the porous carbon materials show methane uptake in the range of 50-160 cm^3/g.[41] A good methane storage material must fulfil few requirements like high maximum adsorption capacity, high deliverable capacity, high hydrophobicity, good adsorption enthalpy and high heat capacity.[41] Together with other porous materials like MOFs and COFs, CTFs have also been studied as methane storage materials in recent years (Table 1). PCTF-1 shows higher CH_4 uptake capacity than PCTF-2 which is 23.6 cm^3/g and 15.1 cm^3/g at 273 K and 298 K respectively.[33] Among the CTFs synthesized from DCA, TCA and TECA monomer, PCTF-5 shows higher CH_4 uptake (20.5 cm^3/g) which is close to the value of PCTF-4 (20.2 cm^3/g) at 273 K and 1 bar.[34] Among the CTFs synthesized form cyanuric chloride by Friedel-Craft reaction, MCTP-1 shows methane uptake capacity of 55.31 cm^3/g, whereas for MCTP-2, PCTP-1 and PCTP-2 the values are 19.97 cm^3/g, 35.75 cm^3/g, 28.07 cm^3/g, respectively.[24,37]

1.4.1.3 Hydrogen storage

Hydrogen has been considered as an alternative energy source of fossil fuel due to its high chemical abundance and high chemical energy density.[4] It is considered as the cleanest fuel as it produce only water as a by-product (eq. 2).[42,43] The heating value of hydrogen is three times higher than petroleum.[43]

$$2H_2 + 2O_2 \longrightarrow 2H_2O \quad ....(2)$$

Hydrogen can be stored as a compressed gas in high pressure tanks or as a liquid, although there are safety issues like the use of compressed gas at high pressure and high energy costs for liquefaction.[42,44] In the gas phase 4kg of hydrogen occupy 45 m^2 of space at room temperature and 1 atm which is a big issue for vehicle related transportation.[42] As an alternative method storage of hydrogen in porous solid has been investigated widely. Microporous materials such as COFs/CTFs have also been studied in this purpose. High surface area and large pore volume relatively favors the hydrogen uptake capacity. For porous materials in most of the cases, hydrogen uptake have been measured at 77 K or 87 K which is far from the temperature range of practical application, but theoretical studies of COFs shows that hydrogen storage at the temperature range 273-298 K is practically possible.[4a] As shown in the Table 1, several CTFs have been studies for hydrogen storage. CTF synthesized from DCBP shows H_2 uptake of 1.55 wt% at 77 K and 1 bar.[17] Zhu and co-workers reported CTFs synthesized from pDCB monomer using $ZnCl_2$ as catalyst in microwave assisted condition which exhibit highest H_2 uptake of 1.7 wt% at 77 K and 1 bar.[45] Among the CTFs synthesized from fluorine motif i.e. fl-CTF400 shows highest H_2 uptake of 4.36 wt% at 77 K and 1 bar.[31] PCTF-1 shows 1.86 wt%, whereas PCTF-5 shows 1.24 wt% of H_2 uptake at 77 K and 1 bar.[33,34] NOP-3 synthesized from TPA exhibit H_2 uptake of 1.14 wt% at 77 K and 1 bar.[30]

1.4.2 Heterogeneous catalysis

Porous materials are highly sought after to perform a variety of catalytic organic reactions. These materials combine the benefits of heterogeneous catalysis, such as easy post reaction separation, catalyst reusability, high stability; and homogeneous catalysis such as high efficiency, selectivity, controllability and mild reaction conditions.[46] Among all porous materials, CTFs possesses some interesting properties including high surface area, basicity, high thermal and chemical stability which make them potential candidates for heterogeneous catalysis. As CTF has basic triazine rings, therefore, it can be used for base catalyzed reactions and as catalytic supports for several metal catalyzed reactions. Palkovits *et al.* developed a triazine based Pt-CTF catalyst for low-temperature oxidation of methane to methanol which exhibits high activity at high selectivity, and stable after several recycling steps (Scheme 2).[47] The Pt-CTF catalyst found to be very stable activity over several runs with TONs above 250.

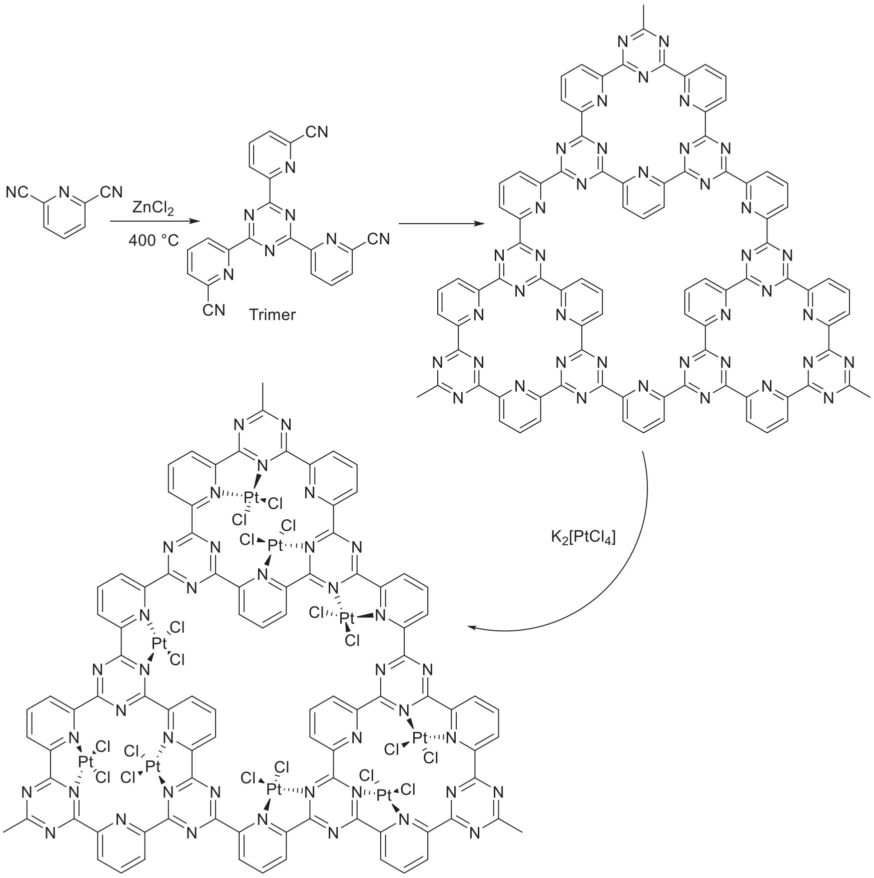

Scheme 2: Schematic diagram of platinum coordination on CTF. Redrawn with permission from ref. 47. Copyright 2009 John Wiley and Sons.

Chan-Thaw *et al.* have prepared Pd nanoparticles on CTFs which is used for liquid phase oxidation of glycerol.[48] This material showed higher activity (982 mol h^{-1} mol^{-1}) than typical Pd/AC (palladium/activated carbon) catalyst (948 mol h^{-1} mol^{-1}). Moreover, glycerol was fully converted after only three hours of reaction; whereas the full conversion was not achieved on Pd/AC. Chang *et al.* have reported Ru/CTF as a catalytic support for ammonia decomposition which shows higher NH_3 conversion rate or turnover frequency rate than conventional Ru/CNT (Ru/carbon nano tube).[49] With 1 wt% of loading Ru/CTF-1 exhibit a TOF value of 0.58 whereas for Ru/CNT the TOF value is 0.19.

Artz *et al.* have attached Ru cluster on various CTFs (Scheme 3) for selective aerobic oxidation of 5-hydroxymethylfurfural (HMF) to 2,5-diformylfuran (DFF).[50] The Ru/CTF shows higher selectivity and catalytic activity than other support material like activated carbon, g-Al_2O_3, hydrotalcite or MgO. They have tested four different nitrile linkers to synthesis the frameworks, among which Ru/CTF-a showed highest catalytic activity (conversion 97.3%, Yield 72.7%) after 3 h of reaction time.

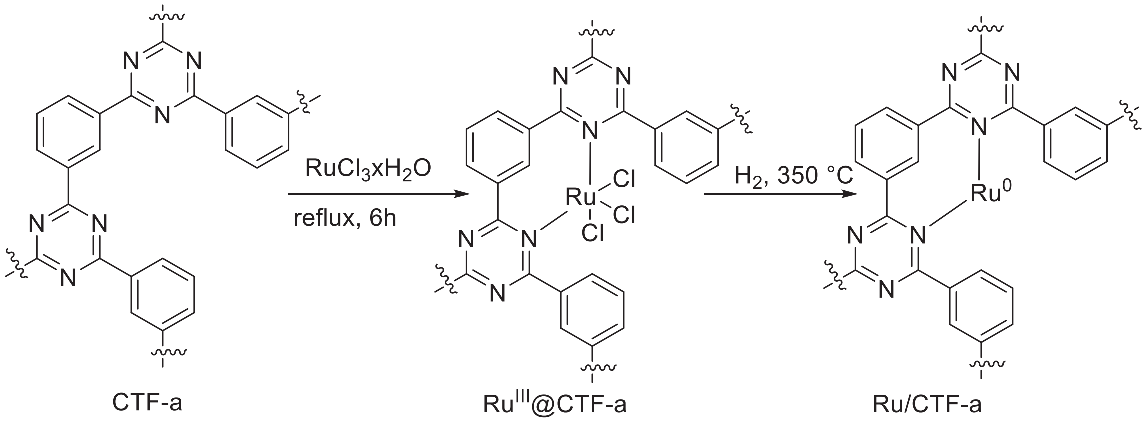

Scheme 3: Synthetic scheme for formation of Ru nanoparticle on CTF-a. Redrawn from ref. 50, Copyright 2015, with permission from John Wiley and Sons.

Katekomol *et al.* have reported CTF as a catalyst for the synthesis of cyclic carbonates via cycloaddition of CO_2 to epoxides.[35] After four hours of reaction, CTF-0 shows 100% conversion with 92% selectivity in the formation of corresponding cyclic chloropropene carbonate from CO_2 and epichlorohydrin.

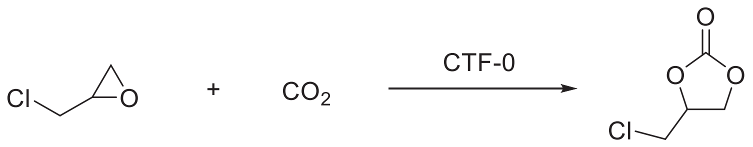

Scheme 4: Transformation of cyclic carbonates from epoxide in presence of CO_2.

Bavykina *et al.* have reported an air stable and recyclable catalyst based on Ir^{III}Cp* (Cp*=pentamethylcyclopentadienyl) attached to a CTF for hydrogen production from formic acid.[51] With 0.2 wt% loading and at 80 °C, the catalyst exhibit a TOF value of 27000 h^{-1}; and 16 % loading, the catalyst shows hydrogen production rates of more than 60 mol L^{-1} h^{-1}.

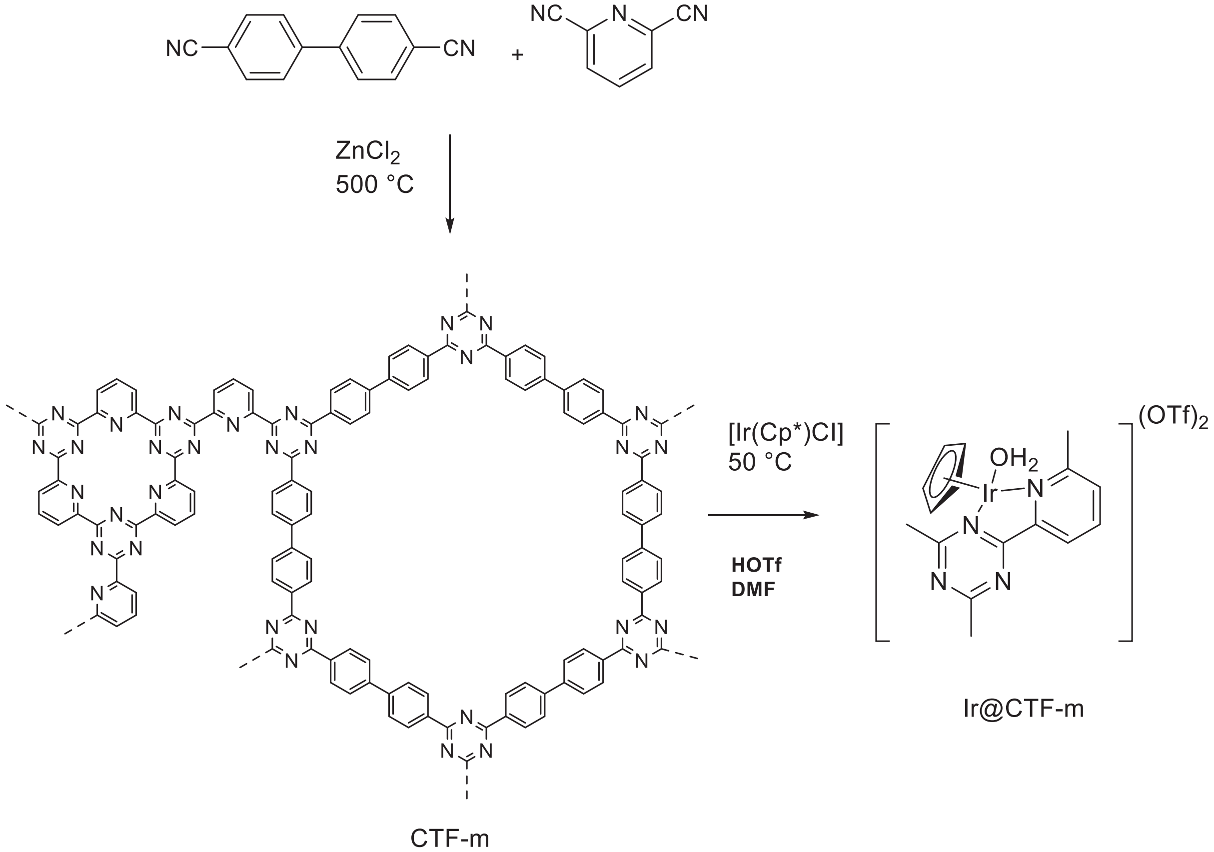

Scheme 5: Synthesis of CTF by using two nitrile monomers i.e. DCP and DCBP and its coordination covalent modification with [Ir(Cp*)Cl]. Redrawn from ref. 51, Copyright 2015, with permission from John Wiley and Sons.

Schwinghammer *et al.* have reported use of CTF as a photocatalyst for light driven hydrogen evolution.[52] Under simulated sunlight illumination, the most active CTF reduce water to hydrogen with an average rate of 1076 (± 278) mmol h^{-1} g^{-1}, which is comparable with other carbon nitride-based and organic photocatalysts.[53] Bi *et al.* reported H_2 and O_2 evaluation on CTF-T1 and RuO2@CTF-T1 via photocatalytic water-splitting reactions (Fig. 7**)**.[54] The efficiency and stability of H_2 production of CTF-T1 are comparable to g-C_3N_4. RuO2@CTF-T1 shows good photoactivity for O_2 evolution under visible light. The activity of O_2 evolution is much smaller than that of H_2 evolution, which can be attributed to the lower thermodynamic driving force for O_2 evolution than that for H_2 evolution.

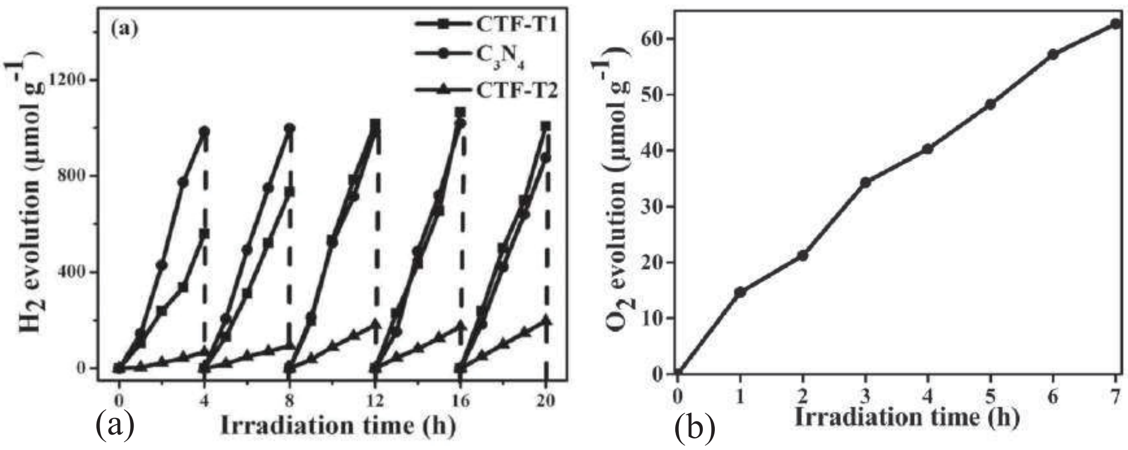

Fig. 7: H_2 and O_2 evoluation (a and b, respectively) by CTF-T1 and RuO2@CTF-T2 under UV light irradiation (λ≥ 420 nm). Reprinted from ref. 54, Copyright 2015, with permission from John Wiley and Sons.

1.4.3 CTFs as sensor

Porous organic materials have attracted considerable interest because of their unique physicochemical properties. Specially, π–conjugated porous organic polymers are an integral part of research for light emitting, light harvesting and chemo-sensing.[14c,55,56,57,58] Ren *et al.* first reported fluorescent CTF synthesized by using trifluoromethanesulfonic acid under room temperature and microwave assisted condition.[21] CTF P1-P6 exhibited bright fluorescence under UV radiation. Upon excitation at 360 nm, CTF P1-P4 and P6 exhibited blue fluorescence having emission in the range of 440-470 nm. CTF P5 showed green fluorescence with an emission wave length of 525 nm (Table 2).

Table 2: Emission spectra for CTF P1-P4

CTF	Monomer	Emission maximum (nm) (λ_{exc} = 360 nm)	Band gap (eV)
P1	pDCB	440-470	2.73
P2	DCBP		2.61
P3	DCDE		3.13
P4	TCBP		2.48
P6	TECPM		2.65
P5	TCPA	525	2.28

Wang *et al.* reported CTFs materials as efficient sensing materials for various nitroaromatic compounds.[59] Framework F-CTF-1 to F-CTF-3 synthesized by trifluoromethanesulfonic acid catalyzed reaction at 0 °C shows strong fluorescence under UV radiation. Upon excitation at 360 nm, the emission spectra appear at 460 nm, 555 nm and at 570 nm for F-CTF-1, F-CTF-2 and F-CTF-3 respectively (Table 3). These CTFs show fluorescence quenching behavior in presence of 4-nitrotoluene, picric acid, nitromethane and 2,4,6-trinitrotoluene as analytes.

Table 3: Emission spectra for F-CTF-1-F-CTF-3

CTF	Monomer	Emission maximum (nm) (λ_{exc} = 360 nm)	Band gap
F-CTF-1	TECB	460	2.73 eV
F-CTF-2	TECTPE	555	2.61 eV
F-CTF-3	TECTBPE	570	3.13 eV

1.4.4 CTFs for mixed matrix membranes (MMMs)

Membranes are very thin layers, which are able to discriminate between components of mixtures by different permeation rates wherefore they can be used in separation technology. Membranes are classified in porous membranes and solution-diffusion membranes.[60] Typically porous membranes (Fig. 7) are made out of zeolites, glass, metal or polymers. The separation is based on size exclusion. Porous membranes are for example used in dialysis, waste water treatment, and in functional clothing. Solution-diffusion membranes (Fig. 8) are produced from dense polymer materials.

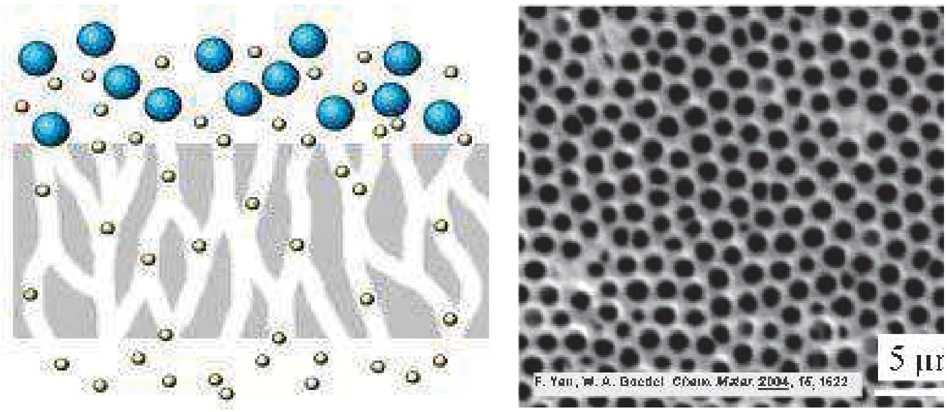

F. Yan, W. A. Goedel Chem. Mater. 2004, 16, 1622

(a) (b)

Fig. 7: Schematic illustration (a) and electron microscopy picture (b) of a porous membrane.[61]

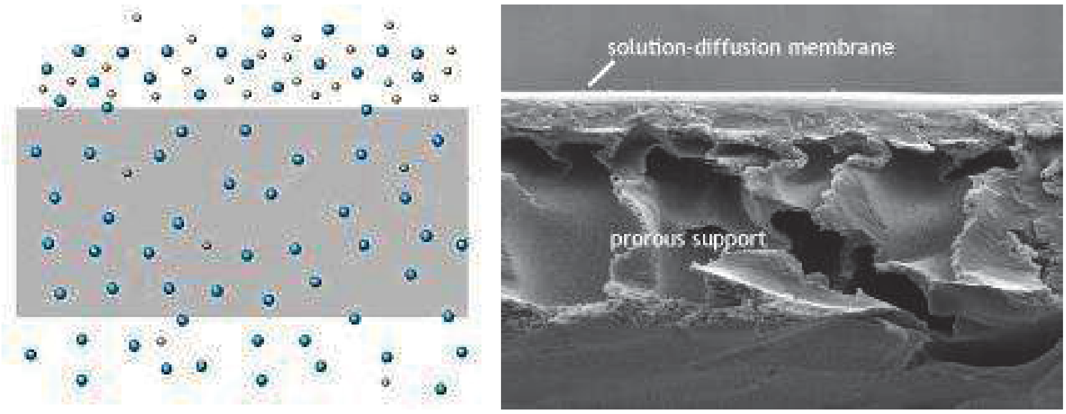

(a) (b)

Fig. 8: Schematic illustration (a) and electron microscopy (b) of a solution-diffusion membrane.[61]

Solution-diffusion membranes are commercially utilized for the separation of air, natural gas conditioning, recycling of gaseous monomers in polymerization reactors and dehydration of alcohols. Depending on pore size; the membrane process can be classified as microfiltration, ultrafiltration, nanofiltration and reverse osmosis.[62] Microfiltration (MF) membranes have the largest pores (0.1 μm to 10 μm) and highest permeability. Ultrafiltration (UF) membranes have smaller pores (2 to 100 nm) and permeability than MF membrane. Nanofiltration (NF) membranes have even smaller pore sizes (around 1 nm) which can remove the micropollutants from waste water. Reverse osmosis membranes are dense membrane without predefined pores. Mixtures of gases are separated by using membranes since the late 1970s.[63,64] Membrane separations have several advantages, such as lower energy cost, lower expenses, ease of operation and environmental friendliness compared to other separation methods.[65] Currently, membrane technology is gaining importance over traditional gas separation processes, such as cryogenic distillation and absorption,[66,67] and present industrial applications include hydrogen separation, nitrogen recovery, oxygen and nitrogen enrichment, and natural gas purification,[68] which are industrially demandable. In chemical industry, it can also recapture CO_2 from processes for further use. Membranes are not only prepared by organic substance (polymer membranes) but also from inorganic substances (inorganic membranes). However inorganic membranes are much more expensive to produce than polymer membranes. Polymer membranes have the advantage of low cost, are easy to fabricate, stable at high pressure (for cross-linked pure polymers), have low energy consumption and high mechanical resistance; but to their disadvantage they follow a trade-off relationship between permeability and selectivity; observed by Robeson. For pure polymer membranes a high permeability correlates with low selectivity and vice versa.[69,70] For gas separation processes, pure polymer membranes have comparatively lower permeability and selectivity than inorganic membranes, such as zeolites. The permeability-selectivity trade-off for pure polymers requires finding new membrane materials. Hence, membranes formed by the combination of polymer and inorganic material, called mixed-matrix membranes (MMMs) were developed. The first MMMs were prepared in the 1980s and have been increasingly investigated in recent years.[65] Porous inorganic material such as zeolites or metal organic frameworks (MOF) could be used for making MMMs.[71,72,73,74,75,76,77] The problem of zeolite/polymer composite MMMs often is their defective morphology; which is illustrated by void spaces between the zeolite particles and the polymeric matrix; leading to poor gas-separation performance; due to gas molecules flow around the zeolite particles. using MOFs for making MMMs due to their various advantages (i.e. organic compounds with different functionalities, accessible porosity, very low defective morphologies, stability, large surface area, easy to handle etc.) over zeolite.[78,79,80,81] The choice of MMMs for gas separations depends on: the pore diameter of the MOF which is larger than the kinetic diameter of one gas component (kinetic diameter of gases: H_2 (2.9 Å), O_2 (3.46 Å), N_2 (3.64 Å), CO_2 (3.3 Å) and CH_4 (3.8 Å)) and lower than the others. This will give very strong enhancement of permeability which is economically very smart (selectivity should not be change) for large scale application. Gas separation processes applied in industrial scale are natural gas treatment (removal of CO_2), hydrogen removal (i.e. in cracking processes) oxygen enrichment from air (medical devices) and nitrogen enrichment from air (used as protecting atmosphere for oxygen sensitive compounds).

Use of new porous materials, namely COFs/CTFs for making new MMMs and study their gas separation process could be of interest. Since COFs/CTFs have advantages such as outstanding thermal stability, permanent porosity with high surface area and light element composition over MOFs, therefore, it will be attractive to use COFs/CTFs in MMMs. While MOF-MMMs have already been studied to some extent, use of COFs/CTFs in membranes is still less. Dai *et al.* developed porous, fluorescent, triazine-framework-based membranes with intrinsic porosity from DCBP through aromatic nitrile trimerization reaction by using CF_3SO_3H as catalyst. With functioalized triazine unit, the membrane shows CO_2/N_2 selectivity of 29±2 CO_2 permeability of 518 ± 25 barrer.[82] Chung and co-workers also reported in situ fabricated membrane via Brønsted-acid-catalyzed cyclotrimerizaiton reaction for dehydration of ethanol.[83] The membrane exhibit a high water permeability of 75600 Barrer and a water/ethanol selectivity of 101 for dehydration of an 85 wt% ethanol aqueous solution at 45 °C. Recently Wang et al. reported triazine framework based membrane synthesized from TCBP which shows good performance for He separation and H_2 purification with a He/H_2 selectivity of 400.[84]

1.5 Method for CTF characterisation

1.5.1 IR spectroscopy

IR spectroscopy is a common technique to identify the bonds present in a chemical structure. It operates in the range of 4000-400 cm^{-1} which can be split into two different region, functional group region (4000-1500 cm^{-1}) and fingerprint region (1500-400 cm^{-1}).[85,86] IR spectroscopy works on the principle that covalent bonds having electrical dipole absorbed energy of electromagnetic radiation and thus causes a change in the dipole of the molecule. The frequency of absorbance can be calculated by using the Hooke´s law[87] by considering a system where two masses (m1 and m2) are connected through bond which acts as a spring,

$$\nu = \frac{1}{2\pi} . \sqrt{\frac{f}{\mu}} \quad \text{.........(3)}$$

Where, ν = frequency; f = force constant; μ = reduced mass = $\frac{m1.m2}{m1+m2}$

Force constant related to the strengths of the bonds connecting the two atoms. Therefore, the frequency will increase with increasing the strengths of the bond and decreasing the reduced mass. The other factors that effect the IR frequency are inductive effect and resonance.

Both liquid and solid samples can be measured using IR spectroscopy technique. For solids, finely powdered sample is mixed with KBr and ground thoroughly to reduce the particle size followed by making a translucent pellet by using mechanical press which is measured then by using FT-IR technique. The ratio of concentration of sample in KBr should be in the range of 1:99. For porous material, IR spectra only measure on solid sample as it is insoluble for common solvent. This technique helps to identify the functional group present in the materials. Specially, POPs often characterized by FT-IR. Fig. 9 shows an example of formation of CTF-2 (from DCN) using this technique.[19] Bojdys *et al.* showed that the strong intensity of the –CN band at 2225 cm^{-1} decreases significantly after 20 h and diminishes further following the course of the reaction, while new bands were appeared at 1535 (stretching mode) and 1315 (breathing modes) cm^{-1} for the triazine unit.[19]

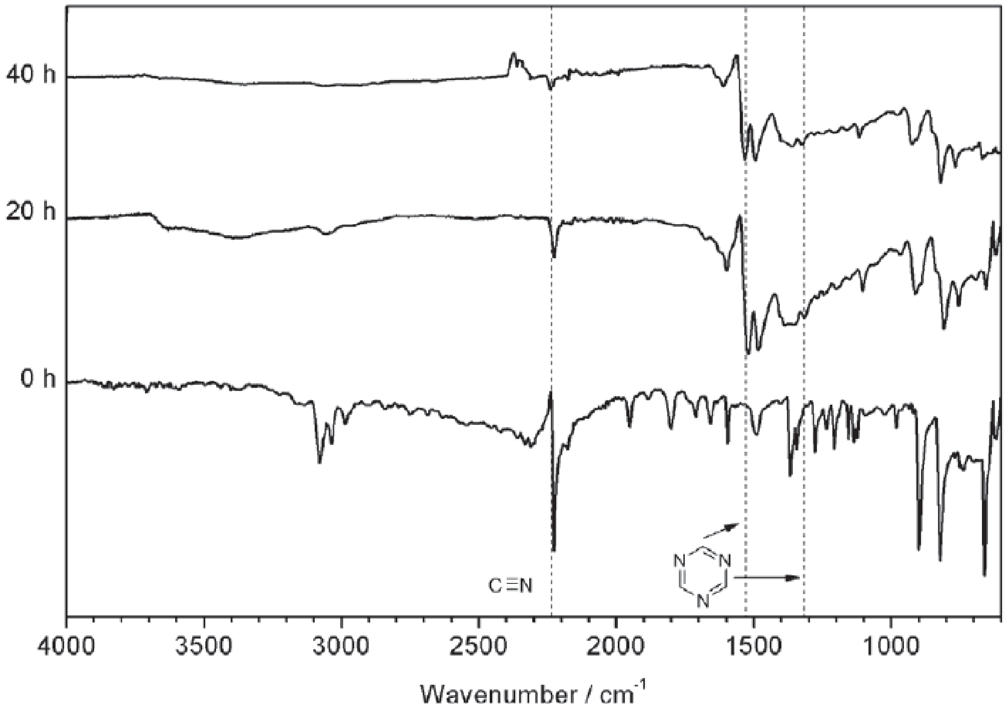

Fig. 9: IR spectra following the formation of CTF-2 from (0 h) and the products after 20 h and 40 h at 400 °C. Reprinted with permission from ref. 19. Copyright 2010 John Wiley and Sons

1.5.2 Thermogravimetric analysis

Thermogravimetric analysis is a technique which determines the mass change of a material as a function of temperature or time. It can provide ideas about thermal stability of the frameworks.

Usually it is carried out in oxygen or in inert gas atmosphere like N_2, He or Ar. TGA technique has been used extensively to study polymeric materials, inorganic materials, metals, ceramic, glasses and composite materials.

For applications of porous frameworks, it is important to consider their thermal stabilities. Therefore, stability is an important issue. This stability mostly determined by TGA. Importantly, CTFs showed high thermal stability (>400 °C). The TGA of a CTF-1 material under N_2 atmosphere was included as an example which can express the thermal stability of about 480 °C (**Fig. 10**).[88]

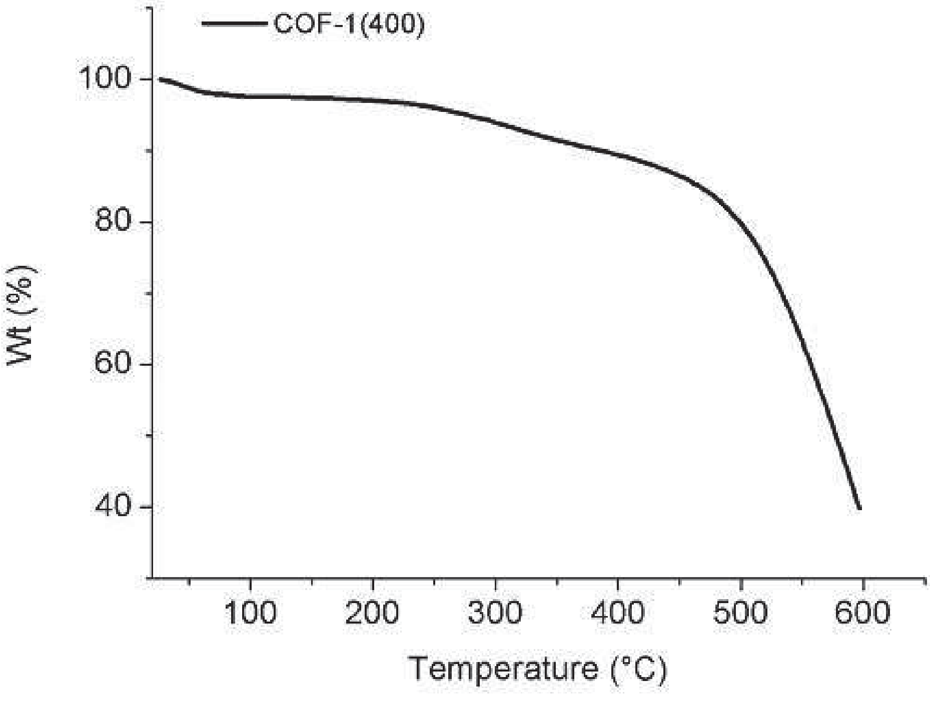

Fig. 10: TGA spectra of CTF-1.[88]

1.5.3 Powder X-ray diffraction

Powder X-ray diffraction (PXRD) is a technique that provides information about crystalline or amorphous nature of a material. The wave length of light, and the distance between the crystal planes can be explained by Braggs law.

$n\lambda = 2d\ sin\theta$ ……..(4) Braggs law

λ = the wavelength of the X-ray; d = the spacing of the crystal layers; θ = the incident angle (the angle between the incident ray and scattered plane); n = integer

Generally COFs or CTFs are mostly amorphous in nature as most of the cases the atoms are arranged in a non-periodic condition. Only few CTFs are crystalline such as CTF-1 and CTF-0 (Fig. 11-12), that is often measure by PXRD. No single crystal of CTF is found so far, therefore, most of cases the Materials Studio Modeling is applied in order to build the 2D or 3D structures.

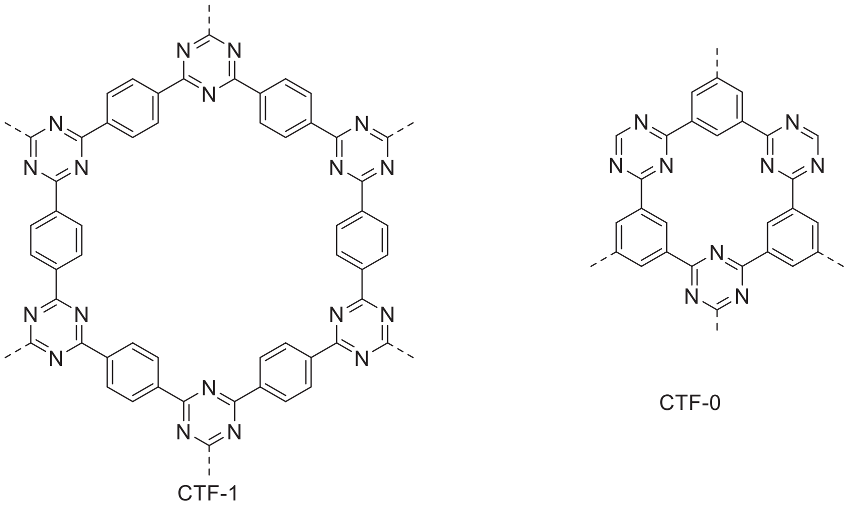
CTF-1

CTF-0

Fig. 11: Idealized structure of CTF-1 and CTF-0.

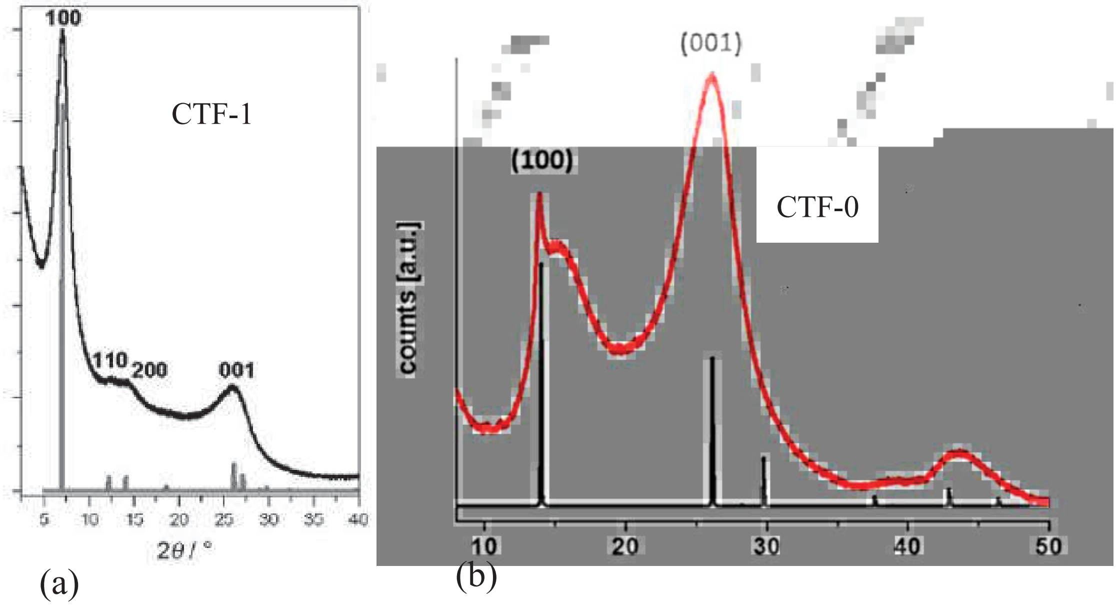

Fig. 12: (a) PXRD pattern of CTF-1. Reprinted with permission from ref. 17. Copyright 2008 John Wiley and Sons (b) PXRD pattern of CTF-0. Reprinted (adapted) with permission from ref. 35. Copyright 2013 American Chemical Society.

1.5.4 Karl–Fischer titration

Karl–Fischer titration is a quantitative technique to determine the water content of a substance. It has several advantages like accuracy, short analysis time, small amount of sample etc. There are two methods for Karl-Fischer titration, coulometric titration and volumetric titration.[89]

In coulometric titration, the lower amount of water can be determined (10 μg-10 mg).[90] On the other hand, the volumetric titration is used for sample having high water content (1 mg-100 mg).[89]

Recently, this technique often used to explain the hydrophilic nature of the porous materials. Fig. 13 is showing an example where amount of water is determined after vacuum draying at 120 °C. This example is for PCTF-8 which can adsorb 10 wt% of moisture from ambient air upon storage under ambient conditions.[34b]

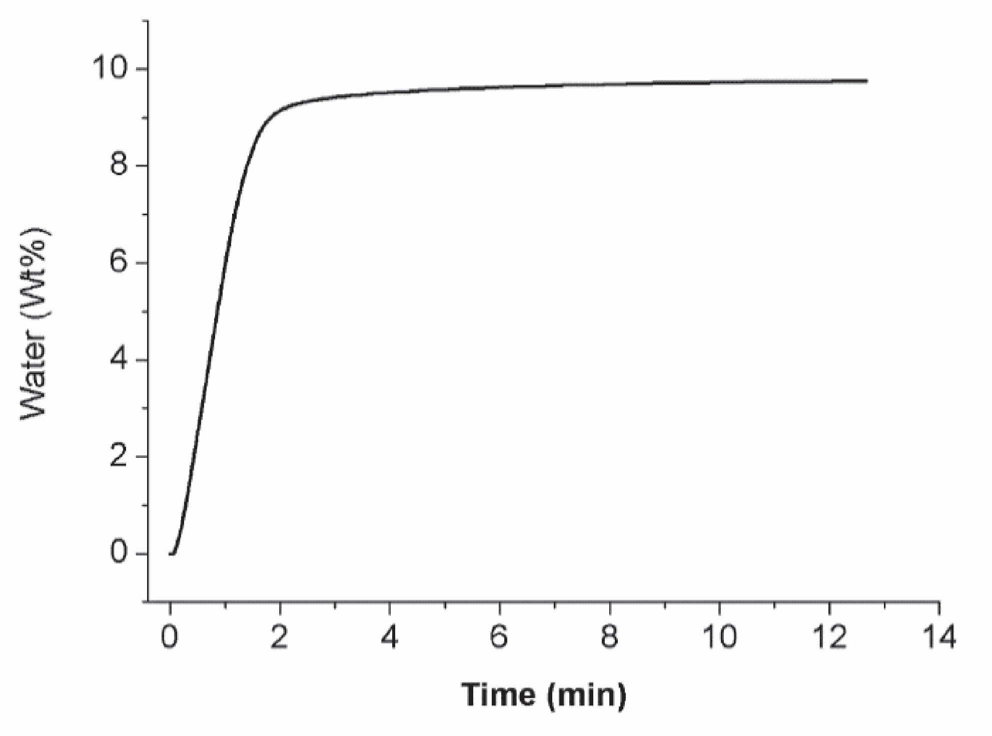

Fig. 13: Karl-Fischer titration plot for PCTF-8 (ref. 34b).

1.5.5 Elemental analysis

Elemental analysis is a technique which determines the elemental composition of a material in order to identify the structure of an unknown compound. This analysis can be qualitative as well as quantitative. From this analysis we often determine the mass fraction of carbon, hydrogen, nitrogen and sulfur. This also can help to ascertain the structure and purity of the material. Since the POPs are amorphous in nature, therefore, chemist often designs the formula units by measuring the elemental analysis. In this view, the elemental analysis of CTF material is crucial. Ionothermal condition based CTFs materials are often show the deviation of calculated and found values of hydrogen and nitrogen atoms due to C–H bond cleavage as we well as homolytic cleavage of the carbon nitrile bonds (Scheme 6).

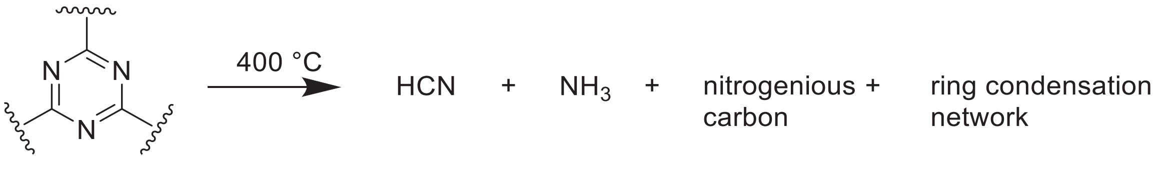

Scheme 6: General schematic representation for the decomposition of a triazine ring.

Mismatch in theoretical and experimental elemental (CHN) analysis of CTFs can also be explained by the hygroscopic nature, impurity, guest solvents etc. present in the synthesized products. Hygroscopic nature of CTFs can explain by the help of KFT analysis. For example, elemental analysis of PCTF-8 is shown in Table 4.[34b]

Table 4: Elemental analysis of PCTF-8

Compound	Calculated (% and molar ratio)					Found (% and molar ratio)				
	C	H	N	C/H	C/N	C	H	N	C/H	C/N
[a]PCTF-8	83.32	3.73	12.95	2	8	74.96	4.55	11.16	1	8
[b]PCTF-8	74.06	4.56	11.52	1	8	74.96	4.55	11.16	1	8

[a]Formula unit without water molecule. [b]Formula unit contain three water molecules.

Elemental analysis (Table 4) suggested that the formula unit ($C_{30}H_{16}N_4$) contain additional three water molecules that can be explained by KFT. The activated PCTF-8 showed about 10 wt% water in the KFT analysis which is in good agreement with the oxygen content found by CHN analysis. Therefore, it became apparent that the PCTF-8 is hygroscopic and adsorbs about 10 wt% of moisture from ambient air upon storage under ambient conditions after vacuum drying at 120 °C. A similar hygroscopic behavior of related CTFs was reported recently by Janiak *et al.* and may be a common phenomenon to CTFs.

1.5.6 NMR spectroscopy

Since most of the COFs/CTFs are insoluble in the common organic solvents, therefore, it is very important to perform solid state NMR measurement in order to find the resulted structure of the frameworks. Unlike solution state spectra, solid state NMR spectra are very broad due to anisotropic chemical shift and dipolar broadening.[91] Fig. 14 showed the structural unit and the solid state ^{13}C NMR spectra of HPF-1.[92] In this NMR, author identifies the chemical shift values and their corresponding carbon atom for the porous materials, HPF-1 (Fig. 14).

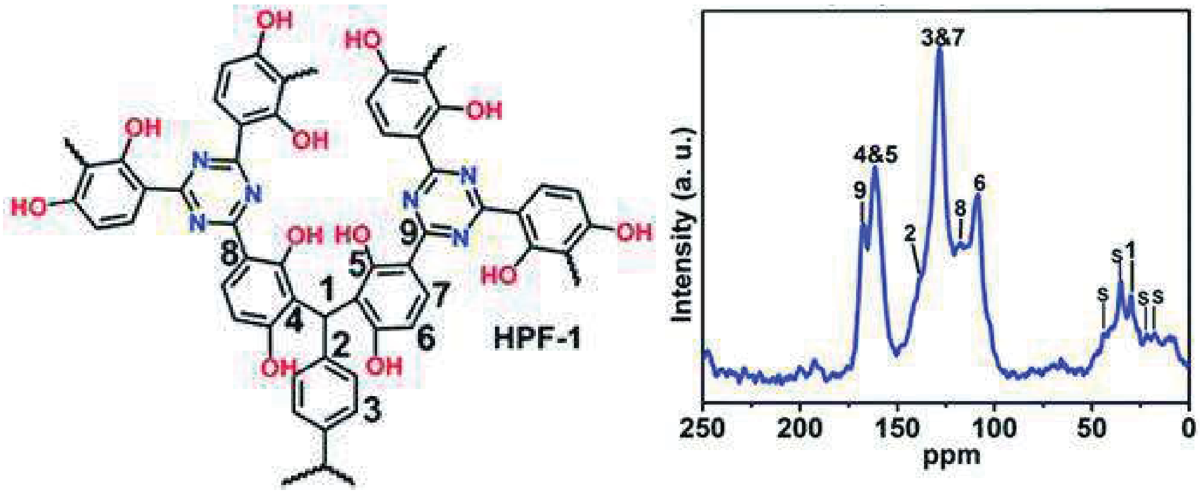

Fig. 14: ^{13}C-MASNMR (400 MHz) of HPF-1, The peaks in the aliphatic region correspond to the occluded THF and dioxane molecule in the polymer labelled as 's'. Fig. taken from ref. 92 Original- Published by The Royal Society of Chemistry.

1.5.7 N_2 adsorption

N_2 adsorption (77K) measurement has frequently been used to evaluate the permanent porosity in porous materials. Typically, porous materials are broadly classified into three types based on their pore sizes (Fig. 15)[93,94]: (1) microporous material (pore width < 20 Å, (2) mesoporous material (pore width = 20-50 Å) (3) macroporous material (pore width >500 Å). However, porous materials have also been classified depend on building frameworks including purely inorganic, organic-inorganic hybrid and purely organic. An arrangement of pores in porous materials is mainly regular (order) or irregular (disorder) shape.[93,94] These shapes are of several types including cylindrical, slits, interstices, spherical or ink bottle and conical (Fig. 16). On the other hand, pores can be closed, blind or through which is depend on accessibility, as shown in the Fig. 15.[93,94] However, each pore can be isolated or connected to other pores to form a porous network.

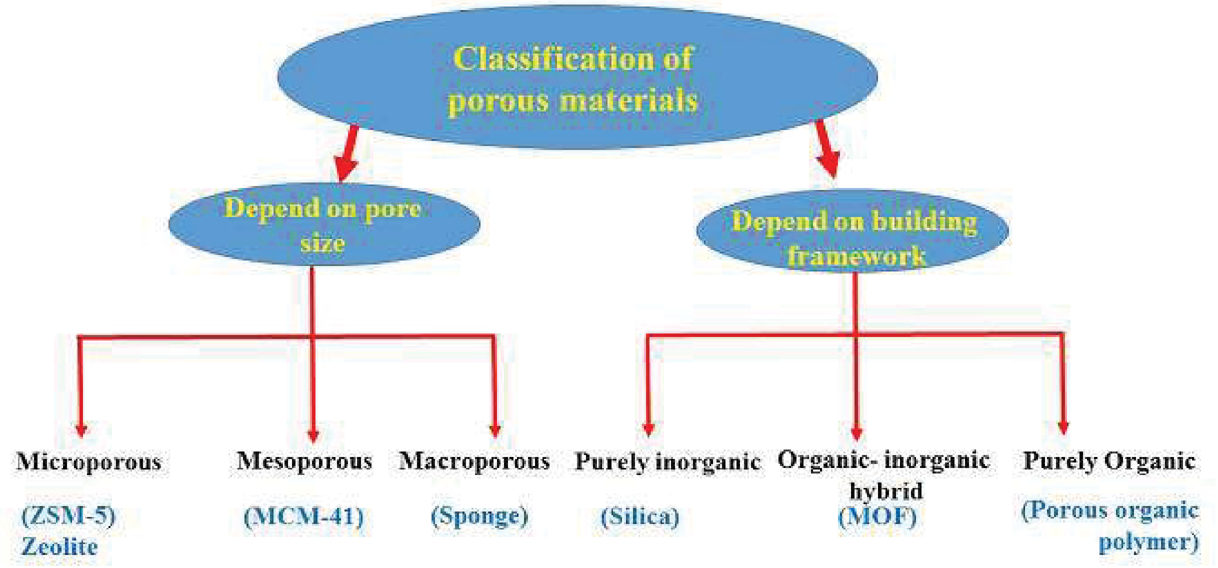

Fig. 15: Schematic diagram for classification of porous materials. Redrawn from ref. 94.

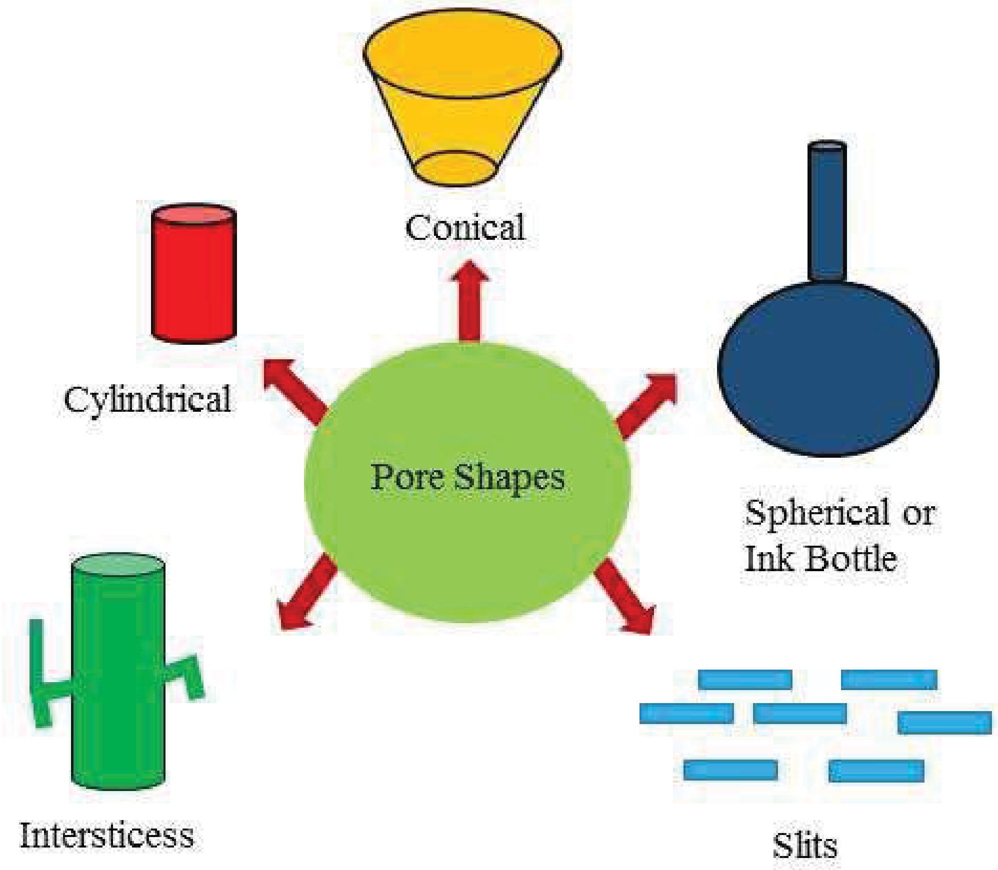

Fig. 16: Image of different pore shapes. Redrawn from ref. 94.

For industrial application of gas storage (H_2/ CO_2/ CH_4) and separation, microporous materials are important. The adsorption of gas molecules on porous materials are mostly occurred by physorption, sometime chemisorption and capillary condensation can also observed, but it depends on the binding energy of the gas molecules and surface. Surface area, pore size and pore volume of porous compounds usually determined by N_2 physisorption isotherm at 77 K.

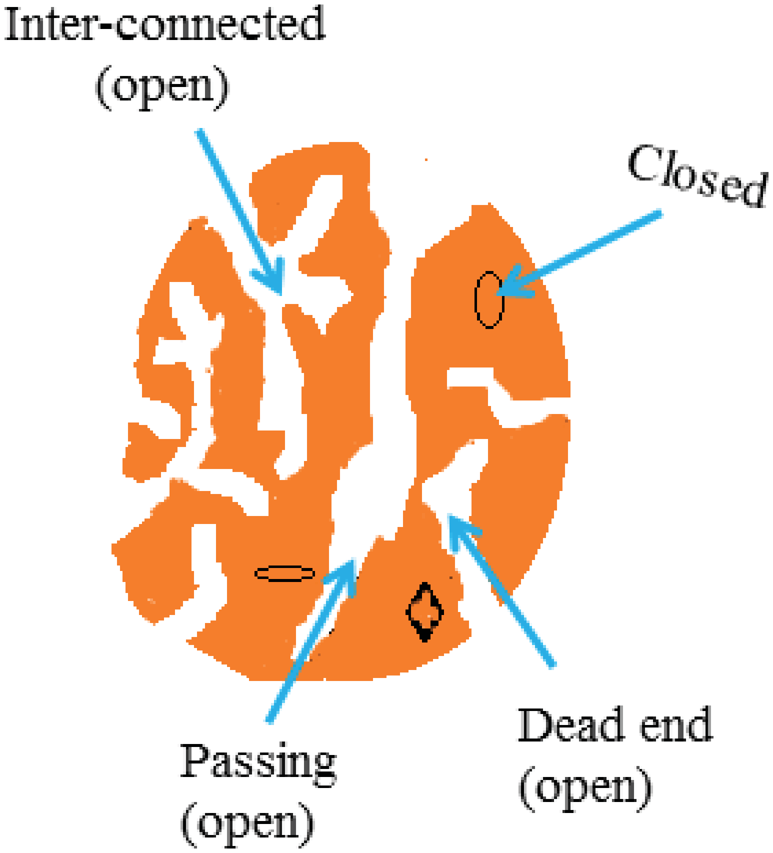

Fig. 17: View of closed and open pores in porous materials depend on accessibility. Redrawn from ref. 94.

The phenomenon of attracting and retaining of molecules on the surface of a solid or liquid is called adsorption. This is a spontaneous process (ΔG negative), and it is exothermic process (ΔH negative). The substance which is adsorbed on the surface is called adsorbate and the substance on which adsorption takes place is called adsorbent. In physical adsorption, the gas molecules are held on the surface of a solid by van der Waals force without formation of any chemical bond. It is a reversible process, forms multi molecular layer and heat of adsorption is low. On the other hand, in chemisorption process gas molecules are held on the surface of a solid by the force similar to a chemical bond. It is an irreversible process, forms unimolecular layer and heat of adsorption is quite high. Amount of a gas adsorbed by a given amount of adsorbent depend upon both temperature and pressure. At constant temperature there exist some definite relationship between the amount of gas adsorbed and the equilibrium pressure. Such relationships are known as adsorption isotherm. According to IUPAC classification in 1985, there are six types of adsorption isotherms. Recently these isotherm has been modified due to various types of porous materials were identified over the last three decades and this isotherms are reflected the relationship between porous structure and adsorption type, as shown in Fig. 18.[95]

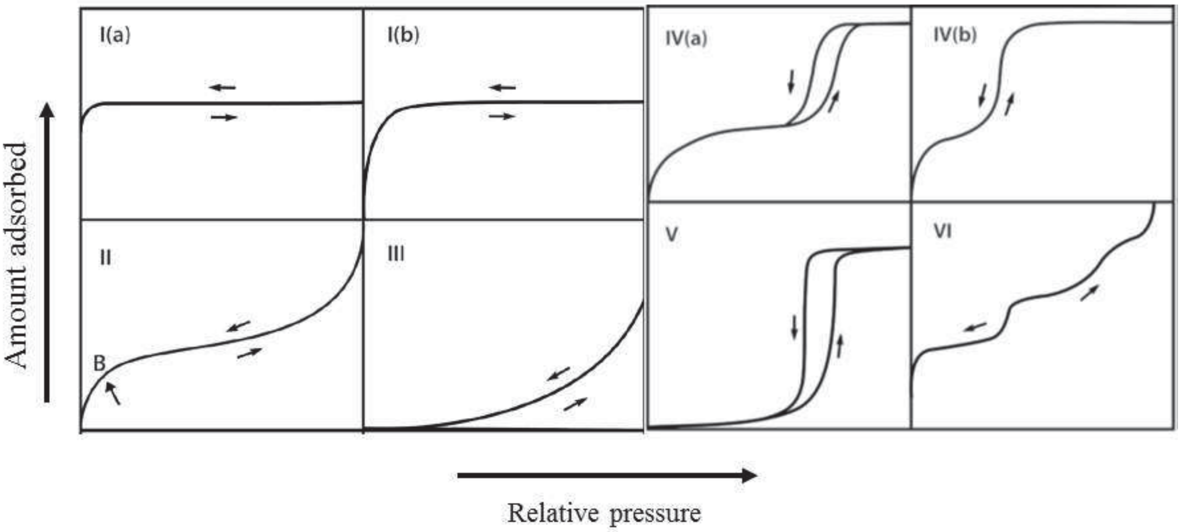

Fig. 18: Types of physisorption isotherms (IUPAC).[95]

Reversible type I isotherm represent the microporosity of the porous material (adsorbent mainly some activated carbons, molecular sieve zeolites and certain porous oxides) with narrow pores, resulting enhancement of adsorbate-adsorbent interaction. Typically, Type I(a) isotherms are found by microporous materials with narrow micropores of width <~ 1 nm. On the other hand, Type I(b) isotherms are observed due broad pore size distributions range including wider micropores and possibly narrow mesopores (< ~ 2.5 nm), and it often found for COFs and POFs. Type II isotherm is observed for non-porous or macroporous material, and it represents unrestricted monolayer-multilayer adsorption. Type III isotherm is generally uncommon and observed for nonporous materials. In this case the interaction between adsorbate and adsorbent act a crucial role. Adsorption of nitrogen on polyethylene shows type III isotherm. Type IV isotherm is generally obtained for mesoporous materials. The initial part of type IV isotherm represents monolayer-multilayer adsorption similar to type II. The characteristic hysteresis loop is due to the capillary condensation occurs in the micropores. Moreover, the type IV isotherms can be divided into two categories: (1) type IVa: capillary condensation is accompanied by hysteresis due to the pore width exceeds a certain critical width, which is dependent on the adsorption system and temperature, (2) type IVb: it is for conical and cylindrical mesopores that are closed at the tapered end. Amorphous materials are often showed the combination of two isotherms: the isotherms of CTFs (*fl*-CTF500 and *fl* -CTF600) showed a combination of isotherms of type I and IV; and this is due to micropore filling as well as mesopore filling.[31]

Type V isotherm is very rare, and found mesoporous materials. This type isotherm represents the weak interaction between adsorbent and adsorbate similar to type III. Type VI isotherms describes adsorption on macroporous or non-porous solid surfaces where stepwise multilayer adsorption occurs. For an example, adsorption of argon or krypton on graphitized carbon blacks at 77 K show type VI isotherm.

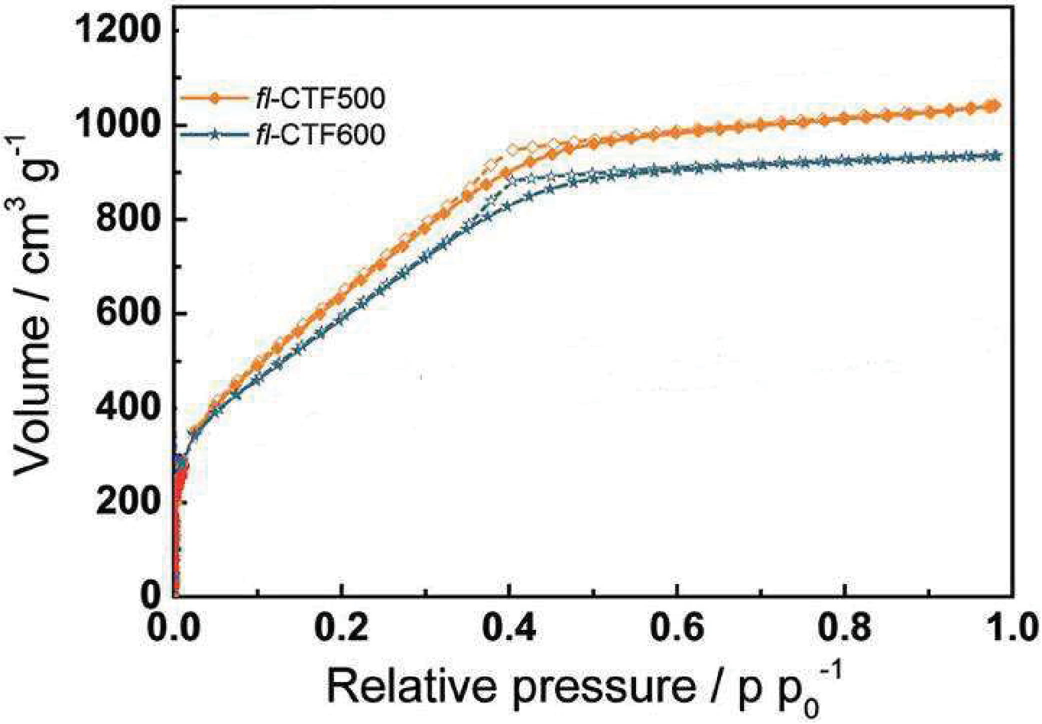

Fig. 19: Argon adsorption (filled symbols) and desorption (open symbols) isotherms at 87 K for fl-CTF500 and fl-CTF600. Picture taken from ref. 31; Published by The Royal Society of Chemistry.

The surface area of a porous solid is usually determined by the classical "Brunauer-Emmett-Teller" method which is based on multilayer adsorption. The BET equation is a modification of monolayer Langmuir adsorption theory.

Adsorption isotherm often exhibit the hysteresis.[95] It appears due to capillary condensation in the mesopores, intrinsic framework flexibility, phase transition and gas trapping within the pore apertures.[96] According to IUPAC (1985), hysteresis loop can be classified into mainly four types which recently modified to six types (H1, H2a, H2b, H3, H4, and H5) as shown in Fig. 20. H1 type of hysteresis appears for the materials (e.g., MCM-41, MCM-48, SBA-15) having ink-bottle pores. H2(a) loops mainly appear for blocking/percolation. Several porous materials including porous glasses, ordered mesoporous materials (e.g., SBA-16 and KIT-5 silicas), silica gel show H2(a) type hysteresis. On the other hand, H2(b) is also due to pore blocking. H3 and H4 type of hysteresis is associated with particle agglomerate resulting slit-shaped pores or spaces between parallel plates. Type H5 loop is found in certain materials which is associated with certain pore structures containing both open and partially blocked mesopores. CTF materials often exhibit hysteresis.[21,31,34a]

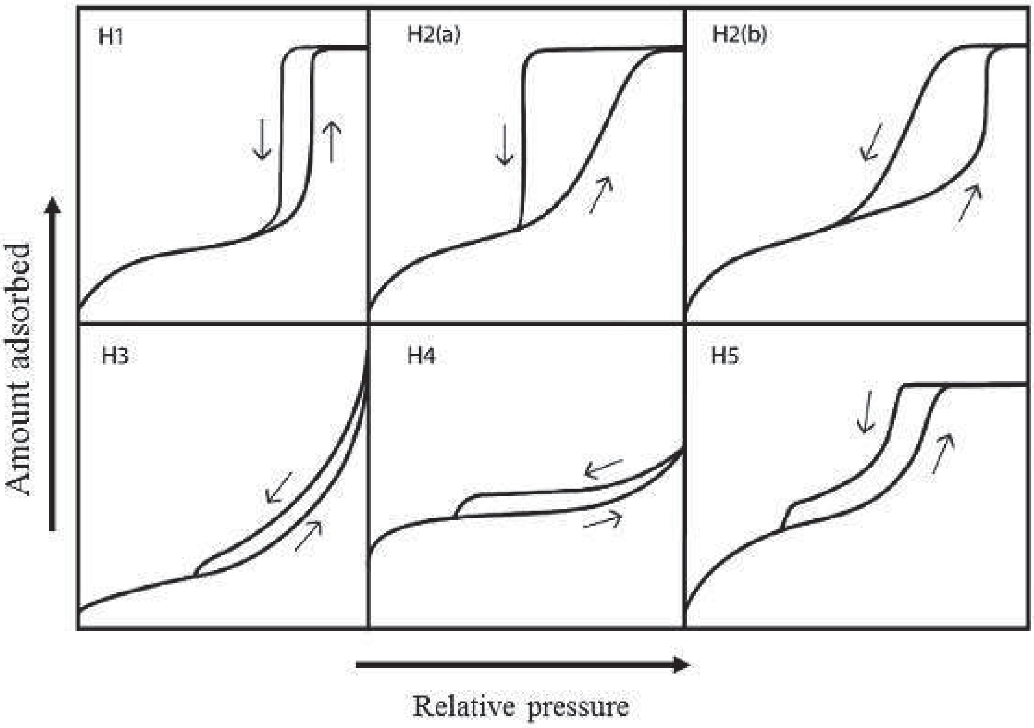

Fig. 20: Type of hysteresis loops (IUPAC).[95]

1.5.8 Water adsorption

Water adsorption on porous materials have several applications like in humidity control, adsorption–driven heat exchanger and heat pumps.[6] For real life application, water uptake at low relative pressure is important ($P/P_0 < 0.1$). Most commonly used water adsorbents are silica gel and zeolite. Recently MOFs and COFs have also been explored as water adsorbents. The water adsorption capacity depend on several factors including structure and chemical composition of the material, hydrophilic/hydrophobic nature of the ligand, effect of functional group, H-bonding capacity, etc.[97,98] According to classical definition, a hydrophilic material is one which have high affinity to water, and a hydrophobic material is one which have low affinity to water.[98] But for water adsorbents the hydrophilicity/hydrophobicity is determined based on the water adsorption loading at particular relative pressure.[98,99] According to IUPAC water adsorption isotherms can be classified into seven types (Fig. 21).[98]

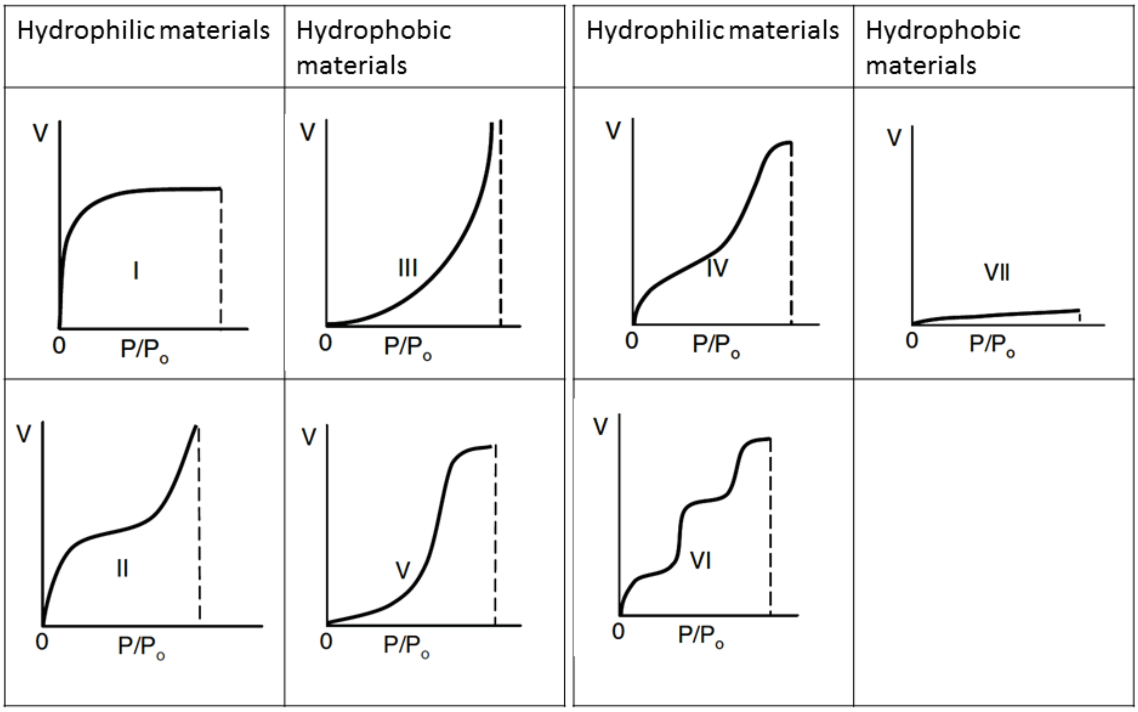

Fig. 21: Adsorption isotherms (IUPAC). Reprinted from ref. 98, Copyright 2008, with permission of Elsevier.

Type I isotherm is considered to be very hydrophilic due to steep rise at low relative pressure. Type II and IV also considered to be hydrophilic due to their high water adsorption capacity at low or medium relative pressure. Uncommon type VI isotherm shows stepwise adsorption express the hydrophilic characteristic. On the other hand type III and type V isotherm considered as hydrophobic or low hydrophilic in nature due to their low adsorption capacity at low relative pressure or sometime moderate adsorption at middle relative pressure and suddenly a high rise in the water adsorption at P/P_0 close to 1. Type VII isotherm is considered as highly hydrophobic in nature due to low water uptake at entire P/P_0 range. As shown in Fig. 22, both of sample (a) and (b) show type I isotherm, but sample (a) is considered to be more hydrophilic than sample (b) due to steep rise in water uptake at low P/P_0. Sample (c) shows type V isotherm with very low water uptake at low pressure region but at high pressure region shows similar water loading of sample (a) and (b) because of similar pore volume of these three materials. Sample (c) considered to be hydrophobic or weakly hydrophilic in nature. Sample (d) is considered as strongly hydrophobic in nature due to its very low water adsorption over the entire relative pressure range.

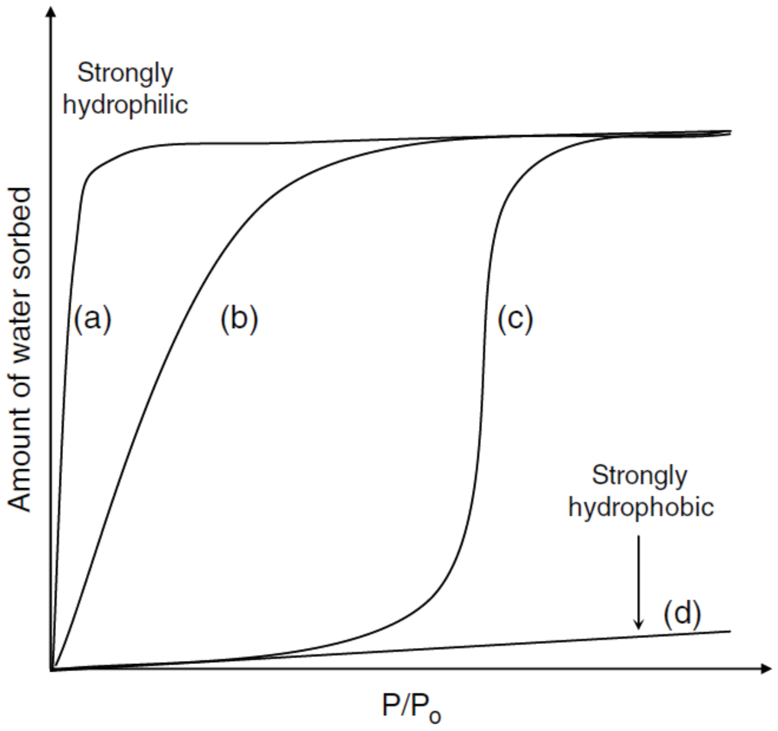

Fig. 22: Water adsorption isotherms for four adsorbents having different hydrophilicities. Reprinted from ref. 98, Copyright 2008, with permission of Elsevier.

2 Aim of the thesis

The objectives of this thesis are to synthesize covalent triazine-based frameworks (CTFs) using variety of linker and studies their liquid (H_2O/surfactant) and gas sorption (N_2, H_2, CO_2 and CH_4) as well as gas separation behavior (CO_2/N_2 and CO_2/CH_4).

To explore this aim, a series of CTF materials should be synthesized by possibly different synthetic routes:

(1) Ionothermal condition ($ZnCl_2$)

(2) Brønsted acid conditions (CF_3SO_3H)

(3) Friedel-Craft ($AlCl_3$) reaction.

For ionothermal synthesis, the following nitrile monomers should be used together with ten equivalent $ZnCl_2$ at 400°C which acts as a Lewis-acid catalyst, molten solvent and porogen for the polymerization (Fig. 23).

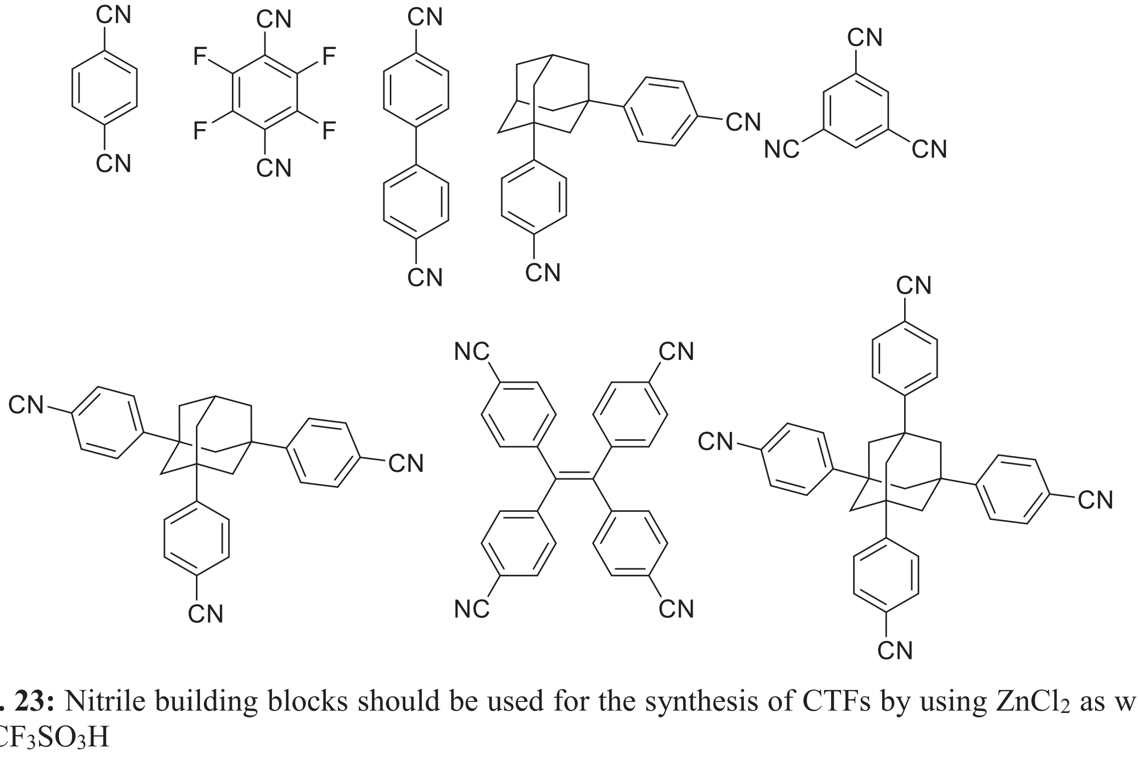

Fig. 23: Nitrile building blocks should be used for the synthesis of CTFs by using $ZnCl_2$ as well as CF_3SO_3H

At the same time, Friedel-Craft ($AlCl_3$) reaction can be used for the several aromatic linkers fluorine (FL), 1,3,5-triphenylbenzene (TPB), triptycene (TPC), tetraphenylethelene (TPE) or tetraphenylsilane (TPS) (See below, Fig. 24) in the presence of cyanuric chloride and 2-amino-4,6-dichloro-1,3,5 triazine to construct triazine-based frameworks.

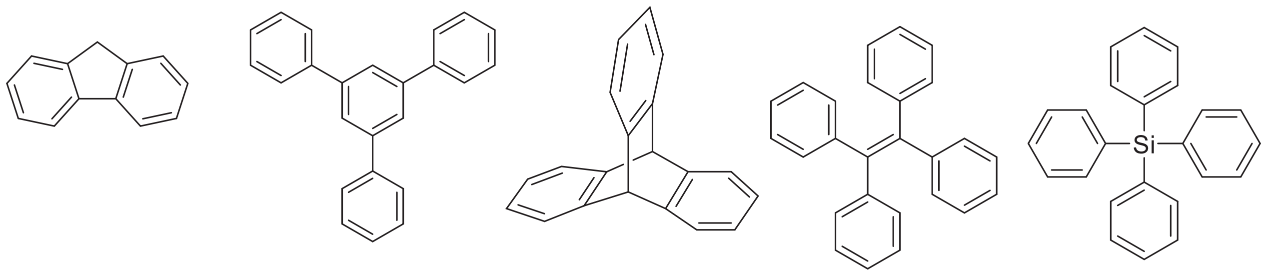

Fig. 24: Building blocks should be used for the synthesis of CTFs using Friedel-Craft ($AlCl_3$) reaction.

3 Cumulative part

Sections 3.1–3.9 describe the published/submitted work of this thesis. All the published works were reprinted with permission from corresponding publisher (reference 100, 88, 103, 104, 105, 34b for section 3.1, 3.4-3.8 respectively).

Each section of this cumulative part contains a short introduction and summary of the work together with assignments of tasks of the authors. Further unpublished work is illustrated in section 4.1-4.2.

3.1 Covalent triazine-based frameworks (CTFs) from triptycene and fluorene motifs for CO_2 adsorption

Subarna Dey, Asamanjoy Bhunia, Dolores Esquivel and Christoph Janiak

J. Mater. Chem. A, 2016, **4**, 6259-6263
DOI: 10.1039/c6ta00638h, (reference 100)
Impact factor 2016: 8.262

Covalent triazine-based frameworks (CTFs) are subclass of POPs that possess high chemical and thermal stability with a high specific surface area. In this work we synthesized two porous triazine based frameworks CTF-TPC and CTF-FL from triptycene and fluorine motif through low temperature and cost-effective $AlCl_3$ catalyzed Friedel-Crafts reaction with BET surface area 1668 and 773 m^2/g respectively. We found that the surface area of the CTF-TPC exceeds than the CTFs materials synthesized by strong Brønsted acid condition and highly comparable with ionothermal synthesis. The synthesized materials were studied for CO_2, CH_4 and H_2 gasses at different temperatures. The H_2 and CH_4 uptake capacities of CTF-TPC and CTF-FL are comparable to many other reported CTFs. At 273 K and 1 bar, CTF-TPC and CTF-FL exhibited good CO_2 uptake capacity of 95.2 cm^3/g and 73.2 cm^3/g with CO_2/N_2 selectivity 30 and 48 respectively. The selectivity of CTF-FL is high comparable with other recent reported CTFs works.

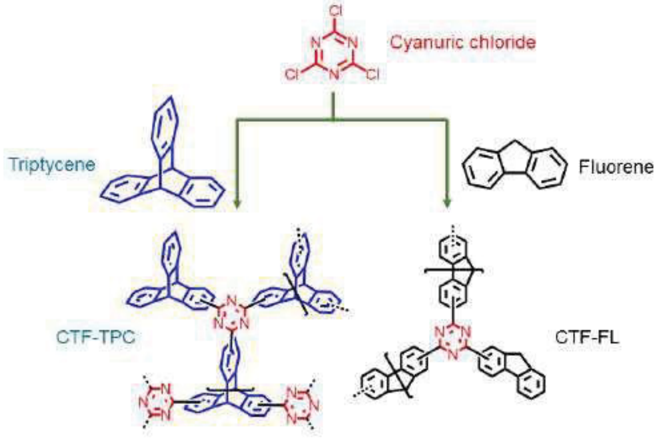

Author's contribution to the work:

- Synthesis and characterization of the CTF materials (except solid state NMR).
- Gas adsorption studies.
- The manuscript was prepared by me, and corrected by Prof. Janiak including the comments from the reviewers during the revision process.

Journal of
Materials Chemistry A

COMMUNICATION

View Article Online
View Journal | View Issue

Cite this: *J. Mater. Chem. A*, 2016, **4**, 6259

Received 22nd January 2016
Accepted 30th March 2016

DOI: 10.1039/c6ta00638h

www.rsc.org/MaterialsA

Covalent triazine-based frameworks (CTFs) from triptycene and fluorene motifs for CO_2 adsorption†

Subarna Dey,[a] Asamanjoy Bhunia,[a] Dolores Esquivel[b] and Christoph Janiak*[a]

Two microporous covalent triazine-based frameworks (CTFs) with triptycene (TPC) and fluorene (FL) backbones have been synthesized through a mild $AlCl_3$-catalyzed Friedel–Crafts reaction, with the highest surface area of up to 1668 $m^2\ g^{-1}$ for non-ionothermal CTFs. CTF-TPC and CTF-FL show an excellent carbon dioxide uptake capacity of up to 4.24 mmol g^{-1} at 273 K and 1 bar.

The burning of fossil fuels increases the CO_2 level in the atmosphere which may contribute to global warming and is more imminent to ocean acidification.[1,2] Therefore, research on carbon capture and storage/sequestration (CCS) has been receiving great attention over the last few decades.[3] It may be necessary to develop CO_2 capture technologies with as little energy penalty as possible. Typically, a flue gas contains N_2 (75–76%), CO_2 (15–16%), H_2O (5–7%), O_2 (3–4%), CO (20 ppm), SO_x (<800 ppm), and NO_x (<500 ppm) with the emission temperatures of 50–75 °C at 1 bar but its exact composition highly depends on the design of the power plant and the source of natural gas or coal.[4] To capture CO_2 at such concentration requires separating CO_2 in the presence of N_2 and H_2O in post-combustion systems. Known CO_2 separations in a post-combustion process are amine scrubbing (amine washing) and chilled ammonia technologies[5] in which the Lewis acid CO_2 interacts with Lewis basic solution resulting in carbamate formation. Drawbacks include regeneration, fouling of the equipment and solvent boil-off. Alternative methods, *e.g.*, chemisorption on solid oxide surfaces or physical adsorption on porous solids, are attracting increasing attention.

Solid adsorbents are zeolites,[6] metal–organic frameworks (MOFs),[4] silica,[7] activated carbons[8] and porous organic polymers (POPs).[9] MOFs and POPs have gained attention due to their high surface area, ability to be functionalized and selectivity for CO_2 over other gases. Classes of POPs are often differentiated according to their building units such as benzimidazole-linked polymers (BILPs),[10] hyper-crosslinked polymers (HCPs),[11] polymers of intrinsic microporosities (PIMs),[12] porous aromatic frameworks (PAFs),[13] conjugated microporous polymers (CMPs),[14] covalent organic frameworks (COFs),[15] Schiff base networks (SNWs),[16] covalent imine polymers (CIP),[17] porous polymer frames/networks (PPFs/PPNs),[18] element–organic frameworks (EOFs)[19] and nitrogen-doped porous carbon materials (NPCs).[20] POPs often have higher stability towards moisture than MOFs which is crucial for post-combustion CO_2 capture materials.

Covalent triazine-based frameworks (CTFs) are another subclass of POPs that possess high chemical and thermal stability with a high specific surface area.[21] CTFs are interesting because of cheap and readily available starting materials, nitrogen content, facile synthesis and certain hydrophilicity. The following strategies for porous CTF preparation have been reported: (1) ionothermal conditions ($ZnCl_2$),[21] (2) strong Brønsted acid conditions (CF_3SO_3H),[22] and (3) Friedel–Crafts ($AlCl_3$) reaction.[23,24] Kuhn, Antonietti and Thomas *et al.* developed CTFs with permanent porosity.[21] By (1) and (2) these materials are made by the trimerization reaction of carbonitriles to form triazine rings. From their elemental composition, we view CTFs from ionothermal reaction with $ZnCl_2$ as in-between well-defined COFs and porous carbon materials. CTFs with surface areas of up to 1152 $m^2\ g^{-1}$ were synthesized by using strong Brønsted acid conditions (CF_3SO_3H) under room temperature and microwave conditions.[22] Brønsted acid conditions usually provide lower surface areas but they avoid decomposition and condensation reactions such as C–H bond cleavage and carbonization and, hence, result in less structural defects. Recently, anhydrous aluminum chloride catalyzed Friedel–Crafts reactions have been used to prepare rather well-

---

[a] *Institut für Anorganische Chemie und Strukturchemie, Heinrich-Heine-Universität Düsseldorf, 40204 Düsseldorf, Germany. E-mail: janiak@uni-duesseldorf.de*

[b] *Department of Organic Chemistry, Nanochemistry and Fine Chemistry Research Institute (IUIQFN), Faculty of Sciences, University of Córdoba, Campus de Rabanales, Marie Curie Building, Ctra. Nnal. IV, 14071 Córdoba, Spain*

† Electronic supplementary information (ESI) available: Synthesis, NMR, powder XRD, elemental analysis, IR, TGA, gas sorption and selectivity. See DOI: 10.1039/c6ta00638h

defined CTF materials with surface areas up to 1452 m^2 g^{-1}.[23,24] Friedel–Crafts catalysis offers the significant advantages of cheap, easy handling, low reaction temperature, facile synthesis conditions and high yield materials with high surface areas.

Here, the porous frameworks CTF-TPC and CTF-FL were synthesized by Friedel–Crafts reactions between the "linkers" triptycene or fluorene with cyanuric chloride as the "node" in the presence of anhydrous $AlCl_3$ as the catalyst in dichloromethane (Scheme 1, see ESI† for details). After purification, the insoluble materials (Fig. S1 in the ESI†) were reproducibly collected in yields greater 80%. The strong triazine electrophile formed by $AlCl_3$, results in the electrophilic aromatic substitution on triptycene or fluorene to give the triazine frameworks. Network formation was supported by FT-IR (Fig. 1) and ^{13}C MAS or ^{13}C cross-polarization with magnetic angle spinning (CP-MAS) NMR spectroscopy (Fig. S2 and S3, ESI†). The absence of a C–Cl stretching band at 849 cm^{-1} suggested that there was no cyanuric chloride left in the materials.[24] The absorption band of the triazine ring is shifted from 1352 cm^{-1} in cyanuric chloride to 1384 cm^{-1} in CTF-TPC and 1346 cm^{-1} in CTF-FL (see Section 6 in the ESI† for comparative literature data).[25]

The signals in the solid-state ^{13}C CP/MAS NMR spectra are in the expected range (Fig. S2 and S3, ESI†),[26–28] which suggests the formation of triazine-based frameworks. CTF-TPC shows a chemical shift at 51 ppm, corresponding to the bridgehead carbons of the triptycene unit. The signals of the phenyl ring of triptycene are in the range of 120–150 ppm, the triazine ring carbons appear at 164 ppm. CTF-FL shows a peak at 37 ppm, which can be assigned to the methylene bridge carbon in the fluorene unit. The other major peaks from 115 ppm to 150 ppm correspond to the aromatic carbons in the fluorene unit; a peak for the triazine ring carbons is detected at 172 ppm.

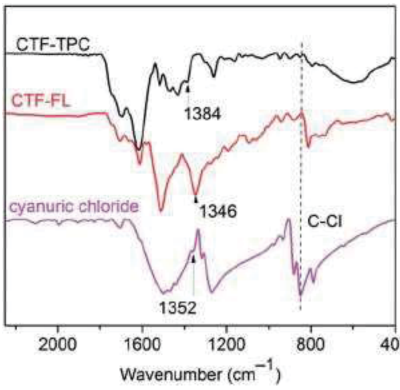

Fig. 1 FT-IR spectra of CTF-TPC and CTF-FL in comparison to that of cyanuric chloride, with proposed triazine bands labelled.

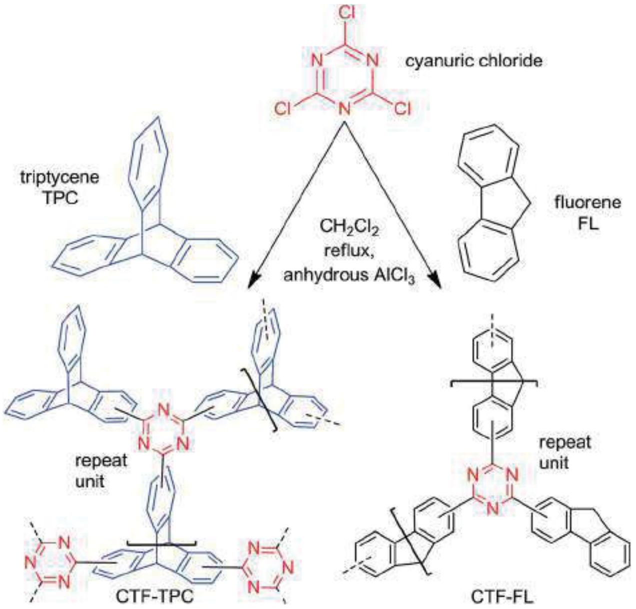

Scheme 1 Synthesis route and model structures for CTF-TPC and CTF-FL (based on elemental analysis, see Section 5 in the ESI†). Both models have a terminal and two bridging ligands for each triazine C_3N_3 ring. For CTF-TPC we do not assume the formation of a symmetric network because of the different possible positions for acylation on the TPC aryl rings. For CTF-FL we assume the formation of a polymer chain which can be crosslinked if the terminal FL occasionally also becomes bridged.

The amorphous nature of the products was assessed by PXRD (Fig. S4, ESI†). The diffractograms show only three broad bands around 17, 30 and 40° 2theta. From TGA, it can be observed that CTF-TPC and CTF-FL start to decompose under an O_2 atmosphere at 380 and 360 °C, respectively (Fig. S5, ESI†). Scanning electron microscopy (SEM) reveals aggregation of spherical particles (Fig. 2).

The porosities of the activated CTFs (degassing at 200 °C for 24 h) were characterized by N_2 sorption measurements at 77 K. The N_2 adsorption isotherm of CTF-TPC exhibits a steep increase in N_2 uptake at low p/p_0 values, and continues to increase at high pressure values. Therefore, the curve could be classified as a combination of types I and IV. The H_4 type hysteresis is often associated with narrow slit-like pores but the type I character indicates microporosity.[29] On the other hand, the isotherm of CTF-FL is only of type I with H_4 type hysteresis. The Brunauer–Emmett–Teller (BET) surface areas (pressure range of $p/p_0 = 0.01–0.05$) of CTF-TPC and CTF-FL are 1668 and 773 m^2 g^{-1}, respectively. BET measurements of three other batches each confirmed the reproducibility of the results

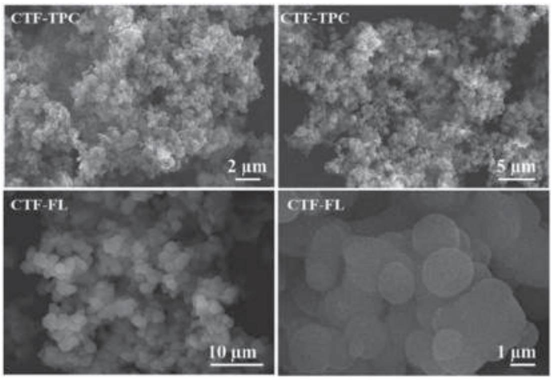

Fig. 2 Scanning electron micrographs (SEM) of CTF-TPC and CTF-FL.

Table 1 Porosity data for CTF-TPC and CTF-FL

Compound	$S_{BET}{}^{a}$ (m^2 g^{-1})	$S_{Lang}{}^{b}$ (m^2 g^{-1})	$V_{0.1}{}^{c}$ (cm^3 g^{-1})	$V_{tot}{}^{d}$ (cm^3 g^{-1})	$V_{0.1}/V_{tot}$	$V_{micro}(CO_2)^{e}$ (cm^3 g^{-1})
CTF-TPC	1668	2041	0.65	0.93	0.70	0.11
CTF-FL	773	936	0.31	0.39	0.79	0.11

[a] Calculated BET surface area over the pressure range of 0.01–0.05p/p_0 values for batches from repeated syntheses are given in Table S4 in the ESI. [b] Langmuir surface area over the pressure range of 0–110 torr. [c] Micropore volume calculated from the N_2 adsorption isotherm at $p/p_0 = 0.1$ for pores ≤2 nm (20 Å). [d] Total pore volume at $p/p_0 = 0.95$ for pores ≤20 nm. [e] Total pore volume for pores with diameters smaller than 1 nm (10 Å, *cf.* Fig. S7, ESI) from the CO_2 NL-DFT model at 273 K.

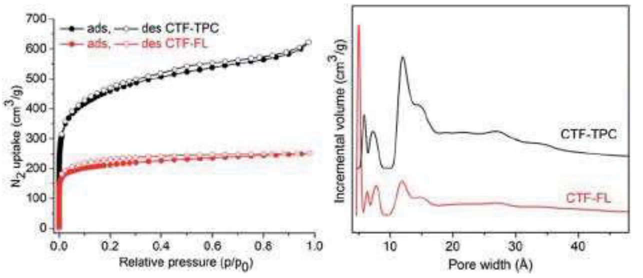

Fig. 3 Nitrogen adsorption–desorption isotherms at 77 K (left) of CTF-TPC and CTF-FL and NLDFT pore size distribution (PSD) curve (right) of CTF-TPC and CTF-FL.

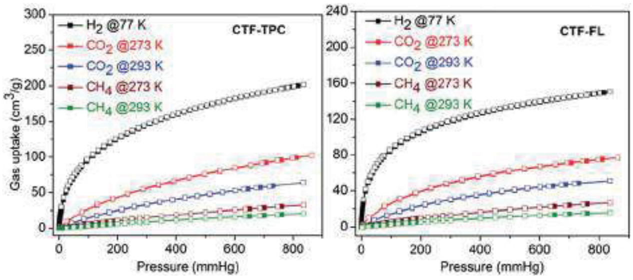

Fig. 4 Gas sorption isotherms of CTF-TPC (left) and CTF-FL (right) (filled symbols for adsorption, empty symbols for desorption).

(Table S4, ESI†). The surface areas are comparable with those of other CTFs (Table S8, ESI†). To the best of our knowledge, the surface area of CTF-TPC, synthesized by $AlCl_3$, exceeds all reported values for similar networks. The surface area of CTF-FL is lower than that of the previously reported fluorene-based CTFs synthesized by $ZnCl_2$.[27] In agreement with the type I isotherms the ratio of micropore volume to total pore volume ($V_{0.1}/V_{tot}$) is in the range of 70–79% (Table 1). Pore size distributions by non-local density functional theory (NLDFT) using the model of "N_2 on carbon, slit-pores method" gave a narrow distribution of micropores centered at 5.9, 7.3, 11.8 and 14.8 Å for CTF-TPC, and 5, 6.4, 8 and 11.8 Å for CTF-FL (Fig. 3). However, a low proportion of mesopores was observed around ~27 Å for both CTFs in agreement with the H_4 hysteresis of the N_2 isotherms.

The H_2 sorption of CTF-TPC and CTF-FL (Table 2 and Fig. 4) is comparable to that of many reported CTF materials.[21a,27,30,31] The CO_2 adsorption of 95.2 cm^3 g^{-1} (4.24 mmol g^{-1}) for CTF-TPC and of 73.2 cm^3 g^{-1} (3.26 mmol g^{-1}) for CTF-FL (Tables 2 and S5, ESI†) agrees with the published data for other CTFs such as FL-CTF (1.27–4.28 mmol g^{-1}),[26a] FCTF-1 (4.67–5.53 mmol g^{-1}),[32] CTF-0 (4.22 mmol g^{-1}),[33] CTF-1 (2.47–3.82 mmol g^{-1}),[32] CTF-Pl–P6 (1.88–3.39 mmol g^{-1}),[22] CTF-P1M–P6M (0.94–4.42 mmol g^{-1}),[22] MCTF-300–500 (2.25–3.16 mmol g^{-1}),[34] PCTF-1–7 (1.85–3.26 mmol g^{-1})[31] and NOP-1–6 (1.31–2.51 mmol g^{-1})[30] (see Table S8 in the ESI† for details). The isosteric heats of adsorption (Q_{st}) from the CO_2 adsorption isotherms at 273 and 298 K near zero loading are 32 and 35 kJ mol^{-1} for CTF-TPC and -FL, respectively (Fig. S6, ESI†), and are again comparable to those of other CTFs (see Section 11 in the ESI†). Upon increasing the loading the Q_{st} values decrease to 26 and 28 kJ mol^{-1} for CTF-TPC and CTF-FL, respectively, which are, however, still well above the heat of liquefaction of bulk CO_2 with 17 kJ mol^{-1}. The high Q_{st} value can be attributed to the high polar framework and the pore size effect. The high adsorption enthalpy at zero coverage is explained by the initial filling of the small ultramicropores with 4 Å diameter (Fig. S7†) with adsorbate–surface interactions to both sides or ends of the CO_2 molecules.

The CH_4 uptake capacities of CTF-TPC and CTF-FL (Fig. 4, Tables 2 and S5 in the ESI†) are comparable with the values for PCTF-1 to -7 from our previous work as well as other CTFs.[24,31] The gas sorption capacity for CH_4 of CTFs follows the increase in surface area and pore volume (Table 1).

Table 2 Gas uptake at 1 bar and selectivity data for CTF-TPC and CTF-FL

Compound	$H_2{}^{a}$ (cm^3 g^{-1})	$CO_2{}^{b}$ (cm^3 g^{-1})	$Q^0_{ads}(CO_2)^{c}$ (kJ mol^{-1})	$CH_4{}^{b}$ (cm^3 g^{-1})	$N_2{}^{b}$ (cm^3 g^{-1})	$CO_2 : N_2{}^{d}$ Henry	$CO_2 : N_2{}^{d}$ IAST
CTF-TPC	195.8	95.2	32	30	9.2	20	30
CTF-FL	146.6	73.2	35	24.9	7.1	25	48

[a] Gas uptake at 77 K. [b] At 273 K. [c] Heat of adsorption for CO_2 at zero loading from adsorption isotherms acquired at 273 and 293 K. [d] Gas selectivity calculated at 273 K.

From the available single-gas adsorption isotherms, the CO_2 selectivities over N_2 or CH_4 for CTF-TPC and CTF-FL were calculated at 273 and 293 by using the Henry equation and the ideal adsorbed solution theory (IAST). From the Henry equation, the adsorption selectivity for CO_2 over N_2 is 20 and 25 at 273 K (16 and 21 at 293 K) for CTF-TPC and CTF-FL, respectively, whereas the corresponding CO_2/CH_4 selectivities were in the range of 4–5 at 273 K and 293 K (Fig. S8 and S9 in the ESI; Tables 2 and S5 in the ESI†). From IAST (Fig. S10, S11 and Tables S6, S7 in the ESI†), the CO_2/N_2 selectivities of CTF-TPC and CTF-FL are 30 and 48 at 273 K (Table 2), which are higher than from the Henry calculation. The selectivity of CTF-FL is high compared with recent work by others.[27] A trade-off relation is observed for the CO_2/N_2 selectivity *versus* porosity: a higher surface area of CTF-TPC (compared to CTF-FL) exhibits lower selectivity, as can be generalized for other CTF-based polymers (see Table S8 in the ESI†).

In summary, the $AlCl_3$ catalyzed Friedel–Crafts reaction can be used for the aromatic linkers triptycene and fluorene to construct triazine-based frameworks. By using this approach, the compound CTF-TPC with 1668 $m^2\ g^{-1}$ gave the highest BET surface area found for such $AlCl_3$-catalyzed cyanuric-chloride based CTFs, so far. It is suggested that the triptycene unit is especially amenable to construct high surface-area porous materials.[35] CTF-TPC and CTF-FL adsorbed 4.24 mmol g^{-1} and 3.26 mmol g^{-1} (273 K/1 bar) of CO_2, respectively. Such high CO_2 uptake together with cost-effective synthesis make CTFs a promising candidate for porous adsorbents. Porosity and gas adsorption behavior can be tuned by changing the linker in this cyanuric-acid/$AlCl_3$-catalysis approach.

Acknowledgements

Support of the work by BMBF project OptiMat 03SF0492C and by the University of Düsseldorf through its strategic research fund (SFF) is gratefully acknowledged. We thank Mrs J. Dechnik, Mrs L. Schmolke, Mr D. Dietrich, Mr S. Glomb, Mr Hastürk and Mr P. Roloff for their help in analytical measurements.

Notes and references

1 R. S. Haszeldine, *Science*, 2009, **325**, 1647.

2 K. Sumida, D. L. Rogow, J. A. Mason, T. M. McDonald, E. D. Bloch, Z. R. Herm, T.-H. Bae and J. R. Long, *Chem. Rev.*, 2012, **112**, 724–781; H. He, W. Li, M. Zhong, D. Konkolewicz, D. Wu, K. Yaccato, T. Rappold, G. Sugar, N. E. David and K. Matyjaszewski, *Energy Environ. Sci.*, 2013, **6**, 488–493.

3 D. M. D'Alessandro, B. Smit and J. R. Long, *Angew. Chem., Int. Ed.*, 2010, **49**, 6058–6082.

4 J. A. Mason, T. M. McDonald, T.-H. Bae, J. E. Bachman, K. Sumida, J. J. Dutton, S. S. Kaye and J. R. Long, *J. Am. Chem. Soc.*, 2015, **137**, 4787–4803.

5 G. T. Rochelle, *Science*, 2009, **325**, 1652–1654; U. Desideri and A. Paolucci, *Energy Convers. Manage.*, 1999, **40**, 1899–1915.

6 J. Zhang, P. A. Webley and P. Xiao, *Energy Convers. Manage.*, 2008, **49**, 346–356.

7 (*a*) G. Qi, Y. Wang, L. Estevez, X. Duan, N. Anako, A.-H. A. Park, W. Li, C. W. Jones and E. P. Giannelis, *Energy Environ. Sci.*, 2011, **4**, 444–452; (*b*) J. C. Hicks, J. H. Drese, D. J. Fauth, M. L. Gray, G. Qi and C. W. Jones, *J. Am. Chem. Soc.*, 2008, **130**, 2902–2903.

8 L. Wang and R. T. Yang, *J. Phys. Chem. C*, 2012, **116**, 1099–1106.

9 V. Guillerm, L. J. Weselinski, M. Alkordi, M. I. H. Mohideen, Y. Belmabkhout, A. J. Cairns and M. Eddaoudi, *Chem. Commun.*, 2014, **50**, 1937–1940; S. Mondal and N. Das, *J. Mater. Chem. A*, 2015, **3**, 23577–23586; G. Liu, Y. Wang, C. Shen, Z. Ju and D. Yuan, *J. Mater. Chem. A*, 2015, **3**, 3051–3058.

10 M. G. Rabbani and H. M. El-Kaderi, *Chem. Mater.*, 2012, **24**, 1511–1517.

11 J. Germain, J. Hradil, J. M. J. Fréchet and F. Svec, *Chem. Mater.*, 2006, **18**, 4430–4435.

12 B. S. Ghanem, K. J. Msayib, N. B. McKeown, K. D. M. Harris, Z. Pan, P. M. Budd, A. Butler, J. Selbie, D. Book and A. Walton, *Chem. Commun.*, 2007, 67–69.

13 H. Zhao, Z. Jin, H. Su, J. Zhang, X. Yao, H. Zhao and G. Zhu, *Chem. Commun.*, 2013, **49**, 2780–2782.

14 J.-X. Jiang, F. Su, A. Trewin, C. D. Wood, N. L. Campbell, H. Niu, C. Dickinson, A. Y. Ganin, M. J. Rosseinsky, Y. Z. Khimyak and A. I. Cooper, *Angew. Chem., Int. Ed.*, 2007, **46**, 8574–8578.

15 (*a*) S.-Y. Ding and W. Wang, *Chem. Soc. Rev.*, 2013, **42**, 548–568; (*b*) Introduction to themed issue on COFs: A. I. Cooper, *CrystEngComm*, 2013, **15**, 1483; (*c*) S. Kandambeth, A. Mallick, B. Lukose, M. V. Mane, T. Heine and R. Banerjee, *J. Am. Chem. Soc.*, 2012, **134**, 19524–19527; (*d*) T. Ben, H. Ren, S. Ma, D. Cao, J. Lan, X. Jing, W. Wang, J. Xu, F. Deng, J. M. Simmons, S. Qiu and G. Zhu, *Angew. Chem., Int. Ed.*, 2009, **48**, 9457–9460; (*e*) S. Dalapati, S. Jin, J. Gao, Y. Xu, A. Nagai and D. Jiang, *J. Am. Chem. Soc.*, 2013, **135**, 17310–17313; (*f*) S. Nandi, U. Werner-Zwanziger and R. Vaidhyanathan, *J. Mater. Chem. A*, 2015, **3**, 21116–21122.

16 M. Shunmughanathan, P. Puthiaraj and K. Pitchumani, *ChemCatChem*, 2015, **7**, 666–673.

17 R. Gomes, P. Bhanja and A. Bhaumik, *Chem. Commun.*, 2015, **51**, 10050–10053.

18 L.-B. Sun, A.-G. Li, X.-D. Liu, X.-Q. Liu, D. Feng, W. Lu, D. Yuan and H.-C. Zhou, *J. Mater. Chem. A*, 2015, **3**, 3252–3256.

19 M. Rose, W. Bohlmann, M. Sabo and S. Kaskel, *Chem. Commun.*, 2008, 2462–2464.

20 M. Nandi, K. Okada, A. Dutta, A. Bhaumik, J. Maruyama, D. Derks and H. Uyama, *Chem. Commun.*, 2012, **48**, 10283–10285.

21 (*a*) P. Kuhn, M. Antonietti and A. Thomas, *Angew. Chem., Int. Ed.*, 2008, **47**, 3450–3453; (*b*) P. Kuhn, A. l. Forget, D. Su, A. Thomas and M. Antonietti, *J. Am. Chem. Soc.*, 2008, **130**, 13333–13337.

22 S. Ren, M. J. Bojdys, R. Dawson, A. Laybourn, Y. Z. Khimyak, D. J. Adams and A. I. Cooper, *Adv. Mater.*, 2012, **24**, 2357–2361.

23 H. Lim, M. C. Cha and J. Y. Chang, *Macromol. Chem. Phys.*, 2012, **213**, 1385–1390.

24 P. Puthiaraj, S.-M. Cho, Y.-R. Lee and W.-S. Ahn, *J. Mater. Chem. A*, 2015, **3**, 6792–6797.

25 (*a*) S. K. Kundu and A. Bhaumik, *RSC Adv.*, 2015, **5**, 32730–32739; (*b*) C. Bai, M. Zhang, B. Li, Y. Tian, S. Zhang, X. Zhao, Y. Li, L. Wang, L. Ma and S. Li, *J. Hazard. Mater.*, 2015, **300**, 368–377; (*c*) P. Puthiaraj, S.-S. Kim and W.-S. Ahn, *Chem. Eng. J.*, 2016, **283**, 184–192.

26 (*a*) C. Zhang, Y. Liu, B. Li, B. Tan, C.-F. Chen, H.-B. Xu and X.-L. Yang, *ACS Macro Lett.*, 2012, **1**, 190–193; (*b*) C. Zhang, T.-L. Zhai, J.-J. Wang, Z. Wang, J.-M. Liu, B. Tan, X.-L. Yang and H.-B. Xu, *Polymer*, 2014, **55**, 3642–3647.

27 S. Hug, M. B. Mesch, H. Oh, N. Popp, M. Hirscher, J. Senker and B. V. Lotsch, *J. Mater. Chem. A*, 2014, **2**, 5928–5936.

28 S. Kuecken, J. Schmidt, L. Zhi and A. Thomas, *J. Mater. Chem. A*, 2015, **3**, 24422–24427.

29 M. Thommes, K. Kaneko, A. V. Neimark, J. P. Olivier, F. Rodriguez-Reinoso, J. Rouquerol and K. S. W. Sing, *Pure Appl. Chem.*, 2015, **87**, 1051–1069.

30 S. Xiong, X. Fu, L. Xiang, G. Yu, J. Guan, Z. Wang, Y. Du, X. Xiong and C. Pan, *Polym. Chem.*, 2014, **5**, 3424–3431.

31 (*a*) A. Bhunia, V. Vasylyeva and C. Janiak, *Chem. Commun.*, 2013, **49**, 3961–3963; (*b*) A. Bhunia, I. Boldog, A. Möller and C. Janiak, *J. Mater. Chem. A*, 2013, **1**, 14990–14999.

32 Y. Zhao, K. X. Yao, B. Teng, T. Zhang and Y. Han, *Energy Environ. Sci.*, 2013, **6**, 3684–3692.

33 P. Katekomol, J. Roeser, M. Bojdys, J. Weber and A. Thomas, *Chem. Mater.*, 2013, **25**, 1542–1548.

34 X. Liu, H. Li, Y. Zhang, B. Xu, S. A, H. Xia and Y. Mu, *Polym. Chem.*, 2013, **4**, 2445–2448.

35 (*a*) G. Zhang, O. Presly, F. White, I. M. Oppel and M. Mastalerz, *Angew. Chem., Int. Ed.*, 2014, **53**, 1516–1520; (*b*) G. Zhang, O. Presly, F. White, I. M. Oppel and M. Mastalerz, *Angew. Chem., Int. Ed.*, 2014, **53**, 5126–5130; (*c*) S. M. Elbert, F. Rominger and M. Mastalerz, *Chem.–Eur. J.*, 2014, **20**, 16707–16720.

Electronic Supplementary Material (ESI) for Journal of Materials Chemistry A.
This journal is © The Royal Society of Chemistry 2016

Covalent triazine-based frameworks (CTFs) from triptycene and fluorene motif for CO_2 adsorption

Subarna Dey,[a] Asamanjoy Bhunia,[a] María Dolores Esquivel[b] and Christoph Janiak*[a]

[a]Institut für Anorganische Chemie und Strukturchemie, Heinrich-Heine-Universität Düsseldorf, 40204 Düsseldorf, Germany.

[b]Department of Organic Chemistry, Nanochemistry and Fine Chemistry Research Institute (IUIQFN), Faculty of Sciences, University of Córdoba, Campus de Rabanales, Marie Curie Building, Ctra. Nnal. IV, 14071 Córdoba, Spain. Email: q12esmem@uco.es

* Corresponding author: E-mail: janiak@uni-duesseldorf.de; Fax: + 49-211-81-12287; Tel: +49-211-81-12286.

Table of contents

1. Materials and methods

All chemicals were purchased from commercial suppliers (Sigma-Aldrich, Acros Organics, and Alfa Aesar chemical company) and used without further purification, unless stated otherwise. Dry dichloromethane (DCM) was collected from an MBraun solvent purification (drying) system under N_2 atmosphere and used for CTF synthesis.

Infrared (IR) spectra were obtained on a Bruker FT-IR Tensor 37 Spectrometer in the 4000-550 cm^{-1} region with 2 cm^{-1} resolution as KBr disks. ^1H and ^{13}C spectra were recorded on an Avance DRX-500 instrument. ^1H and ^{13}C NMR chemical shifts are given in ppm relative to $SiMe_4$ ($\delta = 0.0$ ppm) with calibration against the (residual protonated) solvent signal ($CDCl_3$: 7.26 (^1H) and 77.0 (^{13}C)). Elemental (CNH) analyses were carried out with a PerkinElmer 2400 series 2 elemental analyzer. Powder X-ray diffraction (PXRD) data was collected on a Bruker D2 Phaser diffractometer using a flat sample holder (also a flat silicon, low background sample holder) and Cu $K\alpha_1/\alpha_2$ radiation with $\lambda = 1.5418$ Å at 30 kV covering 2theta angles 5-80° over a time of 2 h, that is. 0.01°/sec. Diffractograms were obtained on flat layer sample holders where at low angle the beam spot is strongly broadened so that only a fraction of the reflected radiation reaches the detector, which leads to low relative intensities measured at $2\theta < 7°$. For hygroscopic or air-sensitive samples, the sample holder can be sealed with a dome. Scanning electron microscopy (SEM) images were obtained using an ESEM Quanta 400 FEG SEM equipped with a secondary electron detector. Thermogravimetric analyses (TGA) were carried out at a ramp rate of 5 °C/min in a N_2 flow with a Netzsch Thermo-Microbalance Aparatus TG 209 F3 Tarsus. The solid-state ^{13}C CP/MAS NMR spectrum was recorded on a Bruker Avance 400 WB spectrometer at 100.61 MHz. The samples were spun at 13 kHz. An overall 10000 free induction decays were accumulated. The excitation pulse and recycle time for ^{13}C CP/MAS NMR were 6 ms and 2 s, respectively.

Sorption isotherms were measured using a Micromeritics ASAP 2020 automatic gas sorption analyzer equipped with oil-free vacuum pumps (ultimate vacuum $<10^{-8}$ mbar) and valves, which guaranteed contamination free measurements. The sample was connected to the preparation port of the sorption analyzer and degassed under vacuum until the outgassing rate, i.e., the rate of pressure rise in the temporarily closed manifold with the connected sample tube, was less than 2 µTorr/min at the specified temperature 200 °C. After weighing, the sample tube was then transferred to the analysis port of the sorption analyzer. All used gases (H_2, He, N_2, CO_2, CH_4) were of ultra-high purity (UHP, grade 5.0, 99.999%) and the STP volumes are given according to the NIST standards (293.15 K, 101.325 kPa). Helium gas was used for the determination of the cold and warm free space of the sample tubes. H_2 and N_2 sorption isotherms were measured at 77 K (liquid nitrogen bath), whereas CO_2 and CH_4 sorption isotherms were measured at 293±1 K (passive thermostating) and 273.15 K (ice/deionized water bath). The heat of adsorption values and the DFT pore size distributions ('N_2 DFT slit pore' model) were calculated out using the ASAP 2020 v3.05 software. Nitrogen sorption isotherms were also obtained on a Quantachrome Nova 4000e at 77 K.

2. Syntheses of CTFs

CTF-TPC: In a typical synthesis, a mixture of triptycene (257 mg, 1.0 mmol), cyanuric chloride (184 mg, 1.0 mmol) and anhydrous $AlCl_3$ (400 mg, 3 mmol) was refluxed in 100 mL of DCM for 16 h. After cooling to room temperature, the orange-colored product was isolated by filtration and washed with water (3 × 50 mL), MeOH (3 × 50 mL), THF (3 × 50 mL), acetone (3 × 50 mL), and dried in vacuum for 12 h. Yield: 0.310 g, 94%.

CTF-FL: A mixture of fluorene (249 mg, 1.5 mmol), cyanuric chloride (184 mg, 1.0 mmol) and anhydrous $AlCl_3$ (600 mg, 4.5 mmol) was refluxed in 100 mL of DCM for 16 h. After cooling to room temperature, the brown-colored product was isolated by filtration and washed with water (3 × 50 mL), MeOH (3 × 50 mL), THF (3 × 50 mL), acetone (3 × 50 mL), and dried in vacuum for 12 h. Yield: 0.302 g, 93%

After drying the samples were cooled down in ambient air and stored in closed vials under air.

Table S1: Yield of the CTF-TPC and CTF-FL for different batches.

No. of batches	CTF-TPC					CTF-FL			
	Triptycene (mg)	Cyanuric chloride (mg)	Yield			Fluorene (mg)	Cynuric chloride (mg)	Yield	
			(mg)	(%)				(mg)	(%)
Batch 1	257	184	310	94		250	185	302	93
Batch 2	257	187	287	87		249	184	280	86
Batch 3	258	188	302	91		249	184	272	84
Batch 4	254	184	297	90		249	184	294	90

(washing with base)									

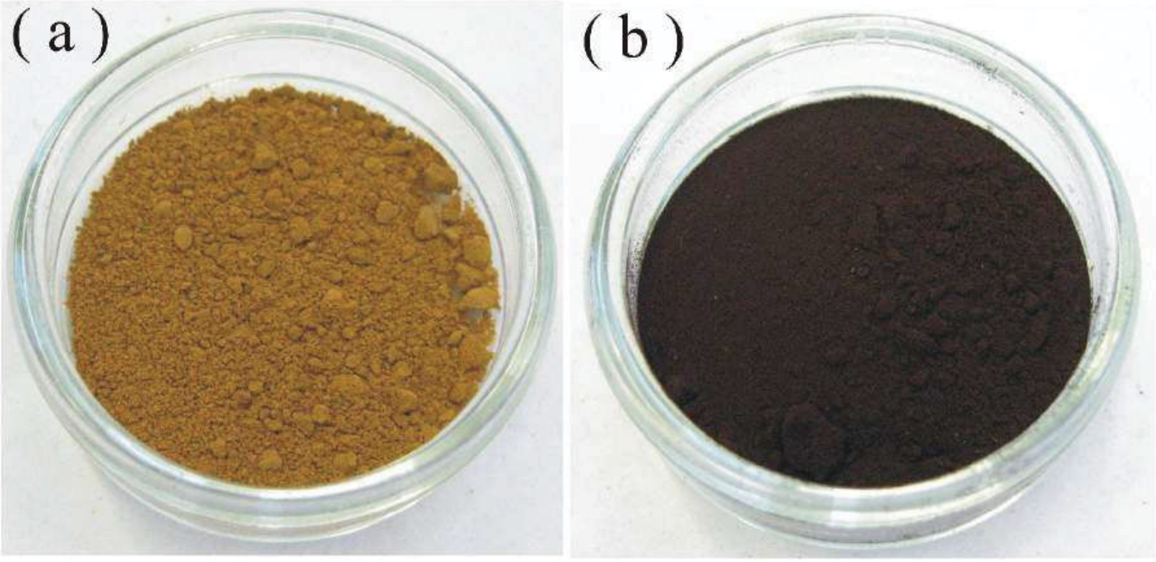

Fig. S1: (a) Photograph of CTF-TPC; (b) photograph of CTF-FL.

3. Solid state NMR

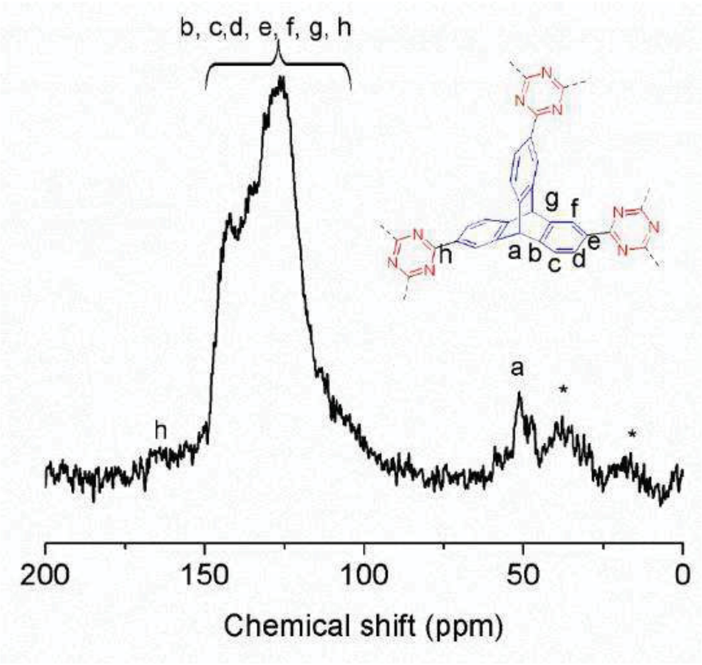

Fig. S2: Solid-state ^{13}C MAS NMR spectrum of CTF-TPC (*spinning sidebands).

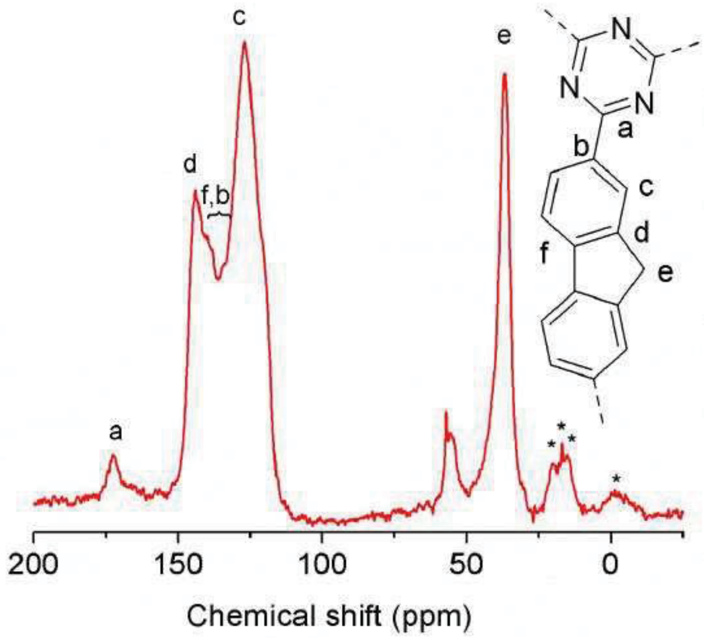

Fig. S3: Solid-state ^{13}C CP/MAS NMR spectrum of CTF-FL (*spinning sidebands).

4. Powder X-ray diffraction patterns

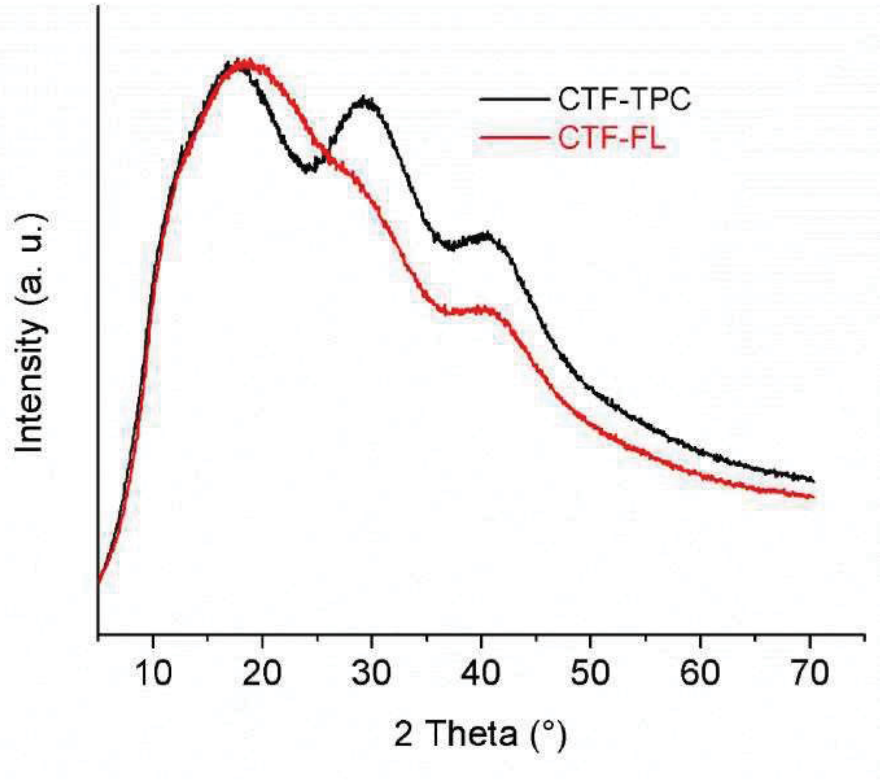

Fig. S4: Powder X-ray patterns of CTF-TPC and CTF-FL.

5. Elemental analysis of CTF-TPC and CTF-FL and formula unit

Table S2 Elemental analysis of CTF materials obtained in this study.[a]

Compound	**Found (wt%)**							
	C	**H**	**N**	**atom C/H**	**atom C/N**	**O**	**Al**	**Cl**
CTF-TPC (batch 1)	77.82	4.44	3.41	1.5	27			
CTF-TPC (batch 2), CHN	71.10	4.80	3.38	1.2	24			
- from EDX [b] +4.5% H	(78.6) 75.2	n.d. 4.3	(4.4) 4.2			(16.5) 15.8	(0.07) 0.07	(0.5) 0.5
CTF-TPC (batch 3), CHN	77.58	4.44	3.35	1.4	27			
- from EDX [b] +4.5% H	(78.7) 75.3	n.d. 4.3	(3.7) 3.5			(16.5) 15.8	(0.4) 0.4	(0.7) 0.7
CTF-TPC (batch 4)	(67.61)[c]	4.25	3.39	1.3	23.2			
average CHN + EDX w. H	75.4	4.4	3.5			15.8	0.2	0.6
CTF-FL (batch 1)	78.18	4.88	7.37	1.3	12			
CTF-FL (batch 2)	76.1	5.27	7.13	1.2	12.4			
CTF-FL (batch 3), CHN	72.95	4.21	5.07	1.4	16.7			
- from EDX [b] +5% H	(76.2) 72.6	n.d. 4.8	(5.8) 5.5			(15.5) 14.8	(0.4) 0.4	(2.1) 2
CTF-FL (batch 4), CHN	75.02	4.73	4.35	1.3	20.1			
- from EDX [b] (+5% H)	(77.8) 74.1	n.d. 4.8	(5.4) 5.1			(16.6) 15.8	0	(0.1) 0.1
average CHN + EDX w. H	74.8	4.8	5.8			15.3	0.2	1

[a] Elemental analysis of CTF-TPC and CTF-FL were measured after drying the materials at 150 °C under vacuum overnight. After drying the samples were cooled down in ambient air and stored in closed vials under air. Elemental analyses were carried out 1-3 days later. Combustion analysis unless noted otherwise.

[b] EDX = energy dispersive X-ray spectroscopy; percentage values are normalized to 100% for the found elements C, N, O, Al and Cl. Hydrogen cannot be detected by EDX. If about 4-5% of H would be included, then the given percentage values would be reduced as indicated. Standard deviations (1 sigma) for element wt% from EDX are at least 10%, hence, EDX values should be considered without decimal digits.

Noteworthy, combustion analysis and EDX agree rather well in their relative C and N content.

[c] excluded in average due to strong deviation from other values

Errors in combustion analysis can be excluded as commercially available triazine compounds gave the expected calculated values:

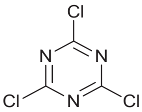

Calculated			**Found**		
C	**H**	**N**	**C**	**H**	**N**
19.54	0.00	22.79	18.91	0.4	22.86

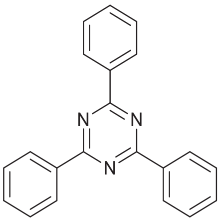

Calculated			**Found**		
C	**H**	**N**	**C**	**H**	**N**
81.53	4.89	13.58	81.58	5.03	13.60

CHN for possible model structures for CTF-TPC:

A) CTF-TPC with TPC ($C_{20}H_{14}$) bridging between three triazine rings:

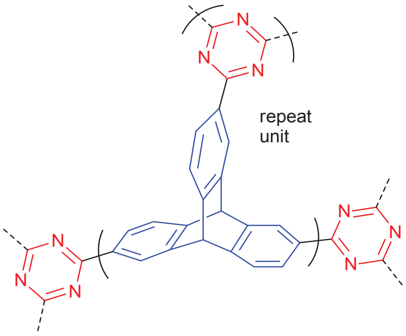

repeat unit: C_3N_3 + (TPC–3H)

C_3N_3+$C_{20}H_{11}$ = $C_{23}H_{11}N_3$; formula weight = 329.362 g/mol: **C 83.87, H 3.37, N 12.76%**

+3.5H_2O (16 wt%,see below): $C_{23}H_{18}N_3O_{3.5}$; M = 392.4 g/mol: **C 70.3, H 4.6, N 10.7**, O 14.3%

B) CTF-TPC with TPC ($C_{20}H_{14}$) terminal on each triazine ring and bridging between two triazine rings:

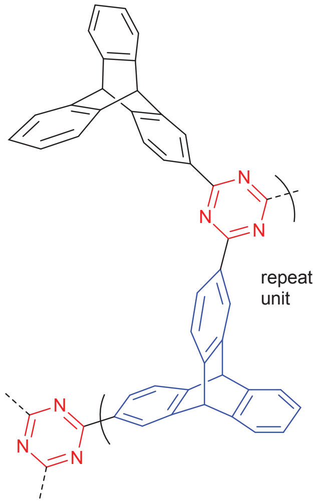

repeat unit: C_3N_3 + (TPC–H) + (TPC–2H)

C_3N_3+$C_{20}H_{13}$+$C_{20}H_{12}$ = $C_{43}H_{25}N_3$; M = 583.694 g/mol: **C 88.48, H 4.32, N 7.20%**

+5H_2O (13 wt%,see below): $C_{43}H_{35}N_3O_5$; M = 673.7 g/mol: **C 76.7, H 5.2, N 6.2**, O 11.9%

C) CTF-TPC with TPC ($C_{20}H_{14}$) terminal on each triazine ring and bridging between three triazine rings:

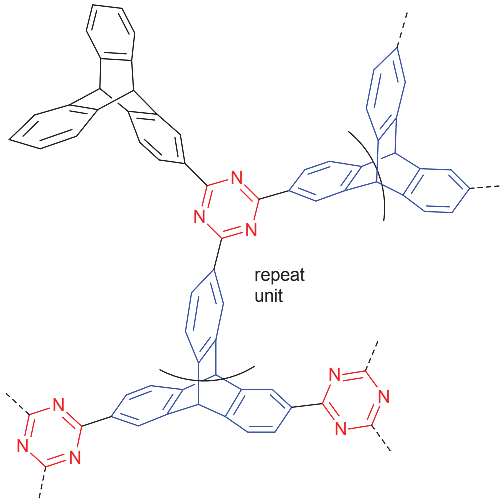

repeat unit: C_3N_3 + (TPC–H) + 2/3(TPC–3H)

C_3N_3+$C_{20}H_{13}$+2/3($C_{20}H_{11}$) = $C_{36.33}H_{20.33}N_3$; M = 498.873: **C 87.47, H 4.11, N 8.42%**

+5H_2O (15 wt%, see below): $C_{36.33}H_{30.33}N_3O_5$; M = 588.9 g/mol: **C 74.1, H 5.2, N 7.1**, O 13.6

CHN for possible model structures for CTF-FL:

A) CTF-FL with FL ($C_{13}H_{10}$) bridging between three triazine rings:

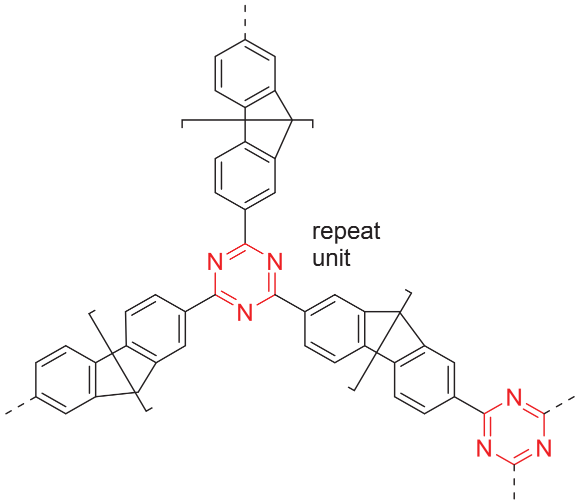

repeat unit: C_3N_3 + 3/2(FL–2H)

C_3N_3+3/2($C_{13}H_8$) = $C_{22.5}H_{12}N_3$; formula weight = 324.365 g/mol: **C 83.32, H 3.73, N 12.95%**

+3.5H_2O (16 wt%,see below): $C_{22.5}H_{19}N_3O_{3.5}$, M = 387.4 g/mol: **C 69.7, H 4.9, N 10.8,** O 14.4%

B) CTF-FL with FL terminal on each triazine ring and bridging between two triazine rings:

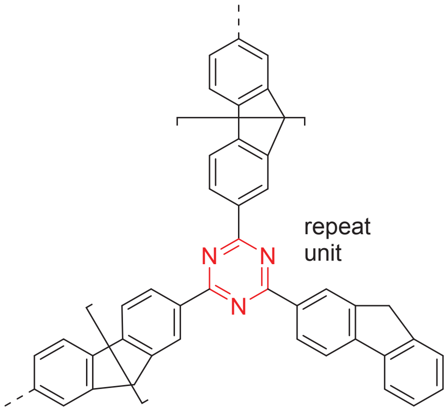

repeat unit: C_3N_3 + (FL–H) + (FL–2H)

C_3N_3+$C_{13}H_9$+$C_{13}H_8$ = $C_{29}H_{17}N_3$; M = 407.476 g/mol: **C 85.48, H 4.20, N 10.31%**

+4H_2O (15 wt%, see below): $C_{29}H_{25}N_3O_4$; M = 479.5: **C 72.6, H 5.2, N 8.8**, O13.3%

Without water the above models A-C still require higher C and N wt% than what has been experimentally determined (see Table S2). Hence, following the analyses for water (see below) we have added water molecules corresponding to about 15wt% for the calculations.

EDX agrees rather well in the C and N wt% with combustion CHN analysis and shows a high oxygen content of ~15%. EDX determined only minor impurities of Al (~0.2) and Cl (~0.6).

Note: The issue of lower than calculated nitrogen content in CTF materials is persistent throughout the literature (see columns in Table S3).

Table S3 CHN data of reported triazine-based frameworks from literature. [a]

Compound	**Reaction condition**	**Calculated**			**Found**			**Ref**
		C	**H**	**N**	**C**	**H**	**N**	
Pre-CTF	Trifluoromethanesulfonic acid	74.99	3.15	21.86	68.67	3.13	19.89	1
CTF	Chlorosulfonic acid	74.99	3.15	21.86	64.49	4.05	12.01	1
CTF [b]	Trifluoromethanesulfonic acid	74.99	3.15	21.86	61.34	3.52	12.82	1
TPOP-2	K_2CO_3	48.85[c]	6.83[c]	44.31[c]	41.83	6.58	36.27	2
CCTS	Dioxane	25.41[c]	2.61[c]	49.38[c]	24.9	3.55	43.75	3
CCTU	Dioxane	37.06[c]	3.49[c]	37.06[c]	26.23	2.63	32.1	3
CCU	Dioxane	34.59[c]	3.19[c]	48.4[c]	28.83	2.54	35.46	3
CTF-T1 [b]	Trifluoromethanesulfonic acid	74.99	3.15	21.86	59.97	4.53	16.44	4
PCTP-2	$AlCl_3$	79.24	0.94	13.2	75.68	2.04	6.17	5

[a] Entries are limited to "mild" synthesis routes and exclude the ionothermal CTFs from $ZnCl_2$ route.

[b] Same material synthesized by different groups using the same reaction conditions.

[c] Calculated by us.

References

1. S. Kuecken, J. Schmidt, L. Zhi and A. Thomas, *J. Mater. Chem. A*, 2015, **3**, 24422-24427.
2. S. K. Kundu and A. Bhaumik, *RSC Adv.*, 2015, **5**, 32730-32739.
3. C. Bai, M. Zhang, B. Li, Y. Tian, S. Zhang, X. Zhao, Y. Li, L. Wang, L. Ma and S. Li, *J. Hazard. Mater.*, 2015, **300**, 368-377.
4. J. Bi , W. Fang , L. Li, J. Wang, S. Liang, Y. He, M. Liu and L. Wu, *Macromol. Rapid Commun.*, 2015, **36**, 1799-1805.
5. P. Puthiaraj, S.-S. Kim and W.-S. Ahn, *Chem. Eng. J.*, 2016, **283**, 184–192.

In the literature of microporous organic polymers the often observed deviation from the expected CHN values is either not addressed at all or explained by "incomplete combustion and trapped adsorbates including gases and water vapor". (e.g. R. Dawson, T. Ratvijitvech, M. Corker, A. Laybourn, Y. Z. Khimyak, A. I. Cooper and D. J. Adams, *Polym. Chem.*, 2012, **3**, 2034-2038; G. Liu, Y. Wang, C. Shen, Z. Ju and D. Yuan, *J. Mater. Chem. A*, 2015, **3**, 3051–3058.)

Analyses for water content

In our case the high oxygen content was followed up with further analyses for water content or uptake:

Karl-Fischer titration (KFT):

A coulometric Karl-Fischer titration for the determination of the water content was carried out with a Karl-Fischer titration apparatus AQUA 40.00 with headspace module. The solid CTF sample was heated to 170 °C in the head space module and the liberated water transferred to the measurement cell.

Samples had been stored in closed vials under ambient air, following their synthesis and drying procedure.

Compound	Sample wt.(mg)	weight-% water
CTF-TPC (batch 1)	15.8	12.0 %
CTF-TPC (batch 2)	13.0	10.2 %
CTF-FL (batch 3)	17.5	12.3 %
CTF-FL (batch 4)	15.0	12.7 %

The water content by KFT for the CTF samples is determined to about 12 wt% which is in good agreement with the oxygen content (~15-16%) found by EDX, considering the larger error margins of EDX for light elements.

Weight uptake of dried sample:

A CTF-TPC sample was dried at 130 °C for 2 h in vacuum at 10^{-5} mbar.

This sample of 36 mg was placed on a scale in ambient air, just covered with a cabinet to avoid disturbance by ventilation. Over the time of 12 h the sample weight increased to ~40 mg. This is explained by water uptake from air.

Water sorption isotherms

Water physisorption isotherms were measured volumetrically on a Quantachrome Autosorb iQ MP at 293 K. For measuring the isotherms the materials were loaded into glass tubes capped with septa. The weighed tubes were attached to the corresponding degassing port of the sorption analyzer, degassed under vacuum (130 °C for 2 h at 10^{-5} mbar), weighed again and then transferred to the analysis port of the sorption analyzer.

Both samples show a water uptake of ~0.12-0.20 g/g (corresponding to 11-17 wt%) up to p/p_0 = 0.50.6 or 50-60% air humidity (typical for the climate in Düsseldorf). This quantifies the hygroscopic nature of the microporous material when stored under ambient air. The water uptake from water sorption isotherms is in agreement with values found from Karl-Fischer titration, with the value from weight uptake of dried sample and with the oxygen content by EDX.

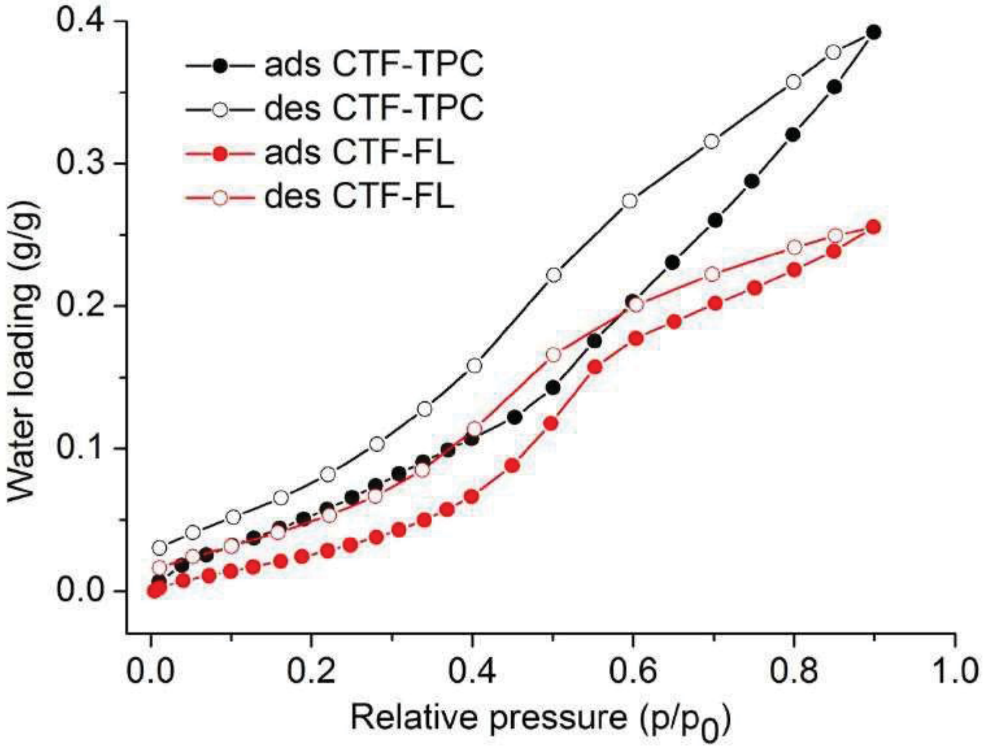

Water sorption isotherms for CTF-TPC and CTF-FL.

Based on the above elemental analyses we suggest

- for CTF-TPC model C – having TPC terminal TPC on each triazine ring and bridging between three triazine rings:

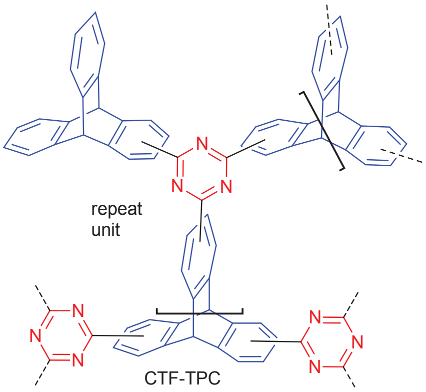

because of the different possible positions for acylation on the TPC aryl rings we do not assume the formation of a symmetric network.

- for CTF-FL model B - with FL terminal on each triazine ring and bridging between two triazine rings:

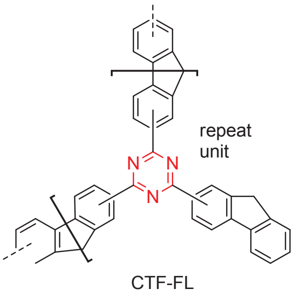

Thereby, we assume formation of a polymer chain which can be occasionally crosslinked if the terminal FL also becomes bridging.

6. Infrared spectroscopy

Comparison to recent literature data of CTF materials with respect to triazine absorption band:

Example 1: S. K. Kundu and A. Bhaumik, *RSC Adv.*, 2015, **5**, 32730-32739.

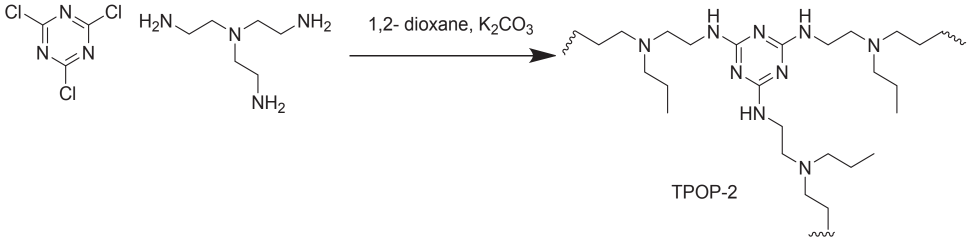

The FT IR spectrum of TPOP-2 shows stretching frequencies of around 1342 and 1572 cm^{-1} which are assigned to the triazine ring**.**

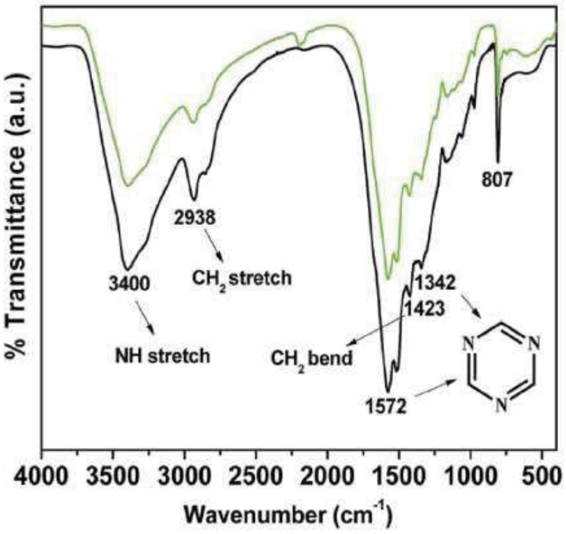

Fig. 4 (in above reference): FTIR spectrum of TPOP-2 (black line) and the reused organocatalyst after fourth reaction cycle (green line). (Figure and caption taken from ref. S. K. Kundu and A. Bhaumik, *RSC Adv.*, 2015, **5**, 32730-32739.

Example 2: P. Puthiaraj, S.-S. Kim and W.-S. Ahn, *Chem. Eng. J.*, 2016, **283**, 184-192.

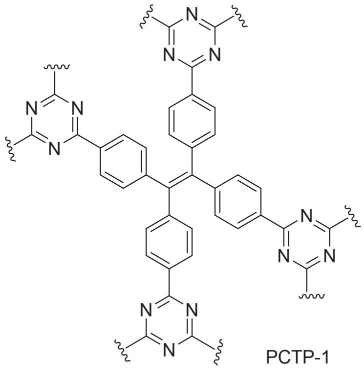

PCTP-1

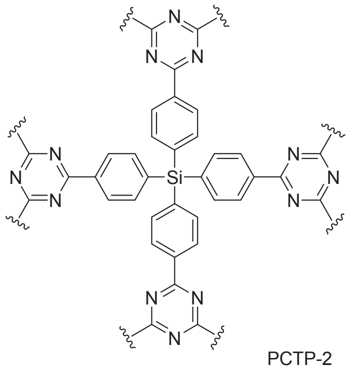

PCTP-2

The triazine weak bands were assigned at 1506–1480 (C=N) and 1386 cm^{-1} (C–N) in the network.

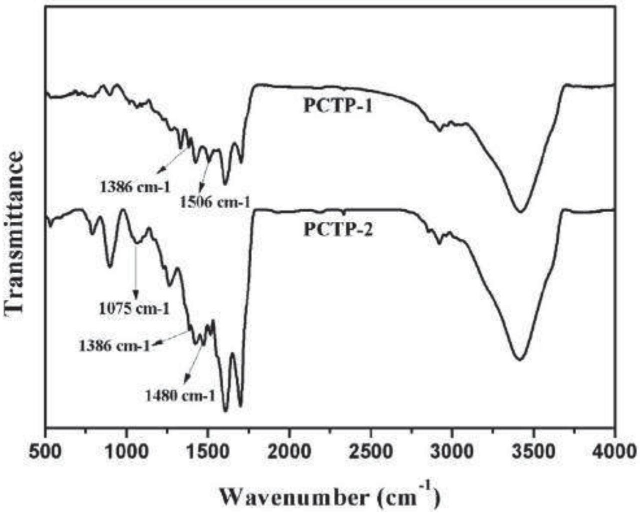

Fig. 1 (in above reference): FT-IR spectra of the PCTPs. (Figure and caption taken from ref. P. Puthiaraj, S.-S. Kim and W.-S. Ahn, *Chem. Eng. J.*, 2016, **283**, 184-192.

Example 3: C. Bai, M. Zhang, B. Li, Y. Tian, S. Zhang, X. Zhao, Y. Li, L. Wang, L. Ma and S. Li, *J. Hazard. Mater.*, 2015, **300**, 368-377.

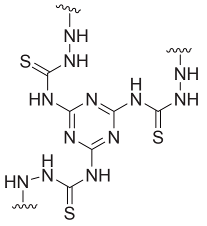

CCTS

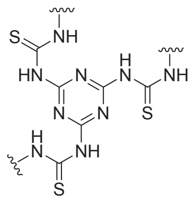

CCTU

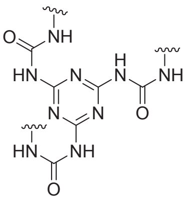

CCU

The typical bands at 1551 cm^{-1} in all IR spectra were assigned to the stretching modes of the aromatic C-N in the triazine unit.

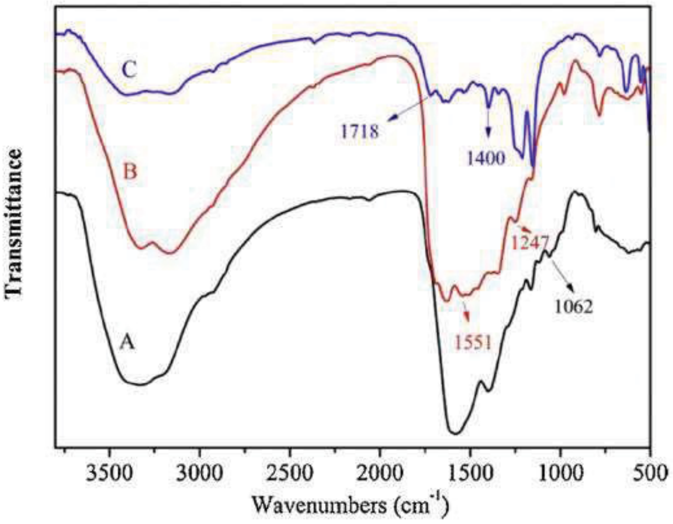

Fig. 1 (in above reference): FT-IR spectra of (A) CCTS, (B) CCTU, and (C) CCU. (Figure and caption taken from ref. C. Bai, M. Zhang, B. Li, Y. Tian, S. Zhang, X. Zhao, Y. Li, L. Wang, L. Ma and S. Li, *J. Hazard. Mater.*, 2015, **300**, 368-377.

7. Thermogravimetric analysis

CTF-TPC:

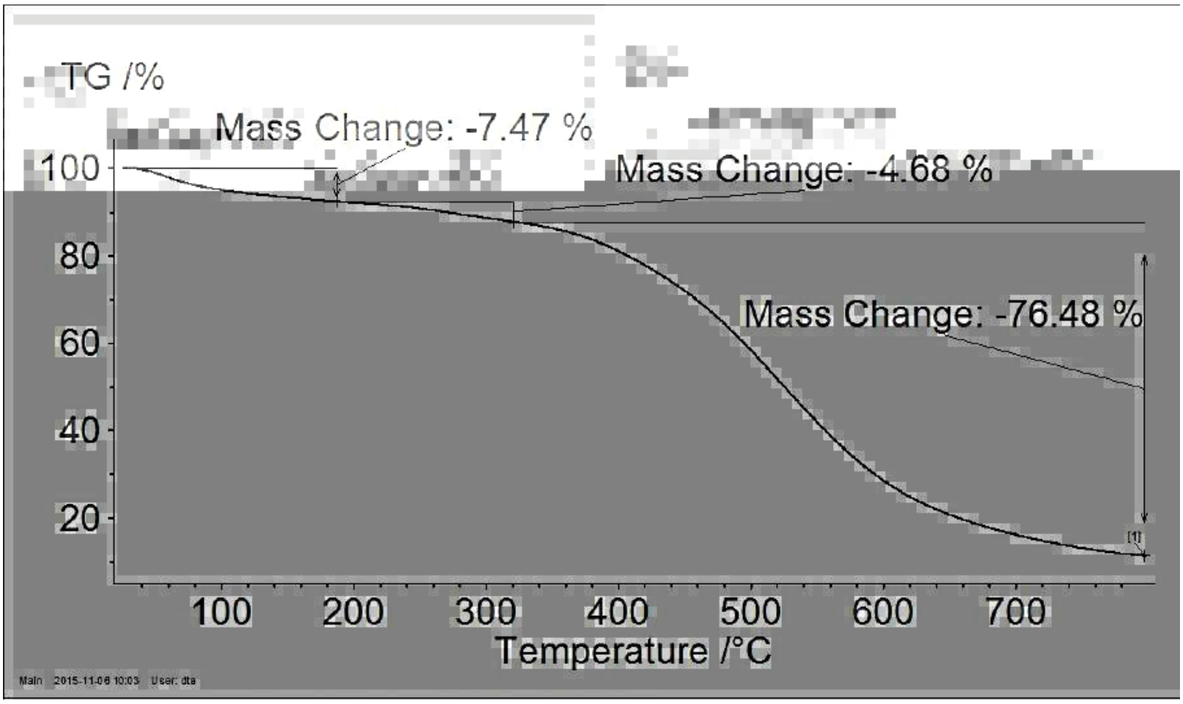

CTF-FL:

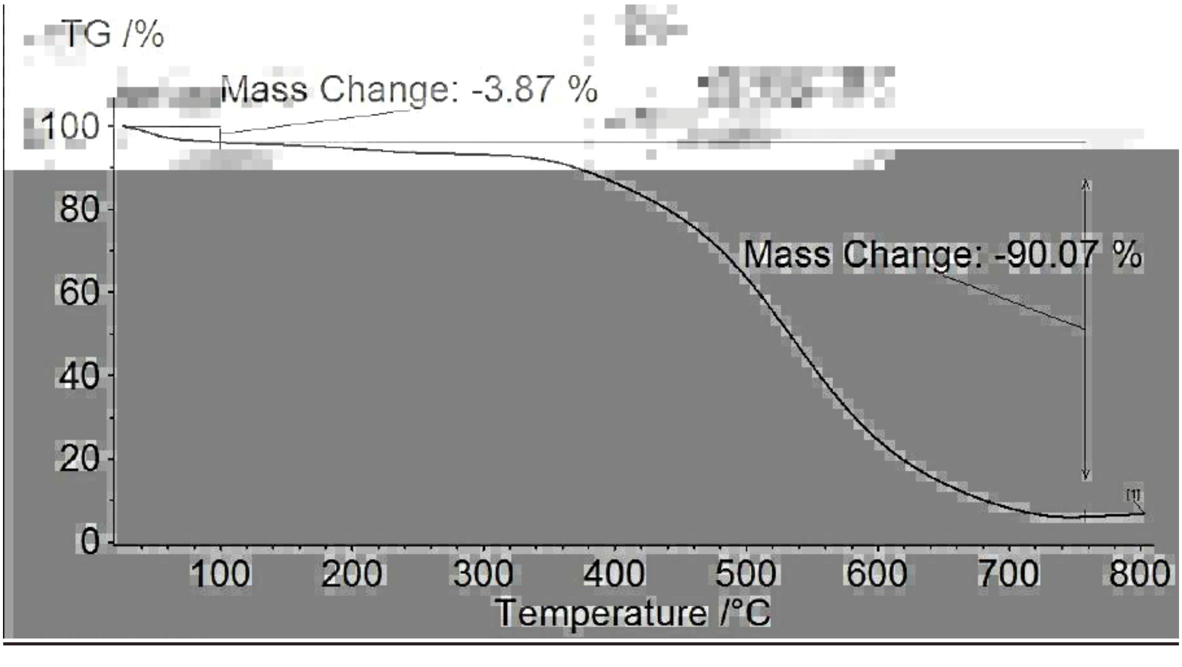

Fig. S5: TGA for CTF-TPC and CTF-FL in temperature range of 25 to 800 °C at the heating rate of 5 °C / min under O_2 atmosphere.

8. Gas Uptake

Table S4 Surface area of CTF-TPC and CTF-FL for different batches.

No. of batch	**CTF-TPC**	**CTF-FL**
	S_{BET} [a] ($m^2\ g^{-1}$)	S_{BET} [a] ($m^2\ g^{-1}$)
Batch 1 [b]	1668	773
Batch 2 [c]	1683	785
Batch 3 [c]	1622	781
Batch 4 [c]	1469	651

[a] Calculated BET surface area from N_2 sorption isotherm at 77 K over the pressure range 0.01-0.05 P/P_0. [b] Measured by using Micromeritics ASAP 2020 automatic gas sorption analyzer. [c] Measured by using Nova 4000e from Quantachrome

Table S5 H_2, CO_2 and CH_4 adsorption as well as selectivity of CTF-TPC and CTF-FL.

Compound	H_2 [a]	CO_2 [b]	CH_4 [b]	$CO_2:N_2$ [c] (293 K)	$CO_2:CH_4$ [c] (293 K)	$CO_2:CH_4$ [d] (273 K)
	($cm^3\ g^{-1}$)	($cm^3\ g^{-1}$)	($cm^3\ g^{-1}$)	Selectivity		
CTF-TPC	195.8	60.4	19	16	5	4
CTF-FL	146.6	48.8	14.9	21	5	5

9. Isosteric heats of adsorption of CO_2 for PCTFs

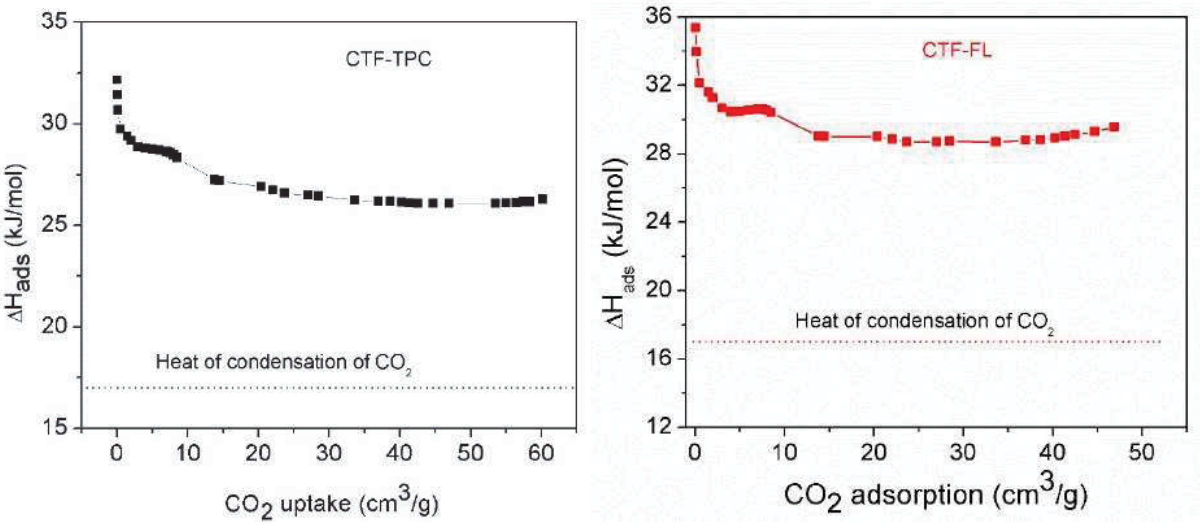

Fig. S6: Isosteric heat of adsorption: calculated from CO_2 adsorption isotherms at 273 K and 293 K for CTF-TPC (left) and CTF-FL (right).

10. Pore Size distribution from CO_2 adsorption isotherm

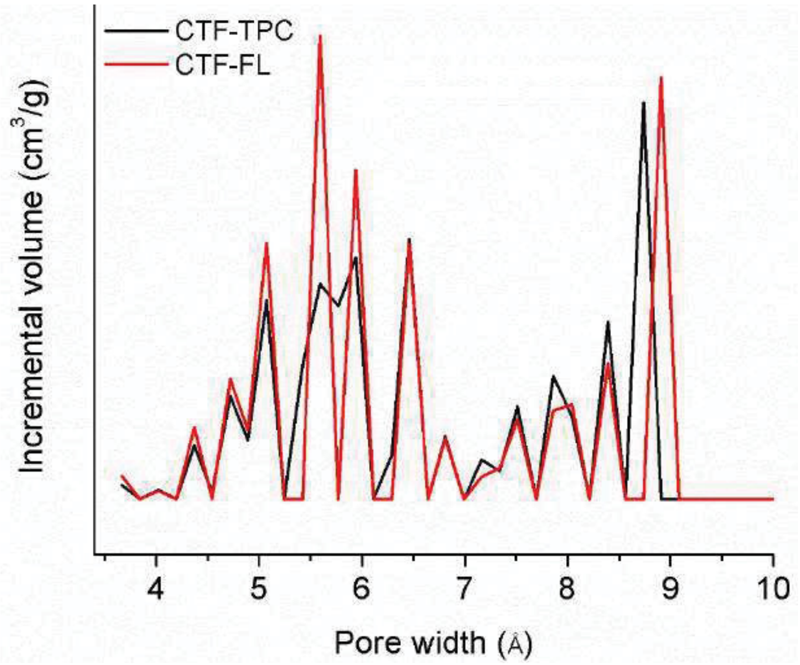

Fig. S7: The pore size distribution from a CO_2 adsorption isotherm at 273 K, calculated by the NL-DFT with a CO_2 on carbon based slit-pore model at 273 K.

11. Selectivity from initial slopes in the Henry region

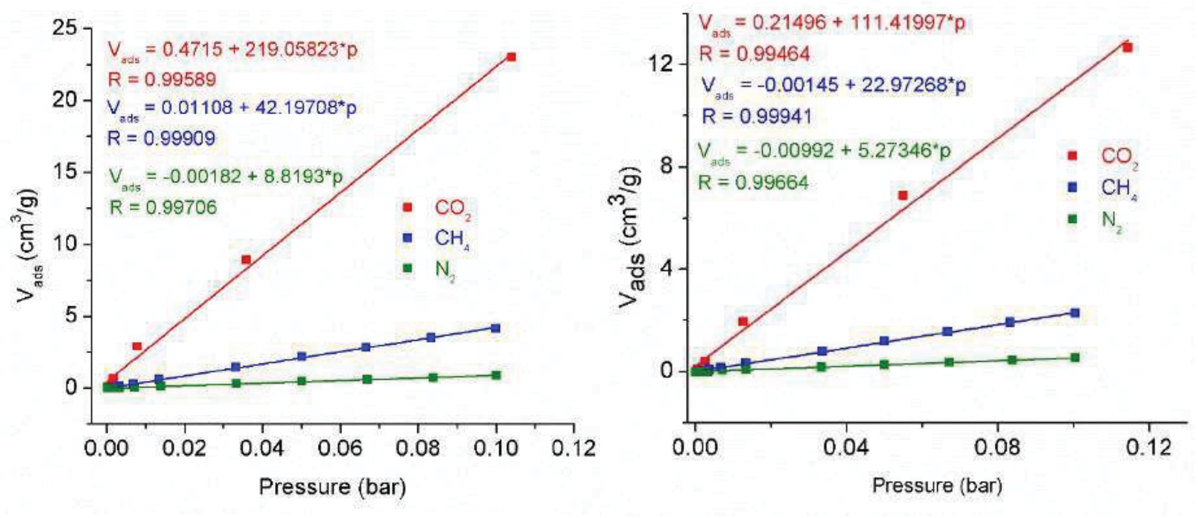

Fig. S8: The initial slopes in the Henry region of the adsorption isotherms for CTF-TPC at 273 K (left) and 293 K (right).

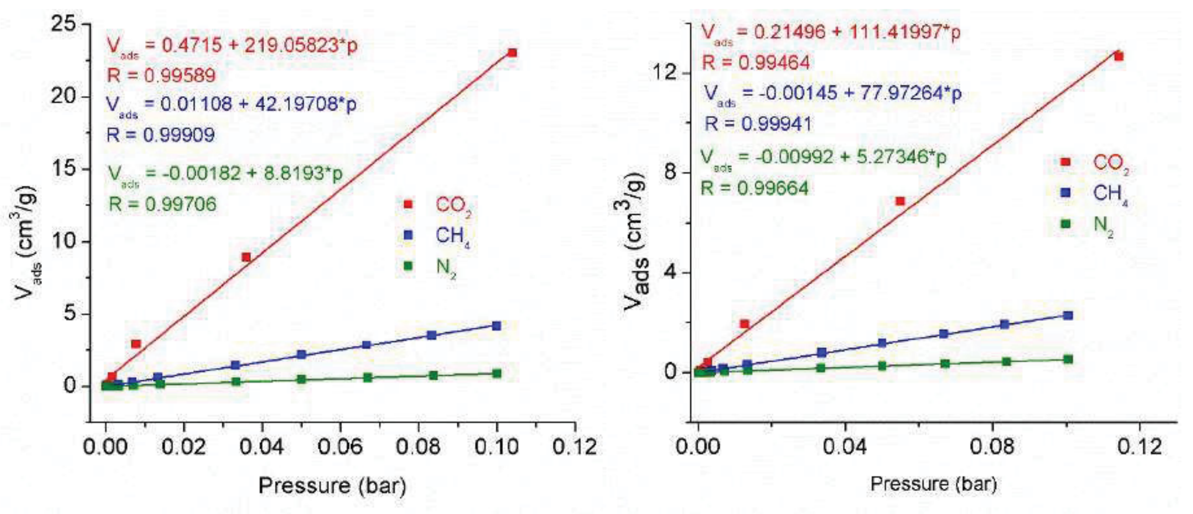

Fig. S9: The initial slopes in the Henry region of the adsorption isotherms for CTF-FL at 273 K (left) and 293 K (right).

12. Ideal Adsorbed Solution Theory (IAST) selectivity studies

IAST selectivities were calculated from the gas adsorption data using a single or dual-site Langmuir model to fit the adsorption isotherms. For CO_2 adsorption isotherm up to 1 bar, we assumed the double-layer adsorption. Therefore, the low pressure (up to 1 bar) adsorption isotherms of CO_2 measured at 273 K was fitted with the dual-site Langmuir (DSL) model. The equation is:

$$q = q_A + q_B = q_{sat,A}\frac{b_A p}{1 + b_A p} + q_{sat,B}\frac{b_B p}{1 + b_B p}$$

Where, q is molar uptake of adsorbate (mmol/g), q_{sat} is saturation uptake (mmol/g), b is the parameter in single component Langmuir isotherm (bar^{-1}), p is the pressure of bulk gas, the subscription of A and B refers to different two sites.

On the other hand, due to the mono-layer adsorption of CH_4 and N_2 adsorption, the single-site Langmuir model were used:

$$q = q_{sat}\frac{bp}{1 + bp}$$

The IAST selectivity S_{ads} can be calculated from the following equation:

$$S_{ads} = \frac{q1/q2}{p1/p2}$$

A CO_2:N_2 ratio of 15:85 was used for calculating the gas mixture selectivities, which is typically the flue gas composition.

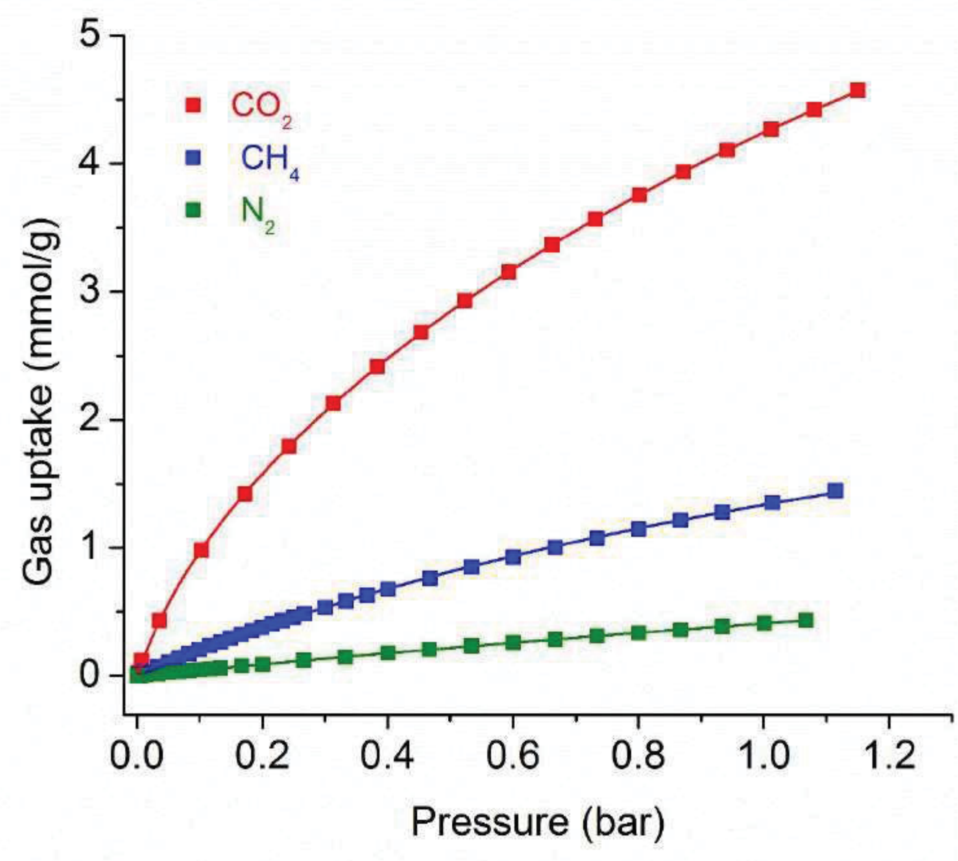

Fig. S10: DSL fitting for CO_2 adsorption and SSL fittings for CH_4 and N_2 adsorption of CTF-TPC at 273 K.

Table S6 Langmuir fitting parameters of CO_2, CH_4, and N_2 adsorption isotherms of CTF-TPC at 273 K and 1 bar.

CTF-TPC@273K	$q_{sat,A}$ (mmol/g)	b_A (bar^{-1})	$q_{sat,B}$ (mmol/g)	b_B (bar^{-1})	Adj. R^2
CO_2	9.63347	0.52412	1.03327	8.98305	0.99999
CH_4	3.71402	0.56223			0.99977
N_2	3.14737	0.15017			0.99999

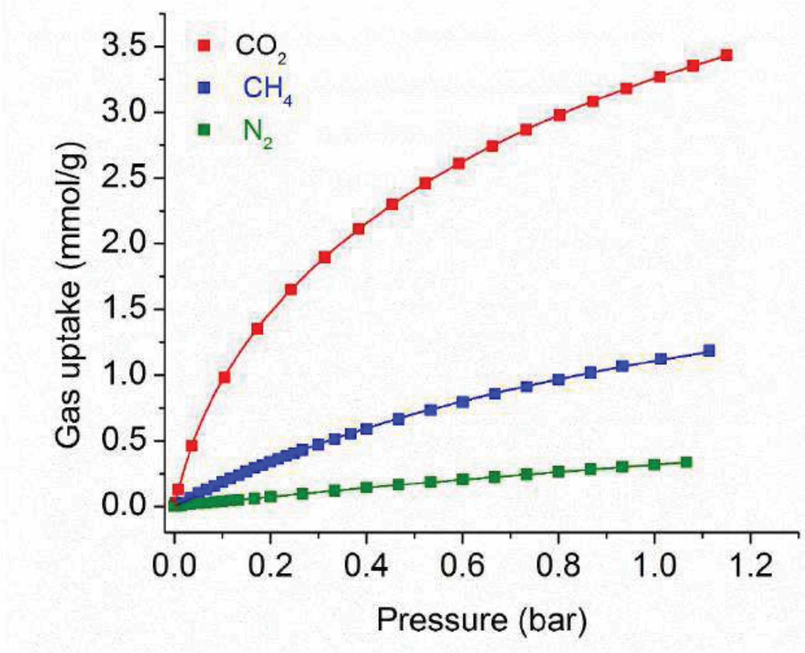

Fig. S11: DSL fitting for CO_2 adsorption and SSL fittings for CH_4 and N_2 adsorption of CTF-FL at 273 K.

Table S7 Langmuir fitting parameters of CO_2, CH_4, and N_2 adsorption isotherms of CTF-FL at 273 K and 1 bar.

CTF-FL@273K	$q_{sat,A}$ (mmol/g)	b_A (bar^{-1})	$q_{sat,B}$ (mmol/g)	b_B (bar^{-1})	Adj. R^2
CO_2	4.71434	1.01096	0.95804	12.39268	0.99999
CH_4	2.59951	0.7417			0.99986
N_2	1.84739	0.20684			0.99996

13. Comparison to other CTFs.

Table S8 Surface area, CO_2 adsorption properties and selectivity of triazine-based polymer.

Compound	BET (m^2/g)	CO_2 uptake (mmol/g) at 1 bar		Q_{st}	CO_2/N_2 selectivity		Ref.
		273 K	298 K[a] or 293 K[b]		Henry	IAST	
CTF-0	2011	4.22					1
CTF-1	746	2.47	1.41	27.5		20	2
CTF-1-600	1533	3.82	2.25	30.0		13	2
FCTF-1	662	4.67	3.21	35.0		31	2
FCTF-1-600	1535	5.53	3.41	32		19	2
CTF-P2	776	1.86				20.3	3
CTF-P3	571	2.25				22.5	3
CTF-P4	867	3.09				16.6	3
CTF-P5	960	2.98				24.1	3
CTF-P6	1152	3.36				16.1	3
CTF-P1M	4	0.93				31.2	3
CTF-P2M	464	1.89				21.0	3
CTF-P3M	523	2.24				15.8	3
CTF-P4M	542	1.85				22.4	3
CTF-P5M	542	2.06				20.1	3
CTF-P6M	947	4.17				14.2	3
MCTP-1	1452	4.64	2.70				4
MCTP-2	859	3.65	2.46				4
Polymer 2	--	--	1.56				5
Polymer 3	646	--	1.68				5
Polymer 4	1266	--	2.09				5
Polymer 2C	427	--	2.99				5
Polymer 3C	1173	--	3.07				5

Polymer 4C	1316	--	3.60				5
NOP-1	978	1.83	1.08	32.8			6
NOP-2	1055	2.37	1.42	34.1			6
NOP-3	1198	2.51	1.41	33.8	27.1	25.6	6
NOP-4	635	1.71	0.84	31.9			6
NOP-5	913	1.45	0.73	30.5			6
NOP-6	1130	1.31	0.50	29.2	33.7	38.7	6
MCTF-300	640	2.25	1.41	24.6			6
MCTF-400	1060	2.36	1.58	25.4			6
MCTF-500	1510	3.16	2.26	26.3			6
fl-CTF300	15	1.27	0.71	43.1	35	37	7
fl-CTF350	1235	4.28	2.29	32.7	27	23	7
fl-CTF400	2862	4.13	1.97	30.7	15	16	7
fl-CTF500	2322	3.26	1.65	31.7	13	12	7
fl-CTF600	2113	3.48	1.80	32.4	14	12	7
COP-1	168	--	1.36				8
COP-2	158		0.93				8
PCTF-1	2235	3.26	1.87	30	13	14	9
PCTF-2	784	1.85	1.00	26	9	14	9
PCTF-3	641	2.17	1.35	27	16	25	9
PCTF-4	1090	2.30	1.51	28	17	26	9
PCTF-5	1183	2.59	1.50	27	17	32	9
PCTF-6	79	--	--		--	--	9
PCTF-7	613	2.18	1.34	25	22	41	9
HPF-1	576	--	2.8	43		120	
CTF-TPC	1668	4.24	2.69	32			This work
CTF-FL	773	3.26	2.18	35			This work

Transformation can be done by considering the molar gas volume 22.414 L (at 273 K), 24.055 L (at 293) and 24.4 L (at 298)

14. References

---

1 P. Katekomol, J. Roeser, M. Bojdys, J. Weber, and A. Thomas, *Chem. Mater.*, 2013, **25**, 1542–1548

2 Y. Zhao, K. X. Yao, B. Teng, T. Zhang and Y. Han, *Energy Environ. Sci*., 2013, **6**, 3684-3692

3 S. Ren, M. J. Bojdys, R. Dawson, A. Laybourn, Y. Z. Khimyak, D. J. Adams and A. I. Cooper, *Adv. Mater*., 2012, **24**, 2357–2361.

4 P. Puthiaraj, S.-M. Cho, Y.-R. Lee and W.-S. Ahn, *J. Mater. Chem. A*, 2015, **3**, 6792-6797

5 H. Lim, M. C. Cha and J. Y. Chang, Macromol. *Chem. Phys*., 2012, **213**, 13, 1385–1390.

6 S. Xiong, X. Fu, L. Xiang, G. Yu, J. Guan, Z. Wang, Y. Du, X. Xiong and C. Pan, *Polym. Chem.*, 2014, **5**, 3424-3431

7 S. Hug, M. B. Mesch, H. Oh, N. Popp, M. Hirscher, J. Senkerd and B. V. Lotsch, *J. Mater. Chem. A*, 2014, **2**, 5928-5936

8 H. A. Patel, F. Karadas,b A. Canlier, J. Park, E. Deniz, Y. Jung, M. Atilhan and C. T. Yavuz, *J. Mater. Chem.*, 2012, **22**, 8431-8437.

9 A. Bhunia, V. Vasylyeva and C. Janiak, Chem. Commun., 2013, 49, 3961–3963; A. Bhunia, I. Boldog, A. Möller and C. Janiak, *J. Mater. Chem. A*, 2013, **1**, 14990–14999.

3.2 Two linkers are better than one: Enhancing CO_2 capture and separation with porous covalent triazine-based frameworks from mixed nitrile linkers

Subarna Dey, Asamanjoy Bhunia and Christoph Janiak

J. Mater. Chem. A, 2016, submitted, (reference 101)

Covalent triazine based frameworks (CTFs) were first developed in 2008 by trimerization reaction of aromatic nitrile groups using $ZnCl_2$ as a molten solvent and Lewis acid catalyst. These porous frameworks exhibit high surface areas which usually depend on the reaction temperature, reaction time and amount of $ZnCl_2$ used. Due to stable chemical bonds and high amount of nitrogen atoms these materials possess good thermal and chemical stability. In this work we approached synthesis of CTFs via ionothermal synthesis route using mixed linker strategy i.e. by mixing two different nitrile monomers which could tune the BET surface area, porosity of the frameworks as well as the gas adsorption properties of the frameworks.

Herein we reacted tetrakis(4-cyanophenyl)ethylene (M) together with terephthalonitrile (M1), tetrafluoroterephthalonitrile (M2), 4,4′-biphenyldicarbonitrile (M3) or 1,3,5-benzene-tricarbonitrile (M4) to form four mixed nitrile-based CTFs (MM1-MM4).

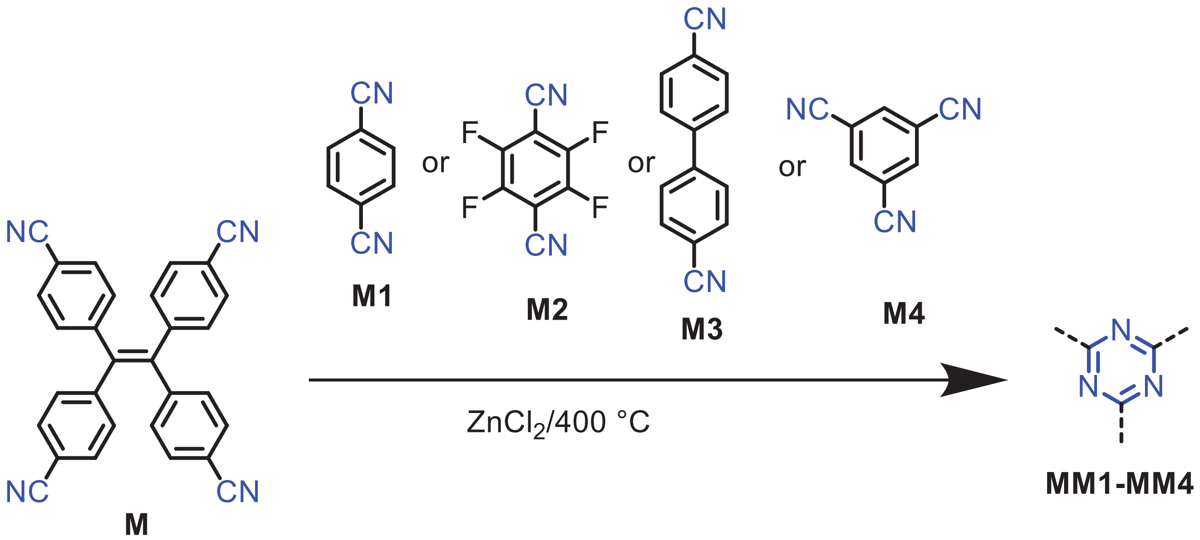

The resulted CTFs exhibited BET surface area in the range of 1360-1884 m^2/g. The frameworks possess good CO_2, CH_4 and H_2 uptake capacity. The CO_2 uptake capacity of MM2 at 273 K is found to be 4.70 mmol/g which is the second highest of all the CTFs known to us. The CTFs also exhibited very high CO_2/N_2 selectivity (at 273 K for MM1-MM4 the values are 130, 97, 77 and 98, respectively) which together with high CO_2 uptake and good thermal and chemical stability makes them promising candidate for gas adsorption and storage.

Author's contribution to the work:

- Synthesis and characterization of the CTF materials.
- Gas adsorption, water adsorption and Karl-Fischer titration.
- The manuscript was prepared by me, and corrected by Prof. Janiak including some schemes and figures.

Journal Name

ARTICLE

Two linkers are better than one: Enhancing CO_2 capture and separation with porous covalent triazine-based frameworks from mixed nitrile linkers†

Received 00th January 20xx,
Accepted 00th January 20xx

DOI: 10.1039/x0xx00000x

www.rsc.org/

Subarna Dey, Asamanjoy Bhunia and Christoph Janiak*

Covalent triazine-based framework (CTF) materials were synthesized by combining two different nitrile building blocks: The tetranitrile tetrakis(4-cyanophenyl)ethylene (M) was reacted with either terephthalonitrile (M1), tetrafluoroterephthalonitrile (M2), 4,4′-biphenyldicarbonitrile (M3) or 1,3,5-benzenetricarbonitrile (M4) under ionothermal conditions ($ZnCl_2$, 400 °C) to yield mixed-nitrile MM'-CTFs MM1 to MM4. Systematic N_2, CO_2 and CH_4 gas sorption studies were performed up to 1 bar at 273 K and 293 K. The specific BET surface areas of MM1-MM4 were 1800, 1360, 1884 and 1407 m^2/g, respectively. The CO_2 uptake capacity of mixed-nitrile MM1, MM2 and MM4 was higher than the CO_2 uptake of the respective individual single-nitrile M- or M'-CTF despite a higher surface area of the M-CTF PCTF-1 (2235 m^2/g). The synergistic increase in CO_2 uptake of the mixed-nitrile MM'-CTFs is due to the higher CO_2-accessible micropore volume $V_{micro}(CO_2)$ and the higher micropore volume fraction $V_{0.1}/V_{tot}$ for the MM'-CTFs when compared to the M- or M'-CTFs. The surface area of porous materials does not play the most important role in CO_2 storage at low pressure but the CO_2-accessible micropore volume is the more decisive factor. Further, MM2 shows the second highest (of known CTFs synthesized at 400 °C) CO_2 uptake capacity of 4.70 mmol/g at 273 K and 1 bar because of its large micropore fraction (82%) and strong electrostatic interactions between high electronegative fluorine atoms and CO_2 gas molecules. CO_2/N_2 adsorption selectivities of mixed-nitrile MM1, MM2 and MM4 CTFs were also higher than the those of the single-nitrile component M- or M'-CTFs.

Introduction

Design and synthesis of porous covalent triazine-based frameworks (CTFs)[1,2,3], a subclass of porous organic polymers (POPs),[4] have received considerable attention over the past few decades in the area of CO_2 post-combustion capture.[3a,5,6,7] Typically, CO_2 gas emitted from power stations and vehicle related transportations is a main component for global warming.[8] Therefore, the research on carbon capture and storage/sequestration (CCS) from point sources is currently probed to reduce carbon emissions.[5] The CCS is mainly a three-step process:[9] (1) CO_2 separation from other flue gas components such as N_2, H_2O, O_2, SO_2, SO_3, NO_x, HCl, CO and hydrocarbons; (2) CO_2 transportation; (3) permanent storage of CO_2. Among these processes, the important step is the CO_2 capture. Well-established technologies such as amine scrubbing and cryogenic cooling are used for CO_2 capture, but these technologies require high energy in the regeneration process. In addition the separation of CO_2/CH_4 is relevant for purification ('sweetening') of natural gas (mainly CH_4) which is typically soured with up to over 40% CO_2 and N_2 and only useable at low CO_2 concentrations.[10,11] Various solid adsorbents such as zeolite,[12] metal organic frameworks (MOFs),[13] silica,[14] activated carbons[15] and (micro)porous organic polymers (POPs)[16,17,18,19,20] have received significant attention for CO_2 sorption. A technical feasible solid adsorbent must fulfill the following criteria: (1) high CO_2 uptake, (2) high surface area, (3) low density, (4) excellent thermal, chemical and water stability. In this regards, selected POPs are considered as promising candidates for CO_2 capture.

In order to improve CO_2 uptake in materials by physisorption π–systems, fluorine atoms and nitrogen atoms have been incorporated. The strong electrostatic interaction of quadrupole CO_2 molecules with the heteroatoms of the pore walls at low pressures favors the CO_2 uptake.[21,22] Also, replacing H by larger F atoms reduces the effective pore size of the materials to less than 0.5 nm, thereby increasing the pore wall interaction and adsorption enthalpy.[23] Classes of POPs or MOPs (microporous organic polymers)[24] are often differentiated according to their building units such as benzimidazole-linked polymers (BILPs),[25] hyper-crosslinked polymers (HCPs),[26] polymers of intrinsic microporosity (PIMs),[27] porous aromatic frameworks (PAFs),[28,29] conjugated microporous polymers (CMPs),[30] covalent organic frameworks (COFs),[4,31] Schiff base networks (SNWs),[32] covalent imine polymers (CIP),[33] porous polymer frameworks (PPFs),[34] porous polymer networks (PPNs),[35] element-organic frameworks (EOFs),[36] nitrogen-doped porous carbon materials (NPCs)[37]. Porous covalent triazine-based frameworks (CTFs) were developed by Kuhn, Antonietti, Thomas *et al.*[1] and possess some of the highest chemical and thermal stabilities of POPs.

---

[a] *Institut für Anorganische Chemie und Strukturchemie, Heinrich-Heine-Universität Düsseldorf, 40204 Düsseldorf, Germany.*

† Electronic Supplementary Information (ESI) available: Synthesis, elemental analysis, PXRD, TGA, gas adsorption selectivity, KFT and water adsorption. See DOI: 10.1039/x0xx00000x

CTFs are made by the idealized trimerization reaction of carbonitriles to triazine rings (C_3N_3). Under ionothermal reaction conditions, molten $ZnCl_2$ is often used in large access (typically 10:1 molar ratio) as a Lewis acid trimerization catalyst and pore-forming (porogen) solvent or templating agent for the polymerization. CTFs are interesting because of cheap and readily available starting materials, facile synthesis and certain hydrophilicity. From their nitrogen-deficient elemental composition, CTFs from ionothermal synthesis with $ZnCl_2$ are in-between ideal triazine-linker frameworks and porous carbon materials. So far, CTFs have been used mainly for gas storage and separation[1,3,38,39] The use of CTFs was also reported for heterogeneous catalysis including light-induced hydrogen evolution and water splitting,[2,40] as catalytic support in liquid phase reactions,[41] and as adsorbents in liquids.[42] Recently, we communicated the transformation of tetrakis(4-cyanophenyl)ethylene (M) under Lewis acidic ($ZnCl_2$) conditions at 400 °C to porous covalent triazine-based frameworks (PCTF-1 and -2) with high surface area (2235 $m^2\ g^{-1}$), high CO_2 and CH_4 uptake and highest hydrogen uptake for a CTF material (1.86 wt% at 77 K, 1 bar).[38] Motivated by this work, we reacted tetrakis(4-cyanophenyl)ethylene (M) together with terephthalonitrile (M1), tetrafluoroterephthalonitrile (M2), 4,4′-biphenyldicarbonitrile (M3) or 1,3,5-benzenetricarbonitrile (M4) to form four mixed nitrile-based CTFs (Scheme 1). The synthesized MM'-CTFs were tested for CO_2, N_2, H_2, and CH_4 adsorption. We are only aware of one other example of mixed-nitrile or mixed-linker CTF from a 1:2 ratio of 2,6-pyridinedicarbonitrile and 4,4-biphenyldicarbonitrile, with the CTF used as catalyst support. This mixed-linker CTF was not investigated for CO_2, CH_4 or H_2 sorption.[43]

Results and discussion

Porous CTFs materials can be synthesized by an ionothermal reaction between aromatic nitriles in $ZnCl_2$ which can be adapted to large scale.[1] Molten $ZnCl_2$ acts as a Lewis-acid catalyst, molten solvent and porogen for the polymerization. A trimerization reaction of nitrile groups can construct triazine rings. Ionothermal reaction of 1:2, 1:2, 1:2 and 1:1.3 molar ratios of tetrakis(4-cyanophenyl)ethylene (M) and terephthalonitrile (M1), tetrafluoroterephthalonitrile (M2), 4,4′-biphenyldicarbonitrile (M3) or 1,3,5-benzenetricarbonitrile (M4) in the presence of anhydrous $ZnCl_2$ resulted in four black colored porous CTFs (MM1-MM4) (Scheme 1 and 2, ESI for the details). A reaction time of 48 h and temperature of 400 °C was used as in our previous work on PCTFs.[38,39] The yield of the frameworks were in the range of 70-80%.

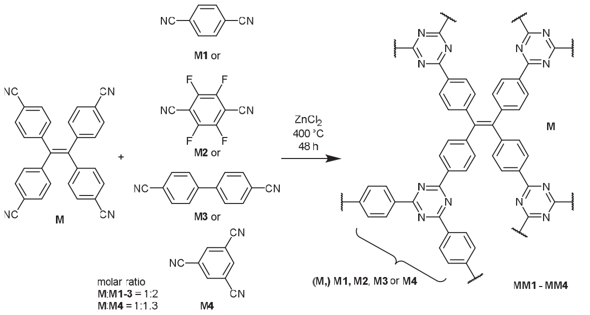

Scheme 1 Monomers reacted to MM' frameworks shown in Scheme 2.

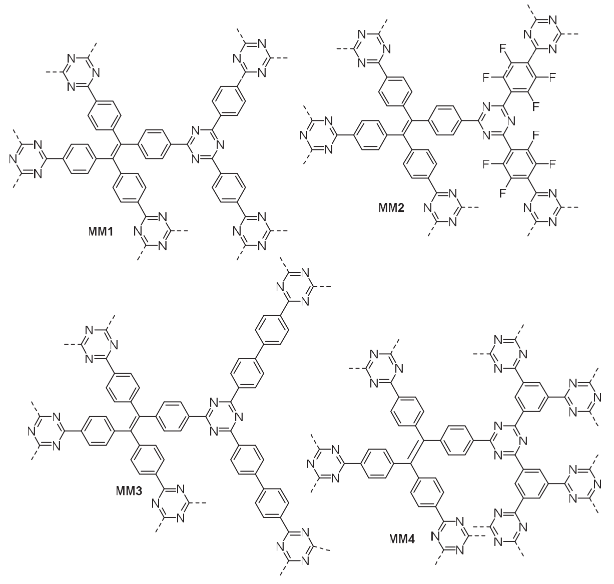

Scheme 2. Idealized building/repeating units of MM'-CTFs.

The IR spectra of MM1, MM2 and MM4 show the presence of a nitrile band (2223 cm^{-1}), indicating that there are unreacted nitrile end groups (Fig. 1).[1,3,44] Only for MM3 the IR spectrum did not show the nitrile band. It is apparently the congestion of the nitrile groups in the short terephthalonitrile, tetrafluoroterephthalonitrile and 1,3,5-benzenetricarbonitrile linkers which prevents the cyclotrimerization reaction at some of the nitrile groups. The IR bands in the region of 1520-1600 cm^{-1} and 1312-1388 (usually weak) cm^{-1} can be assigned to the C-N stretching and breathing mode of the triazine unit, respectively.[3] Powder X-ray diffraction indicates that the materials are amorphous as expected. The diffractograms exhibit only three broad peaks around 17°, 20° with a shoulder at 27° and 41° 2-theta (Fig. S1, ESI†). The peak at 17° is due to $ZnCl_2$. Several articles on CTFs where $ZnCl_2$ was used also demonstrated that minor amounts of zinc chloride are still present in the CTF materials after washing. This difficult to avoid aspect was already established and discussed by Kuhn, Antonietti and Thomas *et al.*[1] CTFs are usually amorphous and there are only three CTFs (CTF-0, CTF-1 and CTF-2) which show some crystallinity.[1a,d]

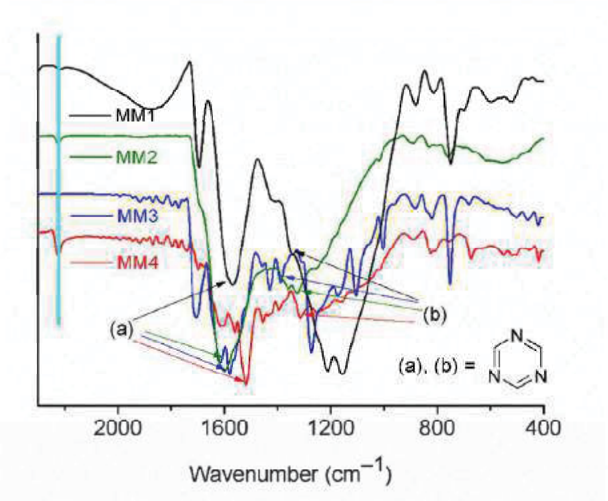

Fig. 1 FT-IR spectra of MM1-MM4 confirming the formation of triazine units. The vertical cyan bar marks the unreacted nitrile band, R-CN of the starting materials (2223 cm^{-1}). The C-N stretching (a) and breathing (b) mode the triazine unit are indicated by arrows.

Elemental analysis of MM1-MM4 indicate nitrogen elimination during the polymerization reaction as reported previously (Table S1, ESI†).[1] It has been noticed that aromatic nitrile decomposition involves C-H and Ar-CN elimination. From thermogravimetric analysis (Fig. S2), MM1-MM4 start to decompose only above 385 °C (Table S2, ESI†). Materials MM1, MM3 and MM4 lose less than 5 wt% until 300 °C and fluorous MM2 loses about 10 wt% until 100 °C due to hydrate or re-adsorbed water (Fig. 2, Table S2 in ESI†).[1,45]

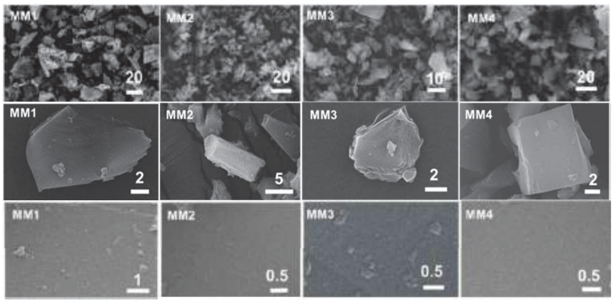

Fig. 2 Scanning electron micrographs of MM1 - MM4 (numbers above the scale bar are in μm). An enlarged version of this figure can be found as Fig. S10 in ESI†.

CTFs have recently been shown to be hygroscopic, with a water uptake of ~0.12-0.20 g/g (corresponding to 11-17 wt%) up to P/P_0 = 0.5-0.6 or 50-60% air humidity when stored under ambient air. The significantly higher water weight loss for MM2 is in agreement with its significantly higher water uptake at P/P_0 from water sorption isotherms (see below). The water loss for MM1, MM2 and MM4 also agrees with absorbed water values found from Karl-Fischer titration (Table S4 in ESI†).Frameworks MM1, MM2, MM3 and MM4 are showing a similar surface morphology from scanning electron microscopy (SEM) studies (Fig. 2), which is in line with their similar porosity characteristics from N_2 sorption studies (cf. Fig. 3-4, Table 1). The SEM images showed that the CTFs MM1-MM4 consist of shard morphology of irregular shape and size with an average particle length of 5 – 20μm.

Gas adsorption properties

The porosities of the four MM'-CTFs were characterized by N_2 sorption measurements at 77 K as the accepted standard for surface area and pore size determination. All materials were activated by degassing at 200 °C for 24 h. In the N_2 sorption isotherms (Fig. 3) a sharp adsorption/desorption step can be noticed at low relative pressure (P/P_0) of 0 to 0.05 for MM1 to MM4, indicating their substantial microporous character (pore widths < 2 nm, 20 Å, Table 1). The similar isotherms of MM1, MM2 and MM4 can be classified as a combination of isotherms of Type I at low and Type II at high P/P_0. Type II isotherms are the result of unrestricted monolayer-multilayer adsorption up to high P/P_0, given on non- or macroporous adsorbents.[46,47] For MM3 with the longer biphenyl linker, the isotherm is more a Type I and IV combination. The adsorption branch has an inflection point at P/P_0 ~0.5 and at high P/P_0 the adsorption branch seems to approach a final saturation plateau, which is the typical feature of Type IV isotherms. All sorption isotherms have a hysteresis loop. For MM1, MM2 and MM4 the adsorbed volume stays almost constant when lowering the pressure down to P/P_0 ~0.5, followed by a gradual desorption upon further pressure lowering. The high-pressure part of the hysteresis loops may look like an H4 hysteresis but lacks the feature of the sharp step-down of the desorption branch at P/P_0 0.4 – 0.5. The gradual desorption below P/P_0 ~0.5 is found in H2(b) loops. H2 hysteresis loops are given by complex pore structures were pore blocking/percolation or cavitation-induced evaporation is important. For H2(b) loops the size distribution of neck widths is much larger than in H2(a) loops with their very steep desorption branches. Type H2(b) loops have been observed with mesocellular silica foams and certain mesoporous ordered silicas after hydrothermal treatment.[46] The surface area was calculated by applying the Brunauer-Emmett-Teller (BET) model over the pressure range of P/P_0 = 0.01-0.05. The surface areas of MM1 to MM4 were 1800, 1360, 1884 and 1407 m^2/g, respectively (Table 1). Surface areas of 1884 m^2/g are at the high end for CTF materials[1e,40] and only surpassed by PCTF-1 (2235 m^2/g, from pure tetrakis(4-cyano-phenyl)ethylene)[38] and fl-CF-400 to -600 (2862-2113 m^2/g from 9*H*-fuorene-2,7-dicarbonitrile)[3b] (see Table S6 for comparative listing of CTFs). As expected, the longest biphenyl linker M3 yields also the highest surface area of 1884 m^2/g. MM2 exhibited the lowest surface area here among the MM' materials which we assign to the large size of fluorine atoms.

Pore size distributions were calculated by non-local density functional theory (NLDFT) using the model of slit-pore carbon' as an adsorbent. All MM' materials show a significant fraction of pore diameters of less than 20 Å (2 nm), which correspond to micropores (Fig. 4). In addition there is a broad mesopore region (20-50Å). For MM3 having the long biphenyl linker the share of mesopores is most dominant, followed by MM1. In line with the N_2 sorption isotherm shapes from which the pore size distributions are derived, MM1 and MM3 have a higher fraction of mesopores compared to MM2 and MM4. Formation of microporous-mesoporous hierarchical materials is a challenge, e.g., for heterogeneous catalysis.[48] In this regard, MM1 and MM3 may be attractive as catalytic support.

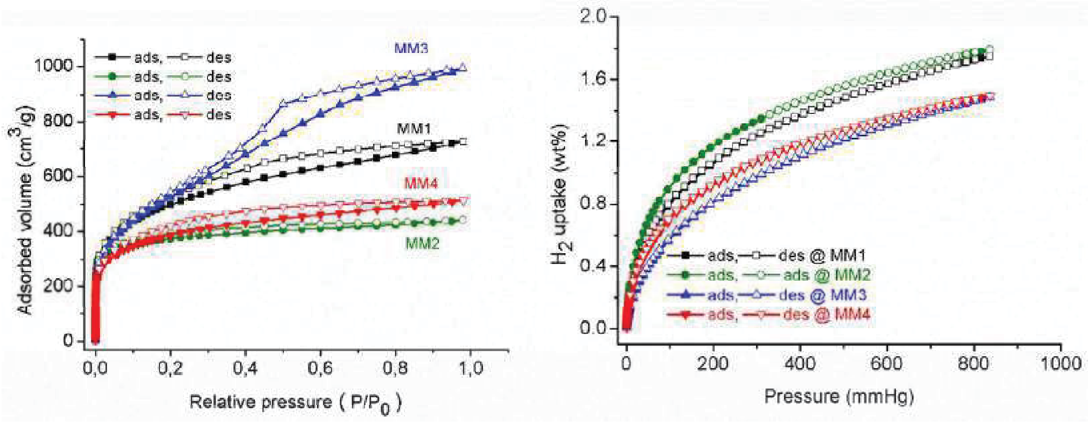

Fig. 3 Nitrogen (left) and hydrogen (right) adsorption-desorption isotherms (closed symbols for adsorption and open symbols for desorption).

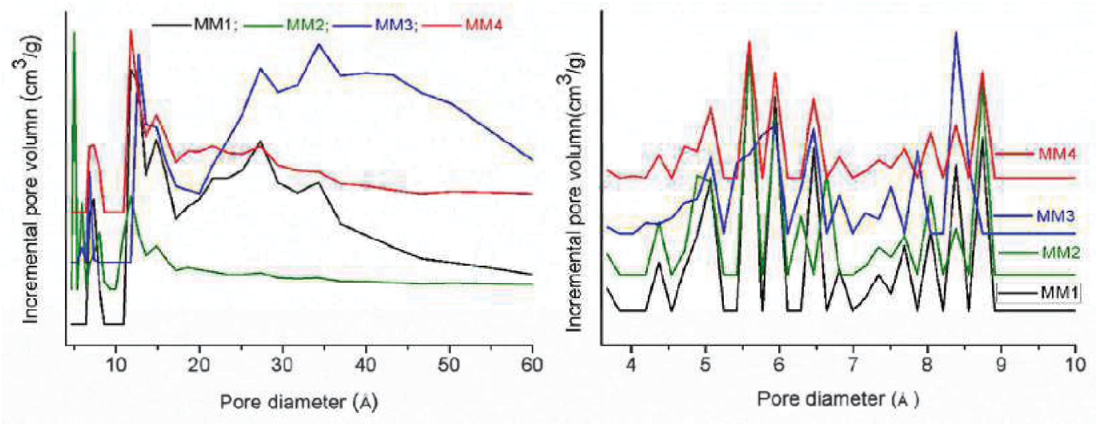

Fig. 4 NLDFT pore size distribution (PSD) curves of MM1-MM4 from (a) N_2 adsorption (at 77 K) and (b) CO_2 adsorption (at 273 K) isotherms (N_2 DFT slit pore' model).

Table 1 Porosity data for MM1-MM4.

Compound	S_{BET} [a] ($m^2\ g^{-1}$)	S_{Lang} [b] ($m^2\ g^{-1}$)	$V_{0.1}$ [c] ($cm^3\ g^{-1}$)	V_{tot} [d] ($cm^3\ g^{-1}$)	$V_{0.1}/V_{tot}$	$V_{micro}(CO_2)$ [e] ($cm^3\ g^{-1}$)
MM1	1800	2216	0.67	1.11	0.60	0.093
MM2	1360	1652	0.55	0.67	0.82	0.14
MM3	1884	2335	0.67	1.52	0.44	0.052
MM4	1407	1734	0.54	0.78	0.69	0.092

[a] Calculated BET surface area over the pressure range 0.01-0.05 P/P_0 from N_2 isotherms at 77 K. [b] Langmuir surface area over the pressure range 0-110 Torr. [c] Micropore volume calculated from N_2 adsorption isotherm at $P/P_0 = 0.1$ for pores ≤ 2 nm (20 Å). [d] Total pore volume at $P/P_0 = 0.95$ for pores ≤ 20 nm. [e] Total pore volume for pores with diameters smaller than 1 nm (10 Å, cf. Fig. 4b) from CO adsorption isotherms at 273 K and the CO_2 NL-DFT model. [f] Data from ref. 2

The presence of ultramicropores was probed by CO_2 adsorption (Fig. 4b) ss the diffusion of dinitrogen molecules at 77 K into ultramicropores (pores smaller than 7 Å) is quite slow.[49] At pore sizes close to the kinetic diameter of N_2 (~3.64 Å) and at 77 K the diffusion limitation can be alleviated by use of CO_2 as an adsorbate at 273 K. The saturation pressure of CO_2 at 0 °C is ~26141 Torr and low relative pressure measurements necessary for micropore analysis are achieved in the range of moderate absolute pressures (1–760 Torr).[50] CO_2 micropore analysis at 273 K versus N_2 analysis at 77 K ensures faster equilibration and slight extension of the range of analysis to pores of smaller sizes that are accessible to CO_2 molecules (kinetic diameter 3.30 Å), but not to N_2.[50,51]

The fractions of micropores with respect to the total pore volume ($V_{0.1}/V_{tot}$)[52] are 60%, 82%, 44% and 69% for MM1 to MM4. Alternatively, MM3 showed the highest amount of mesopores probably due to the long biphenyl linker. H_2 gas sorption for MM1-MM4 was found as 1.68, 1.74, 1.43 and 1.45 wt% H_2 at 77 K and 1 bar (Fig. 3) respectively, which is comparable to many reported CTFs materials.[3,40,41b,44]

Motivated by the high BET surface areas and the presence of nitrogen (favoring quadrupole CO_2 uptake)[22,53,] in the MM' materials, CO_2 sorption (selectivity) was studied in relation to N_2 and CH_4 at 273 and 293 K (Table 2) High selectivities of CO_2 sorption over N_2 and CH_4 are promising for the application of CCS materials and 'sweetening' of natural gas (mainly CH_4), respectively. MM1-MM4 showed fully reversible CO_2 adsorption-desorption isotherms (Fig. 5).

Table 2 Gas sorption at 1 bar and selectivity of MM1-MM4.

Compound	CO_2[a]	CO_2[b]	$Q^0_{ads}(CO_2)$[c]	CH_4[a]	CH_4[b]	N_2[a]	CO_2:N_2[d]	CO_2:N_2[e]	CO_2:CH_4[d]
	($cm^3\ g^{-1}$)	($cm^3\ g^{-1}$)	(kJ mol^{-1})	($cm^3\ g^{-1}$)	($cm^3\ g^{-1}$)	($cm^3\ g^{-1}$)	selectivity		
MM1	83.5	52.8	32	28.8	18.8	9.2	32	130	6
MM2	106.8	70.2	36	32.7	21.1	10.0	23	97	5
MM3	59.5	36.8	43	21.3	13.5	7.0	13	77	4
MM4	77.3	50.0	30	24	14.9	7.5	21	99	5

[a] Gas uptake at 273 K, 1 bar (760 mm Hg); [b] gas uptake at 293 K, 1 bar (760 mm Hg); [c] heat of adsorption for CO_2 at zero loading from adsorption isotherms acquired at 273 and 293 K; [d] gas selectivity calculated at 273 K from the initial slopes in the Henry region; [e] IAST selectivity calculated at 273 K and 1 bar.

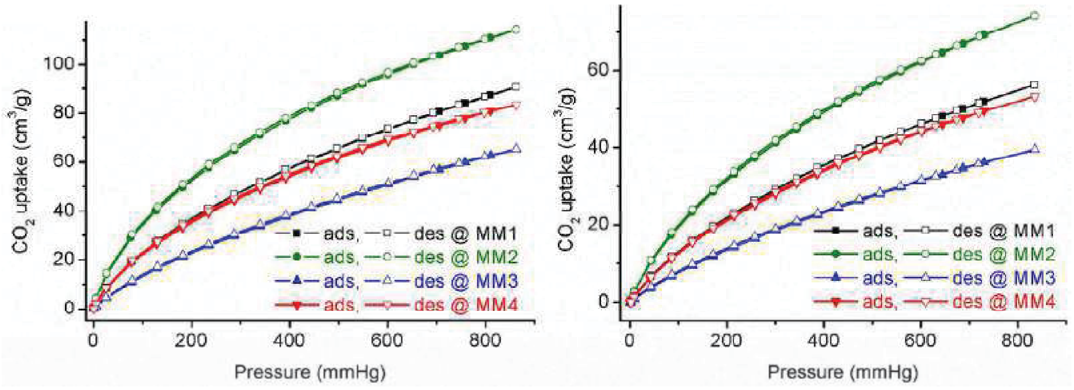

Fig. 5 CO_2 sorption isotherms at 273 K (left) and 293 K (right).

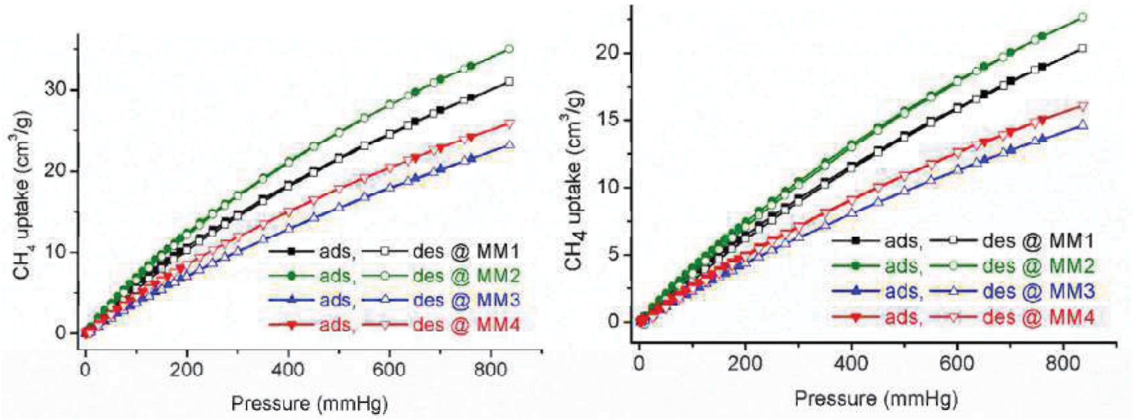

Fig. 6 CH_4 sorption isotherms at 273 K (left) and 293 K (right).

This reversible isotherm suggests that the interaction between CO_2 and the frameworks are favorable enough to regenerate these CTFs materials without too much energy. Among the MM' materials MM2 exhibited highest CO_2 sorption of 106.8 cm^3/g (4.70 mmol/g) at 273 K and 1 bar, which is associated with the large micropore fraction (82%) as well as C-F bonds, despite the lowest surface area in the MM' series. This supports once more the notion that the surface area of porous materials alone does not play the most important role in CO_2 storage at low pressure.[39]

The CO_2 sorption of MM2 at 273 K is second highest of all CTF materials, which we are aware of (cf. Table S6 in ESI†). MM2 surpasses FCTF-1-400 (4.67 mmol/g),[23] MCTP-1 (4.64 mmol/g),[53] and others, with only FCTF-1-600 having, so far, a higher CO_2 uptake (5.53 mmol/g)[23] at 273 K. Even the frameworks MM1, MM3 and MM4, which show CO_2 uptakes of 2.6-3.7 mmol/g, also lie towards the upper end when compared with other CTFs (Table 3, and Table S6 in ESI†) where the higher CO_2 uptake values were 1.27-4.28 mmol/g for fl-CTF,[3b] 1.87-3.08 for *bipy*-CTF300-400,[3a] 3.63-4.55 mmol/g for *lut*-CTF300-400,[3a] 4.67-5.53 mmol/g for FCTF-1,[23] 4.22 mmol/g for CTF-0,[40] 2.47-3.82 mmol/g for CTF-1,[23] 1.88-3.39 mmol/g for CTF-Pl-P6,[44] CTF-P1M-P6M 0.94-4.42 mmol/g for CTF-P1M-P6M,[44] 2.25-3.16 mmol/g for MCTF300-500,[54] 1.85-3.26 mmol/g for PCTF-1-7[39] and 1.31-2.51 mmol/g for NOP-1-6.[55]

It is clearly noticeable from Table 3 that under the same conditions the CO_2 uptake of the CTFs from individual M linkers, such as PCTF-1, CTF-1, FCTF-1 and CTF-0 for M, M1, M2 and M4, respectively are lower than the respective mixed-linker MM' materials. Thus, MM1 has a higher CO_2 uptake than both PCTF-1 (from M) and CTF-1 (from M1) (all prepared at 400 °C). Likewise, MM2 adsorbs more CO_2 than the CTF from M (PCTF-1) or M2 (FCTF-1). MM4 adsorbs more CO_2 than PCTF-1 (from M) and CTF-0 (from M4). MM3 is the only exception with a lower CO_2 uptake than PCTF-1 from M. The higher CO_2 uptake of MM' versus M and M' is especially noteworthy as PCTF-1 (from M) has a higher BET surface area than all MM' materials. We explain this predominently higher CO_2 uptake of the mixed-linker MM'-CTFs primarily by the CO_2-accessible micropore volume $V_{micro}(CO_2)$ (from CO_2 adsorption) and the micropore volume fraction $V_{0.1}/V_{tot}$ (from N_2 adsorption). The pore volume $V_{micro}(CO_2)$ for pores with d ≤ 1 nm (10 Å, from the CO_2 NL-DFT model at 273 K is 0.055 $cm^3\ g^{-1}$ for PCTF-1. Its micropore volume fraction $V_{0.1}/V_{tot}$ is 0.51.[39] These values are lower than the respective values for MM1, MM2 and MM4 (see Table 1), despite the higher surface area of PCTF-1. Only MM3 has lower $V_{micro}(CO_2)$ and $V_{0.1}/V_{tot}$ values than PCTF-1 (but has the highest BET surface area of all MM's). The $V_{micro}(CO_2)$ for CTF-1, FCTF-1 and CTF-0 could not be found in the literature, nor could the values for $V_{0.1}/V_{tot}$ for CTF-1 and FCTF-1. The $V_{0.1}/V_{tot}$ for CTF-0 was found as 0.45 (prepared with 5 mol eq. $ZnCl_2$).[40e] For a CTF-1 sample from our work[42] we measured $V_{0.1}/V_{tot}$ and $V_{micro}(CO_2)$ to 0.79 and 0.1 cm^3/g, respectively. For its relatively small surface area of 970 m^2/g this CTF-1 sample had quite a high CO_2 uptake, in line with the above argument on the importance of micropore volume and volume fraction. Still, when materials have comparative micropore volume then a larger BET surface area will also give higher uptake. However, it is again evident that the surface area of porous materials alone does not play the most important role in CO_2 storage at low pressure.[39] Clearly, the microporosity or micropore volume is the more decisive factor. Overall, this high CO_2 affinity is due to the favorable interactions of the polarizable CO_2 molecule through dipole – quadrupole interactions[22] with the CTF frameworks and their inherent microporosities.

Table 3 Monomers with corresponding CTFs and their CO_2 adsorptions

Monomer	**CTF** [a]	**S_{BET}** [a] **($m^2\ g^{-1}$)**	**CO_2 uptake** [b]	**CO_2/N_2 selectivity** [c]	**Ref.**
M	PCTF-1	2235	3.26	17	39
M1	CTF-1	746	2.47	20	23
	CTF-1	970	3.17	[d]	42
M2	FCTF-1	662	4.67	31	23
M3		1710	[d]	[d]	1e
M4	CTF-0	499 [e]	2.25 [e]	[d]	40e
M + M1	MM1	1800	3.68	130	[f]
M + M2	MM2	1360	4.70	97	[f]
M + M3	MM3	1884	2.62	77	[f]
M + M4	MM4	1407	3.40	99	[f]

[a] All CTFs prepared at 400 °C for comparison. [b] in (mmol/g) at 273 K and 1 bar. [c] IAST selectivity calculated at 273 K and 1 bar, see also Table S6 in ESI†. [d] Not measured. [e] 5 mol equivalent of $ZnCl_2$. [f] This work.

To better understand the adsorption properties, the differential heat of adsorption (negative adsorption enthalpy) $\Delta H_{ads,diff}$ was calculated after determining the required relative pressures p_1 and p_2 from two adsorption isotherms acquired at different temperatures T_1 and T_2 (Fig. 5) using a modified form of the Clausius-Clapeyron equation (eq. (1)).[56] $\Delta H_{ads,diff}$ was calculated over the whole adsorption range from the 273 K and 293 K isotherms for CO_2 in MM1 to MM4. The heat of adsorption at zero loading, Q^0_{ads} is included in Table 2.

$$\Delta H_{ads,diff} = -R ln\left(\frac{p_2}{p_1}\right)\frac{T_1 T_2}{T_2 - T_1} \cdots\cdots\cdots\cdots (1)$$

As shown in the Fig. 7, the isosteric heat of adsorption (ΔH) values at zero coverage are 32, 36, 43 and 30 kJ/mol for MM1 to MM4, respectively, and drop with higher loading. The high adsorption enthalpy at low coverage is explained by the initial filling of the small ultramicropores up to 4 Å with adsorbate–surface interactions to either sides or ends of the CO_2 molecules.[28] At error margins of at least ±3 kJ/mol which we calculated on average for $Q_{ads,diff}$ data points[57] the above differences for MM' materials should not be over interpreted. The more so as a careful evaluation of the performance of a given porous material should consider the heat of adsorption over the entire adsorption range (not just at zero coverage). At zero to low coverage the magnitude of the isosteric heat of adsorption is largely a function of the binding strength of the strongest binding sites within the material. MM3 exhibits the steepest drop in ΔH_{ads} with CO_2 loading, its high energy sites are rapidly saturated already at low CO_2 uptake. The heat of adsorption quickly drops below those of the other MM' materials with increasing coverage and approaches the heat of liquefaction (condensation) of bulk CO_2 with 17 kJ mol^{-1}.[58] The heat of adsorption of MM1 and MM4 develop quite similar with coverage and remain above 25 kJ mol^{-1} until full loading to 1 bar. The heat of adsorption of MM2 is even higher, remaining above 27 kJ mol^{-1}. These latter adsorption enthalpies stays well above the heat of liquefaction of bulk CO_2 and are higher than isosteric enthalpies of adsorption for CO_2 on activated carbons (e.g. BPL 25.7 kJ mol^{-1}, A10 21.6 kJ mol^{-1}, Norit R1 Extra 22.0 kJ mol^{-1}).[59]

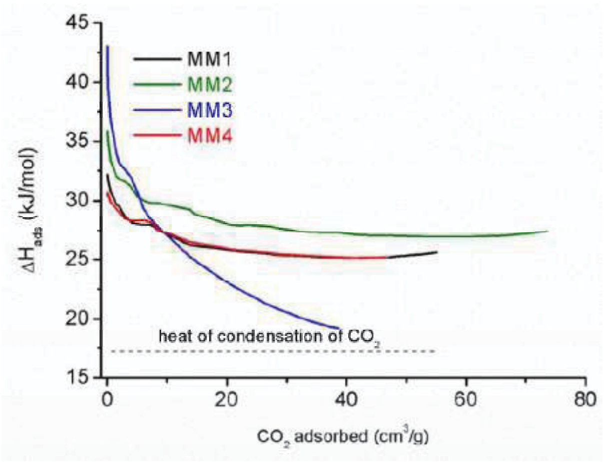

Fig. 7 Isosteric heat of adsorption for MM1-MM4 calculated from CO_2 adsorption isotherms at 273 K and 293 K.

The CH_4 adsorption of MM1-MM4 was investigated at low pressure (up to 1 bar) and 273 K and 293 K. The CH_4 uptake capacities of MM1 to MM4 lie in the range 32.7-21.3 cm^3 g^{-1} at 273 K, which is comparable with the values for PCTF-1 and -2 from tetrakis(4-cyanophenyl)ethylene (M) from our previous work.[38]

The possibility of potential application for CTFs materials as CO_2 sorbents from flue gas or from natural gas, the selectivity of CO_2 over N_2 and CH_4 were calculated by using the Henry equation and the ideal adsorbed solution theory (IAST).[60,61] From the initial slopes of adsorption isotherms, the adsorption selectivities of CO_2/N_2 and CO_2/CH_4 were estimated by the ratios of these slopes at 273 K and 293 K (Fig. S3-S6 and Table 2).

The CO_2/N_2 adsorption selectivities found to be 32, 23, 13 and 21 for MM1-MM4, respectively. As expected, the CO_2/CH_4 sorption selectivies (6, 5, 4 and 5) of MM1-MM4 were lower. These selectivity values also compared very well with the published data (Table S6). From IAST (Fig. S10-S11 and Table S3 and S6 in ESI†), the CO_2/N_2 selectivities of MM1-MM4 are 130, 97, 77 and 98 at 273 K (Table 2), which are higher than the Henry calculation. These selectivities are very high for CTFs materials known to date. Further, the IAST CO_2/N_2 adsorption selectivities of the mixed-nitrile MM' materials are higher than the selectivities of the single-nitrile M materials (Table 3).

To examine the effect of hygroscopic properties**,** water sorptions were measured volumetrically for CTFs MM1-MM4 at 20°C. On the other hand, for a porous material with good water stability, the shape of water vapor sorption isotherm can also offer direct information on the hydrophobicity or hydrophilicity.[62] According to Walton *et al.* the behavior of porous materials often defy the classical definition of a hydrophilic material. Such is the case, for example, for mesoporous silica (MCM-41 and SBA-15) which are classified as hydrophobic, although they absorb more water than microporous zeolite, which is mainly hydrophilic in nature.[62]

This is because the water sorption loadings are directed by the available pore volume due to capillary condensation. Water sorption isotherms of the CTFs MM1-MM4 are shown in Fig. 8 are Type V isotherm.[47,63] Type V isotherms are observed for water adsorption on hydrophobic microporous and mesoporous adsorbents.[47] The S-shaped isotherm is typical for water sorption in metal-organic frameworks (MOFs).[64] MOFs have intermediate and tuneable hydrophilicity-hydrophobicity. The more hydrophilic the MOF, the lower the P/P_0 for the rise of the uptake curve.[57] Hydrophilic MOFs like Al-fumarate[65] and CAU-10-H[66] show the rise between P/P_0 = 0.1-0.2, while more hydrophobic MOFs like MIL-101Cr[67] or fluorinated MIL-47 and MIL-53Al[68] exhibit the rise between P/P_0 = 0.4-0.5.

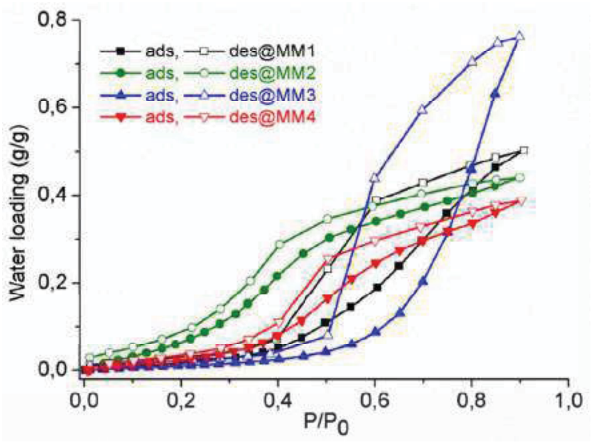

Fig. 8 Water sorption isotherms of MM1-MM4 at 20°C

The MM2-CTFs water sorption isotherm shows an early onset of water uptake which is enhanced between P/P_0 = 0.3-0.4. At low relative pressure (P/P_0 = 0.1) the fluorinated CTF MM2 already shows a water loading of 0.035 g/g (Table S5, ESI†). The MM2 water uptake curve is similar to silica gel with a more or less steady increase because of a broad pore size distribution. This is remarkable as fluorous hydrocarbons would be normally viewed as 'non-sticky' and hydrophobic. Aromatic C-F bonds are, however, relevant H-bond acceptors.[69] So, hydrogen bonding from water to aromatic C-F apparently presents a driving force for water uptake. MM1 and MM3 CTFs with pure hydrocarbon linkers have the rise between P/P_0 = 0.4-0.6 and biphenyl-MM3 even later between P/P_0 = 0.6-0.8 which indicates suggested that these CTFs are hydrophobic to very hydrophobic (MM3) in nature, similar to activated carbon materials.[63b] Pyridine based CTFs such as *bipy*-CTF500 and *pym*-CTF500 both exhibited rather hydrophilic character.[3b] At P/P_0 = 0.9 MM1-MM4 can adsorb in the range of 0.4-0.8 g water/g CTF (548-948 cm^3/g) at 20 °C which is not so much dictated by hydrophilicity but by capillary condensation in the available pore volume (Table S5, ESI†).

Conclusion

In summary, we have introduced a mixed-nitrile linker strategy for the preparation of MM'-CTFs materials with higher CO_2 uptake and higher CO_2/N_2 selectivity than expected from the comparative single-nitrile M- or M'-CTFs. The CO_2 uptake capacity of mixed-nitrile MM1, MM2 and MM4 were synergistically enhanced when compared to the CO_2 uptake of the individual single-nitrile M- or M'-CTFs. At the same time, the BET surface areas of MM' is high (1360-1884 m^2/g) but not higher than the one of the M-CTF PCTF-1 (2235 m^2/g). The synergistic higher CO_2 uptake of the mixed-linker MM'-CTFs is primarily traced to the higher CO_2-accessible micropore volume $V_{micro}(CO_2)$ (from CO_2 adsorption) and the higher micropore volume fraction $V_{0.1}/V_{tot}$ (from N_2 adsorption) for the MM'-CTFs when compared to the M- or M'-CTFs. The finding underscores that the surface area of porous materials alone does not play the most important role in CO_2 storage at low pressure but, the CO_2-accessible micropore volume is the more decisive factor. Further, MM2 shows very high CO_2 uptake capacity of 4.70 mmol/g at 273 K and 1 bar – second highest to all known CTFs – which is due to its large micropore fraction (82%) and to strong electrostatic interactions between high electronegative fluorine atoms and CO_2 gas molecules. These CTFs also exhibit very high CO_2/N_2 adsorption selectivities with the mixed-nitrile MM1, MM2 and MM4 CTFs being again more selective than the single-component M- or M'-CTFs. The high CO_2 adsorptions together with high thermal and chemical stability of these CTFs make them promising candidates for gas capture and storage.

Acknowledgements

‡ Support of the work by BMBF project OptiMat 03SF0492C is gratefully acknowledged.

Notes and references

1 (a) P. Kuhn, M. Antonietti and A. Thomas, *Angew. Chem. Int. Ed.*, 2008, **47**, 3450-3453; (b) P. Kuhn, A. l. Forget, D. Su, A. Thomas and M. Antonietti, *J. Am. Chem. Soc.*, 2008, **130**, 13333-13337; (c) M. J. Bojdys, J. Jeromenok, A. Thomas and M. Antonietti, *Adv. Mater.*, 2010, **22**, 2202-2205; (d) S. Kuecken, J. Schmidt, L. Zhi and A. Thomas, *J. Mater. Chem. A*, 2015, **3**, 24422-24427; (e) P. Kuhn, A. Thomas and M. Antonietti, *Macromolecules*, 2009, **42**, 319-326.

2 (a) X. Jiang, P. Wang and J. Zhao, *J. Mater. Chem. A*, 2015, **3**, 7750–7758; (b) F. Yang, V. Kuznietsov, M. Lublow, C. Merschjann, A. Steigert, J. Klaer, A. Thomas and T. Schedel-Niedriga, *J. Mater. Chem. A*, 2013, **1**, 6407-6415; (c) L. Stegbauer, K. Schwinghammer and Bettina V. Lotsch, *Chem. Sci.*, 2014, **5**, 2789-2793; (d) K. Schwinghammer, S. Hug, M. B. Mesch, J. Senker and B. V. Lotsch, *Energy Environ. Sci.*, 2015, **8**, 3345-3353; (e) K. Schwinghammer, B.Tuffy, M. B. Mesch, E. Wirnhier, C. Martineau, F. Taulelle, W. Schnick, J. Senker and B. V. Lotsch, *Angew.Chem. Int. Ed.*, 2013, **52**, 2435 –2439; (f) X. Wang, K. Maeda, A. Thomas, K.Takanabe, G. Xin, J. M. Carlsson, K. Domen and M. Antonietti, *Nat. Mater.*, 2009, **8**, 76–80.

3 (a) S. Hug, L. Stegbauer, H. Oh, M. Hirscher and B. V. Lotsch, *Chem. Mater.*, 2015, **27**, 8001–8010; (b) S. Hug, M. B. Mesch, H. Oh, N. Popp, M. Hirscher, J. Senker and B. V. Lotsch, *J. Mater. Chem. A*, 2014, **2**, 5928-5936; (c) E. Preis, W. Dong, G. Brunklausb and U. Scherf, *J. Mater. Chem. C*, 2015, **3**, 1582-1587.

4 (a) Y. Xu, S. Jin, H. Xu, A. Nagai and D. Jiang, *Chem. Soc. Rev.*, 2013, **42**, 8012-8031; (b) S.-Y. Ding and W. Wang, *Chem. Soc. Rev.,* 2013, **42**, 548-568.

5 R. Gomes, P. Bhanja and A. Bhaumik, *Chem. Commun.*, 2015, **51**, 10050-10053; Z. Xiang, R. Mercado, J. M. Huck, H. Wang, Z. Guo, W. Wang, D. Cao, M. Haranczyk and B. Smit, *J. Am. Chem. Soc.*, 2015, **137**, 13301–13307.

6 H. Cong, M. Zhang, Y. Chen, K. Chen, Y. Hao, Y. Zhao and L. Feng, *Carbon*, 2015, **92**, 297–304

7 (a) S. Nandi, U. Werner-Zwanziger and R. Vaidhyanathan, *J. Mater. Chem. A*, 2015, **3**, 21116-21122; (b) L.-B. Sun, Y.-H. Kang, Y.-Q. Shi, Y. Jiang, and X.-Q. Liu, *ACS Sustainable Chem. Eng.*, 2015, **3**, 3077–3085; (c) Z. Xiang, X. Zhou, C. Zhou, S. Zhong, X. He, C. Qin and D. Cao, *J. Mater. Chem.*, 2012, **22**, 22663-22669; (d) T. Jin, Y. Xiong, X. Zhu, Z. Tian, D.-J. Tao, J. Hu, D.-e. Jiang, H. Wang, H. Liu and S. Dai, *Chem. Commun.*, 2016, **52**, 4454-4457

8 K. Sumida, D. L. Rogow, J. A. Mason, T. M. McDonald, E. D. Bloch, Z. R. Herm, T.-H. Bae and J. R. Long, *Chem. Rev.,* 2012, **112**, 724-781.

9 Y. Liu, Z. U. Wang and H.-C. Zhou, *Greenhouse Gases: Science and Technology* 2012, **2**, 239-259.

10 J.-R. Li, Y. Ma, M. C. McCarthy, J. Sculley, J. Yu, H.-K. Jeong, P. B. Balbuena and H.-C. Zhou, *Coord. Chem. Rev.*, 2011, **255**, 1791–1823.

11 J. Liu, P. K. Thallapally, B. P. McGrail, D. R. Brown and J. Liu, *Chem. Soc. Rev.*, 2012, **41**, 2308-2322; D. M. D'Alessandro, B. Smit and J. R. Long, *Angew. Chem. Int. Ed.*, 2010, **49**, 6058-6082.

12 J. Zhang, P. A. Webley and P. Xiao, *Energy Conversion and Management*, 2008, **49**, 346-356.

13 A. Khutia and C. Janiak, *Dalton Trans.*, 2014, **43**, 1338-1347.

14 (a) G. Qi, Y. Wang, L. Estevez, X. Duan, N. Anako, A.-H. A. Park, W. Li, C. W. Jones and E. P. Giannelis, *Energy Environ. Sci.*, 2011, **4**, 444–452; (b) J. C. Hicks, J. H. Drese, D. J. Fauth, M. L. Gray, G. Qi and C. W. Jones, *J. Am. Chem. Soc.*, 2008, **130**, 2902–2903.

15 L. Wang and R. T. Yang, *J. Phys. Chem. C*, 2012, **116**, 1099-1106.

16 V. Guillerm, L. J. Weselinski, M. Alkordi, M. I. H. Mohideen, Y. Belmabkhout, A. J. Cairns and M. Eddaoudi, *Chem. Commun.*, 2014, **50**, 1937-1940.

17 T. Islamoglu, M. Gulam Rabbani and H. M. El-Kaderi, *J. Mater. Chem. A*, 2013, **1**, 10259-10266.

18 V. M. Suresh, S. Bonakala, H. S. Atreya, S. Balasubramanian, and T. K. Maji, *ACS Appl. Mater. Interfaces*, 2014, **6**, 4630-4637; H. A. Patel, S. Hyun Je, J. Park, D. P. Chen, Y. Jung, C. T. Yavuz and A. Coskun, *Nat. Commun.*, 2013, **4**, 1357.

19 W. Lu, J. P. Sculley, D. Yuan, R. Krishna, Z. Wei and H.-C. Zhou, *Angew. Chem. Int. Ed.*, 2012, **51**, 7480-7484.

20 H. A. Patel, F. Karadas, J. Byun, J. Park, E. Deniz, A. Canlier, Y. Jung, M. Atilhan and C. T. Yavuz, *Adv. Funct. Mater.*, 2013, **23**, 2270–2276.

21 (a) H.-R. Yu, S. Cho, B. C. Bai, K. B. Yi and Y.-S. Lee, *Int. J. Greenhouse Gas Control*, 2012, **10**, 278–284; (b) S. Cho, H.-R. Yu, K. D. Kim, K. B. Yi and Y.-S. Lee, *Chem. Eng. J.*, 2012, **211**, 89–96.

22 (a) B. Wang, A. P. Cote, H. Furukawa, M. O'Keeffe and O. M. Yaghi, *Nature*, 2008, **453**, 207–211; (b) X.-M. Hu, Q. Chen, Y.-C. Zhao, B. W. Laursen and B. Han, *J. Mater. Chem. A*, 2014, **2**, 14201.

23 Y. F. Zhao, K. X. Yao, B. Y. Teng, T. Zhang and Y. Han, *Energy Environ. Sci.*, 2013, **6**, 3684–3692.

24 (a) A. Patra and U. Scherf, *Chem. Eur. J.*, 2012, **18**, 10074-10080; (b) A. Patra, J.-M. Koenen and U. Scherf, *Chem. Commun.*, 2011, **47**, 9612-9614.

25 M. G. Rabbani and H. M. El-Kaderi, *Chem. Mater.*, 2012, **24**, 1511-1517.

26 J. Germain, J. Hradil, J. M. J. Fréchet and F. Svec, *Chem. Mater.*, 2006, **18**, 4430-4435.

27 B. S. Ghanem, K. J. Msayib, N. B. McKeown, K. D. M. Harris, Z. Pan, P. M. Budd, A. Butler, J. Selbie, D. Book and A. Walton, *Chem. Commun.*, 2007, 67-69.

28 H. Zhao, Z. Jin, H. Su, J. Zhang, X. Yao, H. Zhao and G. Zhu, *Chem. Commun.*, 2013, **49**, 2780-2782.

29 E. Preis, C. Widling, U. Scherf, S. Patil, G. Brunklaus, J. Schmidt and A. Thomas, *Polym. Chem.*, 2011, **2**, 2186-2189; R. S. Sprick, A. Thomas and U. Scherf, *Polym. Chem.*, 2010, **1**, 283-285.

30 J.-X. Jiang, F. Su, A. Trewin, C. D. Wood, N. L. Campbell, H. Niu, C. Dickinson, A. Y. Ganin, M. J. Rosseinsky, Y. Z. Khimyak and A. I. Cooper, *Angew. Chem. Int. Ed.*, 2007, **46**, 8574-8578.

31 Introduction to themed issue on COFs: A. I. Cooper, *CrystEngComm*, 2013, **15**, 1483; S. Kandambeth, A. Mallick, B. Lukose, M. V. Mane, T. Heine and R. Banerjee, *J. Am. Chem. Soc.*, 2012, **134**, 19524-19527.

32 M. Shunmughanathan, P. Puthiaraj and K. Pitchumani, *ChemCatChem*, **2015**, *7*, 666-673.

33 P. Puthiaraj and K. Pitchumani, *Chem. – Eur. J.*, 2014, **20**, 8761-8770.

34 Y. Zhu, H. Long and W. Zhang, *Chem. Mater.*, 2013, **25**, 1630-1635.

35 L.-B. Sun, A.-G. Li, X.-D. Liu, X.-Q. Liu, D. Feng, W. Lu, D. Yuan and H.-C. Zhou, *J. Mater. Chem. A*, 2015, **3**, 3252-3256.

36 M. Rose, W. Bohlmann, M. Sabo and S. Kaskel, *Chem. Commun.,* 2008, 2462-2464.

37 M. Nandi, K. Okada, A. Dutta, A. Bhaumik, J. Maruyama, D. Derks and H. Uyama, *Chem. Commun.,* 2012, **48**, 10283-10285.

38 A. Bhunia, V. Vasylyeva and C. Janiak, *Chem. Commun.*, 2013, **49**, 3961-3963.

39 A. Bhunia, I. Boldog, A. Moller and C. Janiak, *J. Mater. Chem. A*, 2013, **1**, 14990–14999.

40 (a) K. Kailasam, J. Schmidt, H. Bildirir, G. Zhang, S. Blechert, X. Wang and A. Thomas, *Macromol. Rapid Commun.,* 2013, **34**, 1008−1013; (b) K. Kailasam, M. B. Mesch, L. Möhlmann, M. Baar, S. Blechert, M. Schwarze, M. Schröder, R. Schomäcker, J. Senker and A. Thomas, *Energy Technol.*, 2016, **4**, 744–750; (c) R. S. Sprick, B. Bonillo, R. Clowes, P. Guiglion, N. J. Brownbill, B. J. Slater, F. Blanc, M. A. Zwijnenburg, D. J. Adams and A. I. Cooper, *Angew.Chem. Int. Ed.,* 2016, **128**, 1824–1828; (d) R. S. Sprick, J.-X. Jiang, B. Bonillo, S. Ren, T. Ratvijitvech, P. Guiglion, M. A. Zwijnenburg, D. J. Adams and A. I. Cooper, *J. Am. Chem. Soc.*, 2015, **137**, 3265−3270; (e) P. Katekomol, J. Roeser, M. Bojdys, J. Weber and A. Thomas, *Chem. Mater.*, 2013, **25**, 1542–1548; (f) A. Bhunia, D. Esquivel, S. Dey, R. J. Fernández-Terán, Y. Goto, S. Inagaki, P. Van Der Voort and C. Janiak, *J. Mater. Chem A*, 2016, DOI: 10.1039/c6ta04623a.

41 (a) C. E. Chan-Thaw, A. Villa, P. Katekomol, D. Su, A. Thomas and L. Prati, *Nano Lett.*, 2010, **10**, 537–541; (b) J. Roeser, K. Kailasam and A. Thomas, *ChemSusChem*, 2012, **5**, 1793-1799.

42 A. Bhunia, S. Dey, M. Bous, C. Zhang, W. von Rybinski, and C. Janiak, *Chem. Commun.*, 2015, **51**, 484-486.

43 A. V. Bavykina, M. G. Goesten, F. Kapteijn, M. Makkee and J. Gascon, *ChemSusChem*, 2015, **8**, 809 – 812

44 S. Ren, M. J. Bojdys, R. Dawson, A. Laybourn, Y. Z. Khimyak, D. J. Adams and A. I. Cooper, *Adv. Mater.*, 2012, **24**, 2357-2361.

45 S. Dey, A. Bhunia, M. D. Esquivel and C. Janiak, *J. Mater. Chem. A*, 2016, **4**, 6259-6263.

46 (a) K. S. W. Sing, D. H. Everett, R. A. W. Haul, L. Moscou, R. A. Pierotti, J. Rouquerol and T. Siemieniewska, *Pure Appl. Chem.*, 1985, **57**, 603-619; (b) M. Thommes, B. Smarsly, M. Groenewolt, P. I. Ravikovitch and A. V. Neimark, *Langmuir*, 2006, **22**, 756-764.

47 M. Thommes, K. Kaneko, A. V. Neimark, J. P. Olivier, F. Rodriguez-Reinoso, J. Rouquerol and K. S. W. Sing, *Pure Appl. Chem.*, 2015, **87**, 1051–1069.

48 J. Artz, S. Mallmann and R. Palkovits, *ChemSusChem*, 2015, **8**, 672-679.

49 F. Rodriguez-Reinoso and A. Linares-Solano, *in Chemistry and Physics of Carbon*, vol. **21** (P. A. Thrower, Ed.) Marcel Dekker, New York, 1988.

50 Quantachrome Instruments (1900 Corporate Drive, Boynton Beach, FL 33426 USA, www.quantachrome.com) Powder Tech Note 35.

51 A. Bhunia, I. Boldog, A. Möller and C. Janiak. *J. Mater. Chem. A*, 2013, **1**, 14990-14999.

52 R. Dawson, A. Laybourn, R. Clowes, Y. Z. Khimyak, D. J. Adams and A. I. Cooper, *Macromolecules*, 2009, **42**, 8809–8816.

53 P. Puthiaraj, S.-M. Cho, Y.-R. Lee and W.-S. Ahn, *J. Mater. Chem. A*, 2015, **3**, 6792-6797

54 X. Liu, H. Li, Y. Zhang, B. Xu, S. A, H. Xia and Y. Mu*, Polym. Chem.*, 2013, **4**, 2445-2448.

55 S. Xiong, X. Fu, L. Xiang, G. Yu, J. Guan, Z. Wang, Y. Du, X. Xiong and C. Pan, *Polym. Chem.*, 2014, **5**, 3424-3431.

56 F. Rouquerol, J. Rouquerol and K. Sing, *Adsorption by powders and porous solids*, (F. Rouquerol, J. Rouquerol, K. Sing, Eds.), Academic Press, San Diego, 1999, vol. 11.

57 F. Jeremias, A. Khutia, S. K. Henninger and C. Janiak, *J. Mater. Chem.*, 2012, **22**, 10148-10151; F. Jeremias, V. Lozan, S. Henninger and C. Janiak, *Dalton Trans.*, 2013, **42**, 15967-15973.

58 S. Keskin, T. M. van Heest and D. S. Sholl, *ChemSusChem*, 2010, **3**, 879-891.

59 S. Himeno, T. Komatsu and S. Fujita, *J. Chem. Eng. Data*, 2005, **50**, 369-376; K. B. Lee, M. G. Beaver, H. S. Caram and S. Sircar, *Ind. Eng. Chem. Res.*, 2008, **47**, 8048-8062.

60 J. A. Obrien and A. L. Myers, *Ind. Eng. Chem. Res.*, 1988, **27**, 2085–2092

61 A. L. Myers and J. M. Prausnitz, *AIChE J.*, 1965, **11**, 121–127

62 N. C. Burtch, H. Jasuja and K. S. Walton, *Chem. Rev.*, 2014, **114**, 10575-10612

63 (a) E.-P. Ng and S. Mintova, *Micropor. Mesopor. Mater.*, 2008, **114**, 1–26; (b) L. Cossarutto, T. Zimny, J. Kaczmarczyk, T. Siemieniewska, J. Bimer and J.V. Weber, *Carbon*, 2001, **39**, 2339–2346

64 S. K. Henninger, F. Jeremias, H. Kummer and C. Janiak, *Eur. J. Inorg. Chem.*, 2012, **16**, 2625–2634; C. Janiak and S. K. Henninger, *Chimia*, 2013, **67**, 419–424; F. Jeremias, D. Fröhlich, C. Janiak and S. K. Henninger, *New J. Chem.*, 2014, **38**, 1846–1852.

65 F. Jeremias, D. Fröhlich, C. Janiak and S. K. Henninger, *RSC Adv.*, 2014, **4**, 24073–24082.

66 D. Fröhlich, S. K. Henninger and C. Janiak, *Dalton Trans.*, 2014, **43**, 15300–15304.

67 J. Ehrenmann, S. K. Henninger and C. Janiak, *Eur. J. Inorg. Chem.*, 2011, **4**, 471–474; A. Khutia, H. U. Rammelberg, T. Schmidt, S. Henninger and C. Janiak, *Chem. Mater.*, 2013, **25**, 790–798.

68 S. Biswas, S. Couck, D. Denysenko, A. Bhunia, M. Grzywa, J. F. M. Denayer, D. Volkmer, C. Janiak and P. Van Der Voort, *Micropor. Mesopor. Mater.*, 2013, **181**, 175-181.

69 V. R. Thalladi, H.-C. Weiss, D. Bläser, R. Boese, A. Nangia and G. R. Desiraju, *J. Am. Chem. Soc.*, 1998, **120**, 8702-8710; G. Althoff, J. Ruiz, V. Rodríguez, G. López, J. Pérez and C. Janiak, *CrystEngComm*, 2006, **8**, 662‑665; E. D'Oria and J. J. Novoa, *CrystEngComm*, 2008, **10**, 423–436; J. Ruiz, V. Rodríguez, C. de Haro, A. Espinosa, J. Pérez and C. Janiak, *Dalton Trans.*, 2010, **39**, 3290–3301; D. Chopra and T. N. Guru Row, *CrystEngComm*, 2011, **13**, 2175—2186.

Two linkers are better than one: Enhancing CO_2 capture and separation with porous covalent triazine-based frameworks from mixed nitrile linkers.

Subarna Dey, Asamanjoy Bhunia and Christoph Janiak*
Institut für Anorganische Chemie und Strukturchemie, Heinrich-Heine-Universität Düsseldorf, 40204 Duesseldorf, Germany.
* Corresponding author: E-mail: janiak@uni-duesseldorf.de; Fax: + 49-211-81-12287; Tel: +49-211-81-12286.

Emails: subarna.dey@hhu.de, asamanjoy.bhunia@gmail.com,

Table of contents

1. Experimental Section

Materials and methods

All chemicals were purchased from commercial suppliers (Sigma-Aldrich, Acros Organics, and Alfa Aesar chemical company) and used without further purification, unless stated otherwise. Tetrakis(4-cyanophenyl)ethylene was synthesized according to the reported procedures.[1]

Infrared (IR) spectra were obtained on a Bruker FT-IR Tensor 37 Spectrometer in the 4000-550 cm^{-1} region with 2 cm^{-1} resolution as KBr disks. ^{1}H and ^{13}C spectra were recorded on a Avance DRX-500 instruments.. Elemental (CNH) analyses were carried out with a PerkinElmer 2400 series 2 elemental analyzer. Powder X-ray diffraction (PXRD) data was collected on a Bruker D2 Phaser diffractometer using a flat sample holder (also a flat silicon, low background sample holder) and Cu $K\alpha_1/\alpha_2$ radiation with $\lambda = 1.5418$ Å at 30 kV covering 2theta angles 5-80° over a time of 2 h, that is. 0.01°/sec. Diffractograms were obtained on flat layer sample holders where at low angle the beam spot is strongly broadened so that only a fraction of the reflected radiation reaches the detector which leads to low relative intensities measured at $2\theta < 7°$. For hygroscopic or air-sensitive samples, the sample holder can be sealed with a dome. Scanning electron microscopy (SEM) images were obtained using an ESEM Quanta 400 FEG SEM equipped with a secondary electron detector. Thermogravimetric analyses (TGA) were carried out at a ramp rate of 5 °C/min in a N_2 flow with a Netzsch Thermo-Microbalance Aparatus TG 209 F3 Tarsus.

Sorption isotherms were measured using a Micromeritics ASAP 2020 automatic gas sorption analyzer equipped with oil-free vacuum pumps (ultimate vacuum $<10^{-8}$ mbar) and valves, which guaranteed contamination free measurements. The sample was connected to the preparation port of the sorption analyzer and degassed under vacuum until the outgassing rate, i.e., the rate of pressure rise in the temporarily closed manifold with the connected sample tube, was less than 2 μTorr/min at the specified temperature 200 °C. After weighing, the sample tube was then transferred to the analysis port of the sorption analyzer. All used gases (H_2, He, N_2, CO_2, CH_4) were of ultra high purity (UHP, grade 5.0, 99.999%) and the STP volumes are given according to the NIST standards (293.15 K, 101.325 kPa). Helium gas was used for the determination of the cold and warm free space of the sample tubes. H_2 and N_2 sorption isotherms were measured at 77 K (liquid nitrogen bath), whereas CO_2 and CH_4 sorption isotherms were measured at 293±1 K (passive thermostating) and 273.15 K (ice/deionized water bath). The heat of adsorption values and the DFT pore size distributions ('N_2 DFT slit pore' model) were calculated out using the ASAP 2020 v3.05 software.

A coulometric Karl-Fischer titration for the determination of the water content was carried out with a Karl-Fischer titration apparatus AQUA 40.00 with headspace module. The solid CTF sample was heated to 170 °C in the head space module and the liberated water transferred to the measurement cell.

Water sorption isotherms at 20 °C were obtained volumetrically from a Quantachrome Autosorb iQ MP instrument equipped with an all-gas option. Prior to the sorption experiments, the compounds were degassed (130 °C, 2h) under dynamic vacuum.

2. Synthesis of CTFs (MM1-MM4)

MM1: A mixture of tetrakis(4-cyanophenyl)ethylene (100 mg, 0.23 mmol), terephthalonitrile (60 mg, 0.46 mmol) and $ZnCl_2$ (940 mg, 6.19 mmol) were placed into a Pyrex ampoule under inert conditions. The ampoule was evacuated, sealed and heated to 400 °C for 48 h followed by cooling to room temperature. The black product was collected and stirred with water for 72 h. Then the product was isolated by filtration and again stirred with 100 mL of 2 mol/L HCl for 24 h. The resulting black powder was further washed with water (3 × 50 mL), THF (3 × 30 mL), acetone (3 × 30 mL) and dried in vacuum. Yield: 130 mg, 81 %.

MM2: A mixture of tetrakis(4-cyanophenyl)ethylene (100 mg, 0.23 mmol), tetrafluoroterephthalonitrile (92 mg, 0.46 mmol) and $ZnCl_2$ (940 mg, 6.91 mmol) were placed into a Pyrex ampoule under inert conditions. The ampoule was evacuated, sealed and heated to 400 °C for 48 h followed by cooling to room temperature. The black product was collected and stirred with water for 72 h. Then the product was isolated by filtration and again stirred with 100 mL of 2 mol/L HCl for 24 h. The resulting black powder was further washed with water (3 × 50 mL), THF (3 × 30 mL), acetone (3 × 30 mL) and dried in vacuum. Yield: 137 mg, 71 %.

MM3: A mixture of tetrakis(4-cyanophenyl)ethylene (75 mg, 0.17 mmol), 4,4′-biphenyldicarbonitrile (71 mg, 0.35 mmol) and $ZnCl_2$ (713 mg, 5.34 mmol) were placed into a Pyrex ampoule under inert conditions. The ampoule was evacuated, sealed and heated to 400 °C for 48 h followed by cooling to room temperature. The black product was collected and stirred with water for 72 h. Then the product was isolated by filtration and again stirred with 100 mL of 2 mol/L HCl for 24 h. The resulting black powder was further washed with water (3 × 50 mL), THF (3 × 30 mL), acetone (3 × 30 mL) and dried in vacuum. Yield: 127 mg, 87 %.

MM4: A mixture of tetrakis(4-cyanophenyl)ethylene (86 mg, 0.2 mmol), 1,3,5-benzenetricarbonitrile (40 mg, 0.26 mmol) and $ZnCl_2$ (627 mg, 4.6 mmol) were placed into a Pyrex ampoule under inert conditions. The ampoule was evacuated, sealed and heated to 400 °C for 48 h followed by cooling to room temperature. The black product was collected and stirred with water for 72 h. Then the product was isolated by filtration and again stirred with 100 mL of 2 mol/L HCl for 24 h. The resulting black powder was further washed with water (3 × 50 mL), THF (3 × 30 mL), acetone (3 × 30 mL) and dried in vacuum. Yield: 105 mg, 83 %.

3. Table S1 Elemental analysis of MM1-MM4

Frame-work	Calculated (%) [a]					Found (%)				
	C	H	N	C/H	C/N	C	H	N	C/H	C/N
MM1	80.22	3.51	16.27	1.9	5.7	79.09	2.52	5.77	2.6	16
MM2	66.35	1.94	13.45	2.9	5.7	65.43	4.02	10.73	1.4	7
MM3	82.84	3.84	13.33	1.8	7.3	79.15	2.87	3.19	2.4	30
MM4	79.23	3.17	17.6	2.10	5.24	74.99	3.46	9.79	1.8	8.9

[a] Calculated based on the following formulae according to the used stoichiometric ratios (without considering the adsorption of moisture (see below):

MM1 :

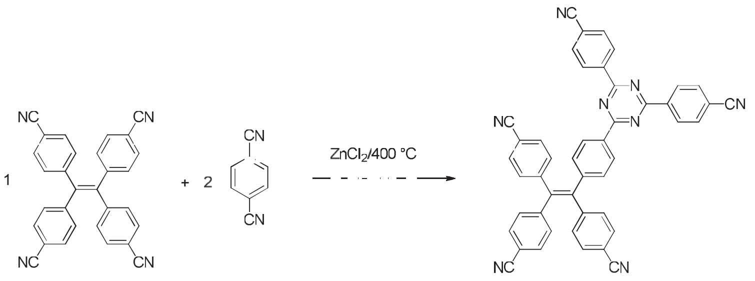

$C_{30}H_{16}N_4$ $C_8H_4N_2$ $C_{46}H_{24}N_8$

Molecular Weight: 688.74

MM2 :

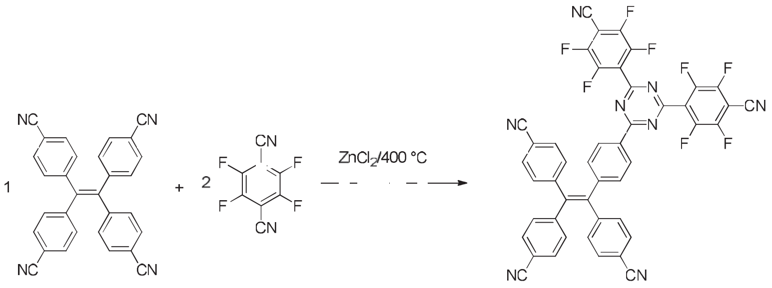

$C_{30}H_{16}N_4$ $C_8F_4N_2$ $C_{46}H_{16}F_8N_8$, *Molecular Weight: 832.66*

MM3 :

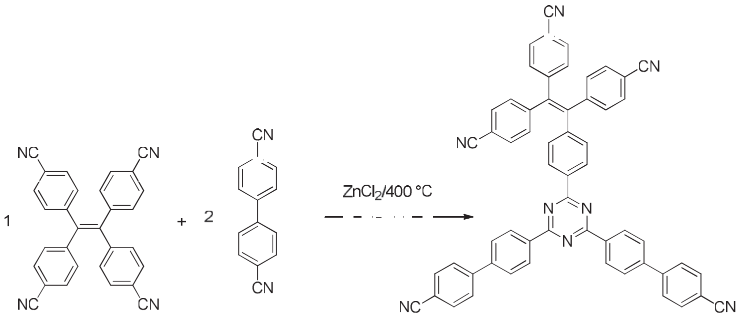

$C_{30}H_{16}N_4$ $C_{14}H_8N_2$ $C_{58}H_{32}N_8$, *Molecular Weight: 840.93*

MM4 :

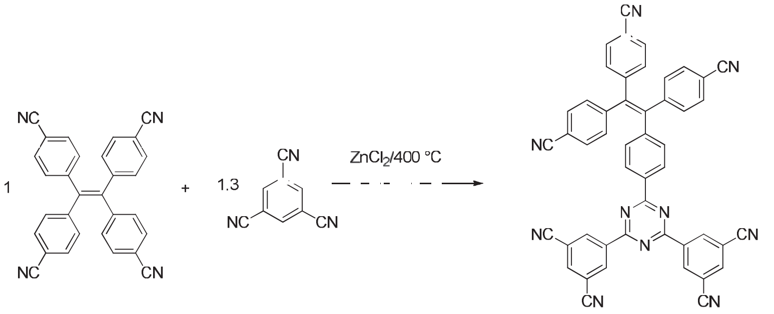

$C_{30}H_{16}N_4$ $C_9H_3N_3$ $\sim C_{42}H_{20}N_8$, *Molecular Weight: 636*

The elemental analysis of MM1-MM4 give a much lower nitrogen content and concomitantly a much higher than calculated C/N ratio. This indicates that most of the nitrogen is lost due to decomposition (Scheme S1).

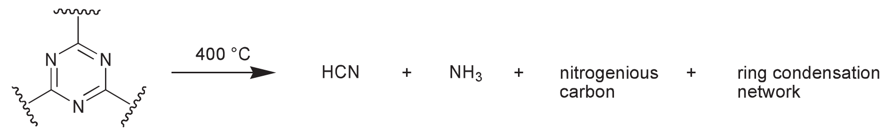

Scheme S1 General schematic representation for the decomposition of a triazine ring.

4. Powder X-ray diffraction patterns of MM1-MM4

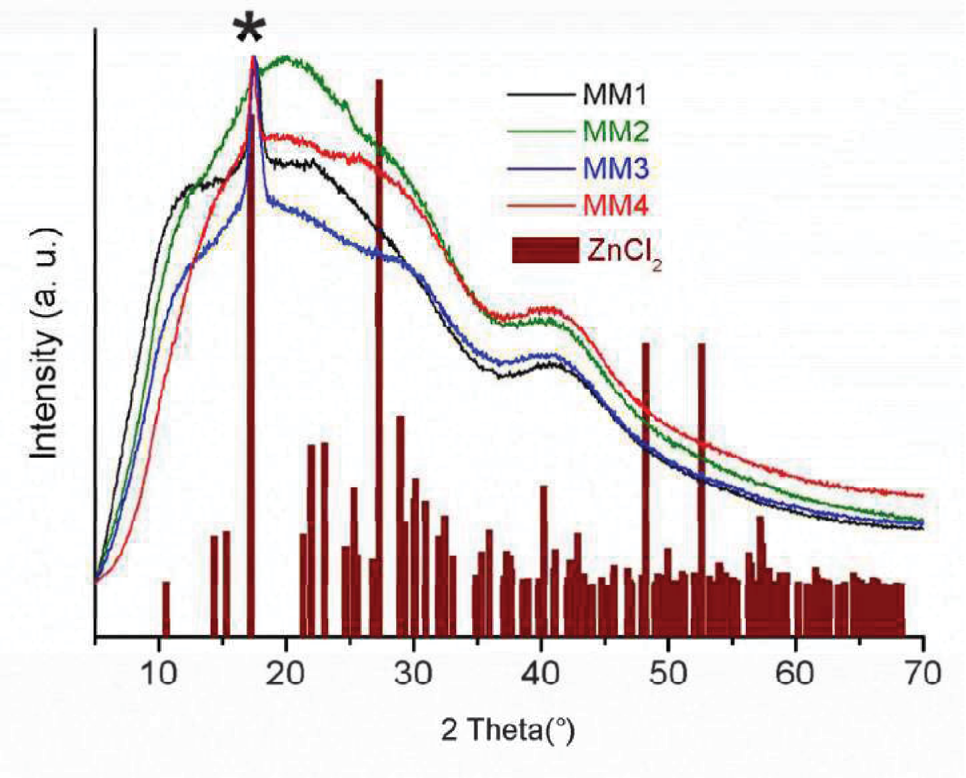

Fig. S1: Powder X-ray pattern of MM1-MM4 and its comparison with ZnCl$_2$. Single peak with * is from ZnCl$_2$ for the (111) plane at 2θ = 17.2°.[2]

5. Thermogravimetric analysis

All materials (MM1-MM4) show definite weight loss before decomposition. Both weight loss and decomposition temperature are summarized in Table S2.

Table S2 Decomposition temperature for MM1-MM4.

Compound	Decomposition Temperature (°C)	Weight loss at decomposition temperature (%)	Weight loss until 100-150 °C temperature range (%)
MM1	440	7.4	3.2
MM2	460	19.02	9.5-10.4
MM3	385	10.96	3.1-3.2
MM4	450	10.95	2.7-2.9

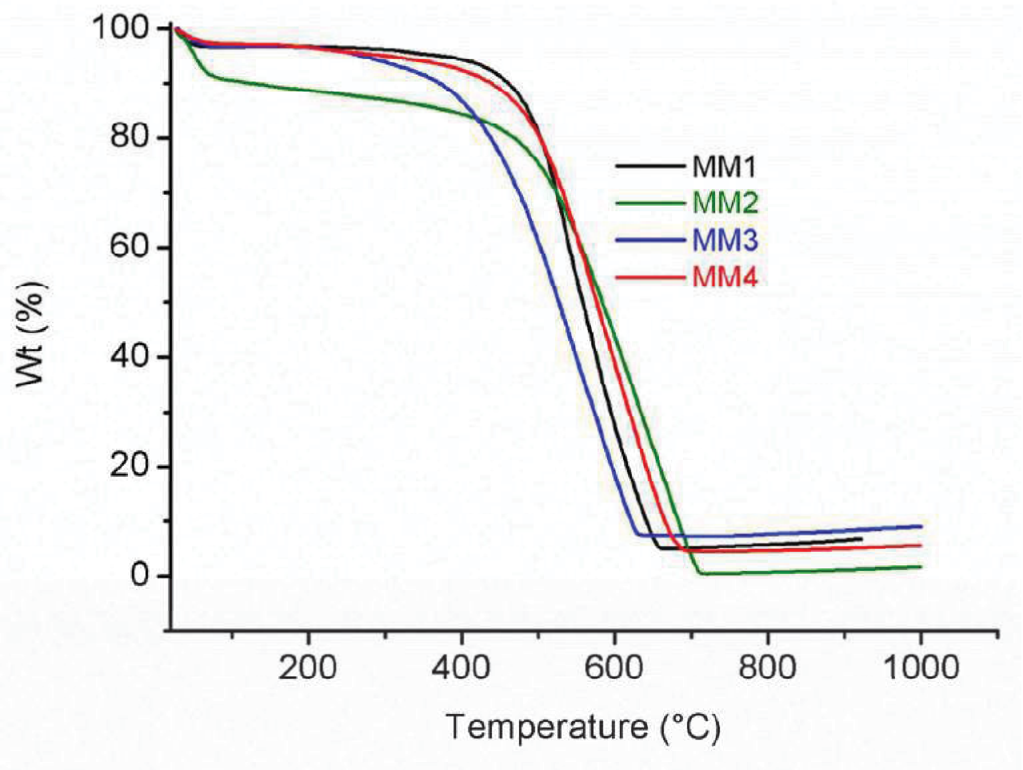

Fig. S2: TGA for MM1-MM4 in temperature range of 25 to 1000 °C at the heating rate of 5 °C / min.

6. Selectivity from initial slopes in the Henry region

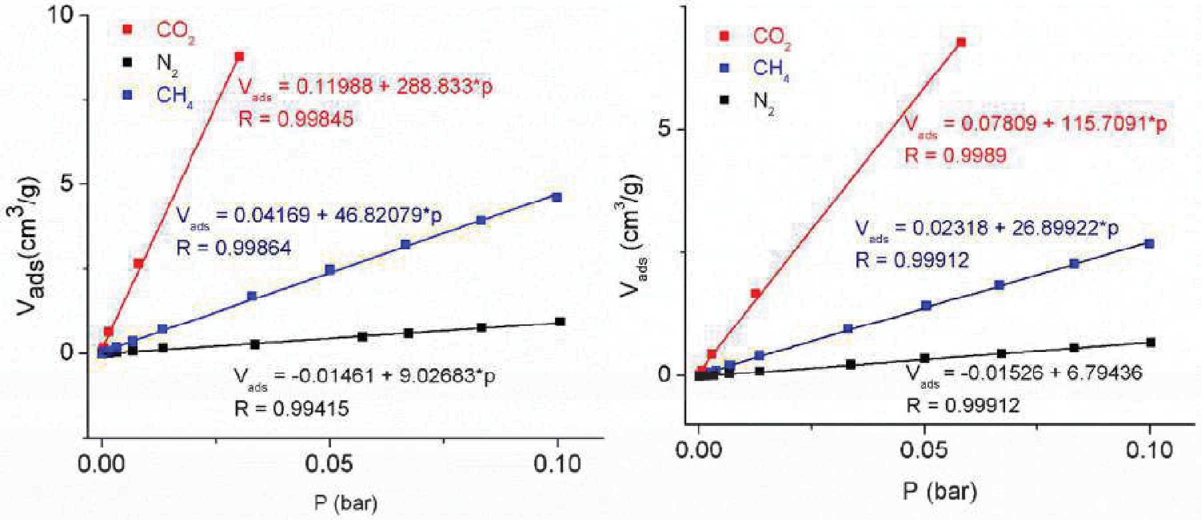

Fig. S3: The initial slopes in the Henry region of the adsorption isotherms for MM1 at 273 K (left) and 293 K (right).

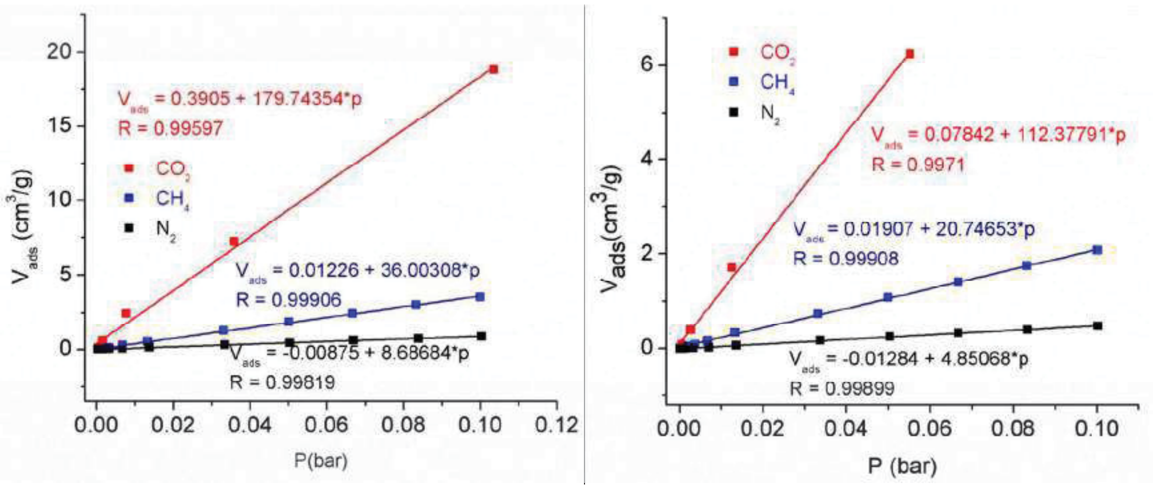

Fig. S4: The initial slopes in the Henry region of the adsorption isotherms for MM2 at 273 K (left) and 293 K (right).

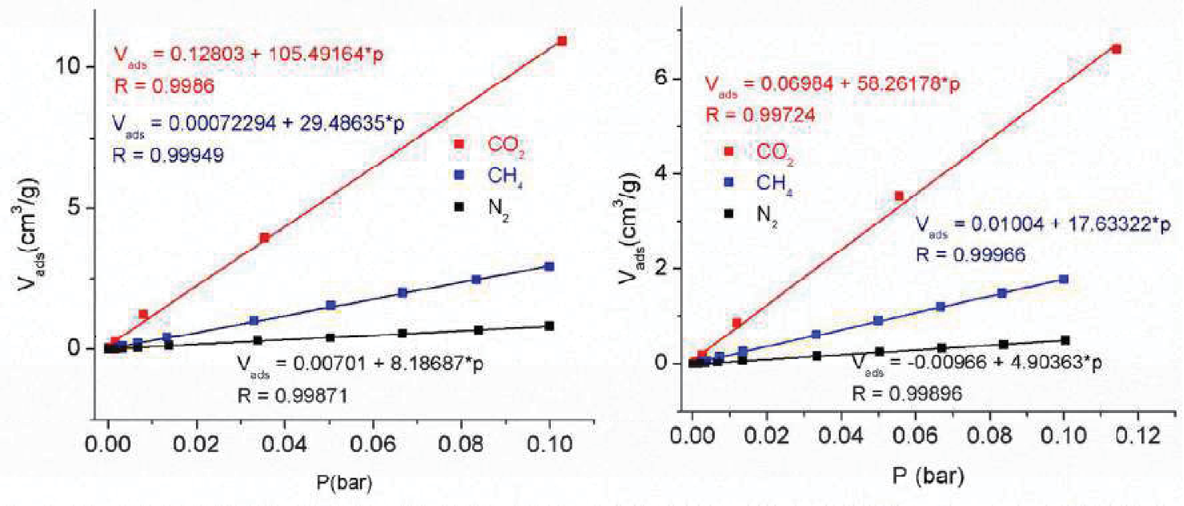

Fig. S5: The initial slopes in the Henry region of the adsorption isotherms for MM3 at 273 K (left) and 293 K (right).

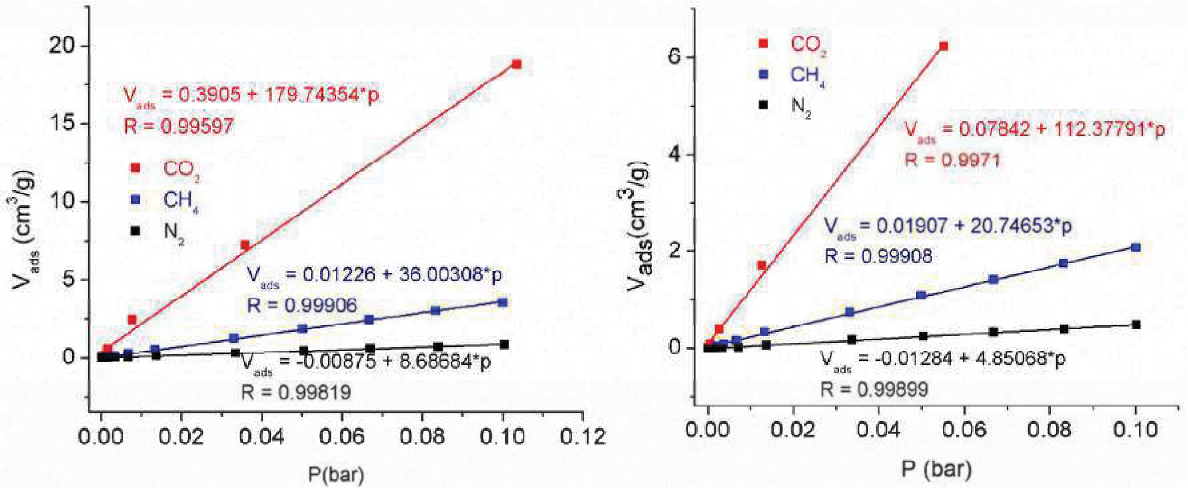

Fig. S6: The initial slopes in the Henry region of the adsorption isotherms for MM4 at 273 K (left) and 293 K (right).

7. Ideal Adsorbed Solution Theory (IAST) selectivity studies

IAST selectivities were calculated from the gas adsorption data using a single or dual-site Langmuir model to fit the adsorption isotherms. For CO_2 adsorption isotherm up to 1 bar, we assumed the double-layer adsorption. Therefore, the low pressure (up to 1 bar) adsorption isotherms of CO_2 measured at 273 K was fitted with the dual-site Langmuir (DSL) model. The equation is:

$$q = q_A + q_B = q_{sat,A}\frac{b_A p}{1 + b_A p} + q_{sat,B}\frac{b_B p}{1 + b_B p}$$

Where, q is molar uptake of adsorbate (mmol/g), q_{sat} is saturation uptake (mmol/g), b is the parameter in single component Langmuir isotherm (bar^{-1}), p is the pressure of bulk gas, the subscription of A and B refers to different two sites.

On the other hand, due to the mono-layer adsorption of CH_4 and N_2 adsorption, the single-site Langmuir models were used:

$$q = q_{sat}\frac{bp}{1 + bp}$$

The IAST selectivity S_{ads} can be calculated from the following equation:

$$S_{ads} = \frac{q1/q2}{p1/p2}$$

A CO_2:N_2 ratio of 15:85 was used for calculating the gas mixture selectivities, which is typically the flue gas composition.

Table S3 Langmuir fitting parameters of CO_2, CH_4, and N_2 adsorption isotherms of MM1, MM2, MM3 and MM4 at 273 K and 1 bar.

MM1@273K	$q_{sat,A}$ (mmol/g)	b_A (bar^{-1})	$q_{sat,B}$ (mmol/g)	b_B (bar^{-1})	Adj. R^2
CO_2	0.79922	12.12842	9.64014	0.44951	0.99999
CH_4	3.33385	0.62106			0.9996
N_2	4.6281	0.0974			0.99997

MM2@273K	$q_{sat,A}$ (mmol/g)	b_A (bar^{-1})	$q_{sat,B}$ (mmol/g)	b_B (bar^{-1})	Adj. R^2
CO_2	1.21485	14.75997	9.04758	0.67154	0.99998
CH_4	3.542	0.693			0.99968
N_2	2.84484	0.18657			0.99997

MM3@273K	$q_{sat,A}$ (mmol/g)	b_A (bar^{-1})	$q_{sat,B}$ (mmol/g)	b_B (bar^{-1})	Adj. R^2
CO_2	0.4344	8.28541	10.16668	0.28643	1
CH_4	3.45169	0.37891			0.9999
N_2	2.88644	0.12548			0.9999

MM4@273K	$q_{sat,A}$ (mmol/g)	b_A (bar^{-1})	$q_{sat,B}$ (mmol/g)	b_B (bar^{-1})	Adj. R^2
CO_2	0.83529	11.16812	7.98059	0.50873	0.9999
CH_4	3.15435	0.51096			0.99985
N_2	2.74336	0.13795			0.99998

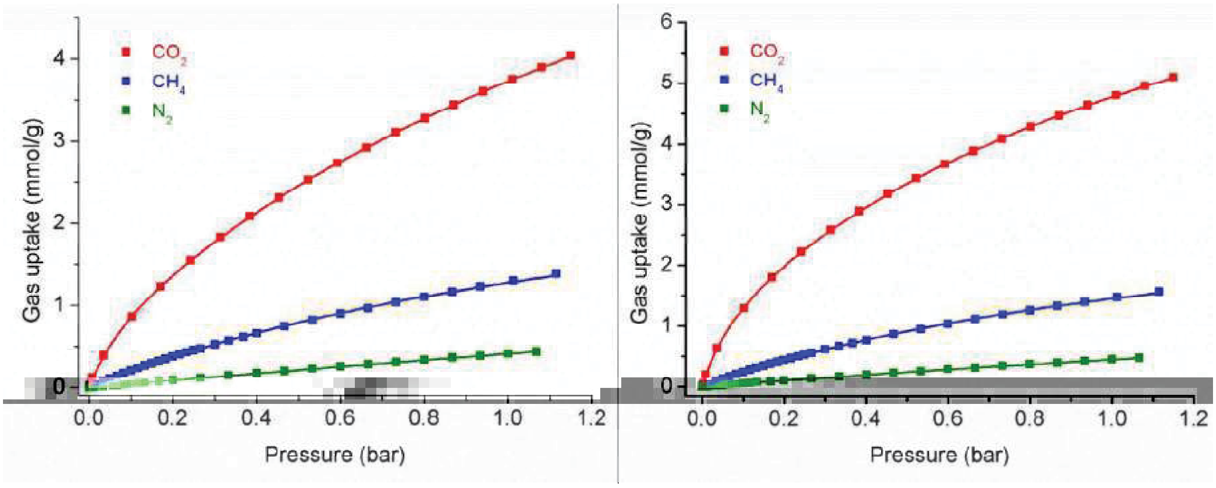

Fig. S7: DSL fitting for CO$_2$ adsorption and SSL fittings for CH$_4$ and N$_2$ adsorption at 273 K for MM1 (left) and MM2 (right).

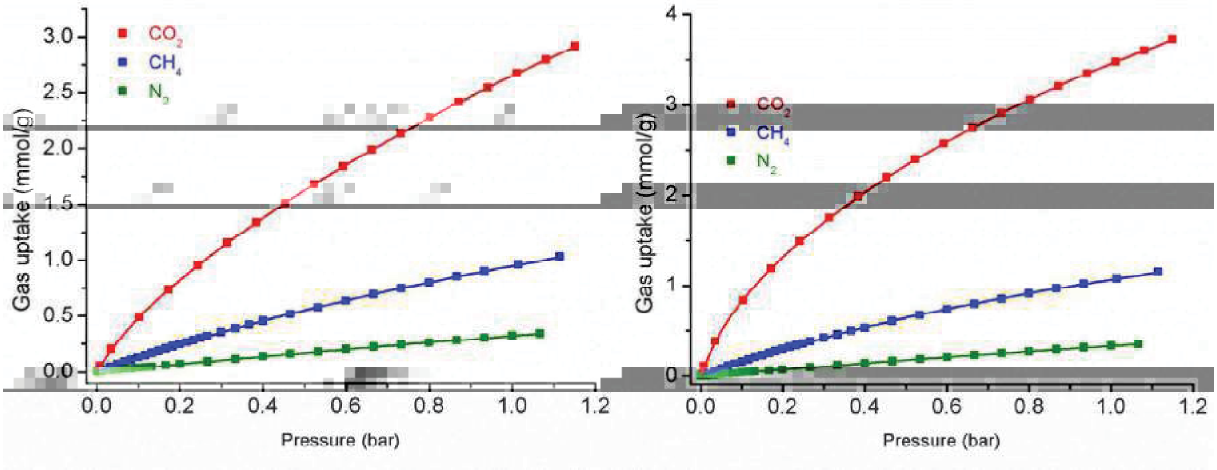

Fig. S8: DSL fitting for CO$_2$ adsorption and SSL fittings for CH$_4$ and N$_2$ adsorption at 273 K for MM3 (left) and MM4 (right).

8. Karl Fischer Titration

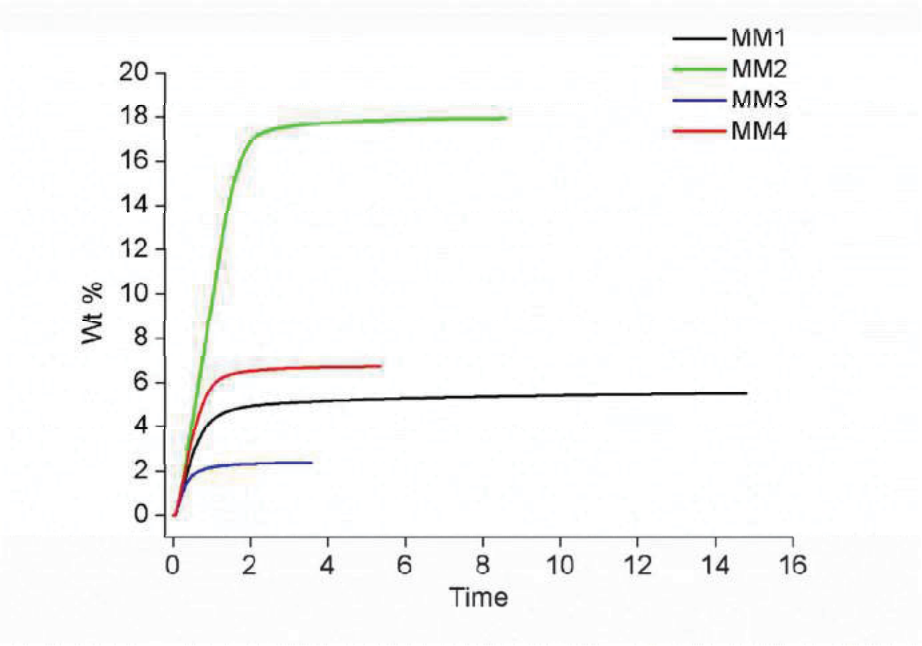

Fig. S9: Karl-Fisher Titration plot for MM1-MM4

Table S4 Amount of water absorbed on CTFs measured by Karl-Fisher Titration

CTFs [a]	Water loading (wt %)
MM1	5.1
MM2	17.5
MM3	1.9
MM4	6.3

[a] Sample had been stored under ambient air with about 50% air humidity.

9. Water adsorption isotherms

Table S5 Water uptake values for MM1- MM4 at 20 °C

CTFs	Uptake at $P/P_0 = 0.1$		Uptake at $P/P_0 = 0.5$		Uptake at $P/P_0 = 0.9$ [a]		V_{tot} [b]
	cm^3/g	g/g	cm^3/g	g/g	cm^3/g	g/g	cm^3/g
MM1	12	0.0096	140	0.11	622	0.498	1.11
MM2	44	0.035	377	0.3	548	0.439	0.67
MM3	7	0.0056	56	0.04	948	0.7596	1.52
MM4	17	0.0136	205	0.17	480	0.384	0.78

[a] The uptake near saturation pressure is not so much determined by the hydrophilicity but by the porosity and available pore volume V_{tot} due to capillary condensation

[b] Total pore volume at $P/P_0 = 0.95$ for pores ≤20 nm (repeated from Table 1 in paper).

10. Comparison to other CTFs

Table S6 Surface area, CO_2 adsorption properties and selectivity of triazine-based polymer.

Compound	BET (m^2/g)	CO_2 uptake (mmol/g) at 1 bar [a]		Q_{st}	CO_2/N_2 selectivity [b]		Ref.
		273 K	298 K or 293 K		Henry	IAST	
CTF-0-400-600	2011	4.22					3
CTF-1	746	2.47	1.41	27.5		20	4
CTF-1-600	1533	3.82	2.25	30.0		13	4
FCTF-1	662	4.67	3.21	35.0		31	4
FCTF-1-600	1535	5.53	3.41	32		19	4
CTF-P2	776	1.84				20.3	5
CTF-P3	571	2.22				22.5	5
CTF-P4	867	3.05				16.6	5
CTF-P5	960	2.94				24.1	5
CTF-P6	1152	3.32				16.1	5

CTF-P1M	4	0.92				31.2	5
CTF-P2M	464	1.87				21.0	5
CTF-P3M	523	2.21				15.8	5
CTF-P4M	542	1.83				22.4	5
CTF-P5M	542	2.03				20.1	5
CTF-P6M	947	4.12				14.2	5
MCTP-1	1452	4.61	2.70				6
MCTP-2	859	3.65	2.46				6
Polymer 2	--	--	1.56				7
Polymer 3	646	--	1.68				7
Polymer 4	1266	--	2.09				7
Polymer 2C	427	--	2.99				7
Polymer 3C	1173	--	3.08				7
Polymer 4C	1316	--	3.61				7
NOP-1	978	1.83	1.06	32.8			8
NOP-2	1055	2.37	1.40	34.1			8
NOP-3	1198	2.51	1.39	33.8	27.1	25.6	8
NOP-4	635	1.71	0.83	31.9			8
NOP-5	913	1.45	0.72	30.5			6
NOP-6	1130	1.31	0.49	29.2	33.7	38.7	8
MCTF-300	640	2.25	1.39	24.6			9
MCTF-400	1060	2.36	1.55	25.4			9
MCTF-500	1510	3.16	2.22	26.3			9
fl-CTF300	15	1.27	0.71	43.1	35	37	10
fl-CTF350	1235	4.28	2.29	32.7	27	23	10
fl-CTF400	2862	4.13	1.97	30.7	15	16	10
fl-CTF500	2322	3.26	1.65	31.7	13	12	10
fl-CTF600	2113	3.48	1.80	32.4	14	12	10
COP-1	168	--	1.33				11

COP-2	158		0.91				11
PCTF-1	2235	3.26	1.84	30	13	17 [b]	12
PCTF-2	784	1.85	0.992	26	9	13 [b]	12
PCTF-3	641	2.17	1.32	27	16	34 [b]	12
PCTF-4	1090	2.30	1.49	28	17	35 [b]	12
PCTF-5	1183	2.59	1.48	27	17	39 [b]	12
PCTF-6	79	--	--		--	--	12
PCTF-7	613	2.18	1.32	25	22	--	12
HPF-1	576	--	2.8	43		120	13
CTF-TPC	1668	4.24	2.47	32			14
CTF-FL	773	3.26	2.00	35			**Error! Bookmark not defined.**
MM1	1800	3.68	2.17	32	32	130	This work
MM2	1360	4.70	2.88	36	23	97	This work
MM3	1884	2.62	1.51	43	13	77	This work
MM4	1407	3.40	2.05	30	21	98	This work

[a] Transformation into cm^3/g can be done by the given value in mmol/g with the molar gas volume at 1 bar of 22.711 L/mol (or mL/mmol = $cm^3/mmol$) (at 273 K), 24.375 L (at 293) and 24.791 L (at 298).

Alternatively, transformation from given cm^3/g into mmol/g:

at 273 K: value in (cm^3/g) : (22.711 $cm^3/mmol$) = value in (mmol/g)
(22.711 L is the molar volume at 1 bar and 273 K for an ideal gas).

at 293 K: value in (cm^3/g) : (24.375 $cm^3/mmol$) = value in (mmol/g)
(24.375 L is the molar volume at 1 bar and 293 K for an ideal gas).

Conversion to value in g/g = value in (mmol/g) x (0.044 g/mmol) from which the value wt% is obtained as g(CO_2)/g(CO_2+adsorbent) x 100%.

[b] at 1 bar for an equimolar gas mixture.

11. Scanning electron micrograph of MM1-MM4

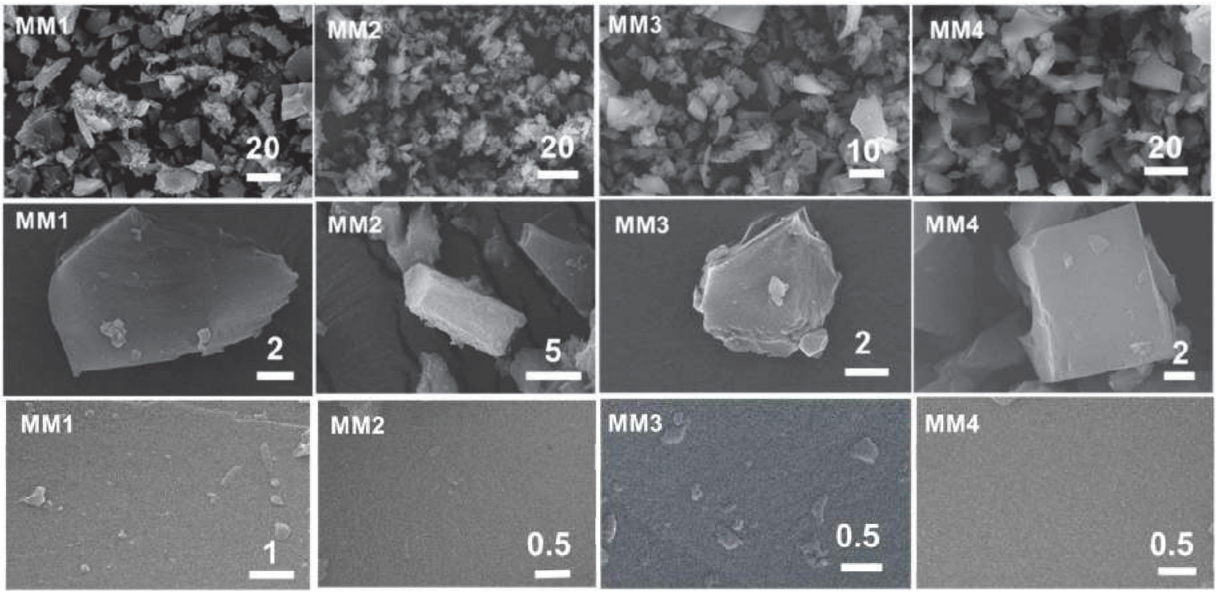

Fig. S10 Scanning electron micrographs of MM1 - MM4 (numbers above the scale bar are in µm). Enlarged version of Fig. 2 in paper.

12. References

---

1 A. Bhunia, V. Vasylyeva and C. Janiak, *Chem. Commun.*, 2013, **49**, 3961-3963.
2 B. Brehler, *Naturwissenschaften*, 1959, **46**, 554.
3 P. Katekomol, J. Roeser, M. Bojdys, J. Weber, and A. Thomas, *Chem. Mater.*, 2013, **25**, 542–1548
4 Y. Zhao, K. X. Yao, B. Teng, T. Zhang and Y. Han, *Energy Environ. Sci.*, 2013, **6**, 3684-3692
5 S. Ren, M. J. Bojdys, R. Dawson, A. Laybourn, Y. Z. Khimyak, D. J. Adams and A. I. Cooper, *Adv. Mater.*, 2012, 24, 2357–2361.
6 P. Puthiaraj, S.-M. Cho, Y.-R. Lee and W.-S. Ahn, *J. Mater. Chem. A*, 2015, **3**, 6792-6797
7 H. Lim, M. C. Cha and J. Y. Chang, Macromol. *Chem. Phys.*, 2012, **13**, 1385–1390.
8 S. Xiong, X. Fu, L. Xiang, G. Yu, J. Guan, Z. Wang, Y. Du, X. Xiong and C. Pan, *Polym. Chem.*, 2014, **5**, 3424-3431.
9 X. Liu, H. Li, Y. Zhang, B. Xu, S. A, H. Xia and Y. Mu, *Polym. Chem.*, 2013, **4**, 2445-2448.
10 S. Hug, M. B. Mesch, H. Oh, N. Popp, M. Hirscher, J. Senkerd and B. V. Lotsch, *J. Mater. Chem. A*, 2014, **2**, 5928-5936.
11 H. A. Patel, F. Karadas, A. Canlier, J. Park, E. Deniz, Y. Jung, M. Atilhan and C. T. Yavuz, *J. Mater. Chem.*, 2012, **22**, 8431-8437.
12 A. Bhunia, V. Vasylyeva and C. Janiak, *Chem. Commun.*, 2013, **49**, 3961–3963; A. Bhunia, I. Boldog, A. Möller and C. Janiak, *J. Mater. Chem. A*, 2013, **1**, 14990–14999.
13 S. Nandi, U. Werner-Zwanziger and R. Vaidhyanathan, *J. Mater. Chem. A*, 2015, **3**, 21116–21122.

3.3 A mixed-linker approach towards improving covalent triazine-based frameworks for CO_2 capture and separation

Subarna Dey, Asamanjoy Bhunia, Ishtvan Boldog and Christoph Janiak

Micropor. Mesopor. Mater., 2016, submitted, (reference 102)

Carbon dioxide is consider as one of the major component of greenhouse gases that contributes to global warming. Carbon capture and storage (CCS) process has becomes of highly potential to reduce the CO_2 emission. Covalent triazine based frameworks (CTFs), as a subclass of POPs, are promising candidate for CCS due to their (1) high surface area (2) high selectivity to CO_2 (3) low density (4) excellent thermal, chemical and water stability.

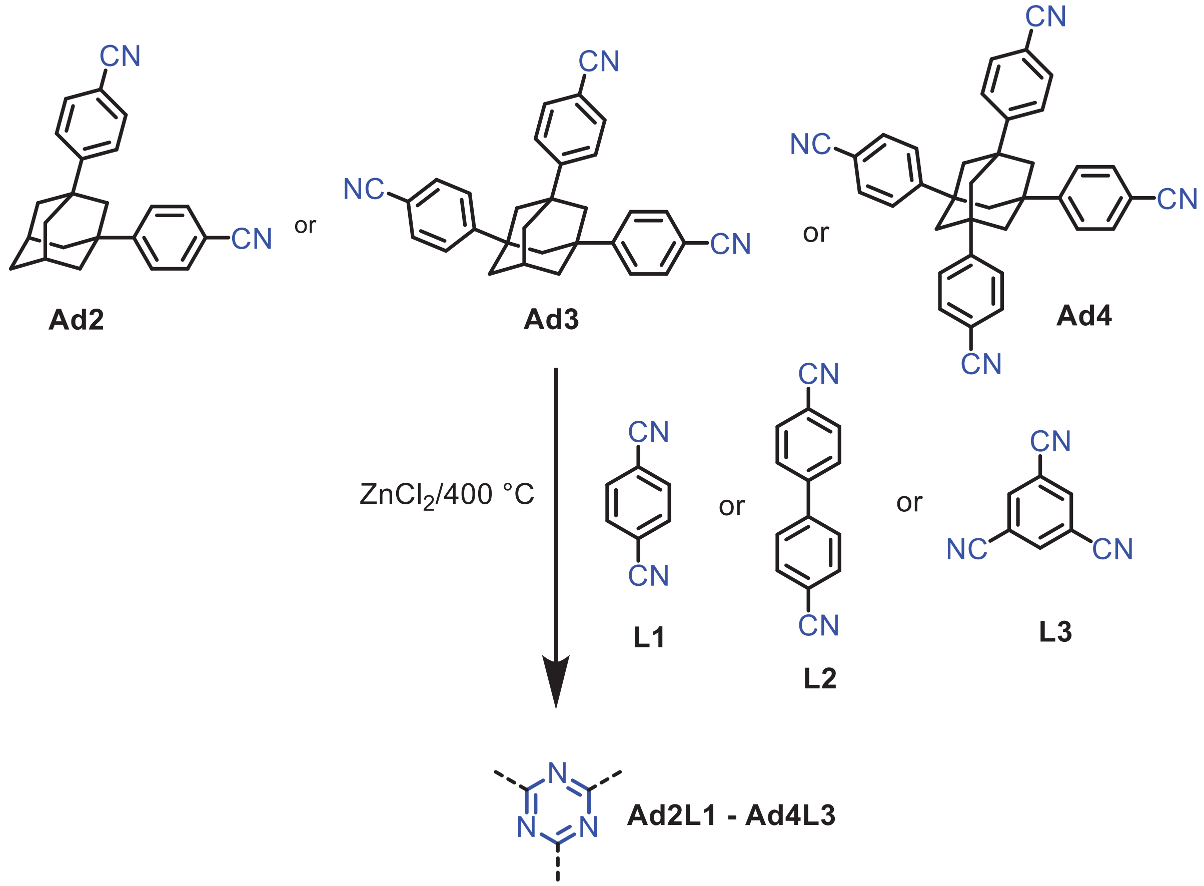

In this work three adamantane nitriles, namely 1,3-bis-, 1,3,5-tris- or 1,3,5,7-tetrakis(4-cyanophenyl)adamantane (**Ad2-Ad4**) with terephthalonitrile (**L1**), 4,4'-biphenyldicarbonitrile (**L2**) or 1,3,5-benzenetricarbonitrile (**L3**) in the presence of anhydrous $ZnCl_2$ resulted in nine CTFs in a form of black solids (**Ad2L1-Ad4L3**). With the mixed-linker strategy, here we have tuned the porosity as well as gas uptake capacity. BET surface areas of the materials were found to be in the range of 918 m^2/g to 1885 m^2/g. **Ad2L1**-**Ad4L3** adsorb significant amounts of CO_2 (40-76 cm^3/g) and CH_4 (14-26 cm^3/g), which are generally in line with other reported CTFs. Water adsorption measurements indicate the hydrophobic nature of the frameworks.

Author's contribution to the work:

- Synthesis and characterization of the CTF materials.
- Gas adsorption, water adsorption and Karl-Fischer titration performances.
- Writing of the manuscript by me, and corrected by Dr. Boldog and Prof. Janiak.

A mixed-linker approach towards improving covalent triazine-based frameworks for CO_2 capture and separation

Subarna Dey, Asamanjoy Bhunia, Ishtvan Boldog and Christoph Janiak*

Institut für Anorganische Chemie und Strukturchemie, Heinrich-Heine-Universität Düsseldorf, 40204 Duesseldorf, Germany.
* Corresponding author: E-mail: janiak@uni-duesseldorf.de; Fax: + 49-211-81-12287; Tel: +49-211-81-12286.

Abstract

Carbon dioxide separation and capture / sequestration are important problems not only in the context of global warming but also for optimization of industrial processes. Porous covalent triazine-based frameworks (CTFs) are a class of promising materials for adsorptive separation of CO_2, which could be and effective alternative to chemisorption based aproaches. We report nine novel CTFs based on mixed building-block approach, synthesized under ionothermal conditions ($ZnCl_2$, 400°C). Angular 1,3-bis(4-cyanophenyl)adamantane (**Ad2**), trigonal-pyramidal 1,3,5-tris(4-cyanophenyl)adamantane (**Ad3**) and tetrahedral 1,3,5,7-tetrakis(4-cyanophenyl)adamantane (**Ad4**) were processed together with the linear terephthalonitrile (**L1**) and 4,4'- biphenyl dicarbonitrile (**L2**) as well as the planar trigonal 1,3,5-benzenetricarbonitrile (**L3**) targeting maximization of surface area and void volume. The thermally (>500 °C) and acid stable CTFs showed a specific surface area (S_{BET}) in the range of 747-1885 $m^2\ g^{-1}$, with the highest surface area achieved for **Ad4L2**, reflecting the generally observed synergism of elongation of L-building blocks with branching of the Ad-building blocks. The CO_2 uptake correlates empirically with the product of BET surface area, micropore volume fraction ($V_{0.1}/V_{tot}$) and CO_2-accessible micropore volume ($V_{micro}(CO_2)$). At low pressure (up to 1 bar) and 273 K, **Ad2L1** - **Ad4L3** adsorb significant amounts of CO_2 (40-76 $cm^3\ g^{-1}$) and CH_4 (14-26 $cm^3\ g^{-1}$), which are generally in line with other reported CTFs, proving the viability of the mixed building-block approach for continuous tuning of properties in the case of CTFs. The obtained CTFs exhibit good ideal selectivity in the range of 17-30 for CO_2 over N_2 (for a 85% N_2/15% CO_2 mixture at 273 K, 1 bar), and represent a prototypal 'tunable' series for efficient adsorption separations. Water vapor sorption by the novel CTS indicates that the adamantane based CTFs are largely hydrophobic.

Keywords: covalent triazine-based frameworks; CTFs; carbon dioxide separation; microporosity; mixed linker

1. Introduction

Porous organic polymers (POPs) are viewed as promising materials for CO_2 sorption and separation because of very high attainable specific surface areas coupled with mechanical (i.e. permanent porosity), chemical and thermal stability suitable for applications and excellent tunability of surface properties [1,2]. The emission of CO_2 has become a major environmental challenge due to rapid industrialization of developing countries and to fast increase of population in them [3,4]. More than 86% of the global energy is supplied by fossil fuels, that induce the high amount of CO_2 in the atmosphere [4], which effects global warming, ocean acidification and stability of ecosystems [5,6]. Therefore, CO_2 capture and separation from flue gases is viewed as a possible solution to control the environmental impact of burning fossil fuels, which is reflected by goals formulated by the 2015 UN Climate Change Conference, 2015 Paris Agreement (COP21) and many more.

Conventional methods for CO_2 separation are based on chemisorption, like in the case of amine scrubbing and chilled ammonia process resulting in carbamate formation [5]. Because of general efficiency issues, including the need of energy demanding regenerative stages and involvement of corrosive solutions, alternative ways for physisorptive CO_2 separation are investigated. Porous materials like zeolite and active carbon are viable adsorbents in this regard, but their inherent disadvantages is the low potential for tunability via functionality-tailoring and hence limited possibilities to achieve high CO_2/N_2 selectivity [4]. Porous organic polymers have gained considerable attention as alternative adsorbents for applications in gas storage and separation. POPs or MOPs (microporous organic polymers) [7] typically consist of solely light elements (e. g. H, B, C, N, O) combined via strong covalent bonds and hence have high specific, i.e., mass-related surface areas and adsorptive capacities. Their synthesis often involves carbon-carbon coupling [8], or condensations / cycloadditions leading to formation of boroxine/boronate esters [9], benzimidazoles [10], imines [11], hydrazones [12], triazines [13], and imides [14,15] using either preferred reversible or irreversible reaction conditions. POPs usually demonstrate higher moisture stability than metal-organic frameworks (MOFs); especially when POPs are sustained solely by chemically robust bonds, typically only accessible under irreversible conditions [11b]. Cyclotrimerization of organic nitriles performed under such conditions yield the stable aromatic triazine ring constituting the hence robust covalent triazine-based frameworks (CTFs) [16]. The CTF class of compounds established by the work of Kuhn, Antonietti, Thomas *et al.* [13] possess high chemical, particularly hydrolytic and thermal stability and are interesting because of high attainable surface areas (beyond 2000 m^2 g^{-1}), [13b] cheap and readily available starting materials, facile synthesis and certain hydrophilicity.

Thomas *et al.* developed CTFs with permanent porosity by ionothermal trimerization (using molten $ZnCl_2$) of aromatic nitrile groups [13]. At high temperature (400-700 °C) $ZnCl_2$ acts as a Lewis acid catalyst and molten pore-forming solvent (porogen) or templating agent for the polymerization [13b]. The surface area of the network depends on the molar ratio of the $ZnCl_2$ to nitrile used (typically 10:1), reaction temperature and reaction time [13]. CTFs from such ionothermal synthesis are considered to be in-between ideal triazine-linker frameworks and porous carbon materials due to nitrogen deficiency in elemental composition compared to their idealized structure [17]. Cooper *et al.* employed strong Brønsted acid conditions (using e.g. trifluoromethane sulfonic acid) to catalyse the trimerization reaction at room temperature or under microwave assisted conditions [18]. Both routes yield CTFs by the idealized trimerization reaction of carbonitriles to triazine rings (C_3N_3). Further, CTFs networks have been obtained using anhydrous $AlCl_3$-catalysed Friedel-Crafts synthesis via coupling of cyanuric chloride with aromatic hydrocarbons [19,20]. Often, CTFs prepared by ionothermal synthesis feature higher surface areas compared to other routes.

Recently, we reported porous triazine based frameworks using a series of bridge-head substituted adamantanes as building blocks, namely 1,3-bis-, 1,3,5-tris- and 1,3,5,7-tetrakis(4-cyanophenyl)adamantanes (encoded as **Ad2**, **Ad3** and **Ad4** in Scheme 1, yielding PCTF-3 to -7 via both ionothermal and strong Brønsted acid catalyzed reaction conditions. The products featured surface areas in the range of 79 to 1183 m^2 $g^{-1}$with moderate CO_2, CH_4 and H_2 uptake around 50 cm^3 g^{-1}, 14-20 cm^3 $g^{-1}$and ~1 wt%, respectively. IAST-derived ideal CO_2:N_2, CO_2:CH_4 and CH_4:N_2 selectivity values were found to be up to 41:1, 7:1 and 6:1, respectively, calculated for $p \rightarrow 0$ at 273 K [17]. The successful use of adamantanes as non-planar building blocks of varied connectivity for the synthesis of 3D network structures motivated us to explore further optimization of porosity characteristics by a mixed-building block approach. Simple spacer building blocks yielding planar structures, when used alone, were viewed as an especially apt target for employing them in combination with 'deplanarizing' building-blocks. 1,3-Bis(4-cyanophenyl)adamantane (**Ad2**), 1,3,5-tris(4-cyanophenyl)adamantane (**Ad3**) and 1,3,5,7-tetrakis(4-cyanophenyl)adamantane (**Ad4**) on one hand and terephthalonitrile (**L1**), 4,4'-biphenyl dicarbonitrile (**L2**) and 1,3,5-benzenetricarbonitrile (**L3**) (Scheme 1) were reacted together aiming to optimize gas adsorption/selectivity as well as to analyse the factors which favor higher micro/meso-porosity and/or surface areas. At present there seems only be one other example of mixed-nitrile or mixed-linker CTF reported, namely from a 1:2 ratio of 2,6-pyridinedicarbonitrile and 4,4-biphenyldicarbonitrile, and this CTF was primarily used as catalyst support and was not investigated for CO_2, CH_4 or H_2 sorption [21].

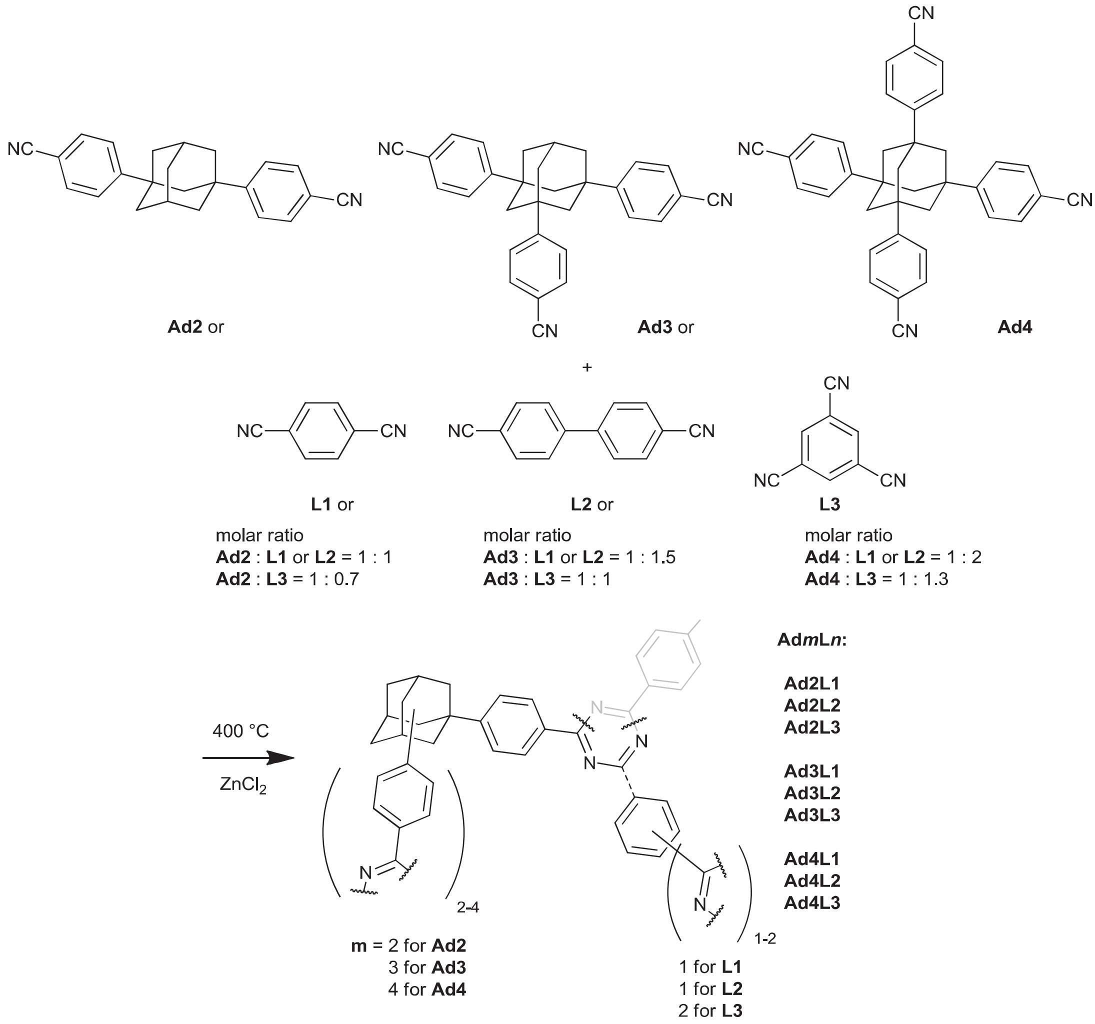

Scheme 1. The co-polymerization reaction scheme towards the **Ad-L** mixed building block CTFs. Selected repeating units of **Ad*m*L*n*** CTFs are depicted in Scheme 2 and Scheme S2 in Supp. Info.

2. Results and discussion

2.1 Synthesis and characterization

Co-polymerization via cyclotrimerization of the nitrile function of the three adamantane nitriles, namely 1,3-bis-, 1,3,5-tris- or 1,3,5,7-tetrakis(4-cyanophenyl)adamantane (**Ad2** - **Ad4**) with terephthalonitrile (**L1**), 4,4'-biphenyldicarbonitrile (**L2**) or 1,3,5-benzenetricarbonitrile (**L3**) in the presence of anhydrous $ZnCl_2$ resulted in nine CTFs in a form of black solids (**Ad2L1 - Ad4L3**) (Scheme 1, Scheme 2 and Scheme S2 in Supp. Info.; see Supp. Info. for experimental details). The reaction conditions (400 °C, 48 h) were the same we used previously for single building block adamantane nitrile-based CTFs. The obtained materials are chemically stable, e.g. treatment by 2 mol L^{-1} aqueous hydrochloric acid for 24 h is part of the purification procedure.

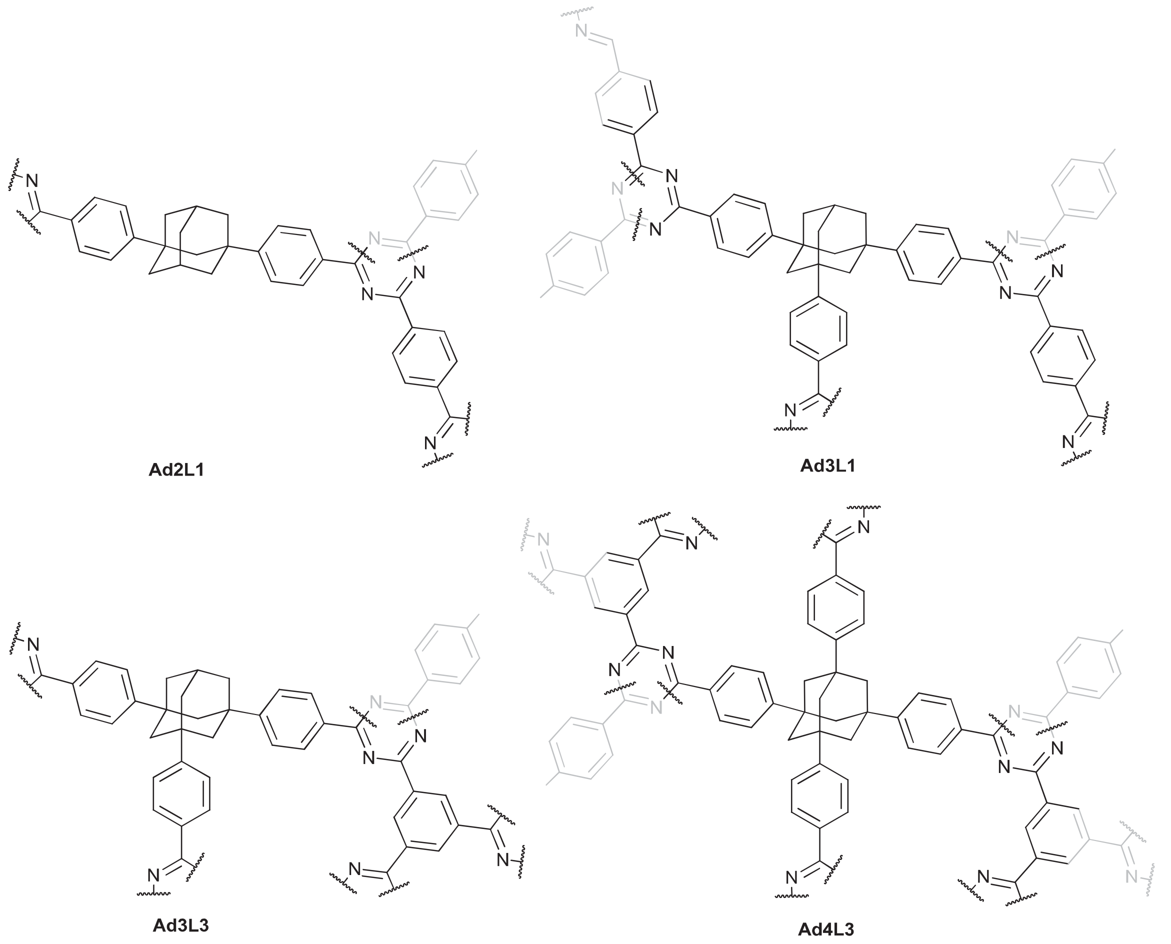

Scheme 2. A representative set of idealized, stoichiometric-average repeating units of **Ad*m*L*n*** CTFs reflecting the 1:1 ratio of the nitrile groups from the two different building blocks (e.g. 1:1, 1:1.5 and 1:2 for **Ad2L1**, **Ad3L1** and **Ad4L1**, respectively). The other repeating units could easily be derived from the depicted ones: the **Ad2L*n*** is a half of the **Ad4L*n*** units regarding the substitution of adamantane, while **Ad*m*L1** units and **Ad*m*L2** are closely related and derived by augmentation of the ligand by a 1,4-phenylene linkage (see Scheme S2 in Supp. Info. for other **Ad*m*L*n*** cases). For clarity the repeating units are extended (light-gray parts).

The formation of triazines and depletion of the starting nitriles were confirmed by FT-IR spectrum (Fig. 1, left). The characteristic nitrile stretching band around 2226 cm^{-1} almost completely disappeared after the reaction except for **Ad4L1** and **Ad4L3** [17,22]. Steric crowding around the **Ad4** units, not relieved by involvement of the short **L1** and **L3** linkers, may prevent the reaction of all **Ad4** nitrile groups. The characteristic bands for the CTF-triazine rings can be found in the regions of 1356-1378 cm^{-1} (often very weak) and 1525-1612 cm^{-1}, slightly shifted from the C-N breathing and stretching mode of a molecular triazine unit (1363 and 1511 cm^{-1}, respectively), in agreement with infrared spectra of other CTFs [13c,18,22]. The powder X-ray diffractograms indicate a largely amorphous material with only three broad peaks at 2θ values centered around 17, 25 and 40° for **Ad2L1**- **Ad2L3**; around 17, 22 and 40° for **Ad3L1 –Ad3L3** and around 17, 29 and 40° for **Ad4L1**-**Ad4L3**. The peak centered around 17° is associated with $ZnCl_2$ (corresponding to the lowest angle strong peak, *hkl* = {111}) [23], which is hard to remove from the pores, as observed by others [13]. Amorphous nature of CTFs prepared using ionothermal conditions is typical, with the most notable exceptions of CTF-0, CTF-1 and CTF-2) [13a,c,24]. Elemental analysis of **Ad2L1**-**Ad4L3** shows much lower nitrogen content in the **Ad-L** CTFs compared to the calculated values according to expections (section 3 in Supp. Info.). The low nitrogen content is a result of aromatic nitrile decomposition to HCN, partial fragmentation with expulsion of CN radicals and other processes taking place during the high-temperature synthesis (400 °C) [13]. Some variation in the results of the elemental analyses may also be explained by variable residual water content in the mildly hydroscopic CTFs (due long storage in ambient air conditions). Depending on their pore size (capillary effect), type and degree of functionalization CTFs were recently shown to exhibit a water uptake of 12-15 wt% from ambient air with about 50-60% humidity (see Supp. Info., ref. 19). Karl-Fischer-Titration (KFT) of the **Ad-L** CTFs which were stored under ambient air revealed a water content between 2.4 wt% (**Ad3L2**) and 12.8 wt% (**Ad4L3**) (Fig. S7 and Table S4 in Supp. Info.). The water content from KFT agrees with the water vapour uptake at around 50% air humidity (*vide infra*).

The **Ad2L1**-**Ad4L3** materials have similar particle morphology, pictured by scanning electron microscopy (SEM), which is in line with similar porosity characteristics found by N_2 adsorption studies (see below). The ‘flake-chip’ particles have irregular form (Fig. 1, right), with average length, i.e., the longer dimension of the particles for the **Ad2L1**-**Ad2L3** materials being 8-18 µm, for the **Ad3L1**-**Ad3L3** 6-8 µm and for **Ad4L1**-**Ad4L3** 10-20 µm.

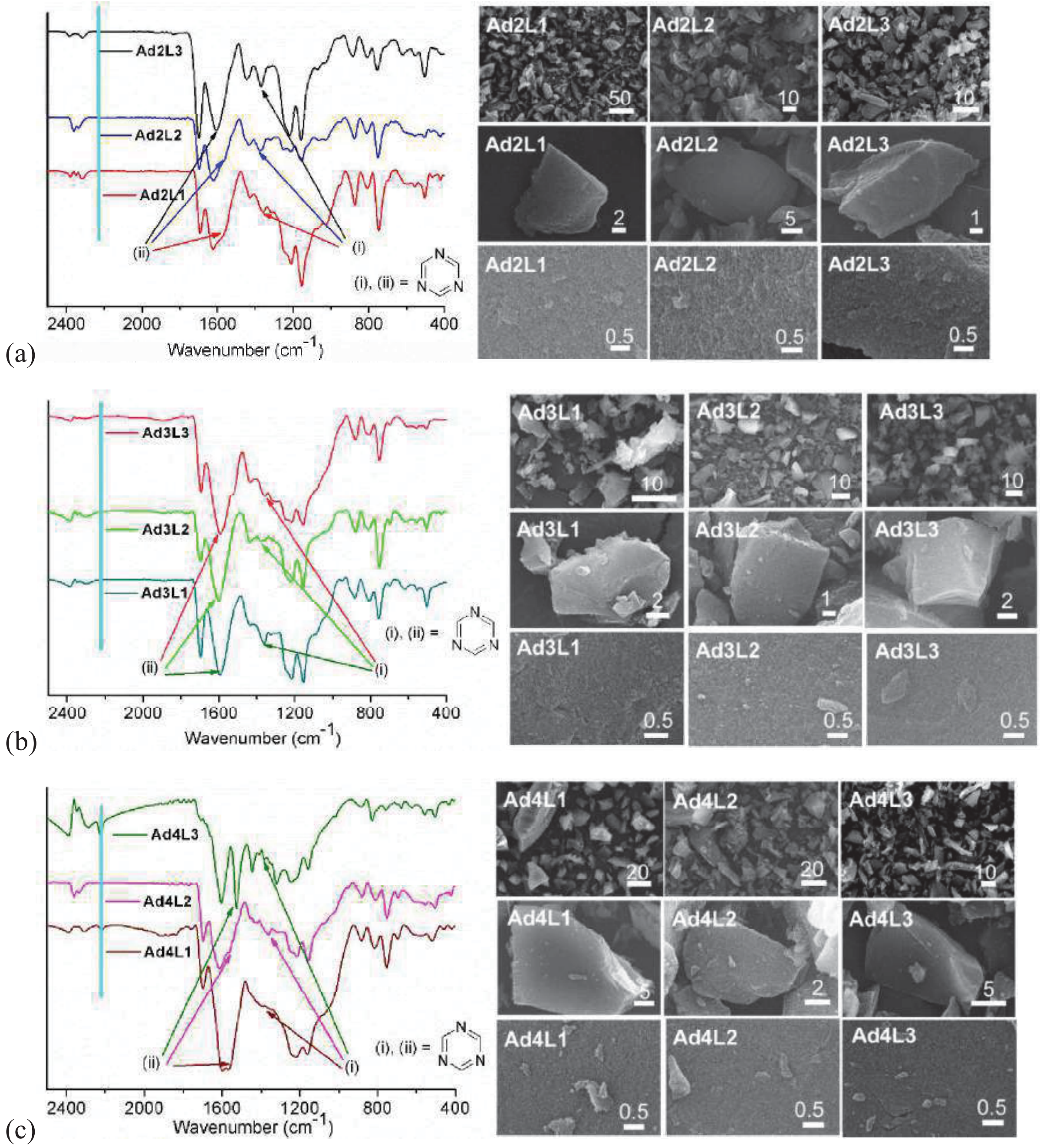

Figure 1. FT-IR spectra (left) and scanning electron micrographs (right) of (a) **Ad2L1-Ad2L3** (b) **Ad3L1-Ad3L3** and (c) **Ad4L1-Ad4L3**. The vertical cyan bar marks the position of the band associated with the unreacted nitrile groups (2223 cm^{-1}). The C=N stretching (ii) and breathing (i) mode the triazine unit are indicated by arrows. In the SEM images the length of the scale bar is given in µm.

2.2 Gas adsorption studies

The porosities of the nine synthesized triazine frameworks were characterised by N_2 sorption measurement at 77K. All materials were activated by degassing at 200 °C for 24 hour. Fig. 2

shows the N_2 sorption isotherms at 77 K for **Ad2L1** to **Ad4L3**. The Brunauer-Emmett-Teller (BET) surface areas were found to be in the range of 918 m^2 g^{-1} to 1885 m^2 g^{-1} (P/P_0 = 0.01-0.05). As a general trend, the increase of the length of the **L** building-block correlates with the increase of CTF surface area, with the exception of **Ad3L2** (Table 1). Among all nine CTFs, **Ad4L2** had the highest surface area of 1885 m^2 g^{-1}, which is in the upper range for CTFs and only surpassed by CTF-0 (2011 m^2 g^{-1}) [24], fl-CTF400-600 (2862-2113 m^2 g^{-1}) [25] and PCTF-1 (2235 m^2 g^{-1}) [22a] (see Table S6 in Supp. Info.). The majority of the adsorption isotherms of the **Ad-L** materials belongs to Type I/I(b) isotherms, with nascent characteristics of a Type II isotherm in some cases (like all the **Ad3L*n*** materials), with the clear exception of **Ad2L2** representing rather a Type II case. A minor H2(b) hysteresis loop is present in all cases, almost disappearing only in **Ad2L3** with lowest porosity. The uptake at low P/P_0 is associated with the filling of micropores. Type I(b) isotherms are characteristic for materials having broader pore size distributions including wider micropores and possibly narrow mesopores. The Type II section at high P/P_0 indicates the physisorption on the non-porous and macroporous part of the sample (including interparticle voids in the aggregated powder particles). The continuous increase at high P/P_0 without the plateau for Type I, IV or V isotherms is the result of unrestricted multilayer adsorption [26]. The hysteresis loops lack a sharp step-down in the desorption branch as for H3, H4 and H5 loops. Instead, the loops gradually close at low P/P_0 and are best assigned to an H2(b) type. Type H2 hysteresis loops are due to more complex pore structures in which network effects are important. The steeper part in some of the desorption branches (within 0.4-0.6 P/P_0 for **Ad2L1**, **Ad3L*n*** and **Ad4L2** CTFs) can be attributed either to pore-blocking/percolation or to cavitation-induced evaporation. H2(b) type hysteresis is associated with broader distribution of bottleneck diameters of the respective pores (narrow pore entrances vs large pore volumes; ‘bottle-neck’ pores) compared to the case of H2(a) type loops [26]. The hysteretic behaviour takes place in the multilayer adsorption / capillary condensation region of the isotherm for a mesoporous structure. The adsorption isotherm of **Ad2L2** (Type II) has an H1 type of hysteresis. **Ad4L1** and **Ad4L3** exhibit a H4 type of hysteresis which is associated with narrow slit like pores.

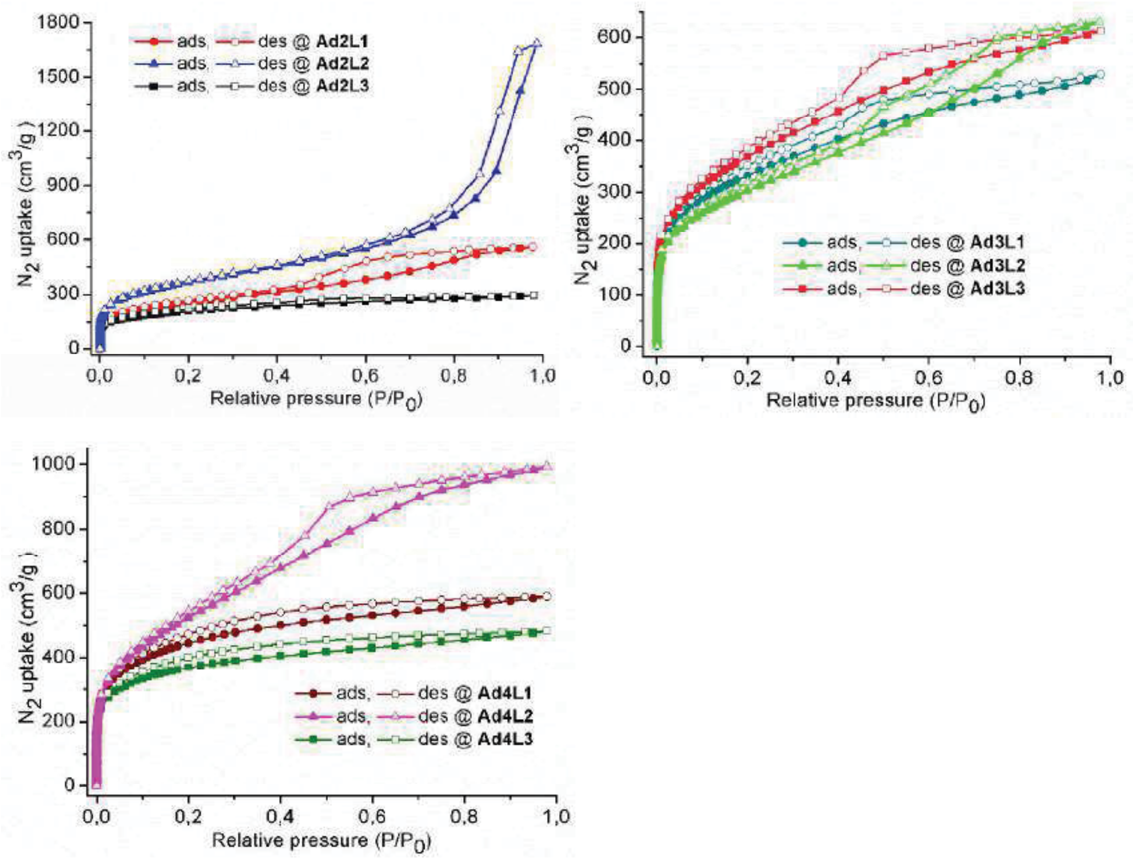

Figure 2. Nitrogen adsorption–desorption isotherms at 77 K (closed symbols for adsorption and open symbols for desorption) for **Ad2L1**-**Ad4L3** (see Fig. S13 in Supp. Info. for enlarged isotherm of **Ad2L3**).

Pore size distributions were calculated by non-local density functional theory (NLDFT) using the 'carbon slit pore' model, according to Tarazona [27]. (Fig. 3). To understand the degree of microporosity of these materials the ratio of micropore volume ($V_{0.1}$) to total pore volume (V_{tot}) was calculated from the N_2 sorption measurement at 77 K (Table 1). All CTFs (except **Ad2L2**) show $V_{0.1}/V_{tot}$ values in the range of 0.4 to 0.7. Compounds **Ad2L3**, **Ad4L1** and **Ad4L3** have a more significant fraction of micro- over mesopores ($V_{0.1}/V_{tot}$ shows over 60% micropores, Table 1), while the remaining **Ad-L** CTFs feature a broad mesopore and macropore region (Fig. 3a,c,e). Comparison of **Ad*m*L1** and **Ad*m*L2** shows an effect of the longer **L2**-biphenyl over shorter **L1**-phenyl linker to increase the fraction of larger pores. The **L2** linker gives the lowest fraction ($V_{0.1}/V_{tot}$) of micropores with each **Ad** node (Table 1). **Ad4L3** shows the highest amount of microporosity (70%), presumably having the densest structure of all the CTF because of the strongest branching of the building blocks, namely the 1,3,5,7-tetrakis(4-cyanophenyl)adamantane and 1,3,5-benzenetricarbonitrile.

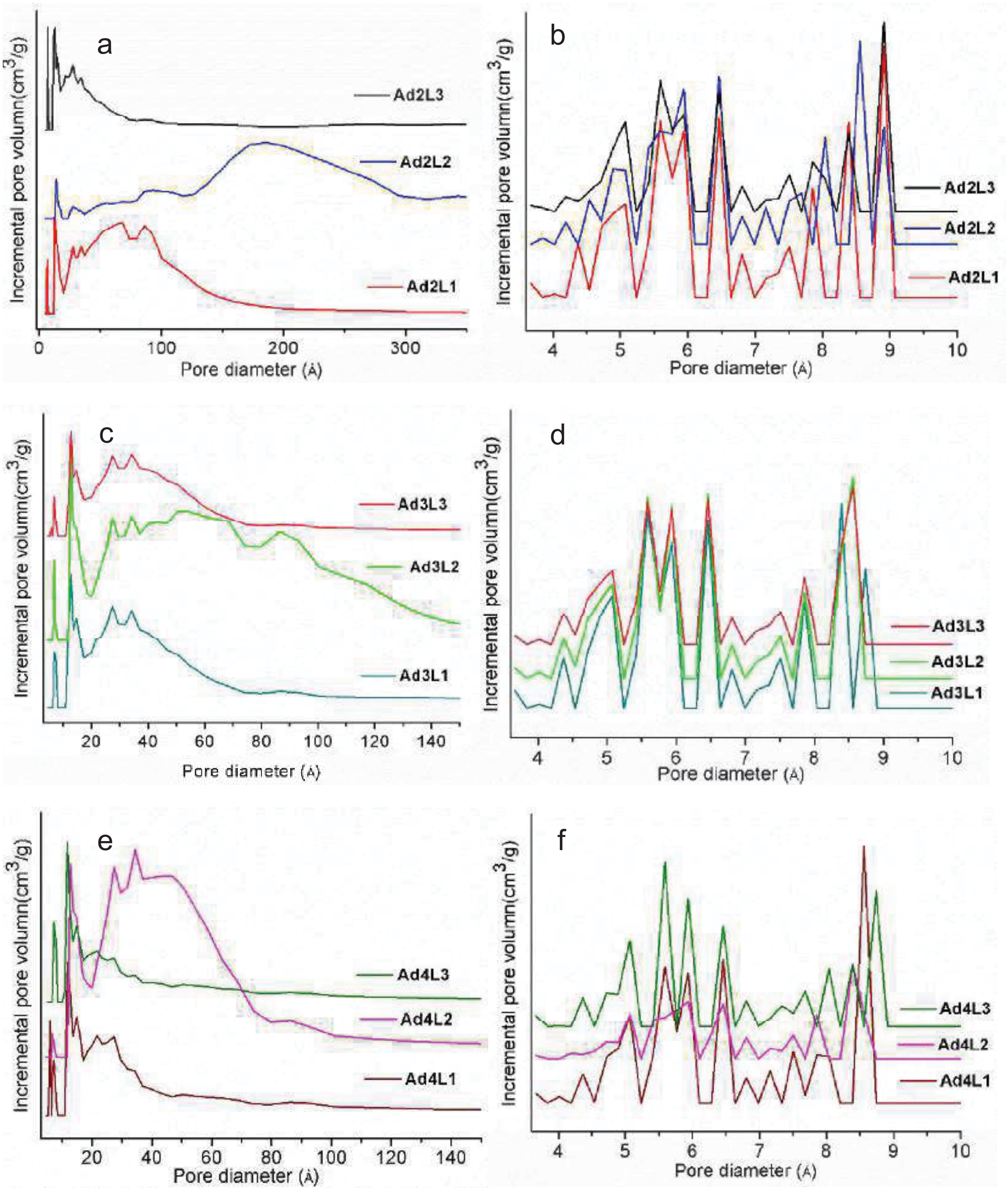

Figure 3. NLDFT pore size distributions for **Ad2L1-Ad4L3** from N_2 adsorption isotherms at 77 K (a, c and e) and CO_2 adsorption isotherms at 273 K (b, d, f). Micropores have diameters of less than 20 Å (2 nm), mesopores range from 20-500 Å (2-50 nm).

Distribution of micropores with diameter smaller than 10 Å and ultramicropores smaller than 7 Å were calculated from CO_2 gas adsorption data collected at 273 K (Fig. 3b, d and f) [28]. At pore sizes close to the kinetic diameter of N_2 (~3.64 Å) and at 77 K the diffusion limitation can be alleviated by use of CO_2 (kinetic diameter 3.30 Å) as an adsorbate at 273 K which ensures faster equilibration [17]. The saturation pressure of CO_2 at 0 °C is ~26141 Torr and low relative pressure measurements necessary for micropore analysis are achieved in the range of moderate absolute pressures (1–760 Torr) [29].

Table 1. Porosity data for **Ad2L1-Ad4L3**.

CTFs	S_{BET} [a] ($m^2\ g^{-1}$)	S_{Lang} [b] ($m^2\ g^{-1}$)	$V_{0.1}$ [c] ($cm^3\ g^{-1}$)	V_{tot} [d] ($cm^3\ g^{-1}$)	$V_{0.1}/V_{tot}$	$V_{micro}(CO_2)$ [e] ($cm^3\ g^{-1}$)
Ad2L1	918	1130	0.34	0.86	0.395	0.0505
Ad2L2	1316	1626	0.48	2.2	0.218	0.0508
Ad2L3	747	916	0.28	0.45	0.622	0.0568
Ad3L1	1199	1476	0.44	0.8	0.55	0.0544
Ad3L2	1093	1351	0.4	0.96	0.416	0.0499
Ad3L3	1328	1639	0.48	0.93	0.516	0.0537
Ad4L1	1617	1984	0.61	0.9	0.677	0.0853
Ad4L2	1885	2339	0.67	1.52	0.44	0.0500
Ad4L3	1341	1644	0.52	0.74	0.702	0.089

[a] Calculated BET surface area from the N_2 adsorption isotherm at 77 K over the pressure range 0.01-0.05 P/P_0 . [b] Langmuir surface area over the 0-0.15 P/P_0 ‘extended’ pressure range for better averaging and consistency between experiments. [c] Micropore volume calculated from N_2 adsorption isotherm at $P/P_0 = 0.1$ for pores ≤2 nm (20 Å). [d] Total pore volume at $P/P_0 = 0.95$ for pores ≤20 nm. [e] Total pore volume for pores with diameters smaller than 1 nm (10 Å, cf. Fig. 3b, d and f) from the CO_2 NLDFT model at 273 K.

Gas uptakes by CTFs obtained from the respective adsorption isotherms for CO_2, CH_4 and N_2 at 1 bar are summarized in Table 2 (Fig. 4, Fig. 5 and Fig. 2). For the applications of carbon-capture-storage (CCS) materials a high selectivity of CO_2 over N_2 at low pressure is required. In addition, the separation of CO_2/CH_4 is relevant for purification ('sweetening') of natural gas, which in raw form contains up to 40% of non-combustible admixtures CO_2 and N_2 additionally to light hydrocarbons, primarily methane, and which is only useable at low CO_2 concentrations [30,31]. Various solid adsorbents such as zeolites [32], metal organic frameworks (MOFs) [33], silica [34], activated carbons [35] and porous organic polymers (POPs) [36,37,38,39,40] have received significant attention for CO_2 sorption. A productive solid adsorbent must fulfill the following criteria: 1) high surface area (2) high selectivity to CO_2 (3) low density (i.e. high material efficiency), (4) excellent thermal, chemical and water stability. In this regards, selected POPs are considered as promising candidates for CO_2 capture [14,41]. Therefore, we studied here CO_2 gas adsorption as well as selectivity.

The CO_2 adsorption by **Ad-L** CTFs at 1 bar is in the range of 1.72 mmol g^{-1} to 3.35 mmol g^{-1} and shows full reversibility, i.e. coincidence of the adsorption and desorption branches (Fig. 4). Among all nine CTFs, **Ad4L1** shows the highest CO_2 adsorption of 3.35 mmol g^{-1} (at 273 K) and 1.97 mmol g^{-1} (at 293 K) at 1 bar. This value is higher than that for the pure **Ad4**-CTF PCTF-5 with 2.55 mmol g^{-1} (at 273 K and 1 bar) [17]. These CO_2 sorption values are highly comparable to previously reported uptake capacities: FCTF-1-400 (4.67 mmol g^{-1}) [42], MCTP-1 (4.64 mmol g^{-1}), and others, with FCTF-1-600 having, so far the highest CO_2 uptake for CTFs at 5.53 mmol g^{-1} [42] (273 K). Other relevant examples are fl-CTF (1.27-4.28 mmol g^{-1}) [25], *bipy*-CTF300-400 (1.87-3.08 mmol g^{-1}) [43], *lut*-CTF300-400 (3.63-4.55 mmol g^{-1}) [43], *pym*-CTF300-400 (0.28-0.45 mmol g^{-1}) [43], FCTF-1 (4.67-5.53 mmol g^{-1}) [42], CTF-0 (4.22 mmol g^{-1}) [24] CTF-1 (2.47-3.82 mmol g^{-1}) [42], CTF-Pl-P6 (1.88-3.39 mmol g^{-1}) [18], CTF-P1M-P6M (0.94-4.42 mmol g^{-1}) [18], MCTF300-500 (2.25-3.16 mmol g^{-1}) [44], PCTF-1-7 (1.85-3.21 mmol g^{-1}) [17] and NOP-1-6 (1.31-2.51 mmol g^{-1}) [45] (all under the same conditions of 273 K and 1 bar). This high CO_2 affinity is due to the favorable interactions of the polarizable CO_2 molecule through dipole-quadrupole interactions [46] with the triazine frameworks [40].

Table 2. Gas adsorption data, including selectivities for **Ad2L1-Ad4L3**.

CTFs	**CO_2**[a]	**CO_2**[b]	**$Q^0_{ads}(CO_2)$**[c]	**CH_4**[a]	**N_2**[a]	**CO_2:N_2**[d]	**CO_2:N_2**[e]	**CO_2:CH_4**[d]
	(cm^3 g^{-1})	**(cm^3 g^{-1})**	**(kJ mol^{-1})**	**(cm^3 g^{-1})**	**(cm^3 g^{-1})**	**selectivity**		
Ad2L1	39.39	28.71	36.8	14.34	5.78	13	21	4
Ad2L2	43.64	26.14	29.5	16.61	5.81	15	19	4
Ad2L3	40.36	25.56	41.3	14.47	5.48	15	27	4
Ad3L1	48.59	30.8	31.8	17.24	5.70	17	24	4
Ad3L2	44.48	27.35	28.1	15.40	5.18	17	24	4
Ad3L3	50.66	29.95	25.3	17.52	6.67	14	20	4
Ad4L1	76.33	48.08	34.3	26.12	8.77	17	23	4
Ad4L2	56.06	47.20	32.6	19.70	6.60	14	17	4
Ad4L3	74.58	34.66	37.1	23.97	7.56	20	30	5

[a] Gas uptake at 273 K, 1 bar (760 mm Hg); [b] gas uptake at 293 K, 1bar (760 mm Hg); [c] heat of adsorption for CO_2 at zero loading from adsorption isotherms acquired at 273 and 293 K; [d] gas selectivity calculated at 273 K from the initial slopes in the Henry region; [e] IAST selectivity calculated at 273 K and 1 bar.

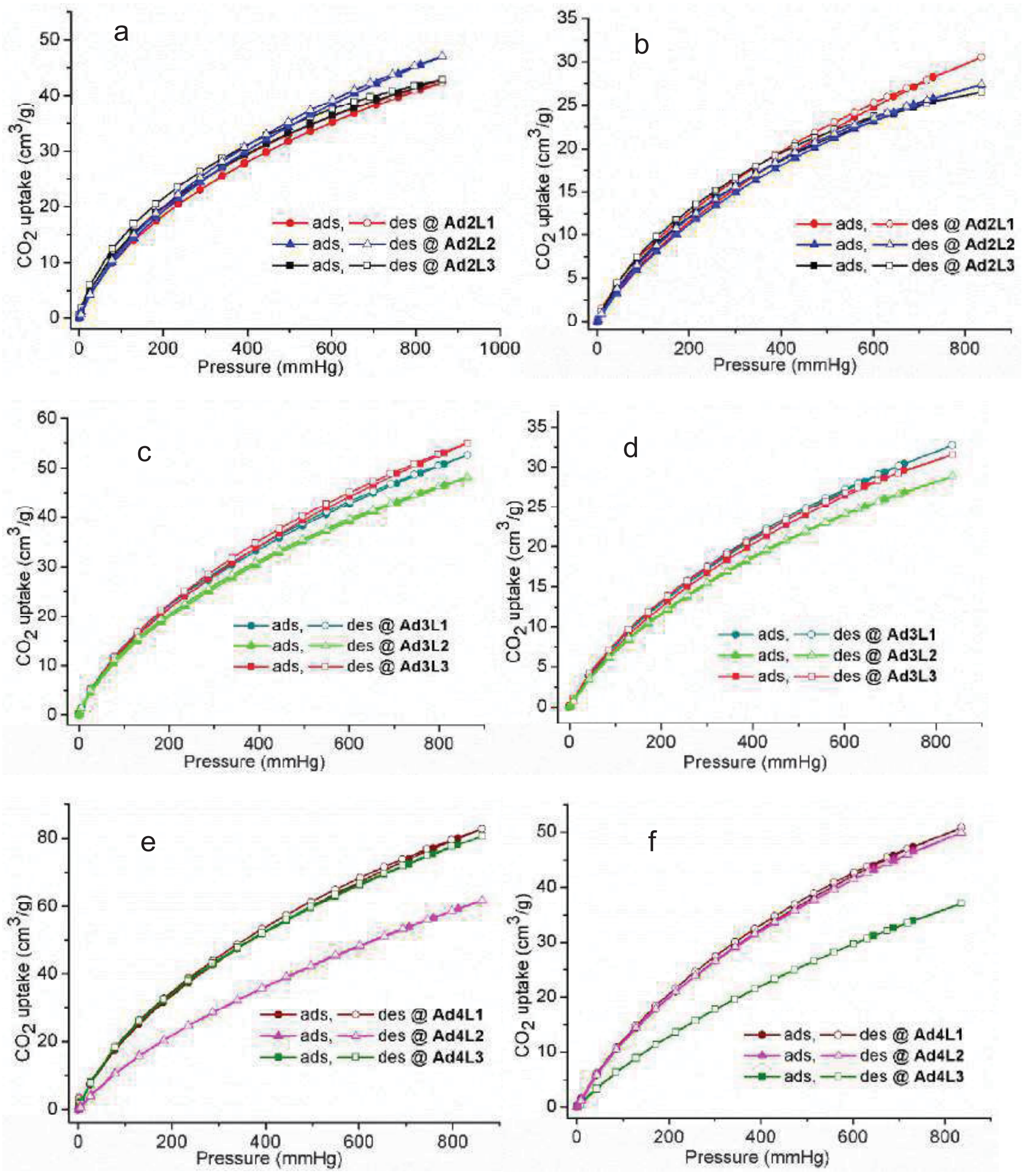

Figure 4. CO$_2$ sorption isotherms for **Ad2L1-Ad4L3**: (a, c, e) 273 K, (b, d, f) 293 K (closed symbols for adsorption and open symbols for desorption).

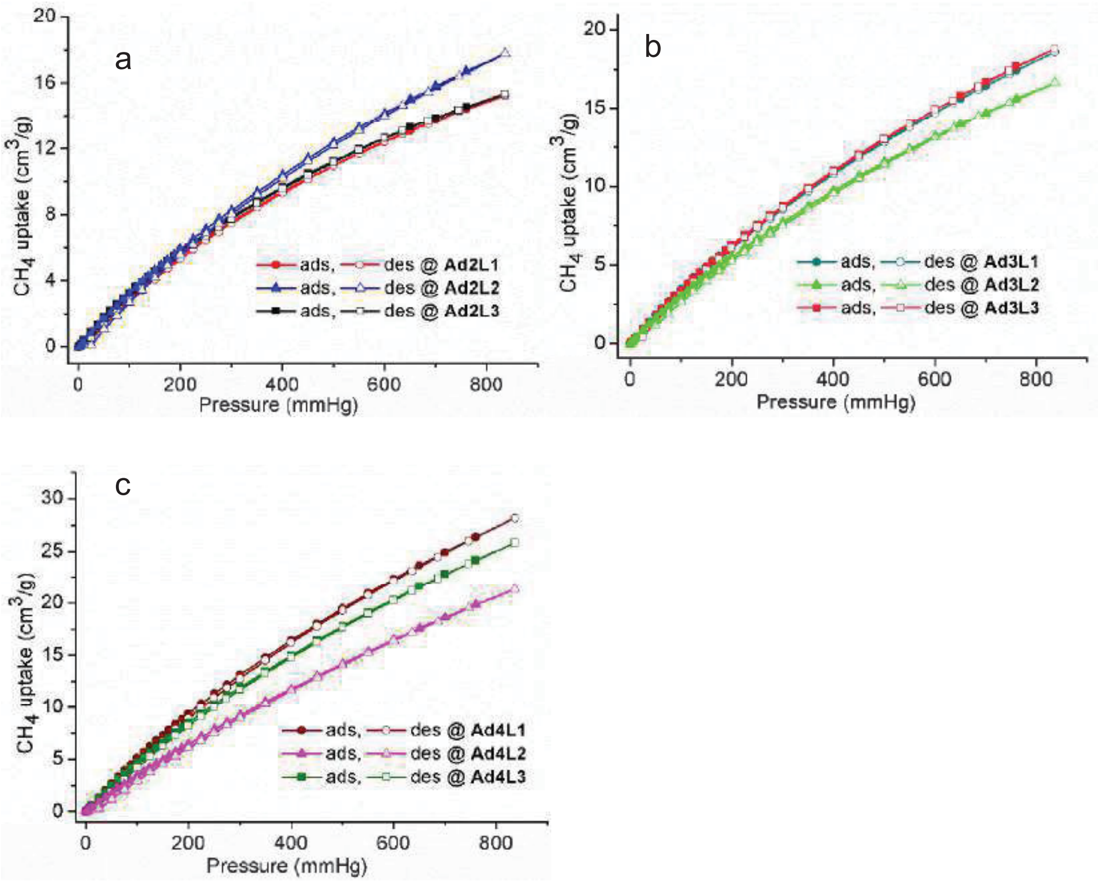

Figure 5. CH_4 sorption isotherms for **Ad2L1-Ad4L3** at 273 K (closed symbols for adsorption and open symbols for desorption).

Ad2L1-Ad4L3 CTFs exhibited CH_4 uptake capacities in the range of 14 cm^3 g^{-1} to 26 cm^3 g^{-1} whereas N_2 sorptions were 5-9 cm^3 g^{-1} which are comparable with our previously reported single building block adamantane-based CTFs, PCTF-3 to PCTF-5 [17]. These low CH_4 and N_2 sorption capacities compared to CO_2 results in good to high CO_2/N_2 and CO_2/CH_4 selectivities for the possible separation of as CO_2 from flue gas or natural gas, respectively. The selectivities of **Ad2L1** to **Ad4L3** were calculated by using the ratio of the initial slopes obtained by a linear fit in the Henry region of the adsorption isotherms (Fig. S8). As shown in Table 2, the calculated CO_2/N_2 and CO_2/CH_4 selectivities of **Ad2L1** to **Ad4L3** were in the range of 13-20 and 4-5, respectively. These values compare well with PCTF-3 to PCFT-5 or other CTFs (Table S6) [17]. Since the Henry region of the adsorption isotherms is only applicable up to 0.1 bar, we estimated the selectivity over the whole pressure region up to 1 bar by the ideal adsorption solution theory (IAST) model [47,48]. By using IAST model, the CO_2/N_2 selectivity of **Ad2L1-Ad4L3** were found in the range of 17-30 at 273 K, thus higher than by initial slope model. Among all the CTFs in this study, **Ad4L3** exhibited the highest selectivity due to its highest micropore volume fraction $V_{0.1}/V_{tot}$ and highest CO_2-accessible micropore volume $V_{micro}(CO_2)$ (Table 1).

Table 3 compares the CO_2 uptake and CO_2/N_2 selectivity to the BET surface area, micropore volume fraction $V_{0.1}/V_{tot}$ and CO_2-accessible micropore volume $V_{micro}(CO_2)$ of the single building block CTFs (from **Ad** or **L** only) to those of the mixed-nitrile building block **Ad-L** CTFs. Interestingly, the surface areas of the materials obtained using the mixed building block approach in a number of cases are higher than the values for the respective materials obtained via the single building approach under the same conditions. This trend is especially clearly visible in the case of ***Ad4Ln*** material, with the highest value attained for **Ad4L2** (1885 m^2 g^{-1}) compared to 1183 and 1710 m^2 g^{-1} for the respective materials by the single building block approach. Alone, the **L1** or **L2** building blocks yield planar hexagonal nets in the ideal case and an addition of ‘de-planarizing’ co-block yields less ordered 3D structures, which still do not have lower surface areas in the best case. It seems that the best results are reached when the de-planarizing block is of high-symmetry and connectivity. The CO_2 uptake correlates, though not perfectly, empirically with the product of BET surface area, micropore volume fraction ($V_{0.1}/V_{tot}$) and CO_2-accessible micropore volume ($V_{micro}(CO_2)$) (Figure 6, Figures S14 in Supp. Info.). The highest uptakes are reached for **Ad4L1** and **Ad4L3** (3.36 and 3.26 mmol g^{-1}) with high but not the largest surface areas. It seems that the volume of micropores, where the adsorption is the most efficient, is an important factor here, as the same two compounds have the largest micropore volumes (0.085 and 0.089 cm^3 g^{-1}, respectively).

Table 3. Monomers with corresponding CTFs and their CO_2 adsorptions.

Monomer	CTF [a]	S_{BET} [a] ($m^2\ g^{-1}$)	CO_2 uptake [b]	CO_2/N_2 selectivity [c]	$V_{0.1}/V_{tot}$	$V_{micro}(CO_2)$ [g] ($cm^3\ g^{-1}$)	Ref.
Ad2	PCTF-3	641	2.14	25	0.57	0.061	17
Ad3	PCTF-4	1090	2.27	26	0.55	0.052	17
Ad4	PCTF-5	1183	2.55	32	0.64	0.072	17
L1	CTF-1	746	2.47	20	[d]	[d]	37
		970	3.17	[d]	0.79	0.1	19b
L2		1710	[d]	[d]	[d]	[d]	12e
L3	CTF-0	499 [e]	2.25 [e]	[d]	0.45	[d]	20
Ad2 + L1	**Ad2L1**	918	1.73	21	0.395	0.0505	[f]
Ad2 + L2	**Ad2L2**	1316	1.92	19	0.218	0.0508	[f]
Ad2 + L3	**Ad2L3**	747	1.77	27	0.622	0.0568	[f]
Ad3 + L1	**Ad3L1**	1199	2.14	24	0.55	0.0544	[f]
Ad3 + L2	**Ad3L2**	1093	1.96	24	0.416	0.0499	[f]
Ad3 + L3	**Ad3L3**	1328	2.23	20	0.516	0.0537	[f]
Ad4 + L1	**Ad4L1**	1617	3.36	23	0.677	0.0853	[f]
Ad4 + L2	**Ad4L2**	1885	2.47	17	0.44	0.0500	[f]
Ad4 + L3	**Ad4L3**	1341	3.28	30	0.702	0.089	[f]

[a] All CTFs were prepared at 400 °C with 10 mol equivalent of $ZnCl_2$. [b] mmol/g at 273 K and 1 bar. [c] IAST selectivity calculated at 273 K and 1 bar, see also Table S6 in Supp. Info. †. [d] Not measured. [e] 5 mol equivalent of $ZnCl_2$. [f] This work. [g] Total pore volume for pores with diameters smaller than 1 nm (10 Å, cf. Fig. 3b, d and f) as given by NLDFT model for the CO_2 data at 273K.

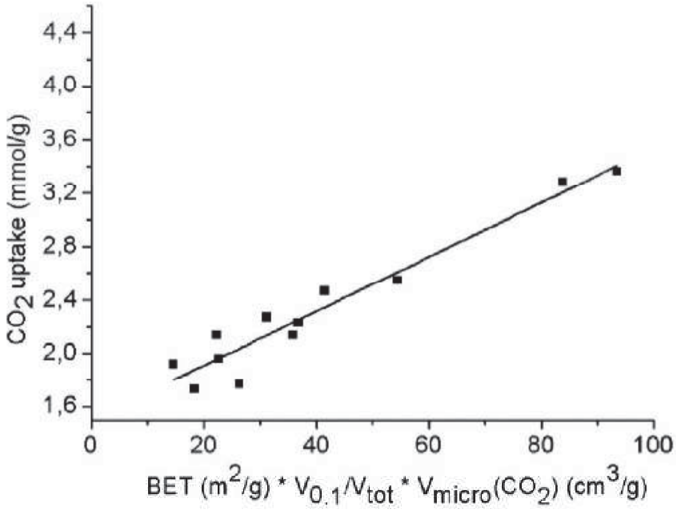

Figure 6. Correlation of CO_2 uptake with the product of BET surface area, micropore volume fraction ($V_{0.1}/V_{tot}$) and CO_2-accessible micropore volume ($V_{micro}(CO_2)$). The 12 data points include the nine values for **Ad*m*L*n*** and PCTF-3 to -5. The root mean-square deviation,

RMSD is 0.931. Compare to Figures S14 in Supp. Info. for other correlations with the best RMSD values being 0.86.

In order to better understand the CO_2 adsorption properties, the differential heat of adsorption (negative adsorption enthalpy, $\Delta H_{ads,diff}$) (Fig. 7) was calculated after determining the required relative pressures p_1 and p_2 from two CO_2 adsorption isotherms acquired at different temperatures T_1 and T_2 using a modified form of the Clausius-Clapeyron equation (eq. (1)) [49]. Q^0_{ads} was calculated over the whole adsorption range from the 273 K and 293 K isotherms for CO_2 in **Ad2L1** to **Ad4L3** (cf. Fig. 4). The heat of adsorption at zero loading, Q^0_{ads} is included in Table 2.

$$\Delta H_{ads,diff} = -Rln\left(\frac{p_2}{p_1}\right)\frac{T_1T_2}{T_2 - T_1} \cdots\cdots\cdots\cdots (1)$$

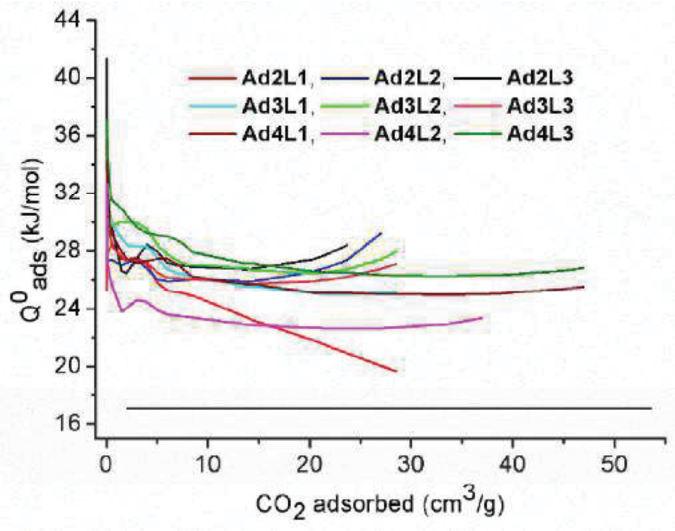

Figure 7. Isosteric heats of adsorption of CO_2 for **Ad2L1-Ad4L3** calculated from a pair of adsorption isotherms measured at 273 K and 293 K.

The isosteric heat of adsorption (Q_{ads}) values at zero coverage are in the range of 25 to 41 kJ mol^{-1} for **Ad2L1** to **Ad4L3**, and quickly decrease at only a few cm^3 g^{-1} of CO_2 adsorbed (Table 2 and Fig. 7). The high adsorption enthalpy at zero coverage is explained by the initial filling of the small ultramicropores with 4 Å diameter (Fig. 3b,d,f) with enhanced adsorbate−surface interactions, which could be modelled as interaction of a single CO2 molecule to two opposite sides of a slit-pore [17]. The heat of adsorption values of these CTFs stay between 23-29 kJ mol^{-1} from quantities adsorbed between 5 cm^3 g^{-1} to 20 cm^3 g^{-1} and beyond except for **Ad2L1** where the decrease steadily continues. However, these heat of

CO_2 adsorption values at 23-29 kJ mol^{-1} stay well above the heat of liquefaction of CO_2 with 17 kJ mol^{-1} [50] or stay around the isosteric enthalpy of adsorption for CO_2 on activated charcoals (e.g. BPL: 25.7 kJ mol^{-1}, A10: 21.6 kJ mol^{-1}, and Norit R1 Extra: 22.0 kJ mol^{-1} [51]. The high Q_{ads} values can be attributed to the enhanced interaction of CO_2 with triazine moieties (very generally speaking to increase of polarity) and for low loadings also to the micropore size effect [40].

When the loading is increased beyond 20 cm^3 g^{-1} the heat of adsorption value appears to increase slightly towards for **Ad2L2, Ad2L3, Ad3L2** and **Ad3L3** (Fig. 7), however this physically improbable condition is within the experimental error margin of ±3 kJ mol^{-1} and not considered as relevant [17,52]. Increase of ΔH_{ads} with CO_2 uptake might potentially take place together with structural changes and/or rearrangement of already adsorbed CO_2 molecules towards an energetically more favorable packing configuration. In this case there are no prerequisites to expect such behavior.

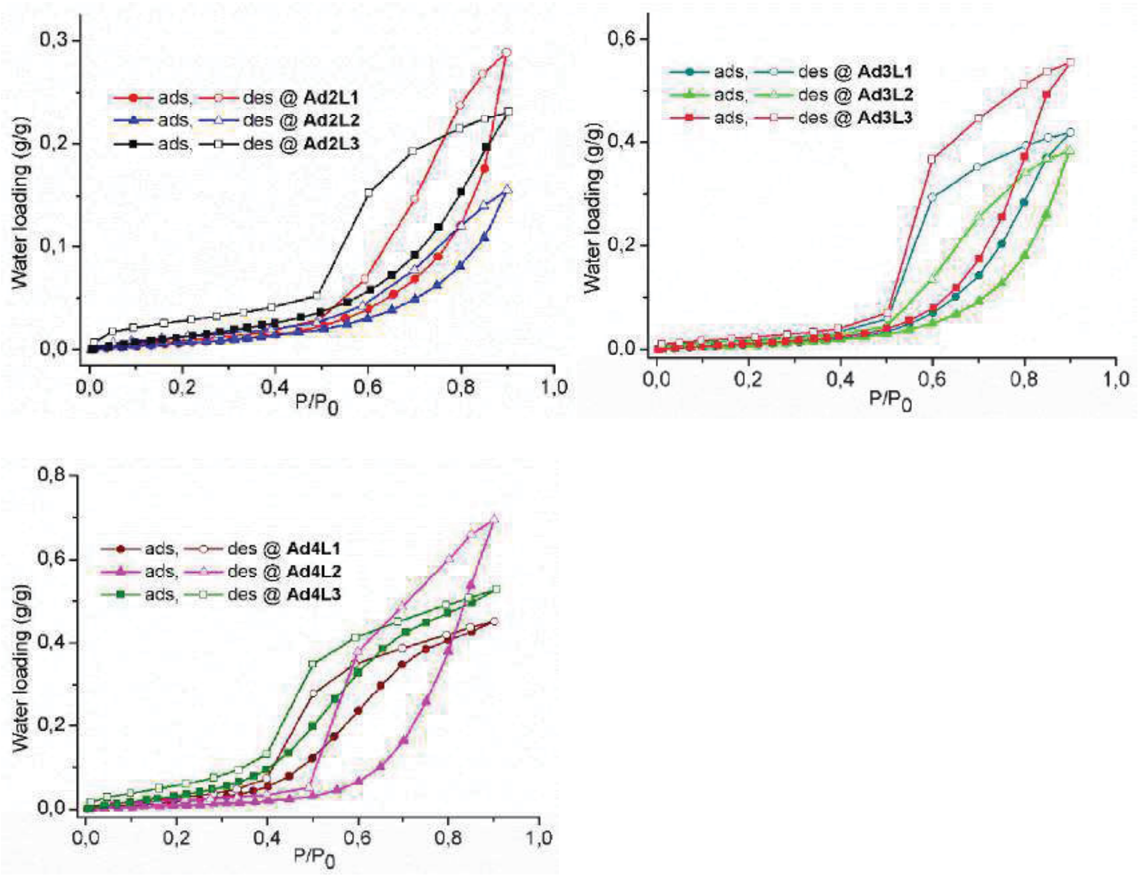

Figure 8. Water sorption isotherms of **Ad2L1-Ad4L3** at 20 °C.

CTFs were recently recognized as more hygroscopic and hydrophilic than expected with a water uptake of 11-17 wt% up to $P/P_0 = 0.5\text{-}0.6$, i.e., from ambient air of 50-60% humidity [19].

To assess the hydrophobic-hydrophilic nature, volumetric water adsorption measurements were carried out for **Ad2L1** to **Ad4L3** (Fig. 8). The water vapour adsorption isotherm provides information on the adsorption loading dependence on relative water vapor pressure, which reflects the hydrophilicity of the material [53]. The **Ad-L** CTFs show largely Type III isotherms for which there is no identifiable monolayer formation and the adsorbent-adsorbate interactions are relatively weak so that the adsorbed molecules are clustered around the most favorable sites on the surface of the solid [26]. The water uptake increase at high vapour pressure comes from the pore condensation of water within the CTFs pore [54]. The H2(b) hysteresis loops are again associated with pore-blocking or percolation by pore necks with a larger size distributions of these necks.

An exception is **Ad4L1** and **Ad4L3** where the sorption isotherms starting to have features of Type V, however still being quite close to Type III. These characteristic S-shape of the Type V isotherms in this case is weakly expressed, and the second flexing is almost flattened out in a line, but still there is some accelerated water uptake between $P/P_0 = 0.4 – 0.6$, followed by a levelling-off at higher P/P_0. Type V isotherms are associated with water adsorption on hydrophobic microporous and mesoporous adsorbents [26]. Yet, the P/P_0 region for the increase in water uptake can occur also at low P/P_0, which is then indicative of a more hydrophilic material. The S-shaped isotherm is typical for water sorption in metal-organic frameworks (MOFs) [55]. MOFs have intermediate and tuneable hydrophilicity-hydrophobicity. The more hydrophilic the MOF, the lower the P/P_0 for the rise of the uptake curve [52]. Hydrophilic MOFs like Al-fumarate [56] and CAU-10-H [57] show the rise between $P/P_0 = 0.1\text{-}0.2$, while more hydrophobic MOFs like MIL-101Cr [58] or fluorinated MIL-47 and MIL-53Al [59] exhibit the increase between $P/P_0 = 0.4\text{-}0.5$.

At 0.9 P/P_0 and 20 °C, the water adsorption of **Ad2L1** to **Ad4L3** is in the range of 0.15 g g^{-1} to 0.68 g g^{-1} (Table S4, Supp. Info.). **Ad4L2** exhibit the highest water vapour uptake of 864 cm^3 g^{-1} STP or 0.7 g g^{-1} at $P/P_0 = 0.9$ and 20 °C. At this high relative pressure the water uptake of **Ad4L2** is even higher than reported for, e.g., bipy-CTF500, pym-CTF500, CTF-TPC and CTF-FL, which also contain N-heterocyclic moieties more hydrophilic then their carbon-only analogues [19,43].

3. Conclusions

Successful systematic application of mixed building block approach for the synthesis of CTFs from two classes of non-planar and planar nitrile building blocks (BB) was demonstrated. Nine covalent triazine frameworks frameworks (CTFs) were synthesized from phenyladamantane based BBs on one side and phenyl/biphenyl substituted ones on the other, using $ZnCl_2$ catalysis. Interestingly, the mixed BB strategy lead in best cases to somewhat larger surface area porosities (747-1885 m^2 g^{-1}) compared to the single BB approach under similar conditions (641-1710 m^2 g^{-1}), contrary to expectable averaged values, thus demonstrating the potential viability of the approach.

The highest surface area was observed for **Ad4L2**, the case when the most branched tetrahedral adamantane BB is used together with the longest biphenyl based 'spacer', which highlights possible future strategies. Conceptually, the introduction of a 'deplanarizing' additive in the case of 'spacer' dinitriles, which, used alone, end up in planar hexagonal network structures, could yield not less porous 3D structures with significant potential towards fine-tuning of properties.

Interestingly, the CO_2 adsorption found did not follow precisely the surface area order. The **Ad4L1** (1617 m^2 g^{-1}) and **Ad4L3** (1341 m^2 g^{-1}), involving the shorter terephthalodinitrile (**L1**) or the more branched trimesonitrile (**L3**) adsorbed the largest amount of CO_2 (ca. 75 cm^3 g^{-1}; 1 bar and 273 K in both cases, which is on the level of the best CTFs). The highest CO_2 and CH_4 adsorption correlates best with the product of BET surface area, micropore volume fraction ($V_{0.1}/V_{tot}$) and CO_2-accessible micropore volume ($V_{micro}(CO_2)$). The micropore volume improves the efficiency of the gas adsorption and, thus, reflects the importance of fine-tuning different porosity aspects. Generally good CO_2 selectivities over N_2 (>13; max. 20-30 for **Ad4L3** by different methods) and average selectivities over CH_4 of 4-5 for all cases were found.

The synthesized CTFs demonstrate relatively low hydrophilicity, still quite good compared to many porous organic polymers. The largest uptake was found for **Ad4L2** at 0.7 g g^{-1} at 90% relative humidity at 20 °C. While practically all the materials demonstrate a Type II isotherm of water sorption, characteristic for surfaces with low affinity, **Ad4L1** and **Ad4L3** materials start to demonstrate also Type V isortherm features, associated with slightly increased affinity to water at high relative humidities.

The most prominent materials found in the screening invariably involved the most symmetric tetrasubstituted adamantane BB, which probably favored the formation of the most ordered structures, hence with the best porosity characteristics. Further development of the mixed BB approach employing the observed trends in fine-tuning of properties is called for development of durable materials with high adsorptive capacities and selectivities for such applications as CO_2 separation/capture.

Acknowledgements

Support of the work by BMBF project OptiMat 03SF0492C is gratefully acknowledged.

References

[1] A.-H. Lu, S. Dai, Porous Materials for Carbon Dioxide Capture, Springer Berlin Heidelberg, 2014.

[2] A.-H. Lu, G.-P. Hao, Annu. Rep. Prog. Chem., Sect. A: Inorg. Chem. 109 (2013) 484-503.

[3] R.K. Pachauri, A. Reisinger, IPCC Fourth Assessment Report (Intergovern-mental Panel on Climate Change, 2007).

[4] Y. Liu, Z.U. Wang, H.-C. Zhou, Greenhouse Gas Sci Technol. 2 (2012) 239–259.

[5] R.S. Haszeldine, Science 325 (2009) 1647.

[6] (a) K. Sumida, D.L. Rogow, J.A. Mason, T.M. McDonald, E.D. Bloch, Z.R. Herm, T.-H. Bae, J.R. Long, Chem. Rev. 112 (2012) 724–781;

(b) H. He, W. Li, M. Zhong, D. Konkolewicz, D. Wu, K. Yaccato, T. Rappold, G. Sugar, N.E. David, K. Matyjaszewski, Energy Environ. Sci. 6 (2013) 488–493.

[7] (a) A. Patra, J.-M. Koenen, U. Scherf, Chem. Commun. 47 (2011) 9612-9614; (b) A. Patra, U. Scherf, Chem. Eur. J. 18 (2012) 10074-10080; (c) E. Preis, C. Widling, U. Scherf, S. Patil, G. Brunklaus, J. Schmidt, A. Thomas, Polym. Chem. 2 (2011) 2186-2189

[8] (a) R.S. Sprick, B. Bonillo, R. Clowes, P. Guiglion, N.J. Brownbill, B.J. Slater, F. Blanc, M.A. Zwijnenburg, D.J. Adams, A.I. Cooper, Angew.Chem. Int. Ed. 128 (2016) 1824 – 1828; (b) R.S. Sprick, J.-X. Jiang, B. Bonillo, S. Ren, T. Ratvijitvech, P. Guiglion, M.A. Zwijnenburg, D.J. Adams, A.I. Cooper, J. Am. Chem. Soc. 137 (2015) 3265−3270.

[9] (a) A.P. Côté, A.I. Benin, N.W. Ockwig, M. O'Keeffe, A.J. Matzger, O.M. Yaghi, Science 310 (2005) 1166; (b) C.J. Doonan, D.J. Tranchemontagne, T.G. Glover, J.R. Hunt, O.M. Yaghi, Nat. Chem. 2 (2010) 235.

[10] M.G. Rabbani, H.M. El-Kaderi, Chem. Mater. 24 (2012) 1511-1517.

[11] (a) F.J. Uribe-Romo, J.R. Hunt, H. Furukawa, C. Klock, M. O'Keeffe, O.M. Yaghi, J. Am. Chem. Soc. 131 (2009) 4570-4571; (b) S. Kandambeth, A. Mallick, B. Lukose, M.V. Mane, T. Heine, R. Banerjee, J. Am. Chem. Soc. 134 (2012) 19524–19527.

[12] F.J. Uribe-Romo, C.J. Doonan, H. Furukawa, K. Oisaki, O.M. Yaghi, J. Am. Chem. Soc. 133 (2011) 11478.

[13] (a) P. Kuhn, M. Antonietti, A. Thomas, Angew. Chem. Int. Ed. 47 (2008) 3450-3453; (b) P. Kuhn, A.l. Forget, D. Su, A. Thomas, M. Antonietti, J. Am. Chem. Soc. 130 (2008) 13333-13337; (c) M.J. Bojdys, J. Jeromenok, A. Thomas, M. Antonietti, Adv. Mater. 22 (2010) 2202-2205; (d) S. Kuecken, J. Schmidt, L. Zhi, A. Thomas, J. Mater. Chem. A 3 (2015) 24422-24427; (e) P. Kuhn, A. Thomas, M. Antonietti, Macromolecules 42 (2009) 319-326; (f) E. Preis, W. Dong, G. Brunklausb, U. Scherf, J. Mater. Chem. C 3 (2015) 1582-1587 (g) A. Bhunia, D. Esquivel, S. Dey, R.J. Fernández-Terán, Y. Goto, S. Inagaki, P. Van Der Voort, C. Janiak, J. Mater. Chem. A 2016, DOI: 10.1039/c6ta04623a

[14] V.M. Suresh, S. Bonakala, H.S. Atreya, S. Balasubramanian, T.K. Maji, ACS Appl. Mater. Interfaces 6 (2014) 4630−4637.

[15] S.K. Dey, N. de Sousa Amadeua, C. Janiak, Chem. Commun. 52 (2016) 7834-7837.

[16] S. Ren, R. Dawson, A. Laybourn, J.-x. Jiang, Y. Khimyak, D.J. Adamsa, A.I. Cooper, Polym. Chem. 3 (2012) 928-934.

[17] A. Bhunia, I. Boldog, A. Moller, C. Janiak, J. Mater. Chem. A 1 (2013) 14990–14999.

[18] S. Ren, M.J. Bojdys, R. Dawson, A. Laybourn, Y.Z. Khimyak, D.J. Adams, A.I. Cooper, Adv. Mater. 24 (2012) 2357-2361.

[19] S. Dey, A. Bhunia, M.D. Esquivel, C. Janiak, J. Mater. Chem. A 4 (2016) 6259-6263.

[20] (a) H. Lim, M.C. Cha, J.Y. Chang, Macromol. Chem. Phys. 213 (2012) 1385–1390; (b) P. Puthiaraj, S.-M. Cho, Y.-R. Lee, W.-S. Ahn, J. Mater. Chem. A 3 (2015) 6792–6797

[21] A.V. Bavykina, M.G. Goesten, F. Kapteijn, M. Makkee, J. Gascon, ChemSusChem 8 (2015) 809–812.

[22] (a) A. Bhunia, V. Vasylyeva, C. Janiak, Chem. Commun. 49 (2013) 3961-3963; (b) A. Bhunia, S. Dey, M. Bous, C. Zhang, W. von Rybinski, C. Janiak, Chem. Commun. 51 (2015) 484-486.

[23] B. Brehler, Naturwissenschaften 46 (1959) 554

[24] P. Katekomol, J. Roeser, M. Bojdys, J. Weber, A. Thomas, Chem. Mater. 25 (2013) 1542–1548.

[25] S. Hug, M.B. Mesch, H. Oh, N. Popp, M. Hirscher, J. Senker, B.V. Lotsch, J. Mater. Chem. A 2 (2014) 5928-5936.

[26] a) M. Thommes, K. Kaneko, A.V. Neimark, J.P. Olivier, F. Rodriguez-Reinoso, J. Rouquerol, K.S.W. Sing, Pure Appl. Chem. 87 (2015) 1051–1069; b) K.S.W. Sing, D.H. Everett, R.A.W. Haul, L. Moscou, R.A. Pierotti, J. Rouquerol, T. Siemieniewska, Pure Appl. Chem. 57 (1985) 603–619.

[27] (a) Micromeretic ASAP2020 software; (b) P. Tarazona, Phys. Rev. A 31 (1985). 2672 (c) P. Tarazona, Phys. Rev. A 32 (1985) 3148; (d) P. Tarazona, U.M.B. Marconi, R. Evans, Mol. Phys. 60 (1987) 573.

[28] F. Rodriguez-Reinoso, A. Linares-Solano, in Chemistry and Physics of Carbon, vol. **21** (P.A. Thrower, Ed.) Marcel Dekker, New York, 1988.

[29] Quantachrome Instruments (1900 Corporate Drive, Boynton Beach, FL 33426 USA, www.quantachrome.com) Powder Tech Note 35.

[30] J.-R. Li, Y. Ma, M.C. McCarthy, J. Sculley, J. Yu, H.-K. Jeong, P.B. Balbuena, H.-C. Zhou, Coord. Chem. Rev. 255 (2011) 1791–1823.

[31] (a) J. Liu, P.K. Thallapally, B.P. McGrail, D.R. Brown, J. Liu, Chem. Soc. Rev. 41 (2012) 2308-2322; (b) D.M. D'Alessandro, B. Smit, J.R. Long, Angew. Chem. Int. Ed. 49 (2010) 6058-6082.

[32] J. Zhang, P.A. Webley, P. Xiao, Energy Conversion and Management 49 (2008) 346-356.

[33] A. Khutia, C. Janiak, Dalton Trans. 43 (2014) 1338-1347.

[34] (a) G. Qi, Y. Wang, L. Estevez, X. Duan, N. Anako, A.-H.A. Park, W. Li, C.W. Jones, E.P. Giannelis, Energy Environ. Sci. 4 (2011) 444–452; (b) J.C. Hicks, J.H. Drese, D.J. Fauth, M.L. Gray, G. Qi, C.W. Jones, J. Am. Chem. Soc. 130 (2008) 2902–2903.

[35] L. Wang, R.T. Yang, J. Phys. Chem. C 116 (2012) 1099– 1106.

[36] V. Guillerm, L.J. Weselinski, M. Alkordi, M.I.H. Mohideen, Y. Belmabkhout, A.J. Cairns, M. Eddaoudi, Chem. Commun. 50, (2014) 1937-1940.

[37] T. Islamoglu, M. Gulam Rabbani, H.M. El-Kaderi, J. Mater. Chem. A 1 (2013) 10259-10266.

[38] H.A. Patel, S. Hyun Je, J. Park, D.P. Chen, Y. Jung, C.T. Yavuz, A. Coskun, Nat Commun. 4 (2013) 1357.

[39] W. Lu, J.P. Sculley, D. Yuan, R. Krishna, Z. Wei, H.-C. Zhou, Angew. Chem. Int. Ed. 51 (2012), 7480-7484.

[40] H. A. Patel, F. Karadas, J. Byun, J. Park, E. Deniz, A. Canlier, Y. Jung, M. Atilhan, C.T. Yavuz, Adv. Funct. Mater. 23 (2013) 2270–2276.

[41] R. Gomes, P. Bhanja, A. Bhaumik, Chem. Commun. 51 (2015) 10050-10053.

[42] Y. Zhao, K.X. Yao, B. Teng, T. Zhang, Y. Han, Energy Environ. Sci. 6 (2013) 3684-3692

[43] S. Hug, L. Stegbauer, H. Oh, M. Hirscher, B.V. Lotsch, Chem. Mater. 27 (2015) 8001–8010

[44] X. Liu, H. Li, Y. Zhang, B. Xu, S. A, H. Xia, Y. Mu, Polym. Chem. 4 (2013) 2445-2448

[45] S. Xiong, X. Fu, L. Xiang, G. Yu, J. Guan, Z. Wang, Y. Du, X. Xiong, C. Pan, Polym. Chem. 5 (2014) 3424-3431

[46] (a) B. Wang, A.P. Cote, H. Furukawa, M. O'Keeffe, O.M. Yaghi, Nature 453 (2008) 207; (b) X.-M. Hu, Q. Chen, Y.-C. Zhao, B.W. Laursen, B. Han, J. Mater. Chem. A 2 (2014) 14201.

[47] J.A. Obrien, A.L. Myers, Ind. Eng. Chem. Res. 27 (1988) 2085–2092.

[48] A.L. Myers, J.M. Prausnitz, AIChE J. 11 (1965) 121–127

[49] F. Rouquerol, J. Rouquerol, K. Sing, Adsorption by powders and porous solids, (F. Rouquerol, J. Rouquerol, K. Sing, Eds.), Academic Press, San Diego, 1999, vol. 11.

[50] S. Keskin, T.M. van Heest, D.S. Sholl, ChemSusChem 3 (2010) 879–891

[51] S. Himeno, T. Komatsu, S. Fujita, J. Chem. Eng. Data 50 (2005) 369–376; K.B. Lee, M.G. Beaver, H.S. Caram, S. Sircar, Ind. Eng. Chem. Res. 47 (2008) 8048–8062

[52] (a) F. Jeremias, A. Khutia, S.K. Henninger, C. Janiak, J. Mater. Chem. 22 (2012) 10148–10151; (b) F. Jeremias, V. Lozan, S. Henninger, C. Janiak, Dalton Trans. 42 (2013) 15967–15973.

[53] N.C. Burtch, H. Jasuja, K.S. Walton, Chem. Rev. 114 (2014) 10575–10612

[54] B.P. Biswal, S. Kandambeth, S. Chandra, D.B. Shinde, S. Bera, S. Karak, B. Garai, U.K. Kharulc, R. Banerjee, J. Mater. Chem. A 3 (2015) 23664-23669

[55] (a) S. K. Henninger, F. Jeremias, H. Kummer, C. Janiak, Eur. J. Inorg. Chem. 16 (2012), 2625–2634; (b) C. Janiak, S.K. Henninger, Chimia 67 (2013) 419–424; (c) F. Jeremias, D. Fröhlich, C. Janiak, S.K. Henninger, New J. Chem. 38, (2014) 1846–1852.

[56] F. Jeremias, D. Fröhlich, C. Janiak, S.K. Henninger, RSC Adv. 4 (2014) 24073–24082.

[57] D. Fröhlich, S.K. Henninger, C. Janiak, Dalton Trans. 43 (2014) 15300–15304.

---

[58] (a) J. Ehrenmann, S.K. Henninger, C. Janiak, Eur. J. Inorg. Chem. 4 (2011) 471–474; (b) A. Khutia, H.U. Rammelberg, T. Schmidt, S. Henninger, C. Janiak, Chem. Mater. 25 (2013) 790–798; (c) M. Wickenheisser, T. Paul, C. Janiak, Micropor. Mesopor. Mater. 220 (2016) 258-269; (d) M. Wickenheisser, A. Herbst, R. Tannert, B. Milow, C. Janiak, Micropor. Mesopor. Mater. 215 (2015) 143-153; (e) M. Wickenheisser, C. Janiak, Micropor. Mesopor. Mater. 204 (2015) 242-250; (f) M. Wickenheisser, F. Jeremias, S. K. Henninger, C. Janiak, Inorg. Chim. Acta 407 (2013) 145-152.

[59] S. Biswas, S. Couck, D. Denysenko, A. Bhunia, M. Grzywa, J.F.M. Denayer, D. Volkmer, C. Janiak, P. Van Der Voort, Micropor. Mesopor. Mater. 181 (2013) 175-181.

A mixed-linker approach towards designing covalent triazine-based frameworks for CO_2 capture and separation

Subarna Dey, Asamanjoy Bhunia, Ishtvan Boldog and Christoph Janiak*

Institut für Anorganische Chemie und Strukturchemie, Heinrich-Heine-Universität Düsseldorf, 40204 Duesseldorf, Germany.
* Corresponding author: E-mail: janiak@uni-duesseldorf.de; Fax: + 49-211-81-12287; Tel: +49-211-81-12286.

Emails: subarna.dey@uni-duesseldorf.de, asamanjoy.bhunia@gmail.com, ishtvan.boldog@gmail.com

Table of contents

1. Experimental Section

Materials and methods

All chemicals were purchased from commercial suppliers (Sigma-Aldrich, Acros Organics, and Alfa Aesar chemical company) and used without further purification, unless stated otherwise. 1,3-di(4-cyanophenyl)adamantane, 1,3,5-tri(4-cyanophenyl)adamantane and 1,3,5,7-tetrakis(4-cyano-phenyl)adamantane were synthesized according to the reported procedures (see below).[1]

Infrared (IR) spectra were obtained on a Bruker FT-IR Tensor 37 Spectrometer in the 4000-550 cm^{-1} region with 2 cm^{-1} resolution as KBr disks. ^1H and ^{13}C spectra were recorded on a Avance DRX-500 instruments. Elemental (CNH) analyses were carried out with a PerkinElmer 2400 series 2 elemental analyzer. Powder X-ray diffraction (PXRD) data was collected on a Bruker D2 Phaser diffractometer using a flat sample holder (also a flat silicon, low background sample holder) and Cu $K\alpha_1/\alpha_2$ radiation with $\lambda = 1.5418$ Å at 30 kV covering 2theta angles 5-80° over a time of 2 h, that is 0.01°/sec. Diffractograms were obtained on flat layer sample holders where at low angle the beam spot is strongly broadened so that only a fraction of the reflected radiation reaches the detector which leads to low relative intensities measured at $2\theta < 7°$. For hygroscopic or air-sensitive samples, the sample holder can be sealed with a dome. Scanning electron microscopy (SEM) images were obtained using an ESEM Quanta 400 FEG SEM equipped with a secondary electron detector. Thermogravimetric analyses (TGA) were carried out at a ramp rate of 10 °C/min in a N_2 flow with a Netzsch Thermo-Microbalance Apparatus TG 209 F3 Tarsus.

Sorption isotherms were measured using a Micromeritics ASAP 2020 automatic gas sorption analyzer equipped with oil-free vacuum pumps (ultimate vacuum $<10^{-8}$ mbar) and valves, which guaranteed contamination free measurements. The sample was connected to the preparation port of the sorption analyzer and degassed under vacuum until the outgassing rate, i.e., the rate of pressure rise in the temporarily closed manifold with the connected sample tube, was less than 2 μTorr/min at the specified temperature 200 °C. After weighing, the sample tube was then transferred to the analysis port of the sorption analyzer. All used gases (H_2, He, N_2, CO_2, CH_4) were of ultrahigh purity (UHP, grade 5.0, 99.999%) and the STP volumes are given according to the NIST standards (293.15 K, 101.325 kPa). Helium gas was used for the determination of the cold and warm free space of the sample tubes. H_2 and N_2 sorption isotherms were measured at 77 K (liquid nitrogen bath), whereas CO_2 and CH_4 sorption isotherms were measured at 293±1 K (passive thermostating) and 273.15 K (ice/deionized water bath). The heat of adsorption values and the DFT pore size distributions ('N_2 DFT slit pore' model) were calculated out using the ASAP 2020 v3.05 software.

A coulometric Karl-Fischer titration for the determination of the water content was carried out with a Karl-Fischer titration apparatus AQUA 40.00 with headspace module. The solid CTF sample was heated to 170 °C in the head space module and the liberated water transferred to the measurement cell.

Water sorption isotherms at 20 °C were obtained volumetrically from a Quantachrome Autosorb iQ MP instrument equipped with an all-gas option. Prior to the sorption experiments, the compounds were degassed (130 °C, 2h) under dynamic vacuum

2. Synthesis of CTFs (Ad2L1-Ad4L3)

Ad2L1: A mixture of 1,3-di(4-cyanophenyl)adamantane (68 mg, 0.2 mmol), terephthalonitrile (26 mg, 0.2 mmol) and $ZnCl_2$ (545 mg, 4 mmol) were placed into a Pyrex ampoule under inert conditions. The ampoule was evacuated, sealed and heated to 400 °C for 48 h followed by cooling to room temperature. The black product was collected and stirred with water for 72 h. Then the product was isolated by filtration and again stirred with 100 mL of 2 mol/L HCl for 24 h. The resulting black powder was further washed with water (3 × 50 mL), THF (3 × 30 mL), acetone (3 × 30 mL) and dried in vacuum. Yield: 80 mg, 85 %.

Ad2L2: The procedure for **Ad2L2** was followed by using the precursor compound 1,3-di(4-cyanophenyl)adamantane, (68 mg, 0.2 mmol), 4,4′-Biphenyldicarbonitrile (41 mg, 0.2 mmol) and $ZnCl_2$ (544 mg, 4 mmol). Yield: 97 mg, 88%.

Ad2L3: The procedure for **Ad2L3** was followed by using the precursor compound 1,3-di(4-cyanophenyl)adamantane, (68 mg, 0.2 mmol), 1,3,5-Benzenetricarbonitrile (21 mg, 0.134 mmol) and $ZnCl_2$ (460 mg, 3.34 mmol). Yield: 78 mg, 87%.

Ad3L1: The procedure for **Ad3L1** was followed by using the precursor compound 1,3,5-tri(4-cyanophenyl)adamantane, (88 mg, 0.2 mmol), terephthalonitrile (38 mg, 0.3 mmol) and $ZnCl_2$ (682 mg, 5 mmol). Yield: 109 mg, 86%.

Ad3L2: The procedure for **Ad3L2** was followed by using the precursor compound 1,3,5-tri(4-cyanophenyl)adamantane, (88 mg, 0.2 mmol), 4,4′-Biphenyldicarbonitrile (61 mg, 0.3 mmol) and $ZnCl_2$ (682 mg, 5 mmol). Yield: 127 mg, 85%.

Ad3L3: The procedure for **Ad3L3** was followed by using the precursor compound 1,3,5-tri(4-cyanophenyl)adamantane, (88 mg, 0.2 mmol), 1,3,5-Benzenetricarbonitrile (31mg, 0.2 mmol) and $ZnCl_2$ (555 mg, 4 mmol). Yield: 102 mg, 85%.

Ad4L1: The procedure for **Ad4L1** was followed by using the precursor compound 1,3,5,7-tetrakis(4-cyanophenyl)adamantane, (54 mg, 0.1 mmol), terephthalonitrile (26 mg, 0.2 mmol) and $ZnCl_2$ (408 mg, 3 mmol). Yield: 58 mg, 72%.

Ad4L2: The procedure for **Ad4L2** was followed by using the precursor compound 1,3,5,7-tetrakis(4-cyanophenyl)adamantane, (81 mg, 0.15 mmol), 4,4′-Biphenyldicarbonitrile (61 mg, 0.3 mmol) and $ZnCl_2$ (614 mg, 4.5 mmol). Yield: 113 mg, 79%.

Ad4L3: The procedure for **Ad4L3** was followed by using the precursor compound 1,3,5,7-tetrakis(4-cyanophenyl)adamantane, (81 mg, 0.15 mmol), 1,3,5-Benzenetricarbonitrile (30 mg, 0.2 mmol) and $ZnCl_2$ (474 mg, 3.5 mmol). Yield: 89 mg, 79%.

Table S1. Nitrile reactant ratio for mixed CTFs synthesis.[a]

CTFs	**Ratio**	
	1,3-bis-, 1,3,5-tris-, or 1,3,5,7-tetrakis(4-cyanophenyl)adamantane (**Ad2-Ad4**)	terephthalonitrile (**L1**)/ or 4,4''-biphenyl dicarbonitrile (**L2**)/ or 1,3,5-benzenetricarbonitrile (**L3**)
Ad2L1	1	1
Ad2L2	1	1
Ad2L3	1	0.7
Ad3L1	1	1.5
Ad3L2	1	1.5
Ad3L3	1	1
Ad4L1	1	2
Ad4L2	1	2
Ad4L3	1	1.3

[a] general conditions: Temperature 400 °C, reaction time 48 h, molar ratio $ZnCl_2$: sum of nitrile groups = 10 : 1

3. Elemental analysis of Ad2L1-Ad4L3

Samples were stored in closed vials under ambient air, following their synthesis and drying procedure

Table S2. CHN values for synthesized CTFs.

Frame-work	**Calculated (%)**					**Found (%)**				
	C	**H**	**N**	**C/H**	**C/N**	**C**	**H**	**N**	**C/H**	**C/N**
Ad2L1	82.38	5.62	12.01	1.23	8.07	74.36	2.84	7.18	2.20	12.00
Ad2L2	84.1	5.57	10.32	1.27	9.46	80.89	2.78	5.39	2.44	14.49
Ad2L3	81.79	5.49	12.72	1.25	7.48	73.31	3.19	4.89	1.93	17.48
Ad3L1	81.75	4.95	13.3	1.38	7.16	78.26	2.7	2.22	2.43	41.10
Ad3L2	83.73	5	11.27	1.40	8.71	78.13	2.58	2.22	2.54	41.17
Ad3L3	81.06	4.76	14.18	1.43	6.68	75.87	3.12	3.07	2.04	28.85
Ad4L1	81.39	4.55	14.06	1.5	6.78	77.66	3.24	6.00	2.01	15.11
Ad4L2	83.52	4.67	11.8	1.5	8.27	78.72	2.87	3.32	2.30	27.65
Ad4L3	80.63	4.33	15.04	1.56	6.27	71.46	2.98	8.14	2.01	10.26

The elemental analysis of **Ad2L1** to **Ad4L3** gave a lower hydrogen and a much lower nitrogen content and concomitantly higher C/H and a much higher than calculated C/N ratio. This indicates that most of the nitrogen is lost to decomposition to HCN, NH_3 (Scheme S1).

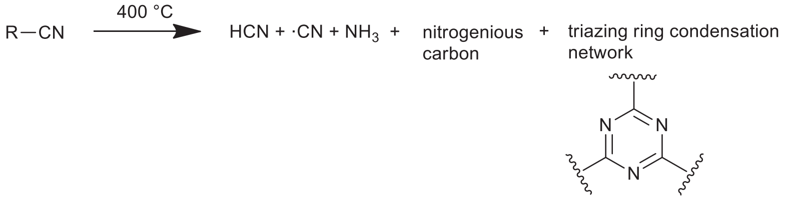

Scheme S1. General schematic representation for the decomposition of a triazine ring.

Some deviation of the CHN elemental analysis can be traced to the water content of the CTFs. Karl-Fischer-Titration of the **Ad-L** CTFs which were stored under ambient air revealed a water content between 2.4 (**Ad3L2**) and 12.8 wt% (**Ad4L3**) (see below Fig. S7 and Table S4).

The following equations are part of Scheme S2, which show the individual idealized repeating units and molecular weights for the **Ad-L** CTFs **Ad2L1** to **Ad4L3**.

Ad2L1:

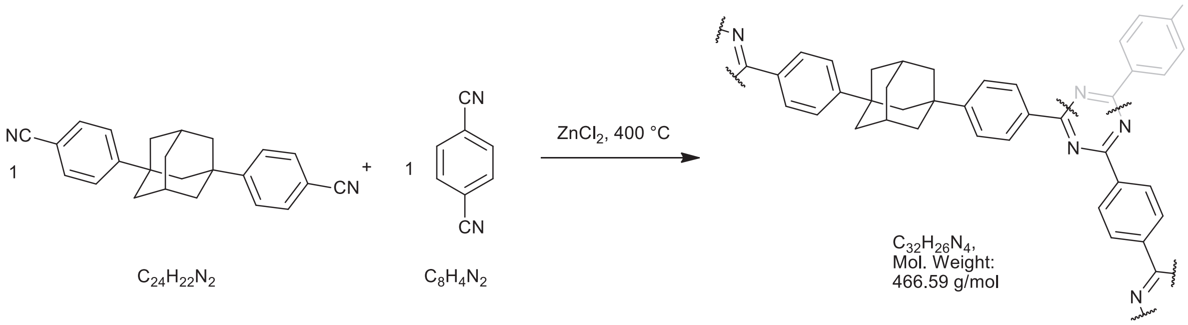

Ad2L2:

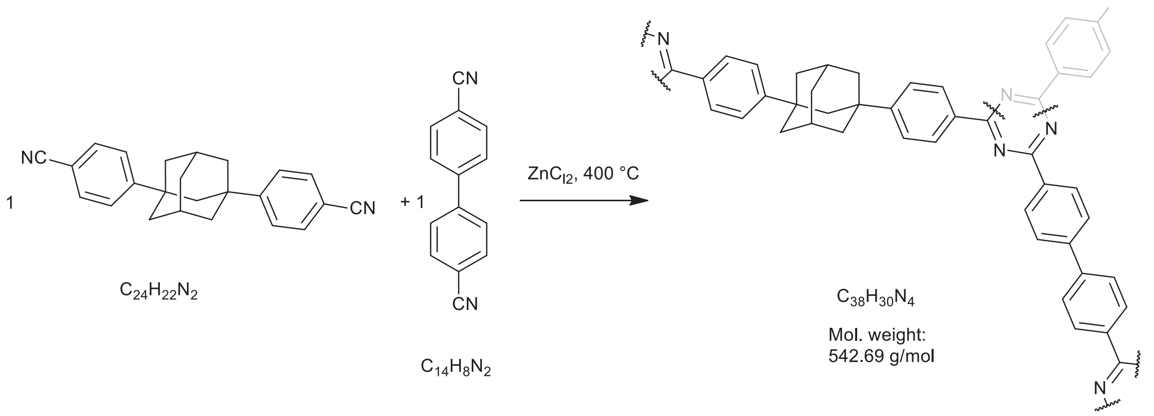

Ad2L3:

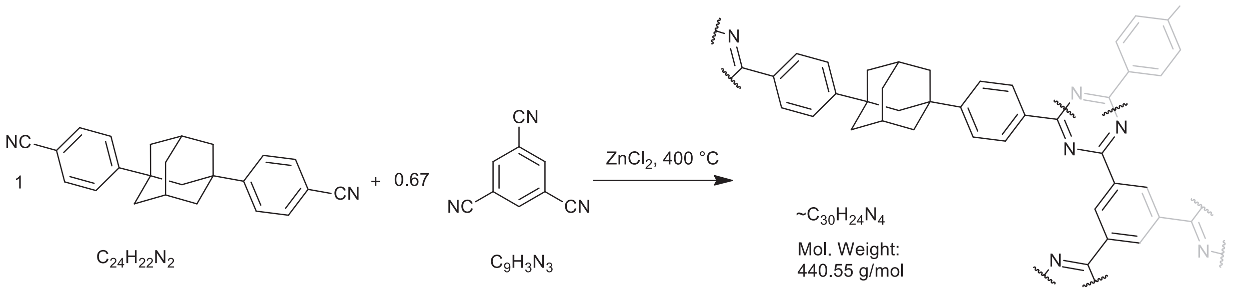

Ad3L1:

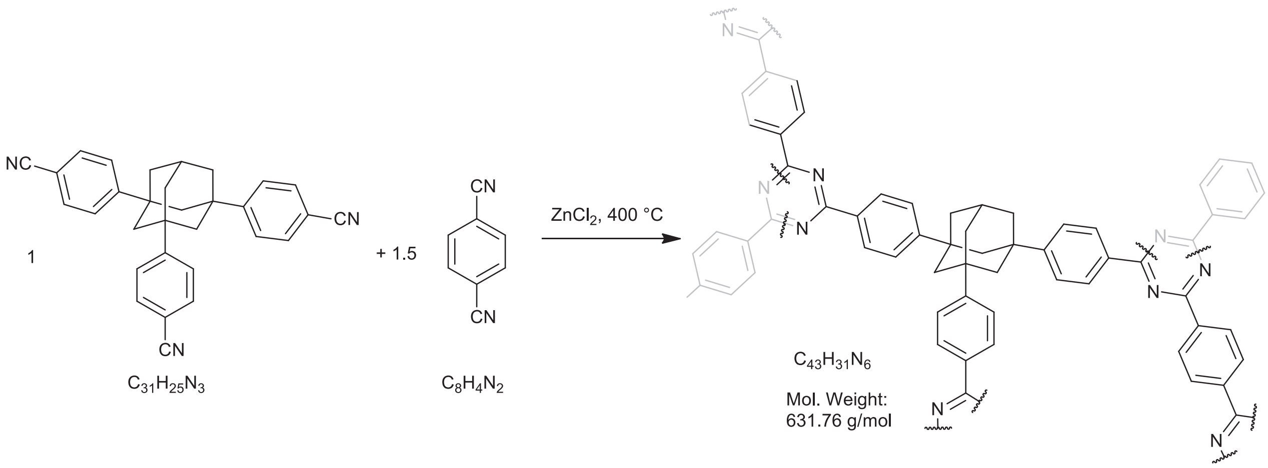

Ad3L2:

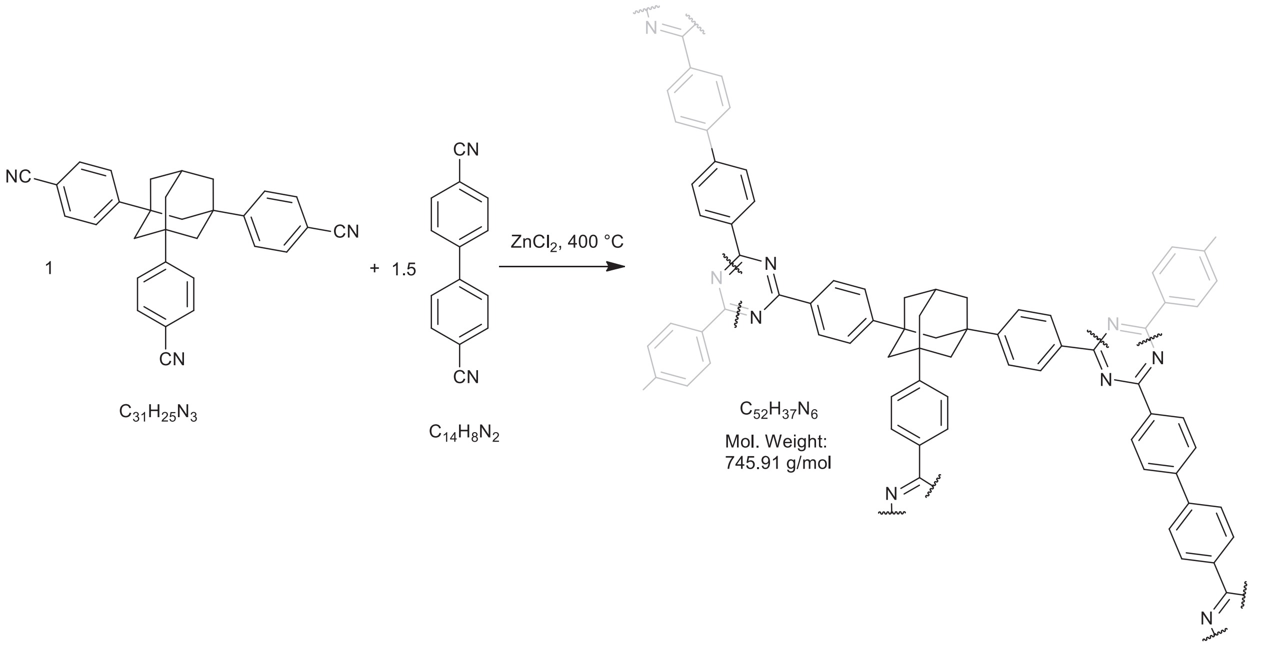

Ad3L3:

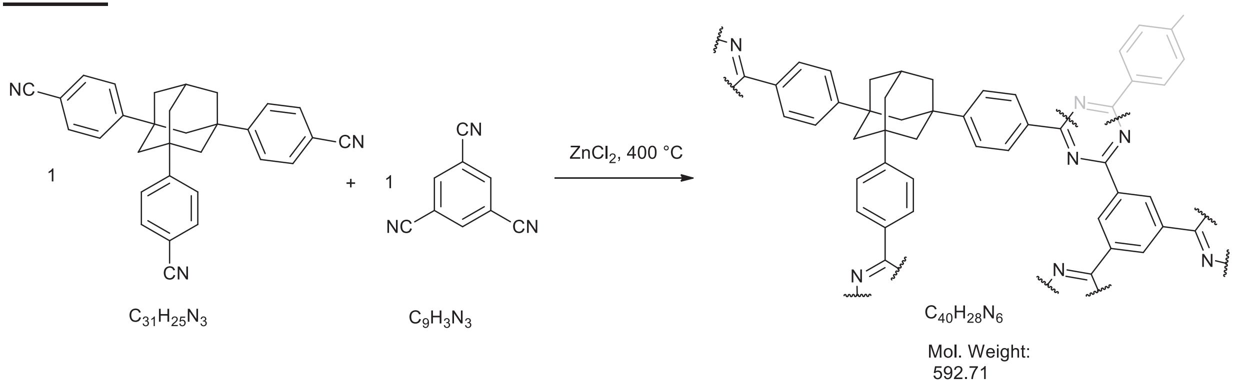

Ad4L1:

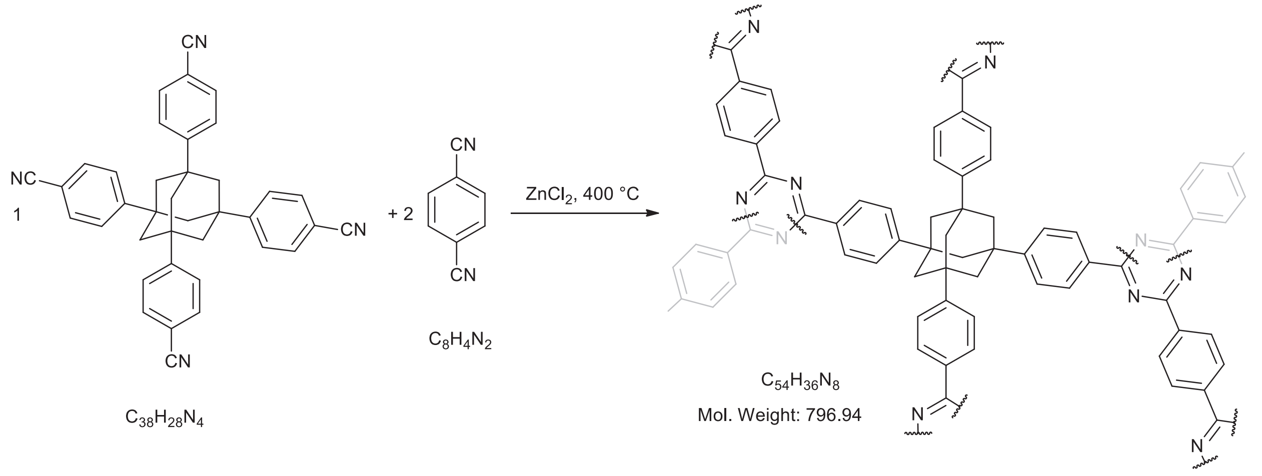

Ad4L2:

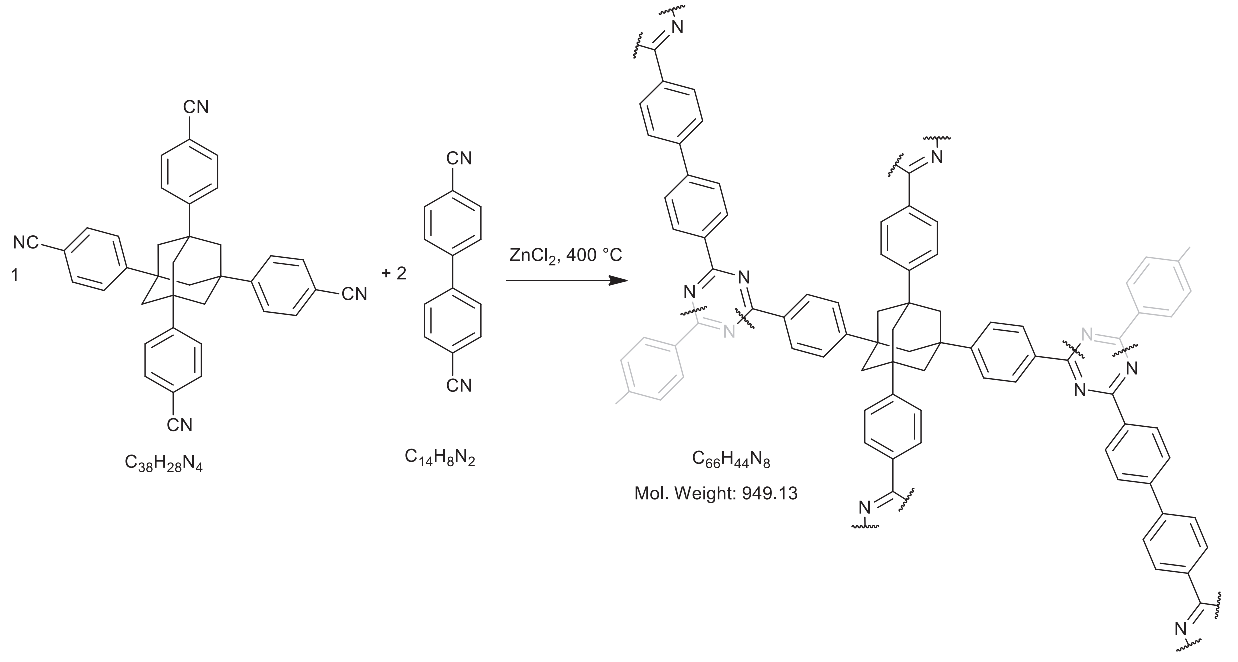

Ad4L3:

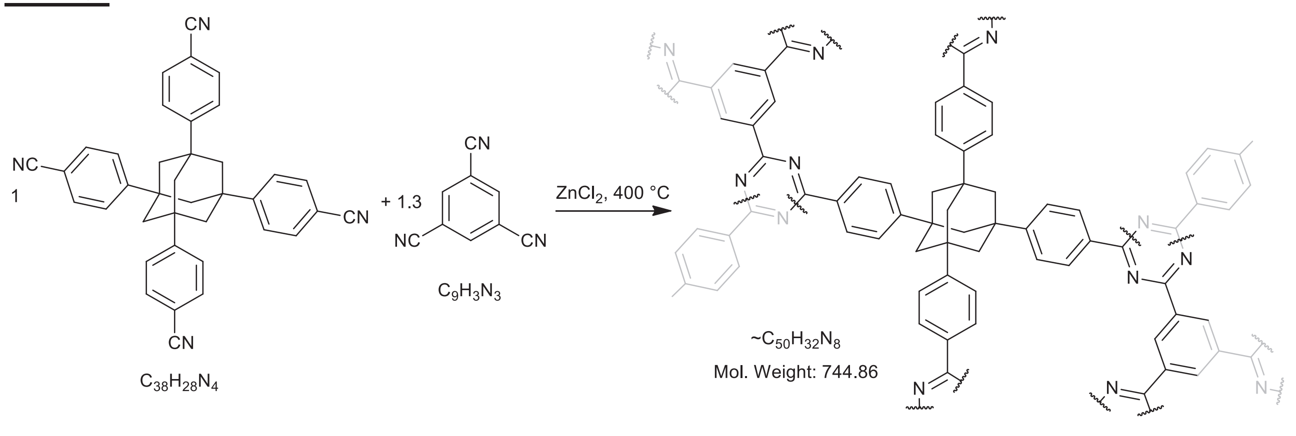

Scheme S2. Reactands and idealized individual repeat units and molecular weights for the **Ad-L** CTFs **Ad2L1** to **Ad4L3**.

4. Powder X-ray diffraction patterns of Ad2L1-Ad4L3

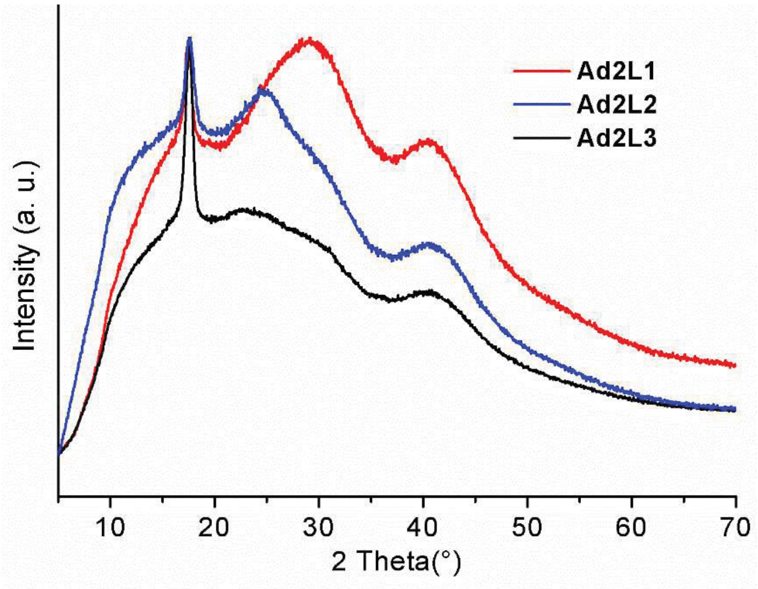

Fig. S1. Powder X-ray pattern of **Ad2L1-Ad2L3**.

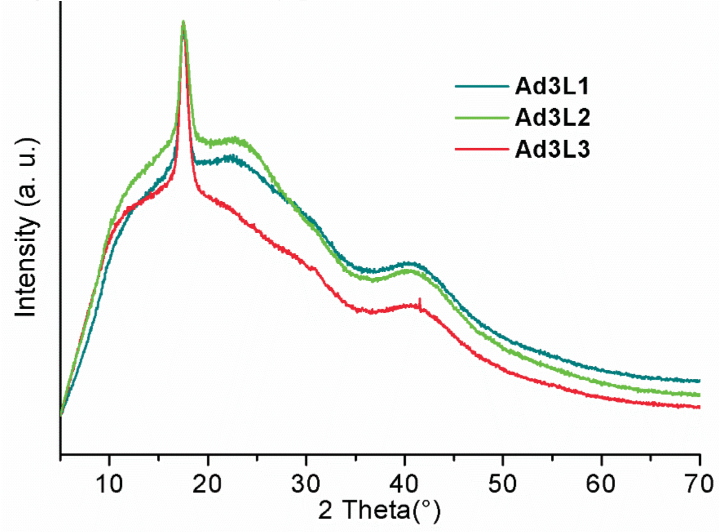

Fig. S2. Powder X-ray pattern of **Ad3L1-Ad3L3.**

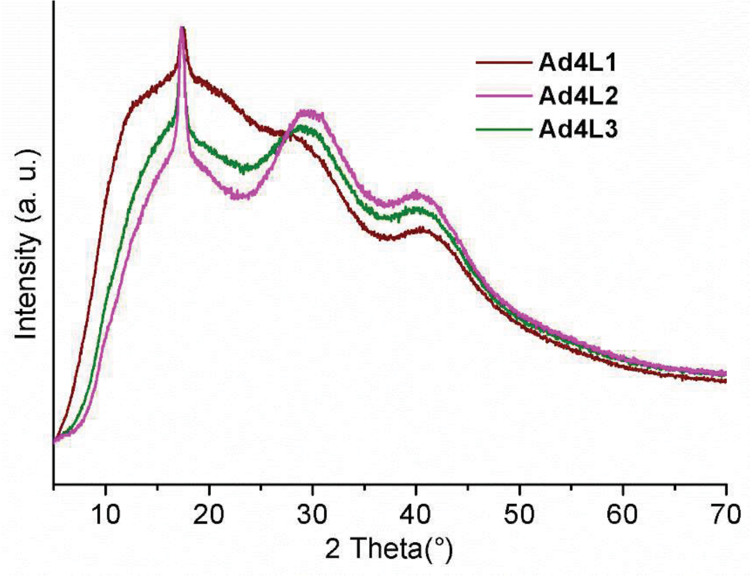

Fig. S3. Powder X-ray pattern of **Ad4L1-Ad4L3.**

5. Thermogravimetric analysis

All materials (**Ad2L1-Ad4L3**) show definite weight loss before decomposition. Both weight loss and decomposition temperature were summarized in Table S2.

Before TGA measurements, sample were dried and stored in closed vials in ambient condition.

Table S3. Decomposition temperature for **Ad2L1-Ad4L3**.

CTFs	Thermal stability (°C)	Weight loss (%)
Ad2L1	510	9
Ad2L2	520	6
Ad2L3	460	6
Ad3L1	510	11
Ad3L2	500	11
Ad3L3	505	13
Ad4L1	530	3
Ad4L2	520	9
Ad4L3	505	15

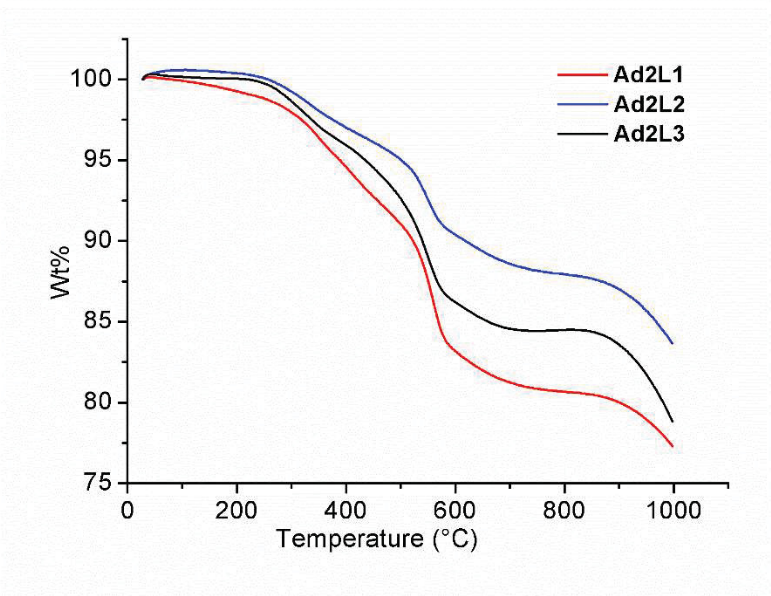

Fig. S4. Thermogravimetric analysis (TGA) for **Ad2L1-Ad2L3**

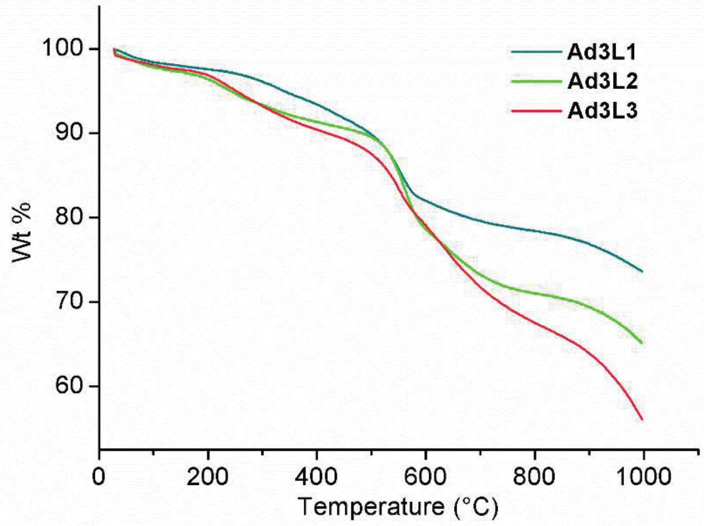

Fig. S5. Thermogravimetric analysis (TGA) for **Ad3L1-Ad3L3**

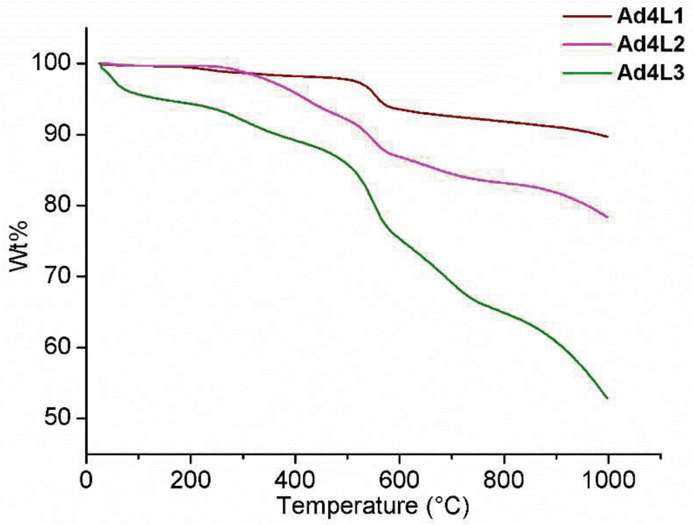

Fig. S6. Thermogravimetric analysis (TGA) for **Ad4L1-Ad4L3**

6. Karl Fischer Titration (KFT):

Analysis for water content was carried out with coulometric Karl-Fischer titration procedure. After synthesis and activation, the samples were stored in closed vials under ambient condition prior to measurement.

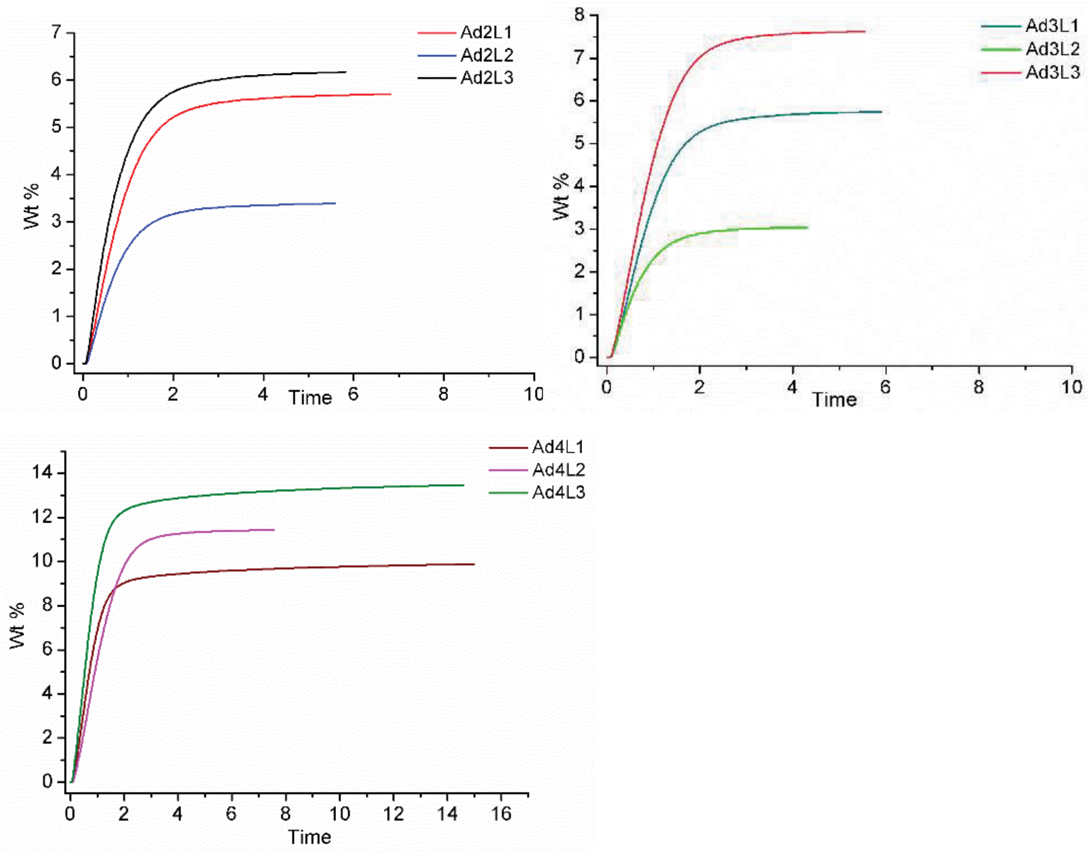

Fig. S7. Karl-Fischer titration plots for **Ad4L1-Ad4L3**.

Table S4. Water adsorption and KFT data for **Ad2L1-Ad4L3**.

CTFs	Uptake atP/P$_0$=0.1		Uptake at P/P$_0$=0.5		Uptake at P/P$_0$ = 0.9		Water loading from KFT
	cm^3 g^{-1}	g g^{-1}	cm^3 g^{-1}	g g^{-1}	cm^3 g^{-1}	g g^{-1}	wt%
Ad2L1		0.003	29	0.023	358	0.288	5.0
Ad2L2	5	0.004	24	0.02	193	0.156	2.7
Ad2L3	8	0.006	45	0.037	287	0.231	5.1
Ad3L1	6	0.005	42	0.035	520	0.419	5.1
Ad3L2	7	0.005	35	0.029	476	0.383	2.4
Ad3L3	7	0.006	48	0.039	690	0.556	6.8
Ad4L1	11	0.010	156	0.123	561	0.451	9.4
Ad4L2	6	0.005	33	0.035	864	0.696	10.7
Ad4L3	22	0.018	246	0.2	654	0.525	12.8

7. Selectivity:

The Henry's law linear isotherm equation and the Langmuir model were applied to calculate the selectivity from pure gas adsorption isotherm. A single or dual-site Langmuir model was fit the adsorption isotherms in order to estimate the selectivity which is often called Ideal Adsorbed Solution Theory (IAST) selectivity.

The Henry's isotherm equation is:

q = KP

where q is the adsorbed amount per unit weight of adsorbent(mmol g $^{-1}$), P is the adsorbate gas pressure at equilibrium (bar) and it is valid in the pressure range up to 0.1 bar, and K is the Henry's law constant (mmol g^{-1} bar^{-1}).

For CO_2 adsorption isotherm up to 1 bar, we assumed the double-layer adsorption. Therefore, the low pressure (up to 1 bar) adsorption isotherms of CO_2 measured at 273 was fitted with the dual-site Langmuir (DSL) model. The equation is:

$$q = q_A + q_B = q_{sat,A}\frac{b_A p}{1 + b_A p} + q_{sat,B}\frac{b_B p}{1 + b_B p}$$

Where, q is molar uptake of adsorbate (mmol/g), q_{sat} is saturation uptake (mmol/g), b is the parameter in single component Langmuir isotherm (bar^{-1}), p is the pressure of bulk gas, the subscription of A and B refers to different two sites.

On the other hand, due to the mono-layer adsorption of CH_4 and N_2 adsorption, the single-site Langmuir model were used:

$$q = q_{sat}\frac{bp}{1 + bp}$$

The IAST selectivity S_{ads} can be calculated from the following equation:

$$S_{ads} = \frac{q1/q2}{p1/p2}$$

A CO_2:N_2 ratio of 15:85 was used for calculating the gas mixture selectivities which is typically the flue gas composition.

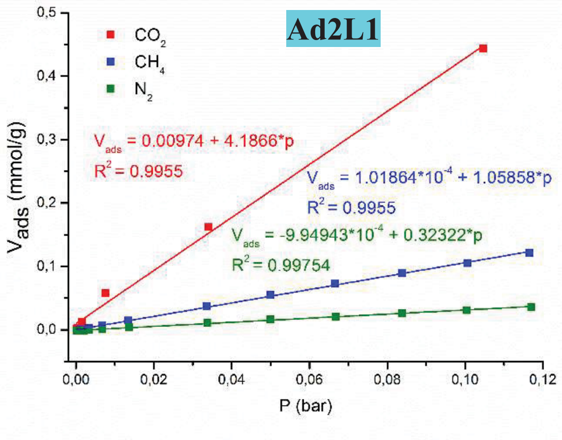
Ad2L1
CO$_2$
CH$_4$
N$_2$
V$_{ads}$ = 0.00974 + 4.1866*p
R^2 = 0.9955
V$_{ads}$ = 1.01864*10^{-4} + 1.05858*p
R^2 = 0.9955
V$_{ads}$ = -9.94943*10^{-4} + 0.32322*p
R^2 = 0.99754
Vads (mmol/g)
0,0
0,1
0,2
0,3
0,4
0,5
0,00
0,02
0,04
0,06
0,08
0,10
0,12
P (bar)

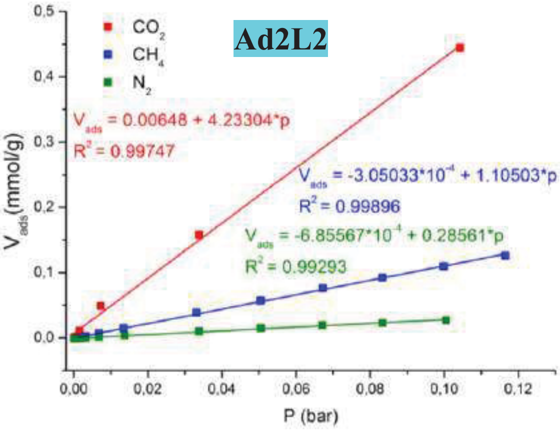
Ad2L2
CO$_2$
CH$_4$
N$_2$
V$_{ads}$ = 0.00648 + 4.23304*p
R^2 = 0.99747
V$_{ads}$ = -3.05033*10^{-4} + 1.10503*p
R^2 = 0.99896
V$_{ads}$ = -6.85567*10^{-4} + 0.28561*p
R^2 = 0.99293
V$_{ads}$ (mmol/g)
0,0
0,1
0,2
0,3
0,4
0,5
0,00
0,02
0,04
0,06
0,08
0,10
0,12
P (bar)

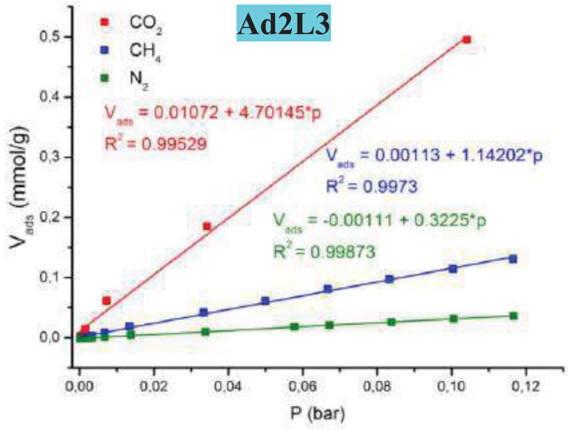
Ad2L3
CO$_2$
CH$_4$
N$_2$
V$_{ads}$ = 0.01072 + 4.70145*p
R^2 = 0.99529
V$_{ads}$ = 0.00113 + 1.14202*p
R^2 = 0.9973
V$_{ads}$ = -0.00111 + 0.3225*p
R^2 = 0.99873
V$_{ads}$ (mmol/g)
0,0
0,1
0,2
0,3
0,4
0,5
0,00
0,02
0,04
0,06
0,08
0,10
0,12
P (bar)

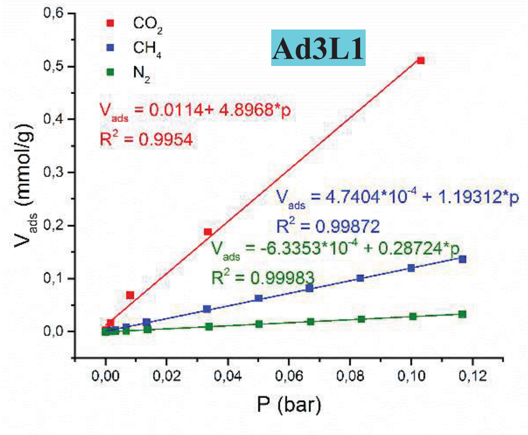
Ad3L1
CO$_2$
CH$_4$
N$_2$
V$_{ads}$ = 0.0114+ 4.8968*p
R^2 = 0.9954
V$_{ads}$ = 4.7404*10^{-4} + 1.19312*p
R^2 = 0.99872
V$_{ads}$ = -6.3353*10^{-4} + 0.28724*p
R^2 = 0.99983
V$_{ads}$ (mmol/g)
0,0
0,1
0,2
0,3
0,4
0,5
0,6
0,00
0,02
0,04
0,06
0,08
0,10
0,12
P (bar)

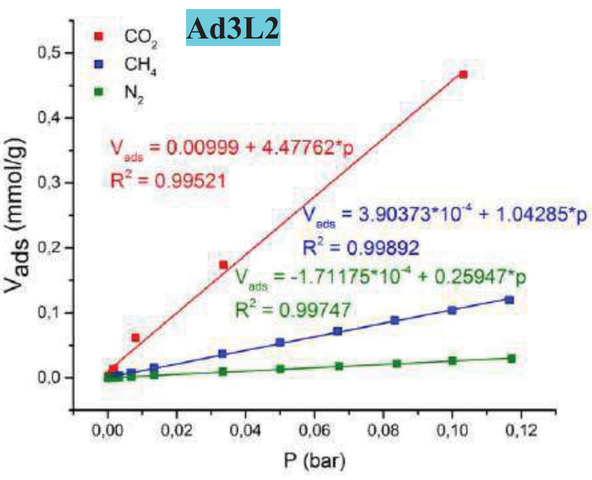
Ad3L2
CO$_2$
CH$_4$
N$_2$
V$_{ads}$ = 0.00999 + 4.47762*p
R^2 = 0.99521
V$_{ads}$ = 3.90373*10^{-4} + 1.04285*p
R^2 = 0.99892
V$_{ads}$ = -1.71175*10^{-4} + 0.25947*p
R^2 = 0.99747
Vads (mmol/g)
0,0
0,1
0,2
0,3
0,4
0,5
0,00
0,02
0,04
0,06
0,08
0,10
0,12
P (bar)

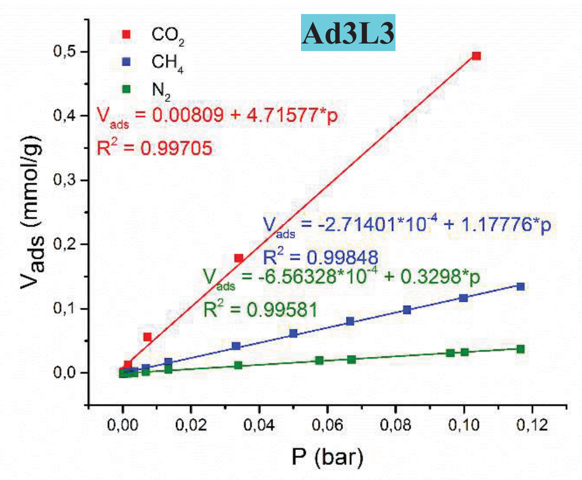
Ad3L3
CO$_2$
CH$_4$
N$_2$
V$_{ads}$ = 0.00809 + 4.71577*p
R^2 = 0.99705
V$_{ads}$ = -2.71401*10^{-4} + 1.17776*p
R^2 = 0.99848
V$_{ads}$ = -6.56328*10^{-4} + 0.3298*p
R^2 = 0.99581
Vads (mmol/g)
0,0
0,1
0,2
0,3
0,4
0,5
0,00
0,02
0,04
0,06
0,08
0,10
0,12
P (bar)

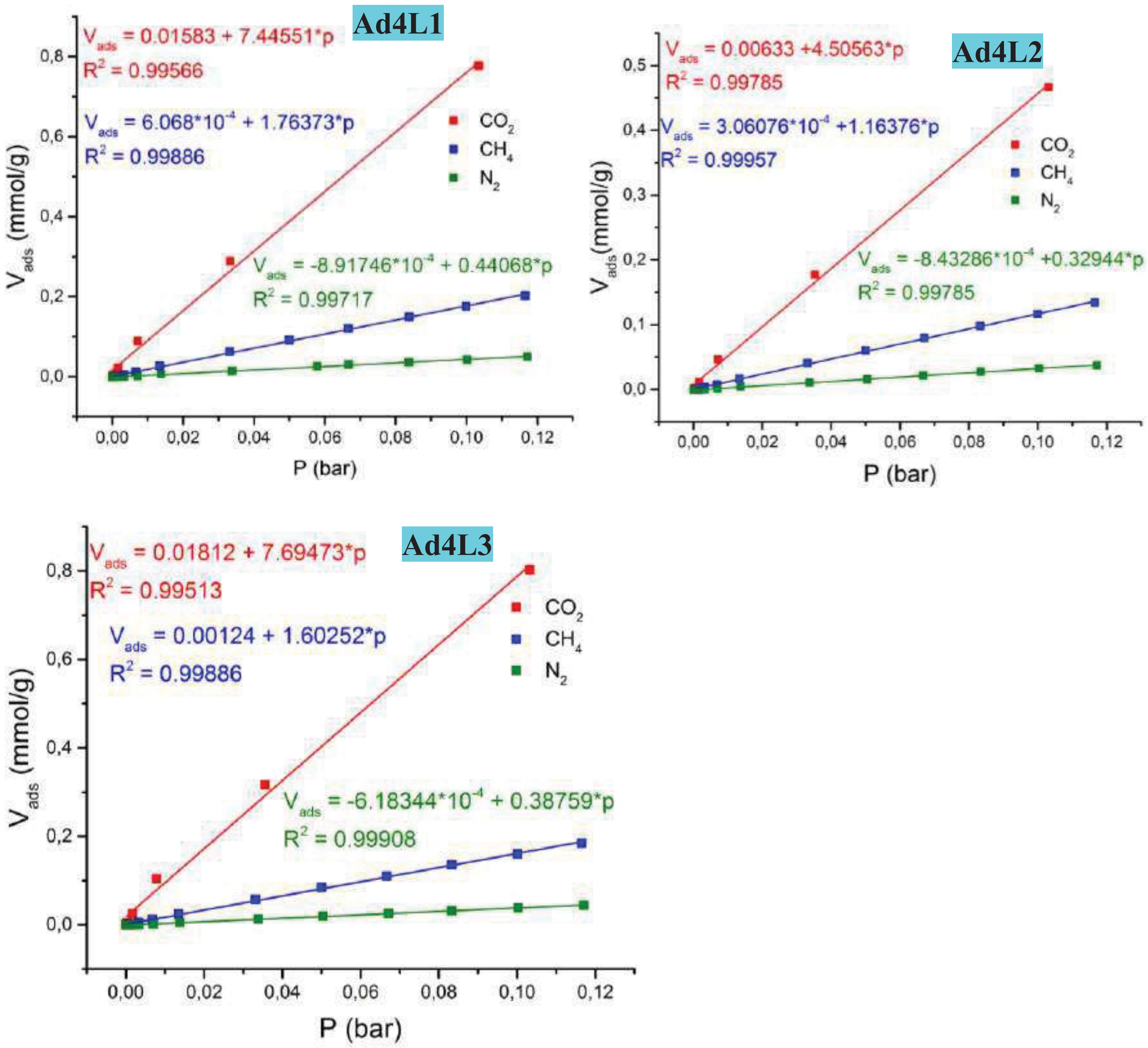

Fig. S8. Initial slopes in the Henry region of the adsorption isotherms for **Ad2L1** to **Ad4L3** at 273 K.

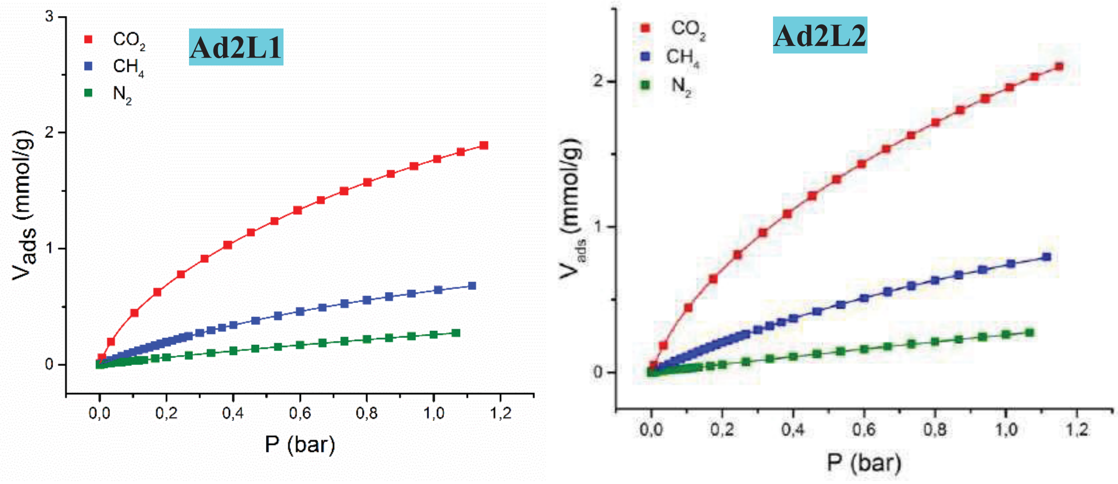

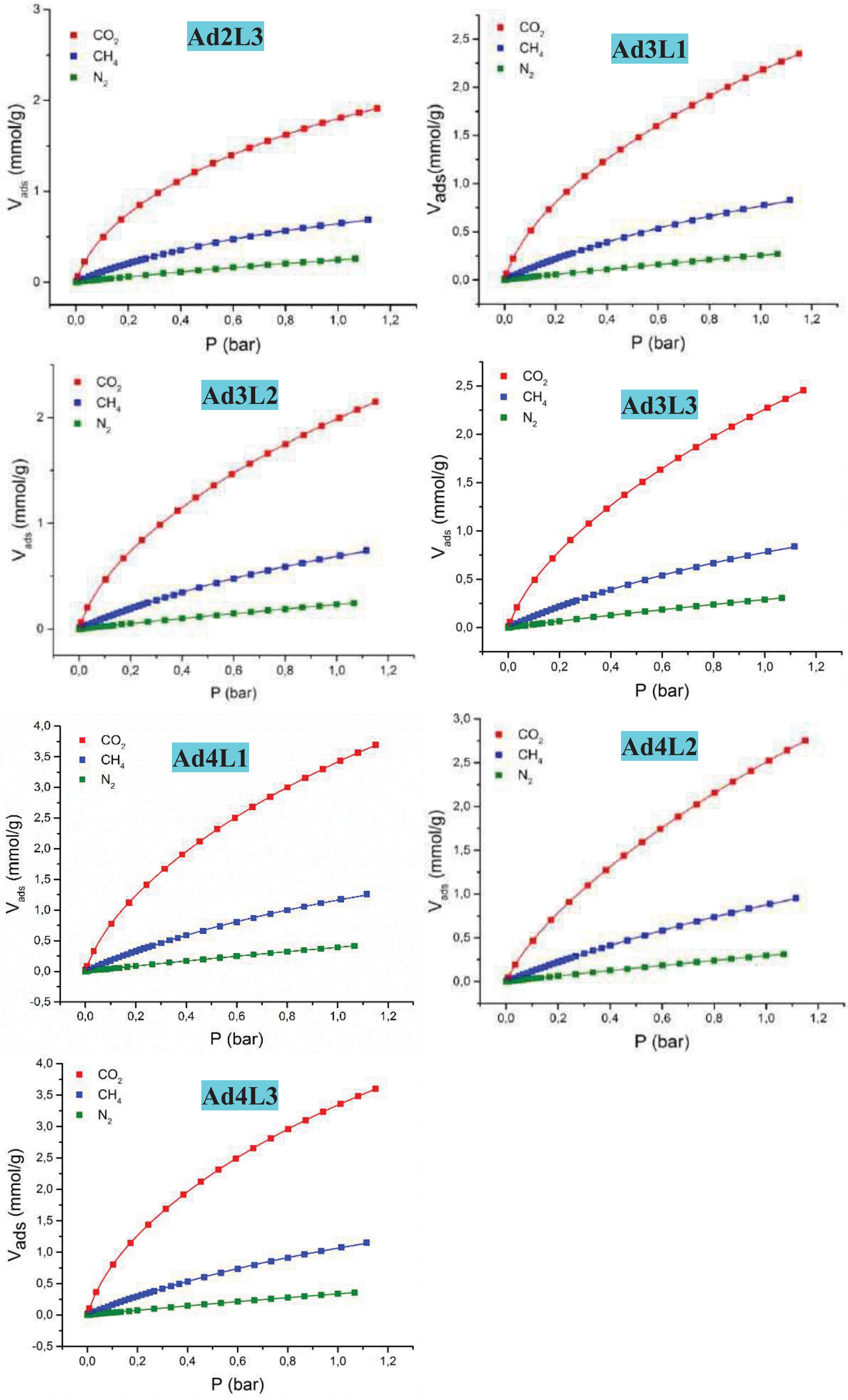

Fig. S9. DSL fitting for CO_2 adsorption and SSL fittings for CH_4 and N_2 adsorption at 273 K for **Ad2L1** to **Ad4L3**.

Table S5. Langmuir fitting parameters of CO_2, CH_4, and N_2 adsorption isotherms of **Ad2L1-Ad4L3** at 273 K and 1 bar.

Ad2L1@273K	$q_{sat,A}$ (mmol/g)	b_A (bar^{-1})	$q_{sat,B}$ (mmol/g)	b_B (bar^{-1})	Adj. R^2
CO_2	3,61969	0.6443	0.37091	13.77752	0.99999
CH_4	1.52345	0.71919			0.99991
N_2	1.27108	0.25577			0.99991

Ad2L2@273K	$q_{sat,A}$ (mmol/g)	b_A (bar^{-1})	$q_{sat,B}$ (mmol/g)	b_B (bar^{-1})	Adj. R^2
CO_2	4.6645	0.50586	0.41892	9.96057	1
CH_4	2.14348	0.52453			0.99991
N_2	3.33536	0.0843			0.99989

Ad2L3@273K	$q_{sat,A}$ (mmol/g)	b_A (bar^{-1})	$q_{sat,B}$ (mmol/g)	b_B (bar^{-1})	Adj. R^2
CO_2	3.15836	0.79083	0.4339	14.08976	1
CH_4	1.39929	0.84922			0.99979
N_2	1.13038	0.27639			0.99992

Ad3L1@273K	$q_{sat,A}$ (mmol/g)	b_A (bar^{-1})	$q_{sat,B}$ (mmol/g)	b_B (bar^{-1})	Adj. R^2
CO_2	0.52072	11.02831	5.60392	0.43289	0.99999
CH_4	2.11868	0.56685			0.99972
N_2	2.24545	0.12787			0.99998

Ad3L2@273K	$q_{sat,A}$ (mmol/g)	b_A (bar^{-1})	$q_{sat,B}$ (mmol/g)	b_B (bar^{-1})	Adj. R^2
CO_2	0.4767	10.80765	5.0526	0.44293	0.9999
CH_4	1.97254	0.5338			0.99983
N_2	1.96588	0.13336			0.99998

Ad3L3@273K	$q_{sat,A}$ (mmol/g)	b_A (bar^{-1})	$q_{sat,B}$ (mmol/g)	b_B (bar^{-1})	Adj. R^2
CO_2	6.40505	0.39929	0.47576	10.00655	0.99999
CH_4	2.25239	0.52751			0.99988
N_2	1.96618	0.17275			0.99988

Ad4L1@273K	$q_{sat,A}$ (mmol/g)	b_A (bar^{-1})	$q_{sat,B}$ (mmol/g)	b_B (bar^{-1})	Adj. R^2
CO_2	8.5502	0.47309	0.73123	10.74697	0.99999
CH_4	3.32195	0.53804			0.99982
N_2	3.2748	0.13588			0.99994

Ad4L2@273K	$q_{sat,A}$ (mmol/g)	b_A (bar^{-1})	$q_{sat,B}$ (mmol/g)	b_B (bar^{-1})	Adj. R^2
CO_2	0.44443	7.73927	9.52662	0.28504	1
CH_4	3.47249	0.33701			0.99992
N_2	3.17044	0.10247			0.99997

Ad4L3@273K	$q_{sat,A}$ (mmol/g)	b_A (bar^{-1})	$q_{sat,B}$ (mmol/g)	b_B (bar^{-1})	Adj. R^2
CO_2	0.78405	11.064	7.60802	0.52579	0.99999
CH_4	3.1143	0.51902			0.99981
N_2	2.66244	0.14519			0.99997

8. Scanning electron micrographs of Ad2L1-Ad4L3

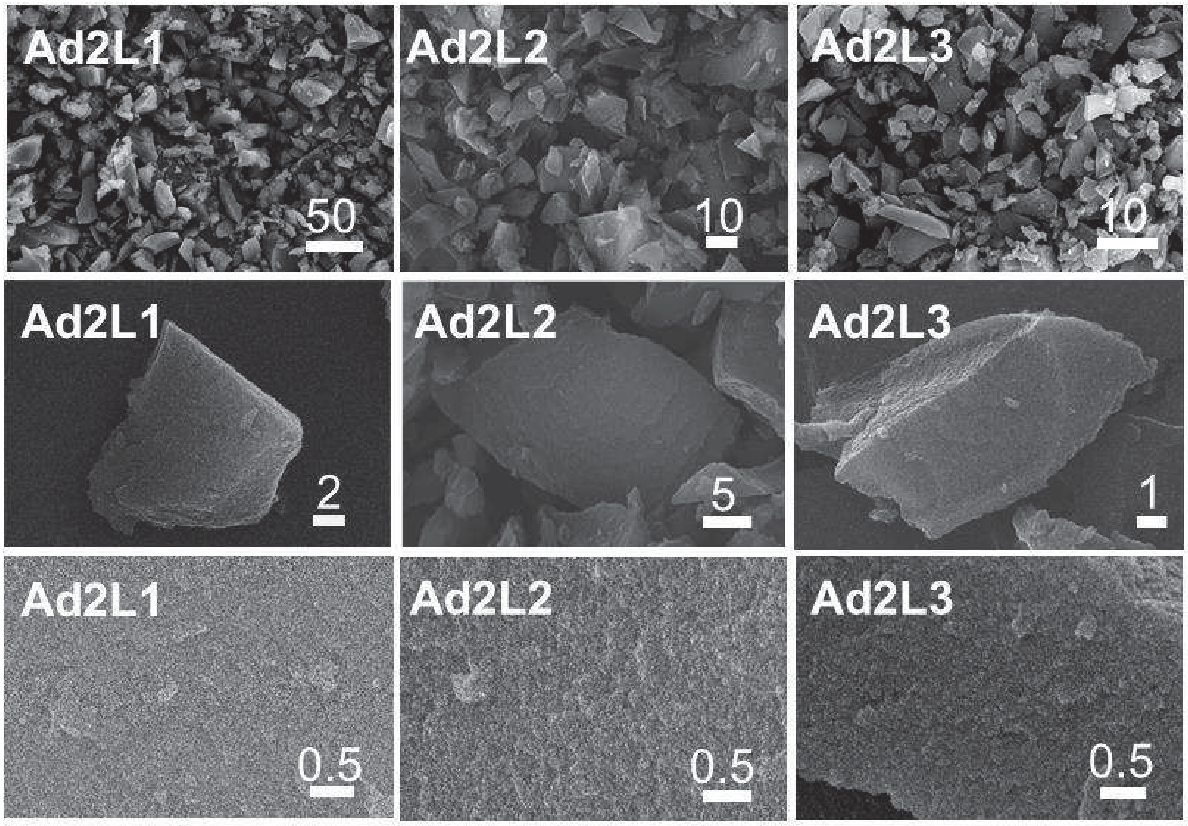

Fig. S10. Scanning electron micrographs of **Ad2L1-Ad2L3** (numbers above the scale bar are in μm). Enlarged version of Fig. 1a (right) in paper.

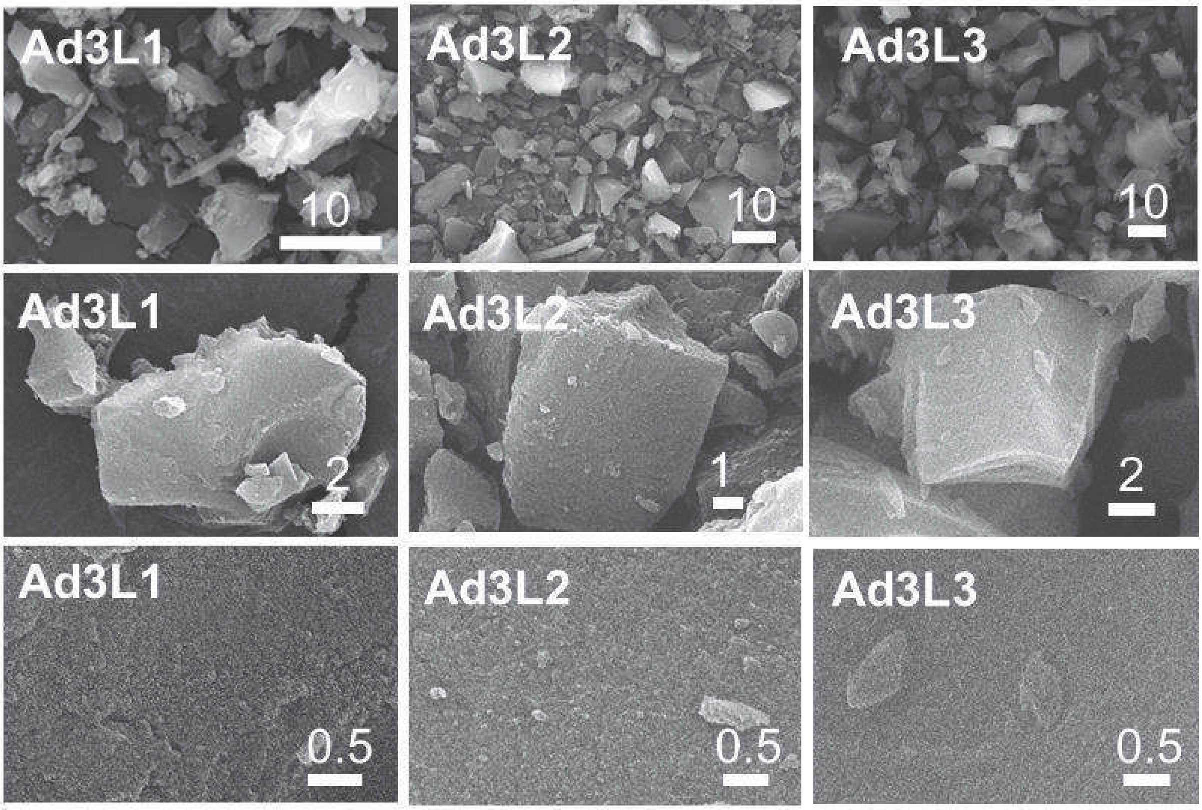

Fig. S11. Scanning electron micrographs of **Ad3L1-Ad3L3** (numbers above the scale bar are in μm). Enlarged version of Fig. 1b (right) in paper.

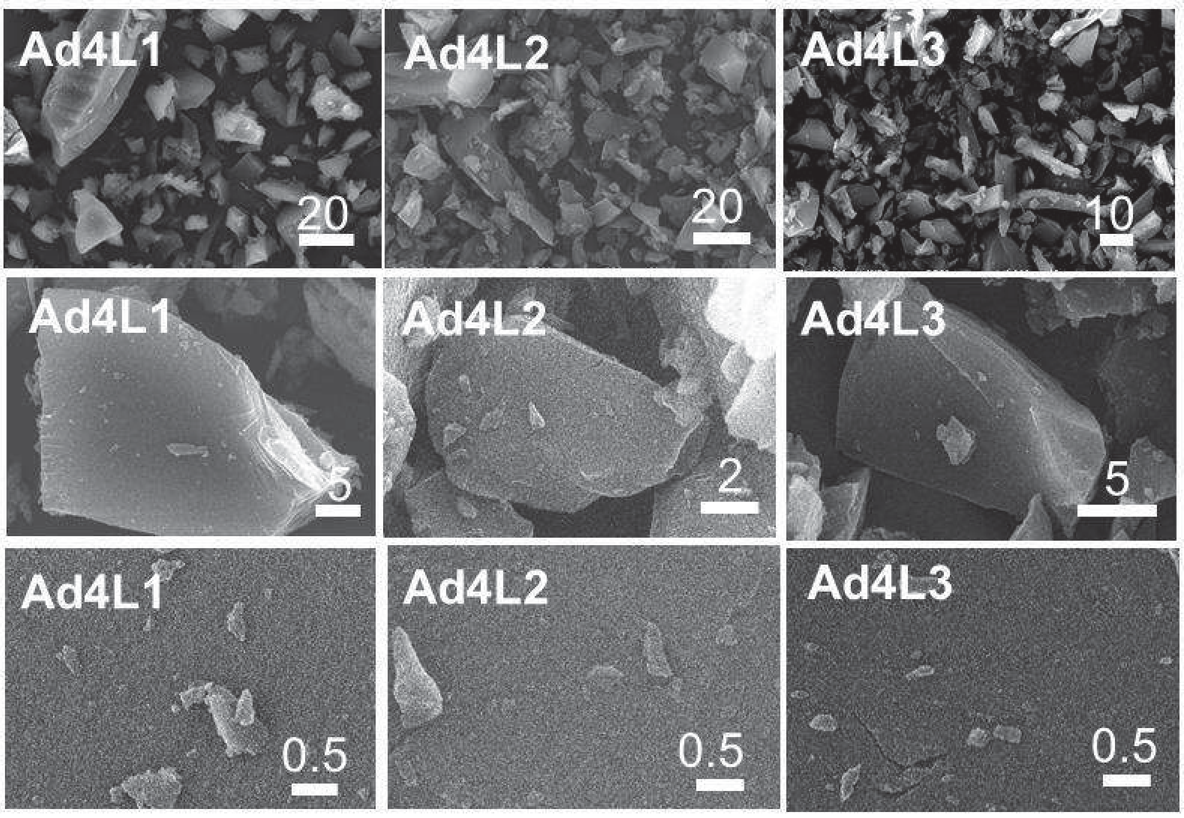

Fig. S12. Scanning electron micrographs of **Ad4L1-Ad4L3** (numbers above the scale bar are in μm). Enlarged version of Fig. 1c (right) in paper.

9. N_2 uptake:

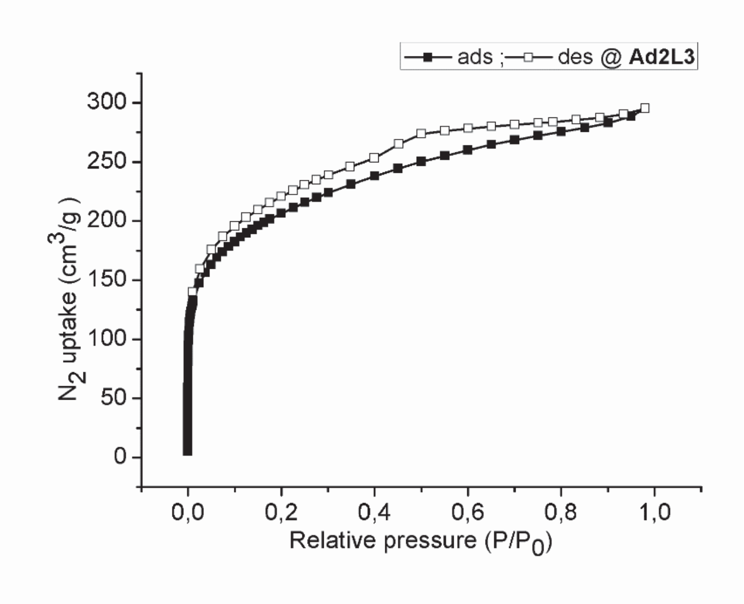

Fig. S13. N2 adsorption isotherm at 77 K for **Ad2L3**. A representation enlarged along y-axis compared to **Fig. 2** in the paper is given here.

10. Comparison to other CTFs

Table S6: Surface area, CO_2 adsorption properties and selectivity of triazine-based polymers.

Compound	BET (m^2/g)	CO_2 uptake (mmol/g) at 1 bar		Q_{st}	CO_2/N_2 selectivity [b]		Ref.
		273 K	298 K or 293 K		Henry	IAST	
CTF-0	2011	4.22					2
CTF-1	746	2.47	1.41	27.5		20	3
CTF-1-600	1533	3.82	2.25	30.0		13	3
FCTF-1	662	4.67	3.21	35.0		31	3
FCTF-1-600	1535	5.53	3.41	32		19	3
CTF-P2	776	1.84				20.3	4
CTF-P3	571	2.22				22.5	4
CTF-P4	867	3.05				16.6	4
CTF-P5	960	2.94				24.1	4
CTF-P6	1152	3.32				16.1	4
CTF-P1M	4	0.92				31.2	4
CTF-P2M	464	1.87				21.0	4

CTF-P3M	523	2.21				15.8	4
CTF-P4M	542	1.83				22.4	4
CTF-P5M	542	2.03				20.1	5
CTF-P6M	947	4.12				14.2	4
MCTP-1	1452	4.61	2.65				5
MCTP-2	859	3.65	2.42				5
Polymer 2	--	--	1.56				6
Polymer 3	646	--	1.68				6
Polymer 4	1266	--	2.09				6
Polymer 2C	427	--	2.99				6
Polymer 3C	1173	--	3.08				6
Polymer 4C	1316	--	3.61				6
NOP-1	978	1.83	1.06	32.8			7
NOP-2	1055	2.37	1.40	34.1			7
NOP-3	1198	2.51	1.39	33.8	27.1	25.6	7
NOP-4	635	1.71	0.83	31.9			7
NOP-5	913	1.45	0.72	30.5			7
NOP-6	1130	1.31	0.49	29.2	33.7	38.7	7
MCTF-300	640	2.25	1.39	24.6			7
MCTF-400	1060	2.36	1.55	25.4			8
MCTF-500	1510	3.16	2.22	26.3			8
fl-CTF300	15	1.27	0.71	43.1	35	37	8
fl-CTF350	1235	4.28	2.29	32.7	27	23	9
fl-CTF400	2862	4.13	1.97	30.7	15	16	9
fl-CTF500	2322	3.26	1.65	31.7	13	12	9
fl-CTF600	2113	3.48	1.80	32.4	14	12	9
COP-1	168	--	1.33				9
COP-2	158		0.91				9
PCTF-1	2235	3.21	1.84	30	13	17 [b]	10
PCTF-2	784	1.83	0.992	26	9	13 [b]	10
PCTF-3	641	2.14	1.32	27	16	34 [b]	11
PCTF-4	1090	2.27	1.49	28	17	35 [b]	11

PCTF-5	1183	2.55	1.48	27	17	39 [b]	11
PCTF-6	79	--	--		--	--	11
PCTF-7	613	2.15	1.32	25	22	--	11
HPF-1	576	--	2.8	43		120	11
CTF-TPC	1668	4.19	2.47	32			12
CTF-FL	773	3.22	2.00	35			13
CTF-FUM-350	230	3.44	2.31		102.4		13
CTF-DCN-500	735	2.66	1.55		37		14
pym-CTF500	208	2.75	1.77	40.5	189	502	14
pym-CTF600	689	3.34	2.15	37.4	126	124	15
bipy-CTF300-600	360-2479	1.87-5.58	0.98-2.95 [a]	33.3-35.2	37-61	24-42	15
lut-CTF300-600	486-2815	3.63-4.99	2.14-2.52 [a]	33.3-38.2	26-76	33-66	15

[a] Transformation into cm^3/g can be done by the given value in mmol/g with the molar gas volume at 1 bar of 22.711 L/mol (or mL/mmol = cm^3/mmol) (at 273 K), 24.375 L (at 293 K) and 24.791 L (at 298 K).

Alternatively, transformation from given cm^3/g into mmol/g:

at 273 K: value in (cm^3/g) : (22.711 cm^3/mmol) = value in (mmol/g)
(22.711 L is the molar volume at 1 bar and 273 K for an ideal gas).

at 293 K: value in (cm^3/g) : (24.375 cm^3/mmol) = value in (mmol/g)
(24.375 L is the molar volume at 1 bar and 293 K for an ideal gas).

Conversion to value in g/g = value in (mmol/g) x (0.044 g/mmol) from which the value wt% is obtained as g(CO_2)/g(CO_2+adsorbent) x 100%.

[b] at 1 bar for an equimolar gas mixture.

11. Correlation of CO_2 uptake with porosity parameters

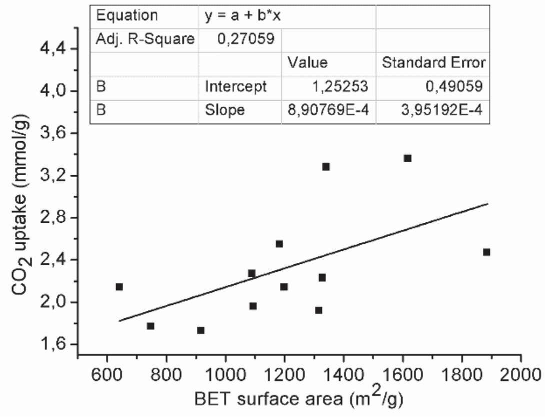

Equation	y = a + b*x		
Adj. R-Square	0,27059		
		Value	Standard Error
B	Intercept	1,25253	0,49059
B	Slope	8,90769E-4	3,95192E-4

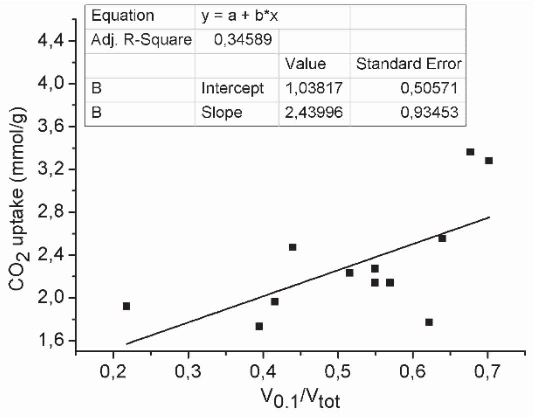

Equation	y = a + b*x		
Adj. R-Square	0,34589		
		Value	Standard Error
B	Intercept	1,03817	0,50571
B	Slope	2,43996	0,93453

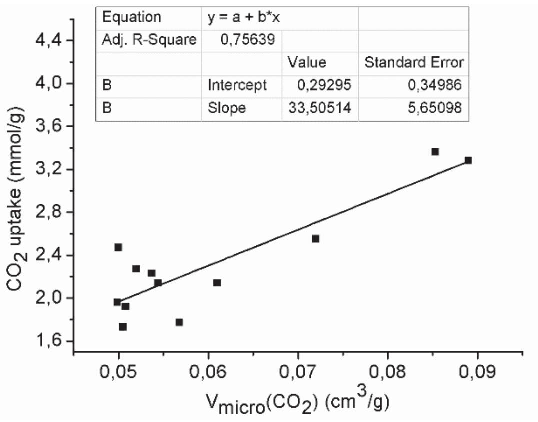

Equation	y = a + b*x		
Adj. R-Square	0,75639		
		Value	Standard Error
B	Intercept	0,29295	0,34986
B	Slope	33,50514	5,65098

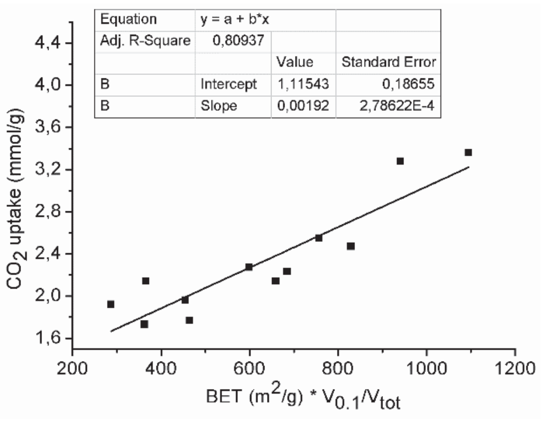

Equation	y = a + b*x		
Adj. R-Square	0,80937		
		Value	Standard Error
B	Intercept	1,11543	0,18655
B	Slope	0,00192	2,78622E-4

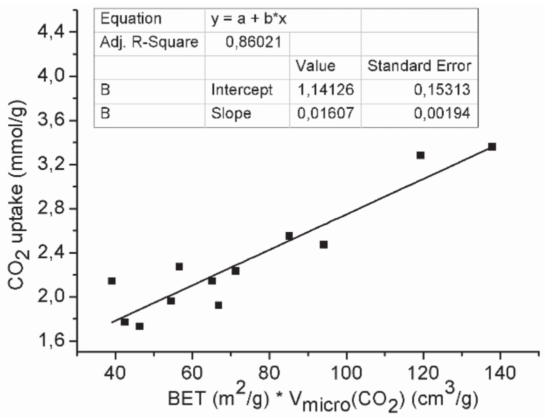

Equation	y = a + b*x		
Adj. R-Square	0,86021		
		Value	Standard Error
B	Intercept	1,14126	0,15313
B	Slope	0,01607	0,00194

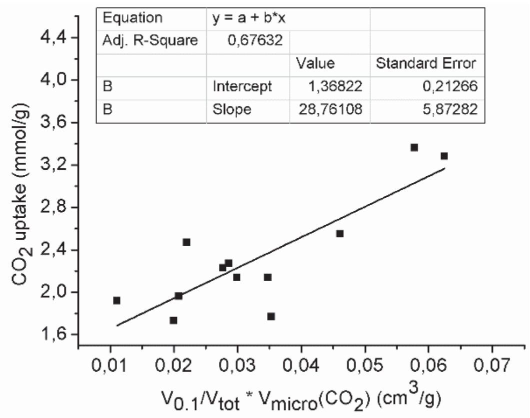

Equation	y = a + b*x		
Adj. R-Square	0,67632		
		Value	Standard Error
B	Intercept	1,36822	0,21266
B	Slope	28,76108	5,87282

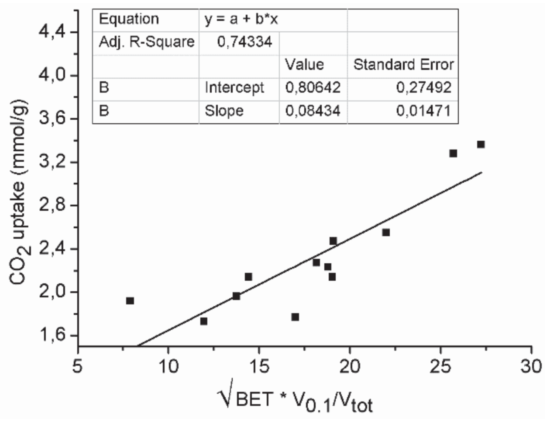

Equation	y = a + b*x		
Adj. R-Square	0,74334		
		Value	Standard Error
B	Intercept	0,80642	0,27492
B	Slope	0,08434	0,01471

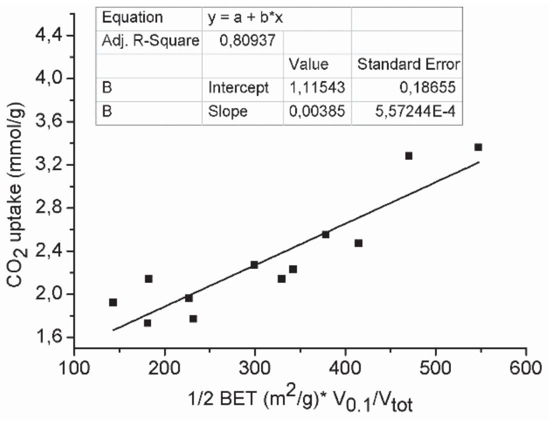

Equation	y = a + b*x		
Adj. R-Square	0,80937		
		Value	Standard Error
B	Intercept	1,11543	0,18655
B	Slope	0,00385	5,57244E-4

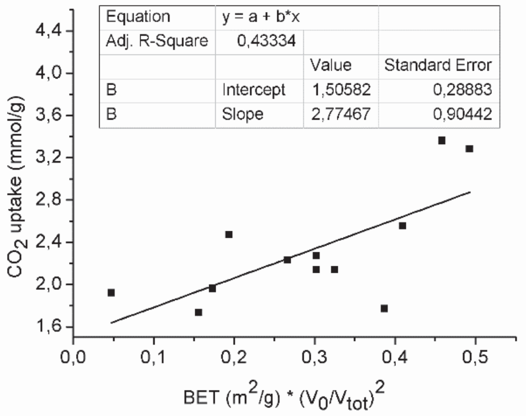

Figure S14. Correlation of CO_2 uptake with the different mathematical combinations (see x-axis title) of the porosity parameters BET surface area, micropore volume fraction ($V_{0.1}/V_{tot}$) and CO_2-accessible micropore volume ($V_{micro}(CO_2)$). The 12 data points include the nine values for **Ad*m*L*n*** and PCTF-3 to -5. The quality of the linear fit is given by the root mean-square deviation, RMSD (Adj. R-square).

12. References

---

[1] V. R. Reichert, L. J. Mathias, Macromolecules 27 (1994) 7015-7023; H. Newman, Synthesis (1972) 692-693.

[2] P. Katekomol, J. Roeser, M. Bojdys, J. Weber, A. Thomas, Chem. Mater. 25 (2013) 542–1548.

[3] Y. Zhao, K. X. Yao, B. Teng, T. Zhang, Y. Han, Energy Environ. Sci. 6 (2013) 3684- 3692.

[4] S. Ren, M. J. Bojdys, R. Dawson, A. Laybourn, Y. Z. Khimyak, D. J. Adams, A. I. Cooper, Adv. Mater. 24 (2012) 2357–2361.

[5] P. Puthiaraj, S.-M. Cho, Y.-R. Lee, W.-S. Ahn, J. Mater. Chem. A 3 (2015) 6792-6797.

[6] H. Lim, M. C. Cha, J. Y. Chang, Macromol. Chem. Phys. 13 (2012) 1385–1390.

[7] X. Liu, H. Li, Y. Zhang, B. Xu, S. A, H. Xia, Y. Mu, Polym. Chem. 4 (2013) 2445-2448.

[8] S. Hug, M. B. Mesch, H. Oh, N. Popp, M. Hirscher, J. Senkerd, B. V. Lotsch, J. Mater. Chem. A 2 (2014) 5928-5936.

[9] H. A. Patel, F. Karadas,b A. Canlier, J. Park, E. Deniz, Y. Jung, M. Atilhan, C. T. Yavuz, J. Mater. Chem. 2 (2012) 8431-8437.

[10] A. Bhunia, V. Vasylyeva and C. Janiak, Chem. Commun. 49 (2013) 3961–3963; A. Bhunia, I. Boldog, A. Möller, C. Janiak, J. Mater. Chem. A 1 (2013) 14990–14999.

[11] S. Nandi, U. Werner-Zwanziger, R. Vaidhyanathan, J. Mater. Chem. A 3 (2015) 21116–21122.

[12] S. Dey, A. Bhunia, D. Esquivel, C. Janiak, J. Mater. Chem. A 4 (2016) 6259-6263.

[13] K. Wang, H. Huang, D. Liu, C. Wang, J. Li, C. Zhong, Environ. Sci. Technol. 50 (2016) 4869–4876.

[14] S. Hug, L. Stegbauer, H. Oh, M. Hirscher, B. V. Lotsch, Chem. Mater. 27 (2015) 8001−8010.

3.4 High adsorptive properties of covalent triazine-based frameworks (CTFs) for surfactants from aqueous solution

Asamanjoy Bhunia, Subarna Dey, Maria Bous, Chenyang Zhang, Wolfgang von Rybinski and Christoph Janiak

Chem. Commun., 2015, **51**, 484-486
DOI: 10.1039/c4cc06393g, (reference 88)
Impact factor 2015: 6.834

Covalent triazine-based frameworks (CTFs) are a subclass of POPs that possess high chemical and thermal stability, thus interesting for variety of applications. In this work we demonstrated high adsorptive properties of CTFs for surfactants. We investigated for the first time these adsorptive properties of a CTF member (CTF-1 synthesized from 1,4-dicyanobenzene by ionothermal reaction condition using $ZnCl_2$) towards a non-ionic and an anionic surfactant (alkyl polyglycolether, $C_{12}EO_7$ and sodium dodecylsulfate, SDS, respectively) from aqueous solution and compare it with a typical carbon black with a specific surface area of 150 m^2/g. Interestingly, CTF-1(600) adsorbed 1.9 g/g and 4.9 g/g SDS and $C_{12}EO_7$, respectively which is much higher than carbon black (0.1 g/g and 0.2 g/g SDS and $C_{12}EO_7$, respectively) and it is due to CTF sheet exfoliation.

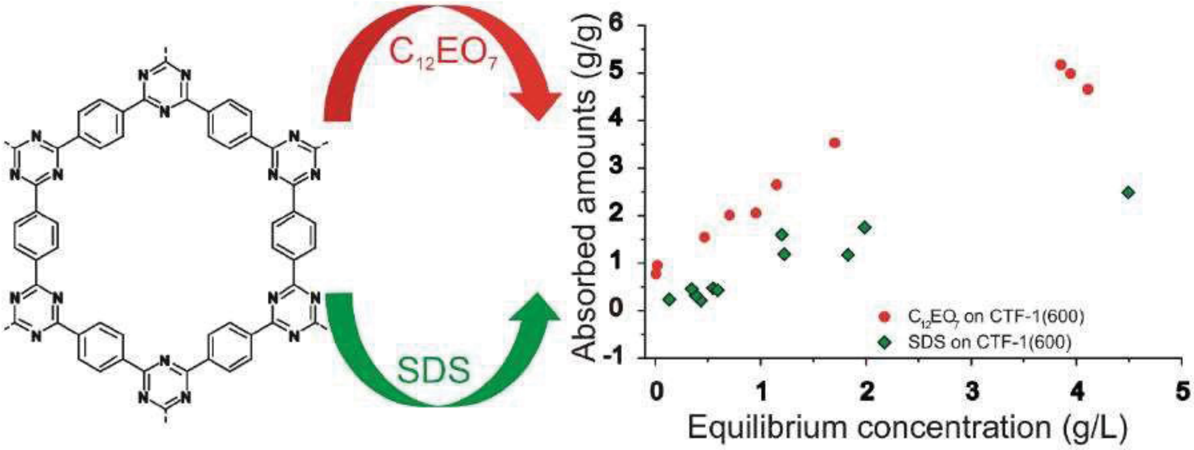

Author's contribution to the work:

- Checking the reproducibility of the CTF materials (CTF-1(400), CTF-1(600)) as well as surfactant adsorption (partly).
- Characterization and gas adsorption studies (partly).
- Writing the manuscript except the introduction and surfactant adsorption studies.

ChemComm

COMMUNICATION

View Article Online
View Journal | View Issue

Cite this: *Chem. Commun.*, 2015, **51**, 484

Received 14th August 2014,
Accepted 6th November 2014

DOI: 10.1039/c4cc06393g

www.rsc.org/chemcomm

High adsorptive properties of covalent triazine-based frameworks (CTFs) for surfactants from aqueous solution†

Asamanjoy Bhunia,[a] Subarna Dey,[a] Maria Bous,[b] Chenyang Zhang,[b] Wolfgang von Rybinski*[b] and Christoph Janiak*[a]

Carbonaceous covalent triazine-based frameworks from 1,4-dicyanobenzene (CTF-1) can adsorb up to about 4 g g^{-1} of the surfactants alkyl polyglycolether, $C_{12}EO_7$ and sodium dodecylsulfate, SDS from aqueous solution (c = 8.0 mmol L^{-1}) which is more than 20-times the gravimetric uptake capacity of a carbon black (Printex L from Evonik). This high uptake is due to CTF sheet exfoliation. Taking into account the thermal and chemical stability of CTFs this first surfactant adsorption study with CTFs shows that CTFs are especially interesting for the uptake of substances from solution.

The adsorptive properties of porous solid substances are of great importance for many applications.[1] Solids based on carbon black structures and graphitic carbons which have a surface area between 100 and 500 m^2 g^{-1} are especially interesting as key sorbents,[2] *inter alia* for separation processes and gas storage.[3,4]

Covalent triazine-based frameworks (CTFs) were developed by Kuhn, Antonietti and Thomas *et al.* as permanently porous substances.[5] They constitute a subclass of POMs (Porous Organic Materials) and possess high chemical and thermal stability. Classes of POMs are often differentiated according to their building units such as benzimidazole-linked polymers (BILPs),[6] hyper-crosslinked polymers (HCPs),[7] polymers of intrinsic microporosity (PIMs),[8] porous aromatic frameworks (PAFs),[9] conjugated microporous polymers (CMPs)[10] and covalent organic frameworks (COFs).[11]

CTFs are made by the idealized trimerization reaction of carbonitriles to triazine rings (Scheme 1). The resulting sheets of CTF-1 can form a hexagonal lattice with an eclipsed AAA structure and tubular channels of 1.2 nm diameter.[5] CTFs are interesting because of cheap and readily available starting materials, facile synthesis and certain hydrophilicity. From their elemental composition, we view CTFs from ionothermal reaction with $ZnCl_2$ as in-between well-defined COFs and porous carbon materials. So far, CTFs have been used in heterogeneous catalysis,[12] as catalytic support in liquid phase reactions,[13] for gas storage and for separation.[14]

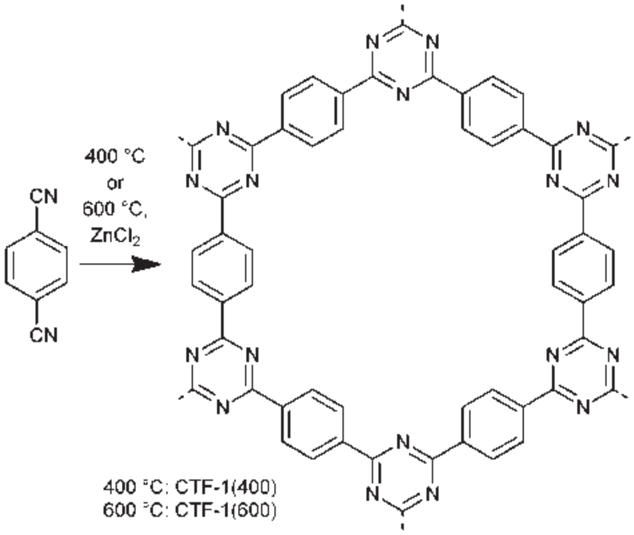

Scheme 1 Idealized synthesis of CTF-1.

For applications of CTFs as adsorbents in liquids,[15] the interaction with substances from solution is decisive.[16] Important substances from solution which strongly interact with surfaces are surfactants. Surfactant adsorption at solid–liquid or liquid–liquid interfaces is crucial in industrial processes such as corrosion inhibition, dispersion stabilization, detergency, crude oil refining, purification and lubrication.[17] Adsorption studies from solution for many types of surfactants and numerous surfaces[18] showed that the adsorbed amounts and the structure within the adsorbed layer depend on the properties of the surfaces, the type of the surfactants and parameters like temperature and pH. Typical gravimetric surfactant uptake capacities for porous graphitized carbon black with a specific surface area of about 100 m^2 g^{-1} were in the range of 0.1 to 0.2 g g^{-1}.[19]

---

[a] *Institute for Inorganic and Structural Chemistry, University Düsseldorf, D-40204 Düsseldorf, Germany. E-mail: janiak@uni-duesseldorf.de*

[b] *Institute for Physical Chemistry, University Düsseldorf, D-40204 Düsseldorf, Germany. E-mail: vonRybinski@uni-duesseldorf.de*

† Electronic supplementary information (ESI) available: Synthesis, IR, powder XRD, elemental analysis, TG analysis, SEM images, N_2 and CO_2 sorption and pore size distribution, adsorption of surfactants. See DOI: 10.1039/c4cc06393g

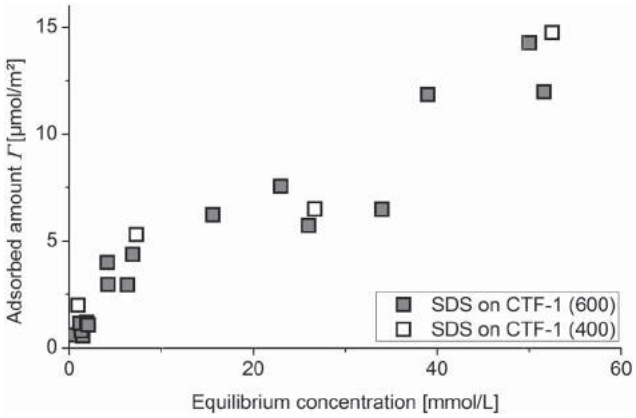

Fig. 1 SDS adsorption isotherms on CTF materials.

Here we investigate for the first time the adsorptive properties of a CTF member (CTF-1 synthesized from 1,4-dicyanobenzene, Scheme 1; see ESI† for further details) towards a non-ionic and an anionic surfactant (alkyl polyglycolether, $C_{12}EO_7$ and sodium dodecylsulfate, SDS, respectively) from aqueous solution and compare it with a typical carbon black with a specific surface area of 150 m^2 g^{-1}.

The amount of surfactant adsorbed on CTFs was determined from the surface tension of the solutions which correlates to the surfactant equilibrium concentration from a calibration curve (see Fig. S8 and details in ESI†). The CTF alone did not influence the surface tension of the aqueous solution.

The adsorption isotherms for SDS onto CTFs (Fig. 1) show two regions. At low SDS concentrations, the adsorbed amount of SDS increases gradually and then the isotherm reaches a plateau and is nearly constant up to an SDS equilibrium concentration of 30 mmol L^{-1}. At higher surfactant content, adsorption again increases nearly linearly up to high equilibrium concentrations. The course of the adsorbed amounts in dependence on SDS equilibrium concentration in the low concentration region corresponds to the formation of a first adsorption layer of SDS on CTF. The almost linear increase of adsorbed SDS amounts at higher SDS concentrations in the second regime correlates with a second adsorption process on the first SDS layer. It is interesting to see that for both CTF-1 samples the adsorbed SDS amounts are the same. Therefore the surface characteristics should be similar despite the different surface area. In desorption experiments, we have seen almost no hysteresis, so that the adsorption process is reversible (data not shown). A more detailed insight into the adsorption mechanism is given by the section of the adsorption isotherm for low solution concentrations (Fig. 2). It shows more clearly the typical shape of an adsorption isotherm in the monolayer region during formation of a surfactant layer on a surface.[16] If compared to the SDS adsorption on a typical carbon black, one can conclude that the adsorption behaviour on CTF at low surfactant concentrations is similar to that of carbon black albeit with higher adsorbed amounts. Typical carbon black adsorbs about 2 µmol(SDS) m^{-2} in the plateau region (Fig. 2).

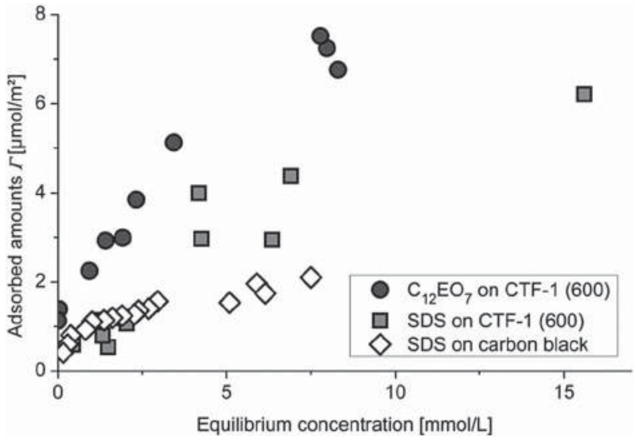

Fig. 2 Adsorption isotherms of SDS and $C_{12}EO_7$ on CTF-1(600) and SDS on carbon black in the low concentration range.

The adsorbed amounts Γ (in mol m^{-2}) represent the number of adsorbed molecules per area on a solid. In Table 1 the values for the area per adsorbed molecule calculated according to eqn (1) are given, assuming that the BET surface area of the CTFs is accessible for the surfactant molecules.

$$a_s = \frac{10^{18}}{N\Gamma} \qquad (1)$$

where, a_s = area per molecule (nm^2); N = Avogadro constant (6.023 × 10^{23} molecules per mol). These a_s data in Table 1 demonstrate that the adsorbed surfactant molecules form a monolayer if the values for the area per molecule are compared with data for the molecules from Langmuir film balance measurement.[20] The assumed arrangement of the molecules is anywhere between horizontal and vertical (see Fig. S9, ESI†).

Also the formation of hemimicelles on the surface can be possible which was shown by measurements with atomic force microscopy on graphite surfaces.[21] If one considers the cross section area of the surfactant with 0.2 nm^2 for the alkyl chain and about 0.5 nm^2 for the ethylenoxide chain,[22] both surfactants could be included into the channels of the solid (cross section area about 1.4 nm^2). On the other hand the fast and thorough desorption of the long chain surfactants suggest no or little adsorption in the channels. Instead of channel filling the layer structure of CTF-1 can lead to interlayer surfactant insertion (similar to graphite) as evidenced by a shift of the (001) peak from $2\theta \approx 25°$ (3.6 Å) to $2\theta \approx 20°$ (4.4 Å) in the powder X-ray pattern (Fig. S2, ESI†). Exfoliation can explain the strong increase of the adsorbed amounts at higher concentrations as multilayer formation or adsorption of micelles which has been claimed for other surfaces[23] becomes possible on the CTF sheet surfaces.

Fig. 2 shows the adsorption of the non-ionic surfactant $C_{12}EO_7$ on CTF-1(600) in comparison to anionic SDS. The adsorption of the non-ionic one is slightly higher than that of the anionic surfactant which could be also shown for the adsorption on carbon black. The reason for the lower adsorption of the anionic compared to the non-ionic surfactant is the electrostatic repulsion of the polar group of the anionic surfactant which leads to lower packing density of the surfactant molecules on the surface.

Table 1 Data for adsorbed surfactant molecules from their adsorption isotherms on CTFs

Surfactant[a]	Solid [S_{BET}/m^2 g^{-1}]	Adsorbed amount Γ^b (μmol m^{-2})	(mg m^{-2})	(g g^{-1})	Area per molecule, $a_s{}^c$ (nm^2)
SDS	CTF-1(600) [1390]	5.0	1.4	1.9	0.33
SDS	CTF-1(400) [970]	5.0	1.4	1.4	0.33
SDS	Carbon black[d] [150]	2.0	0.6	0.1	0.83
$C_{12}EO_7$	CTF-1(600) [1390]	7.0	3.5	4.9	0.24
$C_{12}EO_7$	Carbon black[d] [150]	2.5	1.3	0.2	0.66

[a] SDS = sodium dodecylsulfate; $C_{12}EO_7$ = alkyl polyglycolether. [b] Adsorbed amount Γ at c = 8.0 mmol L^{-1} from eqn (S1) (ESI). [c] From the adsorption isotherms, eqn (1). To be compared with a limiting area per molecule of 1.05 nm^2 in the horizontal orientation and 0.2 nm^2 in the vertical orientation from Langmuir film balance measurements.[20] [d] Printex L from Evonik.

From the gravimetric adsorption of the surfactants (Table 1) related to surface area and mass of the solid adsorbent it is evident that the gravimetric uptake capacity of CTFs is up to 20-times the amount of carbon black by weight (g g^{-1}) and about 2.5 times the amount by surface area (mg m^{-2}) for the ionic SDS surfactant. For the non-ionic $C_{12}EO_7$ surfactant the adsorbed amounts by weight (g g^{-1}) are even increased due to the higher molecular mass of the non-ionic surfactant compared to the anionic surfactant and the higher uptake of the non-ionic surfactant by surface area (mol m^{-2}).

In summary, this comparative study demonstrates the potential for unusually high adsorbed amounts of surfactants on CTF solids due to their high surface area. Hence, CTFs are not only interesting for gas adsorption but also show interesting properties for the application as adsorbents from solutions, taking into account their solvothermal chemical stability. SEM images of before and after SDS adsorption show no evident change in microscopic CTF morphology (Fig. S5, ESI†).

Notes and references

1 F. Rouquerol, J. Rouquerol and K. Sing, *Adsorption by Powders and Porous Solids Principles, Methodology and Applications*, Elsevier, 1999.
2 Introduction to themed issue on porous carbon materials: A.-H. Lu and S. Dai, *J. Mater. Chem. A*, 2013, **1**, 932.
3 J. R. Morris, C. I. Contescu, M. F. Chisholm, V. R. Cooper, J. Guo, L. He, Y. Ihm, E. Mamontov, Y. B. Melnichenko, R. J. Olsen, S. J. Pennycook, M. B. Stone, H. Zhang and N. C. Gallego, *J. Mater. Chem. A*, 2013, **1**, 9341–9350; Y. Xia, Z. Yang and Y. Zhu, *J. Mater. Chem. A*, 2013, **1**, 9365–9381; N. Fechler, S.-A. Wohlgemuth, P. Jäker and M. Antonietti, *J. Mater. Chem. A*, 2013, **1**, 9418–9421; S. J. Yang, J. H. Kang, H. Jung, T. Kim and C. R. Park, *J. Mater. Chem. A*, 2013, **1**, 9427–9432; L. Huang and D. Cao, *J. Mater. Chem. A*, 2013, **1**, 9433–9439.
4 A. G. Hsieh, C. Punckt, S. Korkut and I. A. Aksay, *J. Phys. Chem. B*, 2013, **117**, 7950–7958.
5 P. Kuhn, M. Antonietti and A. Thomas, *Angew. Chem., Int. Ed.*, 2008, **47**, 3450–3453; P. Kuhn, A. l. Forget, D. Su, A. Thomas and M. Antonietti, *J. Am. Chem. Soc.*, 2008, **130**, 13333–13337; M. J. Bojdys, J. Jeromenok, A. Thomas and M. Antonietti, *Adv. Mater.*, 2010, **22**, 2202–2205.
6 M. G. Rabbani and H. M. El-Kaderi, *Chem. Mater.*, 2012, **24**, 1511–1517.
7 J. Germain, J. Hradil, J. M. J. Fréchet and F. Svec, *Chem. Mater.*, 2006, **18**, 4430–4435.
8 B. S. Ghanem, K. J. Msayib, N. B. McKeown, K. D. M. Harris, Z. Pan, P. M. Budd, A. Butler, J. Selbie, D. Book and A. Walton, *Chem. Commun.*, 2007, 67–69.
9 H. Zhao, Z. Jin, H. Su, J. Zhang, X. Yao, H. Zhao and G. Zhu, *Chem. Commun.*, 2013, **49**, 2780–2782.
10 J.-X. Jiang, F. Su, A. Trewin, C. D. Wood, N. L. Campbell, H. Niu, C. Dickinson, A. Y. Ganin, M. J. Rosseinsky, Y. Z. Khimyak and A. I. Cooper, *Angew. Chem., Int. Ed.*, 2007, **46**, 8574–8578.
11 S.-Y. Ding and W. Wang, *Chem. Soc. Rev.*, 2013, **42**, 548–568; introduction to themed issue on COFs: A. I. Cooper, *CrystEngComm*, 2013, **15**, 1483; S. Kandambeth, A. Mallick, B. Lukose, M. V. Mane, T. Heine and R. Banerjee, *J. Am. Chem. Soc.*, 2012, **134**, 19524–19527.
12 P. Katekomol, J. Roeser, M. Bojdys, J. Weber and A. Thomas, *Chem. Mater.*, 2013, **25**, 1542–1548; J. Roeser, K. Kailasam and A. Thomas, *ChemSusChem*, 2012, **5**, 1793–1799.
13 S. Hug, M. E. Tauchert, S. Li, U. E. Pachmayr and B. V. Lotsch, *J. Mater. Chem.*, 2012, **22**, 13956–13964; C. E. Chan-Thaw, A. Villa, P. Katekomol, D. Su, A. Thomas and L. Prati, *Nano Lett.*, 2010, **10**, 537–541.
14 S. Hug, M. B. Mesch, H. Oh, N. Popp, M. Hirscher, J. Senker and B. V. Lotsch, *J. Mater. Chem. A*, 2014, **2**, 5928–5936; A. Bhunia, V. Vasylyeva and C. Janiak, *Chem. Commun.*, 2013, **49**, 3961–3963; A. Bhunia, I. Boldog, A. Möller and C. Janiak, *J. Mater. Chem. A*, 2013, **1**, 14990–14999.
15 T. Wang, K. Kailasam, P. Xiao, G. Chen, L. Chen, L. Wang, J. Li and J. Zhu, *Microporous Mesoporous Mater.*, 2014, **187**, 63–70; J. Liu, H. Chen, S. Zheng and Z. Xu, *J. Chem. Eng. Data*, 2013, **58**, 3557–3562; J. Liu, E. Zong, H. Fu, S. Zheng, Z. Xu and D. Zhu, *J. Colloid Interface Sci.*, 2012, **372**, 99–107; W. Zhang, F. Liang, C. Li, L.-G. Qiu, Y.-P. Yuan, F.-M. Peng, X. Jiang, A.-J. Xie, Y.-H. Shen and J.-F. Zhu, *J. Hazard. Mater.*, 2011, **186**, 984–990.
16 B. Dobias, X. Qiu and W. von Rybinski, *Solid-Liquid Dispersions*, Surfactant Science Series, Marcel Dekker, 1999.
17 M. J. Rosen and M. Dahanayake, *Industrial Utilization of Surfactants: Principles and Practice*, AOCS Press, Illinois, 2001.
18 W. von Rybinski and M. J. Schwuger, Adsorption and Wetting, *Nonionic Surfactants*, ed. M. J. Schick, Marcel Dekker, 1987, pp. 45–107.
19 J. M. Corkill, J. F. Goodman and J. R. Tate, *Trans. Faraday Soc.*, 1966, **62**, 979–986.
20 H. D. Dörfler, *Grenzflächen und kolloid-disperse Systeme*, Springer, Heidelberg, 2002, p. 143.
21 E. J. Wanless and W. A. Ducker, *Langmuir*, 1997, **13**, 1463–1474.
22 H. Lange and P. Jeschke, in *Nonionic Surfactants*, ed. M. Schick, Surfactant Science Series, Marcel Dekker, 1987, pp. 1–44.
23 X. Liu, D. Wu, S. Turgman-Cohen, J. Genzer, T. W. Theyson and O. J. Rojas, *Langmuir*, 2010, **26**, 9565–9574.

Electronic Supplementary Information (ESI)

High adsorptive properties of covalent triazine-based frameworks (CTFs) for surfactants from aqueous solution

Asamanjoy Bhunia[a], Subarna Dey[a], Maria Bous[b], Chenyang Zhang[b], Wolfgang von Rybinski[b]* and Christoph Janiak[a]*

[a] Institut für Anorganische Chemie und Strukturchemie, Heinrich-Heine-Universität Düsseldorf, 40204 Düsseldorf, Germany. Fax: + 49-211-81-12287; Tel: +49-211-81-12286.

[b] Institute for Physical Chemistry and Electrochemistry, Heinrich-Heine-Universität Düsseldorf, 40204 Düsseldorf, Germany. Fax: +49-211-81-12803; Tel: +49-211-81-14867.

* Corresponding author: E-mail: vonRybinski@uni-duesseldorf.de, janiak@uni-duesseldorf.de;

Other Emails:

asamanjoy.bhunia@gmail.com

subarna.dey@uni-duesseldorf.de

maria.bous@uni-duesseldorf.de

chenyang.zhang@uni-duesseldorf.de

1. Experimental Section

Materials and methods

All chemicals were purchased from commercial suppliers (Sigma-Aldrich, Acros Organics, and Alfa Aesar chemical company) and used without further purification, unless stated otherwise.

Infrared (IR) spectra were obtained on a Bruker FT-IR Tensor 37 Spectrometer in the 4000-550 cm^{-1} region with 2 cm^{-1} resolution as KBr disks. Elemental (CNH) analyses were carried out with a PerkinElmer 2400 series 2 elemental analyzer. Powder X-ray diffraction (PXRD) data was collected on a Bruker D2 Phaser diffractometer using a flat sample holder (also a flat silicon, low background sample holder) and Cu Kα_1/α_2 radiation with $\lambda = 1.5418$ Å at 30 kV covering 2theta angles 5-80° over a time of 2 h, that is. 0.01°/sec. Diffractograms were obtained on flat layer sample holders where at low angle the beam spot is strongly broadened so that only a fraction of the reflected radiation reaches the detector which leads to low relative intensities measured at 2θ< 7°. For hygroscopic or air-sensitive samples, the sample holder can be sealed with a dome. Scanning electron microscopy (SEM) images were obtained using an ESEM Quanta 400 FEG SEM equipped with a secondary electron detector. Scanning electron microscopy images of CTF-1 after SDS adsorption (Fig. S5b) were obtained using a Jeol JSM-6510LV analyzer with LaB_6 cathode. Thermogravimetric analyses (TGA) were carried out at a ramp rate of 5 °C/min in a N_2 flow with a Netzsch Thermo-Microbalance Apparatus TG 209 F3 Tarsus.

Sorption isotherms were measured using a Micromeritics ASAP 2020 automatic gas sorption analyzer equipped with oil-free vacuum pumps (ultimate vacuum $<10^{-8}$ mbar) and valves, which guaranteed contamination free measurements. The sample was connected to the preparation port of the sorption analyzer and degassed under vacuum until the outgassing rate, i.e., the rate of pressure rise in the temporarily closed manifold with the connected sample tube, was less than 2 µTorr/min at the specified temperature 200 °C. After weighing, the sample tube was then transferred to the analysis port of the sorption analyzer. All used gases (He, N_2, CO_2) were of ultra-high purity (UHP, grade 5.0, 99.999%) and the STP volumes are given according to the NIST standards (293.15 K, 101.325 kPa). Helium gas was used for the determination of the cold and warm free space of the sample tubes. N_2 sorption isotherms was measured at 77 K (liquid nitrogen bath), whereas CO_2 sorption isotherms was measured at 293±1 K (passive thermostating) and 273.15 K (ice/deionized water bath). The heat of adsorption values and the DFT pore size distributions ('N_2 DFT slit pore' model) were calculated out using the ASAP 2020 v3.05 software.

2. Synthesis

CTF-1(400) and CTF-1(600) were synthesized according to the literature procedure[1]:

A mixture of 1,4-dicyanobenzene (1.28 g, 10 mmol) and anhydrous $ZnCl_2$ (6.8 g, 50 mmol) were placed into a quartz ampoule under inert conditions. The ampoule was evacuated, sealed and heated to 400 or 600 °C for 48 h followed by cooling to room temperature. The black product was collected and stirred with water for 72 h. Then the product was isolated by filtration and again stirred with 200 mL of 2 mol/L HCl for 24 h. The resulting black powder was further washed with water (3 × 75 mL), THF (3 × 75 mL), acetone (3 × 75 mL) and dried in vacuum. Yield: 90 %.

For CTF-1(400): The monomer was heated at 400 °C.

For CTF-1(600): The monomer was heated at 600 °C.

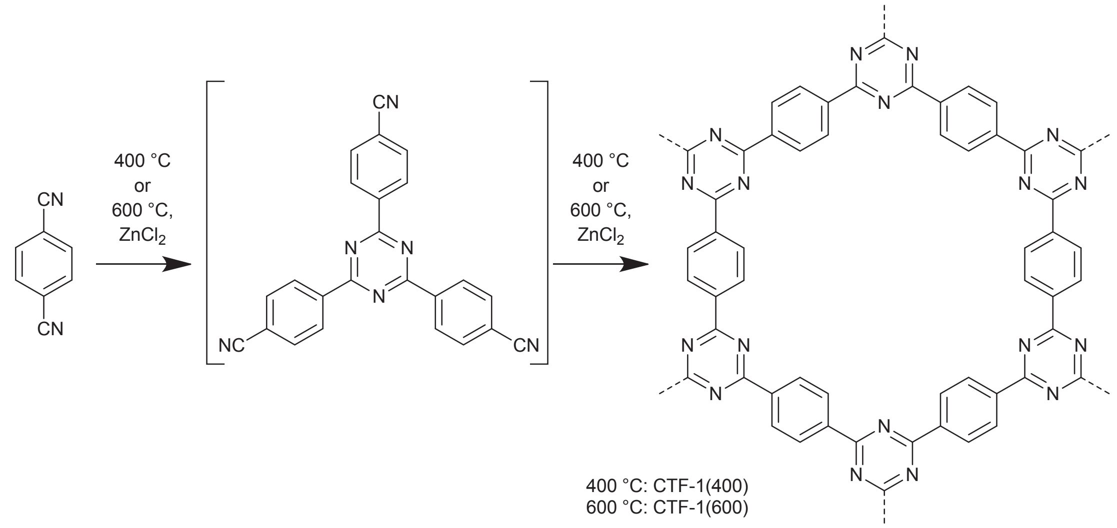

Scheme 1. Synthesis of CTF-1 from 1,4-dicyanobenzene by using the ionothermal reaction with $ZnCl_2$ as porogen and catalyst at two different temperatures.

3. FT-IR Spectrum

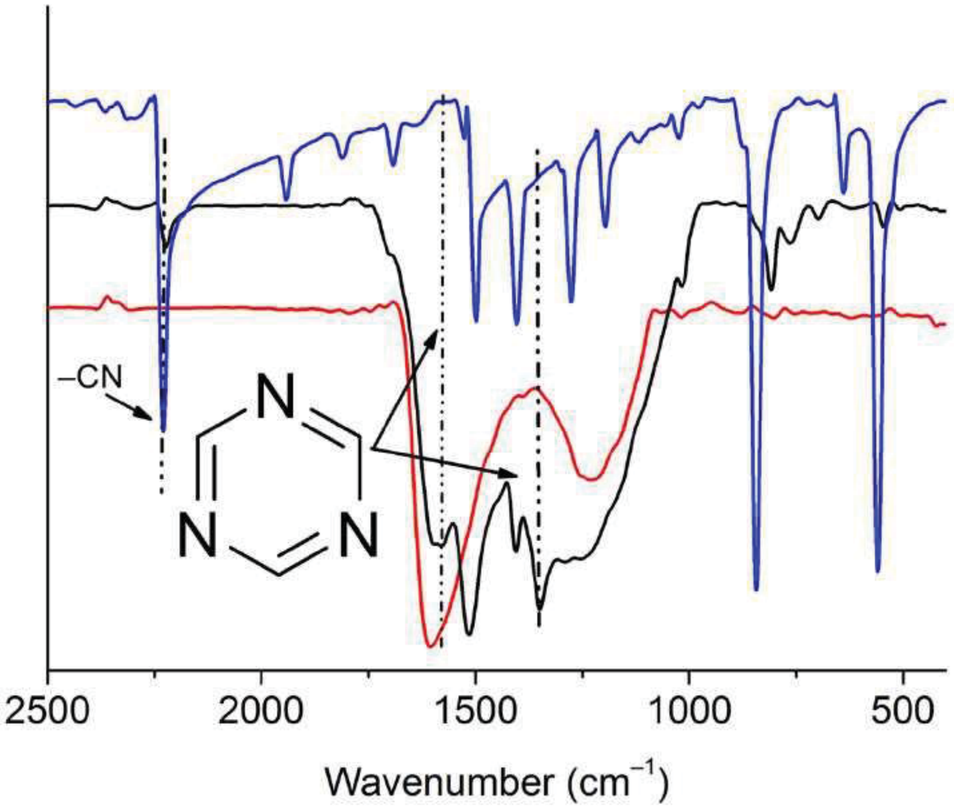

Fig. S1a: FT-IR spectrum of 1,4-dicyanobenzene (blue), CTF-1(400) (black) and CTF-1(600) (red) as synthesized before surfactant adsorption.

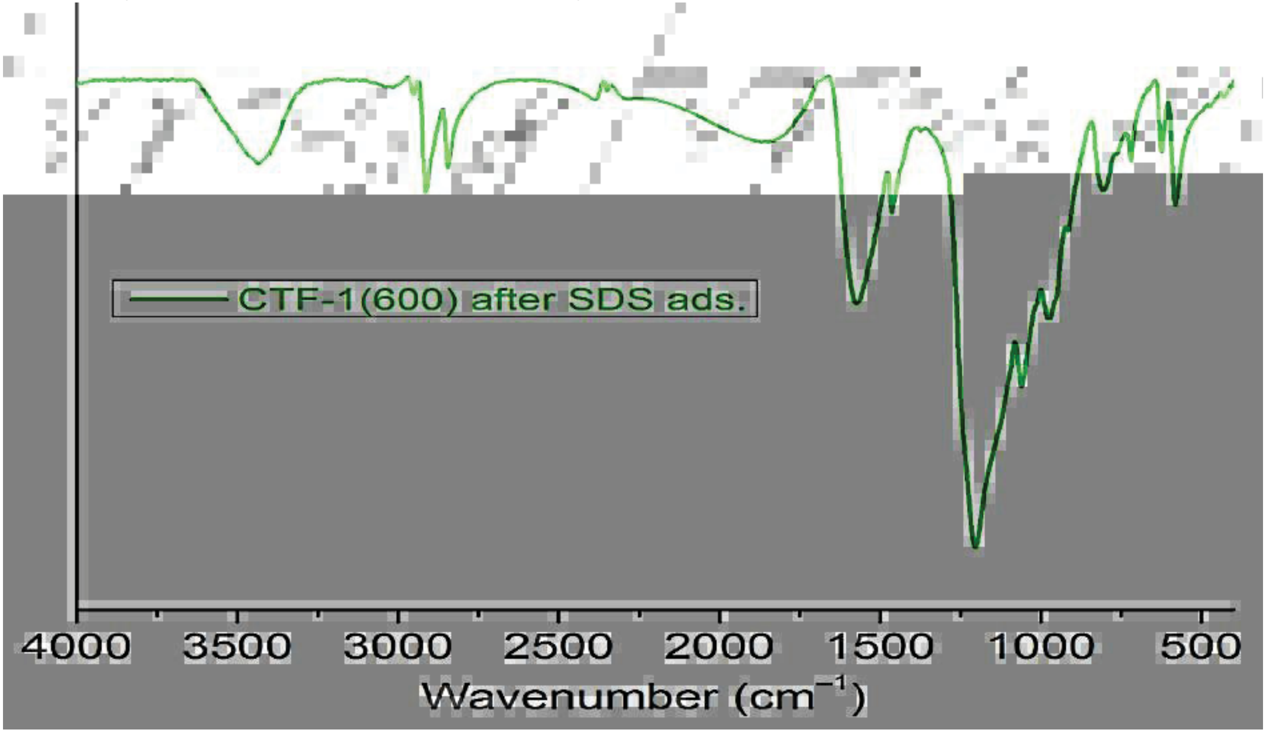

Fig. S1a: FT-IR spectrum of CTF-1(600) after SDS (sodium dodecylsulfate) surfactant adsorption at 20 mmol/L. Bands of SDS are superimposed on the CTF-1(600) bands. The characteristic band at 1570 cm^{-1} of CTF-1(600) in Fig. S1a is retained.

4. Powder X-ray diffraction patterns

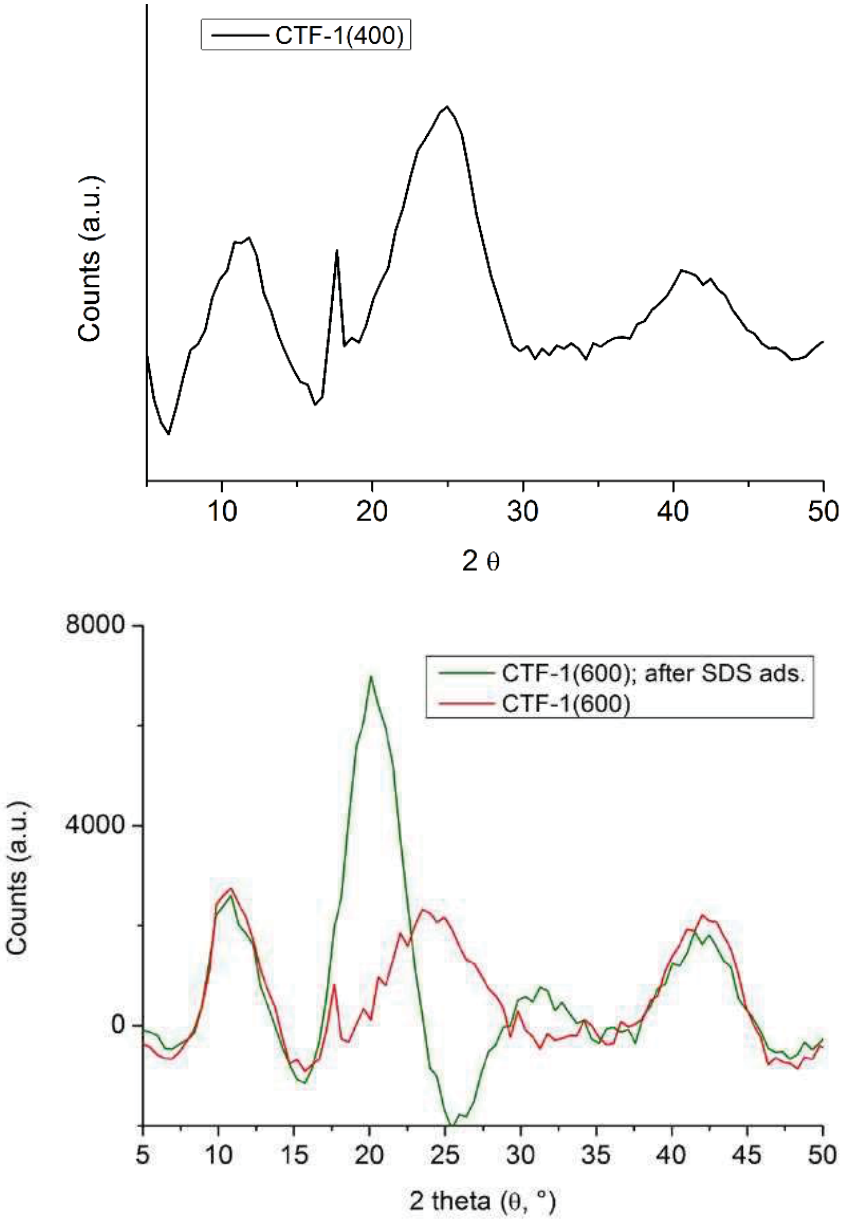

Fig. S2: Powder X-ray diffraction pattern of CTF-1(400) and CTF-1(600) before (*red*) and after SDS (sodium dodecylsulfate) surfactant adsorption at 20 mmol/L (*green)*. The "crystallinity" of the CTF sample is retained albeit with shifts in the peak positions and changes in the relative intensities. The PXRD of CTF-1(600) after SDS has the peak shifted from 25° to 20° with increased intensity. In the work by Kuhn et al.[2] the broad peak at $2\theta = 26.1°$ was assigned to the (001) peak and the distance of the (001) peak in the diffraction pattern was used for the layer distance between the triazine sheets ($c = 3.4$ Å). Here the shift of this peak with its maximum to $2\theta = 20.1°$ indicates an increase of the layer distance between the triazine sheets to 4.4 Å (according to $d = \lambda/2\sin\theta$ with $\lambda = 1.5418$ Å). Interlayer insertion of surfactants can also be observed for layer silicates such as Montmorillonite or Hectorite, which leads to an enhanced distance of the single layers of the solid.[3]

5. Elemental analysis

Compound	Temperature (°C)	Calculated (wt % and molar ratio)					Found (wt% and molar ratio)				
		C	H	N	C/H	C/N	C	H	N	C/H	C/N
CTF-1(400)	400	74.99	3.15	21.86	1.98	4.00	72.03	2.96	13.82	2.03	6.08
CTF-1(600)	600	74.99	3.15	21.86	1.98	4.00	68.13	2.14	8.91	2.7	8.92

6. Thermogravimetric analysis

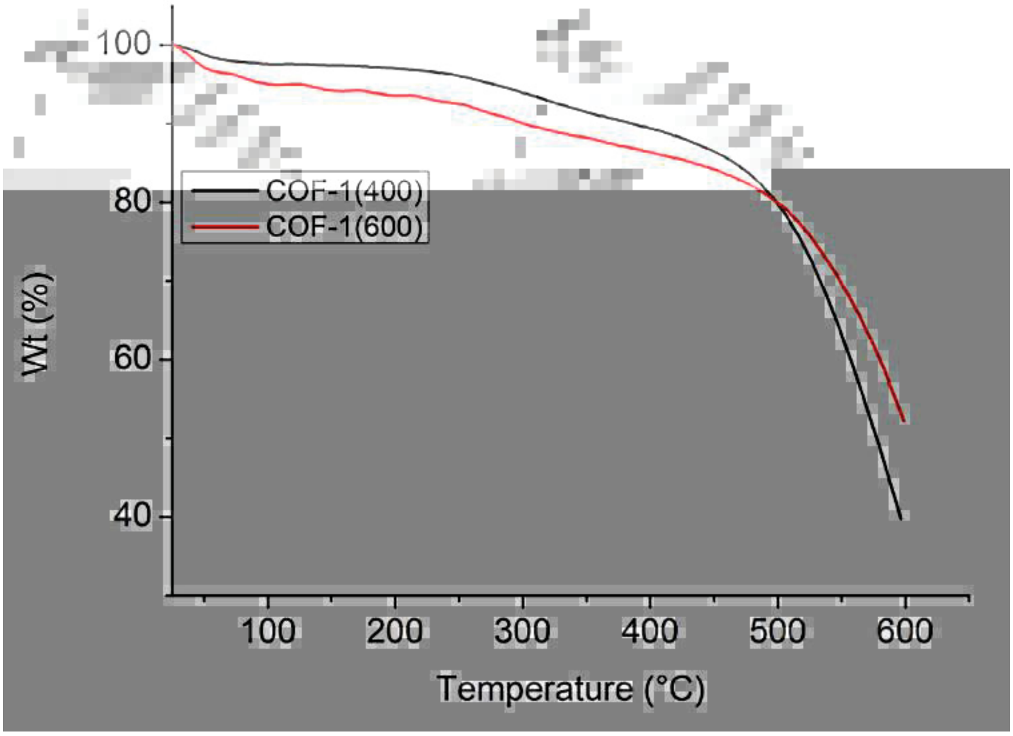

Fig. S3: Thermogravimetric analysis (TGA) data for CTF-1(400) and CTF-1(600).

7. Scanning electron micrographs (SEM) images

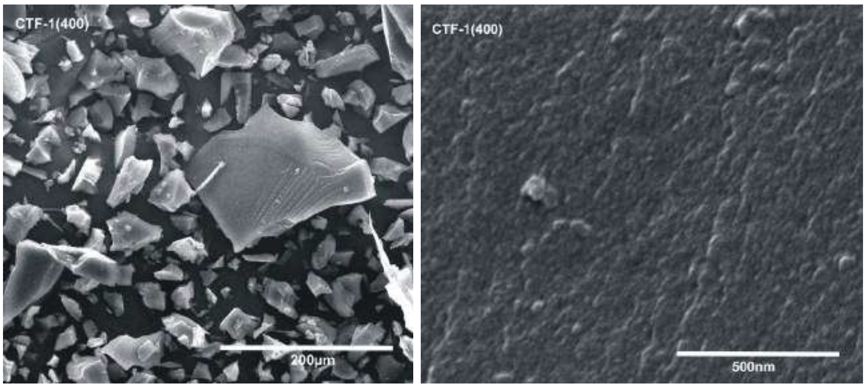

Fig. S4: SEM images for CTF-1(400) before surfactant adsorption.

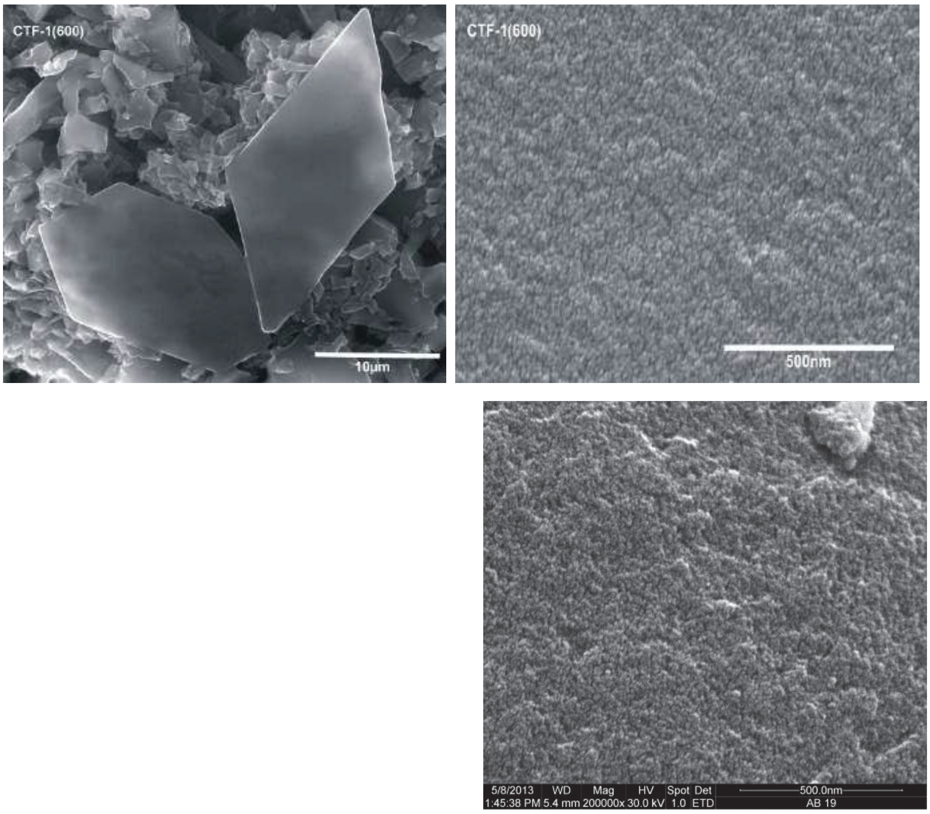

Fig. S5a: SEM images for CTF-1(600) before surfactant adsorption.

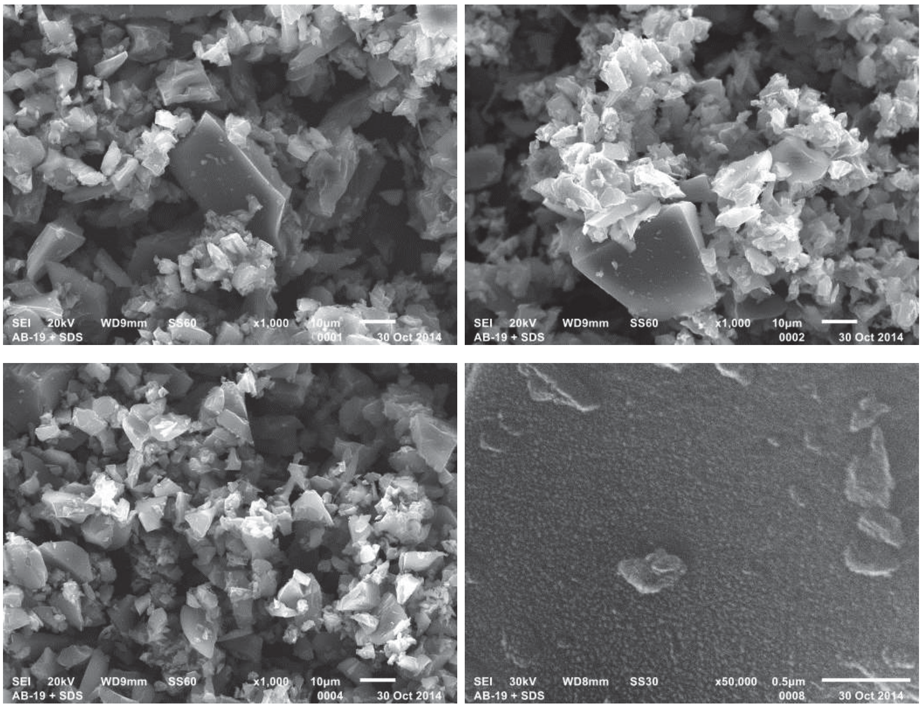

Fig. S5b: SEM images for CTF-1(600) after SDS (sodium dodecylsulfate) surfactant adsorption at an SDS equilibrium concentration of 20 mmol/L. There is no evident change in microscopic morphology after SDS adsorption.

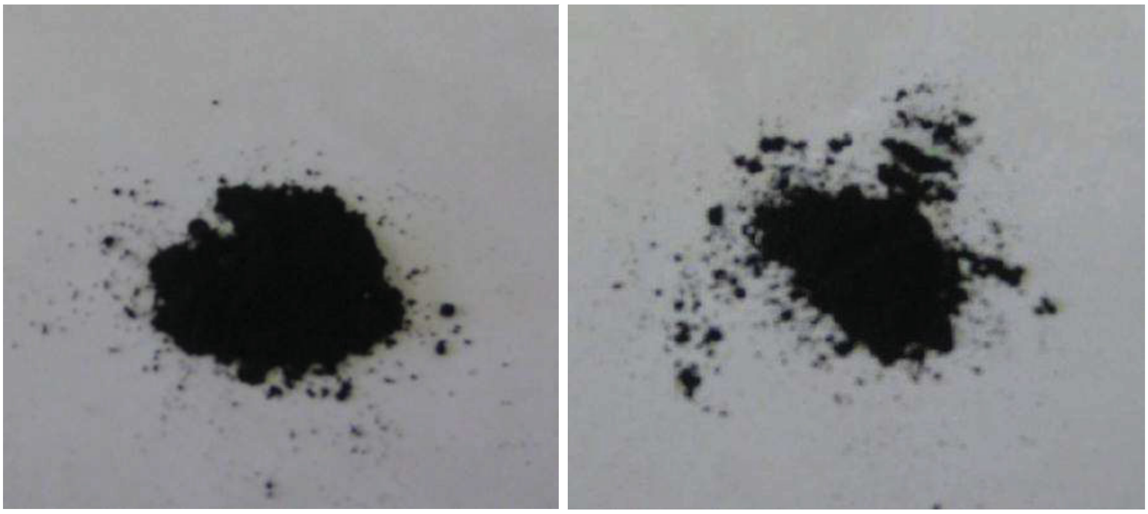

Fig. S5c: Camera photographs of CTF-1(600) before (left) after after SDS adsorption at an SDS equilibrium concentration of 20 mmol/L. The macroscopic black appearance did not change.

8. N_2 Sorption and pore size distribution:

N_2 sorption studies were performed to calculate the porosity. The surface area is calculated by applying the Brunauer–Emmett–Teller (BET) model over the pressure range of P/P_0 = 0.01–0.05. The measured BET surface areas are 970 for CTF-1(400) and and 1390 m^2g^{-1} CTF-1(600).

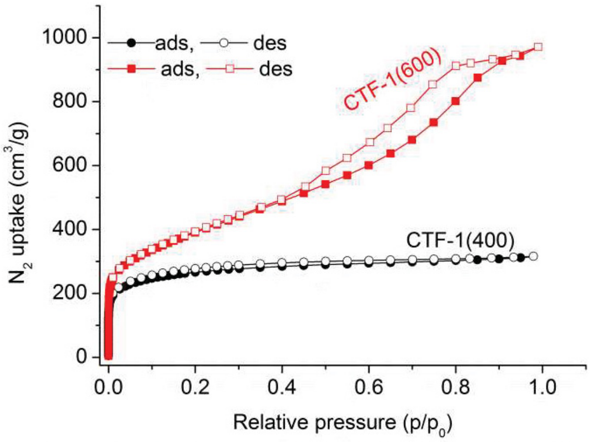

Fig. S6: Nitrogen adsorption-desorption isotherms for CTF-1(600) and CTF-1(400).

To understand the nature of porosity, non-local density functional theory (NLDFT) pore size distributions using a slit-pore model based on the N_2 adsorption isotherms were calculated. A narrow distribution of micropores centered mainly at 5, 6 and 12 Å were observed for CTF-

1(400) leading to small rings and cages associated with triazine formation (Fig. S7). On the other hand, micropores as well as mesopores were found for CTF-1(600).

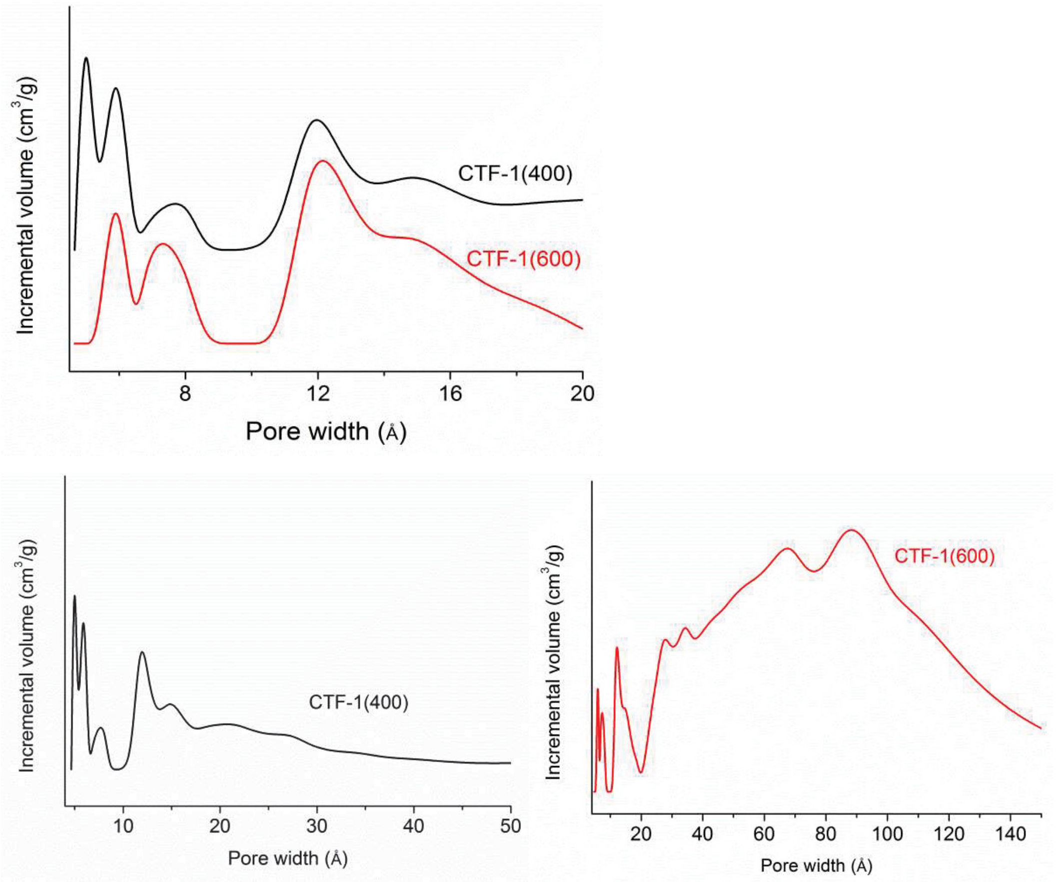

Fig. S7a: NL-DFT pore size distribution curve of CTF-1(400) and CTF-1(600).

Typically, the pore size distribution of a porous solid is evaluated from the analysis of N_2 adsorption isotherms measured at 77 K as was done above (Figure S6). However, that at such cryogenic temperature diffusion of N_2 molecules into carbon micropores is very slow. Moreover, diffusion limitations at this temperature might influence adsorption in ultramicropores (pores smaller than 7 Å).[4] For porous carbons which usually contain a wide range of pore sizes including ultramicropores, this would require time-consuming N_2 adsorption measurements and may still lead to under-equilibration of measured adsorption isotherms, which will give erroneous results of the analysis. For porous carbons problem of this type can be eliminated by using CO_2 adsorption analysis at 273 K.[5] The saturation pressure of CO_2 at 0°C is very high (~26141 Torr), therefore low relative pressure measurements necessary for the micropore analysis are achieved in the range of moderate absolute pressures (1–760 Torr).[6] At 273 K and under higher absolute pressures CO_2 molecules can more easily access ultramicropores than N_2 at ~77 K and the kinetic diameter of CO_2 (3.3 Å) is also a little bit smaller than for N_2 (3.64 Å). So, advantages for of CO_2 micropore analysis at 273 K versus N_2 analysis at 77 K are (i) faster analysis and (ii) greater confidence that measured adsorption points are equilibrated (both due to higher diffusion rates) and (iii) extension of the range of analysis to pores of smaller sizes that are accessible to CO_2 molecules but not to N_2.

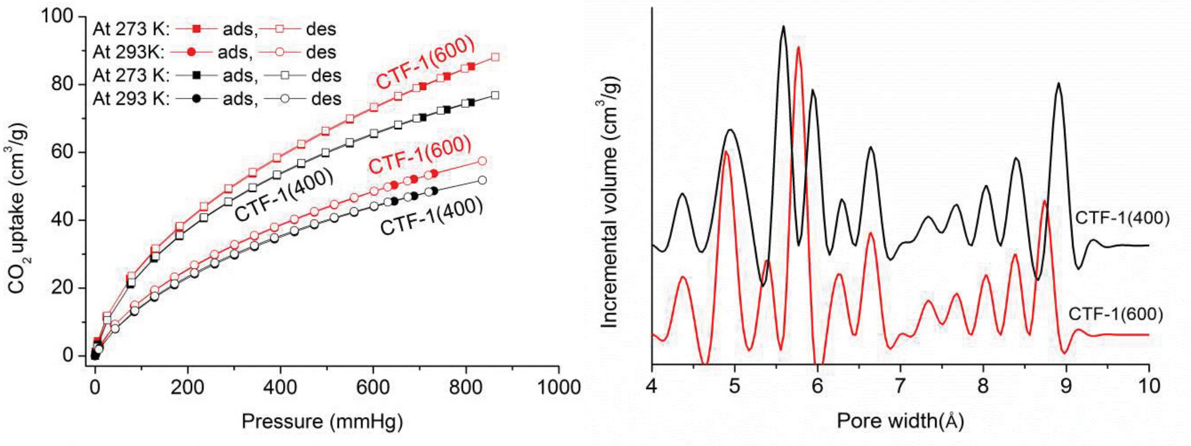

Fig. S7b: CO_2 sorption (left) and NLDFT pore size distribution (PSD) curve from CO_2 sorption (right).

Thus, from CO_2 adsorption isotherms at 273 K, the pore size distribution was derived between 4-10 Å by using NLDFT with a "CO_2 on carbon based slit-pore model" (Figure S7b). CO_2 adsorption with the NLDFT model yields a better resolved PSD towards the ultramicropore end than from N_2 adsorption isotherms. Both PSD values are very similar below 10 Å (1 nm) (Figure S7a and S7b). Moreover, we also studied the CO_2 uptake capacities for both the CTF-1(400) and CTF-1(600) as it is unknown until now. The CO_2 uptake capacities of CTF-1(400) and CTF-1(600) lie between 82 to 49 cm^3 g^{-1} (Figure S7b) which is comparable with the values for PCTFs from our previous work.[7]

9. Adsorption of surfactants

The surfactants for the adsorption studies from solution were sodium dodecylsulfate (SDS) and alkyl polyglycolether ($C_{12}EO_7$) (Table S1). The alkyl polyglycolether was a product with an alkyl chain distribution ranging from C_{12} to C_{18} and an average ethoxylation grade of 7.

Table S1: Surfactants used for the adsorption experiment from solution

Surfactant	Supplier	Structure	Purity
sodium dodecylsulfate (SDS)	Roth	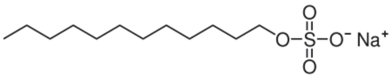	≥99,5 %
alkyl polyglycolether ($C_{12}EO_7$)	BASF	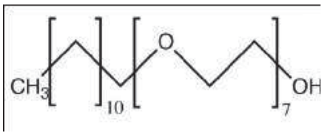	C_{12} main alkyl component (48 %) EO_7 on average

General procedure for surfactant adsorption: A known amount of solid is mixed with a known concentrated surfactant solution with stirring for 1h followed by centrifugation to separate the supernatant. To calculate the amount of, e.g., SDS adsorbed on, e.g., CTF-1(600), we have determined the surface tension of the solution which correlates to the SDS equilibrium concentration from the calibration curve in Figure S8. No influence of the CTF on the surface tension of the aqueous solutions was observed.

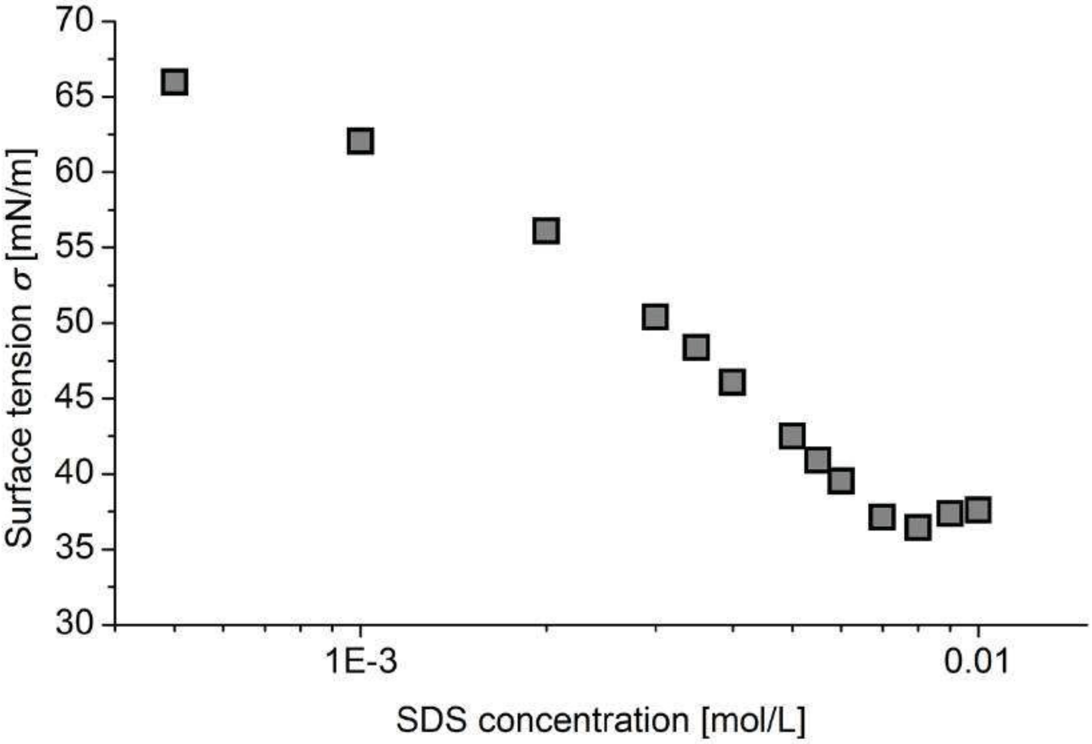

Fig. S8: Surface tension of sodium dodecylsulfate as a function of concentration

The graph in Figure S8 shows the typical surface activity of a surfactant in dependence of the concentration. At low concentrations the surface tension strongly decreases with the concentration, whereas above the critical micelle concentration (cmc) the surface tension remains nearly constant. The slight minimum close to the critical micelle concentration is caused by minor impurities of the surfactant. The linear decrease of surface tension with higher concentration below the cmc was used to calculate the adsorbed amounts on the CTFs. The adsorbed amounts of the surfactants from an aqueous solution on the solids were calculated according to equation S1:

$$\Gamma = \frac{\Delta c V}{m a_s} \qquad \text{(S1)}$$

where, Γ = adsorbed amounts (µmol m^{-2}); Δc = concentration difference before and after the adsorption (mmol L^{-1}); V = volume of the solution (L); m = mass of the adsorbent (g); a_s = specific surface area of the adsorbent (m^2 g^{-1}).

10. Possible arrangements of the adsorbed molecules on the surface of CTFs

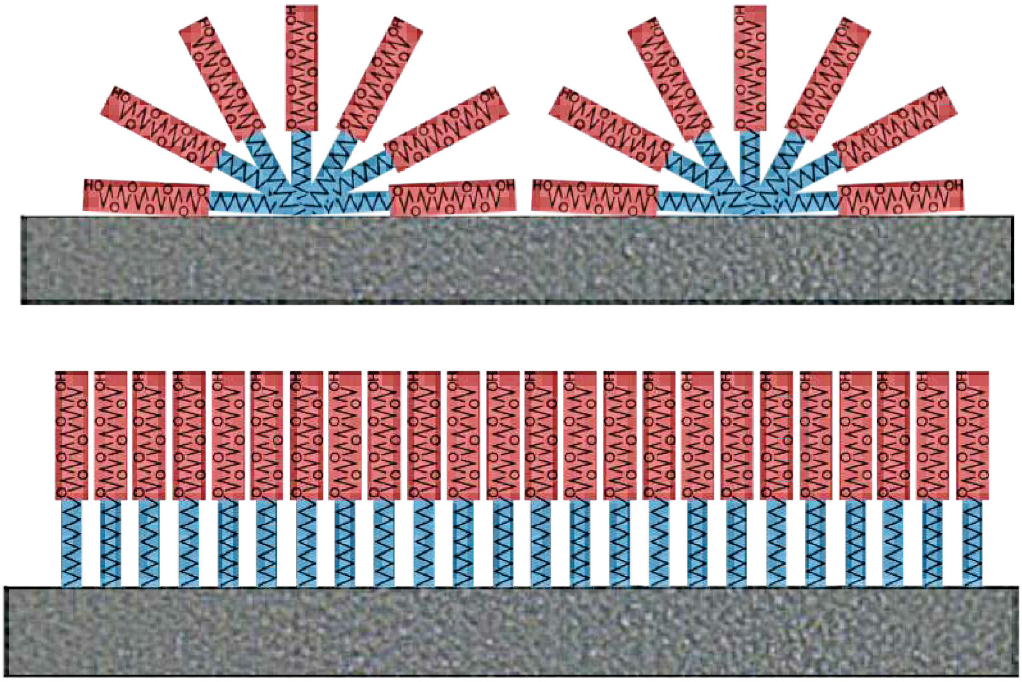

Fig. S9: Possible arrangements of the adsorbed molecules of SDS and $C_{12}EO_7$, respectively, on the surface of CTFs at low surfactant concentrations. Exemplary $C_{12}EO_7$ hemimicellar (top) and monolayer adsorption (bottom) on hydrophobic surface is shown here. The size ratio of hydrophilic head group (red) and hydrophobic tail (blue) is drawn to scale. The size of the sulfate head group of SDS is comparable to $C_{12}EO_7$ in diameter but shorter in length.

Surfactants can either adsorb via hydrogen bonding or electrostatic forces of the polar group to the polar groups of the solid surface or with the non-polar alkyl chain with the triazin ring structure via van der Waals forces like with carbon black surfaces.

Monolayers with horizontal and vertical orientation depending on the surface coverage or bilayers and admicelle and micelle structures are possible.[3,8] As an example the sketch (Fig. S9) shows possible structures for the mentioned non-polar adsorption mechanism between the nonpolar part of the surfactant and the ring structure of the solid, forming close-packed monolayers at higher surface coverage and the hemimicellar structures.[3,8,9]

In ref. 9 (ref. 15 in main article) it is suggested that for aromatic compounds the adsorption follows mainly "non-hydrophobic" mechanisms including hydrogen bonding (hydroxyl- and amino-substituted compounds), electrostatic attraction (anionized compounds), and π–π electron-donor–acceptor (EDA) interaction (nitroaromatic compounds). In the case of surfactants on CTF we think that both non-hydrophobic and van-der-Waals force mechanisms are possible. In any case the adsorbed amounts should be similar for both mechanisms.[3] Many references of the adsorption and adsorption mechanisms of different surfactant types on various surfaces are given in ref. 3.

A trimerization reaction of nitrile groups can construct triazine rings (see Scheme 1 in main text). Each triazine ring can act as a triangular node with phenyl rings and thereby built a continuous sheet or layer network. The resulting sheets can form a hexagonal lattice system with an eclipsed AAA structure where atoms of each layer are placed above their analogues in the next layer.[2]

Surfactants are amphiphilic compounds that adsorb at interfaces such as liquid/liquid, solid/liquid and gas/liquid systems. This is due to the fact that these compounds combine in their structure a non-polar part which is mainly a hydrocarbon alkyl chain containing 8 to 18 carbon atoms and a polar part, as the head-group which can be either from a non-ionic, an ionic (cationic or anionic) or a zwitterionic nature (see Table S1). By adsorption onto a solid surface, a surfactant can convert the surface from a hydrophobic species to a hydrophilic species and vice versa. In hydrophilic surfaces, surfactants can form the quasi two-dimensional admicelles similar to the aggregate structure, name as spherical or cylindrical micelles or bilayer structures.[8] On the other hand, in hydrophobic surfaces, surfactant aggregates tend to form either monolayer or hemimicellar structure such as hemispherical or hemicylindrical (Fig. S9).[10] However, the critical packing factor of the surfactant predicts the admicelles or hemicelles structure.[11]

We note, however, that the surfactants (cf. Table S1) were not chosen with their particular properties to be adapted to the CTF-1 surface. Rather we chose common surfactants which are widely applied in the field.

---

[1] P. Kuhn, A. l. Forget, D. Su, A. Thomas and M. Antonietti, *J. Am. Chem. Soc.*, 2008, **130**, 13333-13337

[2] P. Kuhn, M. Antonietti and A. Thomas, *Angew.Chem. Int. Ed.*, 2008, **47**, 3450-3453.

[3] B. Dobias, X. Qiu and W. von Rybinski, *Solid-Liquid Dispersions,* Surfactant Science Series, Marcel Dekker 1999.

[4] F. Rodriguez-Reinoso and A. Linares-Solano, in Chemistry and Physics of Carbon, Vol. 21 (P. A. Thrower, Ed.) Marcel Dekker, New York, 1988.

[5] J. Garrido, A. Linares-Solano, J. M. Martin-Martinez, M. Molina-Sabio, F. Rodriguez-Reinoso and R. Torregosa, *Langmuir*, 1987, **3**, 76; D. Cazorla-Amoros, J. Alcaniz-Monje and A. Linares-Solano, *Langmuir*, 1996, **12**, 2820; J. Garcia-Martinez and D. Cazorla-

---

Amoros, A. Linares-Solano, in Characterization of Porous Solids V (K. K. Unger, G. Kreysa and J. P. Baselt, Eds.) Elsevier, Amsterdam, 2000, pp. 485-494.

6 Quantachrome Instruments (1900 Corporate Drive, Boynton Beach, FL 33426 USA, www.quantachrome.com) Powder Tech Note 35.

7 A. Bhunia, I. Boldog, A. Moller and C. Janiak, *J. Mater. Chem. A*, 2013, **1**, 14990–14999.

8 F. Tiberg, J. Brinck and L. Grant, Adsorption and surface-induced self-assembly of surfactants at the solid-aqueous interface, *Curr. Opin. J. Colloid Interface Sci.*, 2000, **4**, 411–419.

9 T. Wang, K. Kailasam, P. Xiao, G. Chen, L. Chen, L. Wang, J. Li and J. Zhu, *Microporous Mesoporous Mater.*, 2014, **187**, 63-70; J. Liu, H. Chen, S. Zheng and Z. Xu, *J. Chem. Eng. Data*, 2013, **58**, 3557−3562; J. Liu, E. Zong, H. Fu, S. Zheng, Z. Xu and D. Zhu, *J. Colloid Interface Sci.*, 2012, **372**, 99-107; W. Zhang, F. Liang, C. Li, L.-G. Qiu, Y.-P. Yuan, F.-M. Peng, X. Jiang, A.-J. Xie, Y.-H. Shen and J.-F. Zhu, *J. Hazardous Mater.*, 2011, **186**, 984-990.

10 S. Manne, J. P. Cleveland, H. E. Gaub, G. D. Stucky and P. K. Hansma, Direct visualization of surfactant hemimicelles by force microscopy of the electric double layer, *Langmuir*, 1994, **10**, 4409–4413.

11 M. J. Rosen, *Surfactants and Interfacial Phenomena*, 3rd ed., Wiley-Interscience, New Jersey, 2004, pp. 38–59.

3.5 Syntheses of two imidazolate-4-amide-5-imidate linker-based hexagonal metal–organic frameworks with flexible ethoxy substituent

Suvendu Sekhar Mondal, Subarna Dey, Igor A. Baburin, Alexandra Kelling, Uwe Schilde, Gotthard Seifert, Christoph Janiak and Hans-Jürgen Holdt

CrystEngComm., 2013, **15**, 9394-9399
DOI: 10.1039/c3ce41632a, (reference 103)
Impact factor 2013: 3.858

In this paper syntheses of zinc and cobalt based imidazolate-4-amide-5-imidate frameworks (IFP-9 and -10) form 4,5-dicyano-2-ethoxyimidazole were reported. The gas sorption measurements of N_2, H_2, CH_4, and CO_2 for IFP-9 and IFP-10 were performed at different temperatures up to 1 bar. The BET surface area for IFP-9 and -10 were found 7 and 13 m^2/g, respectively. Due to the polar ethoxy group and narrow pore apertures, wide hysteretic isotherms for H_2, CO_2 and CH_4 were found.

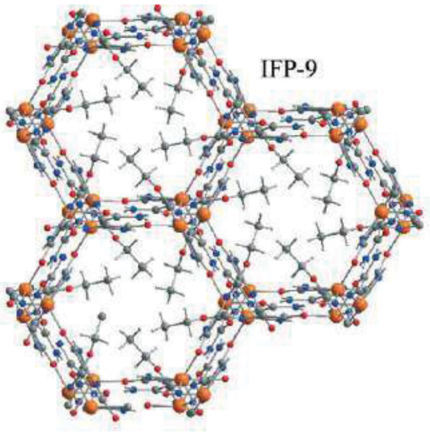

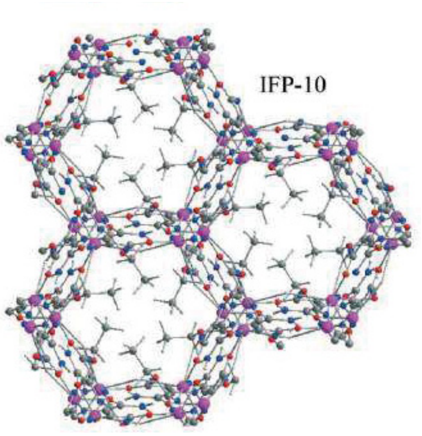

Author’s contribution to the work:

- Performing the gas adsorption studies.
- Writing and drawing figures for the gas adsorption part of the manuscript.

CrystEngComm

RSC Publishing

COMMUNICATION

View Article Online
View Journal | View Issue

Cite this: *CrystEngComm*, 2013, **15**, 9394

Received 16th August 2013,
Accepted 8th October 2013

DOI: 10.1039/c3ce41632a

www.rsc.org/crystengcomm

Syntheses of two imidazolate-4-amide-5-imidate linker-based hexagonal metal–organic frameworks with flexible ethoxy substituent†

Suvendu Sekhar Mondal,[a] Subarna Dey,[b] Igor A. Baburin,[c] Alexandra Kelling,[a] Uwe Schilde,[a] Gotthard Seifert,[c] Christoph Janiak[b] and Hans-Jürgen Holdt*[a]

A rare example of *in situ* linker generation with the formation of soft porous Zn- and Co-MOFs (IFP-9 and -10, respectively) is reported. The flexible ethoxy groups of IFP-9 and -10 protrude into the 1D hexagonal channels. The gas-sorption behavior of both materials for H_2, CO_2 and CH_4 showed wide hysteretic isotherms, typical for MOFs having a flexible substituent which can give rise to a gate effect.

Flexible or soft porous networks are known as third-generation porous coordination polymers that have gained much attention because of their interesting properties.[1–4] Compounds of this exclusive family of materials show a reversible dynamic response dependent on external stimuli, such as the presence/absence of specific guest molecules or even changes in temperature[5] and pressure.[6] As a result of this unique property, flexible MOFs have potential applications in selective gas adsorption/separation or chemical sensing.[3,7,8] Despite the fact that the number of responsive frameworks is still increasing, rational fine-tuning of the dynamic features of flexible MOFs has become more challenging.[3,9,10] The series of pillared-layered frameworks of the type $[M_2L_2P]_n$ (M = Co, Ni, Cu, Zn; L = dicarboxylate ligand; P = neutral pillar) were extensively studied in the past few years.[11–14] Due to the elastic paddlewheel building block, an intrinsic framework flexibility of these MOFs was observed.[11] Thus, the MOFs can exhibit slightly different crystal structures and cell volumes depending on the nature of the guest molecules adsorbed in the pores. In addition, reversible shrinkage and expansion of their unit cells (large pore → narrow pore → large pore) upon adsorption of alcohols was noticed for the reported MOFs.[15,16] In a related study, Fischer and coworkers have reported a series of MOFs by using a specifically functionalized bdc-type linker having dangling alkoxy substituents. Such frameworks exhibit a guest-dependent structural transformation and breathing effect.[17–19]

We have previously developed a new class of metal 2-substituted imidazolate-4-amide-5-imidate based metal–organic frameworks called IFP (Imidazolate Framework Potsdam).[20–22] The chelating 2-substituted imidazolate-4-amide-5-imidate ligands were generated *in situ* by partial hydrolysis of 2-substituted 4,5-dicyanoimidazole in the presence of a metal salt hydrate in *N*,*N'*-dimethylformamide (DMF) under solvothermal conditions, yielding IFP-1 to -4 and IFP-7.[20–22] Zinc-imidazolate-4-amide-5-imidate based IFP-7 showed gate effects due to its flexible methoxy substituent and selective CO_2 capture.[22] Herein, we report the syntheses of zinc and cobalt based imidazolate-4-amide-5-imidate frameworks called IFP-9 and -10, respectively, having a flexible ethoxy substituent. The gas sorption properties of IFP-9 and -10 again indicate flexible MOFs with a gate effect.

The MOFs $\{[Zn(L2)]\cdot 0.5DMF\}_n$ and $\{[Co(L2)]\cdot xH_2O\cdot yDMF\}_n$ (L2 = 2-ethoxyimidazolate-4-amide-5-imidate) are named IFP-9 and IFP-10, respectively. IFP-9 was synthesized by the reaction of 4,5-dicyano-2-ethoxyimidazole (L1) with an equimolar amount of $Zn(NO_3)_2\cdot 4H_2O$ in a mixture of DMF, ethanol and water under solvothermal conditions. The reaction conditions yielded *in situ* the 2-ethoxyimidazolate-4-amide-5-imidate linker (L2). Similarly, IFP-10 was formed by the reaction of L1 with an equimolar amount of $Co(NO_3)_2\cdot 6H_2O$ in DMF under solvothermal conditions (Scheme 1).

The degree of *in situ* hydrolysis of the cyano groups of 4,5-dicyano-2-ethoxyimidazolate (L1) into the corresponding imidazolate-4-amide-5-imidate linker (L2) was studied using infrared (IR) spectroscopy. The IR-spectra of the IFP-9 and IFP-10 manifested no stretching bands related to C≡N in

---

[a] *Institut für Chemie, Anorganische Chemie, Universität Potsdam, Karl-Liebknecht-Straße 24–25, 14476 Potsdam, Germany. E-mail: holdt@uni-potsdam.de; Fax: +49 331 977 5055; Tel: +49 331 977 5180*

[b] *Institut für Anorganische Chemie und Strukturchemie, Heinrich-Heine-Universität Düsseldorf, 40204 Düsseldorf, Germany. E-mail: janiak@uni-duesseldorf.de*

[c] *Institut für Physikalische Chemie und Elektrochemie, Technische Universität Dresden, 01062 Dresden, Germany*

† Electronic supplementary information (ESI) available: Detailed experimental procedure, IR spectra, PXRD patterns, TGA traces, table of X-ray data of IFP-9, gas adsorption data. CCDC 956082. For ESI and crystallographic data in CIF or other electronic format see DOI: 10.1039/c3ce41632a

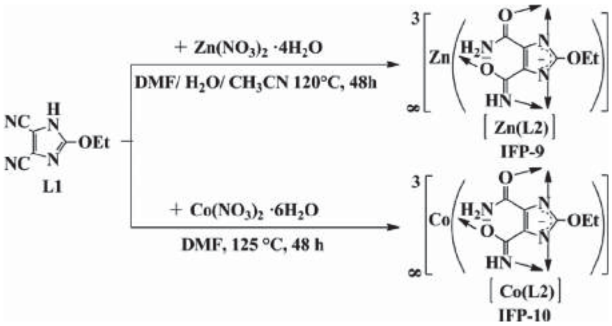

Scheme 1 Syntheses of IFP-9 and IFP-10.

the 2200–2230 cm^{-1} region. Instead, new typical bands for amide and imidate groups were observed at around 1560 cm^{-1} and 1660 cm^{-1}, respectively. Among other prominent IR changes, those associated with N–H resonances were noticeable. Centered at 3341 cm^{-1} (IFP-9) and 3335 cm^{-1} (IFP-10), a broad amide–imidate N–H band with a considerably fine structure was noted (Fig. S1, ESI†).

IFP-9 crystallizes in the highly symmetric rhombohedral space group $R\bar{3}$.[23] The asymmetric unit contains one Zn^{2+} ion and the bridging ligand L2 (Fig. S2, ESI†). The Zn^{2+} ion is pentacoordinated by the donor atoms of three L2 ligands to form a distorted environment with a trigonal-bipyramidal geometry (Fig. 1). In turn, L2 acts as pentadentate linker that coordinates three Zn^{2+} ions. This means that Zn^{2+} ions and bridging L2 ligands act as 3-connected topological species forming a net with a rare uninodal topology, named *etb*.[20,24,25] The topology of IFP-9 is classified by the vertex symbol 3.6.10.15.

In this arrangement, imidates N3 and O2 and the amide O3 reside in equatorial positions and two imidazolate N atoms (N1 and N2) occupy the axial positions (Fig. 1). This five-fold coordination leads to a Zn^{2+} centre with Lewis acid properties.

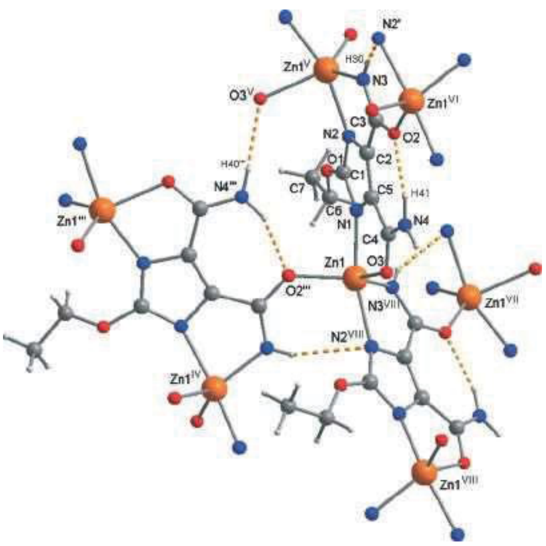

Fig. 1 Section of the crystal structure of IFP-9, showing the coordination environment of Zn^{2+}, the bridging mode of the linker L2 and the hydrogen bonds (dotted lines). For the symmetry codes and details of hydrogen bonds, see the ESI.†

The amide and imidate groups are formed by the *in situ* partial hydrolysis of cyano groups and enable each L2 ligand to participate in the formation of two five-membered chelate rings. One ring forms by coordinating a Zn^{2+} ion to the N1 (imidazolate) atom and the O3 (amide) atom. The other chelate ring forms by coordinating a second Zn^{2+} ion to the N2 (imidazolate) atom and the N3 (imidate) atom. The negatively charged O2 (imidate) atom is coordinated to a third Zn^{2+} ion.

The structure of IFP-9 is further stabilized by three hydrogen bonds (Fig. 1), one intramolecular bond between a nitrogen atom of an amide group and an imidate O atom (N4–H41···O2) and intermolecular hydrogen bonds between an imidate NH group and an imidazolate N atom (N3–H30···N2), as well as between a nitrogen atom and an oxygen atom of the amide groups (N4–H40···O3). The hydrogen-bonding parameters as well as the symmetry operators are listed in Table S4 in the ESI.† The structure of IFP-9 possesses 1D hexagonal channels running along 0, 0, *z*; 1/3, 2/3, *z*; and 2/3, 1/3, *z* (Fig. 2).

The walls of the hexagonal channel in IFP-9 are essentially constructed by the rigid and planar imidazolate-amide-imidate linker L2. The Zn^{2+} ions are located almost on the edges of the hexagonal channels. They are bridged by the L2 linkers through coordination with both N imidazolate atoms. The amide and imidate functional groups of the bridging ligand L2 are embedded in the wall of the channel. The imidate group bridges two Zn^{2+} ions of two channel edges through its N and O atoms. The three different types of hydrogen bonds are all confined to the channel wall as well. The localization of the amide and imidate groups and the hydrogen bonds in the channel walls, and of the pentacoordinated Zn^{2+} ions at the edges of the hexagonal channels, as well as the ethoxy substituents which point into the channels, polarizes and functionalizes the coordination space of this MOF.

Moreover, after several attempts, we could not find a suitable crystal of IFP-10 for single crystal X-ray measurement. Hence, the structural model of IFP-10 was constructed by using the single-crystal X-ray refinement of IFP-1[20] which was further optimized by using an *ab initio* density functional theory (DFT) method. The PXRD pattern of the optimized IFP-10 structure is in good agreement with the experimental data (Fig. 3). The theoretically optimized structure of IFP-10 also possesses 1D hexagonal channels (Fig. 2b). The ethoxy groups protrude into the open channels and determine their pore aperture. The ethyl group of the ethoxy moiety is disordered over two equally occupied sites. By considering the van der Waals radii, the pore aperture diameter of the channels in IFP-9 was estimated as 0.60 and 0.35 Å for the corresponding disordered species. For IFP-10, a diameter of 0.30 Å was calculated from the theoretically estimated structure. The void spaces in IFP-9 and IFP-10 represent 23% and 26%, respectively. For the void calculation, the PLATON toolkit was used.[26,27]

Thermogravimetric analysis (TGA) for as-synthesized IFP-9 indicated a gradual weight-loss of about 5% starting from 200 °C up to 325 °C which corresponds to partial loss of DMF guest species, followed by framework decomposition above 325 °C. As-synthesized IFP-10 showed a negligible weight-loss

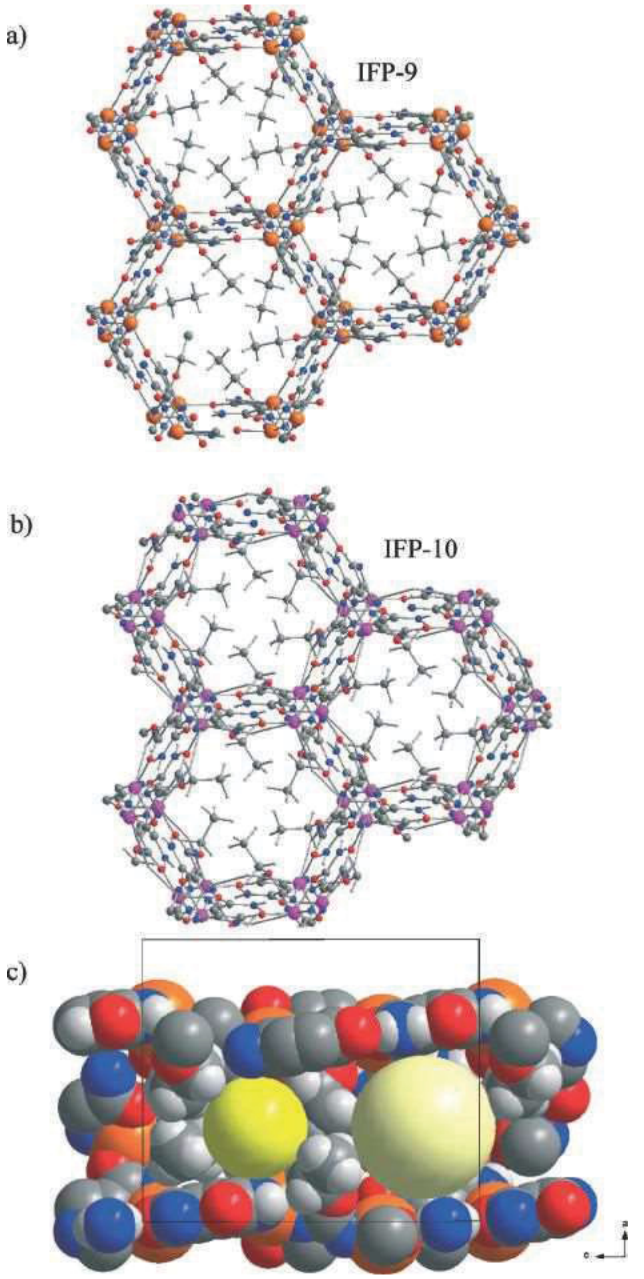

Fig. 2 Hexagonal channels with different accessible diameters – a) for IFP-9 (Zn-centre), b) for IFP-10 (Co-centre); orange – Zn, pink – Co, blue – N, red – O, dark gray – C, light gray – H; the ethyl group in IFP-9 is disordered; only one species is drawn. The structure of IFP-10 is based on *ab initio* density functional calculations. (c) Insight into one channel of IFP-9 (running along *c*) with two different void volumes – for details, see the squeeze output at the end of the cif.

step of 5% at 25–225 °C, corresponding to the release of solvent molecules (Fig. S3, ESI†). TGA traces show that after solvent removal, both IFPs are stable up to 300 °C. Materials were activated at 200 °C at 10^{-3} mbar pressure for 24 h. Powder X-ray diffraction patterns (PXRD) of activated samples exhibited sharp diffraction peaks similar to the as-synthesized samples (Fig. 3). Thus, the porous frameworks maintained crystalline integrity even without solvent molecules.

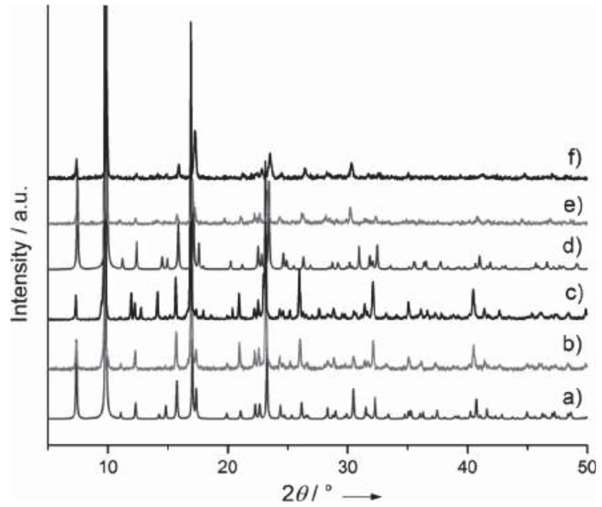

Fig. 3 Powder X-ray diffraction patterns of IFP-9; a) simulated, b) as-synthesized and c) activated, and of IFP-10; d) simulated, e) as-synthesized and f) activated.

Activated IFP-9 and -10 are expected to show gas-sorption selectivity towards small polar molecules due to their polar and flexible ethoxy side chains. The gas sorption isotherms of N_2, H_2, CH_4, and CO_2 for IFP-9 are recorded at various temperatures up to 1 bar (Fig. 4 and 5). IFP-9 and -10 barely adsorbed N_2 at 77 K, which can be attributed to a narrow pore size of the channels (0.60 and 0.35 Å for IFP-9 and 0.30 Å for IFP-10). Hence, N_2 molecules (kinetic diameter of 3.64 Å) cannot diffuse into the small channels. From the estimated Brunauer–Emmett–Teller (BET) surface area for IFP-9 and -10 of 7 and 13 $m^2 g^{-1}$, respectively, it can be concluded that N_2 is adsorbed at the outer surface only. The CO_2, CH_4 and H_2 sorption isotherms show very different sorption behaviors. The low-pressure CO_2 sorption measurements for IFP-9 (at 273 K, Fig. 4a) and IFP-10 (at 273 K and 298 K, Fig. 5a) indicate CO_2 uptake with a broad hysteresis for the desorption branch. Such hysteretic behavior was also observed for flexible MOFs like IFP-7 and other MOFs having flexible substituents.[17–19,22] The uptake of CO_2 by IFP-9 and IFP-10 at 273 K and 1 bar is 5 $cm^3 g^{-1}$ and 39 $cm^3 g^{-1}$, respectively. Because of the small-pore aperture windows (see above), the CO_2 molecules are preferably located in cavities ("zero-dimensional closed space").[28] Notably, IFP-9 and IFP-10 also adsorb 2.5 $cm^3 g^{-1}$ and 6 $cm^3 g^{-1}$ CH_4 at 273 K and 1 bar, respectively, despite their narrow pore apertures (Fig. 4a for IFP-9 and Fig. 5b for IFP-10). Also, H_2 is adsorbed at 77 K up to 8.8 and 5.2 $cm^3 g^{-1}$ in IFP-9 and -10, respectively, at 1 bar (Fig. 4b for IFP-9 and Fig. 5b for IFP-10).

The reason that N_2 at 77 K is not adsorbed presumably because of activated diffusion effects associated with the low thermal energy of the adsorbate relative to the high barrier for diffusion through the small-pore aperture windows.[29] In other words, at slow thermal motion at 77 K, the N_2 molecule will statistically only seldom approach the small-pore aperture with the correct orientation for penetration, that is, in line with its molecule axis. While H_2 and CO_2 are adsorbed at 77 K and 273 K, respectively, N_2 is not adsorbed at 77 K,

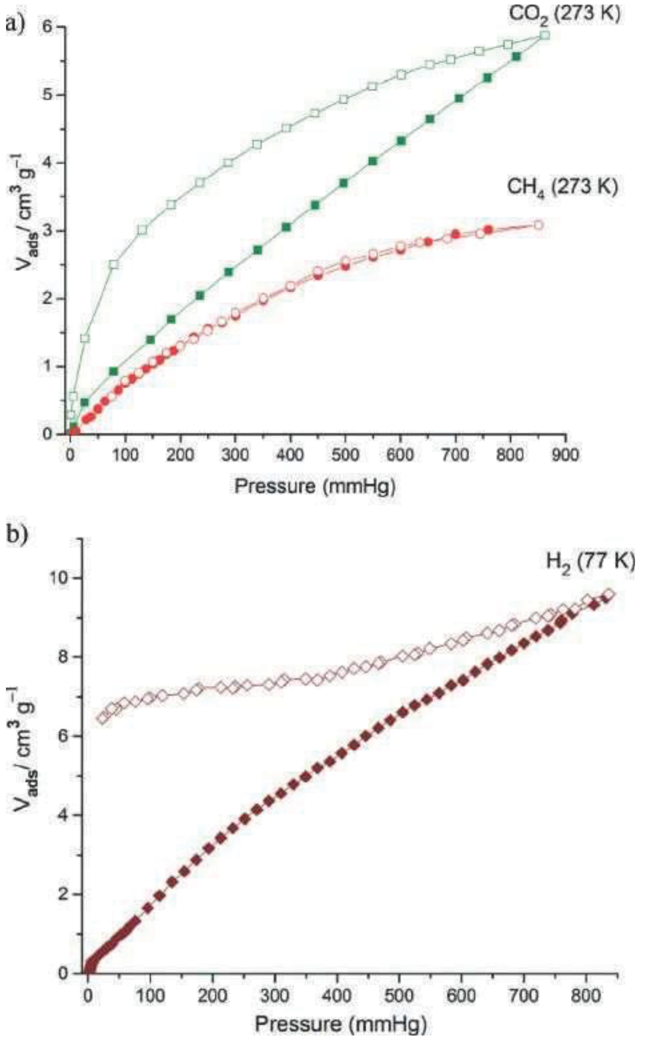

Fig. 4 Gas sorption isotherms for activated IFP-9. Adsorption and desorption branches are indicated by closed and open symbols, respectively.

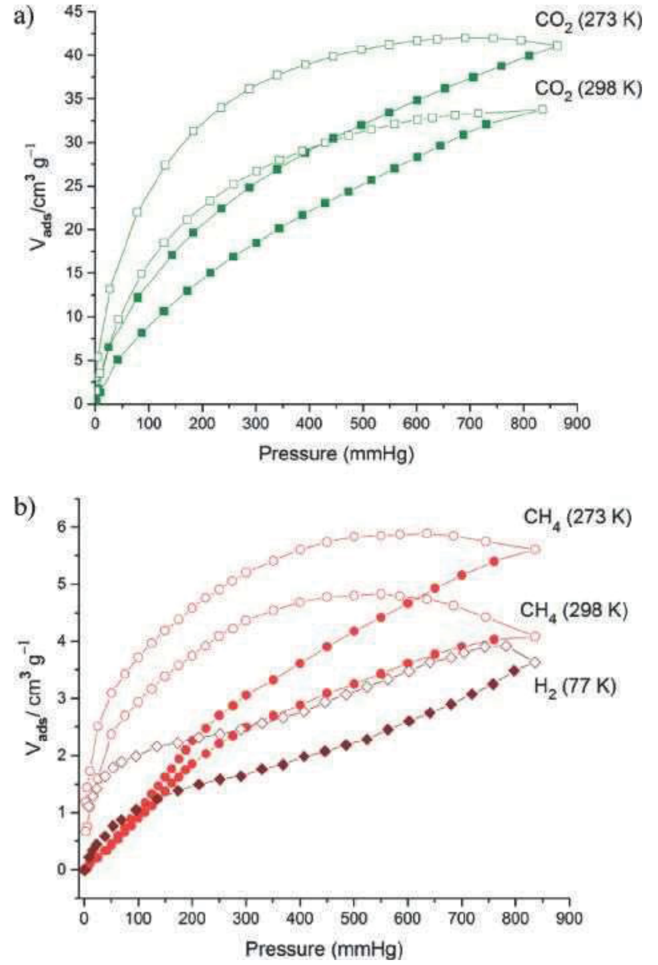

Fig. 5 Gas sorption isotherms for activated IFP-10. Adsorption and desorption branches are indicated by closed and open symbols, respectively.

which is a frequently encountered phenomenon characterized by the kinetic hindrance of small pores or pore aperture windows.[30] It is suggested that the passage of guest molecules through the small-pore aperture windows in and out of the cavities proceeds through a temporary expansion of the window size. The desorption branches of CH_4 isotherms for IFP-10 show a wide desorption hysteresis. The CH_4 sorption behavior of IFP-10 can be attributed to a kinetic trap created by the polar flexible ethoxy substituent and imidazolate-amide-imidate channel walls, acting as a gate that regulates the access and release of CH_4 into and from the channels. Such broad desorption behaviour for the CH_4 isotherm at atmospheric pressure is rarely observed in microporous MOFs.[22,31] Another way to prove the flexibility of the frameworks is by H_2 sorption. Although IFPs adsorb a low amount of H_2 at atmospheric pressure, they show a wide desorption hysteresis. As already mentioned, IFP-9 possesses pore aperture windows of 0.35 Å to the solvent-depleted cavities of 8.0 and 5.8 Å diameter (see Fig. 2c), and ethoxy groups from the ligand form the pore aperture windows. Incoming gas molecules have to widen the windows by changing the conformation of the ethoxy groups arranged on the C2-atom of the imidazole ring. Because of the lower kinetic diameter of CO_2 (3.3 Å), in comparison to that of CH_4 (3.8 Å), the twist of the ethyl groups for incoming CO_2 has to be smaller as it has to be for CH_4. Moreover, this behavior demonstrates that the selective uptake for CO_2 over N_2, CH_4 and H_2 could be attributed to the difference in polarizability of adsorbate molecules (average electric dipole polarizabilities: CO_2 2.911 × 10^{-24} cm^3, N_2 1.7403 × 10^{-24} cm^3, CH_4 2.593 × 10^{-24} cm^3).[32] The interactions are expected between the polar functional groups (amide and imidate) and CO_2, which has a significant quadrupole moment, while CH_4 has none. Therefore, IFP-10 also shows a higher CO_2 uptake compared to IFP-9 due to the presence of an unsaturated metal site of the paramagnetic Co centre (d^7-system). The Zn centre has the electronic state d^{10} and is a diamagnetic system. We anticipated that the Co centres in IFP-10 have a higher potential to polarize CO_2 molecules than the Zn-based IFP-9. This behaviour was also previously observed for the Co-based isostructural IFP-5.[33] A similar wide hysteretic H_2 uptake was observed by a nanoporous octanuclear Cu^{2+} structure and its Co^{2+} ion-exchanged material.[34]

In conclusion, we report an *in situ* formed 2-ethoxyimidazolate-4-amide-5-imidate linker with its isostructural MOFs IFP-9 and-10. Porous 3D frameworks with 1D hexagonal channels with pore aperture diameters of 0.35 Å and 0.30 Å are formed for IFP-9 (Zn) and IFP-10 (Co), respectively. The structure of IFP-9 was determined by X-ray crystallographic analysis. The structure of IFP-10 was determined by a combination of PXRD and structure modelling and was confirmed by IR spectroscopy. Due to the polar ethoxy group and narrow pore apertures, wide hysteretic isotherms for H_2, CO_2 and CH_4 were observed. The very broad desorption hysteretic behaviour of CH_4 uptake for IFP-10 is not commonly observed for microporous MOFs. Such gas-sorption behaviour is typical for the MOFs having flexible substituents. Due to the narrow pore apertures with flexible ethoxy groups, IFP-9 and -10 could be useful for potential gas mixture separation in comparison with other IFP materials at high pressure measurements. Moreover, research to extend this approach to other transition metal ions and other flexible substituent-based IFPs is in progress.

Acknowledgements

This work is financially supported by Priority Program 1362 of the German Research Foundation on "Metal–Organic Frameworks." We thank Dr. C. Günter (Institut für Erd- und Umweltwissenschaften, Universität Potsdam, Germany) for powder X-ray diffraction measurements.

Notes and references

1 S. Kitagawa and K. Uemura, *Chem. Soc. Rev.*, 2005, **34**, 109–119.

2 G. Férey and C. Serre, *Chem. Soc. Rev.*, 2009, **38**, 1380–1399.

3 (*a*) S. Horike, S. Shimomura and S. Kitagawa, *Nat. Chem.*, 2009, **1**, 695–704; (*b*) K. Sumida, D. L. Rogow, J. A. Mason, T. M. McDonald, E. D. Bloch, Z. R. Herm, T. H. Bae and J. R. Long, *Chem. Rev.*, 2012, **112**, 724–781.

4 R. Kitaura, K. Seki, G. Akiyama and S. Kitagawa, *Angew. Chem., Int. Ed.*, 2003, **42**, 428–431.

5 Y. Liu, J. Her, A. Dailly, A. J. Ramirez-Cuesta, D. A. Neumann and C. M. Brown, *J. Am. Chem. Soc.*, 2008, **130**, 11813–11818.

6 P. G. Yot, Q. Ma, J. Haines, Q. Yang, A. Ghoufi, T. Devic, C. Serre, V. Dmitriev, G. Férey, C. Zhong and G. Maurin, *Chem. Sci.*, 2012, **3**, 1100–1104.

7 J.-R. Li, J. Sculley and H.-C. Zhou, *Chem. Rev.*, 2012, **112**, 869–932.

8 L. E. Kreno, K. Leong, O. K. Farha, M. Allendorf, R. P. Van Duyne and J. T. Hupp, *Chem. Rev.*, 2012, **112**, 1105–1125.

9 P. Horcajada, F. Salles, S. Wuttke, T. Devic, D. Heurtaux, G. Maurin, A. Vimont, M. Daturi, O. David, E. Magnier, N. Stock, Y. Filinchuk, D. Popov, C. Riekel, G. Férey and C. Serre, *J. Am. Chem. Soc.*, 2011, **133**, 17839–17847.

10 T. Lescouet, E. Kockrick, G. Bergeret, M. Pera-Titus, S. Aguado and D. Farrusseng, *J. Mater. Chem.*, 2012, **22**, 10287–10293.

11 D. N. Dybtsev, H. Chun and K. Kim, *Angew. Chem., Int. Ed.*, 2004, **43**, 5033–5036.

12 K. L. Mulfort and J. T. Hupp, *J. Am. Chem. Soc.*, 2007, **129**, 9604–9605.

13 N. Yanai, T. Uemura, M. Inoue, R. Matsuda, T. Fukushima, M. Tsujimoto, S. Isoda and S. Kitagawa, *J. Am. Chem. Soc.*, 2012, **134**, 4501–4504.

14 H. C. Hoffmann, B. Assfour, F. Epperlein, N. Klein, S. Paasch, I. Senkovska, S. Kaskel, G. Seifert and E. Brunner, *J. Am. Chem. Soc.*, 2011, **133**, 8681–8690.

15 K. Uemura, Y. Yamasaki, F. Onishi, H. Kita and M. Ebihara, *Inorg. Chem.*, 2010, **49**, 10133–10143.

16 J. S. Grosch and F. Paesani, *J. Am. Chem. Soc.*, 2012, **134**, 4207–4215.

17 S. Henke, R. Schmid, J.-D. Grunwaldt and R. A. Fischer, *Chem.–Eur. J.*, 2010, **16**, 14296–14306.

18 S. Henke, A. Schneemann, A. Wütscher and R. A. Fischer, *J. Am. Chem. Soc.*, 2012, **134**, 9464–9474.

19 S. Henke and R. A. Fischer, *J. Am. Chem. Soc.*, 2011, **133**, 2064–2067.

20 F. Debatin, A. Thomas, A. Kelling, N. Hedin, Z. Bacsik, I. Senkovska, S. Kaskel, M. Junginger, H. Müller, U. Schilde, C. Jäger, A. Friedrich and H.-J. Holdt, *Angew. Chem., Int. Ed.*, 2010, **49**, 1258–1262.

21 F. Debatin, K. Behrens, J. Weber, I. A. Baburin, A. Thomas, J. Schmidt, I. Senkovska, S. Kaskel, A. Kelling, N. Hedin, Z. Bacsik, S. Leoni, G. Seifert, C. Jäger, C. Günter, U. Schilde, A. Friedrich and H.-J. Holdt, *Chem.–Eur. J.*, 2012, **18**, 11630–11640.

22 S. S. Mondal, A. Bhunia, I. A. Baburin, C. Jäger, A. Kelling, U. Schilde, G. Seifert, C. Janiak and H.-J. Holdt, *Chem. Commun.*, 2013, **49**, 7599–7601.

23 Crystal data for IFP-9: $C_{8.5}H_{11.5}N_{4.5}O_{3.5}Zn$, $M_r = 298.09$ g mol^{-1}, crystal dimensions 0.30 × 0.21 × 0.12 mm, trigonal, space group $R\bar{3}$, $a = b = 18.0166(5)$, $c = 18.6077(5)$ Å, $V = 5230.8(2)$ Å^3, $Z = 18$, $\rho_{\mathrm{calcd}} = 1.70$ g cm^{-1}; $\mu(\mathrm{Mo}_{\mathrm{K}\alpha}) = 2.12$ mm^{-1}, $T = 210$ K, $2\theta_{\max} = 55.0°$, 29 403 reflections measured, 2681 unique ($R_{\mathrm{int}} = 0.0211$), $R = 0.0212$, w$R = 0.0559$ ($I > 2\sigma(I)$). For details of the data collection and the structure solution and refinement see ESI.† CCDC 956082 contains the supplementary crystallographic data for this paper. These data can be obtained free of charge from the Cambridge Crystallographic Data Centre *via* www.ccdc.cam.ac.uk/data_request/cif.

24 N. L. Rosi, J. Kim, M. Eddaoudi, B. Chen, M. O'Keeffe and O. M. Yaghi, *J. Am. Chem. Soc.*, 2005, **127**, 1504–1518.

25 O.-R. Fang, G.-S. Zhu, Z. Jin, Y.-Y. Ji, J.-W. Ye, M. Xue, H. Yang, Y. Wang and S.-L. Qui, *Angew. Chem., Int. Ed.*, 2007, **46**, 6638–6642.

26 A. Bondi, *J. Phys. Chem.*, 1964, **68**, 441–451.

27 A. L. Spek, *PLATON: A Multipurpose Crystallographic Tool*, Utrecht University, Utrecht, The Netherlands, 2001.

28 S.-I. Noro, S. Kitagawa, T. Akutagawa and T. Nakamura, *Prog. Polym. Sci.*, 2009, **34**, 240–279.

29 A. J. Fletcher, E. J. Cussen, T. J. Prior, M. J. Rosseinsky, C. J. Kepert and K. M. Thomas, *J. Am. Chem. Soc.*, 2001, **123**, 10001–10011.

30 (*a*) C. Janiak, *Chem. Commun.*, 2013, **49**, 6933–6937; (*b*) C. Heering, I. Boldog, V. Vasylyeva, J. Sanchiz and C. Janiak, *CrystEngComm*, 2013, DOI: 10.1039/C3CE41426D, in press.

31 D. Zhao, D. Yuan, R. Krishna, J. M. van Baten and H.-C. Zhou, *Chem. Commun.*, 2010, **46**, 7352–7354.

32 D. R. Lide, *CRC Handbook of Chemistry and Physics*, CRC Press, Boca Raton, FL, 2009, Table 4, pp. 10–196.

33 F. Debatin, J. Möllmer, S. S. Mondal, K. Behrens, A. Möller, R. Staudt, A. Thomas and H.-J. Holdt, *J. Mater. Chem.*, 2012, **22**, 10221–10227.

34 J. Zhao, L. Mi, J. Hu, H. Hou and Y. Fan, *J. Am. Chem. Soc.*, 2008, **130**, 15222–15223.

Electronic Supplementary Material (ESI) for CrystEngComm

Syntheses of two Imidazolate-4-amide-5-imidate Linker Based Hexagonal Metal-Organic Frameworks with Flexible Ethoxy Substituent

Suvendu Sekhar Mondal,[a] Subarna Dey,[b] Igor A. Baburin,[c] Alexandra Kelling,[a] Uwe Schilde,[a] Gotthard Seifert,[c] Christoph Janiak,[b] and Hans-Jürgen Holdt*[a]

[a] *Institut für Chemie, Anorganische Chemie, Universität Potsdam, Karl-Liebknecht-Straße 24-25, 14476 Potsdam, Germany.*
Fax: +49 331-977-5055; Tel: +39 331-977-5180; E-mail: holdt@uni-potsdam.de
[b] *Institut für Anorganische Chemie und Strukturchemie, Heinrich-Heine-Universität Düsseldorf, 40204 Düsseldorf, Germany; E-mail: janiak@uni-duesseldorf.de*
[c] *Institut für Physikalische Chemie und Elektrochemie, Technische Universität Dresden, 01062 Dresden, Germany*

CONTENTS

1 Experimental Details

The linker precursors 2-ethoxy-4,5-dicyanoimidazole (L1)[1] was synthesized following published procedure. Elemental analysis (C, H, N) was performed on Elementar Vario EL elemental analyzer.

Materials

All chemicals were purchased from commercial suppliers (Sigma-Aldrich, Fluka, Alfa Aesar and others) and used without further purification.

Synthetic procedure

IFP-9:

In a sealed tube (Typ A, company: Ace) 0.20 g of (1.35 mmol) 4,5-dicyano-2-ethoxy-imidazole (L1), $Zn(NO_3)_2 \cdot 4H_2O$ (0.39 g, 1.35 mmol) were dissolved in DMF/EtOH/H_2O (v:v =. 2:1:0.5 mL). The sealed tube was closed and the mixture was heated at 120 °C for 48 h and then allowed to cool down to room temperature with 5 °C per hour. The obtained fine crystalline material was named IFP-9. Yield for IFP-9: ~ 65 % based on $Zn(NO_3)_2 \cdot 4H_2O$; elemental analysis of activated IFP-9; $C_7H_8N_4O_3Zn$; calcd., C 32.15, H 3.08, N 21.42; found, C 31.91, H 3.44, N 21.08; IR (KBr pellet): $\tilde{v}$ = 3341 (br), 3280 (vs), 3116 (s), 1657 (s), 1552 (m), 1466 (m), 1104 (m), 802 cm^{-1} (m).

IFP-10:

In a sealed tube (Typ A, company: Ace) 0.20 g of (1.35 mmol) 4,5-dicyano-2-ethoxy-imidazole (L1), $Co(NO_3)_2 \cdot 6H_2O$ (0.39 g, 1.35 mmol) were dissolved in DMF (5 mL). The sealed tube was closed and the mixture was heated at 125 °C for 48 h and then allowed to cool down to room temperature with 5 °C per hour. The obtained material was named IFP-10. Yield for IFP-10: ~ 58 % based on $Co(NO_3)_2 \cdot 6H_2O$; elemental analysis of activated IFP-10; $C_7H_8N_4O_3Co$; calcd., C 32.96, H 3.16, N 21.96; found, C 32.81, H 3.44, N 21.66; IR (KBr pellet): $\tilde{v}$ = 3335 (br), 3116 (vs), 1660 (s), 1547 (s), 1473 (m), 1282 (m), 1104 (m), 802 cm^{-1} (m),684 cm^{-1} (m).

2 IR spectra

IR spectra were recorded on a FT-IR Nexus from Thermo Nicolet in the region of 4000- 400 cm-^{1} as KBr pellets.

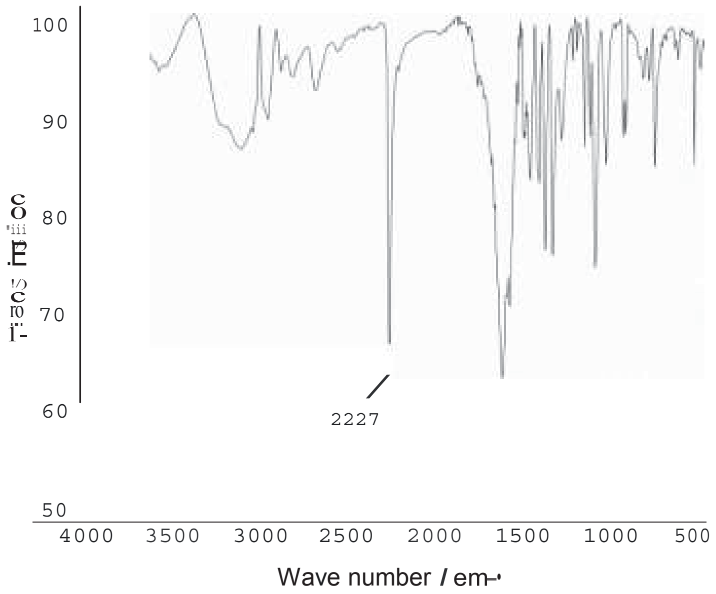

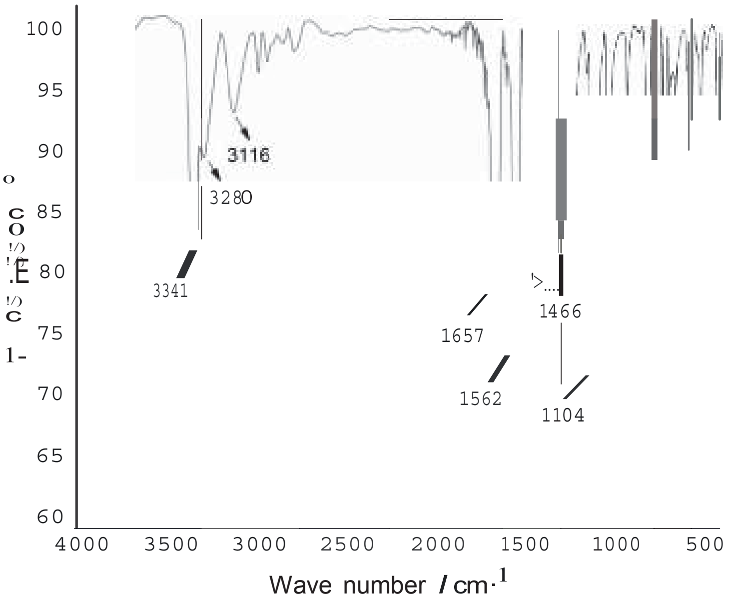

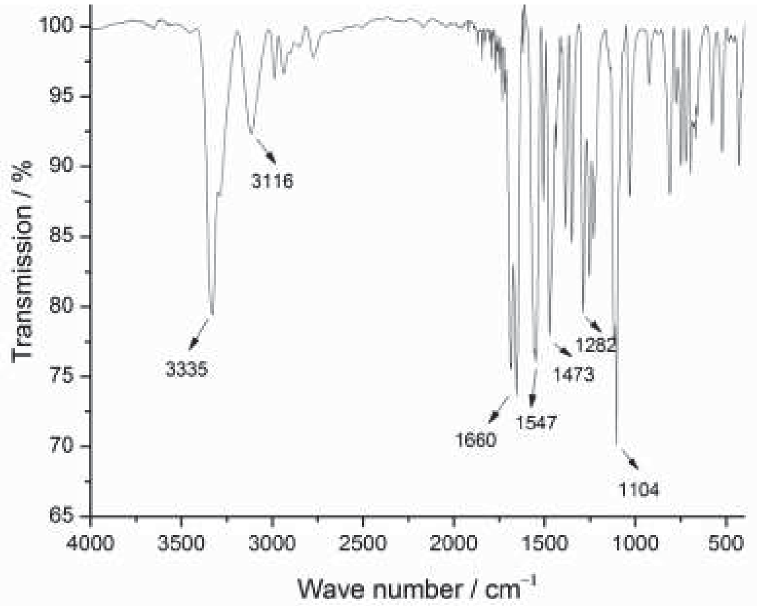

Fig. S1. IR-spectra of: **A**) 4,5-dicyano-2-ethoxy-imidazole (L1); **B**) as-synthesized IFP-9; **C**) as-synthesized IFP-10.

3 Powder X-ray-diffraction patterns

Powder X-ray diffraction (PXRD) patterns were measured on a Siemens Diffractometer D5005 in Bragg-Brentano reflection geometry. The diffractometer was equipped with a copper tube, a scintillation counter, automatical incident- and diffracted-beam soller slits and a graphite secondary monochromator. The generator was set to 40 kV and 40 mA. All measurements were performed with sample rotation. Data were collected digitally from 3° to 70° 2θ using a step size of 0.02° 2θ and a count time of 4 seconds per step. The simulated powder pattern for IFPs was calculated using single-crystal X-ray diffraction data and processed by the free Mercury v1.4.2 program provided by the Cambridge Crystallographic Data Centre.

4 Single crystal X-ray structure determination of IFP-9

The crystals were embedded in perfluoropolyalkylether oil and mounted on a glass fibre. Intensity data were collected at 210 K using a STOE Imaging Plate Diffraction System IPDS-2 with graphite monochromatized $\mathrm{Mo}_{K\alpha}$ radiation (λ = 0.71073 Å) at 50 kV and 40 mA (360 frames, $\Delta\omega$=1°, exposure time per frame: 4 min. The data were corrected by a numerical absorption correction using the program X-Area (Stoe, 2004) as well as for Lorentz and polarisation effects. The structure was resolved with direct methods using SHELXS-97[2] and refined with full-matrix least-squares on F^2 using the program SHELXL-97[3] (Sheldrick, 1997). All non-hydrogen atoms were refined anisotropically.

The amide and imidate hydrogen atoms were located from the differences in Fourier map and refined with $U_{iso}(H) = 1.2\ U_{eq}(N)$. The other hydrogen atoms were calculated in their expected positions and refined with $U_{iso}(H) = 1.2\ U_{eq}(CH_2)$ or $U_{iso}(H) = 1.2\ U_{eq}(CH_3)$. The unit cell contains channels filled with disordered solvent molecules. In spite of several attempts, no chemically reasonable solution could be received for the solvent species in the channels of the crystal material. Very high displacement parameters, high estimates and partial occupancy due to the disorder make it impossible to determine accurate atomic positions for that molecules. PLATON/SQUEEZE[4] calculated a solvent-accessible void volume in the unit cell of 1196.2 Å^3 (22.9 % of the total cell volume), corresponding to 336 electrons (residual electron density after the last refinement cycle) per cell. This number agrees with about 0.5 molecules of DMF (0.5x40x18=360) per asymmetric unit. The contributions of the disordered solvent species was subtracted from the structure factor calculations, but included in D(calc), F_{000} and the Molecular weight. The deposited atom data (cif) reflect only the known cell content.

CCDC 956082 for IFP-9 contains the supplementary crystallographic data for this paper. These data can be obtained free of charge from The Cambridge Crystallographic Data Centre via www.ccdc.cam.ac.uk/data_request/cif.

Table S1 Crystal Data, Details of Intensity Measurements, and Structure Refinement for IFP-9.

Chemical formula	$C_{8.5}H_{11.5}N_{4.5}O_{3.5}Zn$
Formula Mass	298.09
Crystal system	trigonal
Space group	$R\bar{3}$
a/Å	18.0166(5)
b/Å	18.0166(5)
c/Å	18.6077(5)
α/°	90.00
β/°	90.00
γ/°	120.00
Unit cell volume/Å^3	5230.8(2)
Temperature/K	210
No. of formula units per unit cell, *Z*	18
Radiation type	MoKα
Absorption coefficient, μ/mm^{-1}	1.873
Reflections collected	29403
No. of independent reflections	2681
R_{int}	0.0211
R_1 / wR_2 [$I > 2\sigma(I)$]	0.0212/0.0559
R_1 / wR_2 (all data)	0.0236/0.0569
Goodness of fit on F^2	1.049

Table S2 Selected bond lengths [Å] for [Zn(L2)] 0.5 DMF (IFP-9).

N1–Zn1	2.075(1)
N2–Zn1^{V}	2.131(1)
N3–Zn1^{V}	1.997(1)
O2–Zn1	2.004(1)
O3–Zn1	2.166(1)

Table S3 Selected bond angles [°] for Zn(L2)] 0.5 DMF (IFP-9).

N3–Zn1–O2$^{\mathrm{VIII}}$	120.68(6)
N3–Zn1–N1$^{\mathrm{VIII}}$	103.96(5)
O2–Zn1–N1$^{\mathrm{III}}$	89.46(5)
N3–Zn1–N2$^{\mathrm{VIII}}$	79.61(5)
O2–Zn1–N2$^{\mathrm{III}}$	105.52(5)
N1–Zn1–N2$^{\mathrm{III}}$	160.32(5)
N3–Zn1–O3$^{\mathrm{VIII}}$	120.32(6)
O2–Zn1–O3$^{\mathrm{III}}$	118.99(5)
N1–Zn1–O3	77.30(4)
N2–Zn1–O3$^{\mathrm{VIII}}$	84.19(4)

Table S4 Hydrogen-bonding parameters [Å, °] for [Zn(L2)] 0.5 DMF (IFP-9).

	D-H	H ... A	D ... A	D-H ... A
N3 - H30 … N2$^{\mathrm{I}}$	0.76(2)	2.50(2)	3.211(2)	156(2)
N4 - H40 … O3$^{\mathrm{II}}$	0.86(2)	2.17(2)	3.030(2)	175(2)
N4 - H41 … O2	0.91(2)	1.93(3)	2.788(2)	156(2)

Symmetry Operators: $^{\mathrm{I}}$ x-y+1/3, x-1/3, 2/3-z; $^{\mathrm{II}}$ 1-x, 1-y, -z; $^{\mathrm{III}}$ 2/3+x-y, 1/3+x, 1/3-z
$^{\mathrm{IV}}$ y, 1-x+y, -z; $^{\mathrm{V}}$ 2/3-x+y, 4/3-x, 1/3+z; $^{\mathrm{VI}}$ y-1/3, 1/3-x+y, 1/3-z
$^{\mathrm{VII}}$ 1+x-y, x, -z; $^{\mathrm{VIII}}$ 4/3-y, 2/3+x-y, z-1/3

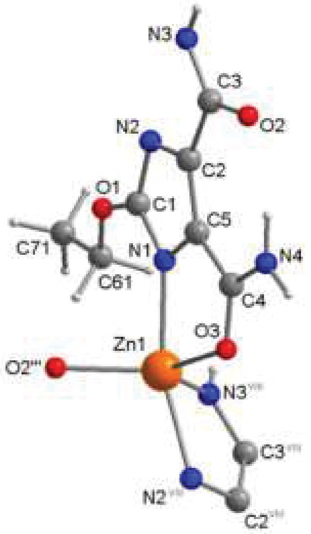

Fig. S2. Asymmetric unit with coordination site of IFP-9.

5 Theoretical calculations of crystal structure of IFP-10

DFT calculations (PBE functional[5]) were performed by using the SIESTA program package.[6] The DZP basis set used in the calculations was first tested on the structure of IMOF-3 (later, we named IMOF-3 as IFP-1) solved from single-crystal X-ray data,[7] and showed very good agreement with respect to unit cell parameters (compare; a_{calcd} = 17.9119 Å and c_{calcd} = 18.2982 Å vs. a_{exptl} = 17.9244 Å and c_{exptl} = 18.4454 Å), bond lengths and angles. Due to the large unit cell sizes, it was sufficient to include only the Γ-point of the Brillouin zone for the evaluation of integrals in the reciprocal space.

6 Thermogravimetric (TG) analysis

The TG measurements were performed in a stationary air atmosphere (no purge) from room temperature up to 850 °C using a Linseis thermal analyzer (Linseis, Germany) working in the vertical mode. The heating rate was 10 °C/min. The samples were placed in cups of aluminium oxide.

A)

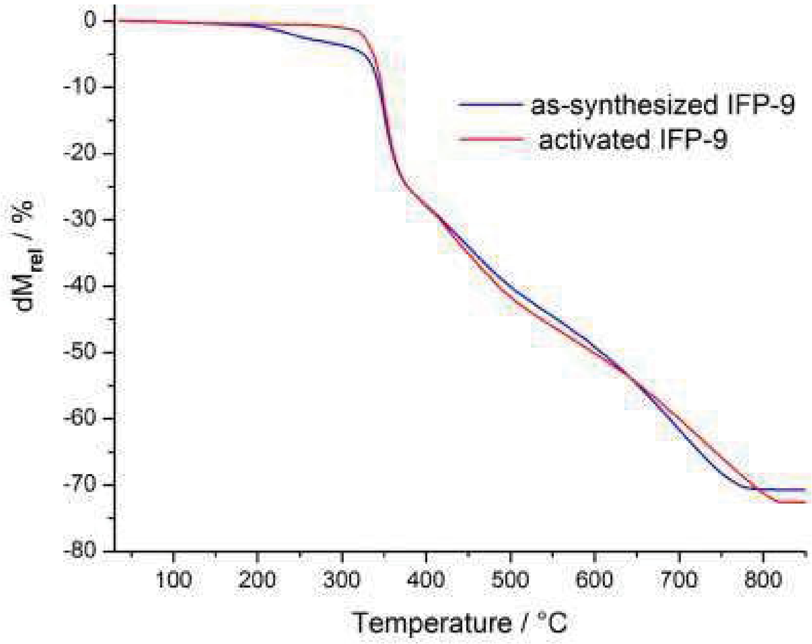

B)

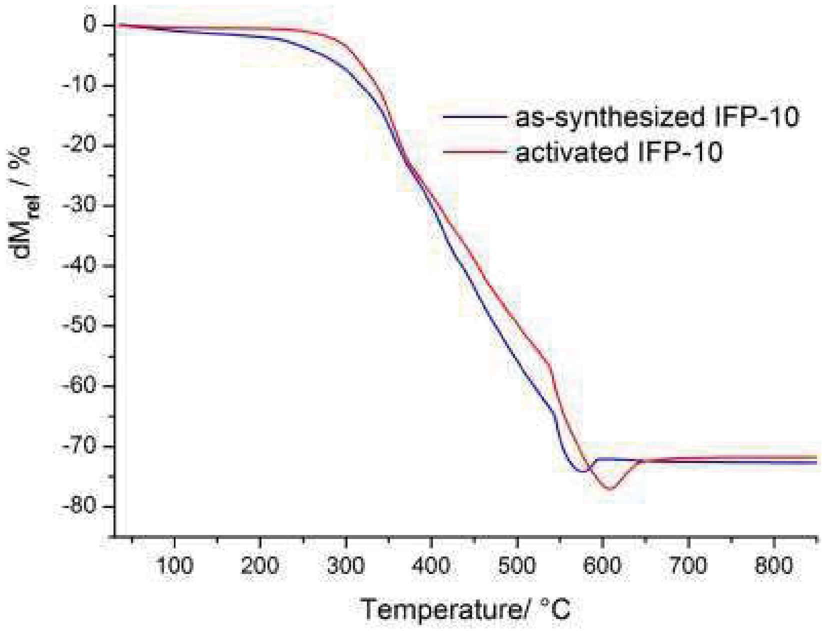

Fig. S3. TGA curves **A)** for IFP-9 and **B)** IFP-10.

7 Gas-sorption measurement

The sample was connected to the preparation port on a Micromeritics ASAP 2020 automatic gas sorption analyzer and degassed under vacuum until the out gassing rate, i.e., the rate of pressure rise in the temporarily closed manifold with the connected sample tube, was less than 2 µTorr/min at the specified temperature 200 °C for 24 h. After weighing, the sample tube was then transferred to the analysis port of the sorption analyzer. All used gases (H_2, He, N_2, CO_2, CH_4) were of ultra high purity (UHP, grade 5.0, 99.999%) and the STP volumes are given according to the NIST standards (293.15 K, 101.325 kPa). Helium gas was used for the determination of the cold and warm free space of the sample tubes. H_2 and N_2 sorption isotherms were measured at 77 K (liquid nitrogen bath), whereas CO_2 and CH_4 sorption isotherms were measured at 298±1 K (passive thermostating) and 273.15 K (ice/deionized water bath). The heat of adsorption value was calculated by using the ASAP 2020 v3.05 software.

References

1 W. K. Anderson, D. Bhattacharjee, and D. M. Houston, *J. Med. Chem.*, 1989, **32**, 119−127.

2 Sheldrick, G. M. SHELXS-97 Program for the Crystal Structure Solution, University of Göttingen, Germany, 1997.

3 Sheldrick, G. M. SHELXL-97 Program for the Crystal Solution Refinement, University of Göttingen, Germany, 1997.

4 (*a*) V. Blatov, Nanocluster analysis of intermetallic structures with the program package TOPOS, Struct. Chem., 2012, **23**, 955–963; (*b*) A. L. Spek, *PLATON*, Multipurpose Crystallographic Tool, Utrecht University, Utrecht, The Netherlands, 2008.

5 J. P. Perdew, K. Burke, M. Ernzerhof, *Phys. Rev. Lett.,* 1996, **77**, 3865–3868.

6 J. M. Soler, E. Artacho, J. D. Gale, A. García, J. Junquera, P. Orde-jón and D. Sánchez Portal, *J. Phys.: Condens. Matter.,* 2002, **14**, 2745 –2779.

7 F. Debatin, A. Thomas, A. Kelling, N. Hedin, Z. Bacsik, I. Senkovska, S. Kaskel, M. Junginger, H. Müller, U. Schilde, C. Jäger, A. Friedrich and H.-J. Holdt, *Angew. Chem. Int. Ed.,* 2010, **49**, 1258–1262.

3.6 Microporous La–Metal–Organic Framework (MOF) with Large Surface Area

Souvik Pal, Asamanjoy Bhunia, Partha P. Jana, Subarna Dey, Jens Möllmer, Christoph Janiak, and Hari Pada Nayek

Chem. Eur. J., 2015, **21**, 2789 – 2792
DOI: 10.1002/chem.201405168, (reference 104)
Impact factor 2015: 5.731

A microporous La–metal-organic framework (MOF) was synthesized by the reaction of $La(NO_3)_3{\cdot}6H_2O$ with 4,4',4"-s-triazine-1,3,5-triyltri-*p*-aminobenzoic acid under solvothermal conditions. The gas sorption measurements of N_2, H_2, CH_4, and CO_2 for IFP-9 and IFP-10 were performed at different temperatures up to 1 bar. The Langmuir and BET surface area were found to be 1295 and 1074 m^2/g, respectively. This MOF showed H_2 uptake of 158.4 cm^3/g at 77 K. At 273 K, the CO_2 and CH_4 uptake values were 76.8 cm^3/g and 19.7 cm^3/g respectively with CO_2/N_2 and CO_2/CH_4 selectivities 12 and 4, respectively.

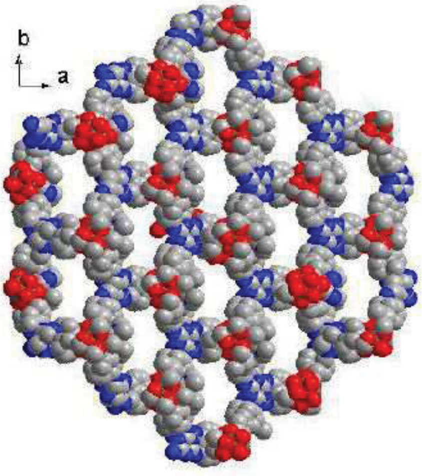

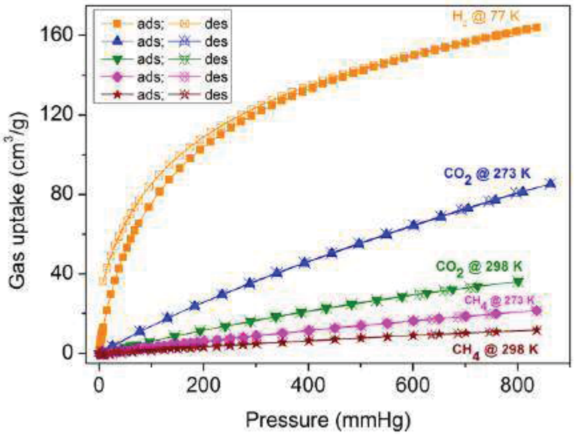

Author's contribution to the work:

- Performing the gas adsorption studies.
- Writing and drawing figures for the gas adsorption part of the manuscript.
- MOF stability test by using H_2O, MeOH and benzene.

ChemPubSoc Europe
DOI: 10.1002/chem.201405168
CHEMISTRY A European Journal
Communication

Lanthanide MOF

Microporous La–Metal–Organic Framework (MOF) with Large Surface Area

Souvik Pal,[a] Asamanjoy Bhunia,[b] Partha P. Jana,[c] Subarna Dey,[b] Jens Möllmer,[d] Christoph Janiak,[b] and Hari Pada Nayek*[a]

Abstract: A microporous La–metal-organic framework (MOF) has been synthesized by the reaction of $La(NO_3)_3\cdot 6H_2O$ with a ligand 4,4′,4′′-s-triazine-1,3,5-triyltri-*p*-aminobenzoate (TATAB) featuring three carboxylate groups. Crystal structure analysis confirms the formation of 3D MOF with hexagonal micropores, a Brunauer–Emmett—Teller (BET) surface area of 1074 $m^2 g^{-1}$ and high thermal and chemical stability. The CO_2 adsorption capacities are 76.8 $cm^3 g^{-1}$ at 273 K and 34.6 $cm^3 g^{-1}$ at 293 K, a highest measured CO_2 uptake for a Ln–MOFs.

Permanent porosity metal–organic frameworks (MOFs) have been successfully employed in such areas as, for example, gas adsorption,[1–4] catalytic organic transformation,[5,6] separation,[7] sensing,[8–10] and drug delivery.[11] Generally, MOFs are synthesized from rigid organic linkers and a transition metal containing secondary building units (SBUs). Lanthanide MOFs with large surface area are rare.[12–14] Yet, lanthanide MOFs have recently gained tremendous attention due to their luminescence and magnetic properties.[15–23] Large coordination sphere and flexible coordination geometry make the control of the final topology and properties of lanthanide MOFs difficult. This often results in the formation of interpenetrated frameworks, which limit the size of the pores, thus affecting the gas adsorption properties of the MOFs.[24–26] Moreover, coordinated solvents (in most cases, H_2O or DMF) to lanthanides play important roles to determine the stability of the lanthanide MOFs. Removal of these solvents from lanthanides often causes collapse of the whole framework. Due to these difficulties, most of the MOFs reported to date were only interesting in terms of their magnetic and luminescence properties. Therefore, construction of lanthanide MOFs with permanent porosity and stability suitable for gas adsorption and separation is still a challenging task.[27]

We have recently engaged in the synthesis of lanthanide MOFs by using a tritopic ligand, 4,4′,4′′-s-triazine-1,3,5-triyltri-*p*-aminobenzoic acid (H_3TATAB)[28] featuring three carboxylate groups (Scheme 1). Ligand H_3TATAB was previously utilized for synthesizing transition metals containing MOFs.[29,30] Herein, we report that a three-dimensional (3D) lanthanum MOF, $[La(TATAB)(H_2O)]\cdot 6H_2O$ (**1**), which has been synthesized by treating H_3TATAB with $La(NO_3)_3\cdot 6H_2O$ in DMF/H_2O/EtOH at 60 °C under solvothermal conditions (detailed experimental procedures and characterizations techniques are provided in the Supporting Information).

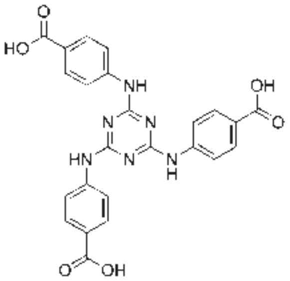

Scheme 1. Structure of ligand, 4,4′,4′′-s-triazine-1,3,5-triyltri-*p*-aminobenzoic acid (H_3TATAB).

The solid-state structure of **1** was obtained by single-crystal X-ray diffraction analysis. According to structural analysis, **1** is crystallized in monoclinic space group *Cc* with four formula units per unit cell. The solid-state structural data showed that **1** is a non-interpenetrated three-dimensional MOF formed by the trivalent cations La^{3+} bridged by TATAB ligands. The asymmetric unit contains one TATAB anion, one La^{3+} ion coordinated by one H_2O molecule, and six water molecules. Each TATAB ligand coordinates six La^{3+} ions by exclusively its carboxylate groups, each of which is situated in a coordination sphere bridging/chelating over two La^{3+} ions (Figure 1 a). The La^{3+} ions are decacoordinate by nine oxygen atoms from six TATAB ligands and one oxygen atom of a coordinated water molecule (Figure 1 b). The La polyhedron has ten vertices, 24 edges, and 16 triangular faces, and thus, represents a distorted gyroelongated square bipyramid (Figure S3 in the Supporting Information). The bridging interactions are responsible for organization

---

[a] S. Pal, Dr. H. P. Nayek
Department of Applied Chemistry, Indian School of Mines
Dhanbad-826004, Jharkhand (India)
E-mail: hpnayek@yahoo.com

[b] Dr. A. Bhunia, S. Dey, Prof. Dr. C. Janiak
Institut für Anorganische Chemie und Strukturchemie
Heine-Universität Düsseldorf, 40204 Düsseldorf (Germany)

[c] Dr. P. P. Jana
Centre for Analysis and Synthesis, Department of Chemistry
Lund University, Getingevagen 60, Box 124, SE-22100, Lund (Sweden)

[d] Dr. J. Möllmer
Institut für Nichtklassische Chemie e.V. Leipzig, 04318 Leipzig (Germany)

Supporting information for this article is available on the WWW under http://dx.doi.org/10.1002/chem.201405168.

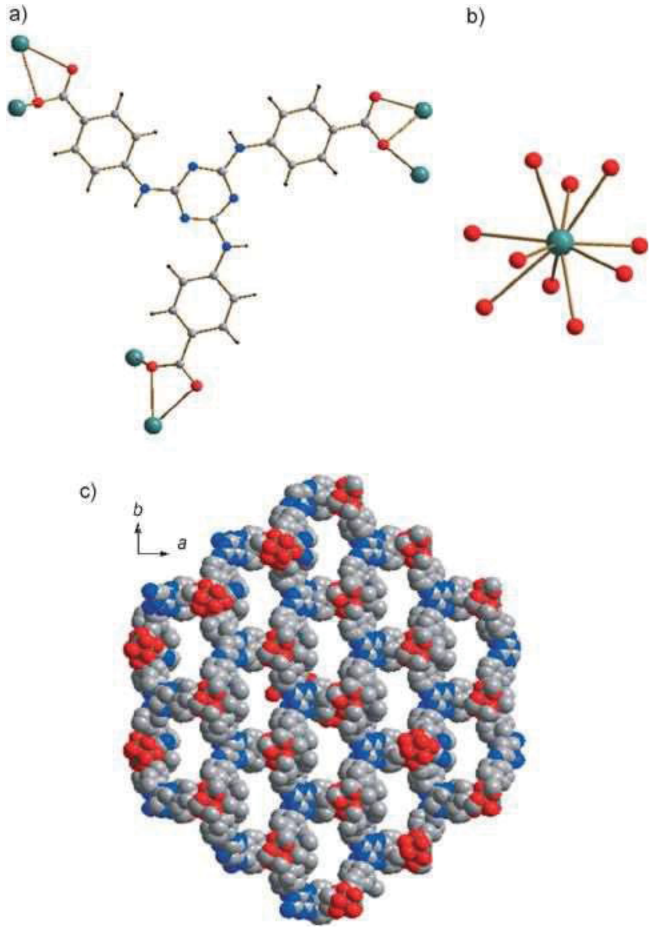

Figure 1. a) TATAB ligand bridging La^{3+} ions; b) one SBU, a decacoordinate La^{3+} ion; and c) view of microporous channels along crystallographic *c* axis.

of the metal atoms into a three-dimensional porous framework structure with microporous channels along the crystallographic *c* axis (Figure 1 c). Remarkably, compound **1** crystallizes in the non-centrosymmetric polar space group *Cc*. Accordingly, all parts of the structure must be oriented in the same direction along the polar axis: with their aqua ligands: for example, the La polyhedra are all pointing in the same direction (roughly along the *a* axis in Figure S4 a, c in the Supporting Information). The polar packing within the chain and of adjacent chains in the crystal of **1** probably originates from the hydrogen-bonding interactions of the aqua ligands with solvent molecules in the channels.[31–35] The thermal stability of **1** was investigated by thermogravimetric (TG) analysis. The TG curve shows an initial weight loss up to 130 °C (Figure S5 in the Supporting Information). This is due to the removal of six free water molecules and the aqua ligand.

The remaining framework is stable up to 437 °C and slowly decomposes upon further temperature increase. To confirm the chemical stability of **1**, we suspended **1** in boiling benzene, methanol, and water, upon heating for three days. PXRD analysis was applied after such extensive treatments, and it showed that full crystallinity remained (Figure S6 in the Supporting Information). The porosity of **1** was characterized by N_2 sorption measurements. The isotherm shows a steep slope at low P/P_0 values with a type I character, which is typical for microporous materials (Figure 2).[36] The calculated Langmuir and Brunauer–Emmett—Teller (BET) surface area were found to be 1295 and 1074 $m^2 g^{-1}$, respectively. The absence of hysteresis during the adsorption and desorption points indicated that the frameworks were stable and rigid. To the best of our knowledge, this surface area lies towards the upper end compared to other lanthanide (Ln = La–Lu)-based MOFs (Table 1). It is comparable even with highest reported surface area for rare-earth-based MOF.[37] The pore-size distribution of **1** was determined by non-local density functional theory (NL DFT) by using a slit-pore model based on the N_2 adsorption isotherms. A narrow distribution of micropores cantered at 6, 7, and 13 Å were observed (insert in Figure 2). The adsorption isotherm of other gases, such as H_2, CO_2, and CH_4, were also obtained at low pressure (up to 1 bar; Figure 3). MOF **1** showed H_2 sorption of 158.4 $cm^3 g^{-1}$ at 77 K with very small hysteresis over the pressure range 0–0.3 bar. Although the BET surface area of **1** was higher than previously reported Ln–MOFs, its H_2 adsorption was lower than the PCM-16. CO_2 sorption of **1** was measured at 273 K and 293 K, which showed fully reversible adsorption and desorption curve. The CO_2 adsorption capacities were

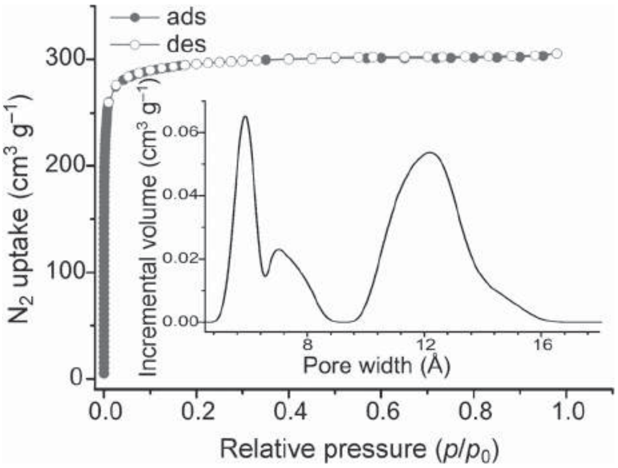

Figure 2. N_2 sorption isotherm at 77 K. Inset: NL-DFT pore-size distribution curve of **1**.

Table 1. Comparison of gas-sorption data of selected extrinsic Ln–MOFs.

Ln–MOF (Ln = La–Lu)	S_{BET} [$m^2 g^{-1}$][a]	H_2 [$cm^3 g^{-1}$][b]	CO_2 [$cm^3 g^{-1}$][c]	CH_4 [$cm^3 g^{-1}$][c]
1	1074	158.4	76.8	19.7
MIL-103[12]	730–930	–[d]	–[d]	–[d]
Dy(btc)(H_2O)·DMF[43][e]	655	147.9	–[d]	–[d]
Tb(btc)[44][e]	678	–[d]	–[d]	–[d]
PCN-17[38,24]	606–930	90–123	–[d]	–[d]
PCM-16[45]	620	295.61	–[d]	–[d]
PCM-15[32]	674	218.08	63 (278 K)	–[d]

[a] Calculated BET surface area over the pressure range 0.01–0.05 P/P_0. [b] H_2 uptake at 77 K. [c] Gas uptake at 273 K. [d] Not reported. [e] btc = 1,3,5-Benzenetricarboxylate.

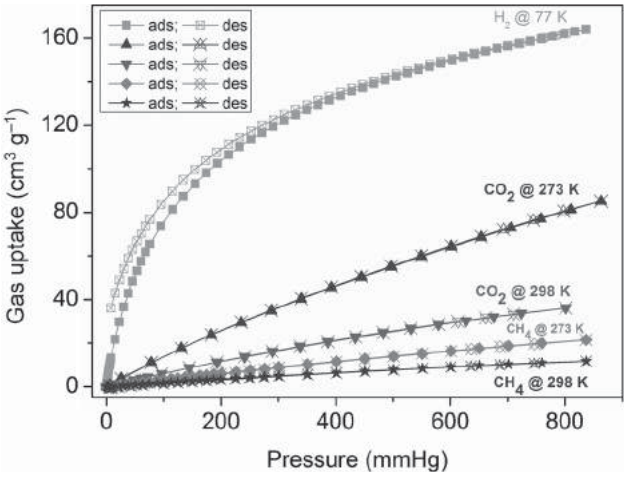

Figure 3. H_2, CO_2, and CH_4 sorption isotherm at 1 bar.

76.8 cm^3 g^{-1} at 273 K and 34.6 cm^3 g^{-1} at 293 K (Figure 3). Interestingly, such sorption values represent the highest measured CO_2 uptake for a Ln–MOFs.[38] The high CO_2 uptake of compound **1** is due to the strong hydrogen bonding between NH groups of ligand (H_3TATAB) and CO_2 molecules.[39,40] To further understand the adsorption properties, the isosteric heats of adsorption were calculated from the CO_2 adsorption isotherms at 273 and 293 K (Figure S10 in the Supporting Information). At zero loading, the Q_{st} value (isosteric heats of adsorption; $-\Delta H$) is 32 kJ mol^{-1}. Upon increasing the loading, the Q_{st} value decreased rapidly to 22 kJ mol^{-1}, which is still well above the heat of liquefaction of bulk CO_2 with 17 kJ mol^{-1}.[41] The high Q_{st} value can be attributed to the high polar framework and the pore-size effect.

The high adsorption enthalpy at zero coverage can be explained by the initial filling of the small ultra micropores with 4 Å diameter (Figure S8 in the Supporting Information) with adsorbate–surface interactions to both sides or ends of the CO_2 molecules. CH_4 sorption value of **1** were 19.7 cm^3 g^{-1} at 273 K and 10.8 cm^3 g^{-1} at 293 K (Figure 3). Noteworthy, for Ln–MOFs, no CH_4 sorption data have been recorded to date. From the available single-gas adsorption isotherms, the ratio of the initial slopes in the Henry region (0 to ca. 0.12 bar) of the adsorption isotherms (Figure S11 in the Supporting Information) can be used to determine the gas selectivities exhibited by **1**. CO_2/N_2 and CO_2/CH_4 selectivities were found to be 12:1 and 4:1 at 273 K, respectively. The selectivity does not depend only on the size of the gas components (kinetic diameter: CO_2 3.3 Å, N_2 3.64 Å, and CH_4 3.8 Å), but also on the polarizability of the surface and of the gas components. The selectivity for CO_2 over N_2 and CO_2 over CH_4 can be ascribed to the combined effects of the size of the pore apertures and the strong quadrupolar interactions of CO_2 with nitrogen atoms present on the pore surface. Moreover, the gas selectivities for CO_2/N_2 and CO_2/CH_4 were also predicted by ideal adsorbed solution theory (IAST; Figure S12 in the Supporting Information).[42] The CO_2/N_2 selectivity at 273 K was higher than 20, whereas the CO_2/CH_4 selectivity at 273 was higher than four (Figure S12 in the Supporting Information). Interestingly, **1** maintained its crystallinity after gas-sorption studies (Figure S7 in the Supporting Information).

We have constructed a highly stable microporous lanthanum metal–organic framework, [La(TATAB)(H_2O)]·6 H_2O (**1**) exhibiting exceptional surface area for N_2 gas adsorption. H_2, CO_2 adsorption, and for the first time CH_4 gas adsorption was investigated for any lanthanide-based MOF. The MOF **1** showed high selectivity for CO_2 over N_2 and CO_2 over CH_4, and retained its crystallinity after gas adsorption. The MOF also showed high chemical stability towards boiling benzene, methanol, and water. Current work includes the synthesis of various lanthanide–MOFs suitable for gas adsorption, catalysis, and luminescence studies.

Experimental Section

Synthesis of [La(TATAB)(H_2O)]·6 H_2O (1)

A mixture of H_3L(24 mg, 0.049 mmol) and La(NO)$_3$·6 H_2O (21 mg, 0.049 mmol) were dissolved in a mixed solvent of DMF (2.5 mL), EtOH (2.5 mL), H_2O (1 mL), and triethylamine (TEA,0.024 mL) at RT. HNO_3 (2 M) was added dropwise, until the mixture has become clear. The mixture was sealed in a 30 mL Teflon-lined autoclave. The autoclave was heated to 60 °C, held for 72 h, and cooled to RT. Colorless needle-shaped crystals of **1** were collected. Yield: 30 %, 0.011 g; elemental analysis calcd (%) for $C_{24}H_{29}N_6O_{13}La$ (M_w = 748.44 g mol^{-1}): C 38.52, H 3.91, N 11.23; found: C 38.23, H 3.66, N 11.07; IR (KBr pellet): $\tilde{\nu}$ = 3410 (br), 1625 (m), 1487 (s), 1394 (s), 1348 (s), 1237 (m), 1172 (m), 860 (w), 784 (m), 692 (w), 654 (w), 498 (w), 460 cm^{-1} (w).

Acknowledgements

This work was financially supported by SERB, DST, India under FAST Track Scheme (Order No. SR/FT/CS-96/2011, dated 15/06/2012). We also thank Indian School of Mines, Dhanbad.

Keywords: adsorption · chemical stability · lanthanides · metal–organic frameworks · structure elucidation

[1] O. K. Farha, I. Eryazici, N. C. Jeong, B. G. Hauser, C. E. Wilmer, A. A. Sarjeant, R. Q. Snurr, S. T. Nguyen, A. Ö. Yazaydın, J. T. Hupp, *J. Am. Chem. Soc.* **2012**, *134*, 15016 – 15021.

[2] D. Zhao, D. Yuan, D. Sun, H.-C. Zhou, *J. Am. Chem. Soc.* **2009**, *131*, 9186 – 9188.

[3] K. Sumida, D. L. Rogow, J. A. Mason, T. M. McDonald, E. D. Bloch, Z. R. Herm, T.-H. Bae, J. R. Long, *Chem. Rev.* **2012**, *112*, 724 – 781.

[4] M. P. Suh, H. J. Park, T. K. Prasad, D.-W. Lim, *Chem. Rev.* **2012**, *112*, 782 – 835.

[5] A. Corma, H. García, F. X. Llabrés i Xamena, *Chem. Rev.* **2010**, *110*, 4606 – 4655.

[6] R. F. D'Vries, M. Iglesias, N. Snejko, E. Gutiérrez-Puebla, M. A. Monge, *Inorg. Chem.* **2012**, *51*, 11349 – 11355.

[7] Z. Lin, R. Zou, J. Liang, W. Xia, D. Xia, Y. Wang, J. Lin, T. Hu, Q. Chen, X. Wang, Y. Zhao, A. K. Burrell, *J. Mater. Chem.* **2012**, *22*, 7813 – 7818.

[8] L. E. Kreno, K. Leong, O. K. Farha, M. Allendorf, R. P. Van Duyne, J. T. Hupp, *Chem. Rev.* **2012**, *112*, 1105 – 1125.

[9] A. Carné-Sánchez, C. S. Bonnet, I. Imaz, J. Lorenzo, É. Tóth, D. Maspoch, *J. Am. Chem. Soc.* **2013**, *135*, 17711 – 17714.

[10] Y. Zhou, B. Yan, *Inorg. Chem.* **2014**, *53*, 3456 – 3463.

[11] P. Horcajada, R. Gref, T. Baati, P. K. Allan, G. Maurin, P. Couvreur, G. Férey, R. E. Morris, C. Serre, *Chem. Rev.* **2012**, *112*, 1232 – 1268.

[12] T. Devic, C. Serre, N. Audebrand, J. Marrot, G. Férey, *J. Am. Chem. Soc.* **2005**, *127*, 12788 – 12789.
[13] L. Pan, K. M. Adams, H. E. Hernandez, X. Wang, C. Zheng, Y. Hattori, K. Kaneko, *J. Am. Chem. Soc.* **2003**, *125*, 3062 – 3067.
[14] Q. Tang, Y. Liu, S. Liu, D. He, J. Miao, X. Wang, G. Yang, Z. Shi, Z. Zheng, *J. Am. Chem. Soc.* **2014**, *136*, 12444 – 12449.
[15] L.-N. Jia, L. Hou, L. Wei, X.-J. Jing, B. Liu, Y.-Y. Wang, Q.-Z. Shi, *Cryst. Growth Des.* **2013**, *13*, 1570 – 1576.
[16] B. D. Chandler, J. O. Yu, D. T. Cramb, G. K. H. Shimizu, *Chem. Mater.* **2007**, *19*, 4467 – 4473.
[17] Q. Tang, S. Liu, Y. Liu, J. Miao, S. Li, L. Zhang, Z. Shi, Z. Zheng, *Inorg. Chem.* **2013**, *52*, 2799 – 2801.
[18] Y.-G. Huang, F.-L. Jiang, M.-C. Hong, *Coord. Chem. Rev.* **2009**, *253*, 2814 – 2834.
[19] J. Rocha, L. D. Carlos, F. A. A. Paz, D. Ananias, *Chem. Soc. Rev.* **2011**, *40*, 926 – 940.
[20] Y. Zhou, M. Hong, X. Wu, *Chem. Commun.* **2006**, 135 – 143.
[21] Q.-Y. Yang, K. Wu, J.-J. Jiang, C.-W. Hsu, M. Pan, J.-M. Lehn, C.-Y. Su, *Chem. Commun.* **2014**, *50*, 7702 – 7704.
[22] Y.-H. Zhang, X. Li, S. Song, *Chem. Commun.* **2013**, *49*, 10397 – 10399.
[23] D. F. Sava, L. E. S. Rohwer, M. A. Rodriguez, T. M. Nenoff, *J. Am. Chem. Soc.* **2012**, *134*, 3983 – 3986.
[24] S. Ma, D. Yuan, X.-S. Wang, H.-C. Zhou, *Inorg. Chem.* **2009**, *48*, 2072 – 2077.
[25] T. M. Reineke, M. Eddaoudi, M. O'Keeffe, O. M. Yaghi, *Angew. Chem. Int. Ed.* **1999**, *38*, 2590 – 2594; *Angew. Chem.* **1999**, *111*, 2712 – 2716.
[26] H. He, H. Ma, D. Sun, L. Zhang, R. Wang, D. Sun, *Cryst. Growth Des.* **2013**, *13*, 3154 – 3161.
[27] Z.-J. Lin, Z. Yang, T.-F. Liu, Y.-B. Huang, R. Cao, *Inorg. Chem.* **2012**, *51*, 1813 – 1820.
[28] Q.-R. Fang, D.-Q. Yuan, J. Sculley, J.-R. Li, Z.-B. Han, H.-C. Zhou, *Inorg. Chem.* **2010**, *49*, 11637 – 11642.
[29] X.-S. Wang, S. Ma, D. Sun, S. Parkin, H.-C. Zhou, *J. Am. Chem. Soc.* **2006**, *128*, 16474 – 16475.
[30] X. Zhao, H. He, F. Dai, D. Sun, Y. Ke, *Inorg. Chem.* **2010**, *49*, 8650 – 8652.
[31] W.-W. Zhou, J.-T. Chen, G. Xu, M.-S. Wang, J.-P. Zou, X.-F. Long, G.-J. Wang, G.-C. Guo, J.-S. Huang, *Chem. Commun.* **2008**, 2762 – 2764.
[32] M. D. Stephenson, M. J. Hardie, *Dalton Trans.* **2006**, 3407 – 3417.
[33] A.-C. Chamayou, M. A. Neelakantan, S. Thalamuthu, C. Janiak, *Inorg. Chim. Acta* **2011**, *365*, 447 – 450.
[34] J. Ruiz, V. Rodriguez, C. de Haro, A. Espinosa, J. Perez, C. Janiak, *Dalton Trans.* **2010**, *39*, 3290 – 3301.
[35] C. Janiak, A.-C. Chamayou, A. K. M. Royhan Uddin, M. Uddin, K. S. Hagen, M. Enamullah, *Dalton Trans.* **2009**, 3698 – 3709.
[36] D. H. E. K. S. W. Sing, R. A. W. Haul, L. Moscou, R. A. Pierotti, J. Rouqurol, T. Siemieniewska, in *Reporting Physisorption Data for Gas/Solid Systems with Special Reference to the Determination of Surface Area and Porosity* (Recommendations 1984), *Pure and Appl. Chem. Vol. 57*, **1985**, pp. 603 – 619.
[37] K. Tang, R. Yun, Z. Lu, L. Du, M. Zhang, Q. Wang, H. Liu, *Cryst. Growth Des.* **2013**, *13*, 1382 – 1385.
[38] S. Ma, X.-S. Wang, D. Yuan, H.-C. Zhou, *Angew. Chem. Int. Ed.* **2008**, *47*, 4130 – 4133; *Angew. Chem.* **2008**, *120*, 4198 – 4201.
[39] A. Khutia, C. Janiak, *Dalton Trans.* **2014**, *43*, 1338 – 1347.
[40] N. Planas, A. L. Dzubak, R. Poloni, L.-C. Lin, A. McManus, T. M. McDonald, J. B. Neaton, J. R. Long, B. Smit, L. Gagliardi, *J. Am. Chem. Soc.* **2013**, *135*, 7402 – 7405.
[41] A. Bhunia, I. Boldog, A. Moller, C. Janiak, *J. Mater. Chem. A* **2013**, *1*, 14990 – 14999.
[42] W.-M. Liao, H.-T. Shi, X.-H. Shi, Y.-G. Yin, *Dalton Trans.* **2014**, *43*, 15305 – 15307.
[43] X. Guo, G. Zhu, Z. Li, F. Sun, Z. Yang, S. Qiu, *Chem. Commun.* **2006**, 3172 – 3174.
[44] N. A. Khan, M. M. Haque, S. H. Jhung, *Eur. J. Inorg. Chem.* **2010**, 4975 – 4981.
[45] I. A. Ibarra, J. W. Yoon, J.-S. Chang, S. K. Lee, V. M. Lynch, S. M. Humphrey, *Inorg. Chem.* **2012**, *51*, 12242 – 12247.

Received: September 6, 2014

CHEMISTRY
A European Journal

Supporting Information

Microporous La–Metal–Organic Framework (MOF) with Large Surface Area

Souvik Pal,[a] Asamanjoy Bhunia,[b] Partha P. Jana,[c] Subarna Dey,[b] Jens Möllmer,[d]
Christoph Janiak,[b] and Hari Pada Nayek*[a]

chem_201405168_sm_miscellaneous_information.pdf

Materials and General Characterizations:

All chemicals and solvents employed for the synthesis were of analytical grade and used as received without further purifications. 4,4′,4″-s-triazine-1,3,5-triyltri-p-aminobenzoic acid (H_3TATAB) was prepared according to the literature procedure.[1] Elemental analyses were performed on a VARIO MICRO cube analyser by Elemental analyser system GMBH. IR spectra in KBr (4500-500 cm^{-1}) were recorded using a Perkin–Elmer RXI FT-IR spectrometer. The simulated powder patterns were calculated using data from single crystal X-ray diffraction.Energy dispersive X-ray analysis (EDX)analysis was performed by Hitachi S3400N instrument.Thermogravimetric analyses (TGA) were performed with a NETZSCH leading Thermal analysis STA449F_3 Jupiter thermal analyser system in a dynamic atmosphere of N_2 at a heating rate of 10 °C/min. Powder X-ray diffraction (PXRD) data was collected on a Bruker D2 Phaserdiffractometer using a flat sample holder (also a flat silicon, low background sample holder) and Cu $K\alpha_1/\alpha_2$ radiation with $\lambda = 1.5418$ Å at 30 kV covering 2theta angles 5-50° over a time of 2 h. Diffractograms were obtained on flat layer sample holders where at low angle the beam spot is strongly broadened so that only a fraction of the reflected radiation reaches the detector which leads to low relative intensities measured at $2\theta < 7°$. For hygroscopic or air-sensitive samples, the sample holder can be sealed with a dome. Sorption isotherms were measured using a Micromeritics ASAP 2020 automatic gas sorption analyzer equipped with oil-free vacuum pumps (ultimate vacuum $<10^{-8}$ mbar) and valves, which guaranteed contamination free measurements. The sample was connected to the preparation port of the sorption analyzer and degassed under vacuum until the outgassing rate, i.e., the rate of pressure rise in the temporarily closed manifold with the connected sample tube, was less than 2 μTorr/min at the specified temperature 180 °C. After weighing, the sample tube was then transferred to the analysis port of the sorption analyzer. All used gases (H_2, He, N_2, CO_2, CH_4) were of ultra high purity (UHP, grade 5.0, 99.999%) and the STP volumes are given according to the NIST standards (293.15 K, 101.325 kPa). Helium gas was used for the determination of the cold and warm free space of the sample tubes. H_2 and N_2 sorption isotherms were measured at 77 K (liquid nitrogen bath), whereas CO_2 and CH_4 sorption isotherms were measured at 293±1 K (passive thermostating)and 273.15 K (ice/deionized water bath). The heat of adsorption values and the DFT pore size distributions (‘N_2 DFT slit pore’ model) were calculated out using the ASAP 2020 v3.05 software.

Synthesis of [La(TATAB)(H_2O)].6 H_2O (1):

A mixture of H_3L(24 mg, 0.049 mmol) and $La(NO)_3{\cdot}6\ H_2O$(21 mg, 0.049 mmol) was dissolved in a mixed solvent of DMF (2.5 mL), EtOH (2.5 mL), H_2O (1 mL) and triethylamine (TEA, 0.024 mL) at a room temperature. HNO_3 (2 M) was added drop wise until the mixture become clear. This mixture sealed in a 30 mL Teflon-lined autoclave. The autoclave was heated to 60 ℃, held for 72 h and cooled to a room temperature. Colorless needle shaped single crystal of **1** were collected. Yield: 30%. Anal. Calc. for $C_4H_{29}N_6O_{13}La$ (%): C, 38.52; H, 3.91; N, 11.23; Found: C, 38.23; H, 3.66; N, 11.07; IR (KBr pellet, cm^{-1}): 3410 (br), 1625 (m), 1487 (s), 1394 (s), 1348 (s), 1237 (m), 1172 (m), 860 (w), 784 (m), 692 (w), 654 (w), 498 (w), 460 (w).

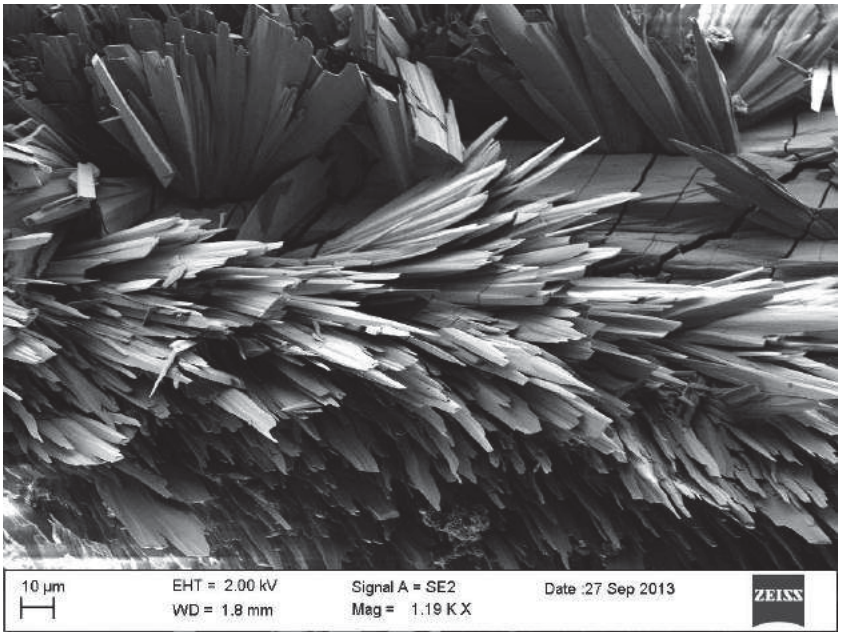

Figure S1: Fe-SEM picture of single crystals of **1**.

IR analysis:

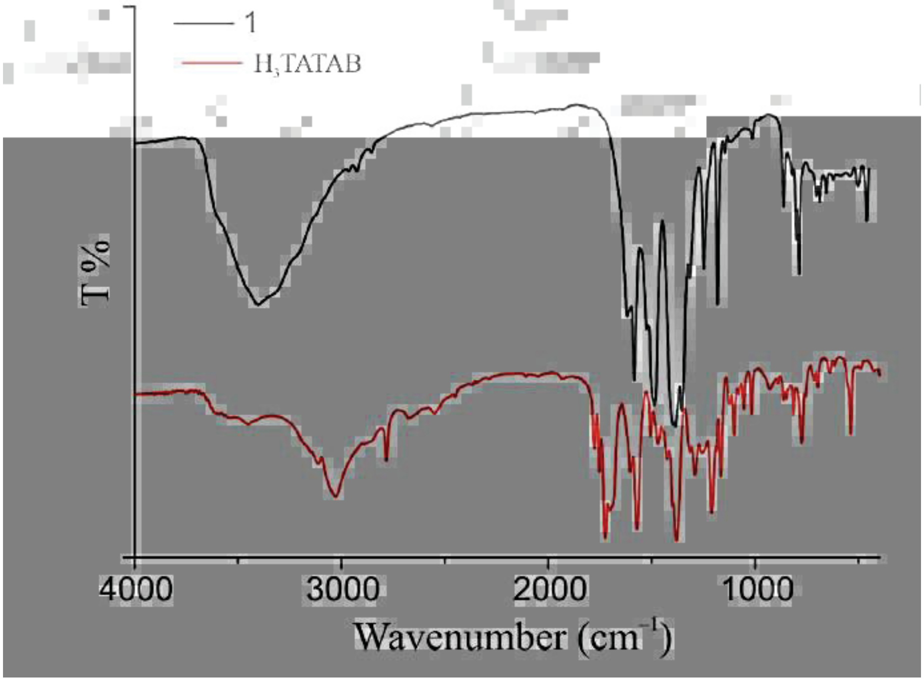

Figure S2: IR spectra of **H$_3$TATAB** and **1**.

The IR spectrum of **1** shows strong absorption bands at 1584 and 1480 cm^{-1} which are attributed to the asymmetric and symmetric stretching vibrations of the coordinated carboxylate groups of H$_3$TATAB respectively. [**ν**(C=N)] stretching vibrations appear at 1525 and 1352 cm^{-1}. The bands at 1726 and 3031 cm^{-1} of H$_3$TATAB owing to [**ν**(COOH)] and [**ν**(OH)]stretching respectively disappear in **1** due to complete deprotonation carboxylic moiety. A broad brand at 3401 cm^{-1} appears due to [**ν**(OH)] stretching of the water molecules

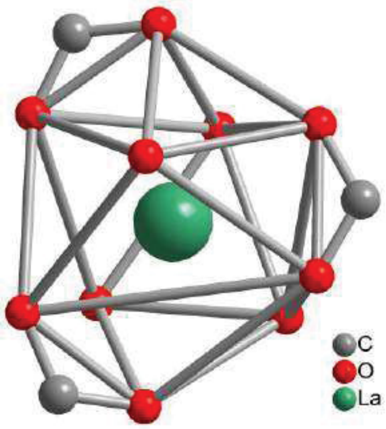

(a)

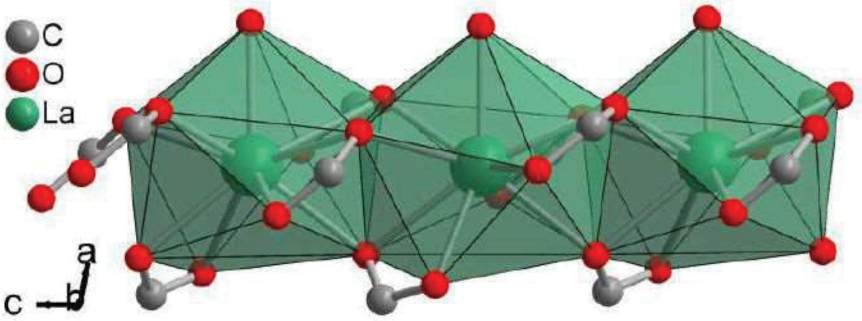

(b)

Figure S3: (a) Polyhedra around a La ion in **1** as a distorted gyroelongated square dipyramid. Only the C atoms of chelating carboxyl groups are shown for an understanding of the distortion. (b) Chain of face-sharing La polyhedra.

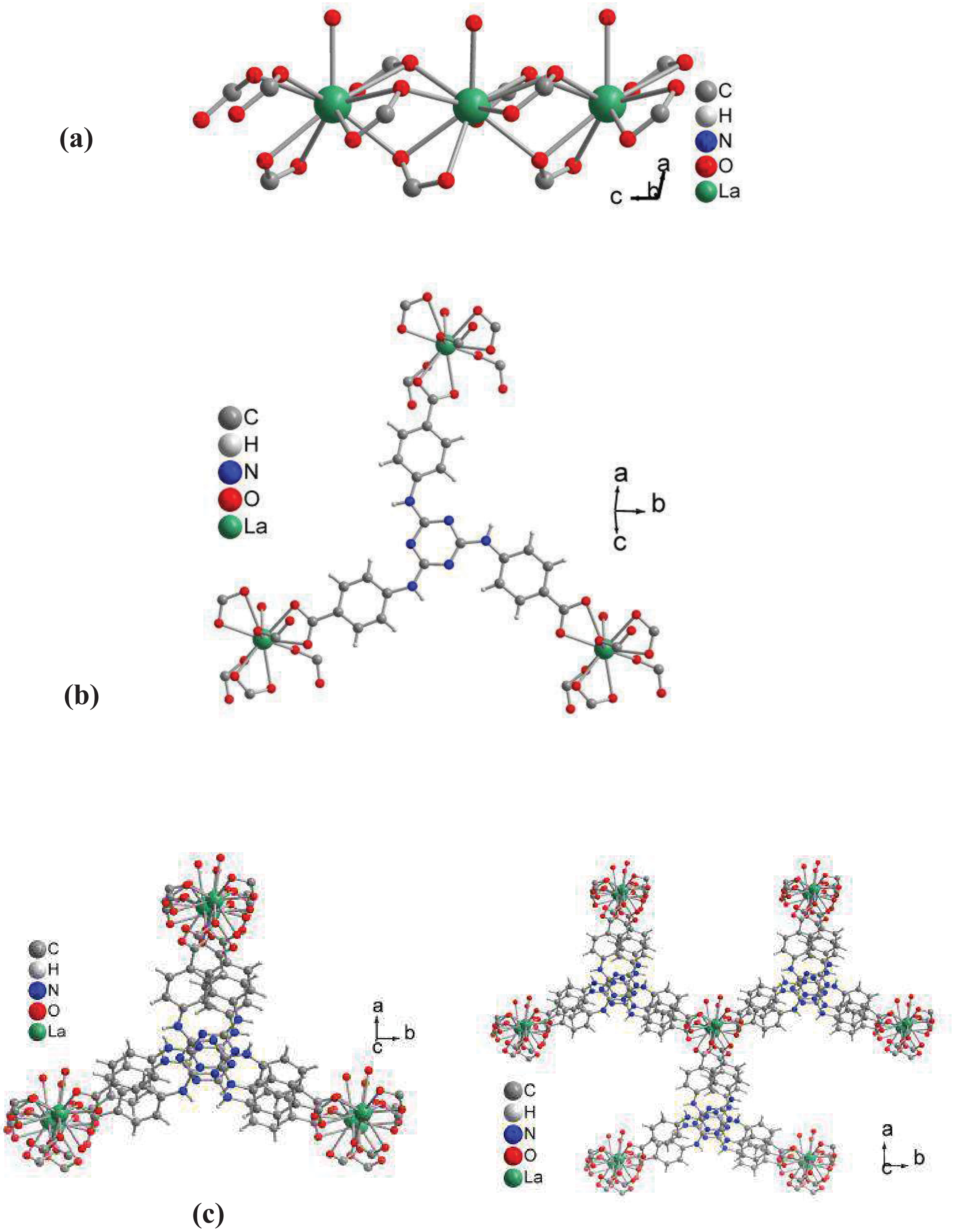

Figure S4: (a) Chain of carboxylate-bridged La ions. (b) Connections of La atoms from adjacent chains and (c) Connection of adjacent, parallel La-carboxylate chains into a 3D network with hexagonal channels.

Thermogravimetric Analysis:

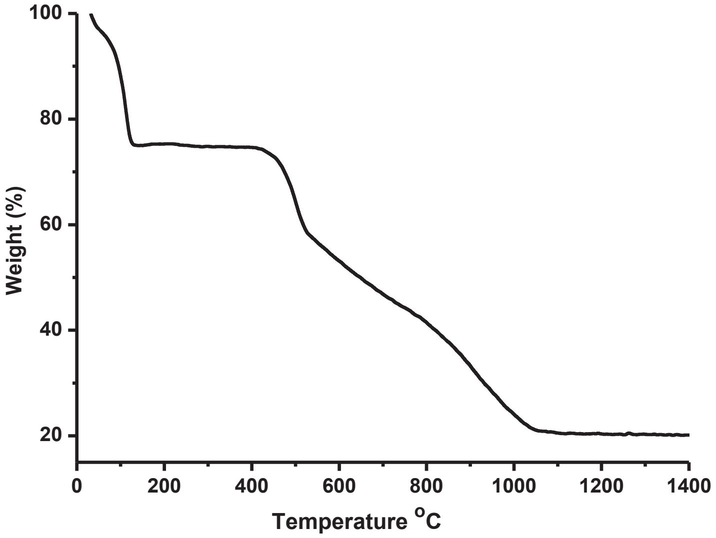

Figure S5: TGA curve of **1**.

Chemical Stability

The chemical stability of **1** was studied by suspending the compound in boiling benzene, methanol and water condition for three days that reflect extreme operational parameters of typical industrial chemical processes. After such extensive experiment, **1** was retained fully crystalline integrity as confirmed by powder X-ray diffraction patterns.

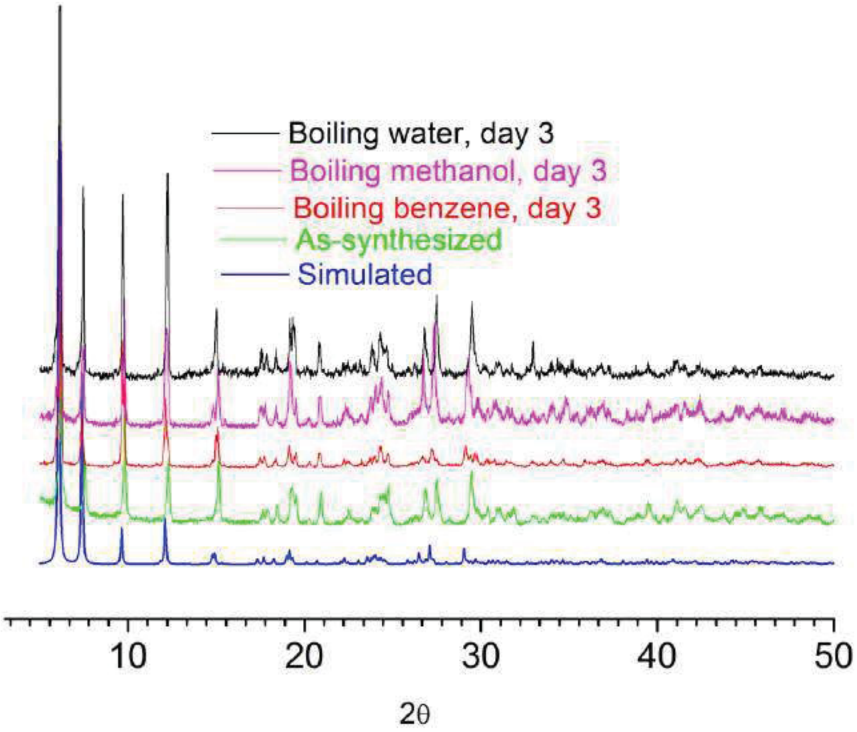

Figure S6: Powder X-ray diffraction patterns of as synthesized and after stability tests in refluxing methanol, benzene and water.

Powder X-ray diffraction:

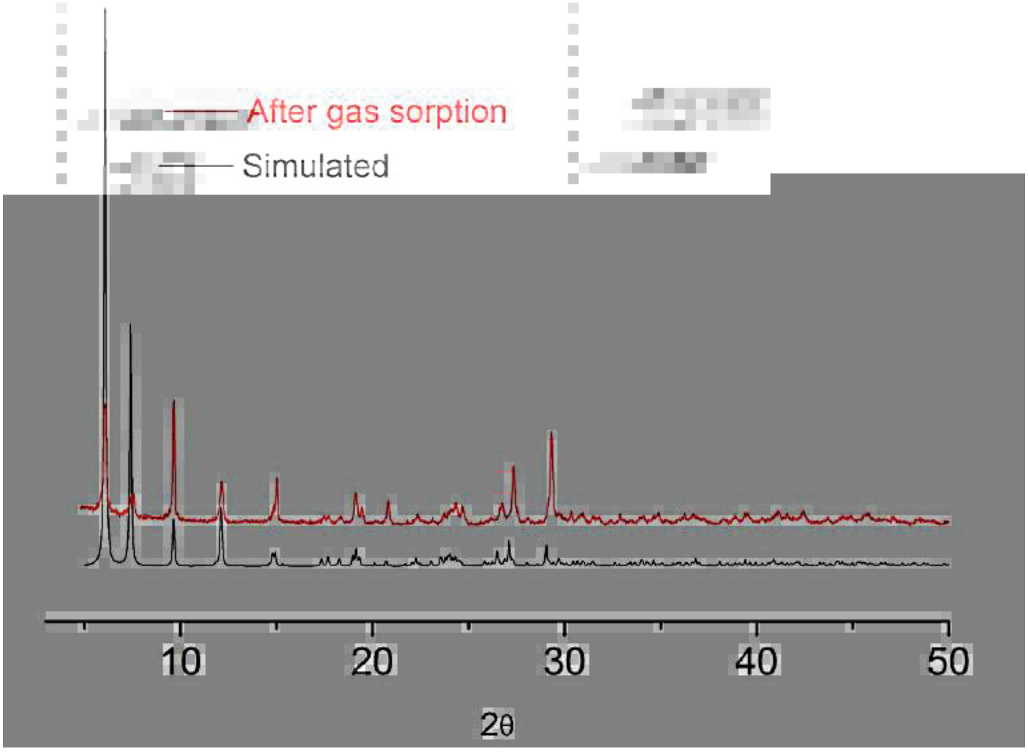

Figure S7: Powder X-ray diffraction patterns of as synthesized **1**.

Pore size distribution:

Fig. S8 show the micropore distribution plot of N_2 measurement at 77 K as well as CO_2 measurement at 273 K. A narrow distribution of micropores centered at 6.7 and 13 Å were observed which is comparable with the small and larger channel diameter (~ 6.4 and 13.1 Å, respectively) obtained from X-ray structure. At 273 K and under higher absolute pressures CO_2 molecules can more easily access ultramicropores than N_2 at ~77 K and the kinetic diameter of CO_2 (3.3 Å) is also a little bit smaller than for N_2 (3.64 Å). So, advantages for of CO_2 micropore analysis at 273 K versus N_2 analysis at 77 K are (i) faster analysis and (ii) greater confidence that measured adsorption points are equilibrated (both due to higher diffusion rates) and (iii) extension of the range of analysis to pores of smaller sizes that are accessible to CO_2 molecules but not to N_2.[1] From the CO_2 adsorption isotherm at 273 K, the pore size distribution was derived between 4-10 Å by using NLDFT with a "CO_2 on carbon based slit-pore model"(see Figure S8, bellow) and showed a relative maximum at around ~ 6 Å which is comparable with the small channel diameter (~6.4 Å) found from X-ray structure.

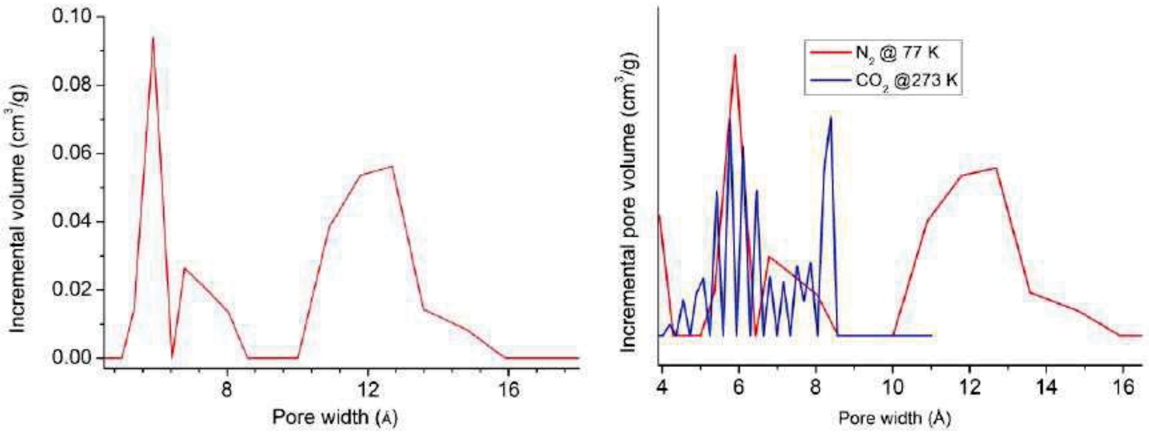

Figure S8: Left: NL-DFT pore size distribution curve of 1 at 77 K. Right: Pore size distribution of 1 from N_2 (red) and CO_2 (blue) adsorption isotherm analysis at 77 K and 273 K, respectively.

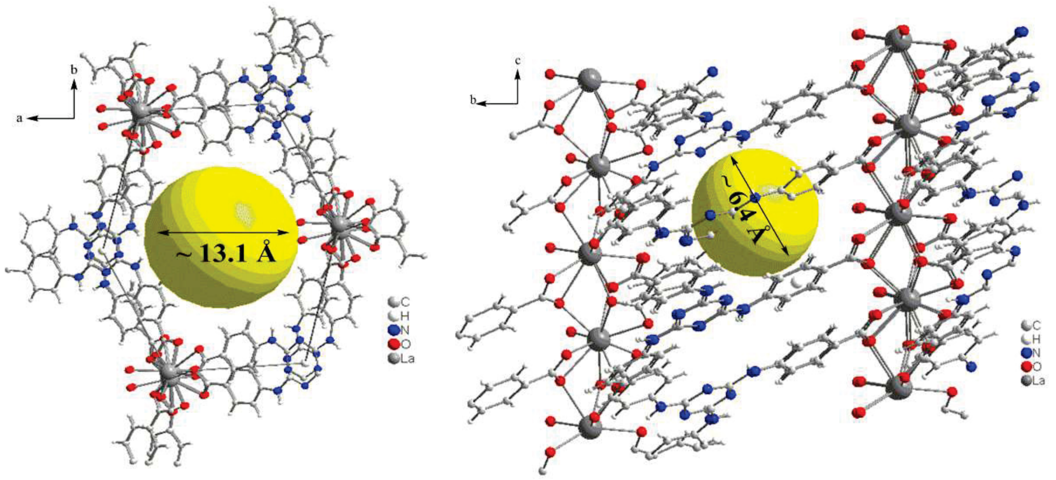

Figure S9: Ball-and-stick view of the two cages

Heat of adsorption

From two adsorption isotherms acquired at different temperatures T_1 and T_2, the differential heat of adsorption $\Delta H_{ads,diff}$ can be calculated for any amount of adsorbed substance after determining the required relative pressures p_1 and p_2. A modified form of the Clausius-Clapeyron equation is used (eq (1)).$\Delta H_{ads,diff}$ was calculated over the whole adsorption range from the 273 K and 293 K isotherms for CO_2.

(1)

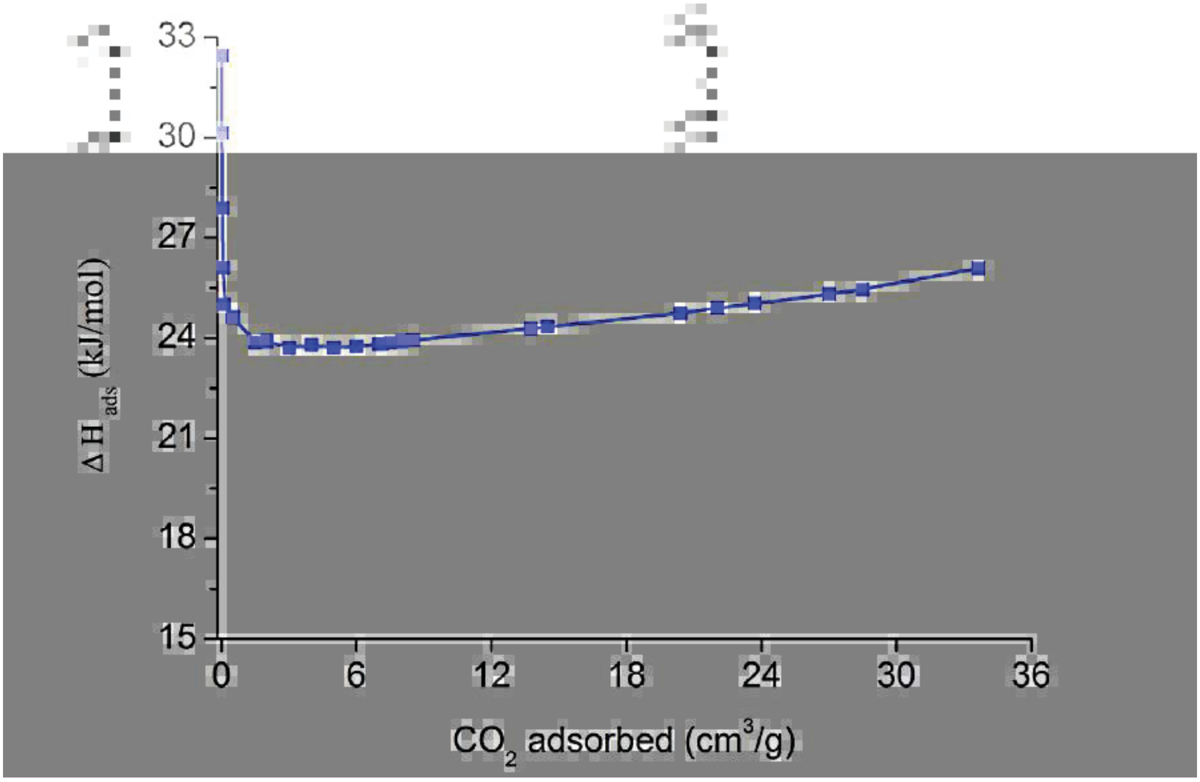

Figure S10: Isosteric heat of adsorption: calculated from CO_2 adsorption isotherms at 273 K and 293 K.

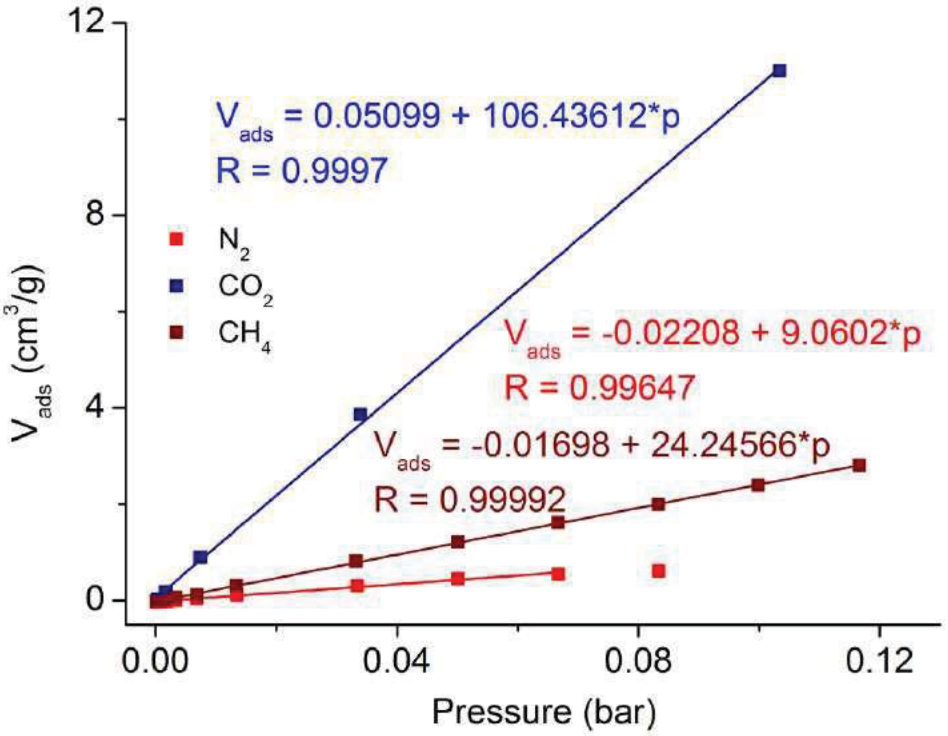

Figure S11: The initial slopes in the Henry region of the adsorption isotherms for **1** at 273 K.

IAST calculation

The ideal adsorbed solution theory was published in 1965 by Myers and Prausnitz.[2] The main feature of this model is the possibility of calculating binary adsorption equilibria depending on partial pressure and temperature by using only pure component adsorption data. Assumption of an ideal adsorbed phase, which is in an equilibrium with a perfect gas phase, leads to the activity coefficients equal to 1. Comparison to Raoult's law thus

$$\mathbf{y_i P = P_i^0(\pi) \cdot x_i}, \tag{1}$$

with the mixture pressure P, the mol fraction of the gas phase y_i and of the adsorbed phase x_i for component i and the equilibrium gas phase pressure P_i^0 of the pure component i corresponding to temperature and spreading pressure π of the mixture. Assuming the equality of the spreading pressure for each component to the spreading pressure of the mixture, one can write

$$\boldsymbol{\pi_1^0 = \pi_2^0} \tag{2}$$

and

$$\boldsymbol{\pi_i^0 = \psi_i(P_i^0)}, \tag{3}$$

with the pressure dependent spreading pressure. This dependency can then be expressed by using the Gibbs adsorption isotherm[3] to be

$$\frac{\pi_i^0 \cdot A_{OF}}{RT} = \int_0^{P_i^0} n \cdot d\ln P . \tag{4}$$

The spreading pressure can now be calculated for both pure components i by using a pure gas adsorption isotherm model, which represents the experimental pure gas adsorption data.[3,4] Herein, we used the Langmuir isotherm model (5) for this purpose.[3]

$$\theta = \frac{n}{n_{max}} = \frac{b \cdot p}{1 + b \cdot p} \tag{5}$$

Thus, by solving equation (1) to (4) simultaneously for given y_i and P, the adsorbed phase molar fraction x_i can be calculated. Subsequently, applying the Lewis rule[5]

$$\frac{1}{n_m^s} = \frac{x_1}{n_1^0} + \frac{x_2}{n_2^0} \tag{6}$$

leads us to the adsorbed amount of both components in a gas mixture equilibrium.

Here we used the IAST method to calculate the binary sorption equilibrium of CO_2/CH_4 and CO_2/N_2 at 273 K on **1** for two different pressure, P_{total} = 0.01 MPa and P_{total} = 0.05 MPa, respectively. The resulting selectivity as a function of gas phase mol fraction of CO_2 is given in Figure S11 for a mixture containing CO_2 and CH_4 and in Figure S12 for a mixture of CO_2 and N_2.

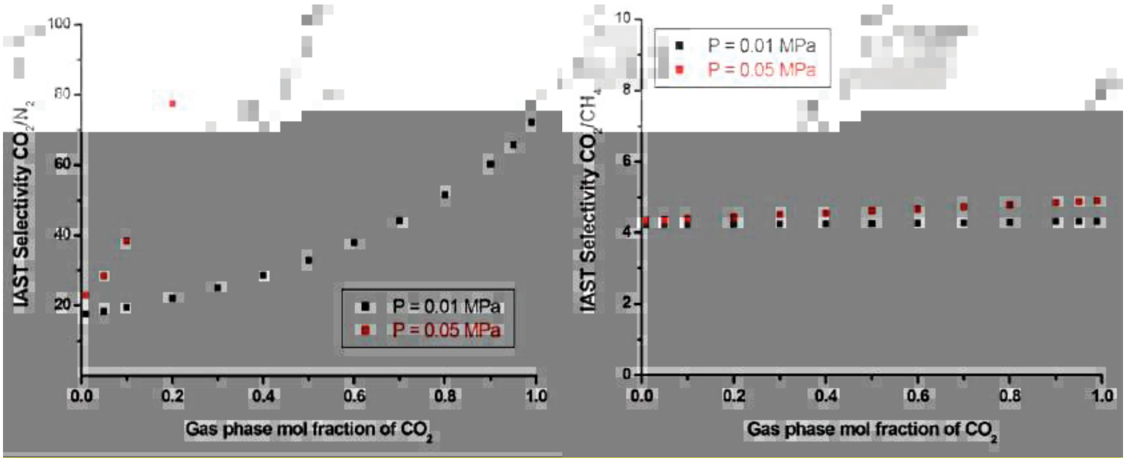

Figure S12: Predicted Selectivity of compound **1** from IAST calculation for CO_2/N_2 (left) and CO_2/CH_4 (right) at 273K.

Table S1: Langmuir model fitting parameter and Henry constants for sorption of CO_2, CH_4 and N_2 at 273 K on **1**.

	Parameter	**unit**	**CO_2 / 273 K**	**CH_4 / 273 K**	**N_2 / 273 K**
Langmuir	n_{max}	mmol g^{-1}	13.42	4.60	0.18
	b	MPa^{-1}	3.406	2.380	15.779
	Henry constant	mmol (g MPa)$^{-1}$	45.708	10.950	2.840

X-ray Crystallography:

Diffraction intensities of **1** were measured with an Oxford Diffraction XCalibur Eos instrument equipped with Mo Kα radiation (λ = 0.71073 Å, 50 kV, 40 mA) at ambient temperature. Data collection and reduction were performed with the Oxford diffraction Crysalis system. The structure was solved by direct methods (SIR92)[6] and refined on F^2 by full-matrix least-squares methods using SHELXL-97.[7-8] Non-hydrogen atoms were anisotropically refined. H-atoms were included in the refinement on calculated positions riding on their carrier atoms. H-atoms of water molecules were not calculated, but those were included in molecular formula of **1**. The function minimized was $[\sum w(Fo^2 - Fc^2)^2]$ ($w = 1 / [\sigma^2 (Fo^2) + (aP)^2 + bP]$), where $P = (\mathrm{Max}(Fo^2,0) + 2Fc^2) / 3$ with $\sigma^2(Fo^2)$ from counting statistics. The function $R1$ and $wR2$ were $(\sigma||Fo| - |Fc||) / \sigma|Fo|$ and $[\sigma w (Fo^2 - Fc^2)^2 / \sigma(wFo^4)]^{1/2}$, respectively. Crystallographic data (excluding structure factors) for the structures reported in this paper have been deposited in the Cambridge Crystallographic Data Centre as a supplementary publication no. CCDC 1007740. Copies of the data can be obtained free of charge on application to CCDC, 12 Union Road, Cambridge CB21EZ, UK (fax: + (44)1223-336-033; email: deposit@ccdc.cam.ac.uk).

Table S2: Single crystal data and structure refinement parameters for **1**.

Compound	**1**
Formula	$C_{24}H_{29}N_6O_{13}La$
Formula weight	748.44
Temperature(K)	293(2)
Crystal system	monoclinic
Space group	C*c*
a(Å)	24.434
b(Å)	18.364
c(Å)	8.259
β (°)	101.72

Z	4
d_{calc} (g cm-3)	1.370
μ(mm-1)	1.238
F(000)	1504
Total Reflections	7337
Unique Reflections	4914
Observed data [I > 2 σ (I)]	3736
No. of parameters	398
R(int)	0.0579
R_1[I > 2 σ (I)]	0.0633
wR2 (all data)	0.1427
GooF (all data)	1.061
Max. peak/hole	0.824/-0.659

Table S3: Selected bond lengths (Å) and angles (°) for **1**.

La1-O1	2.628(8)
La1-O2	2.823(8)
La1-O3	2.522(8)
La1-O4	2.630(8)
La1-O5	2.658(8)
La1-O8	2.607(8)
La1-O6	2.585(10)
La1-O1-La1'	1.987(2)
La1-O2-La1'	2.202(3)
La1-O5-La1'	2.002(3)

References:

1. Q.-R. Fang, D.-Q. Yuan, J. Sculley, J.-R. Li, Z.-B. Han and H.-C. Zhou, *Inorg. Chem.*, 2010, 49, 11637.
2. A.L. Myers and J.M. Prausnitz, *AIChE J.* 1965, **11**, 121.
3. D.D. Do, Adsorption Analysis: Equilibria and Kinetics, Imperial College Press, UK, 1998.
4. O. Talu and A. Myers, *AIChE J.* 1988, **34**, 1887.
5. W.K. Lewis, E.R. Gilliland, B. Chertow and W.P. Cadogan, *Ind. Eng. Chem.* 1950, **42**, 1319.
6. M. Sheldrick SHELXS-97, Program of Crystal Structure Solution, University of Göttingen, Germany, 1997.
7. G. M. Sheldrick SHELXL-97, Program of Crystal Structure Refinement, University of Göttingen, Germany, 1997.
8. G. M. Sheldrick, *Acta Cryst*. A64, 2008, 112-122.

3.7 A homochiral vanadium–salen based cadmium bpdc MOF with permanent porosity as an asymmetric catalyst in solvent-free cyanosilylation

Asamanjoy Bhunia, Subarna Dey, José María Moreno, Urbano Diaz, Patricia Concepcion, Kristof Van Hecke, Christoph Janiak and Pascal Van Der Voort

Chem. Commun., 2016, **52**, 1401-1404
DOI: 10.1039/c5cc09459c, (reference 105)
Impact factor 2016: 6.567

Chiral metal-organic frameworks (MOFs), which are a class of crystalline nanoporous materials, have received significant attention due to their high specific surface area, porosity, excellent thermal stability, solvent resistance, etc. Thus, these materials are promising with various applications including gas storage/separation, catalysis and drug delivery. In this work, a chiral vanadium–salen based Cd-MOF has reported using the chiral ligand (R,R)-(-)-1,2-cyclohexanediamino-N,N' -bis(3-*tert*-butyl-5-(4-pyridyl)salicylidene (H_2L) via *in situ* synthesis under solvothermal conditions. The BET surface area was found to be 574 m^2/g which to the best of our knowledge is the highest surface area amongst all metalloligand-based MOFs. Adsorption properties for CO_2, CH_4 and H_2 gasses were performed at low pressure for different temperatures. This framework shows excellent performance as asymmetric catalyst in solvent-free cyanosilylation.under solvent-free conditions.

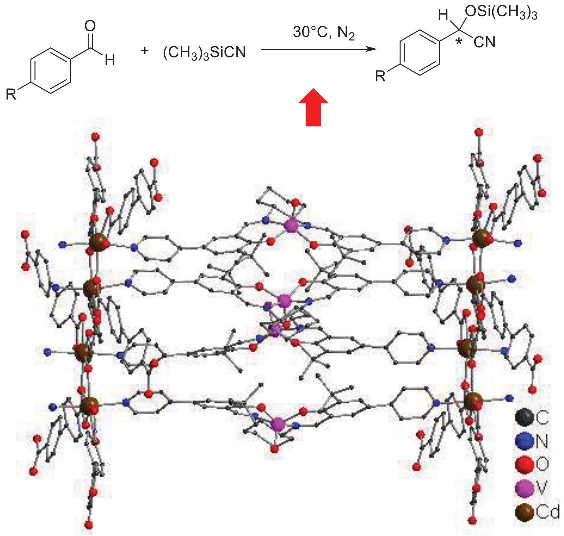

Author’s contribution to the work:

- Performing the gas adsorption studies.
- Writing and drawing figures for the gas adsorption part of the manuscript.

ChemComm

COMMUNICATION

View Article Online
View Journal | View Issue

Cite this: *Chem. Commun.*, 2016, **52**, 1401

Received 15th November 2015,
Accepted 18th November 2015

DOI: 10.1039/c5cc09459c

www.rsc.org/chemcomm

A homochiral vanadium–salen based cadmium bpdc MOF with permanent porosity as an asymmetric catalyst in solvent-free cyanosilylation†

Asamanjoy Bhunia,[a] Subarna Dey,[b] José María Moreno,[c] Urbano Diaz,[c] Patricia Concepcion,[c] Kristof Van Hecke,[d] Christoph Janiak[b] and Pascal Van Der Voort*[a]

A homochiral vanadium–salen based MOF with the pcu topology is constructed *via in situ* synthesis under solvothermal conditions. The synthesized MOF exhibits BET surface areas of 574 m^2 g^{-1}, showing the highest H_2 adsorption capacity (1.05 wt% at 77 K, 1 bar) and the highest CO_2 uptake (51 cm^3 g^{-1} at 273 K, 1 bar) for currently known salen-based MOFs. This framework shows excellent performance as an asymmetric catalyst in solvent-free cyanosilylation.

Metal organic frameworks (MOFs) are exciting hybrid materials for a plethora of potential applications including gas storage, gas separation, catalysis, and drug delivery.[1–3] They are crystalline nanoporous materials comprised of ordered networks formed from organic electron donor linkers and metal cations or clusters.[3] In MOF-based catalysis, either unsaturated metal coordination sites[4] or active linker sites in between the metals can be used as the catalytic active sites.[5,6] This second approach is much more challenging but offers unique opportunities to design highly selective and/or chiral catalysts. The most active linkers that have been developed to synthesize the chiral MOFs to date for asymmetric catalysis are based on BINOL and salen ligands.[6–9]

One possible strategy in the synthesis of chiral MOFs is the use of metalloligands.[7,10–12] In the metalloligand approach, metal-containing homo- and heteronuclear complexes (mostly salen types) that exhibit free coordination sites to connect to other metal atoms are allowed to form 1D, 2D or 3D networks. The additional linkers such as dicarboxylic or bipyridine groups are mostly used to construct a 3D structure that is mostly responsible for porosity.[10,11] Since metalloligands are more extended and flexible with respect to traditional organic linkers, it is however very hard to stabilize the framework. Although a few MOFs with salen struts have been examined as heterogeneous catalysis or as gas storage/separation vehicles, in most of the cases the framework suffered from severe diffusion limitations, even during the surface area measurements using nitrogen sorption.

Chen *et al.* reported several salen-containing MOFs called M′MOFs (mixed-metal organic frameworks) with surface areas ranging from 90 to 602 m^2 g^{-1}, albeit only measurable by the CO_2 uptake at 195 K.[10,11] The authors argued that the N_2 adsorption at 77 K on the activated M′MOFs was too slow because of diffusion effects. On the other hand, Hupp *et al.* reported that the surface area of the Mn^{III}SO-MOFs and Mn^{II}SO-MOFs was 478 and 385 m^2 g^{-1} using N_2 adsorption at 77 K.[13]

Many examples of asymmetric catalysis have been used by chiral MOFs for the synthesis of chiral molecules while metal centers in the metallosalen linkers are catalytically active. Cui *et al.* reported hydrolytic kinetic resolution and chiral sulfoxidation reactions for Co– and Ti–salen based MOFs, respectively, but again the N_2 sorption of their frameworks at 77 K showed only surface adsorption.[14,15] Hupp and Lin reported Mn– and Ru–salen MOFs for asymmetric catalytic alkene epoxidation and cyclopropanation reactions.[5,12,16] However, these MOFs also did not show permanent porosity. Therefore, the synthesis of permanently porous salen-based chiral frameworks is a huge challenge for asymmetric catalysis and gas sorption within the same frameworks.

In the last few years, one of the most important and rapidly growing concepts has been the development of green synthesis methods that are efficient, selective, high yielding and environmentally favorable.[17,18] Therefore, solvent-free reaction conditions offer significant advantages such as decreased energy consumption, reduced reaction times, fewer by-products, no purification and a large reduction in the reactor size. Also, one-step *in situ*

---

[a] *Department of Inorganic and Physical Chemistry, Center for Ordered Materials, Organometallics and Catalysis, Ghent University, Krijgslaan 281-S3, 9000 Ghent, Belgium. E-mail: pascal.vandervoort@ugent.be*

[b] *Institut für Anorganische Chemie und Strukturchemie, Universität Düsseldorf, 40204 Düsseldorf, Germany*

[c] *Instituto de Tecnología Quimica (UPV-CSIC), Avenida de los Naranjos s/n, 46022 Valencia, Spain*

[d] *Department of Inorganic and Physical Chemistry, Ghent University, Krijgslaan 281-S3, 9000 Ghent, Belgium*

† Electronic supplementary information (ESI) available: Experimental details, characterization data, solvent-free cyanosilylation, crystallographic data (CIF), and additional tables and figures. CCDC 1422004. For ESI and crystallographic data in CIF or other electronic format see DOI: 10.1039/c5cc09459c

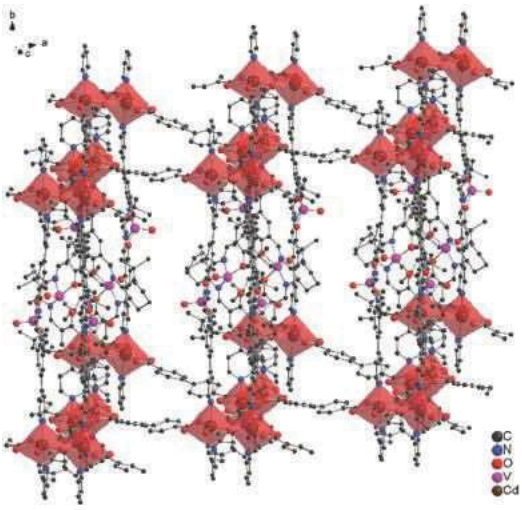

Fig. 1 Section of the packing of V–salen Cd-bpdc MOF from a single-crystal X-ray structure (hydrogen atoms omitted for clarity). Polyhedra depict the edge-sharing pentagonal bipyramidal coordination environment around two adjacent Cd atoms.

processes save time and consumables. Therefore, *in situ* synthesis as well as solvent-free organic transformation is a great challenge in current research.

Herein, we report a chiral vanadium–salen based Cd-MOF using the chiral ligand (*R*,*R*)-(−)-1,2-cyclohexanediamino-*N*,*N*′-bis(3-*tert*-butyl-5-(4-pyridyl)salicylidene) (H_2L) *via in situ* synthesis under solvothermal conditions instead of a multi-step[19] process. We tested its potential application in solvent-free cyanosilylation catalysis and its gas adsorption properties.

The reaction of the chiral ligand H_2L, $VOSO_4$, $Cd(NO_3)_2\cdot(H_2O)_4$ and biphenyl-4,4′-dicarboxylic acid (bpdc) in the presence of DMF/EtOH/H_2O at 100 °C resulted in the formation of a 3D MOF (see the ESI† for synthesis and characterization). This compound was characterized by standard analytical/spectroscopic techniques and the solid-state structure was determined by single-crystal X-ray diffraction techniques (Fig. 1).‡ The resulting product is stable in air and insoluble in common organic solvents such as chloroform, acetone, acetonitrile, THF, MeOH, EtOH, *etc.* The bulk purity of the compound was confirmed by a comparison of their activated and X-ray diffraction simulated powder (PXRD) patterns (Fig. S2 in the ESI†). From thermogravimetric (TG) analysis, it was observed that the activated compound starts to decompose with significant weight loss only above 350 °C (Fig. S3 in the ESI†).

Single-crystal X-ray crystallography showed that the compound crystallized in the orthorhombic non-centrosymmetric space group $P222_1$.[19] The asymmetric unit consists of two cadmium(II) ions, two V–salen units ($V^{IV}OL$), and two biphenyldicarboxylate ligands (bpdc). However, both the linkers (VO–salen and bpdc) are parallel to each other in the 1D channel of the framework in which a distorted rectangular aperture of $\sim 7 \times 3.5$ Å^2 along the *a* direction (considering the van der Waals radii of the H and C wall atoms) is estimated, respectively (Fig. S18, ESI†). The guest solvent molecules in the channel could not be determined by X-ray crystallography due to their disordered nature, so that the Squeeze option in PLATON was utilized (see the details in the ESI†). Each cadmium(II) atom is hepta-coordinated by five oxygen atoms from three carboxylate groups of bpdc ligands and two nitrogen atoms from the V–salen pyridine units. Two neighboring cadmium(II) atoms are bridged by two μ_2-η^2:η^1 bpdc carboxylate groups and form a secondary building block (SBU) leading to the formation of a 3D network with a **pcu** topology (Fig. S16 and S17, ESI†). In the V–salen unit, oxygen atoms and the vanadium(IV) atom are disordered over two positions.[20,21] As expected, in the center of each salen ligand, the vanadium(IV) atom adopts a distorted square pyramidal coordination geometry. The framework topology was simplified to its underlying net, using the ToposPro program package (see the framework topology in the ESI† for full details).[22] The structure shows two equivalent, interpenetrating frameworks (Fig. S11, ESI†). In the standard representation, the underlying net of each framework (Fig. S12, ESI†) can be considered to be a 2-nodal 3,5-coordinated net with (3-c)(5-c) nodes stoichiometry, resulting in the formation of a **fet** topology (Fig. S13, ESI†), while in the cluster representation, a uninodal 6-coordinated net with the **pcu** topology (Fig. S16, ESI†) is observed, with 4 short edges (16.8 Å) and two long, double bridged, opposite (*trans*) edges (24.0 Å) (running down the [010] direction).

The porosity was characterized by standard N_2 sorption measurements at 77 K. The material was activated by degassing at 100 °C under high vacuum (10^{-6} Torr) for 24 h. The isotherm shows a steep slope at low P/P_0 values with a type I isotherm, which is typical for microporous materials (Fig. 2).[23,24]

The calculated Langmuir and BET surface area were found to be 697 and 574 m^2 g^{-1}, respectively. The total pore volume was estimated to be 0.24 cm^3 g^{-1} at a relative pressure P/P_0 = 0.97. The absence of hysteresis during the adsorption and desorption points indicated that the framework was stable as well as rigid. To the best of our knowledge, this compound exhibits the highest surface area amongst all metalloligand-based MOFs characterized by standard nitrogen sorption (*i.e.* at 77 K) (Table S1, ESI†). Even, the surface area lies in the upper end when compared to other M′MOFs that showed BET surface areas (measured by CO_2

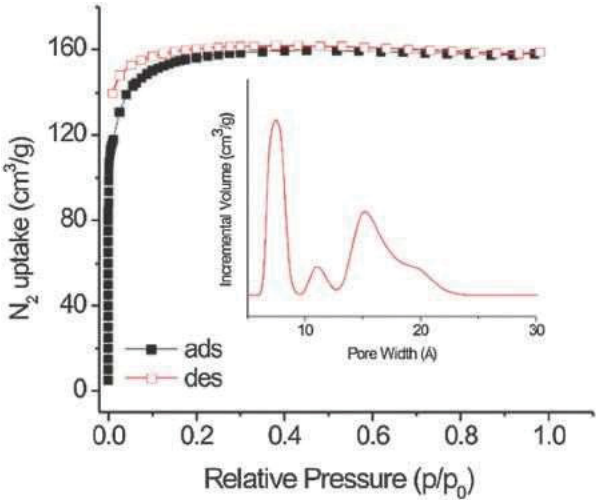

Fig. 2 N_2 sorption isotherm at 77 K. Inset: NL-DFT pore-size distribution curve of V–salen Cd-bpdc MOF.

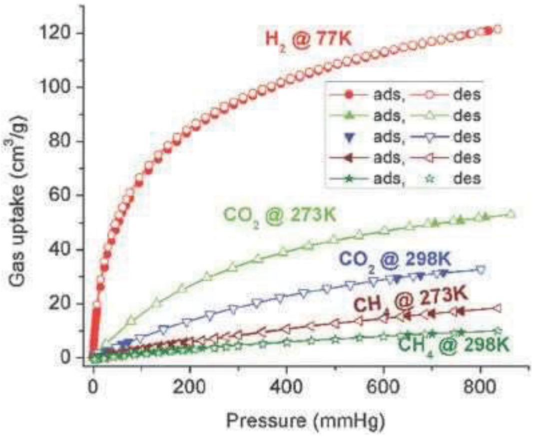

Fig. 3 Low-pressure H_2, CO_2 and CH_4 sorption isotherms.

Table 1 Asymmetric cyanosilylation of aldehydes catalyzed by vanadium–salen Cd-bpdc MOF[a]

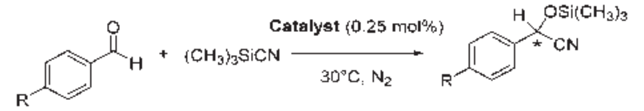

Entry	R	Time	Yield[b] (%)	ee[c] (%)
1	H	14	95	78
2	Me	14	93	76
3	OMe	14	76	80
4	Cl	14	98	72
5	Br	14	98	76
6[d]	H	9	91	57

[a] Reaction conditions: catalyst (0.25 mol%), aldehyde (0.82 mmol) and trimethylsilyl cyanide (3 eq.), and time 14 h. [b] Calculated by GC. [c] Determined by chiral GC. [d] Catalyst: VO–salen in the homogeneous phase.

at 195 K) of 90–602 m^2 g^{-1}.[10,11] The pore size distribution was determined by non-local density functional theory (NL-DFT) using a slit-pore model based on the N_2 adsorption isotherms. A narrow distribution of micropores centered at 7, 11, and 15 Å were observed (inset in Fig. 2). However, the major peak was at 7 Å, which matches with the calculated value (Fig. S19, ESI†) obtained from the single-crystal structure (ultramicropores <7 Å cannot be detected from N_2 sorption isotherms).

Because of the porosity of the V–salen Cd-bpdc MOF, as well as the large number of nitrogen atoms (imine and pyridine nitrogen atoms) in the framework, we decided to examine its adsorption properties at low pressure (*i.e.* 1 bar) for CO_2 and other gases (*i.e.* H_2 and CH_4). The CO_2 adsorption capacities in the activated material are 51 cm^3 g^{-1} at 273 K and 32 cm^3 g^{-1} at 298 K (Fig. 3), which is again higher than that of any known M'MOF material.[10,11]

To further understand the adsorption properties, the isosteric heats of adsorption were calculated from the CO_2 adsorption isotherms at 273 K and 298 K (Fig. S4, ESI†), as they describe the interaction with the hydrophobic pore surfaces. At zero loading the Q_{st} value ($-\Delta H$) is 30 kJ mol^{-1}. Upon increasing the loading the Q_{st} value decreases rapidly to 28 kJ mol^{-1}, which is still well above the heat of liquefaction of bulk CO_2 with 17 kJ mol^{-1} or the isosteric enthalpy of adsorption for CO_2 on activated carbons (*e.g.* BPL 25.7 kJ mol^{-1}, A10 21.6 kJ mol^{-1}, Norit R1 Extra 22.0 kJ mol^{-1}).[25,26] The high Q_{st} value can be attributed to the high polar framework and the pore size effect. The high adsorption enthalpy at zero coverage is explained by the initial filling of the small ultramicropores with 4 Å diameter (Fig. S5, ESI†) with adsorbate–surface interactions on both sides or ends of the CO_2 molecules. In contrast to CO_2, only 17 and 9 cm^3 g^{-1} of nonpolar CH_4 were adsorbed at 273 and 298 K. Interestingly, the material adsorbs 120 cm^3 g^{-1} (or 1.05 wt%) H_2 at 77 K and 1 bar (Fig. 3). This uptake is higher than that of other M'MOF materials, and it is mainly due to size exclusion effects.

We wished to examine if the VO–salen unit was accessible for asymmetric catalytic reactions (Table 1). Therefore, we studied the catalytic activity for cyanosilylation reactions of aromatic aldehydes under solvent-free conditions. However, chiral VO-salen complexes are active homogeneous asymmetric catalysts for various types of organic reactions.[27] To optimize the reaction conditions, the study was carried out in the reaction of benzaldehyde (0.82 mmol) and trimethylsilyl cyanide (2.46 mmol) by using 0.25 mol% catalyst in an N_2 atmosphere at 30 °C. The resulting yield of the reaction reached up to 95% after 14 h. Upon increasing the time, the yield of the reaction did not improve, the cyanosilylation reaction being performed with a 1 : 3 mol ratio of the selected aldehyde and TMSCN in an N_2 atmosphere at 30 °C for 14 h as the optimal working conditions (Fig. S6 and ESI†). To confirm the leaching, the catalyst is separated by filtration or centrifugation when the yield reaches 35% and then the reaction was continued (hot filtration test) (Fig. S6 in the ESI†). After 14 h, we observed that the reaction yield did not increase further.

MOF materials are structured from coordination bonds between metallic clusters and organic ligands that can be easily modified upon contact with organic solvents. In fact, leaching phenomena are frequently observed when solid MOF catalysts are used in different catalytic processes. In our case, the use of solvent-free conditions, during the cyanosilylation of aldehydes, favors the preservation of the V–salen-MOF structure, avoiding the decomposition and disorganization of the pristine MOF, and preventing the presence of homogeneous active sites in the reaction media. Experiments carried out in the presence of different solvents (chloroform and acetonitrile) confirmed this fact because leaching is clearly detected, showing the convenience of avoiding the use of organic solvents during the catalytic processes (Fig. S10a and b in ESI†). Further, chiral centers are influenced by their chemical environment. The presence of organic solvents as the reaction medium together with the hydrophobic properties of MOF materials could favor the excessive presence of solvent molecules adsorbed around chiral active sites. The consequence could be an activity decrease of asymmetric centers. Considering this, solvent-free conditions would be preferred for chiral solid catalysts. Therefore, we investigated the catalytic reaction in the absence of any solvent. Under these optimized conditions, the cyanosilylation of benzaldehyde gave 95% yield with 78% ee (Fig. 4 and Table 1), which is high compared with the recent work by the Duan and Cui groups.[19,28] They carried out the heterogeneous asymmetric cyanosilylation reaction by using an organic solvent such as CH_3CN and DCM.

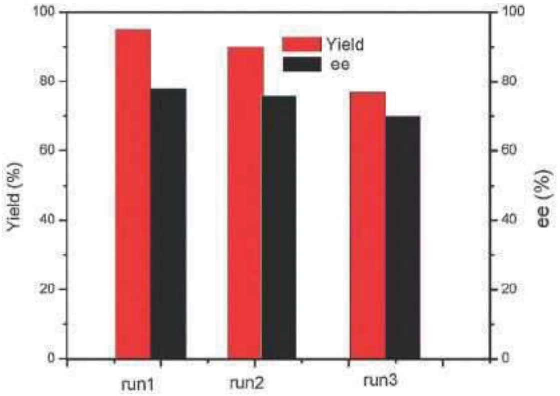

Fig. 4 Yield and enantiomeric excess (ee) for cyanosilylation reaction of benzaldehyde during 1st, 2nd and 3rd runs.

Even, the Cui group used Ph_3PO as a base to promote cyanosilylation.[19] To the best of our knowledge, no solvent-free cyanosilylation has been reported for salen-based MOFs. In our study, we not only use solvent-free conditions, but also a smaller amount of the catalyst. Moreover, the heterogeneous nature of the reaction was further confirmed by recyclability and reusability tests of the catalyst in the cyanosilylation of benzaldehyde (Fig. 4 and Fig. S6, S7 in the ESI†). We observed that the activity was maintained for the following two runs without significant change in the ee value (Fig. 4 and Table S2, ESI†). In the 3rd run, the yield and ee were decreased, which is associated with the modification of the surrounding environment of chiral centers or undesirable adsorption of organic compounds. After the 3rd run, the catalyst still maintained its crystalline structure, which was confirmed by PXRD (Fig. S7, ESI†). Moreover, the UV-vis spectrum of the fresh and reused catalyst (after the 3rd run) did not show remarkable changes in the vanadium species (Fig. S7, ESI†). In order to prove the effect of introduction of different substituents in the aromatic ring at the *para*-position, we further used aromatic aldehydes with an electron-withdrawing (–Cl and –Br) and an electron-donating (–Me and –OMe) group (Table 1 and Fig. S8 in the ESI†). The electron-withdrawing (–Cl and –Br) group gave higher yield whereas the electron-donating group decreased the yield with respect to benzaldehyde. This tendency is explained by the higher electropositive charge on the carbonyl group of aldehyde achieved in the presence of electron-withdrawing groups, resulting in a higher activation of the substrate. In contrast, for the electron-donating group, the activation of the carbonyl group is lower. Moreover, in all cases the ee value is higher than 72% (Table 1).

In conclusion, we have reported a chiral vanadium–salen based Cd-bpdc MOF using a chiral salen ligand (*R*,*R*)-(−)-1,2-cyclohexanediamino-*N*,*N*′-bis(3-*tert*-butyl-5-(4-pyridyl)salicylidene) (H_2L) *via in situ* synthesis under solvothermal conditions. This MOF shows to be intrinsically microporous with a high BET surface area of 574 $m^2\ g^{-1}$. At 273 K and 1 bar, this framework exhibits a higher CO_2 uptake capacity than other metallosalen-based MOFs. We tested this compound as a chiral catalyst for asymmetric cyanosilylation of aromatic aldehydes under solvent-free conditions. The catalyst is recyclable and reusable and showed a good conversion and ee. This green and solvent-free approach can be highly suitable for the synthesis of various chiral products such as α-hydroxy acids, α-hydroxy aldehydes and β-amino alcohols through the corresponding cyanohydrin in biomedicinal chemistry.

This research was funded by Ghent University, GOA grant number 01G00710.

Notes and references

‡ Crystal data for V–salen Cd-bpdc MOF: $C_{104}H_{100}Cd_2N_8O_{13.63}V_2$, M = 2006.69, orthorhombic, space group $P2221$ (No. 17), a = 17.0460(5) Å, b = 24.0462(6) Å, c = 28.8442(6) Å, V = 11823.0(5) Å^3, Z = 4, T = 100 K, ρ_{calc} = 1.127 g cm^{-3}, μ(Cu-Kα) = 4.565 mm^{-1}, F(000) = 4124.1, 68 492 reflections measured, 24 063 unique (R_{int} = 0.0926), which were used in all calculations. The final R_1 was 0.0564 ($I > 2\sigma(I)$) and wR_2 was 0.1393 (all data). CCDC 1422004.

1 H. Furukawa, K. E. Cordova, M. O'Keeffe and O. M. Yaghi, *Science*, 2013, **341**, 1230444.
2 K. Sumida, D. L. Rogow, J. A. Mason, T. M. McDonald, E. D. Bloch, Z. R. Herm, T.-H. Bae and J. R. Long, *Chem. Rev.*, 2012, **112**, 724–781.
3 G. Férey, *Chem. Soc. Rev.*, 2008, **37**, 191–214.
4 A. Corma, H. García and F. X. Llabrés i Xamena, *Chem. Rev.*, 2010, **110**, 4606–4655.
5 S.-H. Cho, B. Ma, S. T. Nguyen, J. T. Hupp and T. E. Albrecht-Schmitt, *Chem. Commun.*, 2006, 2563–2565.
6 L. Ma, J. M. Falkowski, C. Abney and W. Lin, *Nat. Chem.*, 2010, **2**, 838–846.
7 R. Kitaura, G. Onoyama, H. Sakamoto, R. Matsuda, S.-I. Noro and S. Kitagawa, *Angew. Chem., Int. Ed.*, 2004, **43**, 2684–2687.
8 A. Bhunia, Y. Lan, V. Mereacre, M. T. Gamer, A. K. Powell and P. W. Roesky, *Inorg. Chem.*, 2011, **50**, 12697–12704.
9 A. Bhunia, M. A. Gotthardt, M. Yadav, M. T. Gamer, A. Eichhöfer, W. Kleist and P. W. Roesky, *Chem. – Eur. J.*, 2013, **19**, 1986–1995.
10 S.-C. Xiang, Z. Zhang, C.-G. Zhao, K. Hong, X. Zhao, D.-R. Ding, M.-H. Xie, C.-D. Wu, M. C. Das, R. Gill, K. M. Thomas and B. Chen, *Nat. Commun.*, 2011, **2**, 204.
11 M. C. Das, Q. Guo, Y. He, J. Kim, C.-G. Zhao, K. Hong, S. Xiang, Z. Zhang, K. M. Thomas, R. Krishna and B. Chen, *J. Am. Chem. Soc.*, 2012, **134**, 8703–8710.
12 F. Song, C. Wang, J. M. Falkowski, L. Ma and W. Lin, *J. Am. Chem. Soc.*, 2010, **132**, 15390–15398.
13 A. M. Shultz, A. A. Sarjeant, O. K. Farha, J. T. Hupp and S. T. Nguyen, *J. Am. Chem. Soc.*, 2011, **133**, 13252–13255.
14 C. Zhu, G. Yuan, X. Chen, Z. Yang and Y. Cui, *J. Am. Chem. Soc.*, 2012, **134**, 8058–8061.
15 W. Xuan, C. Ye, M. Zhang, Z. Chen and Y. Cui, *Chem. Sci.*, 2013, **4**, 3154–3159.
16 J. M. Falkowski, C. Wang, S. Liu and W. Lin, *Angew. Chem., Int. Ed.*, 2011, **50**, 8674–8678.
17 J. M. DeSimone, *Science*, 2002, **297**, 799–803.
18 P. J. Walsh, H. Li and C. A. de Parrodi, *Chem. Rev.*, 2007, **107**, 2503–2545.
19 W. Xi, Y. Liu, Q. Xia, Z. Li and Y. Cui, *Chem. – Eur. J.*, 2015, **21**, 12581–12585.
20 Y. N. Belokon, P. Carta, A. V. Gutnov, V. Maleev, M. A. Moskalenko, L. V. Yashkina, N. S. Ikonnikov, N. V. Voskoboev, V. N. Khrustalev and M. North, *Helv. Chim. Acta*, 2002, **85**, 3301–3312.
21 P. Adão, J. Costa Pessoa, R. T. Henriques, M. L. Kuznetsov, F. Avecilla, M. R. Maurya, U. Kumar and I. Correia, *Inorg. Chem.*, 2009, **48**, 3542–3561.
22 V. A. Blatov, A. P. Shevchenko and D. M. Proserpio, *Cryst. Growth Des.*, 2014, **14**, 3576–3586.
23 K. S. W. Sing, D. H. Everett, R. A. W. Haul, L. Moscou, R. A. Pierotti, J. Rouquerol and T. Siemieniewska, *Pure Appl. Chem.*, 1985, **57**, 603–619.
24 G. Leofanti, M. Padovan, G. Tozzola and B. Venturelli, *Catal. Today*, 1998, **41**, 207–219.
25 K. B. Lee, M. G. Beaver, H. S. Caram and S. Sircar, *Ind. Eng. Chem. Res.*, 2008, **47**, 8048–8062.
26 S. Himeno, T. Komatsu and S. Fujita, *J. Chem. Eng. Data*, 2005, **50**, 369–376.
27 (*a*) V. Chechik, M. Conte, T. Dransfield, M. North and M. Omedes-Pujol, *Chem. Commun.*, 2010, **46**, 3372–3374; (*b*) Y. N. Belokon, M. North and T. Parsons, *Org. Lett.*, 2000, **2**, 1617–1619.
28 D. Dang, P. Wu, C. He, Z. Xie and C. Duan, *J. Am. Chem. Soc.*, 2010, **132**, 14321–14323.

Electronic Supplementary Information (ESI)

A Homochiral Vanadium-Salen-Cadmium bpdc MOF with Permanent Porosity as Asymmetric Catalyst in Solvent-Free Cyanosilylation

Asamanjoy Bhunia,[a] Subarna Dey,[b] José María Moreno,[c] Urbano Diaz,[c] Patricia Concepcion,[c] Kristof Van Hecke,[d] Christoph Janiak[b] and Pascal Van Der Voort*[a]

[a]*Dept. of Inorganic and Physical Chemistry, Center for Ordered Materials, Organometallics and Catalysis, Ghent University, Krijgslaan 281-S3, 9000 Ghent, Belgium*

[b]*Institut für Anorganische Chemie und Strukturchemie, Universität Düsseldorf, 40204 Düsseldorf, Germany*

[c]*Instituto de Tecnología Quimica (UPV-CSIC), Avenida de los Naranjos s/n, 46022 Valencia, Spain*

[d]*Department of Inorganic and Physical Chemistry, Ghent University, Krijgslaan 281-S3, 9000 Ghent, Belgium*

* To whom correspondence should be addressed. E-mail: pascal.vandervoort@ugent.be; Tel: (+)32-92644442; Fax: (+)32-92644983.

Supporting information
13 pages

Table of contents

1. Experimental Section

Materials and methods

All chemicals were purchased from commercial suppliers (Sigma-Aldrich and TCI Europe) and used without further purification, unless stated otherwise. Ligands (R,R)-(-)-1,2-cyclohexanediamino-N,N' -bis(3-tert-butyl-5-(4-pyridyl)salicylidene (H_2L) was synthesized according to the reported procedures.[1]

Diffuse-reflectance infrared Fourier transform (DRIFT) spectra were obtained with a Thermo Nicolet 6700 FTIR spectrometer equipped with a nitrogen-cooled MCT detector and a KBr beam splitter. Elemental analyses (C, H, N) were carried out with a Thermo Scientific Flash 2000 CHNS-O analyzer equipped with a TCD detector. Thermogravimetric analysis (TGA) was performed with a Netzsch STA-409CD thermal analyzer in a temperature range of 25–600 °C under an air atmosphere at a heating rate of 2 °C min^{-1}. Powder X-ray diffraction (PXRD) data were recorded with a Thermo Scientific ARL X'Tra diffractometer operated at 40 kV, 40 mA with Cu-$K\alpha$ (λ = 1.5406 Å) radiation. Sorption isotherms were measured using a Micromeritics ASAP 2020 automatic gas sorption analyzer equipped with oil-free vacuum pumps (ultimate vacuum $<10^{-8}$ mbar) and valves, which guaranteed contamination free measurements. The sample was connected to the preparation port of the sorption analyzer and degassed under vacuum until the outgassing rate, i.e., the rate of pressure rise in the temporarily closed manifold with the connected sample tube, was less than 2 μTorr/min at the specified temperature 80 °C. After weighing, the sample tube was then transferred to the analysis port of the sorption analyzer. All used gases (H_2, He, N_2, CO_2, CH_4) were of ultra-high purity (UHP, grade 5.0, 99.999%) and the STP volumes are given according to the NIST standards (293.15 K, 101.325 kPa). Helium gas was used for the determination of the cold and warm free space of the sample tubes. H_2 and N_2 sorption isotherms were measured at 77 K (liquid nitrogen bath), whereas CO_2 and CH_4 sorption isotherms were measured at 293±1 K (passive thermostating) and 273.15 K (ice/deionized water bath). The heat of adsorption values and the DFT pore size distributions ('N_2 DFT slit pore' model) were calculated out using the ASAP 2020 v3.05 software. The yield of the cayanosilylations were determined by capillary gas chromatography. They were carried out in a Varian 3900 equipped with a Sapiens 5MS column (30m*0.25mm*0.25μm) and was operated at 280 ºC in the injector temperature and 300 ºC in the detector temperature (FID). Moreover, the *ee* was determinated by chiral chromatography in a Varian 3900 with a Chiraldex γ-TA column (30m*0.25mm*0.25μm) and was operated at 230ºC both in the injector temperature and the detector temperature (FID).

2. a. Synthesis of V-salen Cd-bpdc MOF

A mixture of H_2L (16 mg, 0.027 mmol), $VOSO_4{\cdot}(H_2O)_x$ (8 mg, 0.05 mmol), $Cd(NO_3)_2{\cdot}(H_2O)_4$ (15 mg, 0.05 mmol) and biphenyl-4,4′-dicarboxylic acid (6 mg, 0.025 mmol) were combined in 1.5 mL of DMF with stirring for 3 h at room temperature followed by addition of 1.5 mL ethanol and 15 µL H_2O. The resulting solution was then sealed in a 10 mL glass vial. The glass vial was heated at 100 °C for 2 d in an oven and cooled to room temperature. The green needle shaped crystals were collected and washed three times with DMF followed by MeOH and dried in air. Yield: 16 mg, 32% (based on vanadium salt).

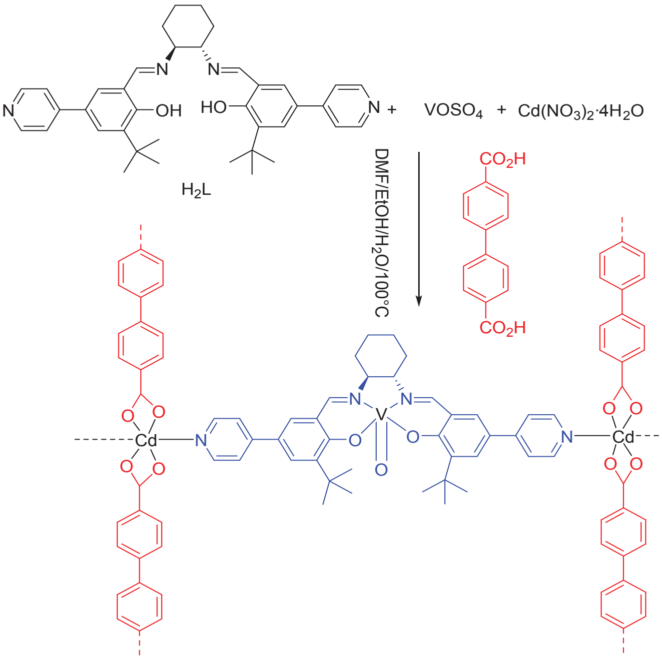

Scheme S1: Synthesis of V-salen Cd-bpdc MOF. The structure of MOF is heavily simplified. The exact connectivity are not shown.

2. b. Synthesis of VO-salen complex: A solution of ligand H_2L (0.088g, 1 mmol) was dissolved in 20 mL of MeOH. The reaction mixture was stirring for 5 min and then $VO(acac)_2$ (0.040g, 1 mmol) was added. The mixture was refluxed for 4 h at 70 °C and then mixture was filtered and washed with 10 mL cold MeOH and dried in vacuo. Yield: 76 mg, 77% for $VO(acac)_2$. ESI-MS m/z: 654.8 (Calcd m/z 654.28 for $[M+H]^+$). IR (KBr pellet): ν =3493 (w), 2943 (s), 2863 (m), 1601 (s), 1543 (m), 1432 (w), 1394 (s), 1349 (m), 1308 (s), 1264 (s), 1172 (s), 1081 (m), 1032 (w), 985 (s), 930 (m), 898 (w), 820 (s), 782 (m), 727 (w), 634 (m), 571 (s), 495 (s), 455 (w) cm^{-1}.

3. FT-IR Spectrum

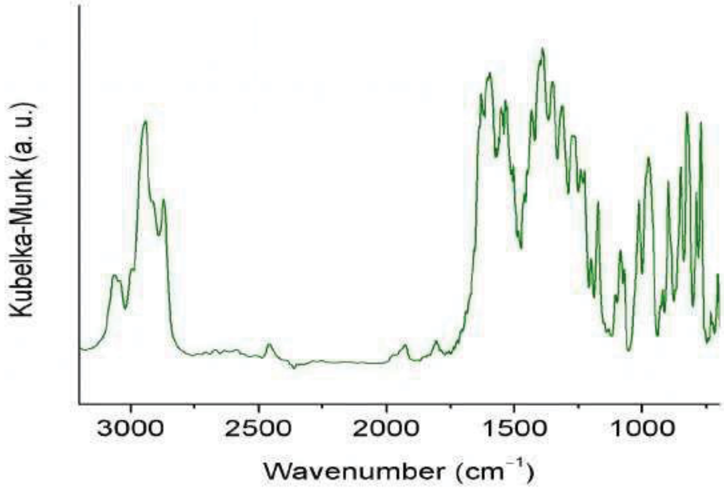

Fig. S1: IR spectrum of V-salen Cd-bpdc MOF.

4. Powder X-ray diffraction patterns

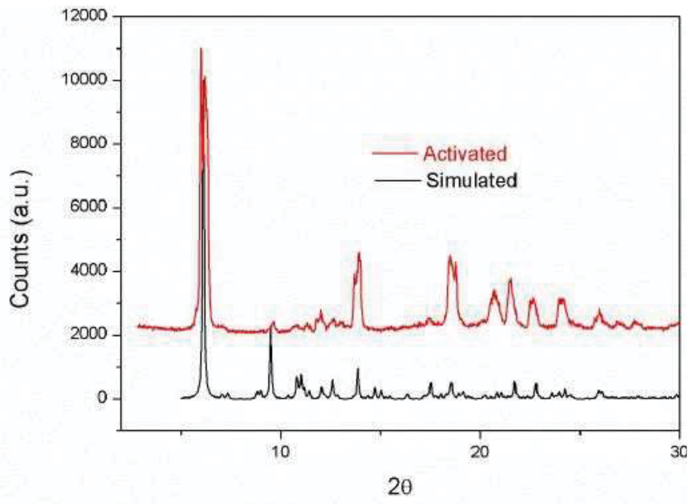

Fig. S2: Powder X-ray pattern of V-salen Cd-bpdc MOF (simulated and activated).

5. Thermogravimetric analysis (TGA)

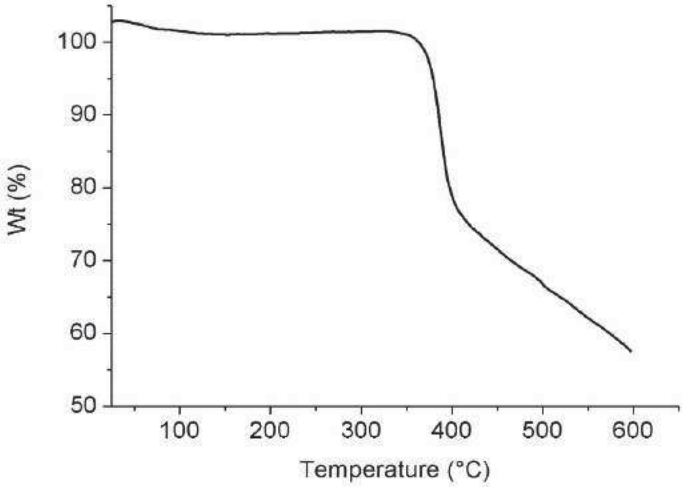

Fig. S3: TGA plot for V-salen Cd-bpdc MOF.

6. Isosteric heats of adsorption of CO_2

From two adsorption isotherms acquired at different temperatures T_1 and T_2, the differential heat of adsorption $\Delta H_{ads,diff}$, that is isosteric heat of adsorption Q_{st}can be calculated for any amount of adsorbed substance after determining the required relative pressures p_1 and p_2. A modified form of the Clausius-Clapeyron equation is used (eq (1))[2] $\Delta H_{ads,diff}$ was calculated over the whole adsorption range from the 273 K and 298 K isotherms for CO_2.

$$\Delta H_{ads,diff} = Q_{st} =- R ln\left(\frac{p_2}{p_1}\right)\frac{T_1 T_2}{T_2 - T_1} \qquad (1)$$

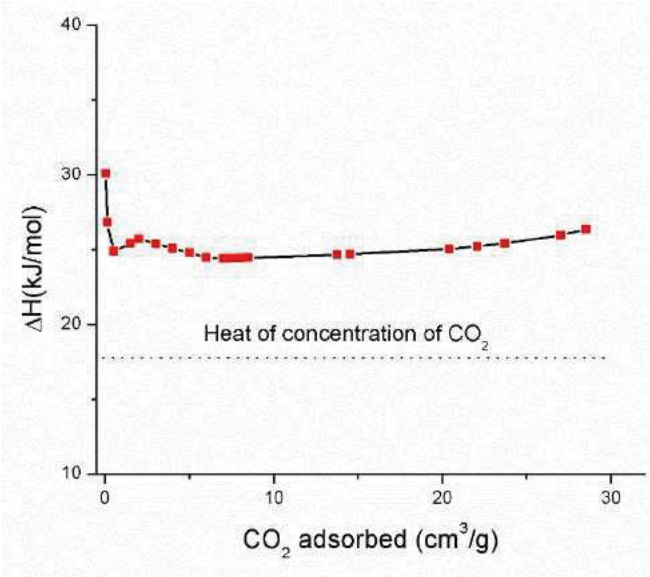

Fig. S4: Isosteric differential heat of adsorption (adsorption enthalpy, $Q_{ads,diff}$) as a function of CO_2 uptake for V-salen Cd-bpdc MOF.

7. Pore size distribution from a CO_2 adsorption isotherm

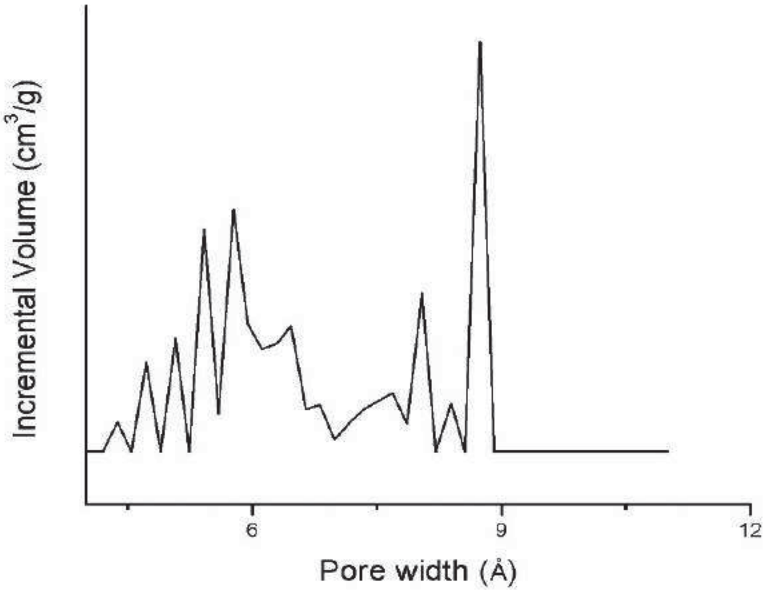

Fig. S5. The pore size distribution from a CO_2 adsorption isotherm at 273 K, calculated by the NL-DFT with a "CO_2 on carbon based slit-pore" model at 273 K.

8. BET surface area and gas uptake capacities (H_2, CO_2 and CH_4) of reported salen-based MOFs.

a. Table S1. BET surface area and gas uptake capacities (H_2, CO_2 and CH_4) of reported salen-based MOFs.

Compound	BET (m^2/g), from N_2 at 77 K	BET (m^2/g), from CO_2 at 195K	H_2 (mmol/g)	CO_2 (cm^3/g) at 273K, 1 bar	CH_4 (cm^3/g) at 273K, 1 bar	Reference
V-salen Cd-bpdc MOF	574	Not measured	5.35 (1.05 wt%)	51	17	Present work
M′MOF 1	Not measured	Not measured	4.78	Not measured	Not measured	J. Am. Chem. Soc. 2008, 130, 6411−6423
M′MOF- 2	Not measured	388	Not measured	~36	Not measured	Nat. Commun. 2011, 2, 204
M′MOF-3	Not measured	110	Not measured	~18	Not measured	Nat. Commun. 2011, 2, 204
M'MOF-4a	Not measured	602	Not measured	Not measure	Not measured	J. Am. Chem. Soc. 2012, 134, 8703−8710
M'MOF-5a	Not measured	202	Not measured	Not measured	Not measured	J. Am. Chem. Soc. 2012, 134, 8703−8710
M'MOF-6a	Not measured	369	Not measured	Not measured	Not measured	J. Am. Chem. Soc. 2012, 134, 8703−8710
M'MOF-7a	Not measured	90	Not measured	Not measured	Not measured	J. Am. Chem. Soc. 2012, 134, 8703−8710

9. Catalysis: Cyanosilylation of benzaldehyde

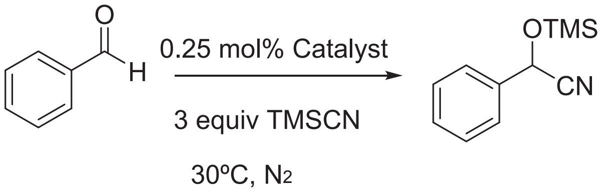

a. Cyanosilylation of benzaldehyde under solvent-free condition, catalyzed by vanadium-salen Cd-bpdc MOF:

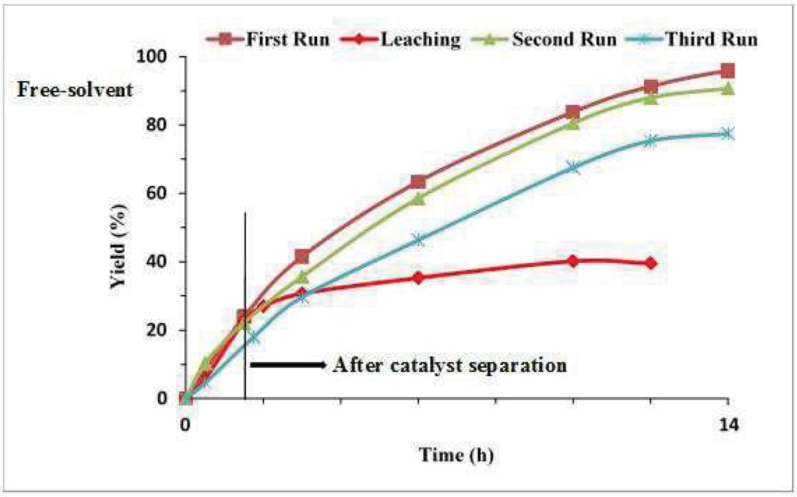

Fig. S6: Yield of the leaching test for cyanosilylation of benzaldehyde under solvent-free condition. The catalyst was separated by centrifugation at 1.5 h of the reaction. Reaction conditions: Catalyst (0.25 mol %), benzaldehyde (0.87 mmol), TSMCN (2.61 mmol), Temperature (30°C), N_2 atmosphere. Yield of blank of reaction 14 % (14 h), without catalyst.

The enantiomeric excess (ee) was determined by chiral GC, being obtained negative values from optical parameters. It was concluded that the higher enantiomeric product was the compound (S).[3]

Table S2: Asymmetric cyanosilylation of benzaldehyde catalyzed by V-salen Cd-bpdc MOF.

Run	Substrate	Yield^a (%)	ee^a (%)	TON^b	TOF^b (h^{-1})	r_o^b (moles·L^{-1} h^{-1})
1	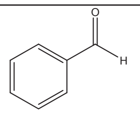	95	78	23	46	0.8
2		90	76	12	24	0.4
3		77	70	5	11	0.2

^{a}ee at 14 h of reaction. ^{b}Values at 0.5 h of reaction and considering all vanadium sites as actives (4.16 wt%).

b. Recyclability of the catalyst:

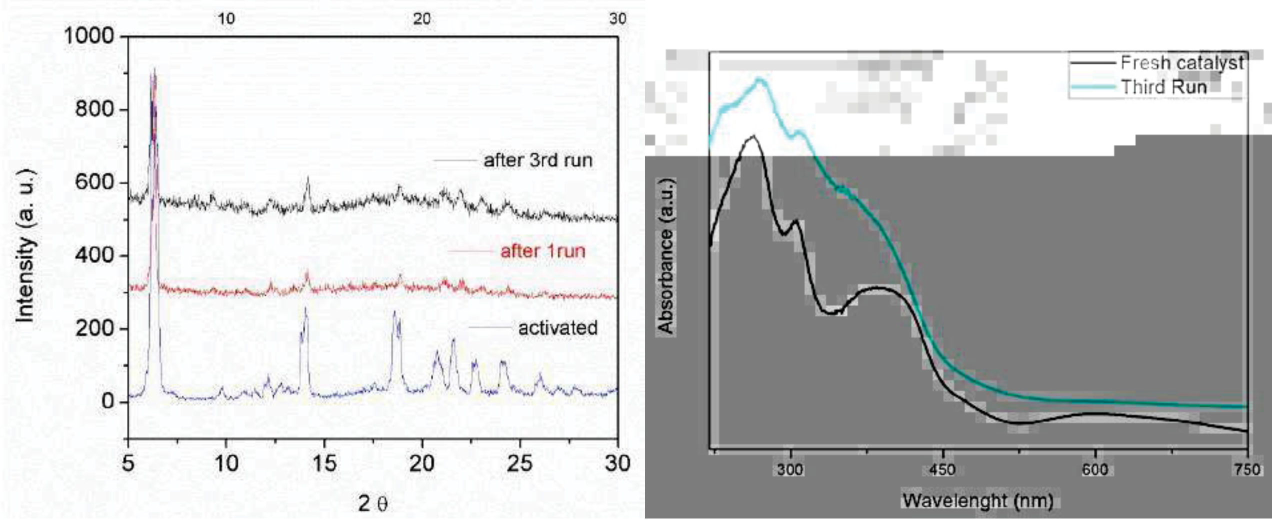

Fig. S7: Recyclability of the catalyst. Left: powder X-ray diffraction patterns of the catalyst before and after. Right: UV-vis spctrum of fresh catalyst and after 3rd run.

c. Catalysis: Cyanosilylation of aromatic aldehyde

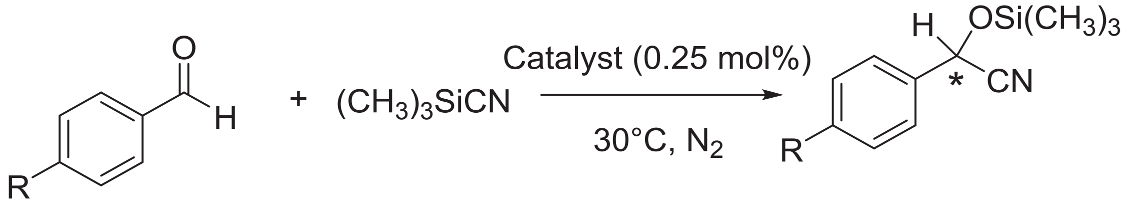

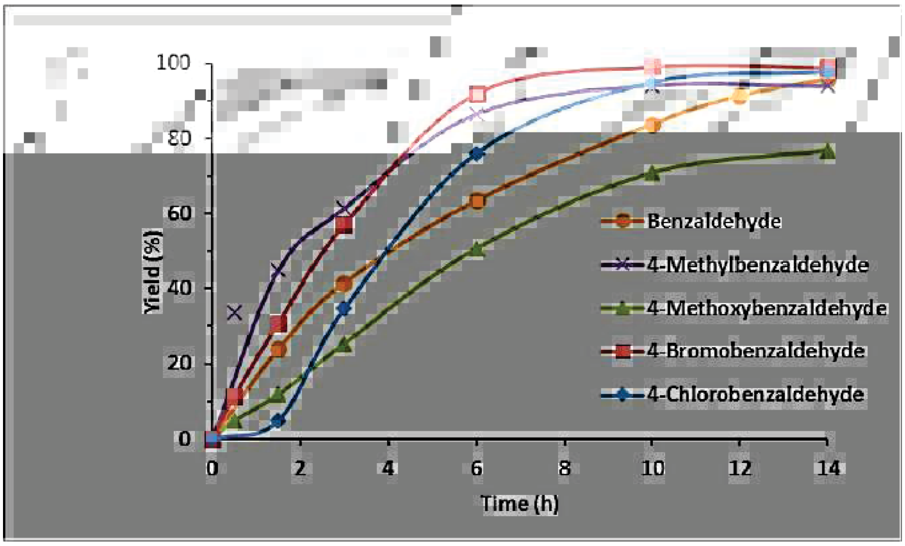

Fig. S8: Asymmetric cyanosilylation of aldehydes catalyzed by V-salen Cd-bpdc MOF.

c. Comparison of the catalytic activity between the homogeneous catalyst and the MOF

The comparison between homogeneous VO-salen complex and the solid V-salen Cd-bpdc MOF was performed in the same reaction conditions (Table 1 and Fig. S9) and the results obtained showed that yield of 91% was obtained after 9 hours, although the achieved *ee* (57%) was lower compared with heterogeneous catalytic tests using V-salen Cd-bpdc MOF recyclable solid (Fig. S9).

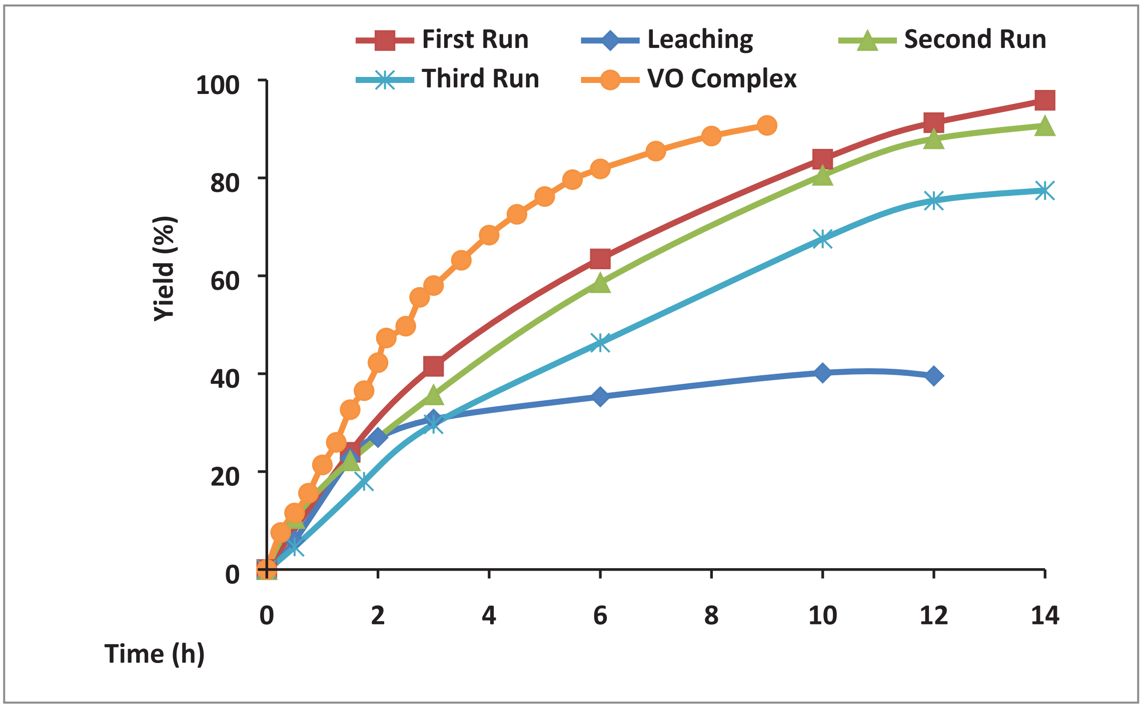

Fig. S9: Asymmetric cyanosilylation of benzaldehydes catalyzed by VO-Salen complex and V-salen Cd-bpdc MOF. Condition: Catalyst (0.25 mol %), benzaldehyde (0.87 mmol), TSMCN (2.61 mmol), Temperature (30°C), N_2 atmosphere.

10. Cyanosilylation of benzaldehyde by using chloroform and acetonitrile as solvent

we studied the catalytic activity for cyanosilylation reactions of aromatic aldehydes in dry acetonitrile and chloroform under N_2 atmosphere at 30 °C. By using dry chloroform as solvent, the yield of the reaction reached up to 95 % (Fig. S10a, ESI). Similarly, a value of 80 % was achieved in the presence of acetonitrile (Fig. S10b, ESI). The obtained results suggested that chloroform is a better solvent compared to acetonitrile, but we anticipated significant leaching of vanadium atoms (Fig. S10a-S10b, in ESI). To confirm the leaching, the solid catalyst was separated by filtration or centrifugation when the yield had reached 35 % and the reaction was continued (hot filtration test) (Fig. S10a-S10b, in ESI). We observed that the reaction did indeed continue further in the filtrate for both solvents chloroform and acetonitrile, at similar rate as for the reaction without solid catalyst separation. Therefore, we investigated the catalytic reaction in the absence of any solvent.

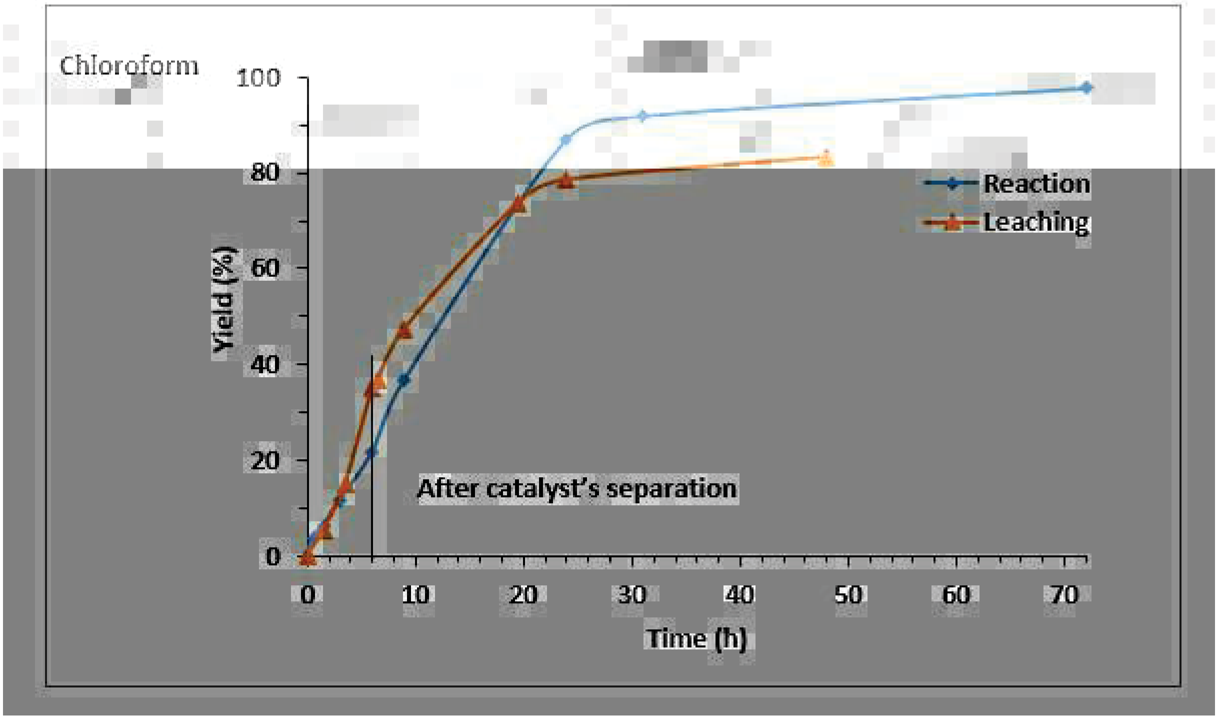

Fig. S10a: Yield of the leaching test for cyanosilylation of benzaldehyde using chloroform as solvent. For the leaching test the catalyst was separated by centrifugation when the yield was 35%, that is, after ~6 h. Reaction conditions: Catalyst (0.25 mol %), benzaldehyde (0.87 mmol), TSMCN (2.61 mmol), Temperature (30°C), N_2 atmosphere.

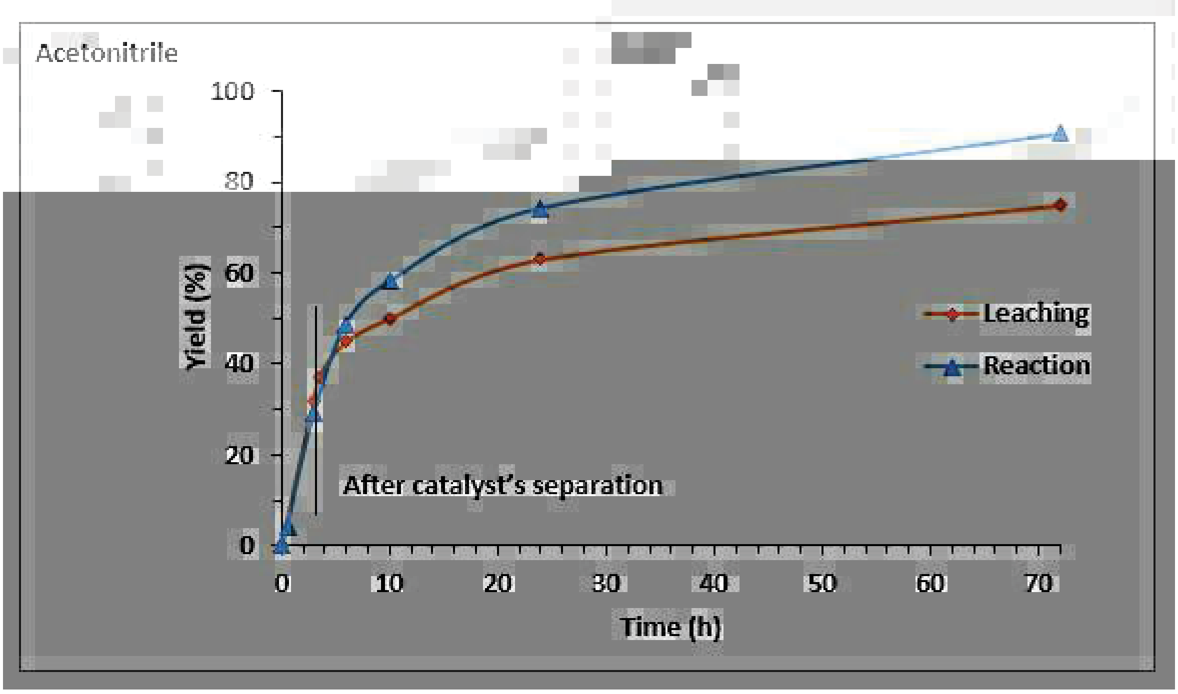

Fig. S10b: Yield of the leaching test for cyanosilylation of benzaldehyde using acetonitrile as solvent. For the leaching test the catalyst was separated by centrifugation when the yield was 35%, that is after ~3 h. Reaction conditions: Catalyst (0.25 mol %), benzaldehyde (0.87 mmol), TSMCN (2.61 mmol), Temperature (30°C), N_2 atmosphere

11. Chiral GC spectra

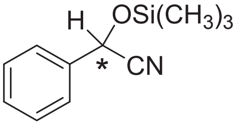

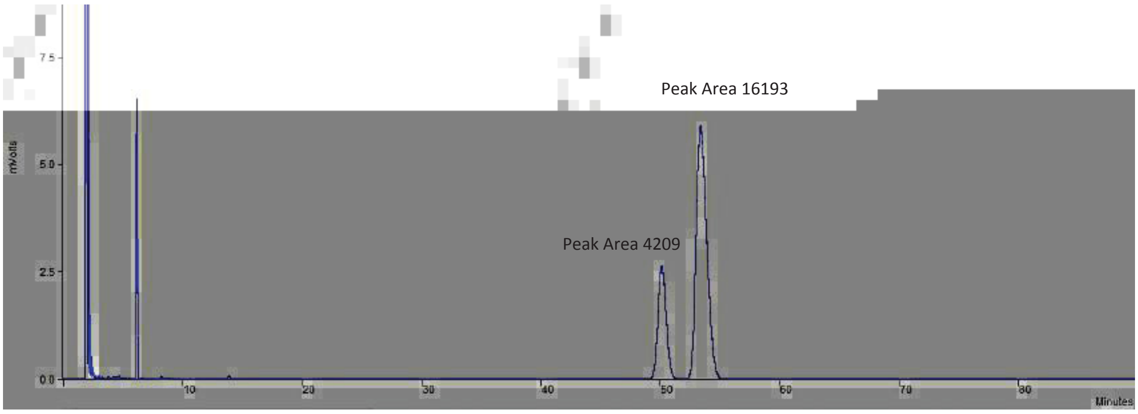

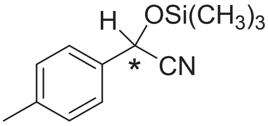
H
OSi(CH3)3
*
CN

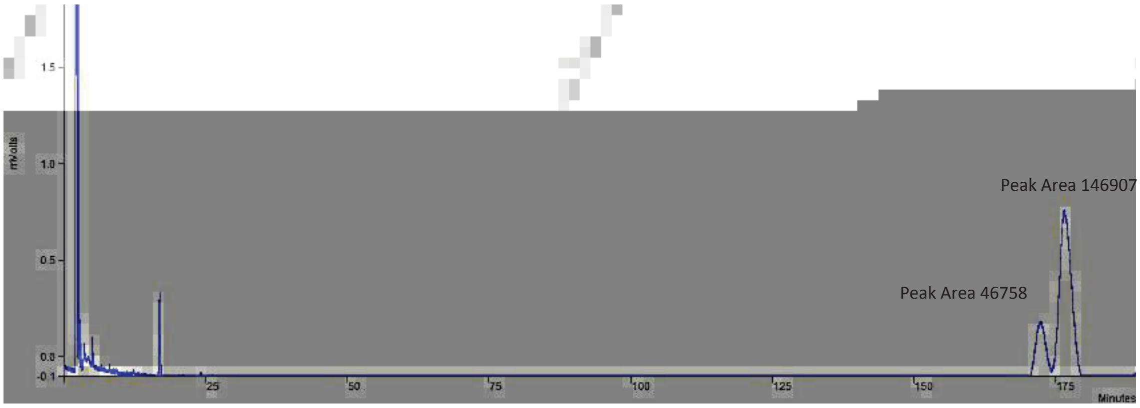
1.5
1.0
0.5
0.0
-0.1
mVolts
Peak Area 146907
Peak Area 46758
25
50
75
100
125
150
175
Minutes

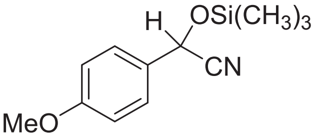
H
OSi(CH3)3
CN
MeO

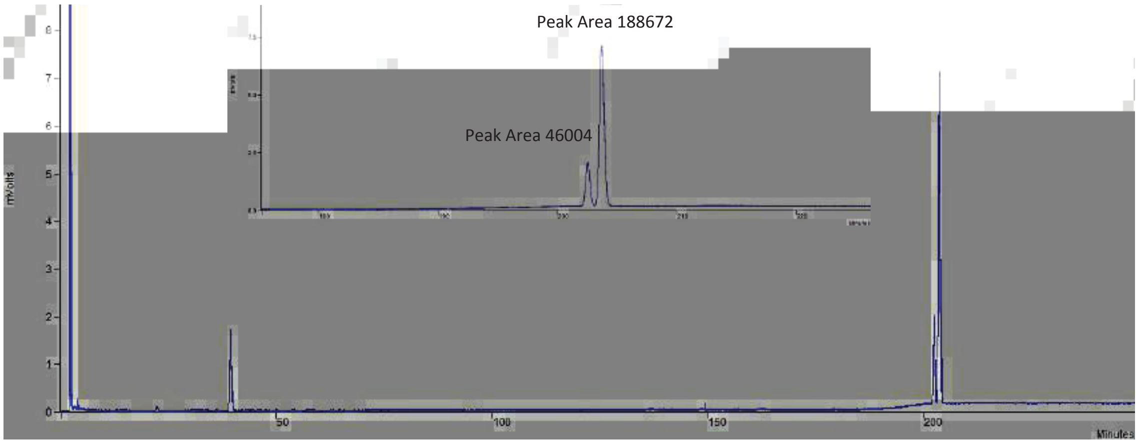
8
7
6
5
4
3
2
1
0
mVolts
Peak Area 188672
Peak Area 46004
50
100
150
200
Minutes

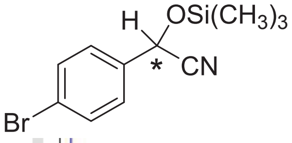
H
OSi(CH3)3
*
CN
Br

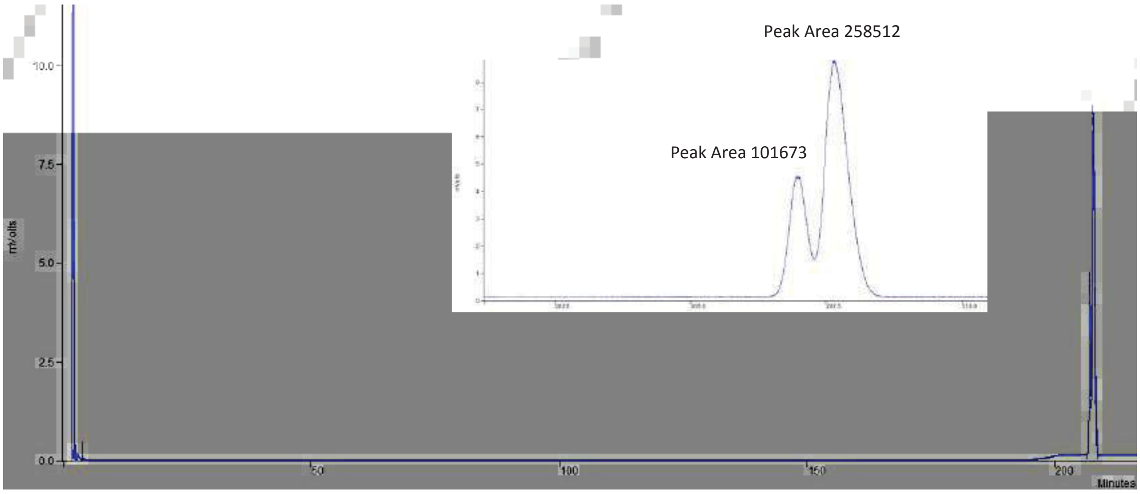
Peak Area 258512
Peak Area 101673
mVolts
10.0
7.5
5.0
2.5
0.0
50
100
150
200
Minutes

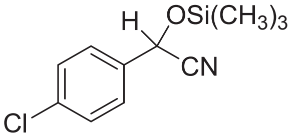
H
OSi(CH3)3
CN
Cl

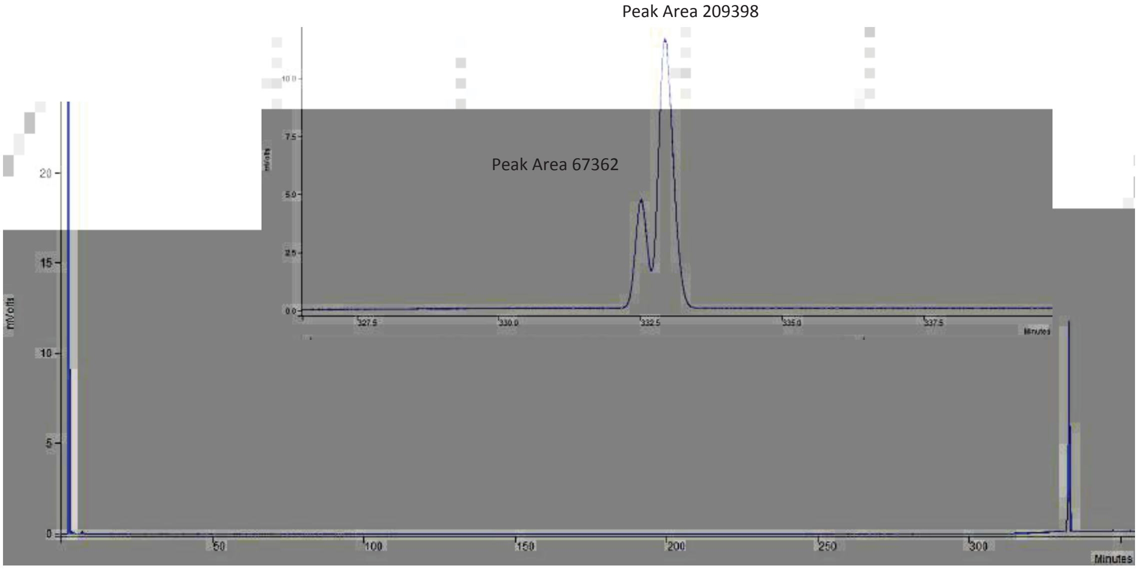
Peak Area 209398
Peak Area 67362
10.0
7.5
5.0
2.5
0.0
327.5
330.0
332.5
335.0
337.5
Minutes
mVolts
20
15
10
5
0
50
100
150
200
250
300
Minutes

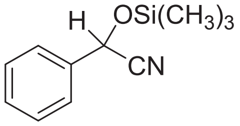

ee = 57%, Catalyzed by VO-salen in the homogeneous phase

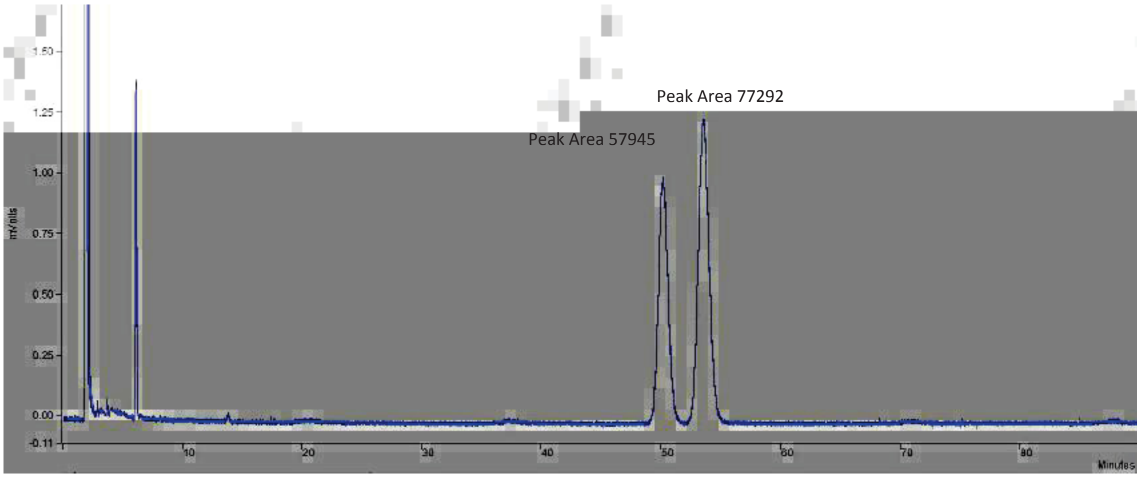

12. Framework topology

Analysis was performed with the ToposPro program package[4]. The structure is interpenetrated 2-fold (Fig. S11), each of the two equivalent frameworks can be simplified to its underlying net in two ways: (1) standard (2) cluster representation.[5] Four oxygen and four vanadium atoms of the structure are disordered over two positions, we will consider the structure with maximum occupation. The disorder does not affect the underlying topologies.

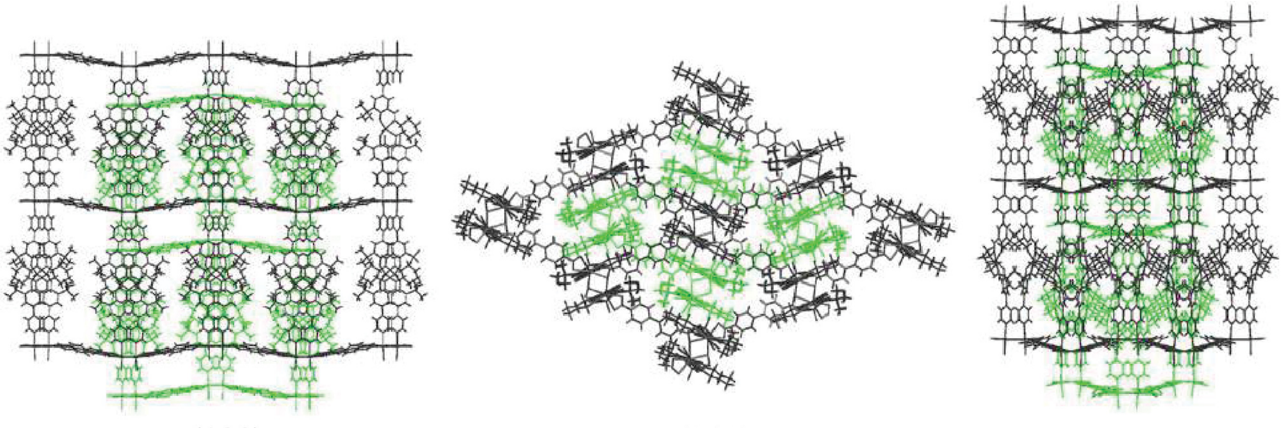

(100) (010) (001)

Fig. S11: Views along the cell axes for the two interpenetrated frameworks of the structure.

(1) Standard representation

The underlying net of the framework (Fig. S12) in the standard representations is 2-nodal 3,5-coordinated net with stoichiometry of nodes (3-c)(5-c). The net has a **fet** topology (Fig. S13). See also http://rcsr.net/nets/fet

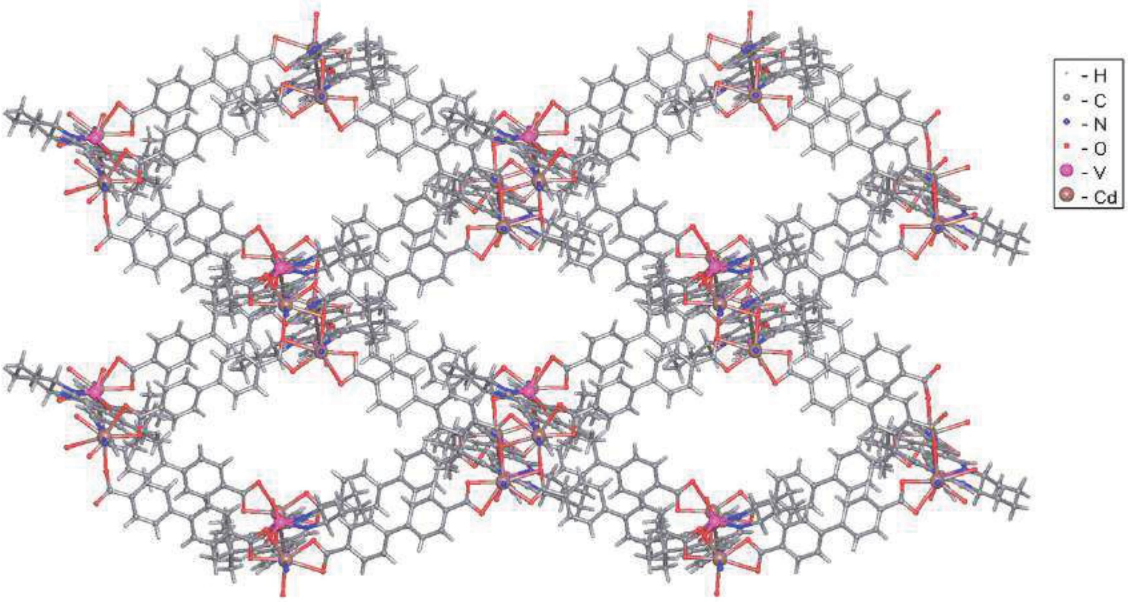

Fig. S12: A single framework of the structure.

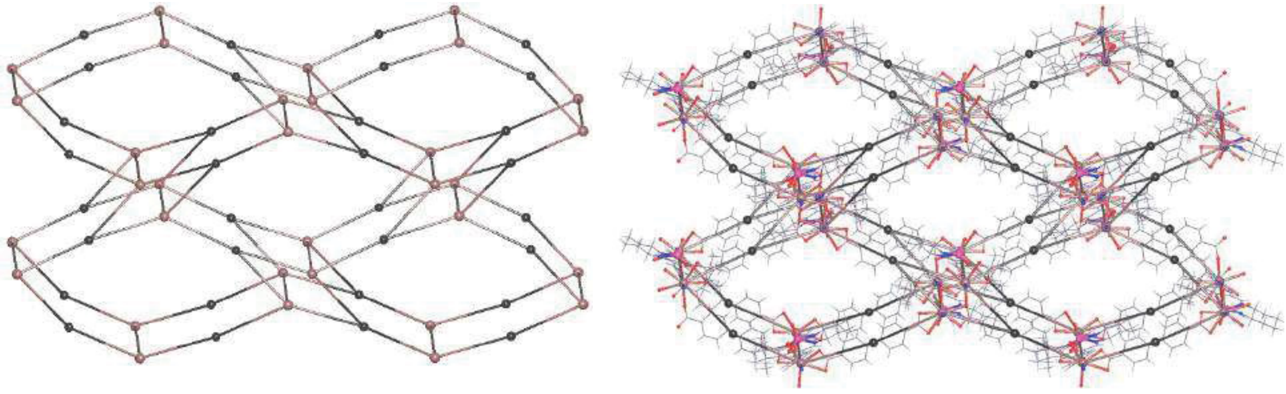

Fig. S13: Illustration of the underlying net **fet** in the standard representation (left) and the net merged with the corresponding fragment of the framework (right).

Each node of the underlying net corresponds to a ligand or an atom in the structure. In our case, the 5-coordinated nodes of the underlying net **fet** correspond to the Cd atoms in the structure (Fig. S14).

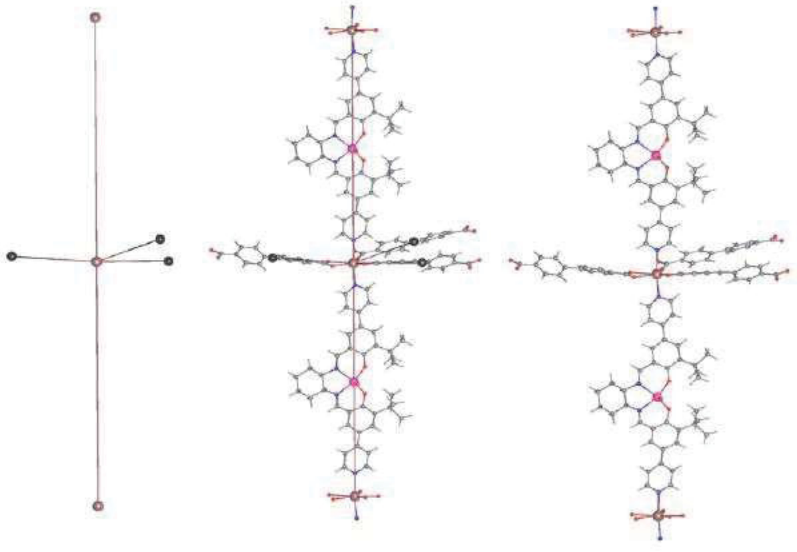

Fig. S14: 5-coordinated node of the underlying net **fet** and the corresponding fragment of the structure.

The 3-coordinated nodes of the underlying net **fet** correspond to the 4-(4-carboxyphenyl)benzoic acid ligand (Fig. S15). The trans long edges of the underlying net **fet** that connect the 5-coordinated nodes correspond to chelated vanadium atoms (Fig. S14).

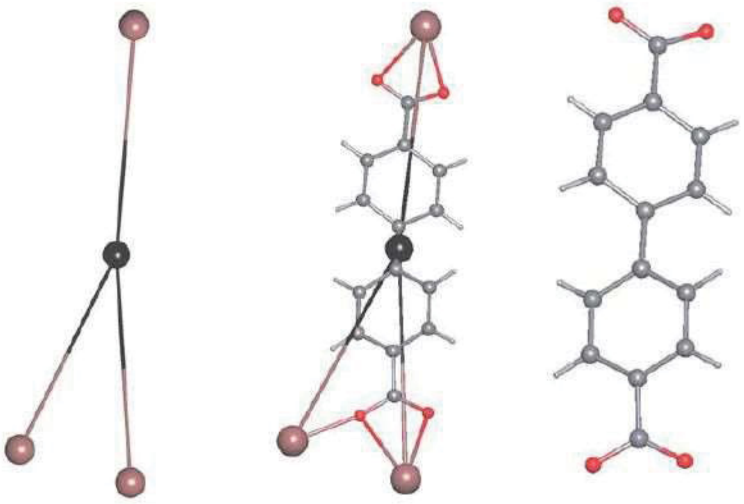

Fig. S15: 3-coordinated node of the underlying net **fet** and the corresponding fragment of the structure.

(2) Cluster representation

The underlying net of the framework in the cluster representations is a uninodal 6-coordinated net with the **pcu** topology (Fig. S16) with 4 edges short (16.8 Å) and two long (24.0 Å) opposite (trans) edges double bridged (running down b axis [010]). Fig. S17 shows the conformity of the underlying net elements and fragments of the structure.

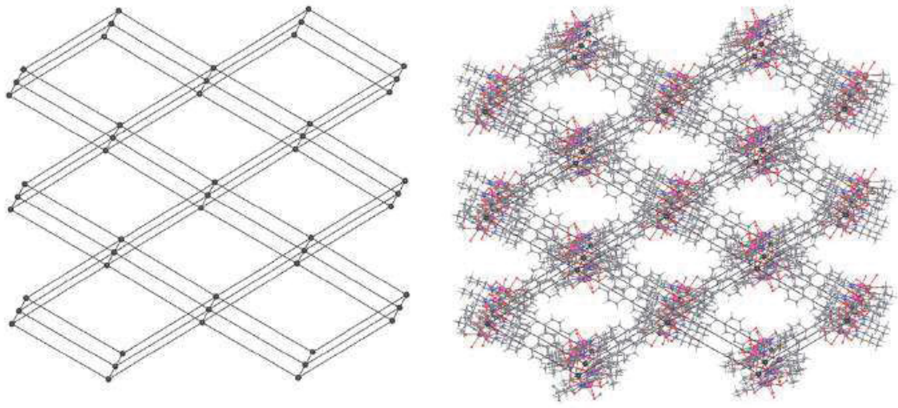

Fig. S16: The **pcu** underlying net in the cluster representation (left) and the net merged with the corresponding fragment of the framework (right).

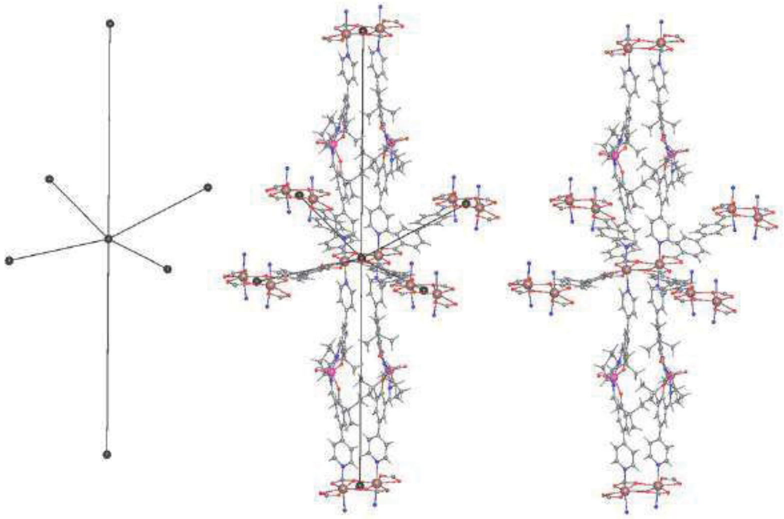

Fig. S17: The nodes and edges of the underlying 6-coordinated net **pcu** and the corresponding fragment of the structure.

Symmetry interpenetration of V-salen Cd-bpdc MOF
There are two identical interpenetrating nets[6] related by the 2-fold axis as full interpenetration symmetry (non-translating) element. So, it belongs to class of interpenetration IIa.[7]

Summary of the framework topology:
In the ToposPro TTO collection there are 97 MOF structures, whose underlying nets in the standard representation have the **fet** topology as well as 2025 MOF structures, whose underlying nets in the cluster representation have the **pcu** topology. Six structures have the same pattern of interpenetration (2-fold interpenetrated related by the 2-fold axis as full interpenetration symmetry. Class IIa) and the same topology in the cluster and standard representations as the $C_{104}H_{100}Cd_2N_8O_{13.63}V_2$ structure.

13. X-ray Crystallography:

For the structure of compound the V-salen Cd-bpdc MOF, X-ray intensity data were collected on a Agilent Supernova Dual Source (Cu at zero) diffractometer equipped with an Atlas CCD detector using CuKα radiation (λ = 1.54178 Å) and ω scans. The images were interpreted and integrated with the program CrysAlisPro (Agilent Technologies)[8]. Using Olex2[9], the structures were solved by direct methods using the ShelXS structure solution program and refined by full-matrix least-squares on F^2 using the ShelXL program package[10]. Non-hydrogen atoms were anisotropically refined and the hydrogen atoms in the riding mode and isotropic temperature factors fixed at 1.2 times U(eq) of the parent atoms (1.5 times for methyl groups). The contribution of heavily disordered solvent molecules was taken into account and suppressed using the SQUEEZE procedure in PLATON[11].

CCDC-1422004 contains the supplementary crystallographic data for this paper and can be obtained free of charge via www.ccdc.cam.ac.uk/conts/retrieving.html (or from the Cambridge Crystallographic Data Centre, 12, Union Road, Cambridge CB2 1EZ, UK; fax: +44-1223-336033; or deposit@ccdc.cam.ac.uk).

Crystal data. $C_{104}H_{100}Cd_2N_8O_{13.63}V_2$, $M = 2006.69$, orthorhombic, space group $P222_1$ (No. 17), $a = 17.0460(5)$, $b = 24.0462(6)$ Å, $c = 28.8442(6)$ Å, $V = 11823.0(5)$ Å^3, $Z = 4$, $T = 100$ K, $\rho_{calc} = 1.127$ g cm^{-3}, μ(Cu-Kα) = 4.565 mm^{-1}, $F(000) = 4124.1$, 68492 reflections measured, 24063 unique ($R_{int} = 0.0926$) which were used in all calculations. The final $R1$ was 0.0564 ($I > 2\sigma(I)$) and $wR2$ was 0.1393 (all data).

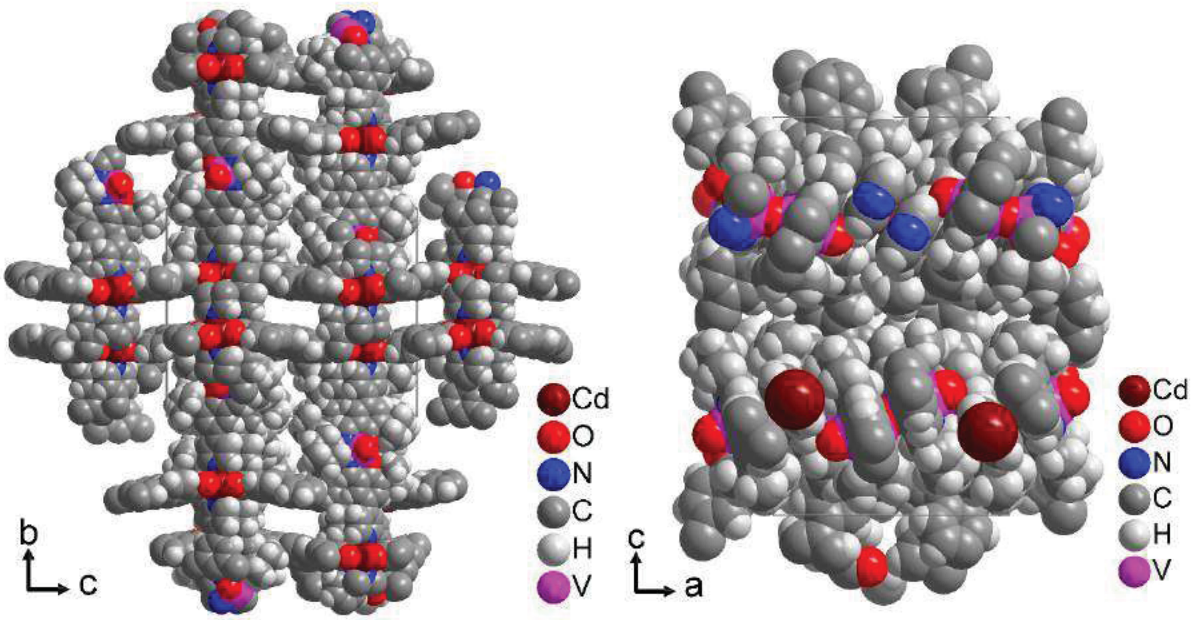

Fig.S18: View of the structure of the V-salen Cd-bpdc MOF (Left: along a-axis; right: along b-axis).

14. References

---

1 Y. Huang, T. Liu, J. Lin, J. Lü, Z. Lin, and R. Cao, *Inorg. Chem.*, 2011, **50**, 2191–2198.

2 F. Rouquerol, J. Rouquerol and K. Sing, *Adsorption by powders and porous solids*, F. Rouquerol, J. Rouquerol and K.Sing, ed. Academic Press, San Diego, 1999, vol. 11.

3 B. Heller, D. Redkin, A. Gutnov, C. Fischer, W. Bonrath, R. Karge and M. Hapke, *Synthesis*, 2008, **1**, 69–74.

4 V. A. Blatov, A. P. Shevchenko and D. M. Proserpio, *Cryst. Growth Des.*, 2014, **14**, 3576–3586.

5 E. V. Alexandrov, V. A. Blatov, A. V. Kochetkov and D. M. Proserpio, *CrystEngComm,* 2011**, 13**, 3947-3958.

6 L. Carlucci, G. Ciani, and D. M. Proserpio, *Coord. Chem. Rev.,* 2003, **246**, 247-289.

7 V.A. Blatov, L. Carlucci, G. Ciani and D. M. Proserpio, *CrystEngComm,* 2004**, 6**, 378-395.

8 Agilent. *CrysAlis PRO.* Agilent Technologies UK Ltd, Yarnton, England, 2013

9 O.V. Dolomanov, L. J. Bourhis, R. J. Gildea, J. A. K. Howard and H. Puschmann, *J. Appl. Cryst.*, 2009, **42**, 339-341.

10 G.M. Sheldrick, *Acta Cryst*., 2008, **A64**, 112-122.

11 A.L. Spek, *Acta Cryst.*, 2009, **D65**, 148-155.

3.8 A photoluminescent covalent triazine framework: CO_2 adsorption, light-driven hydrogen evolution and sensing of nitroaromatics

Asamanjoy Bhunia, Dolores Esquivel, Subarna Dey, Ricardo Fernández-Terán, Yasutomo Goto, Shinji Inagaki, Pascal Van Der Voort and Christoph Janiak

J. Mater. Chem. A, 2016, **4**, 13450-13457
DOI: 10.1039/c6ta04623a, (reference 34b)
Impact factor 2016: 8.262

A highly photoluminescent (PL) porous covalent triazine-based framework (PCTF-8) is synthesized from tetra(4-cyanophenyl)ethylene by using trifluoromethanesulfonic acid as catalyst with a high fluoresencence quantum yield (31%) at room temperature. The BET specific surface area of PCTF-8 was found to be 625 m^2/g. At 77 K PCTF-8 showed a H_2 uptake of 112 cm^3/g. The CO_2 and CH_4 uptake capacities of PCTF-8 were found to be 56 and 17 cm^3/g, respectively at 273 K upto 1 bar. Photoluminescence properties as well as the sensing behaviour towards nitroaromatics have been demonstrated. The fluorescence emission intensity of PCTF-8 is quenched by ca. 71 % in presence of 2,4,6-trinitrophenol (TNP). This high photoluminescence property is applied for hydrogen evolving organic photocatalysis from water in presence of a sacrificial electron donor and a cocatalyst.

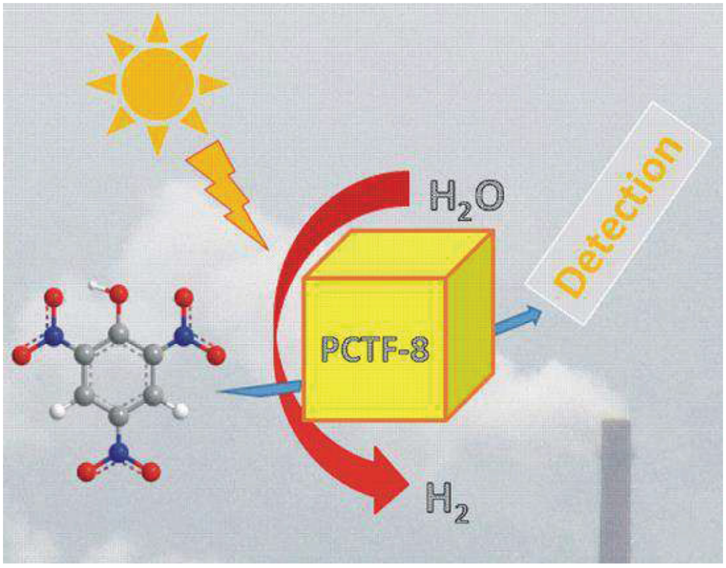

Author's contribution to the work:

- Performing the gas adsorption studies and Karl-Fischer titration.
- Writing and drawing figures for the gas adsorption part
- Helping the fluorescent quenching titration experiments.

Journal of
Materials Chemistry A

Cite this: *J. Mater. Chem. A*, 2016, **4**, 13450

A photoluminescent covalent triazine framework: CO_2 adsorption, light-driven hydrogen evolution and sensing of nitroaromatics†

Asamanjoy Bhunia,*[ab] Dolores Esquivel,[ac] Subarna Dey,[b] Ricardo Fernández-Terán,[d] Yasutomo Goto,[e] Shinji Inagaki,[e] Pascal Van Der Voort[a] and Christoph Janiak*[b]

A highly photoluminescent (PL) porous covalent triazine-based framework (PCTF-8) is synthesized from tetra(4-cyanophenyl)ethylene by using trifluoromethanesulfonic acid as the catalyst at room temperature. Due to triazine units in the framework, the PCTF-8 exhibits excellent thermal stability (>400 °C). The Brunauer–Emmett–Teller (BET) specific surface area of PCTF-8 is 625 $m^2\ g^{-1}$ which is lower than the one obtained from the synthesis under Lewis acid conditions ($ZnCl_2$). At 1 bar and 273 K, the PCTF-8 adsorbs a significant amount of CO_2 (56 $cm^3\ g^{-1}$) and CH_4 (17 $cm^3\ g^{-1}$) which is highly comparable to nanoporous 1,3,5-triazine frameworks (NOP-1-6, 29–56 $cm^3\ g^{-1}$). This nitrogen rich framework exhibits good ideal selectivity (61 : 1 (85% N_2 : 15% CO_2) at 273 K, 1 bar). Thus, it can be used as a promising candidate for potential applications in post-combustion CO_2 capture and sequestration technologies. In addition, photoluminescence properties as well as the sensing behaviour towards nitroaromatics have been demonstrated. The fluorescence emission intensity of PCTF-8 is quenched by *ca.* 71% in the presence of 2,4,6-trinitrophenol (TNP). From time-resolved studies, a static quenching behaviour was found. This high photoluminescence property is used for hydrogen evolving organic photocatalysis from water in the presence of a sacrificial electron donor and a cocatalyst.

Received 2nd June 2016
Accepted 2nd August 2016

DOI: 10.1039/c6ta04623a

www.rsc.org/MaterialsA

Introduction

Porous organic materials have attracted considerable interest because of their unique physicochemical properties in various technological and energy-related applications such as gas storage, separation, catalysis, *etc.*[1,2] In particular, π-conjugated porous organic polymers are an integral part of research for light emission, light harvesting and chemo-sensing.[3] Due to their rigidity at the molecular level, they have a high affinity to aggregate in solution and the solid state, resulting typically in aggregation caused quenching (ACQ) effects.[4] The aggregation of conjugated polymers can be prevented by molecular approaches based on site isolation with bulky polymeric matrices.[5] This approach can improve the luminescence properties of the polymeric materials. At the same time, π-conjugated materials are also a promising platform for CO_2 capture because of the interaction between the quadrupole moments of CO_2 and the π-clouds in the porous organic materials.[6] The incorporation of high amounts of nitrogen into the porous materials can facilitate CO_2 capture. Such multifunctionality has been a long term challenge for the development of porous photofunctional materials which have attracted great interest as chemical sensors, *e.g.* to detect explosive nitroaromatic compounds.[7] The sensitivity and selectivity in the detection of these compounds by using porous materials suffer from analyte–host interactions, chemical stability and so on. π-Conjugated triazine based porous materials may be attractive chemical sensors because of their high stability and high porosity. Due to the high electron mobilities and electron withdrawing character of the triazine ring, these materials have been widely used in synthetic chemistry and optoelectronics.[8]

Currently, these types of materials have attracted great interest as organic photocatalysts for hydrogen production *via* photocatalytic water splitting under visible light.[9] Their chemical structures, analogous to that of g-C_3N_4, in combination with their tunable porosity make them attractive candidates for light-induced hydrogen evolution.[10] Lostch *et al.* reported the first

---

[a] *Department of Inorganic and Physical Chemistry, Centre for Ordered Materials, Organometallics and Catalysis, Ghent University, Krijgslaan 281-S3, 9000 Ghent, Belgium. E-mail: asamanjoy.bhunia@gmail.com*

[b] *Institut für Anorganische Chemie und Strukturchemie, Universität Düsseldorf, 40204 Düsseldorf, Germany. E-mail: janiak@uni-duesseldorf.de*

[c] *Department of Organic Chemistry, Nanochemistry and Fine Chemistry Research Institute (IUIQFN), Faculty of Sciences, University of Córdoba, Campus of Rabanales, Marie Curie Building, Ctra. Nal. IV, km 396, 14071 Córdoba, Spain*

[d] *Department of Chemistry – Ångström Laboratory, Uppsala University, Box 523, SE-751 20, Uppsala, Sweden*

[e] *Toyota Central R&D Laboratories, Inc., Nagakute, Aichi 480-1192, Japan*

† Electronic supplementary information (ESI) available: TGA, XRD, elemental analysis, KFT, isosteric heat of adsorption and pore size distribution of CO_2, adsorption, IAST selectivity, emission spectra of PCTF-1, and detection of nitroaromatic explosives. See DOI: 10.1039/c6ta04623a

example of a covalent organic framework (COF) which was active in visible light-induced hydrogen production from water using platinum as a cocatalyst.[9a] More recently, a yellow coloured phenyl-triazine oligomer with high crystallinity exhibited the highest activity obtained for metal-free organic photocatalysts in the absence of noble metal catalysts.[9b]

Herein we report a new strategy for the construction of photoluminescent materials based on π-conjugated building blocks. We employed tetra(4-cyanophenyl)ethylene as a single component for the synthesis of a porous covalent triazine-based framework (PCTF) using trifluoromethanesulfonic acid (TFMS) as the catalyst at room temperature, in which the tetraphenylethylene (TPE) units are directly connected to strong electron accepting triazine rings. Recently, some of us reported PCTFs with the TPE unit by using the ionothermal $ZnCl_2$ route.[11] The structures of CTFs from ionothermal reactions with $ZnCl_2$ are in-between well-defined COFs and porous carbon materials.[12] TFMS-catalyzed condensation frameworks[13,14] offer significant advantages: (1) lower temperature and shorter reaction time, (2) avoiding undesired decomposition and condensation reactions such as C–H bond cleavage and carbonization which otherwise lead to defects in the framework and (3) absence of $ZnCl_2$ contamination in the porous materials. These advantages are attractive to obtain reasonably well-defined CTFs which can exhibit a broad variety of physical properties including chemical sensing, gas storage/separation and organic photocatalysis. So far, CTFs have been used mainly in gas storage and separation.[11,13] There are also few reports on the use of CTFs for heterogeneous catalysis including light-induced hydrogen evolution,[9,15] as catalytic supports in liquid phase reactions,[16] and as adsorbents in liquids,[17] due to their chemical and thermal stabilities. In spite of their many applications, their photoluminescence was only briefly noted[14] to the best of our knowledge. Thus, we show in this paper that PCTF-8 can not only be used for gas adsorption/separation but also exhibits high selectivity for the detection of 2,4,6-trinitrophenol (TNP) over other nitroaromatic analytes such as 4-nitrotoluene (NT), nitrobenzene (NB), 2,6-dinitrotoluene (2,6-DNT), 2,4-dinitrotoluene (2,4-DNT), 2,4-dinitrophenol (DNP) together with light-induced hydrogen evolution.

Experimental section

Materials

All chemicals were purchased from commercial suppliers (Sigma-Aldrich, Acros Organics, and Alfa Aesar chemical company) and used without further purification, unless stated otherwise. Tetra(4-cyanophenyl)ethylene was synthesized according to the reported procedures.[11] Chloroform was distilled from P_2O_5 under a nitrogen atmosphere.

Instrumentation

Infrared (IR) spectra were obtained on a Bruker FT-IR Tensor 37 Spectrometer in the 4000–550 cm^{-1} region with 2 cm^{-1} resolution as KBr disks. UV-vis absorption and fluorescence emission spectra were obtained using Jasco V-670 and FP-6500 spectrometers, respectively. Fluorescence quantum yields were evaluated using an absolute photoluminescence quantum yield measurement system equipped with a calibrated integrating sphere and a multi-channel spectrometer (C9920-02, Hamamatsu Photonics). The excitation wavelength was 395 nm. ^1H and ^{13}C spectra were recorded on a Bruker Avance DRX-500 instrument. ^1H and ^{13}C NMR chemical shifts are given in ppm relative to $SiMe_4$ ($\delta = 0.0$ ppm) with calibration against the residual protonated solvent signal ($CDCl_3$: 7.26 (^1H) and 77.0 (^{13}C)). ^{13}C cross-polarization (CP) MAS NMR measurements were performed at 100.6 MHz at a sample spinning frequency of 5 or 6 kHz using a Bruker Avance 400 spectrometer with a 7 mm zirconia rotor. For the ^{13}C CP-MAS NMR measurements, the repetition delay was 5 s, the contact time was 1.75 ms, and the pulse width was 4.5 μs (^1H 90° pulse). Elemental (CNH) analyses were carried out with a PerkinElmer 2400 series 2 elemental analyser. Powder X-ray diffraction (PXRD) data were collected on a Bruker D2 Phaser diffractometer using a flat sample holder (also a flat silicon, low background sample holder) and Cu $K\alpha_1/\alpha_2$ radiation with $\lambda = 1.5418$ Å at 30 kV covering 2theta angles 5–80° over a time period of 2 h, that is 0.01° s^{-1}. Diffractograms were obtained on flat layer sample holders where at low angles, the beam spot is strongly broadened so that only a fraction of the reflected radiation reaches the detector which leads to low relative intensities measured at $2\theta < 7°$. For hygroscopic or air-sensitive samples, the sample holder can be sealed with a dome. Scanning electron microscopy (SEM) images were obtained using an ESEM Quanta 400 FEG SEM equipped with a secondary electron detector. Thermogravimetric analyses (TGA) were carried out at a ramp rate of 5 °C min^{-1} under air with a Netzsch Thermo-Microbalance Apparatus TG 209 F3 Tarsus. A coulometric Karl–Fischer titration (KFT) for the determination of the water content was carried out with a Karl–Fischer titration apparatus AQUA 40.00 with a headspace module. The solid CTF sample was heated to 170 °C in the head space module and the liberated water was transferred to the measurement cell.

Sorption isotherms were measured using a Micromeritics ASAP 2020 automatic gas sorption analyser equipped with oil-free vacuum pumps (ultimate vacuum $<10^{-8}$ mbar) and valves, which guaranteed contamination free measurements. The sample was connected to the preparation port of the sorption analyser and degassed under vacuum until the outgassing rate, *i.e.* the rate of pressure rise in the temporarily closed manifold with the connected sample tube, was less than 2 μTorr min^{-1} at the specified temperature of 200 °C. After weighing, the sample tube was then transferred to the analysis port of the sorption analyser. All used gases (H_2, He, N_2, CO_2, and CH_4) were of ultra-high purity (UHP, grade 5.0, 99.999%) and the STP volumes are given according to the NIST standards (293.15 K, 101.325 kPa). Helium gas was used for the determination of the cold and warm free spaces of the sample tubes. H_2 and N_2 sorption isotherms were measured at 77 K (liquid nitrogen bath), whereas CO_2 and CH_4 sorption isotherms were measured at 293 ± 1 K (passive thermostating) and 273.15 K (ice/deionized water bath). The heat of adsorption values and the DFT pore size distributions ('N_2 DFT slit pore' model) were calculated using the ASAP 2020 v3.05 software.

Photocatalytic H_2 production experiments were performed with a Solar Box 3000 equipped with a Xe lamp (300 W). For each experiment, the polymer powder (10 mg) was suspended in a phosphate buffer solution (pH-7, 9 mL) containing triethanolamine (TEoA) or MeOH as a sacrificial donor (1 mL). Dihydrogen hexachloroplatinate (5 μL, 8 wt% aqueous solution) was added as the precursor for the *in situ* formation of a platinum cocatalyst. The solution was ultrasonicated for 15 min before being degassed by nitrogen bubbling for 30 min. The flask was illuminated at a 90° angle at a distance of 22 cm with a 300 W Xe lamp for the time specified. Gas samples were taken with a gas-tight syringe and quantified by using a gas chromatograph (Shimadzu GC-2010 Plus) equipped with a barrier discharge ionization detector (BID).

Time-correlated single photon counting (TCSPC) measurements were performed using a pulsed diode laser source (Edinburgh Instruments EPL405) operating at 404.6 nm with a pulse FWHM of *ca.* 77.1 ps. A neutral density filter was used to attenuate the beam to obtain photon counts of approx. 1% or less of the incoming light intensity. The detector used was a Hamamatsu MCP-photomultiplier tube R3809U-51 (cooled to *ca.* −40 °C), the signal was passed to a discriminator (Ortec 9307) and then into a TAC (Ortec 566, 50 ns time range used). The electrical trigger signal from the laser was also passed through a discriminator (Tennelec TC454) and onto the TAC (Ortec 566). The TAC output was read by a DAQ-1 MCA computer card using 4096 channels and collected with Horiba Jobin Yvon DataStation 2.3 software. All measurements were done in the reverse mode at 10 MHz and under magic angle polarisation. A cut-off filter (GG3) was used to block scattered excitation light. The instrument response function (IRF) was collected by using a dilute solution of Ludox as a standard scattering sample. Fluorescence lifetimes were obtained by iterative reconvolution of the IRF and the collected decay curves, by fitting to a multiexponential decay model using in-house scripts.

Synthesis

A 50 mL Schlenk flask was charged with trifluoromethanesulfonic acid (0.45 g, 3.0 mmol) in 8 mL dry $CHCl_3$ under a N_2 atmosphere. The reaction mixture was stirred and cooled to 0 °C. Tetra-(4-cyanophenyl)ethylene (217 mg, 0.5 mmol) in 30 mL dry $CHCl_3$ was added dropwise into the acid solution with stirring over 30 min and the temperature of 0 °C was maintained for another 2 h. Then, the resulting solution was stirred for 12 h at room temperature. An NH_3/H_2O solution (0.5 mol L^{-1}) was added until the reaction mixture became neutral and the mixture was stirred for another 2 h. The yellow product was isolated by filtration and washed with water (3 × 50 mL), THF (3 × 30 mL), acetone (3 × 30 mL), chloroform (3 × 30 mL) and further purified by Soxhlet extraction for 24 h with acetone. The final product was dried in a vacuum. The yield was 180 mg, 83% for $(C_{30}H_{16}N_4)_n$.

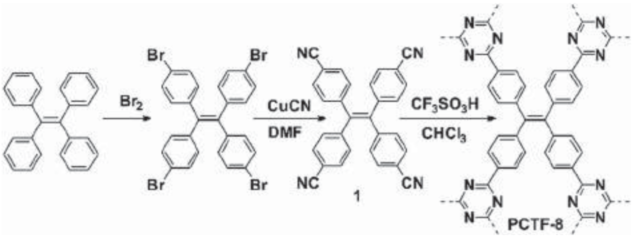

Scheme 1 Synthesis of the nitrile linker and PCTF-8.

Results and discussion

Synthesis and spectroscopic characterization

PCTF-8 was synthesized by the TFMS catalyzed reaction from tetra(4-cyanophenyl)ethylene (**1**) at room temperature as a yellow powder in 83% yield (Scheme 1). In FT-IR, the carbonitrile band

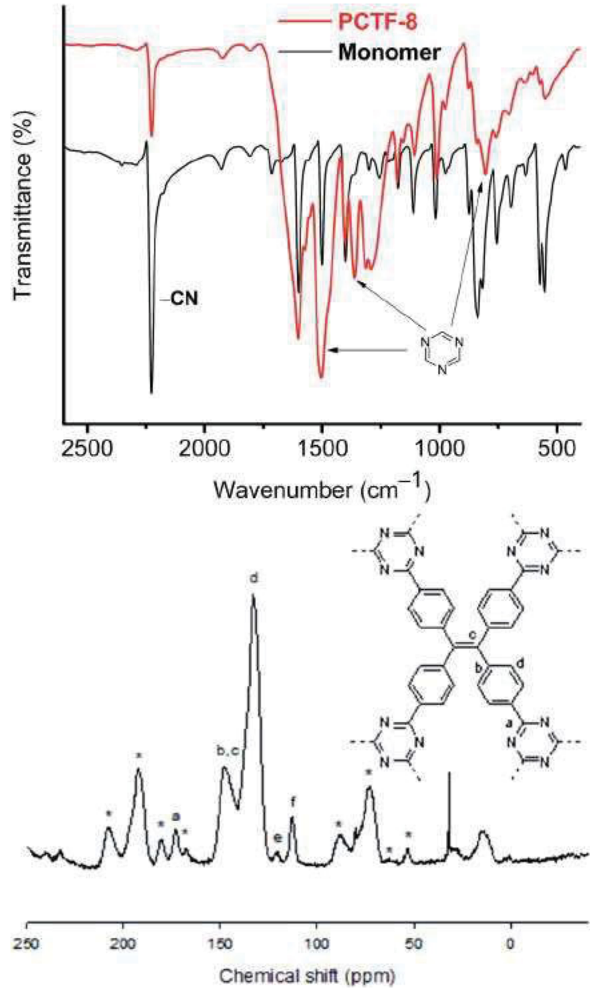

Fig. 1 IR spectra of the monomer and PCTF-8 (top). Solid-state ^{13}C CP/MAS NMR spectrum of PCTF-8 (bottom). Signals e and f are associated with residual cyano end groups and * belongs to sidebands.

in the precursors around 2226 cm^{-1} has significantly decreased in intensity which indicates only a few free nitrile groups in PCTF-8 (Fig. 1, top). The intense bands around 1503, 1362 and 800 cm^{-1} correspond to the formed triazine rings.[12] In the solid-state ^{13}C CP/MAS NMR spectrum (Fig. 1, bottom), the major resonances at 174, 141 and 134 ppm can be assigned to the triazine ring (–CAr=N–), ethylene carbon (–C=C–) and aromatic carbon (Ar) atoms, respectively.[12] The peaks around 124 and 114 ppm were associated with residual cyano end groups.[14] Powder X-ray diffraction of PCTF-8 confirmed its expected amorphous nature (Fig. S1, ESI†).

Thermogravimetric analysis (TGA) showed that PCTF-8 exhibited good thermal stability up to 420 °C under air (Fig. S2, ESI†). Elemental analysis (Table S1, ESI†) of PCTF-8 nearly matches the calculated values corrected with the results of KFT analysis which determined the water content of the sample (Fig. S3, ESI†). It became apparent that the PCTF-8 is hygroscopic and adsorbs about 10 wt% of moisture from ambient air upon storage under ambient conditions after vacuum drying at 120 °C. A similar hygroscopic behaviour of related CTFs was reported recently by Janiak *et al.*[18] and may be a common phenomenon to CTFs which may also explain the frequently observed mismatch in theoretical and experimental elemental (CHN) analysis. Under SEM, the PCTF-8 particles are small and largely irregular as well as angular shaped with a wide range of sizes (greater than 1 μm) (Fig. 2).

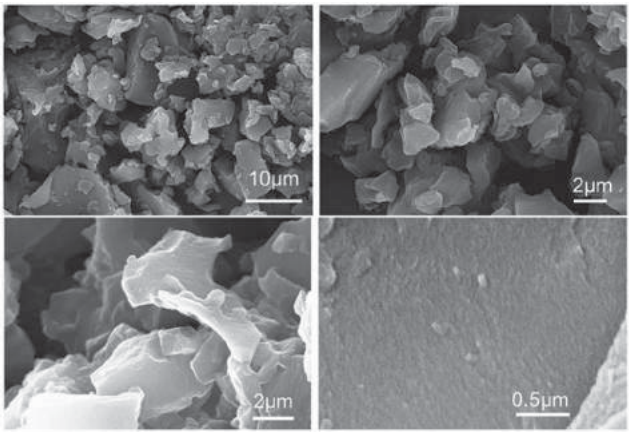

Fig. 2 SEM images of PCTF-8.

Gas sorption

The N_2 sorption isotherm shows a steep slope at low P/P_0 values and a type I character typical for microporous materials (Fig. 3 and Table S2, ESI†).[19] The calculated BET surface area of 625 m^2 g^{-1} is higher than for similar tetrakis(4-carboxyphenyl)ethylene linker-based fluorescent MOFs (244–317 m^2 g^{-1}).[20] The surface area of PCTF-8 is in the range of other TFMS-catalysed CTFs with 2 to 1152 m^2 g^{-1}.[14] The ratio of micropore volume to total pore volume ($V_{0.1}/V_{\mathrm{tot}}$) of 0.78 suggests that the material contains a very high fraction of micropores. A narrow distribution of micropores centered at 5, 5.9, 6.8, 11.8 and 14.8 Å was observed (insert in Fig. 3). PCTF-8 showed a H_2 sorption of 112 cm^3 g^{-1} at 77 K (with no hysteresis) that is very close to those of other CTFs.[13] The CO_2 adsorption capacities in activated PCTF-8 are 56 cm^3 g^{-1} at 273 K and 35 cm^3 g^{-1} at 293 K, respectively (Fig. 4). The CO_2 uptake of PCTF-8 was comparable to that of CTF-type polymers synthesized by TFMS, which showed CO_2 uptakes of 20–93 cm^3 g^{-1} at 273 K and 1 bar.[14] Such uptake capacity is also comparable to that of nanoporous 1,3,5-triazine frameworks (NOP-1-6, 29–56 cm^3 g^{-1}).[21] The CO_2 uptake of PCTF-8 is comparable to that of PCTF-1 which has about three times the BET surface area of PCTF-8.[11] This is due to the higher nitrogen content and intact triazine units of PCTF-8 from the milder synthesis conditions as CO_2 interacts with the triazine nitrogen due to its large polarizability and quadrupole moment.

The isosteric heat of adsorption from the CO_2 adsorption isotherms at 273 and 293 K (Fig. S4, ESI†) at zero loading is 37 kJ mol^{-1} and rapidly drops at adsorbate loadings of only a few cm^3 g^{-1}. The heat of adsorption stays around 29 kJ mol^{-1}

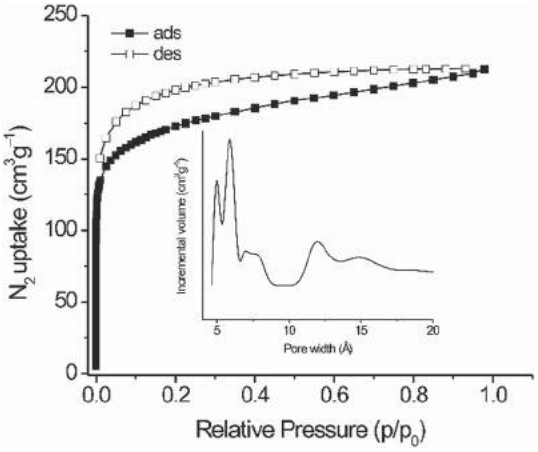

Fig. 3 N_2 sorption isotherms at 77 K and a NL-DFT pore size distribution profile (inset) of PCTF-8.

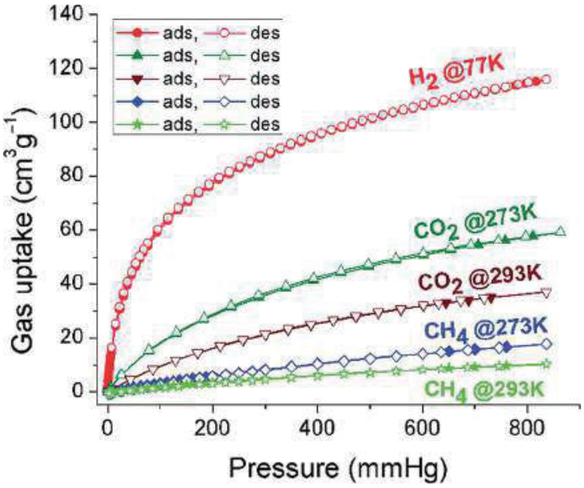

Fig. 4 H_2, CO_2, and CH_4 isotherms at 1 bar of PCTF-8.

for loadings between 3 and ~30 $cm^3\ g^{-1}$. When the loading is increased beyond 30 $cm^3\ g^{-1}$ the heat of adsorption value appears to increase slightly which should not be over-interpreted however in view of the error margin of readily ±3 kJ mol^{-1}.[13,22] This heat of CO_2 adsorption of ~29 kJ mol^{-1} for PCTF-8 stays well above the heat of liquefaction of bulk CO_2 with 17 kJ mol^{-1} [23] or around the isosteric enthalpy of adsorption for CO_2 on activated charcoals (*e.g.* BPL: 25.7 kJ mol^{-1}, A10: 21.6 kJ mol^{-1}, and Norit R1 Extra: 22.0 kJ mol^{-1}).[24] The high Q_{st} value can be attributed to the high polar framework and the pore size effect. The high adsorption enthalpy at zero coverage is explained by the initial filling of the small ultramicropores with 4 Å diameter (Fig. S5, ESI†) with adsorbate–surface interactions to both sides or ends of the CO_2 molecules.[13]

If the heat of adsorption would indeed exhibit an increase with CO_2 uptake, this means that a simultaneous, exothermic process must take place, such as possibly the rearrangement of already adsorbed CO_2 molecules towards a closer, energetically, more favorable configuration.

CH_4 sorption values of PCTF-8 were 17 $cm^3\ g^{-1}$ at 273 K and 10 $cm^3\ g^{-1}$ at 293 K (Fig. 4) which are comparable with the values for CTFs from our previous work.[11,13] From the available single-gas adsorption isotherms, the CO_2 selectivity over N_2 of PCTF-8 was calculated at 273 K by using the Henry equation and the ideal adsorbed solution theory (IAST) in order to understand greater affinity toward CO_2. The calculated adsorption selectivity of CO_2/N_2 is 24 and 61 at 273 K using the Henry equation and the ideal adsorbed solution theory (IAST), respectively (Fig. S6 and Section 8 in the ESI†), which are comparable with the values for PCTF-1 to −7 from our previous work as well as other CTFs.[11,13,14,25,26] This comparably large value of PCTF-8 for CO_2 may be attributed to the presence of more basic nitrogen moieties.

Photophysical properties

Absorption and photoluminescence spectra of PCTF-8 and its monomer (**1**) were measured at room temperature (Fig. 5). The monomer **1** dispersed in CH_2Cl_2 shows several absorption bands below 400 nm attributed to the π–π* transitions of the TPE chromophore.[27,28] Upon excitation at 350 nm, the monomer emits a weak blue emission with $\lambda_{max} = 389$ nm (Fig. 5a). This type of subunit is known to show an aggregation induced emission in the solid state or concentrated solutions. The weak emission is due to the non-restricted rotation of phenyl rings in dilute solutions.[29,30] On the other hand, a solid-state absorption spectrum of PCTF-8 exhibits a broad absorption band centred at around 400 nm ranging from 300 to 600 nm, which can be attributed to the TPE units (Fig. 5b). These different absorption profiles are responsible for the different colours; the monomer shows a light yellowish colour owing to absorbing UV light but reflecting all visible light, while PCTF-8 is a bright yellow powder due to absorbing blue light (Fig. 5).

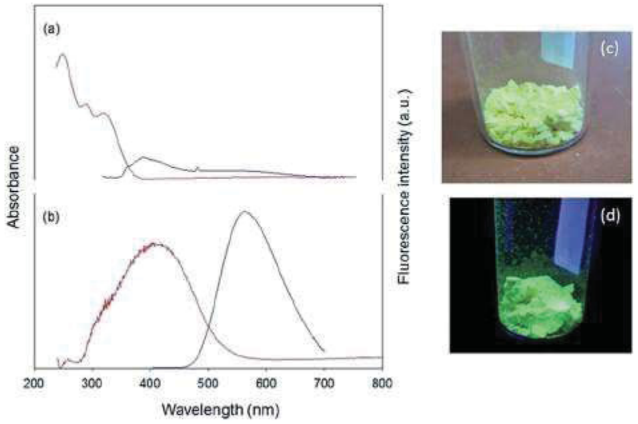

Fig. 5 Absorption (red line) and fluorescence spectra (blue line) of (a) monomer 1 (in CH_2Cl_2, λ_{exc} 350 nm) and (b) the corresponding PCTF-8 solid (λ_{exc} 395 nm). Photos of PCTF-8 are shown under ambient light (c) and UV-light (d).

To compare the emission behaviour of PCTF-8 synthesized under different conditions (Brønsted acid and ionothermal conditions), we have measured the emission spectrum of black coloured PCTF-1 that was synthesized under ionothermal conditions (Fig. S5, ESI†). PCTF-1 does not show appreciable emission because of partial carbonization in the framework. Therefore, highly emissive properties of CTFs seem only possible when avoiding carbonization by preparation at room temperature. In the solid-state, PCTF-8 shows a strong greenish-yellow fluorescence with an emission maximum at 562 nm when excited at 395 nm and a fluorescence quantum yield (Φ_f) of 31% at room temperature (Fig. 5b). This high value, compared to the extremely low quantum yield observed for the monomer in solution, is primarily attributed to the immobilization and restricted rotation of the aromatic rings in the tetraphenylethene units of the framework.[30,31]

From its ultraviolet-visible spectrum, the optical band gap of PCTF-8 was estimated to be 2.25 eV. In principle, this band gap is large enough to overcome the endothermic character of the water-splitting reaction. To investigate this property, photocatalytic hydrogen evolution experiments were performed with PTCF-8 and Pt-loaded PCTF-8 in the presence of a methanol or triethanolamine sacrificial electron donor (10 mol%) in buffered aqueous solutions. Without any platinum co-catalyst, no hydrogen evolution was observed. After loading with 2.3 wt% Pt, PCTF-8 showed H_2 production from buffered (pH 7) aqueous solutions containing sacrificial electron donors under simulated sunlight (Fig. S8, ESI†). The total amount of H_2 evolved of

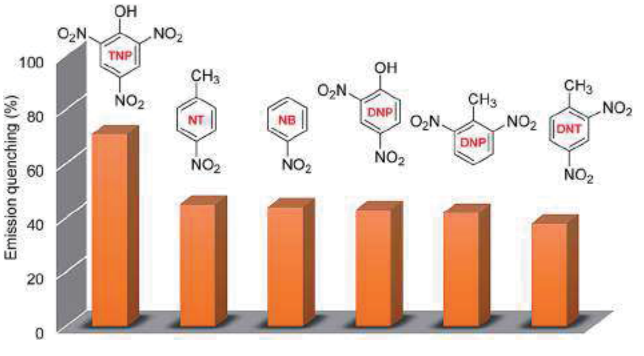

Fig. 6 Fluorescence quenching (%) of PCTF-8 with nitroaromatic analytes in acetonitrile dispersion.

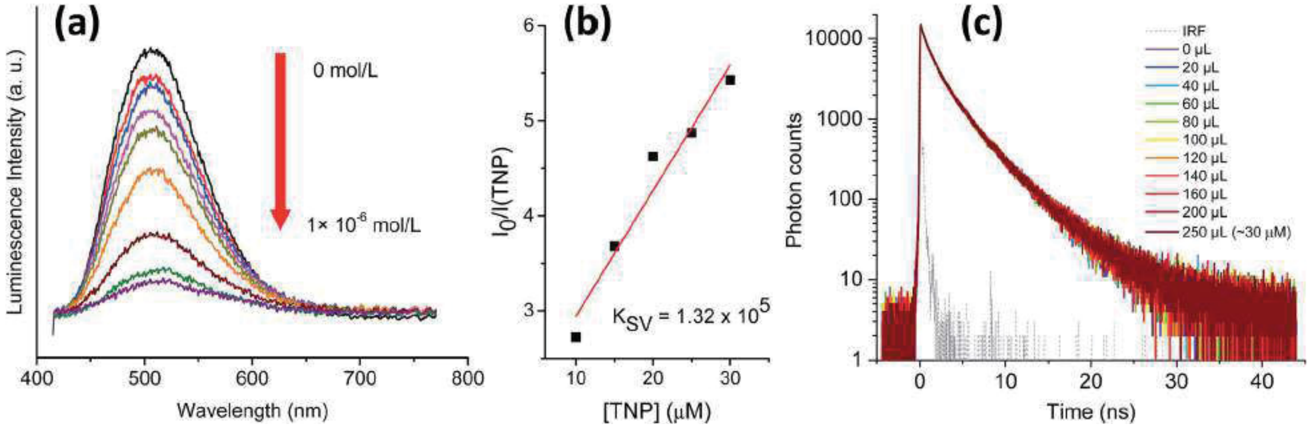

Fig. 7 (a) Fluorescence quenching of PCTF-8 by TNP (0 to 1×10^{-6} M) at room temperature (1 mg in 3 mL acetonitrile, $\lambda_{exc} = 395$ nm); (b) Stern–Volmer plots for the quenching of PCTF-8 by TNP in acetonitrile dispersion ($\lambda_{exc} = 395$ nm); (c) fluorescence decay profile of PCTF-8 ($\lambda_{exc} = 405$ nm) with different aliquots of TNP added, for a maximum quencher concentration of *ca.* 30 μM.

Pt-loaded PCTF-8 (10 mg) in a buffered aqueous methanol or TEoA solutions when irradiated for 20 h was 1780 and 2370 μmol g^{-1}, respectively. These moderate values of hydrogen production could be due to the poor crystallinity of PCTF-8 which hinders the diffusion of light-induced charge carriers to the surface.[9]

To examine the sensing behaviour of PCTF-8, luminescence spectrometric quenching titration experiments were performed by gradual addition of nitroaromatic analytes (TNP, NT or NB, 2,4-DNP, 2,6-DNT, 2,4-DNT, *cf.* Fig. 6) to PCTF-8 dispersed in acetonitrile at room temperature (Fig. 6 and 7a, and Section 11 in the ESI†).

Upon successive additions of nitroaromatic analytes, the fluorescence emission intensity was increasingly quenched, with TNP being the most effective quencher, for a maximum quenching of *ca.* 71% of the fluorescence emission intensity. The other analytes show similar quenching behaviour in the following order: TNP ≫ NT > NB > DNP > 2,6 DNT > 2,4 DNT (Fig. 6). Following the quenching experiment over time up to sixty minutes, it is evident that the quenching occurs very rapidly and does not increase over time (Fig. S16, ESI†).

To quantify the sensitivity towards the nitroaromatic analytes, the Stern–Volmer (SV) quenching constants (K_{SV}) were calculated by using the standard linear curve-fitting of the fluorescence intensity (I_0/I) in the presence of different concentrations of the analytes (1×10^{-5} to 5×10^{-5} mol L^{-1}) (Fig. 7b, S17–S21 in ESI†). The obtained quenching constants (K_{SV}) are in the order TNP ≫ DNP > NB > 2,6-DNT > 2,4-DNT > NT. The K_{SV} of TNP was 1.32×10^5 L mol^{-1} (Fig. 7b), which is comparable with those of previously reported frameworks.[32]

To further understand the nature of the quenching process involved in "turn-off" fluorescence sensing by PCTF-8, we measured the emission decays by time-correlated single photon counting at different concentrations of TNP (added as aliquots of a stock solution in acetonitrile), as it has the highest quenching efficiency of the studied nitroaromatic compounds. From the decays shown in Fig. 7c, it can be observed that the lifetime is independent of the concentration of the quencher in the studied range, which strongly suggests that a static quenching mechanism takes place. The static quenching behaviour of PCTF-8 with TNP can be explained in terms of the formation of a ground-state complex due to a strong interaction with the analyte (see the ESI† for discussion).[33] The lifetime of PCTF-8 was fitted to three exponential decay components ($\chi^2 = 1.324$, Fig. S22 in the ESI†): 0.5 ns (49%), 2.1 ns (42%) and 5 ns (1%). This decay behaviour can be rationalised in terms of the size distribution of the polymer, and due to the fact that emission comes from a heterogeneous suspension, where different aggregation behaviours can be observed.

Conclusions

In conclusion, we have used TPE units in the preparation of a porous and photoluminescent covalent triazine-based framework (PCTF) by using TFMS as the catalyst. This PCTF-8 showed photoluminescence behaviour under UV light, whereas the material PCTF-1 prepared by the high-temperature $ZnCl_2$ route was completely non-emissive. PCTF-8 shows sensitive detection towards nitroaromatic analytes with trinitrophenol (TNP) quenching *ca.* 71% of the PCTF-8 fluorescence emission intensity. The quenching mechanism was found to be static in nature because the emission lifetimes did not change with increasing addition of the analytes. From optical transmission measurements, we estimated a band gap of about 2.25 eV which determines its efficiency as a photocatalyst for hydrogen evolution. The total amount of H_2 evolved of Pt-loaded PCTF-8 in aqueous methanol or TEoA was 1780 and 2370 μmol g^{-1}, when irradiated for 20 h. Hence, CTFs are not only interesting for gas adsorption/separation but also hold great potential for hydrogen production and for the development of new luminescent chemosensors.

Acknowledgements

A. B. thanks Ghent Univ. (GOA nr. 01G00710). D. E. thanks the Scientific Research-Foundation Flanders (FWO), the Spanish Ministry of Economy and Competitiveness (Project MAT2013-44463-R), Junta de Andalucia (Project P10-FQM-6181 and Andalucia Talent Hub) and FEDER Funds. This work was partly supported by ACT-C, Japan Science and Technology Agency (JST), BMBF project OptiMat 03SF0492C and the HHU SFF fund. We thank Prof. Romero-Salguero of the University of Córdoba for his suggestions and support.

Notes and references

1 (*a*) A. I. Cooper, *Adv. Mater.*, 2009, **21**, 1291–1295; (*b*) M. E. Davis, *Nature*, 2002, **417**, 813–821; (*c*) J. R. Holst and A. I. Cooper, *Adv. Mater.*, 2010, **22**, 5212–5216; (*d*) V. Guillerm, L. J. Weselinski, M. Alkordi, M. I. H. Mohideen, Y. Belmabkhout, A. J. Cairns and M. Eddaoudi, *Chem. Commun.*, 2014, **50**, 1937–1940; (*e*) M. H. Alkordi, Ł. J. Weseliński, V. D'Elia, S. Barman, A. Cadiau, M. N. Hedhili, A. J. Cairns, R. G. AbdulHalim, J.-M. Basset and M. Eddaoudi, *J. Mater. Chem. A*, 2016, **4**, 7453–7460.

2 (*a*) S.-Y. Ding and W. Wang, *Chem. Soc. Rev.*, 2013, **42**, 548–568; (*b*) Y. Xu, S. Jin, H. Xu, A. Nagai and D. Jiang, *Chem. Soc. Rev.*, 2013, **42**, 8012–8031.

3 (*a*) J. Weber and A. Thomas, *J. Am. Chem. Soc.*, 2008, **130**, 6334–6335; (*b*) L. Chen, Y. Honsho, S. Seki and D. Jiang, *J. Am. Chem. Soc.*, 2010, **132**, 6742–6748; (*c*) A. Patra, J.-M. Koenen and U. Scherf, *Chem. Commun.*, 2011, **47**, 9612–9614; (*d*) X. Liu, Y. Xu and D. Jiang, *J. Am. Chem. Soc.*, 2012, **134**, 8738–8741; (*e*) A. Patra and U. Scherf, *Chem.–Eur. J.*, 2012, **18**, 10074–10080.

4 I. A. Levitsky, K. Kishikawa, S. H. Eichhorn and T. M. Swager, *J. Am. Chem. Soc.*, 2000, **122**, 2474; S. Wang, W. J. J. Oldham, R. A. J. Hudack and G. C. Bazan, *J. Am. Chem. Soc.*, 2000, **122**, 5695.

5 (*a*) Y. Xu, L. Chen, Z. Guo, A. Nagai and D. Jiang, *J. Am. Chem. Soc.*, 2011, **133**, 17622–17625; (*b*) L. Martelo, A. Jimenez, A. J. M. Valente, H. D. Burrows, A. T. Marques, M. Forster, U. Scherf, M. Peltzer and S. M. Fonseca, *Polym. Int.*, 2012, **61**, 1023–1030.

6 V. M. Suresh, S. Bonakala, S. Roy, S. Balasubramanian and T. K. Maji, *J. Phys. Chem. C*, 2014, **118**, 24369–24376.

7 (*a*) S. Pramanik, C. Zheng, X. Zhang, T. J. Emge and J. Li, *J. Am. Chem. Soc.*, 2011, **133**, 4153–4155; (*b*) D. Banerjee, Z. Hu and J. Li, *Dalton Trans.*, 2014, **43**, 10668–10685; (*c*) S. Dalapati, S. Jin, J. Gao, Y. Xu, A. Nagai and D. Jiang, *J. Am. Chem. Soc.*, 2013, **135**, 17310–17313; (*d*) G. Das, B. P. Biswal, S. Kandambeth, V. Venkatesh, G. Kaur, M. Addicoat, T. Heine, S. Verma and R. Banerjee, *Chem. Sci.*, 2015, **6**, 3931–3939; (*e*) L. Zhang, Z. Kang, X. Xin and D. Sun, *CrystEngComm*, 2016, **18**, 193.

8 (*a*) L. Stegbauer, K. Schwinghammer and B. V. Lotsch, *Chem. Sci.*, 2014, **5**, 2789–2793; (*b*) S. Ren, R. Dawson, A. Laybourn, J.-X. Jiang, Y. Khimyak, D. J. Adamsa and A. I. Cooper, *Polym. Chem.*, 2012, **3**, 928–934; (*c*) T. Ishi-i, K. Yaguma, T. Thiemann, M. Yashima, K. Ueno and S. Mataka, *Chem. Lett.*, 2004, **33**, 1244–1245.

9 (*a*) L. Stegbauer, K. Schwinghammer and B. V. Lotsch, *Chem. Sci.*, 2014, **5**, 2789–2793; (*b*) K. Schwinghammer, S. Hug, M. B. Mesch, J. Senker and B. V. Lotsch, *Energy Environ. Sci.*, 2015, **8**, 3345–3353; (*c*) K. Schwinghammer, B. Tuffy, M. B. Mesch, E. Wirnhier, C. Martineau, F. Taulelle, W. Schnick, J. Senker and B. V. Lotsch, *Angew. Chem., Int. Ed.*, 2013, **52**, 2435–2439; (*d*) K. Kailasam, J. Schmidt, H. Bildirir, G. Zhang, S. Blechert, X. Wang and A. Thomas, *Macromol. Rapid Commun.*, 2013, **34**, 1008–1013; (*e*) K. Kailasam, M. B. Mesch, L. Möhlmann, M. Baar, S. Blechert, M. Schwarze, M. Schröder, R. Schomäcker, J. Senker and A. Thomas, *Energy Technol.*, 2016, **4**, 744–750; (*f*) R. S. Sprick, B. Bonillo, R. Clowes, P. Guiglion, N. J. Brownbill, B. J. Slater, F. Blanc, M. A. Zwijnenburg, D. J. Adams and A. I. Cooper, *Angew. Chem., Int. Ed.*, 2016, **128**, 1824–1828; (*g*) R. S. Sprick, J.-X. Jiang, B. Bonillo, S. Ren, T. Ratvijitvech, P. Guiglion, M. A. Zwijnenburg, D. J. Adams and A. I. Cooper, *J. Am. Chem. Soc.*, 2015, **137**, 3265–3270.

10 X. Wang, K. Maeda, A. Thomas, K. Takanabe, G. Xin, J. M. Carlsson, K. Domen and M. Antonietti, *Nat. Mater.*, 2009, **8**, 76–80.

11 A. Bhunia, V. Vasylyeva and C. Janiak, *Chem. Commun.*, 2013, **49**, 3961–3963.

12 P. Kuhn, M. Antonietti and A. Thomas, *Angew. Chem., Int. Ed.*, 2008, **47**, 3450–3453; P. Kuhn, A. l. Forget, D. Su, A. Thomas and M. Antonietti, *J. Am. Chem. Soc.*, 2008, **130**, 13333–13337; M. J. Bojdys, J. Jeromenok, A. Thomas and M. Antonietti, *Adv. Mater.*, 2010, **22**, 2202–2205.

13 A. Bhunia, I. Boldog, A. Möller and C. Janiak, *J. Mater. Chem. A*, 2013, **1**, 14990–14999.

14 S. Ren, M. J. Bojdys, R. Dawson, A. Laybourn, Y. Z. Khimyak, D. J. Adams and A. I. Cooper, *Adv. Mater.*, 2012, **24**, 2357–2361.

15 P. Katekomol, J. Roeser, M. Bojdys, J. Weber and A. Thomas, *Chem. Mater.*, 2013, **25**, 1542–1548.

16 (*a*) C. E. Chan-Thaw, A. Villa, P. Katekomol, D. Su, A. Thomas and L. Prati, *Nano Lett.*, 2010, **10**, 537–541; (*b*) J. Artz, S. Mallmann and R. Palkovits, *ChemSusChem*, 2015, **8**, 672–679.

17 A. Bhunia, S. Dey, M. Bous, C. Zhang, W. von Rybinski and C. Janiak, *Chem. Commun.*, 2015, **51**, 484–486.

18 S. Dey, A. Bhunia, D. Esquivel and C. Janiak, *J. Mater. Chem. A*, 2016, **4**, 6259–6626.

19 K. S. W. Sing, D. H. Everett, R. A. W. Haul, L. Moscou, R. A. Pierotti, J. Rouquérol and T. Siemieniewska, *Pure Appl. Chem.*, 1985, **57**, 603.

20 N. B. Shustova, B. D. McCarthy and M. Dincă, *J. Am. Chem. Soc.*, 2011, **133**, 20126–20129.

21 S. Xiong, X. Fu, L. Xiang, G. Yu, J. Guan, Z. Wang, Y. Du, X. Xiong and C. Pan, *Polym. Chem.*, 2014, **5**, 3424–3431.

22 F. Jeremias, A. Khutia, S. K. Henninger and C. Janiak, *J. Mater. Chem.*, 2012, **22**, 10148–10151; F. Jeremias, V. Lozan, S. Henninger and C. Janiak, *Dalton Trans.*, 2013, **42**, 15967–15973.

23 S. Keskin, T. M. van Heest and D. S. Sholl, *ChemSusChem*, 2010, **3**, 879–891.

24 S. Himeno, T. Komatsu and S. Fujita, *J. Chem. Eng. Data*, 2005, **50**, 369–376; K. B. Lee, M. G. Beaver, H. S. Caram and S. Sircar, *Ind. Eng. Chem. Res.*, 2008, **47**, 8048–8062.

25 S. Xiong, X. Fu, L. Xiang, G. Yu, J. Guan, Z. Wang, Y. Du, X. Xiong and C. Pan, *Polym. Chem.*, 2014, **5**, 3424–3431.

26 X. Liu, H. Li, Y. Zhang, B. Xu, S. A, H. Xia and Y. Mu, *Polym. Chem.*, 2013, **4**, 2445–2448.

27 Y. Xu, A. Nagai and D. Jiang, *Chem. Commun.*, 2013, **49**, 1591.

28 W. Lluo, Y. Zhu, J. Zhang, J. He, Z. Chi, P. W. Miller, L. Chen and C. Su, *Chem. Commun.*, 2014, **50**, 11942–11945.

29 Y. Hong, J. W. Y. Lam and B. Z. Tang, *Chem. Soc. Rev.*, 2011, **40**, 5361–5388.

30 V. M. Suresh, S. Bonakala, S. Roy, S. Balasubramanian and T. K. Maji, *J. Phys. Chem. C*, 2014, **118**, 24369–24376.

31 Z. Wei, Z. Gu, R. K. Arvapally, Y. Chen, R. N. McDougald, J. F. Ivy, A. A. Yakovenko, D. Feng, M. A. Omary and H. Zhou, *J. Am. Chem. Soc.*, 2014, **136**, 8269–8276.

32 S. Shanmugaraju and P. S. Mukherjee, *Chem. Commun.*, 2015, **51**, 16014–16032.

33 J. R. Lakowicz, *Principles of Fluorescence Spectroscopy*, Springer, New York, 3rd edn, 2006.

Electronic Supplementary Information (ESI)

A photoluminescent covalent triazine framework: CO_2 adsorption, light-driven hydrogen evolution and sensing of nitroaromatics

Asamanjoy Bhunia,*[a,b] Dolores Esquivel,[a,c] Subarna Dey,[b] Ricardo Fernández-Terán,[d] Yasutomo Goto,[e] Shinji Inagaki,[e] Pascal Van Der Voort,[a] and Christoph Janiak*[b]

[a]Department of Inorganic and Physical Chemistry, Centre for Ordered Materials, Organometallics and Catalysis, Ghent University, Krijgslaan 281-S3, 9000 Ghent, Belgium.
[b]Institut für Anorganische Chemie und Strukturchemie, Universität Düsseldorf, 40204 Düsseldorf, Germany.
[c]Department of Organic Chemistry, Nanochemistry and Fine Chemistry Research Institute (IUIQFN), Faculty of Sciences, University of Córdoba, Campus of Rabanales, Marie Curie Building, Ctra. Nal. IV, km 396, 14071 Córdoba, Spain.
[d]Department of Chemistry – Ångström Laboratory, Uppsala University, Box 523, SE-751 20, Uppsala, Sweden.
[e]Toyota Central R&D Laboratories., Inc., Nagakute, Aichi 480-1192, Japan.

Supporting information
16 pages

Table of contents

1. Powder X-ray diffraction pattern

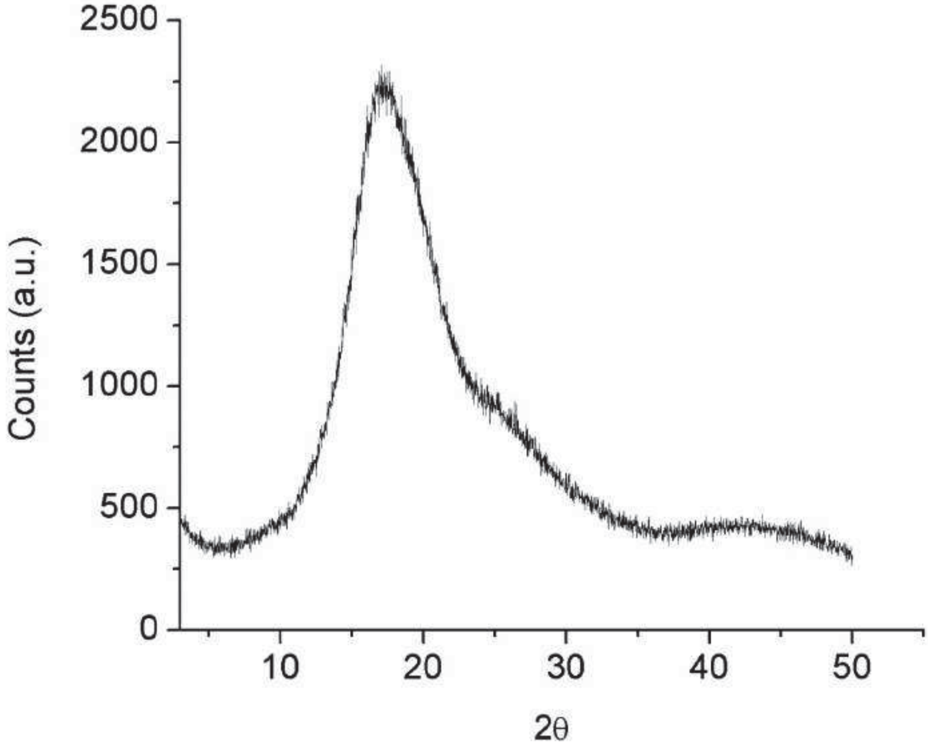

Fig. S1: Powder X-ray pattern of PCTF-8.

2. Elemental analysis of PCTF-8

Elemental analysis suggested that the formula unit ($C_{30}H_{16}N_4$) contain additional three water molecules which is in good agreement with results found by Karl-Fischer titration (KFT). The calculated and found values are in the Table S1.

Table S1: Elemental analysis of PCTFs

Compound	Calculated (% and molar ratio)					Found (% and molar ratio)				
	C	H	N	C/H	C/N	C	H	N	C/H	C/N
[a]PCTF-8	83.32	3.73	12.95	2	8	74.96	4.55	11.16	1	8
[b]PCTF-8	74.06	4.56	11.52	1	8	74.96	4.55	11.16	1	8

[a]Formula unit without water molecule. [b]Formula unit contain three water molecules.

3. Thermogravimetric analysis (TGA)

PCTF-8 is thermally stable up to 420 °C. The weight loss step that occurs below the decomposition temperature of the PCTF-8 can be ascribed to the removal of the solvent molecules as well as guest molecules from the pore.

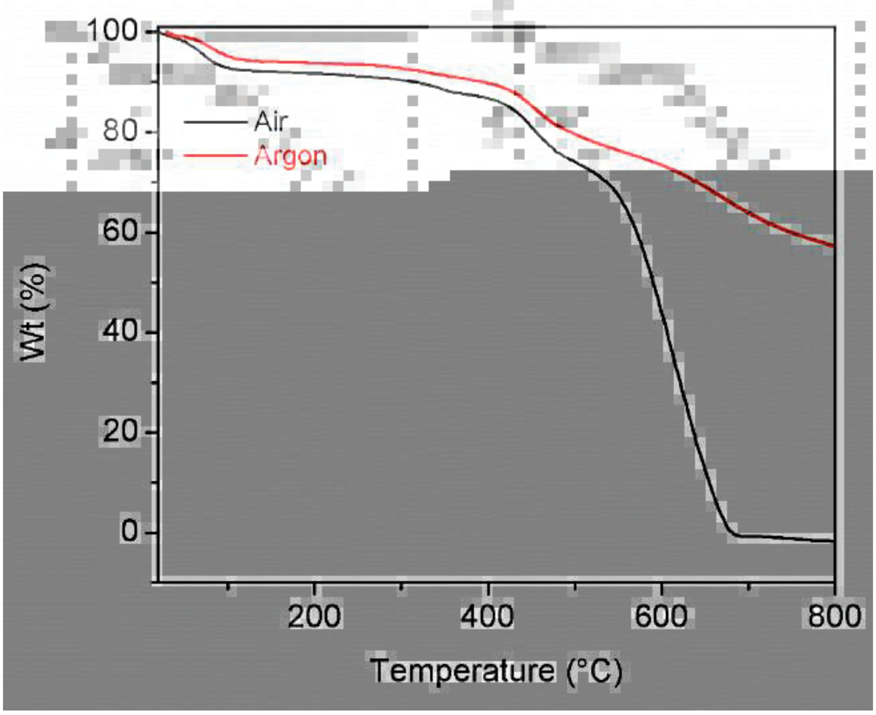

Fig. S2: TGA plot for PCTF-8 under air (black colour) and argon (red colour).

4. Analyses for water content

Karl-Fischer titration (KFT):

Water content of a PCTF-8 sample was determined by KFT. We found about 10 wt% water in the material which is in good agreement with the oxygen content found by CHN analysis. The PCTF-8 material had been stored under ambient air after vaccum drying at 120°C for 24 h.

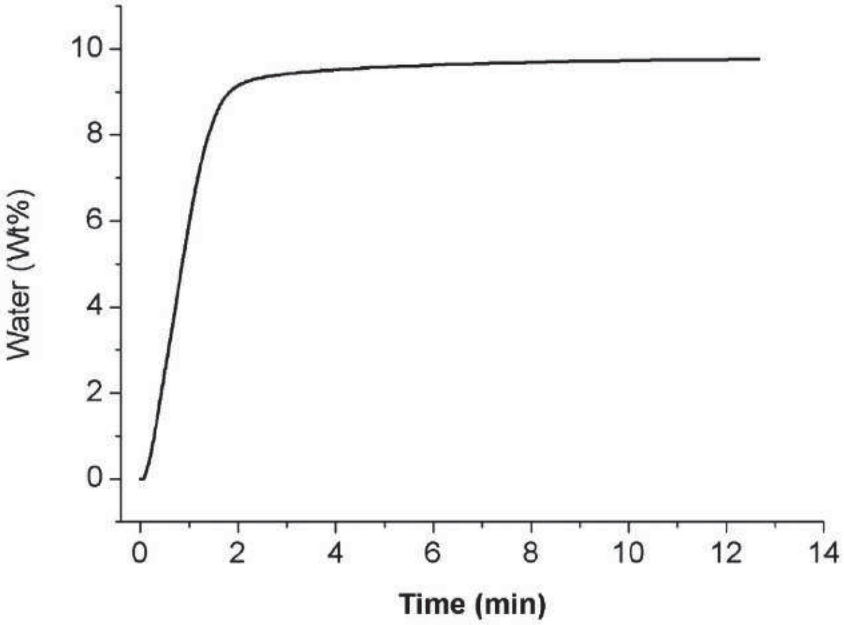

Fig. S3: Karl-Fischer titration plot for PCTF-8.

5. Surface area and pore volume data for PCTF-8

Table S2: Porosity data for PCTF-8 from N_2 isotherms at 77 K

Compound	S_{BET} [a]	S_{Lang} [a]	$V_{0.1}$ [b]	V_{tot} [c]	$V_{0.1}/V_{tot}$
	(m^2 g^{-1})	(m^2 g^{-1})	(cm^3 g^{-1})	(cm^3 g^{-1})	
PCTF-8	625	758	0.25	0.32	0.78

[a]Calculated BET surface area over the pressure range 0.01–0.05 P/P_0; [b]Pore volume at $P/P_0 = 0.1$; [c]Total pore volume at $P/P_0 = 0.95$.

6. Isosteric heat of adsorption of CO_2 for PCTF-8

From two adsorption isotherms acquired at different temperatures T_1 and T_2, the differential heat of adsorption $\Delta H_{ads,diff}$, that is isosteric heat of adsorption Q_{st} can be calculated for any amount of adsorbed substance after determining the required relative pressures p_1 and p_2. A modified form of the Clausius-Clapeyron equation is used (eq (1)).[1] $\Delta H_{ads,diff}$ was calculated over the whole adsorption range from the 273 K and 293 K isotherms for CO_2.

$$\Delta H_{ads,diff} = Q_{st} =- Rln\left(\frac{p_2}{p_1}\right)\frac{T_1T_2}{T_2-T_1} \qquad (1)$$

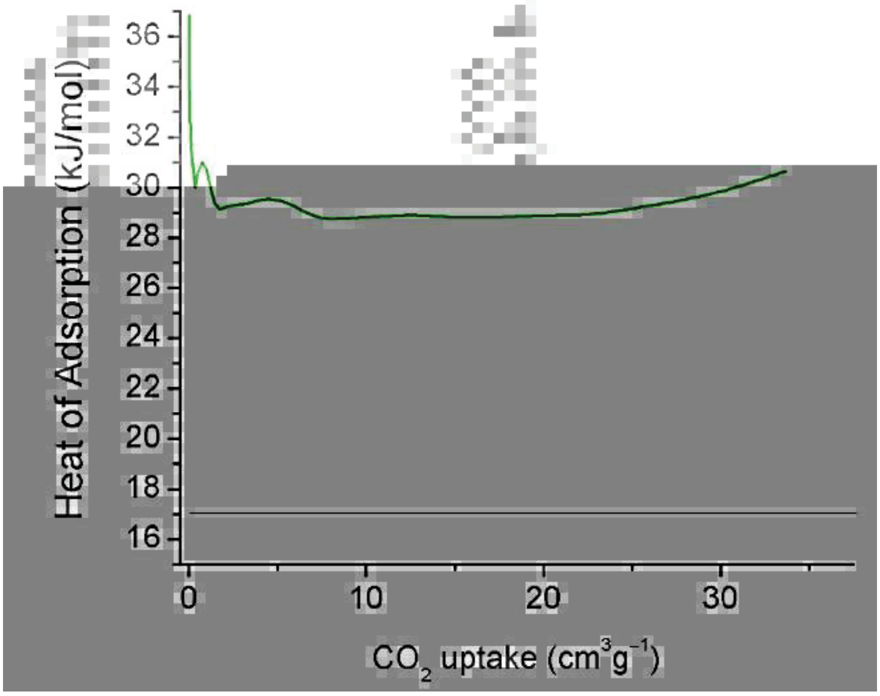

Fig. S4: Isosteric differential heat of adsorption (adsorption enthalpy, $Q_{ads,diff}$) as a function of CO_2 uptake for PCTF-8.

7. Pore size distribution from a CO_2 adsorption isotherm

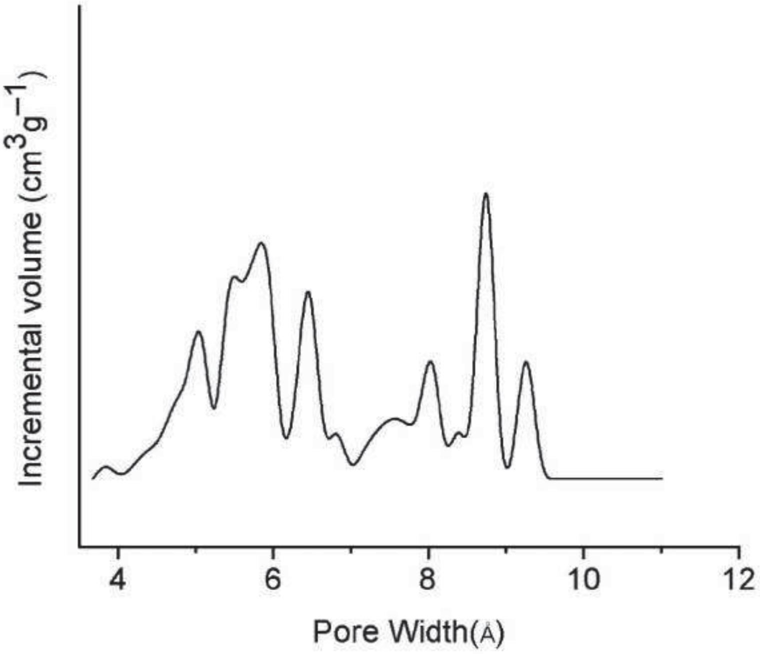

Fig. S5: The pore size distribution from a CO_2 adsorption isotherm at 273 K, calculated by the NL-DFT with a "CO_2 on carbon based slit-pore" model at 273 K.

8. Selectivity studies

TableS3: Langmuir fitting parameters of CO_2, CH_4, and N_2 adsorption isotherms of PCTF-8 at 273 K and 1 bar.

PCTF-8@273K	$q_{sat,A}$ (mmol/g)	b_A (bar^{-1})	$q_{sat,B}$ (mmol/g)	b_B (bar^{-1})	Adj. R^2
CO_2	0.76614	8.44818	3.87379	0.8761	1
CH_4	2.14138	0.52433			0.99997
N_2	1.29082	0.21243			0.99997

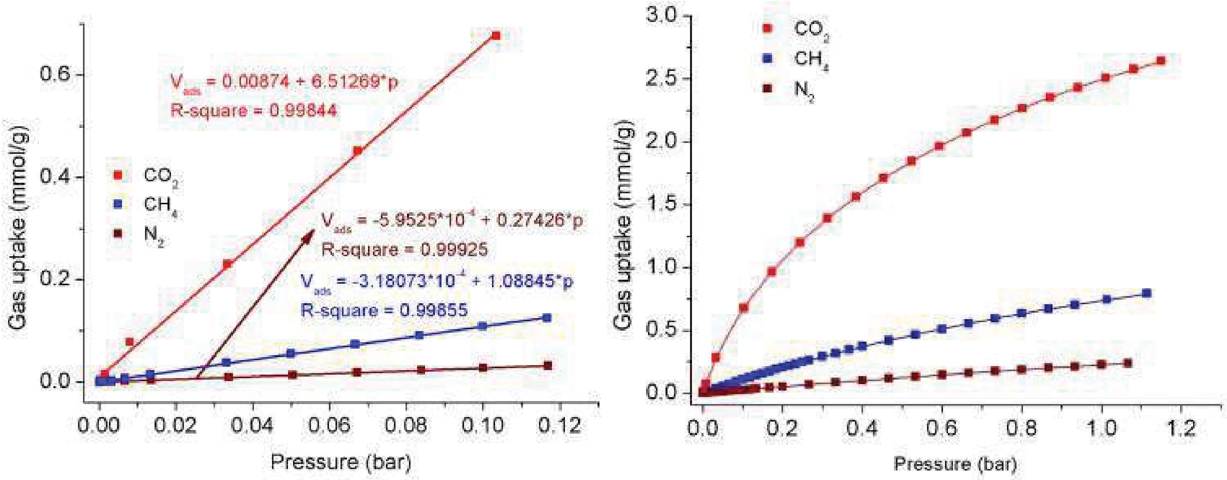

Fig. S6: Adsorption selectivity for PCTF-8 using Henry equation (left) and IAST (right).

9. Emission spectrum of PCTF-1

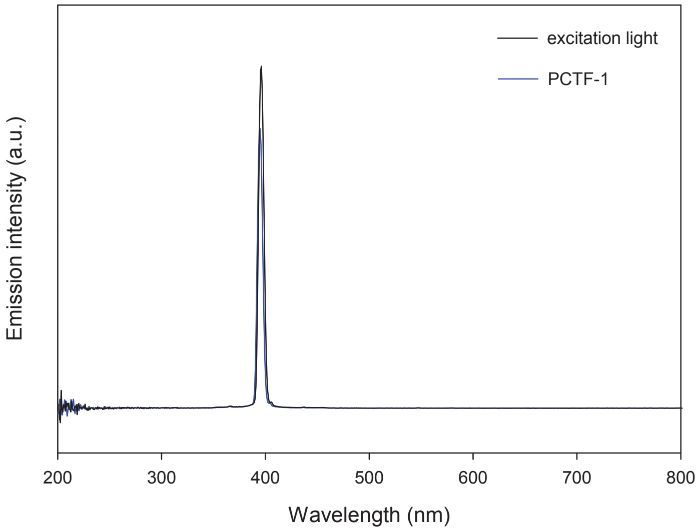

Fig. S7: Emission spectrum of PCTF-1 and the excitation light.

10. H_2 Evolution Experiments

Fig. S8: Gas chromatograms: The peak of hydrogen evolution for Pt-loaded PCTF-8 in the presence of methanol (blue colour line) and triethanolamine (magenta colour line) sacrificial electron donor (10%) under simulated light for 24 h. Black colour line represent the hydrogen evolution experiment of PCTF-8 without using cocatalyst (Dihydrogen hexachloroplatinate).

11. Nitroaromatic Explosives Detections

The fluorescence quenching of dispersed PCTF-8 were investigated at room temperature. The dispersions were prepared using 1 mg PCTF-8 in 3 mL acetonitrile. The resulting suspensions were ultrasonicated for 10 min before adding different analytes (TNP, 2,4-DNP, 2,6-DNT, 2,4-DNT, NT and NB). The analytes (0 to 1× 10^{-6} mol/L) were added into the dispersion of PCTF-8 via micro pipette. After 2-3 minutes, the fluorescence emission spectra were recorded ($\lambda_{exc} = 395\ nm$ for all spectra).

The K_{SV} values we report are not corrected for the inner filter effect for two main reasons. Out of the six studied nitroaromatic analytes, four (2,4-DNP, 2,4-DNT, NB and NT) have negligible absorption at either 395 nm or 405 nm, as shown in Fig. S9. In spite of the fact that the NIST database page does not report the solvent used for the measurements, we do not expect any significant shift in the absorption which can involve an increase in the extinction coefficients above 390 nm. In the same way, the absorption bands of these compounds are far from the onset of the emission of PCTF-8, and therefore no primary nor secondary inner filter effect contributions are expected to arise from these analytes, making any correction of the reported K_{SV} unnecessary. In the case of TNP and 2,6-DNT, in spite of the fact that the absorption spectra of these compounds (Fig.

S10) overlap with the absorption spectrum of PCTF-8, given that the concentrations we used for the quenching experiments were extremely low (30 μM at most), we do not expect any significant impact of the possible corrections for the inner filter effect, which we estimate to be less than the experimental error in the determination of the fluorescence intensities. At the same time, even for Anthracene (example given in J. R. Lakowicz, Principles of fluorescence spectroscopy, Springer, New York, 3rd ed., 2006 page 56, Figure 2.47), the linear range of the fluorescence emission intensity vs. concentration goes up to the Mm scale, while in our work we are using μM concentrations of the analytes.

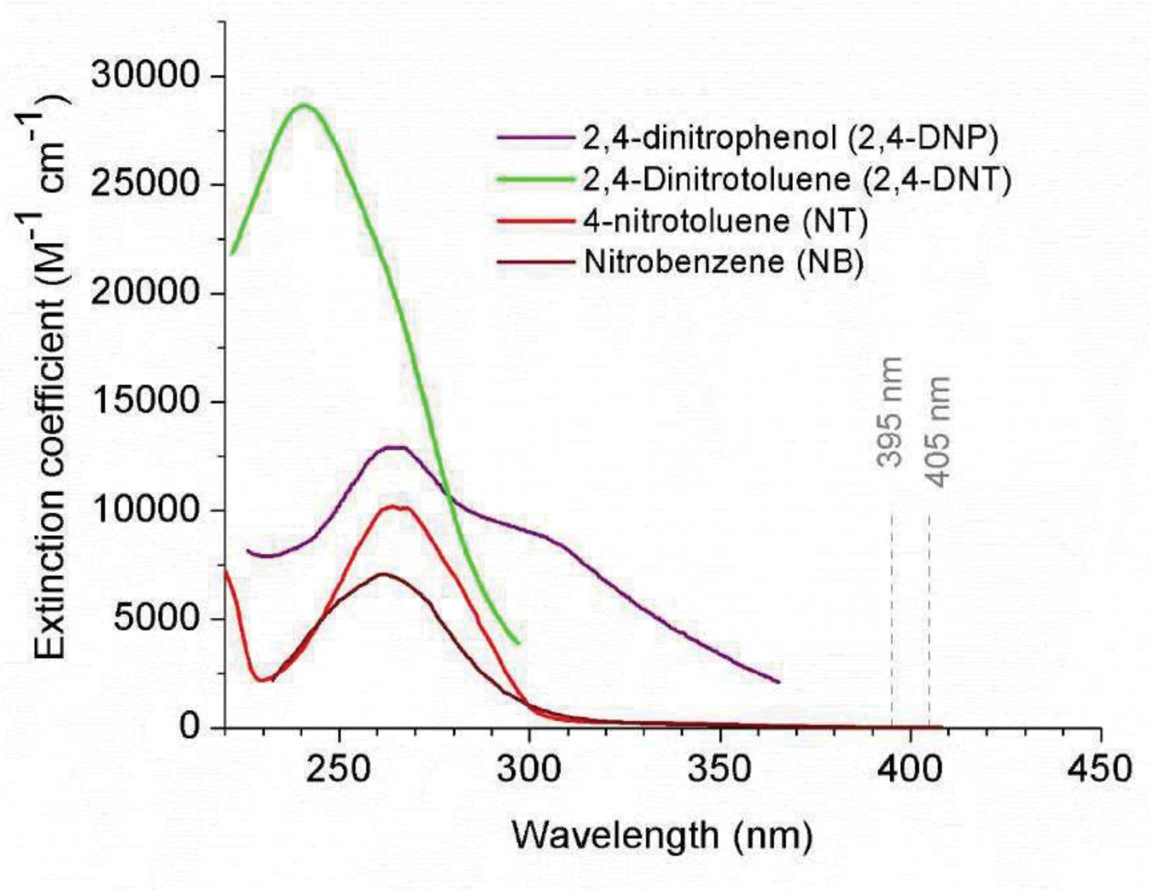

Fig. S9: Extinction coefficients of four nitroaromatic analytes. Data from NIST Standard Reference Database. 2,4-dinitrophenol has negligible absorption beyond 360 nm.

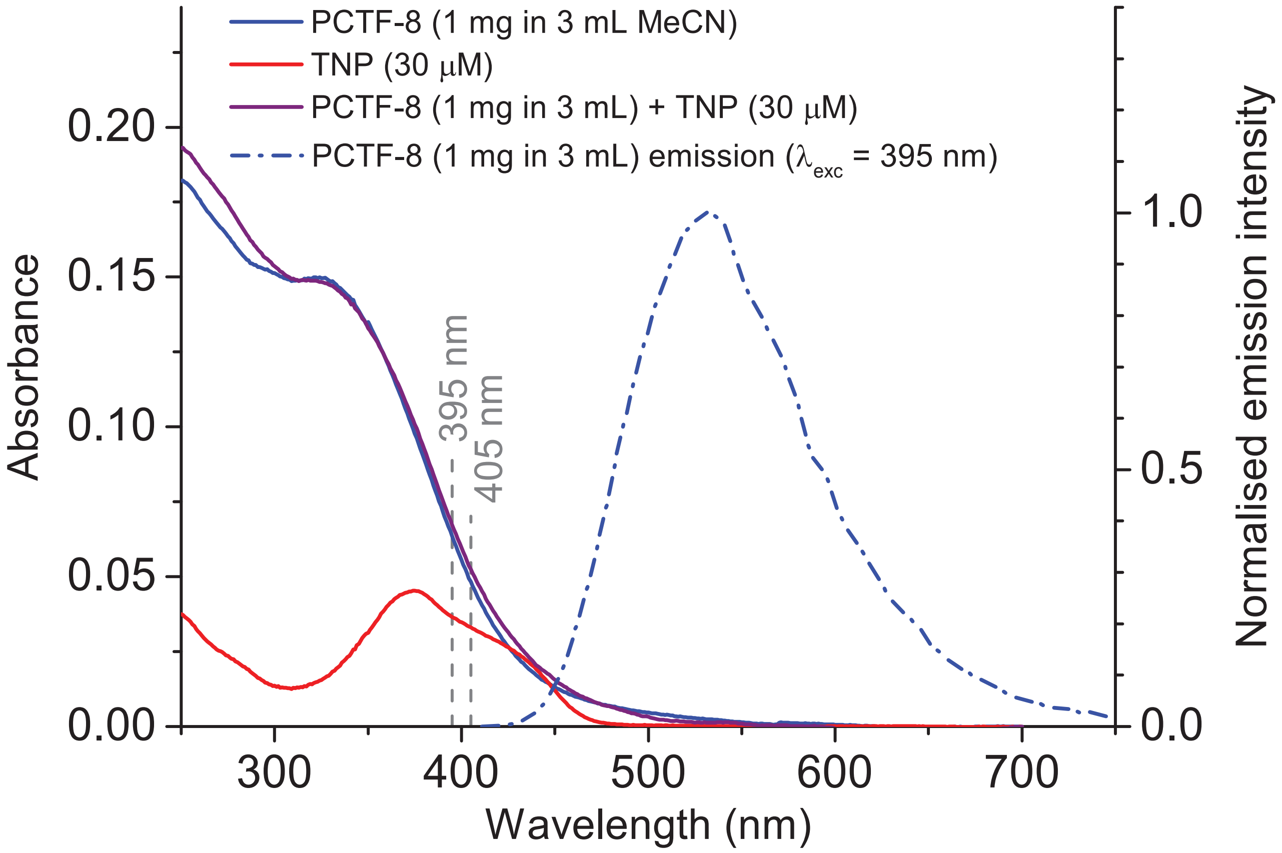

Fig. S10: Absorption and emission spectra of PCTF-8 (1 mg in 3 mL MeCN, $\lambda_{exc} = 395\ nm$), together with absorption spectra of TNP (30 μM) and a mixture of TNP and PCTF-8 (1 mg in 3 mL)

In the range of concentrations that we used, and as evidenced in Fig. S10, the absorption of picric acid (TNP, 30 μM solution in MeCN) and of PCTF-8 (1 mg in 3 mL MeCN), as well as a solution containing both the TNP analyte and PCTF-8 (identical concentrations) at either 395 nm (wavelength used for steady-state quenching experiments) or at 405 nm (wavelength used for TCSPC studies) is below 0.1 (approx. 0.06, as shown in Fig. S10), and therefore we conclude that corrections to our reported K_{SV} values are not necessary, as no significant contributions from the inner filter effect are expected with this very low absorbance. As an additional comment, the linearity of our Stern-Volmer plots also reflects the absence of inner filter effects and other possible deviations from the standard behavior in the concentration range of the analytes that we employed. 2,6-dinitrophenol has a lower extinction coefficient than TNP at either 395 or 405 nm, and therefore no corrections are expected to be needed for this analyte in the studied concentration range, either.

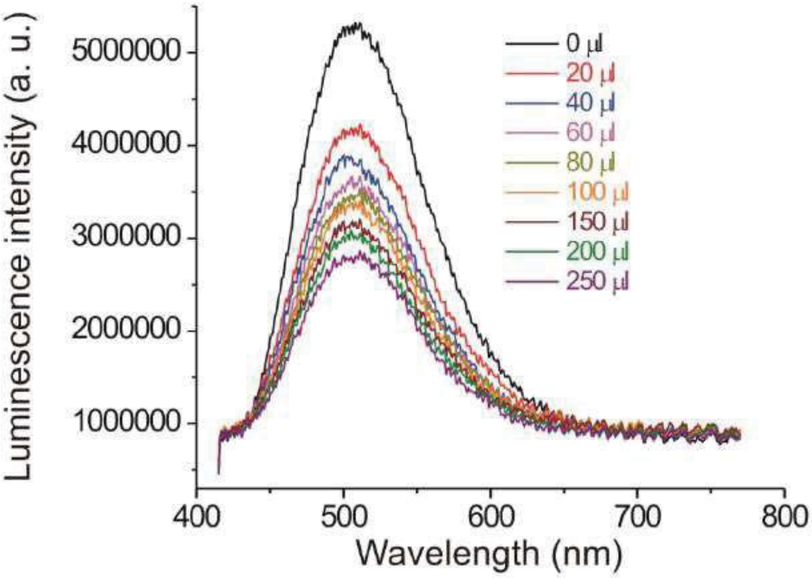

Fig. S11: Fluorescence quenching ($\lambda_{exc} = 395\ nm$) of PCTF-8 by 2,4-DNP (0 – 1×10^{-6} mol/L) at room temperature (1 mg PCTF-8 in 3 mL acetonitrile).

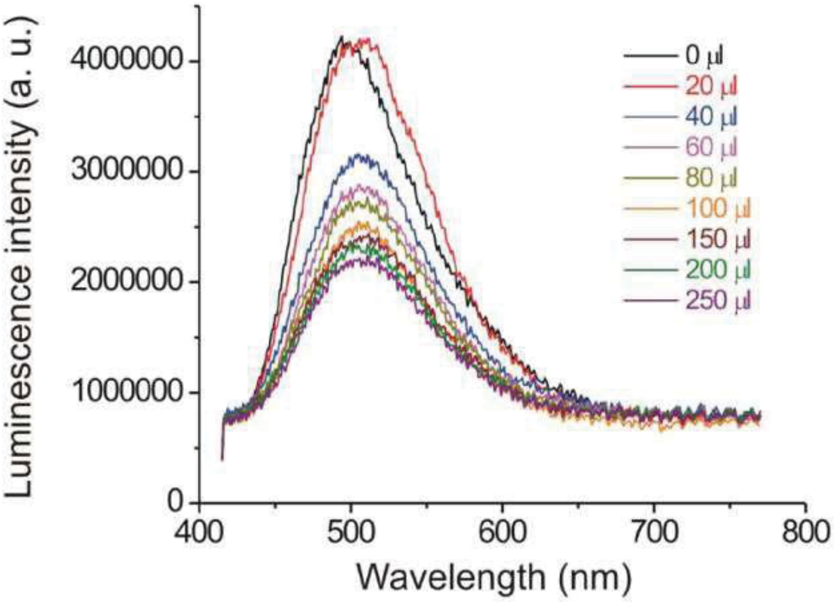

Fig. S12: Fluorescence quenching ($\lambda_{exc} = 395\ nm$) of PCTF-8 by 2,6-DNT (0–1×10^{-6} mol/L) at room temperature (1 mg PCTF-8 in 3 mL acetonitrile).

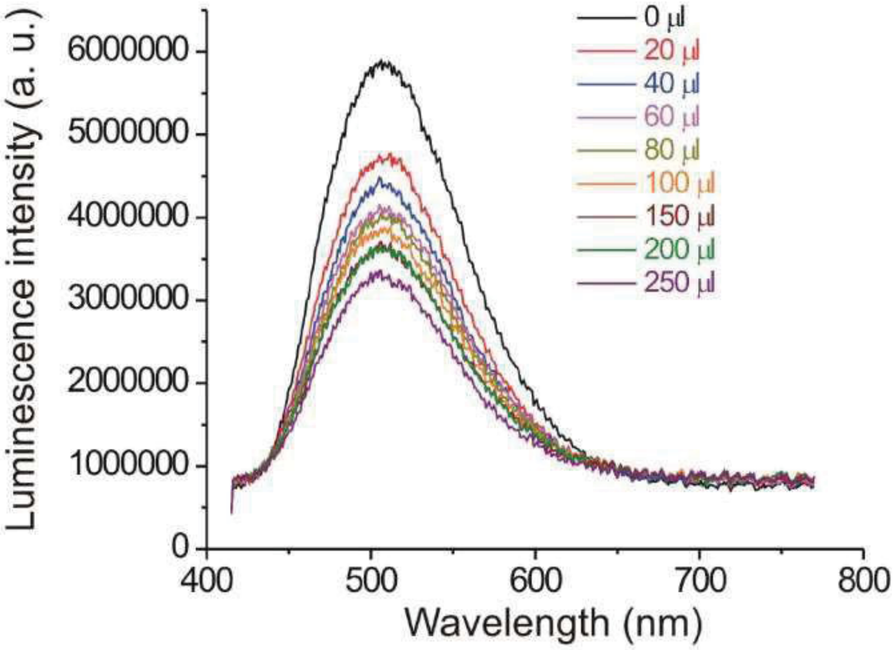

Fig. S13: Fluorescence quenching ($\lambda_{exc} = 395\ nm$) of PCTF-8 by 2,4-DNT (0 – 1×10^{-6} mol/L) at room temperature (1 mg PCTF-8 in 3 mL acetonitrile).

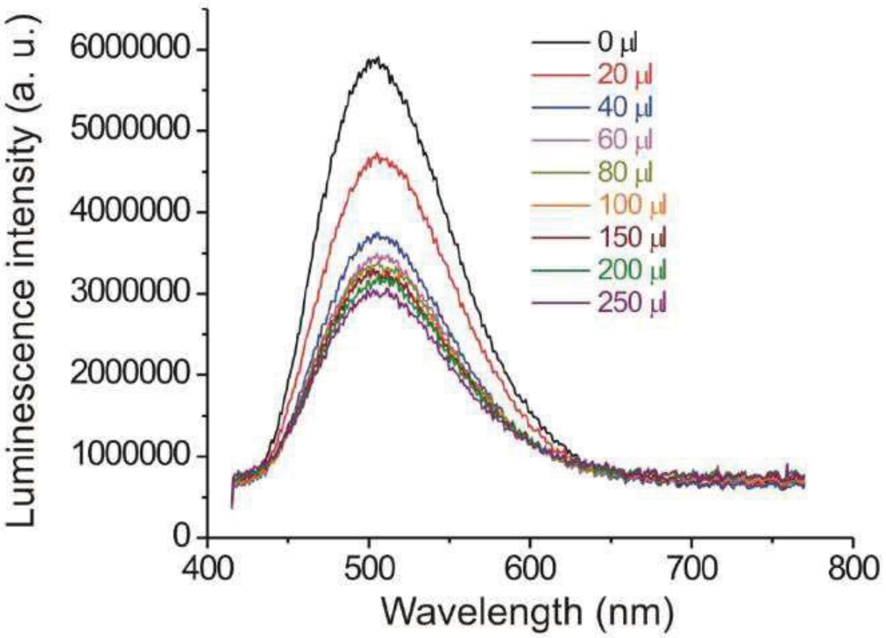

Fig. S14: Fluorescence quenching ($\lambda_{exc} = 395\ nm$) of PCTF-8 by NT (0–1×10^{-6} mol/L) at room temperature (1 mg PCTF-8 in 3 mL acetonitrile).

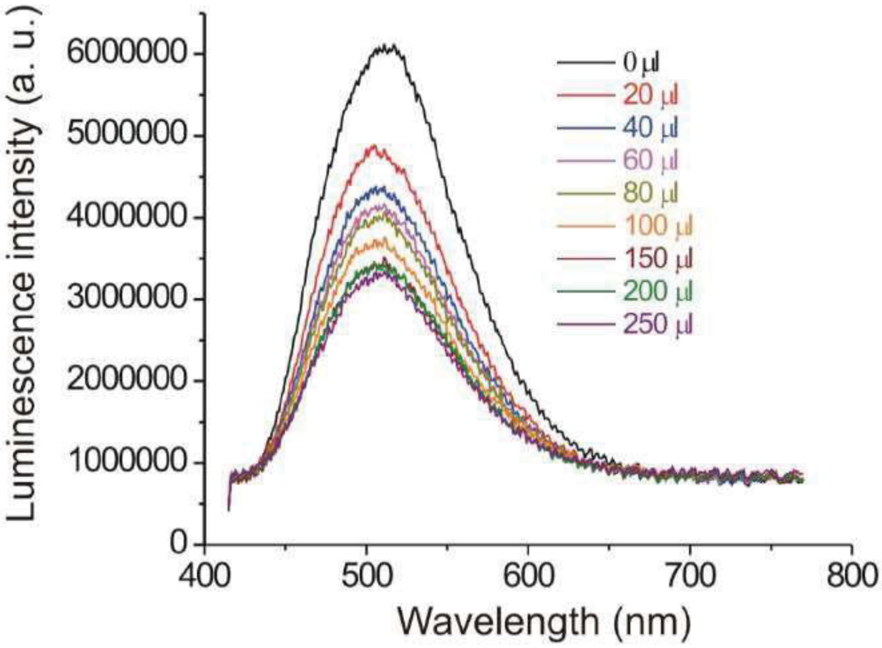

Fig. S15: Fluorescence quenching ($\lambda_{exc} = 395\ nm$) of PCTF-8 by NB ($0 - 1 \times 10^{-6}$ mol/L) at room temperature (1 mg PCTF-8 in 3 mL acetonitrile).

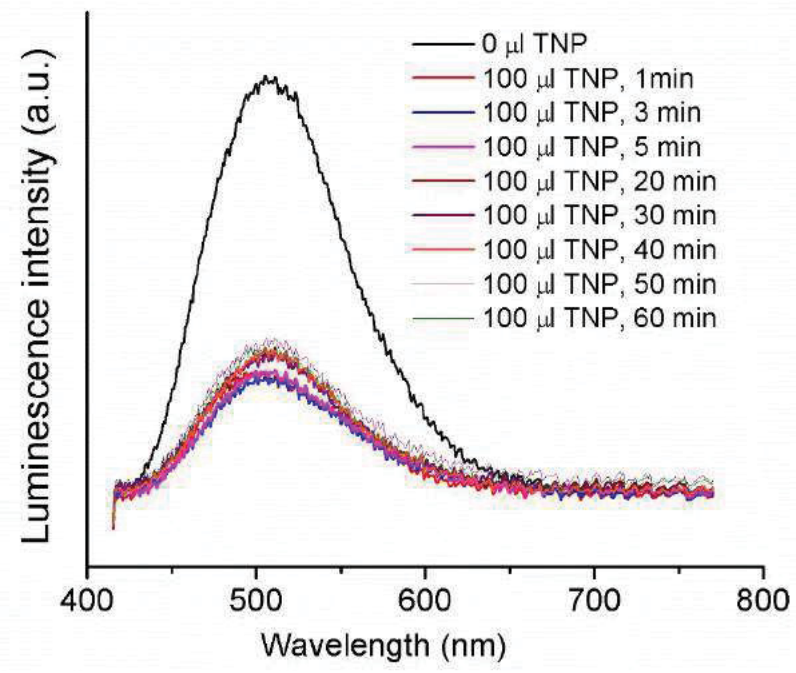

Fig. S16: Fluorescence quenching ($\lambda_{exc} = 395\ nm$) of PCTF-8 with time by TNP (5×10^{-4} mol/L) at room temperature.

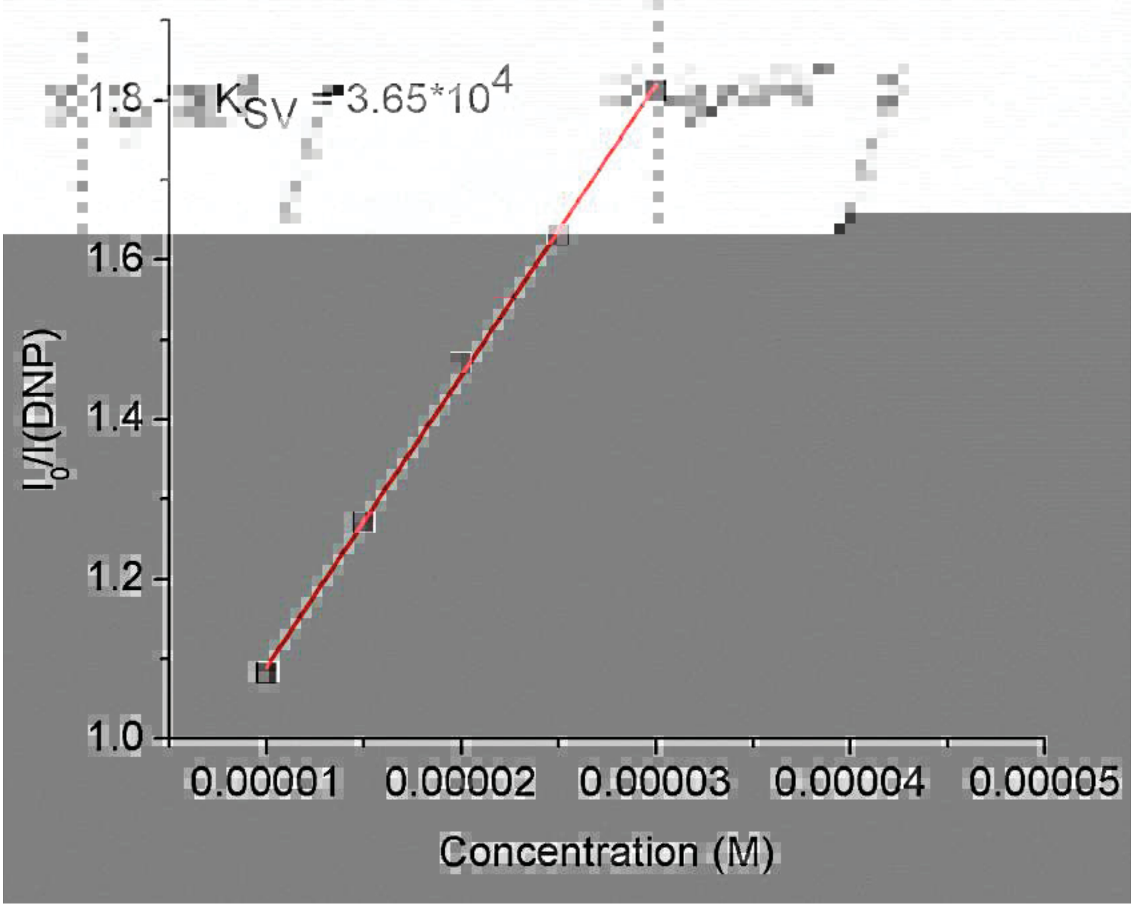

Fig. S17: Linear Stern–Volmer plots for the quenching of PCTF-8 by DNP.

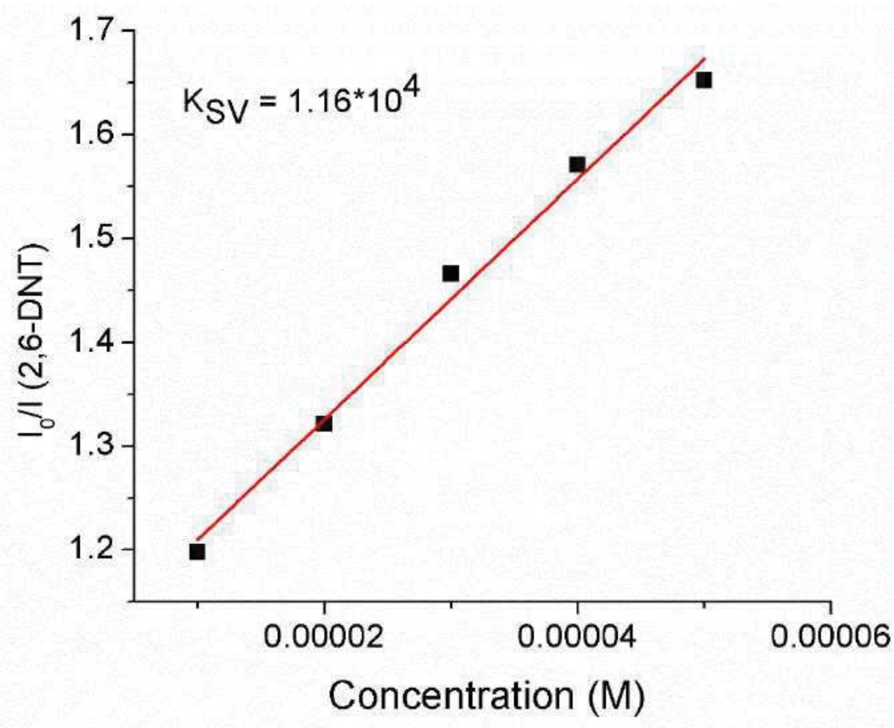

Fig. S18: Linear Stern–Volmer plots for the quenching of PCTF-8 by 2,6-DNT.

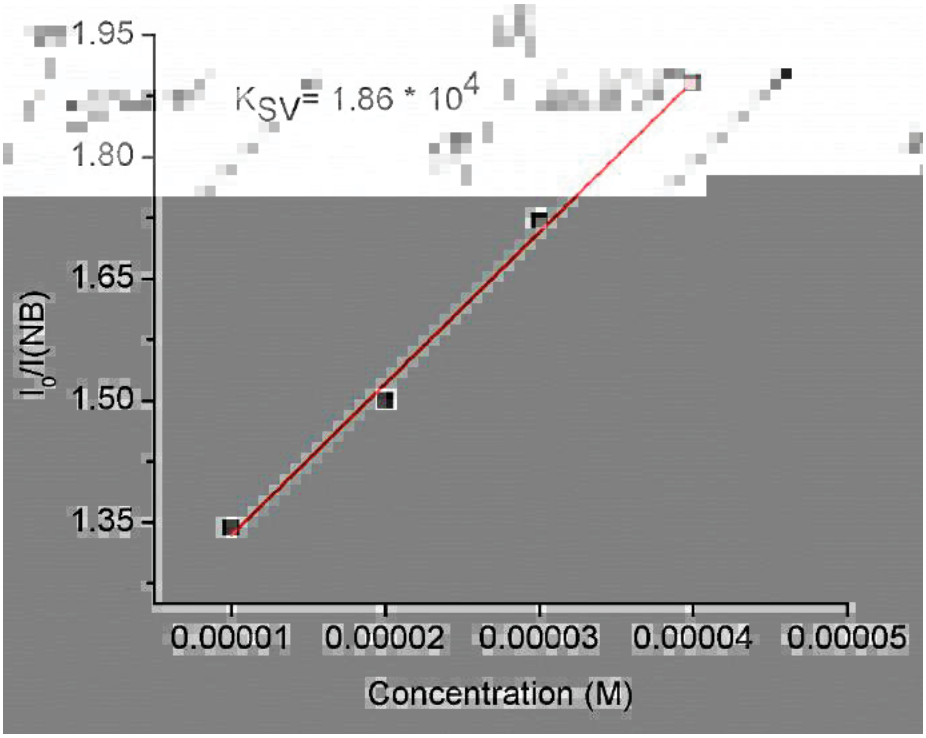

Fig. S19: Linear Stern–Volmer plots for the quenching of PCTF-8 by NB.

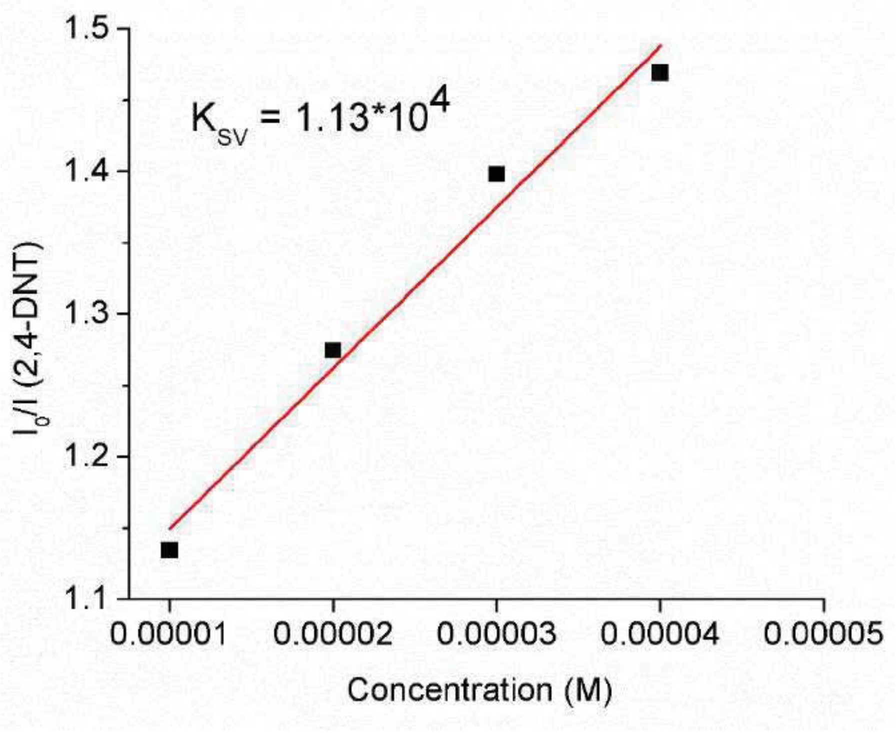

Fig. S20: Linear Stern–Volmer plots for the quenching of PCTF-8 by 2,4-DNT.

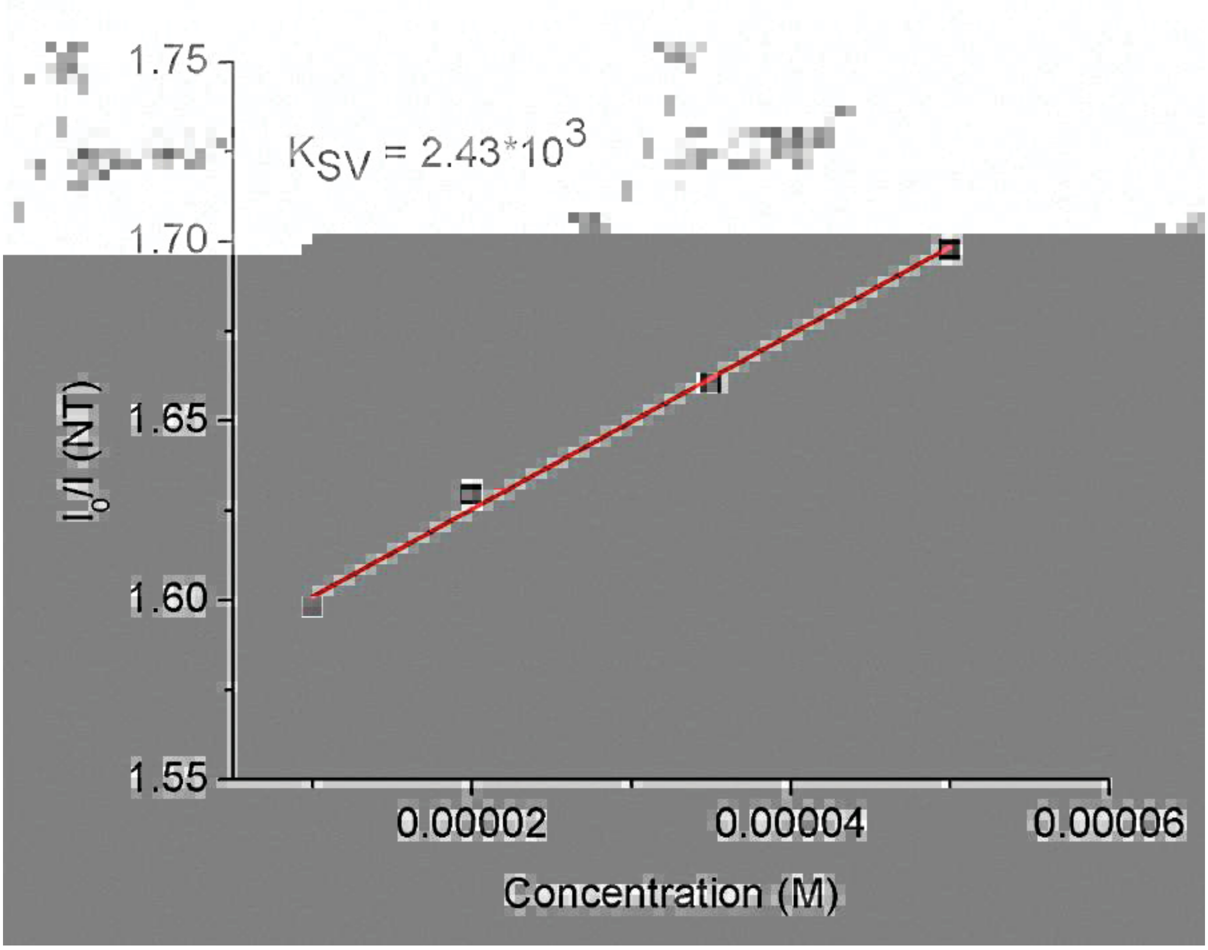

Fig. S21: Linear Stern–Volmer plots for the quenching of PCTF-8 by NT.

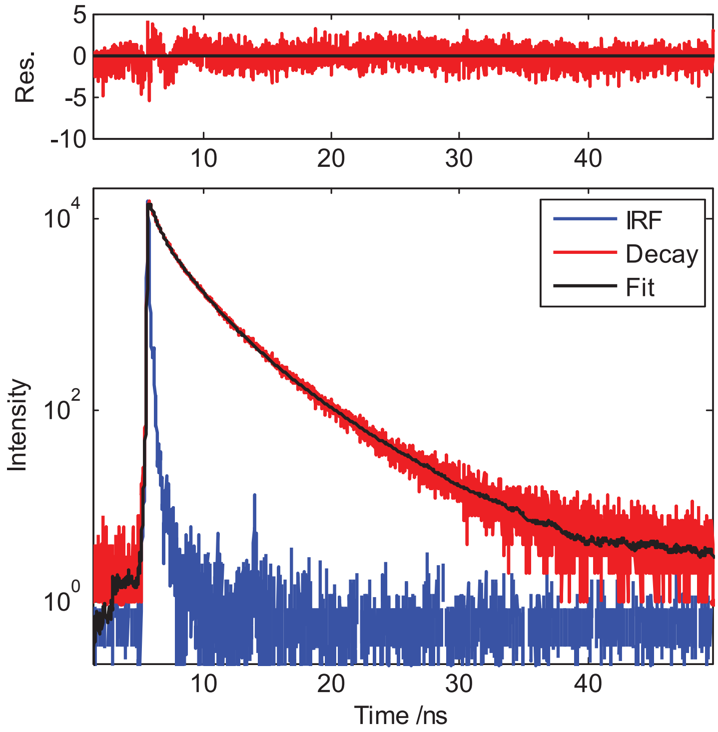

Fig. S22: TCSPC fit of pure PCTF-8 in acetonitrile.

The static quenching behaviour of PCTF-8:

In a recent paper (*J. Mater. Chem. A*, 2015, 3, 4604), the selective detection of TNP by microspheres from poly(cyclotriphosphazene-co-curcumin) is reported. The authors of this paper propose a mechanism to explain the selective detection of TNP, based on the combination of excited-state energy transfer and the formation of a ground-state non-fluorescent complex via proton transfer from the acidic phenol to the basic nitrogen sites in the cyclotriphosphazene ring (Fig. S23, reproduced from *J. Mater. Chem. A*, 2015, 3, 4604 with permission).

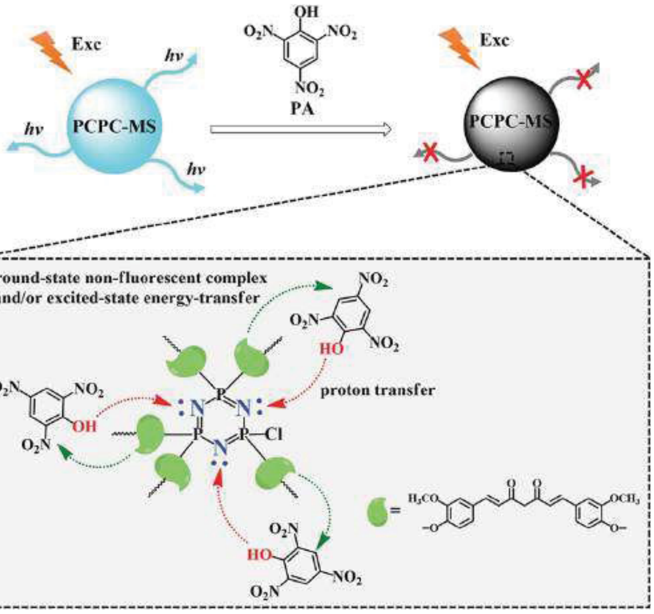

Fig. S23: Proposed mechanism to explain selective detection of TNP by cyclotriphosphazene-based framework (Fig. S23 reproduced from *J. Mater. Chem. A*, 2015, 3, 4604 with permission).

As seen in Fig. S10 it can be evidenced that none of the analytes have overlapping absorption bands with the emission of the fluorophore, thus ruling out any possible excited-state energy transfer to the phenols. At the same time, a similar chemical feature of the building unit of PCTF-8 presented in our work are the triazine rings. In this sense, the basic nitrogen atoms in triazine can be involved in a ground-state proton transfer reaction as the proton acceptors, especially considering the relative acidity of 2,4,6-trinitrophenol vs. other nitroaromatic compounds, which could be a possible explanation for the increased quenching observed by this analyte. Further studies are needed to ascertain the nature of the quenching mechanism.

12. References

1 F. Rouquerol, J. Rouquerol and K. Sing, Adsorption by powders and porous solids, F. Rouquerol, J. Rouquerol and K. Sing, ed. Academic Press, San Diego, 1999, vol. 11.

3.9 Missing Building Blocks Defects in a Porous Hydrogen-bonded Amide-Imidazolate Network Proven by Positron Annihilation Lifetime Spectroscopy

Suvendu Sekhar Mondal, Subarna Dey, Ahmed G. Attallah, Asamanjoy Bhunia, Alexandra Kelling, Uwe Schilde, Reinhard Krause-Rehberg, Christoph Janiak, and Hans-Jürgen Holdt

ChemistrySelect, 2016, in revision, (reference 106)

A three-dimensional hydrogen-bonded molecular building block (MBB) based network [$Cd_{14}(L2)_{12}(O)(OH)_2(H_2O)_6(DMF)_2$] (where, L2= imidazolate-4,5-diamide-2-olate), named as HIF-3, have been synthesized under conventional electrical (CE) heating and microwave (MW) assisted conditions. To prove the porosity, low pressure gas adsorption (N_2, H_2 and CO_2) were tested. The evacuated materials exhibit good N_2, CO_2, and H_2 gas sorption, in comparison with other H-bonded networks.

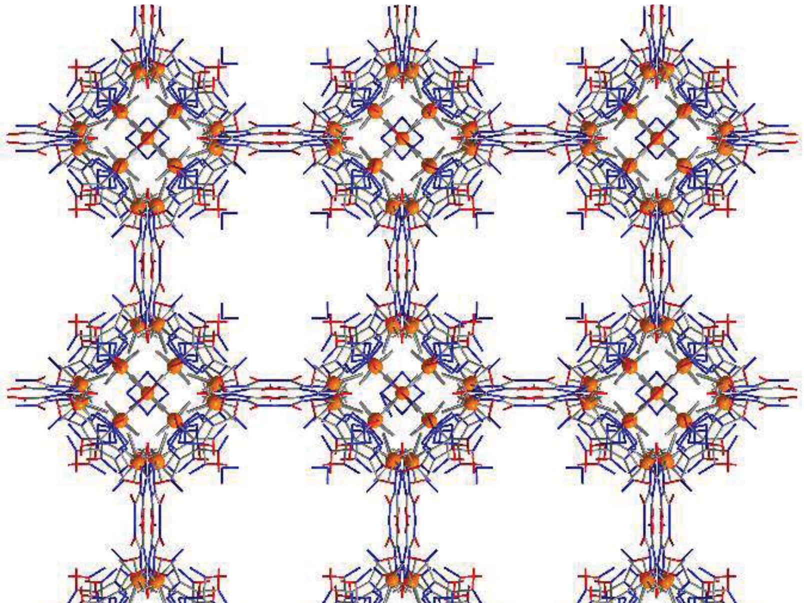

Author's contribution to the work:

- Performing the gas adsorption studies.
- Drawing gas adsorption figures.

Missing Building Blocks Defects in a Porous Hydrogen-bonded Amide-Imidazolate Network Proven by Positron Annihilation Lifetime Spectroscopy

Suvendu Sekhar Mondal,[a] Subarna Dey,[b] Ahmed G. Attallah,[c,d] Asamanjoy Bhunia,[b] Alexandra Kelling,[a] Uwe Schilde,[a] Reinhard Krause-Rehberg,[c] Christoph Janiak,[b] and Hans-Jürgen Holdt*[a]

[a] Dr. S. S. Mondal, A. Kelling, Prof. U. Schilde, Prof. H.-J. Holdt
Institut für Chemie, Anorganische Chemie, Universität Potsdam, Karl-Liebknecht-Straße 24-25, 14476 Potsdam, Germany
E-mail: holdt@uni-potsdam.de; Fax: (+49) 331-977-5055
[b] S. Dey, Dr. A. Bhunia, Prof. C. Janiak
Institut für Anorganische Chemie und Strukturchemie, Heinrich-Heine-Universität Düsseldorf, Universitätsstraße 1, 40225 Düsseldorf, Germany
[c] A. G. Attallah, Prof. R. Krause-Rehberg
Institut für Physik, Martin-Luther-Universität Halle-Wittenberg, Von-Danckelmann-Platz 3, 06120 Halle, Germany
[d] Physics Department, Faculty of Science, Minia University, P.O. 61519, Egypt.

Supporting information for this article is available on the WWW.

Abstract: In situ imidazolate-4,5-diamide-2-olate (L2) linker generation under conventional electrical (CE) heating and microwave (MW) assisted conditions leads to the formation of the porous three-dimensional hydrogen-bonded molecular building block (MBB) $[Cd_{14}(L2)_{12}(O)(OH)_2(H_2O)_4(DMF)_4]$ based network, named as HIF-3. In the MBB a Cd_6 octahedron is inscribed in a Cd_8 cube. The evacuated materials show good N_2, CO_2, and H_2 gas sorption, in comparison with other H-bonded networks. The desorption branches exhibit a broad hysteresis, suggesting that the materials show flexible behavior during gas uptake. Positron annihilation lifetime spectroscopy (PALS) shows inherent crystal defects of the materials. PALS indicates that the contribution of mesopores (10 and 14% for HIF-3-CE and -MW, respectively) due to missing building blocks, makes the frameworks structurally flexible.

Main text:

Research on porous materials, from zeolites, activated carbons, and mesoporous materials to metal–organic frameworks (MOFs) and covalent–organic frameworks (COFs) has demonstrated the potential roles of such materials for the advancement of science and technology.[1–5] The extensive studies of MOFs and COFs over the past two decades have not only led to new porous materials that can mimic traditional zeolites and porous carbons, but also generated a number of novel materials with interesting properties, thus rendering them promising for gas storage/separation, sensing, catalysis, photovoltaics, and drug release.[3–5] Compared with MOFs and COFs, the hydrogen-bonded organic frameworks (HOFs) and also including the rare class of hydrogen- bonded molecular building blocks (MBBs), self-assembled frameworks through weaker hydrogen-bonding interactions among molecular organic linkers, are much more fragile and difficult to stabilize.[6–8]

Some progress has been made to stabilize of porous HOFs materials and thus to establish permanent porosities and a few of them even exhibit properties superior to other porous materials for the mixture gas separation, exemplifying the bright future of these materials as a new category of functional materials.[9-12] Although the research on HOFs has been developed for quite a long time, those with both established permanent porosities by gas sorption isotherms or other techniques, and functional properties are still rare. Therefore, it is necessary to investigate the reason of the behaviour of structural backbone of H-bonded networks is less porous as it is expected.

Recently, there has been a renewed interest in the exploration of defects MOFs.[13] The defects in MOFs have been defined as the sites that locally break the regular periodic arrangement of atoms or ions of the static crystalline parent framework because of missing or dislocated atoms or ions. Introduction of defect sites into ordered structures is also a useful strategy to realize unusual heterogeneous structures and properties. The weak H-bonding networks are more fragile, so the potentially "porous" networks typically may collapse or show structural change after solvent removal. Therefore, in-depth systematically studies, including the exploration of new H-bonding motifs, and organic linkers for the construction of HOFs and framework robustness and flexibility, are certainly necessary before we can harness the rich chemistry of HOFs to rationally design and synthesize porous functional materials.

Herein, we report an optimized synthesis of an imidazolate- 4,5-diamide-2-olate (L2) linker based H-bonded Cd_{14}-MBBs network, named as HIF-3 (HIF = Hydrogen-bonded Imidazolate Framework) and its gas uptake properties. We undertook an in-depth study of positron annihilation lifetime spectroscopy (PALS)[14-16] to investigate the temperature dependent porosity of HIF-3, and to explain the behavior of the inner surface property and defects crystalline structures due to missing of MBBs.

HIF-3-CE is formed by in situ hydrolysis of 4,5-dicyano-2-methoxyimidazole (L1) with an equimolar amount of $Cd(ClO_4)_2 \cdot 6H_2O$ in *N,N′*-dimethylformamide (DMF) under solvothermal conditions by conventional electrical (CE) heating at 135 °C with a reaction time of 6 days (Scheme 1). Partial hydrolysis of the cyano groups of L1 to amide groups and of the methoxy to the hydroxy group followed by two-fold deprotonation generates the L2 linker. The linker L2 is only stable in the deprotonated and metal-coordinated state. Under these reaction conditions, in addition to HIF-3-CE, the in situ functionalized linker, 2-methoxy imidazolate 4-amide-5-imidate (L3) and its MOF IFP-14 (IFP = Imidazolate Framework Potsdam), is also formed as a minor by-product (Scheme 1 and Experimental section in the SI). IFP-14 was separated using the sieving technique.[17] We reported previously the synthesis of zinc or cobalt-L2 based H-bonded MBB networks[18,19] respectively, as minor products from the same reaction conditions and along with this, the L3 linker based MOFs IFP-7 and -8, respectively, as a major product.[18,19] We reasoned that the CE-synthetic conditions could be "thermodynamically" driven, allowing long time (6 days) for crystal growth in a reversible self-assembly synthesis process. Under this slow process, both the in situ L2 and L3 linkers were generated and, hence there should have been a competition for coordinating to the metal-center, forming L2 linker based hydrogen-bonded MBB structures or L3 based MOFs. Noteworthy, in the hydrogen-bonded MBB structure, the metal centers, e.g., Zn and Co required higher coordination number of six or seven.[18,19] In contrast, Zn and Co in the MOFs IFP-7 and -8, respectively were five-fold coordinated by the L3 linker.[19–21] Due to the bigger size of Cd, the reaction preferably yields six-fold coordinated Cd center, forming the HIF-3-CE structure, as the major product.

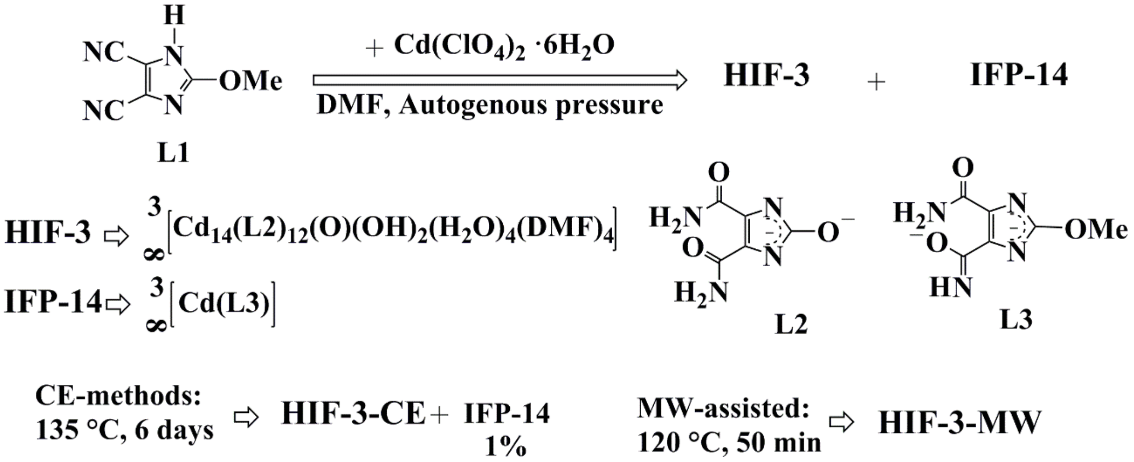

Scheme 1. Generation of in situ imidazolate-4,5-diamide-2-olate (L2) and 2-methoxy imidazolate-4-amide-5-imidate (L3) linker under solvothermal conditions in DMF.

Interestingly, when the reaction was done under microwave (MW)-assisted conditions (Scheme 1 and at SI), only phase pure, HIF-3-MW was formed and no by-product IFP-14 was detected. For the first time, in the MOFs areas, we have shown that MW-assisted condition has an advantage to the formation of a single product, where the conventional CE-heating methods gave a product mixture (Scheme 1).[22] Nevertheless, MW-assisted condition has been shown to be particularly favourable to avoid uneven heating of the reaction chamber, resulting in the formation of only a high-temperature product, HIF-3-MW in having greatly reduced reaction times associated with rapid heating through the dipole effect rather than convection and conduction.[22] The reason of forming only HIF-3-MW can be inferred that under a MW-assisted fast heating process the reaction rate of the double hydrolysis of L1 to L2 is enhanced (Scheme 1), resulting only in the "kinetically controlled" single product of HIF-3-MW.

As-synthesized HIF-3-CE was characterized by single-crystal X-ray diffraction as $[Cd_{14}(L2)_{12}(O)(OH)_2(H_2O)_4(DMF)_4]$ $(DMF)_8$. Compound HIF-3-CE crystallizes in the high-symmetry space group $I\,4_1/acd$ of the tetragonal crystal system (see SI). The asymmetric unit contains five different cadmium centres (Cd1, Cd2, Cd3, Cd4 and Cd5), three L2 linkers and oxido ion (O^{2-}), hydroxido ion (OH^-), terminal H_2O and DMF (Figure 1a). Moreover, the combination of five different types of coordination environments around the Cd atoms in one compound is rarely observed.[23] Twelve L2 ligands, one O^{2-}, two OH^- ions, four water and four DMF molecules, assemble with fourteen Cd ions to form a tetradecanuclear $Cd(II)_{14}$-MBB with peripheral amide groups (Figure 1b). The oxido ion (O1) is located in the centre of the MBB, surrounded by two Cd1, two Cd2 and two Cd5 atoms in a octahedral coordination environment (Figure 1b). This Cd_6 octahedron, created by two Cd1, Cd2 and Cd5 with having the μ_6-O^{2-} ion in the core was inscribed into a distorted Cd_8 cube ($Cd_6@Cd_8$) whose vertices are formed by four Cd3 and four

Cd4 atoms (Figure 1b). The MBB contains amide groups at its vertices and edges. Each cubic-like MBB is connected through its vertices with eight MBBs in a body-centered cubic packing (Figure 1c) by intermolecular N–H···O hydrogen bonding (Table S4 at SI) between the peripheral amide groups, generating the 3D supramolecular assembly of HIF3-CE (Figure 1c). The framework exhibits one type of infinite 1D channels with openings of ~1.16 nm between the van-der-Waals surfaces (Figure 1c). The channels of as-synthesized HIF-3-CE contain two DMF molecules per formula unit, in a solvent-accessible void volume of 24% of the unit cell volume (SI for details). The structure of minor product, IFP-14 was found to be isostructural to Zn based IFP-7 (SI for details).[20,21]

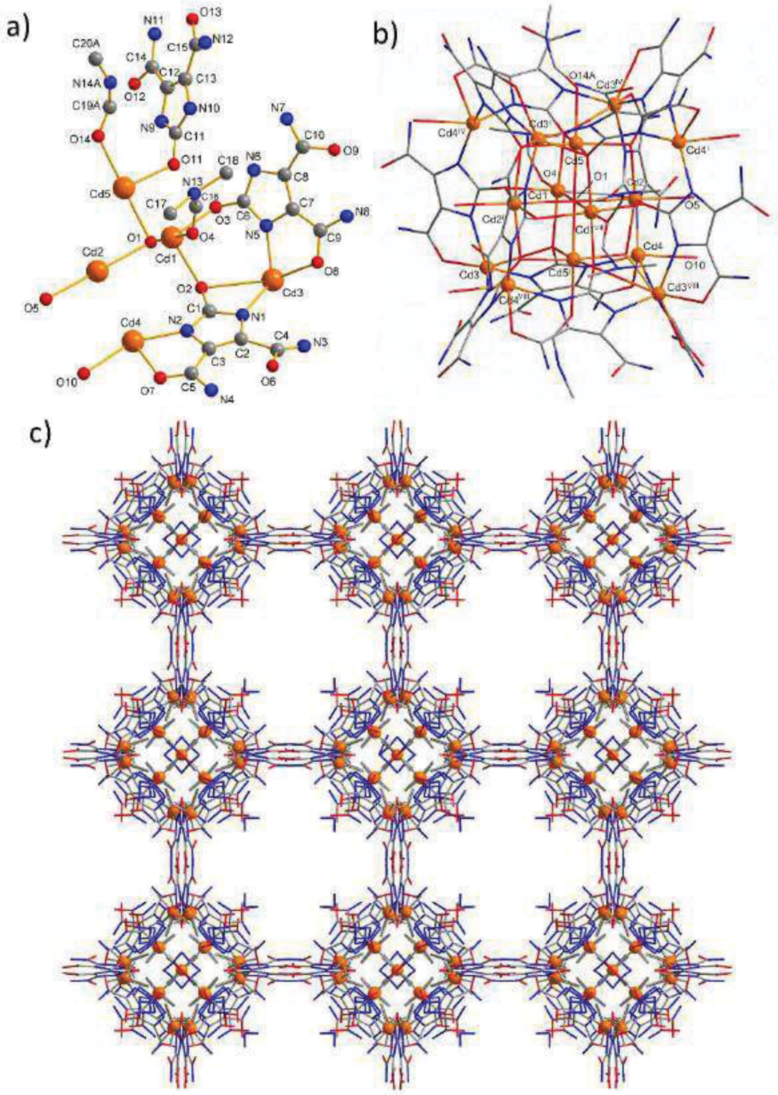

Figure 1. Crystal structure of HIF-3: a) asymmetric unit, b) tetradecanuclear Cd_{14}-MBB (for symmetry operators see legend of Table S4) and c) hydrogen-bonded supramolecular assembly of HIF-3-CE (orange Cd, blue N, red O, and dark gray C; H atoms are omitted for clarity).

Additionally, in situ hydrolysis of the L1 linker was proven by IR spectroscopy (Figure S3) and liquid state NMR spectra of a digested sample of HIF-3-CE (Figure S4). The purity of the as-synthesized materials, HIF-3-CE and -MW was confirmed by powder X-ray diffraction (PXRD) patterns (Figure S5). The as-synthesized sample of HIF-3-CE exhibited a weight loss 11.4% at

25–230 °C, upon heating, corresponding to the release of coordinated water and some of void occupied DMF molecules (Figure S10). For the removal of solvents, we decided not to activate the HIF-3 materials thermally to avoid any stress for the hydrogen-bonding pattern. Instead, the material was placed in a Soxhlet extractor and extracted with dry methanol over 5 days. The solvent-exchanged material was activated by degassing at 60 °C under high vacuum (10^{-6} Torr) for 24 h, prior to gas-sorption measurements.

N_2 isotherms for activated HIF-3 were measured at 77.4 K up to a relative pressure p/p_0 of 0.995, giving a Type II curvature. The estimated Brunauer–Emmett–Teller (BET) surface areas for HIF-3-CE and -MW are 127 and 43 $m^2\ g^{-1}$, respectively (Figure 2a). The CO_2 adsorption capacities in activated HIF-3-CE and -MW are 18 and 14 $cm^3\ g^{-1}$, respectively at 273 K, 1 bar (Figure 2b). The CO_2 uptake value is comparable to other known H-bonded materials, such as TBC[4]DHQ,[9e] SOF1a,[9a] SOF-3a,[10b] SOF7a,[10c] B2,[9f] and TTP[9g], but lower than other classes of benchmark H-bonded materials, H-bonded Zn_{14}-MBBs,[18] HOF-1a,[10a] and CBDU[11c] (Table S6).

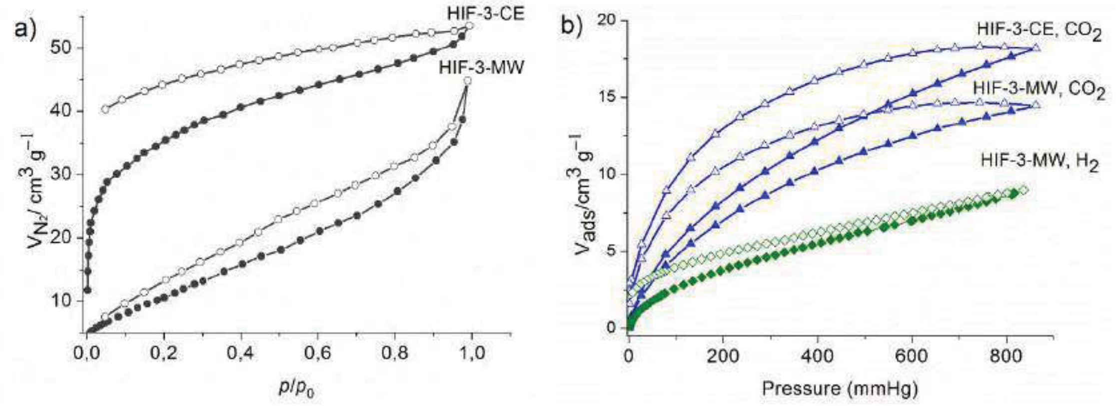

Figure 2. a) N_2, and b) H_2 and CO_2 sorption isotherms of HIF-3 (adsorption and desorption branches are indicated in closed and open symbols, respectively).

From the CO_2 adsorption isotherm at 273 K, the pore size distribution was derived between 0.4 and 1.0 nm by using NLDFT with a "CO_2 on carbon-based slit-pore model" (Figure S11) which showed a relative maximum at ~ 0.88 nm that is comparable with the channel (1.16 nm) obtained from the X-ray structure. At 273 K and under higher absolute pressures, CO_2 molecules can more easily access ultramicropores than N_2 at 77 K, and the kinetic diameter of CO_2 (3.3 Å) is also a little bit smaller than for N_2 (3.64 Å). So, advantages of micropore analysis by CO_2 adsorption at 273 K versus N_2 adsorption at 77 K are (i) faster analysis, (ii) greater confidence that measured adsorption points are equilibrated (both due to higher diffusion rates), and (iii) extension of the range of analysis to pores of smaller sizes that are accessible to CO_2 molecules but not to N_2.[24] HIF-3-CE and -MW adsorb 15 and 9 $cm^3\ g^{-1}$ of H_2, respectively at 77 K and 1 bar (Figure S12 and Figure 2b). Surprisingly, all desorption branches show a wide hysteresis, suggesting that both the materials are flexible behavior during gas uptake. The weak hydrogen-bonding barely stabilizes the framework, so the potentially "porous" networks typically collapse or yield to structural transformation, once the solvent guest molecules are removed after thermal and/or vacuum activation. This is proven by a certain degree of hysteretic desorption isotherms of many H-bonded porous materials.[9d,10]After gases uptake, the HIF-3-CE structure is transformed into an unknown crystalline material, although the crystallinity is maintained (Figure S5) that could complementarily supported by broad desorption hysteretic isotherms during gas uptake. We were interested to analyze the inner porosity and stability of the soft frameworks when the materials were heated at elevated temperature. Variable temperature PALS was employed to probe the inner surface of HIF-3.

Positron interaction with dielectric materials can form positronium, the atom-like bound state of a positron and an electron.[14] The electron and positron comprising a positronium atom can have either parallel or antiparallel spins. The species with parallel spins, orthopositronium (Ps), has a characteristic lifetime in vacuum of 142 ns. In a porous dielectric material, the lifetime of Ps is reduced in a manner directly related to the size of pores within that material. By bombarding a sample with positrons and detecting γ rays emitted from Ps decay, a Ps lifetime (or a distribution of lifetimes) can be determined and correlated to a precise pore size (or pore size distribution) for the analyzed material. Gidley, Matzger, and co-workers have proven that PALS has inherent advantages over gas sorption techniques as an analytical tool to study porous MOFs such as Zn-HKUST-1 and MOF-5.[15,16] The PALS method can provide an evidence for the presence of inner pores at HIF-3-CE. For comparison, PALS of HIF-3-MW was measured under similar conditions.

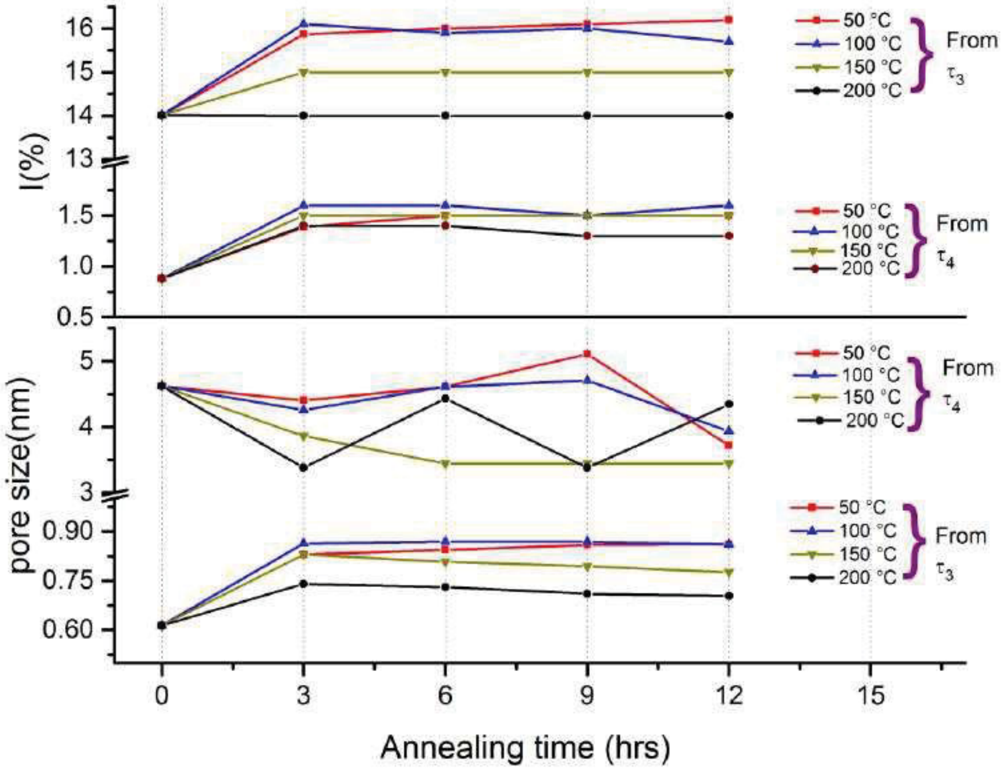

Figure 3. Lifetimes and their intensities for HIF-3-CE as a function of annealing time. Pore sizes for considering the spherical shapes of HIF-3-CE as a function of annealing time.

We accumulated 5×10^6 counts for the two spectra (2.5×10^6 stored in each spectrum) of digital PALS, using a low activity 22-Na source (7 μCi). We analyzed the data with LT10 routine to extract positron lifetime values which gave four positron lifetime components (τ) with the following physical meanings (τ_1 represents the p-Ps annihilation (0.125 ns), τ_2 is the free positron annihilation in the material matrix (varies from 0.3~0.6 ns), τ_3 indicates positronium annihilation in the materials and/or the annihilation in small pores (micropores <2 nm) (2~3.5 ns), and τ_4 means the positronium annihilation in the larger pores).

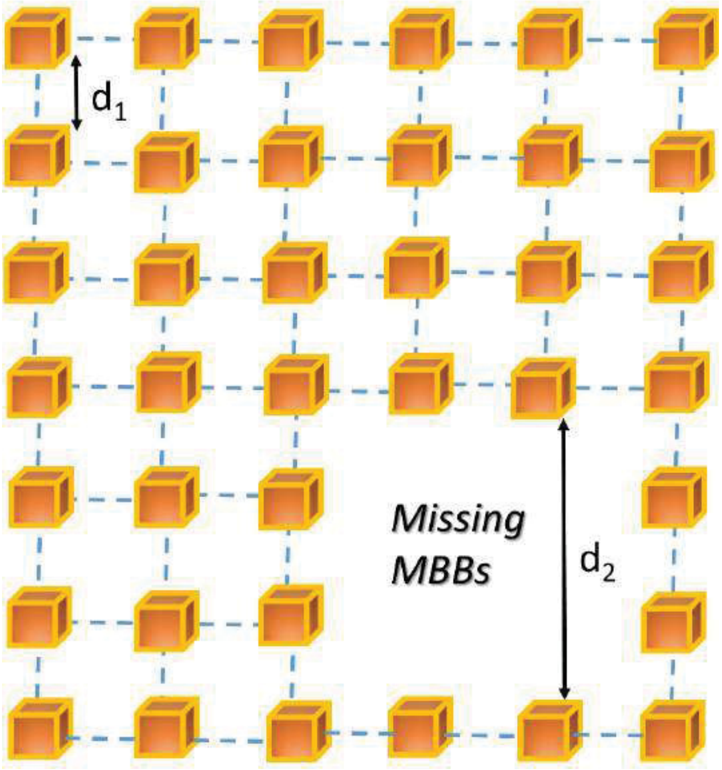

Figure 4. Schematic illustration of H-bonding patterns with missing MBBs in HIF-3-CE.

The effect of the activation temperatures during different periods on the positron lifetime (and hence the pore size) of HIF-3-CE are shown in Figure 3. The pore size, derived from τ_3 is smaller and more stable than the pore size, getting from τ_4, and at 50, 100, and 200 °C, it is constant after 12 hours annealing time while for 150 °C, the pore size is slightly reduced. The small pore size is reduced with the increasing of the activation temperature, indication the pore construction upon heating the material. Interestingly, the PXRD reflections of activated HIF-3-CE are shifted toward higher Bragg angles, suggesting a structure contraction upon activation of the material (Figure S6). The larger pore, obtained from τ_4 has changed drastically during heating above 150 °C and τ_4 is inversely proportional to the annealing temperature along with all periods (except at 100 °C for 12 hours). Importantly, at 200 °C activation temperature, more dynamic behavior of the large pore is observed. The small pore and large pore size, after 12 hours annealing time at the activation temperature at 100 °C, are 0.87 and ~3.9 nm, respectively. The small pore diameter, obtained from the pore size of annealing time is comparable with the pore size distribution of "CO_2 on carbon-based slit-pore model" (relative maximum at ~ 0.88 nm) and also close to X-ray structure (1.16 nm). It has been also noted that $I_4<I_3$ (Figure 3 and S14) during all periods of activation which means that the HIF-3-CE has a small concentration (~10% at 100 °C activation temperature after 6 h annealing time, Figure S15) of large pores and the remaining of small pores. However, the crystal structure does not indicate the small concentration (10%)

of large pores with having of the pore size of 3.9 nm. This could probable the missing molecular building blocks at a few areas of crystal structure, creating the mesopore regions that make instability of the H-bonded network (Figure 4), and also a complementary proof by the hysteretic desorption isotherms. This phenomenon also suggests that at first the MBBs are formed and after that these are connected by H-bonds.

For HIF-3-MW, it has been also observed that $I_4<I_3$ (Figure S16 and S17) during all periods of activation, confirming a small concentration (~14%, at 100 °C activation temperature after 6 h annealing time, Figure S18) of large pores which are comparatively higher than HIF-3-CE (10%). The fixed intensities of I_4 (Figure S16) may suggest that these pores are closed and contained with the protonated form of non-coordinated L2 linkers which are stable in reaction medium and unable to leave the pores. Additionally, inductively coupled plasma optical emission spectrometry (ICP OES) results (Table S7) for HIF-3 suggest that MW-assisted condition showed less Cd-content and indirectly supported the extra non-coordinated L2 linker incorporation and defects in the structure. The reasons can be inferred that very fast crystal growth under MW-assisted conditions may not ensure enough time for the MBBs to quantitatively adhere to the growing crystal lattice at the right place, and hence, more pronounced missing MBBs defects are obtained, where the linkers are trapped inside pores, reducing the pore sizes obtained from τ_3 and τ_4 (small and large pore of 0.65 and 2.4 nm, respectively at 100 °C activation time). Moreover, MW-assisted conditions, the pore size i.e. mesopore formation, getting from τ_4 values, is highly dominant than CE-methods. Hence, the material synthesized under MW-assisted conditions is more flexible to the structural transformation during activation, proven by less gas uptake, compared to the material synthesized under CE-conditions.

In summary, we describe an in situ linker generation method for the synthesis of a rare class of molecular building blocks that are connected by H-bonds into a porous supramolecular network. Also we have solved the problem of getting two products formed at CE-conditions into only one product under MW-assisted conditions. Thermodynamically driven HIF-3-CE exhibited slightly larger N_2, CO_2, and H_2 uptakes than the kinetically controlled HIF-3-MW. CO_2 uptake capacities are comparable with the known H-bonded porous organic compounds, although the broad hysteretic desorption isotherms imply structural changes during gas sorption. For a deeper understanding of the porosity, for the first time we performed PALS investigations to demonstrate a unique ability of exposing nanoscale porosity, vindicating the presence of mesopores into the microporous H-bonded material. Such indication clearly suggests that missing building blocks defects (10 and 14% for HIF-3-CE and -MW, respectively) are formed in the crystalline materials. A small portion of mesopores showed more dynamic structural changes during annealing and activation process wherein, micropores remain static in annealing time and decrease with increasing the activation temperatures. We realize that in-depth porosimetry studies by using PALS enable the basic understanding of the H-bonding patterns and defects as well as porosity of the H-bonded porous materials.

Acknowledgements: The authors thank Dr. C. Günter (Universität Potsdam) for help with X-ray powder diffraction measurements, S. Lubahn (Universität Potsdam) for the ICP-OES measurements and Y. Linde (Universität Potsdam) for the C, H, and N elemental analysis. This work is financially supported by the German Research Foundation (SPP 1362 “Porous Metal-Organic Frameworks,” HO 1706/ 7-1 and HO 1706/7-2).

Keywords: hydrogen-bonding • N,O ligands • porosity • positron • supramolecular chemistry

References:

[1] a) N. Linares, A. M. Silvestre-Albero, E. Serrano, J. Silvestre-Albero, J. García-Martínez, *Chem. Soc. Rev*. **2014**, *43*, 7681–7717; b) W. J. Roth, P. Nachtigall, R. E. Morris, Čejka, J. *Chem. Rev*. **2014**, *114*, 4807–4837.

[2] a) V. Valtchev, L. Tosheva, *Chem. Rev.* **2013**, *113*, 6734–6760; b) S. Navalon, A. Dhakshinamoorthy, M. Alvaro, H. Garcia, *Chem. Rev*. **2014**, *114*, 6179–6212.

[3] a) H.-C. Zhou, S. Kitagawa, *Chem. Soc. Rev*. **2014**, *43*, 5415–5418; b) H. Furukawa, U. Muller, O. M. Yaghi, *Angew. Chem. Int. Ed*. **2015**, *54*, 3417–3430; *Angew. Chem.* **2015**, *127*, 3480–3494; c) E. López-Maya, C. Montoro, L. M. Rodríguez-Albelo, S. D. A. Cervantes, A. A. Lozano-Pérez, J. L. Cenís, E. Barea, J. A. R. Navarro, *Angew. Chem. Int. Ed*. **2015**, *54*, 6790–6794; *Angew. Chem*. **2015**, *127*, 6894–6898; d) A. Bhunia, S. Dey, J. M. Moreno, U. Diaz, P. Concepcion, K. Van Hecke, C. Janiak, P. Van Der Voort, *Chem. Commun.* **2016**, *52*, 1401–1404; e) M. Leroux, N. Mercier, M. Allain, M.-C. Dul, Jens Dittmer, A. H. Kassiba, J.-P. Bellat, G. Weber, I. Bezverkhyy, *Inorg. Chem*. **2016**, DOI: 10.1021/acs.inorgchem.6b01119.

[4] Z. Zhang, M. J. Zaworotko, *Chem. Soc. Rev.* **2014**, *43*, 5444–5455.

[5] Y.-H. Xu, S.-B. Jin, H. Xu, A. Nagai, D.-L. Jiang, *Chem. Soc. Rev*. **2013**, *42*, 8012–8031.

[6] a) J. Tian, P. K. Thallapally, B. P. McGrail, *CrystEngComm* **2012**, *14*, 1909–1919; c) N. B. McKeown, *J. Mater. Chem.* **2010**, *20*, 10588–10597.

[7] a) K. T. Holman, A. M. Pivovar, J. A. Swift, M. D. Ward, *Acc. Chem. Res.* **2001**, *34*, 107–118; b) K. E. Maly, E. Gagnon, T. Maris, J. D. Wuest, *J. Am. Chem. Soc.* **2007**, *129*, 4306–4322; c) A. Yamamoto, T. Hamada, I. Hisaki, M. Miyata, N. Tohna, *Angew. Chem. Int. Ed.* **2013**, *52*, 1709–1712; *Angew. Chem.* **2013**, *125*, 1753–1756; d) W. Xiao, C. Hu, M. D. Ward, *J. Am. Chem. Soc.* **2014**, *136*, 14200–14206.

[8] a) V. Guillerm, D. Kim, J. F. Eubank, R. Luebke, X. Liu, K. Adil, M. S. Lah, M. Eddaoudi, *Chem. Soc. Rev.* **2014**, *43*, 6141–6172; b) M. H. Alkordi, J. A. Brant, L. Wojtas, V. Ch. Kravtsov, A. J. Cairns, M. Eddaoudi, *J. Am. Chem. Soc.* **2009***, 131,* 17753–17755.

[9] a) W. Yang, A. Greenaway, X. Lin, R. Matsuda, A. J. Blake, C. Wilson, W. Lewis, P. Hubberstey, S. Kitagawa, N. R. Champness, M. Schröder, *J. Am. Chem. Soc.* **2010**, *132*, 14457–14469; b) X.-Z. Luo, X.-J. Jia, J.-H. Deng, J.-L. Zhong, H.-J. Liu, K.-J. Wang, D.-C. Zhong, *J. Am. Chem. Soc.* **2013**, *135*, 11684–11687; c) M. Mastalerz, I. M. Oppel, *Angew. Chem. Int. Ed.* **2012**, *51*, 5252–5255; *Angew. Chem.* **2012**, *124*, 5345–5348; d) I. Hisaki, S. Nakagawa, N. Tohnai, M. Miyata, *Angew. Chem. Int. Ed.* **2015**, *54*, 3008–3012; *Angew. Chem.* **2015**, *127*, 3051–3055; e) P. K. Thallapally, B. P. McGrail, J. L. Atwood, C. Gaeta, C. Tedesco, P. Neri, *Chem. Mater.* **2007**, *19*, 3354–3357; f) R. S. Patil, D. Banerjee, C. Zhang, P. K. Thallapally, J. L. Atwood, *Angew. Chem. Int. Ed.* **2016**, *55*, 4523–4526; *Angew. Chem.* **2016***, 128,* 4599–4602; g) P. Sozzani, S. Bracco, A. Comotti, L. Ferretti, R. Simonutti, *Angew. Chem. Int. Ed.* **2005**, *44*, 1816–1820; *Angew. Chem.* **2005**, *117*, 1850–1854.

[10] a) Y. He, S. Xiang, B. Chen, *J. Am. Chem. Soc.* **2011**, *133*, 14570–14573; b) P. Li, Y. He, H. D. Arman, R. Krishna, H. Wang, L. Weng, B. Chen, *Chem. Commun*. **2014**, *50*, 13081–13084; c) W. Yang, B. Li, H. Wang, O. Alduhaish, K. Alfooty, M. Aldin Zayed, P. Li, H. D. Arman, B. Chen, *Cryst. Growth Des*. **2015**, *15*, 2000–2004; d) H. Wang, B. Li, H. Wu, T. L. Hu, Z. Yao, W. Zhou, S. Xiang, B. Chen, *J. Am. Chem. Soc.* **2015**, *137*, 9963–9970.

[11] a) R. S. Patil, H. Kumari, C. L. Barnes, J. L. Atwood*, Chem. Commun*. **2015**, *51*, 2304–2307; b) R. S. Patil, H. Kumari, C. L. Barnes, J. L. Atwood, *Chem. Eur. J.* **2015**, *21*, 10431–10435; c) M. B. Dewal, M.W. Lufaso, A. D. Hughes, S. A. Samuel, P. Pellechia, L. S. Shimizu, *Chem. Mater*. **2006**, *18*, 4855–4864.

[12] a) D. F. Sava, V. Ch. Kravtsov, J. Eckert, J. F. Eubank, F. Nouar, M. Eddaoudi, *J. Am. Chem. Soc.* **2009**, *131*, 10394–10396; b) S. Wang, T. Zhao, G. Li, L. Wojtas, Q. Huo, M. Eddaoudi, Y. Liu, *J. Am. Chem. Soc.* **2010**, *132*, 18038–18041.

[13] a) Z. Fang, B. Bueken, D. E. De Vos, R. A. Fischer, *Angew. Chem. Int. Ed.* **2015**, *54*, 7234–7254; *Angew. Chem.* **2015**, *127*, 7340–7362; b) J. Canivet, M. Vandichel, D. Farrusseng, *Dalton Trans.* **2016**, *45*, 4090–4099; c) A. K. Cheetham, T. D. Bennett, F.-X. Coudert, A. L. Goodwin, *Dalton Trans.* **2016**, *45*, 4113–4126; d) A. W. Thornton, R. Babarao, A. Jain, F. Trousselet, F.-X. Coudert, *Dalton Trans.* **2016**, *45*, 4352–4359; e) W. Liang, C. J. Coghlan, F. Ragon, M. Rubio-Martinez, D. M. D'Alessandro, R. Babarao, *Dalton Trans*. **2016**, *45*, 4496–4500.

[14] a) D. W. Gidley, H.-G. Peng, R. S. Vallery, *Annu. Rev. Mater. Res*. **2006**. *36*, 49–79; b) Y. Kobayashi, K. Ito, T. Oka, K. Hirata, *Radiation Physics and Chemistry* **2007**, *76*, 224–230; c) H. B. Tanh Jeazet, T. Koschine, C. Staudt, K. Raetzke, C. Janiak, *Membranes* **2013**, *3*, 331–353; d) J. I. Feldblyum, D. Dutta, A. G. Wong-Foy, A. Dailly, J. Imirzian, D. W. Gidley, A. J. Matzger, *Langmuir* **2013**, *29*, 8146–8153; e) P. Guo, D. Dutta, A. G. Wong-Foy, D. W. Gidley, A. J. Matzger, *J. Am. Chem. Soc.* **2015**, *137*, 2651–2657; f) S. S. Mondal, A. Bhunia, A. G. Attallah, P. R. Matthes, A. Kelling, U. Schilde, K. Müller-Buschbaum, R. Krause-Rehberg, C. Janiak, H.-J. Holdt, *Chem. Eur. J.* **2016***, 22,* 6905–6913; g) P. Crivelli, D. Cooke, B. Barbiellini, B. L. Brown, J. I. Feldblyum, P. Guo, D. W. Gidley, L. Gerchow, A. J. Matzger, *Phys. Rev. B*, **2014**, *89*, 241103(R).

[15] J. I. Feldblyum, M. Liu, D. W. Gidley, A. J. Matzger, *J. Am. Chem. Soc.* **2011**, *133*, 18257–18263.

[16] M. Liu, A. G. Wong-Foy, R. S. Vallery, W. E. Frieze, J. K. Schnobrich, D. W. Gidley, A. J. Matzger, *Adv. Mater*. **2010**, *22*, 1598–1601.

[17] T. D. Keene, D. J. Price, C. J. Kepert, *Dalton Trans.* **2011**, *40*, 7122–7126.

[18] S. S.Mondal, A. Bhunia, A. Kelling, U. Schilde, C. Janiak, H.-J. Holdt, *J. Am. Chem. Soc.* **2014**, *136*, 44–47.

[19] S. S.Mondal, A. Bhunia, A. Kelling, U. Schilde, C. Janiak, H.-J. Holdt, *Chem. Commun.* **2014**, *50*, 5441–5443.

[20] S. S. Mondal, A. Bhunia, I. A. Baburin, C. Jäger, A. Kelling, U. Schilde, G. Seifert, C. Janiak, H.-J. Holdt*, Chem. Commun*. **2013**, *49*, 7599–7601.

[21] F. Debatin, A. Thomas, A. Kelling, N. Hedin, Z. Bacsik, I. Senkovska, S. Kaskel, M. Junginger, H. Müller, U. Schilde, C. Jäger, A. Friedrich, H.-J. Holdt, *Angew. Chem. Int. Ed.* **2010**, *49*, 1258–1262; *Angew. Chem.* **2010**, *122*, 1280–1284.

[22] a) J. Klinowski, F. A. A. Paz, P. Silva, J. Rocha, *Dalton Trans.* **2011**, *40*, 321–330; b) E. A. Flügel, A. Ranft, F. Haase, B. V. Lotsch, *J. Mater. Chem.* **2012**, *22*, 10119–10133; c) W. Xu, Z. Bao, B. Yuan, J. Wang, Y. Sun, H. Luo, S. Deng, *Micropor. Mesopor. Mater.* **2013**, *180*, 114–122; d) W. Liang, D. M. D'Alessandro, *Chem. Commun.* **2013**, *49*, 3706–3708; e) K. Behrens, S. S. Mondal, R. Nöske, I. A. Baburin, S. Leoni, C. Günter, J. Weber, H.-J. Holdt, *Inorg. Chem.* **2015**, 54, 10073–10080.

[23] G. Anantharaman, H. W. Roesky, J. Magull, *Angew. Chem. Int. Ed.* **2002**, *41*, 1226–1229; *Angew. Chem.* **2002**, *114*, 1274–1277.

[24] a) J. Garrido, A. Linares-Solano, J. M. Martin-Martinez, M. Molina-Sabio, F. Rodriguez-Reinoso, R. Torregosa, *Langmuir* **1987**, *3*, 76–81; b) D. Cazorla-Amoros, J. Alcaniz-Monje, A. Linares-Solano, *Langmuir* **1996**, *12*, 2820–2824; c) J. Garcia-Martinez, D. Cazorla-Amoros, A. Linares-Solano, *In Characterization of Porous Solids V*; K. K. Unger, G. Kreysa, J. P. Baselt, Elsevier: Amsterdam, **2000**; pp 485–494.

CONTENTS

1. General Remarks

All reagents and solvents were used as purchased from commercial suppliers (Sigma-Aldrich, Fluka, Alfa Aesar, and others) without further purification, if not stated otherwise. $Cd(ClO_4)_2 \cdot 6H_2O$ was handled with precaution. MW-assisted synthesis was performed on the microwave system *CEMDiscove*r. Elemental analysis (C, H, N) was performed on Elementar Vario EL elemental analyzer. SEM- measurements was done on a JEOL JSM 6510 SEM. ICP-OES measurements was performed on the Perkin Elmer Optical Emission Spectrometer Optima 5300 DV (Scott-Chamber/Cross-Flow-Nebulizer). For measurements all samples were activated under vacuum by 60 °C for 12 hours and then coated with carbon (POLARON CC7650 Carbon Coater). The linker precursor 4,5-dicyano-2 methoxyimidazole (L1) was synthesized following a published procedure.[1]

2. Experimental Section

Synthesis of $[Cd_{14}(L2)_{12}(O)(OH)_2(H_2O)_6(DMF)_4]$ $(DMF)_{12}$ (= HIF-3-CE) and $[Cd(L3)]$ $(H_2O)_3$ (= IFP-14):

In a sealed tube (Type A, company: Ace) 0.121 g (0.81 mmol) of 4,5-dicyano-2-methoxyimidazole (L1) and 0.342 g of $Cd(ClO_4)_2 \cdot 6H_2O$ (0.81 mmol) were dissolved in DMF (5 mL). The sealed tube was closed and the mixture was heated at 135 °C for 6 days and was then allowed to cool down to room temperature with 5 °C per hour. Light orange crystals are formed (~ 99 wt%) together with another type of a few crystals which was named as IFP-14 (Scheme 1). The light orange crystals, named as HIF-3-CE were separated by a sieving technique, wherein the IFP-14 were trapped by a mesh (mesh size: 20 µm) while the HIF-3-CE filtered through it. The fine crystalline product was washed with DMF and EtOH and dried in air. Yield for HIF-3-CE: 0.172 g (~55%) based on L1; elemental analysis: $[Cd_{14}(L2)_{12}(O)(OH)_2(H_2O)_4(DMF)_4]$ $(DMF)_8$ = $C_{96}H_{142}N_{60}O_{55}Cd_{14}$; Calcd., C 25.12, H 3.12, N 18.31, Found: C 25.57, H 3.46, N 17.84; IR (KBr pellet): ν_{max} = 3444 (m), 3342 (m), 3252 (m), 1650 (vs), 1587 (s), 1510 (s), 1285 (s), 1253 (m), 1100 (m), 1023 (m), 727 cm^{-1} (m).

Synthesis of HIF-3-MW: A total of 0.062 g (0.41 mmol) of L1 and 0.175 g (0.41 mmol) of $Cd(ClO_4)_2 \cdot 6H_2O$ were dissolved in 3 mL of DMF. Under MW-assisted conditions at 120 °C and 50 min of reaction time. The light yellow powder was obtained. Yield: 0.091 g (~57%) based on L1; elemental analysis for HIF-3-MW: Calcd., C 25.12, H 3.12, N 18.31, Found: C 25.73, H 3.42, N 17.71; IR (KBr pellet): ν_{max} = 3439 (m), 3335 (m), 3260 (m), 1653 (vs), 1587 (s), 1510 (s), 1280 (s), 1257 (m), 1104 (m), 1025 (m), 723 cm^{-1} (m).

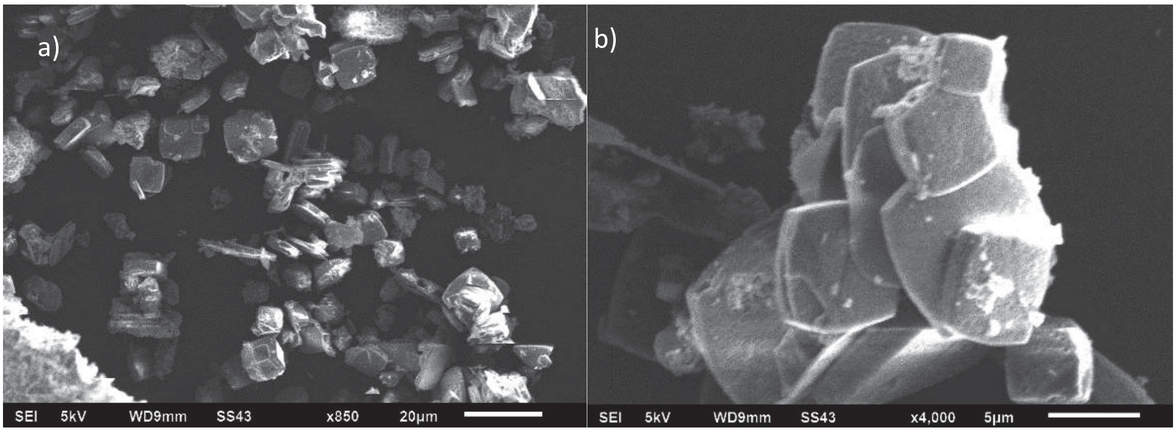

Figure S1. Scanning electron micrograph (SEM); a) and b) for HIF-3-CE.

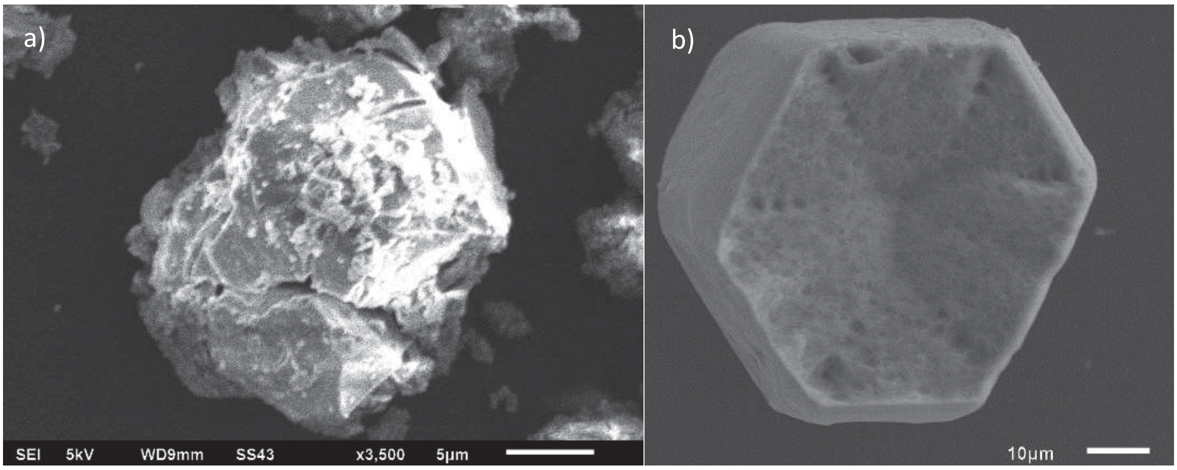

Figure S2. SEM a) HIF-3-MW, and b) IFP-14.

3. IR spectra

IR spectra were recorded on FT-IR Nexus from Thermo Nicolet in the region of 4000–400 cm^{-1} using KBr pellet.

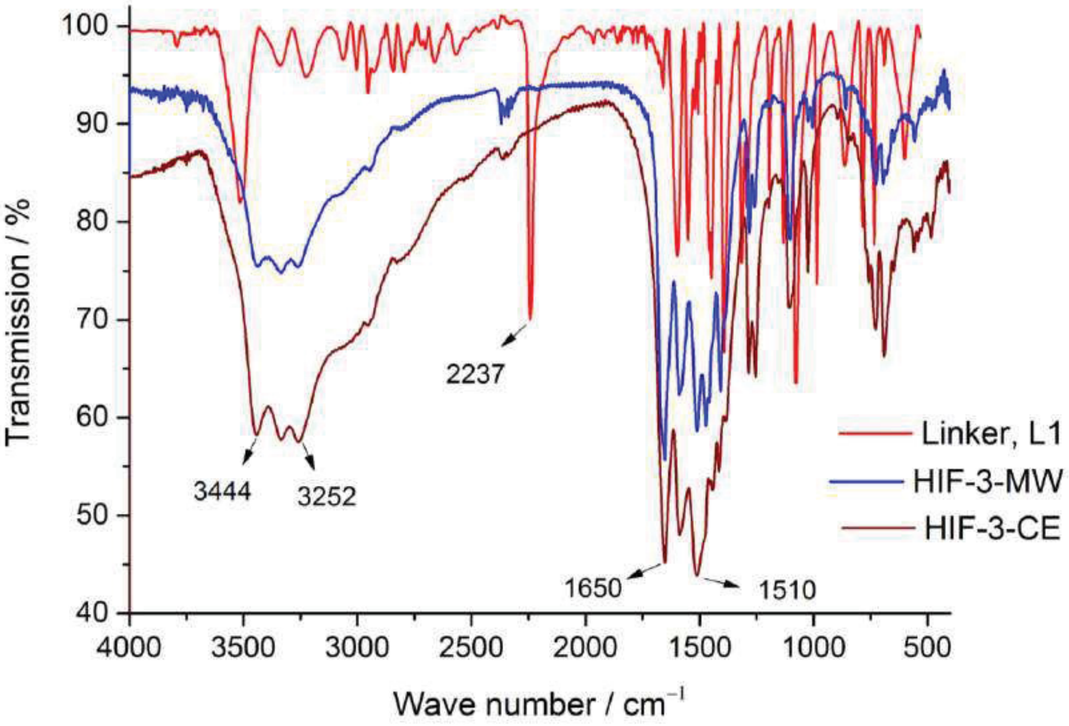

Figure S3. IR-spectra of 4,5-dicyano-2-methoxyimidazole (L1), as-synthesized HIF-3-CE, and as-synthesized HIF-3-MW.

The degree of in situ hydrolysis of the cyano groups of L1 into the corresponding L2 was studied with infrared (IR) spectroscopy. The IR-spectra of the HIF-3-CE/-MW manifest no stretching bands related to C≡N in the region of 2237 cm^{-1}. Instead, the typical absorption bands for an amide are observed between 3444 and 3252 cm^{-1} and at 1650 and 1510 cm^{-1} (Figure S3).

4. Liquid-phase ^{13}C NMR spectroscopy of activated HIF-3-CE

NMR spectra were recorded with a Bruker Advance 300 spectrometer. Resonances for NMR spectra are reported relative to Me_4Si (δ = 0.0 ppm) and calibrated based on the solvent signal for ^{1}H and ^{13}C. Liquid-phase^{1}H and ^{13}C NMR spectroscopy of activated HIF-3-CE sample (28 mg) was digested in 0.5 mL [D$_6$] DMSO and 0.05 mL DCl (20%)/D_2O.

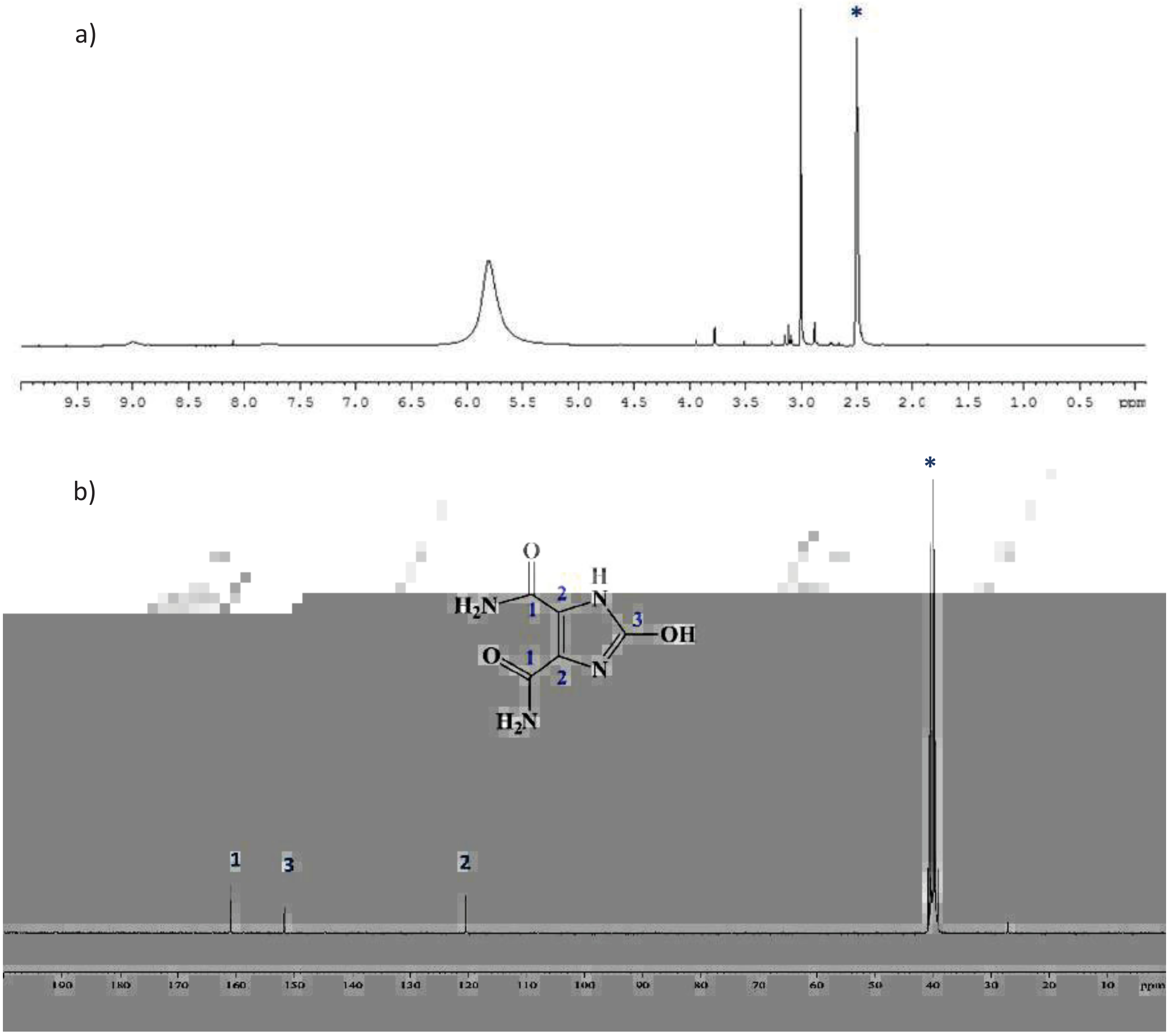

Figure S4. a) ^{1}H- and b) ^{13}C- NMR spectra of a digested activated sample HIF-3-CE in 0.05 mL DCl (20%)/D_2O and 0.5 mL [D$_6$] DMSO. Solvent signals ([D$_6$] DMSO) are marked with an asterisk (*). At ^{1}H NMR spectra 2.8–3.2 ppm, weak triplet peaks are observed due to slow HDO intermolecular rate of exchange.[2] ^{1}H-NMR spectrum the proton peak of amide group (at 5.8 ppm) is noted. Digested sample of HIF-3-CE in DMSO-d$_6$ and DCl/D_2O, there is no coordination to cadmium. Moreover, olate group and imidazolate may be protonated.

The degree of in situ hydrolysis of the methoxy to hydroxyl group of L1 into the corresponding L2 was proven by liquid-phase ^{13}C- NMR spectrum, no peak related to methoxy group at 54–60 ppm region was observed. Additionally, ^{13}C- NMR spectrum is a good evidence of the in situ functionalization of cyano groups, as specifically around 162 ppm one peak appeared for the carbon atom of the amide group (Figure S4).

5. Powder X-ray-diffraction patterns

Powder X-ray diffraction (PXRD) patterns were measured on a Siemens diffractometer D5005 in Bragg-Brentano reflection geometry. The diffractometer was equipped with a copper tube, a scintillation counter, automatic incident- and diffracted-beam soller slits and a graphite secondary monochromator. The generator was set to 40 kV and 40 mA. All measurements were performed with sample rotation. Data were collected digitally from 3° to 70° 2ϑ using a step size of 0.02° 2ϑ and a count time of 4 seconds per step. The simulated powder pattern for HIF-3-CE/-MW were calculated using single-crystal X-ray diffraction data and processed by the free Mercury v1.4.2 program provided by the Cambridge Crystallographic Data Centre.

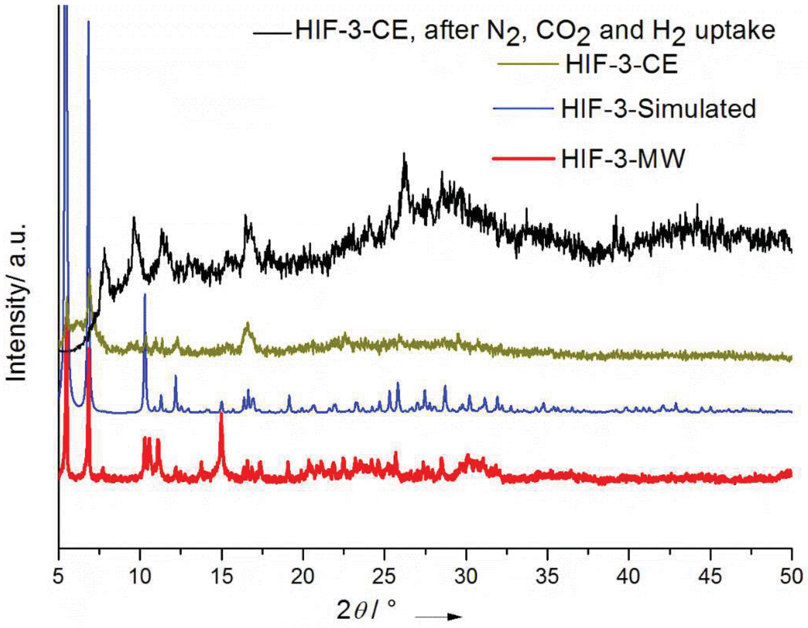

Figure S5. a) Powder X-ray diffraction patterns of as-synthesized HIF-3-CE and as-synthesized HIF-3-MW; Difference in the relative intensities is because of the simulated pattern does not account for the disordered solvent molecules in the HIF-3 pores.

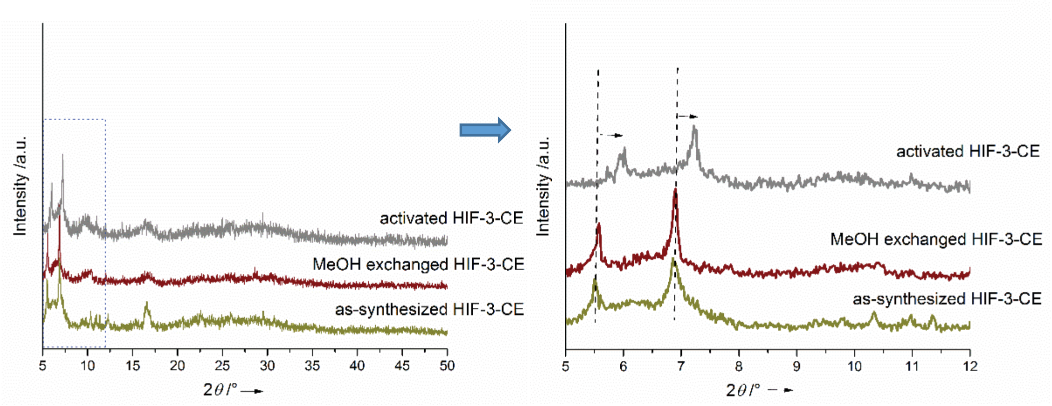

Figure S6. Comparison of the PXRD patterns of the HIF-3-CE. In the close up (right side) of the lower angle region from 2ϑ = 5−12° the shifting reflections belonging to equivalent lattice planes are marked with a black arrow.

It may be common of the fact that due to presence of defects in the H-bonded network, the PXRD patterns is slightly varied in compare with simulated pattern. Chan et al. and others reported HOFs structures where the PXRD patterns of H-bonded network slightly deviated from the simulated patterns.[3]

6. Single Crystal X-ray Structure Determination of HIF-3-CE and IFP-14

For X-ray structure determinations the crystals were embedded in perfluoropolyalkylether oil and mounted within a MicroGripper (HIF-3-CE) or on a glass fibre (IFP-14). The data collection of HIF-3-CE was performed at 210 K on a STOE StadiVari diffractometer equipped with a four-circle goniometer (open Eulerian cradle), a Genix Microfocus X-ray source (Mo) with a graded multilayer mirror and a Dectris 200 K detector (801 frames, Δω=0.5°, 10 s exposure time per frame). For structure analysis of IFP-14, the intensity data were collected at 150 K using a STOE Imaging Plate Diffraction System IPDS-2 with graphite monochromatized Mo-Kα radiation at 50 kV and 40 mA (360 frames, Δω=1°, 5 min exposure time per frame). The data were corrected for absorption as well as for Lorentz and polarization effects using the program X-Area (Stoe, 2004). The structures were solved by direct methods using SHELXS-2013/2[4] and refined by full-matrix least squares on F^2 using the program SHELXL-2014/7.[5] All non-hydrogen atoms were refined anisotropically, with the exception of the atoms of the coordinated DMF molecules, which were refined isotropically. In HIF-3-CE, the hydrogen atoms could not be located from the electron density map. Therefore the hydrogen atoms of the amino groups and methyl hydrogen atoms of one of the coordinated DMF molecules were calculated in their expected positions and refined as riding atoms. In IFP-14, the hydrogen atoms of the amino group could be found from the Fourier map. The hydrogen atoms of the DMF were calculated and refined with a riding model. The unit cell contains channels filled with disordered solvent molecules. In spite of several attempts, no chemically reasonable solution could be received for the solvent species in the channels of the crystal material. Very high displacement parameters, high estimates and partial occupancy due to the disorder make it impossible to determine accurate atomic positions for that molecules. For PLATON/SQUEEZE[6] calculated the solvent-accessible void volume and the corresponding number of electrons in the unit cell (HIF-3-CE: 7938 A^3, 23.6 % of the total cell volume, 2480 electrons, agreeing with about 2 molecules of dimethylformamide (1.94x40x32=2656); IFP-14: 2093 Å^3, 36.4 % of the total cell volume, corresponding to 546 electrons, agreeing with about 3 molecules of water (3.03x10x18=546). For IFP-14, the contribution of the disordered solvent species was subtracted from the structure factor calculations by the SQUEEZE instruction of PLATON. For HIF-3-CE, with the SQUEEZE generated structure factors no improvement of the refinement could be achieved. Hence the original data were used.

CCDC 1488819 (HIF-3-CE) and CCDC 1488842 (IFP-14) contain the supplementary crystallographic data for this paper. These data can be obtained free of charge from The Cambridge Crystallographic Data Centre.

Table S1. Crystal Data, Details of Intensity Measurements, and Structure Refinement for $[Cd_{14}(L2)_{12}(O)(OH)_2(H_2O)_4(DMF)_4]$ $(DMF)_8$ (= HIF-3-CE) and $[Cd(L2)]$ $(H_2O)_3$ (=IFP-14)

	HIF-3-CE	IFP-14
Empirical formula	$C_{18}H_{18.25}Cd_{3.50}N_{13}O_{11.75}$	$C_6H_{11}N_4O_6Cd$
Formula weight / g·mol^{-1}	998.10	347.59
Crystal system	tetragonal	trigonal
Space group	$I\,4_1/a\,c\,d$	R-3
Cell dimensions $a = b$ / Å c / Å $\alpha = \beta$ / ° γ / °	 32.6744(11) 31.5400(13) 90 90	 18.6157(8) 19.1658(8) 90 120
Volume / Å^3	33673(3)	5752.0(5)
Temperature / K	210(2)	150(2)
Z	32	18
Density (calculated) / g·cm^{-3}	1.58	1.81
Absorptions coefficient / cm^{-1}	1.80	1.73
2Θ range / °	4.77 - 50.00	3.30 - 49.50
Crystal shape / color	prism / light orange	prism / light yellow
Crystal size / mm	0.11 x 0.16 x 0.19	0.06 x 0.12 x 0.15
F(000)	15336	3078
Index ranges	$-34 \leq h \leq 38$ $-28 \leq k \leq 38$ $-37 \leq l \leq 23$	$-21 \leq h \leq 21$ $-21 \leq k \leq 21$ $-22 \leq l \leq 22$
Reflections collected	74292	23440
Independent reflections	7404	2165
Data / restraints / parameters	7404 / 10 / 423	2165 / 0 / 144
R_1 / wR_2 [$I > 2\sigma(I)$]	0.0542 / 0.1328	0.0340 / 0.0848
R_1 / wR_2 (all data)	0.1085 / 0.1463	0.0519 / 0.0905
Goodness of fit on F^2	0.800	0.949
Largest diff. peak and hole / e·Å^{-3}	1.865 and -0.590	0.846 and -0.569

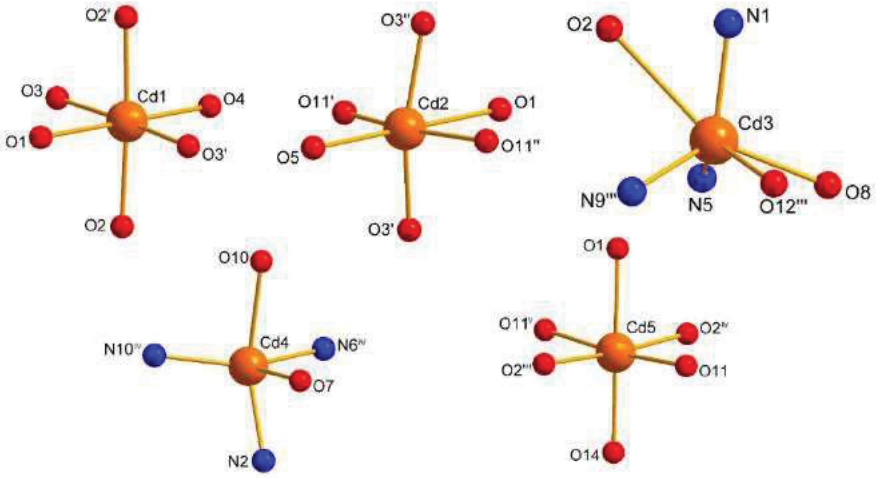

Figure S7. The five cadmium centres (Cd1, Cd2, Cd3, Cd4 and Cd5) of HIF-3-CE in the MBB, for symmetry operators see legend of Table S4.

At MBB, each of two Cd1 atoms is coordinated by four olate oxygen atoms of four imidazolate ligands (two O2 and two O3), one oxido ion (O1) and one DMF (O4) forming a distorted octahedral coordination geometry (Figure S7). The two Cd2 centres are surrounded by four olate oxygen atoms (O3, O11), one oxido ion (O1) and one hydroxido ion (O5), and two Cd5 centres are surrounded by four olate oxygen atoms (O2, O11), one O^{2-} (O1) and two DMF (O4, O14) to form a distorted octahedral coordination geometry (Figure S7). The Cd3 atoms are each coordinated by three nitrogen atoms (N1, N5 and N9) from three imidazolate ligands, two amide oxygen atoms (O8 and O12) and an olate ion (O2) as the linker in a one-fold face capped distorted square pyramid (Figure S7). Cd4 atoms are each coordinated by three nitrogen atoms (N2, N6 and N10) from three imidazolate ligands, one amide oxygen atoms (O7) and one H_2O (O10) in a distorted trigonal-bipyramidal geometry (Figure S7).

Table S2. Selected bond lengths [Å] for HIF-3-CE.

Cd1- O1	2.3545(9)	Cd3 - N5	2.184(8)
Cd1 - O2	2.322(5)	Cd3 - N9^{I}	2.183(9)
Cd1 - O3	2.266(6)	Cd4 - O7	2.373(9)
Cd1 - O4	2.258(12)	Cd4 - O10	2.498(12)
Cd2 - O1	2.5535(10)	Cd4 - N2	2.157(12)
Cd2 - O3^{IV}	2.272(6)	Cd4 - N6^{IV}	2.222(8)
Cd2 - O5	2.469(7)	Cd4 - N10^{IV}	2.208(10)
Cd2 - O11^{IV}	2.309(5)	Cd5 - O1	2.3950(7)
Cd3 - O8	2.333(7)	Cd5 - O2^{IV}	2.287(6)
Cd3 - O12^{I}	2.420(9)	Cd5 - O11	2.281(6)
Cd3 - N1	2.176(10)	Cd5 - O14	2.298(9)

Table S3. Selected bond angles [°] for HIF-3-CE.

O4 - Cd1 - O3	92.88(15)	N9^{I} - Cd3 - O12^{I}	71.2(3)
O4 - Cd1 - O2^{IV}	91.90(15)	O8 - Cd3 - O12^{I}	74.3(3)
O3 - Cd1 - O2^{IV}	89.1(2)	N2 - Cd4 - N10^{IV}	102.7(4)
O4 - Cd1 - O1	180.0	N2 - Cd4 - N6^{IV}	97.8(3)
O3 - Cd1 - O1^{IV}	87.12(15)	N10^{IV} - Cd4 - N6^{IV}	151.8(3)
O2 - Cd1 - O1	88.10(15)	N2 - Cd4 - O7	70.8(4)
O3^{IV} - Cd2 - O11^{IV}	80.2(2)	N10^{IV} - Cd4 - O7	104.2(3)
O3 - Cd2 - O5^{IV}	97.62(15)	N6^{IV} - Cd4 - O7	100.7(3)
O3 - Cd2 - O1^{IV}	82.38(15)	N2 - Cd4 - O10	149.1(4)
O11 - Cd2 - O1^{IV}	83.06(14)	N10^{IV} - Cd4 - O10	85.7(4)
O5 - Cd2 - O1	180.0(5)	N6^{IV} - Cd4 - O10	86.5(3)
N1 - Cd3 - N5	117.8(3)	O7 - Cd4 - O10	78.4(5)
N1 - Cd3 - O8	106.2(4)	O11 - Cd5 - O2^{I}	88.5(2)
N5 - Cd3 - O8	72.6(3)	O11 - Cd5 - O14	92.69(13)
N9 - Cd3 - O8^{I}	129.4(3)	O2^{I} - Cd5 - O14	92.07(13)
N1 - Cd3 - O12^{I}	97.9(4)	O11 - Cd5 - O1	87.31(13)
N5 - Cd3 - O12^{I}	136.6(3)	O2^{I} - Cd5 - O1	87.93(13)
		O14 - Cd5 - O1	180.0

Table S4. Hydrogen bond geometry in HIF-3-CE.

	H···A	D···A	D−H···A
N3−H3B···O12^{I}	2.12	2.94(2)	158.2
N4−H4A····O9^{II}	2.64	3.25(2)	128.0
N4−H4B···O6	1.79	2.63(2)	160.9
N7−H7A···O7^{III}	**2.18**	**3.00(1)**	**155.9**
N7−H7B···O7^{IV}	**2.16**	**2.95(1)**	**152.5**
N8−H8A···O8^{V}	**1.97**	**2.83(1)**	**171.6**
N8−H8B···O9	1.84	2.67(1)	159.0
N11−H11A···O9^{VI}	**2.51**	**3.35(2)**	**163.8**
N11−H11B···O13	1.80	2.62(3)	155.3
N12−H12A···O9^{VII}	**2.59**	**3.24(2)**	**132.8**
N12−H12B···O7^{IV}	2.20	3.01(2)	154.8

Hydrogen bonds connecting two MBBs are in **bold**.

Symmetry Operators: ^{I} y-0.25, x+0.25, 0.25-z ^{II} y+0.25, x+0.25, z+0.25 ^{III} y-0.25, x-0.25, z-0.25 ^{IV} 1.25-y, 1.25-x, 0.25-z ^{V} x, 1-y, 0.5-z ^{VI} 0.75-y, x+0.25, z-0.25 ^{VII} 1-x, 1-y, -z ^{VIII} 1-x, 1.5-y, z.

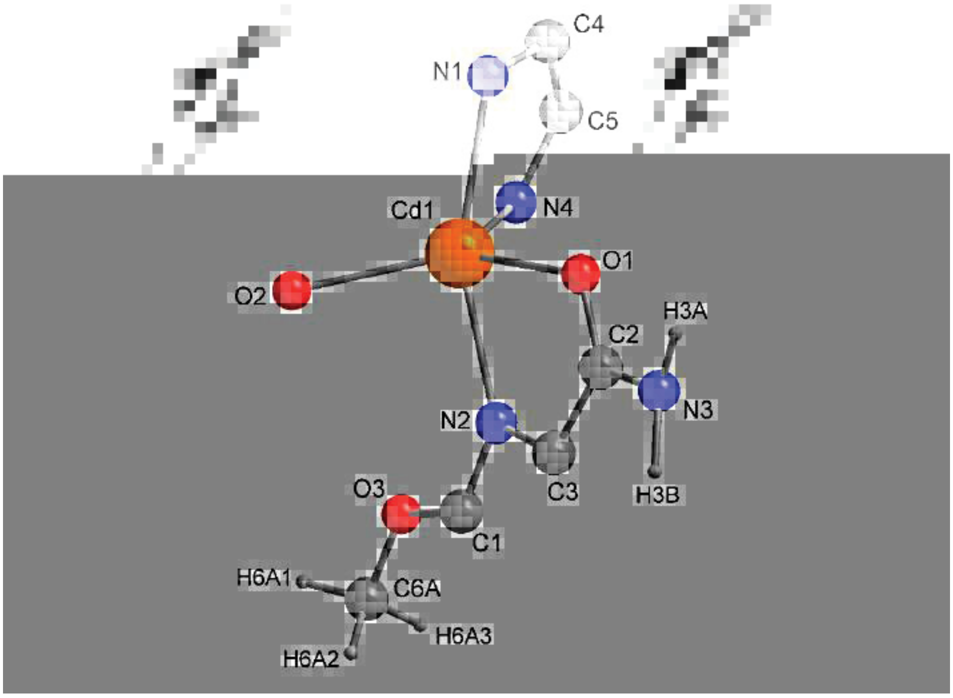

Figure S8. Asymmetric unit of IFP-14. The methyl group is disordered over two equally occupied sites (only one is drawn).

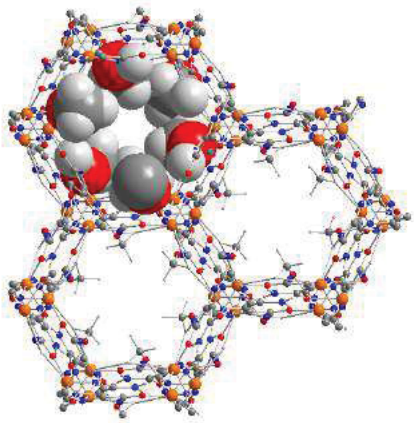

Figure S9. Hexagonal channels in IFP-14 (the methyl substituents at the linker L3 are presented in a space filling mode (orange Cd, blue N, red O, dark gray C, light gray H).

The structure of IFP-14 was found to be isostructural to Zn based IFP-1 with the same *etb* topology.[7] The cadmium ion in the IFP-14 structure is penta-coordinated by the L3 linkers to form a distorted trigonal–bipyramidal geometry (Figure S8). The structure possesses 1D hexagonal channels running along *c* axis (Figure S9). The methoxy groups protrude into the open channels and determine their accessible diameter (Figure S9). By considering the van der Waals radii, the accessible diameter of the channels in IFP-14 was estimated to be 3.2 Å. Calculations with the PLATON toolkit indicated that IFP-14 contains 35% void space. Moreover, we are unable to examine the gas uptake capacities as well as other physical properties for IFP-14 in the present study due to low yield. We are in the process of optimizing the synthetic conditions for obtaining a better yield.

Table S5. Hydrogen-bonding parameters [Å, °] for [Cd(L3)] ·$3H_2O$ (IFP-14).

	D-H	H···A	D···A	D-H··A
C6B–H6B3–O2	0.98	2.45	3.274(15)	141.4
N3–H3A–O1^{I}	0.93(8)	2.18(8)	3.106(6)	174(7)
N3–H3B–O2^{II}	1.08(8)	1.74(8)	2.734(6)	150(6)

Symmetry operators: ^{I} -x+1.33, -y+0.66, -z+0.66 ^{II} x-y, x-1, -z+2

7. Thermogravimetric analysis

TG measurements were performed in a static air atmosphere from room temperature up to 900 °C with a Perkin Elmer TGA 4000 thermal analyzer. The heating rate was 10 °C min^{-1}. The samples were placed in ceramic pans.

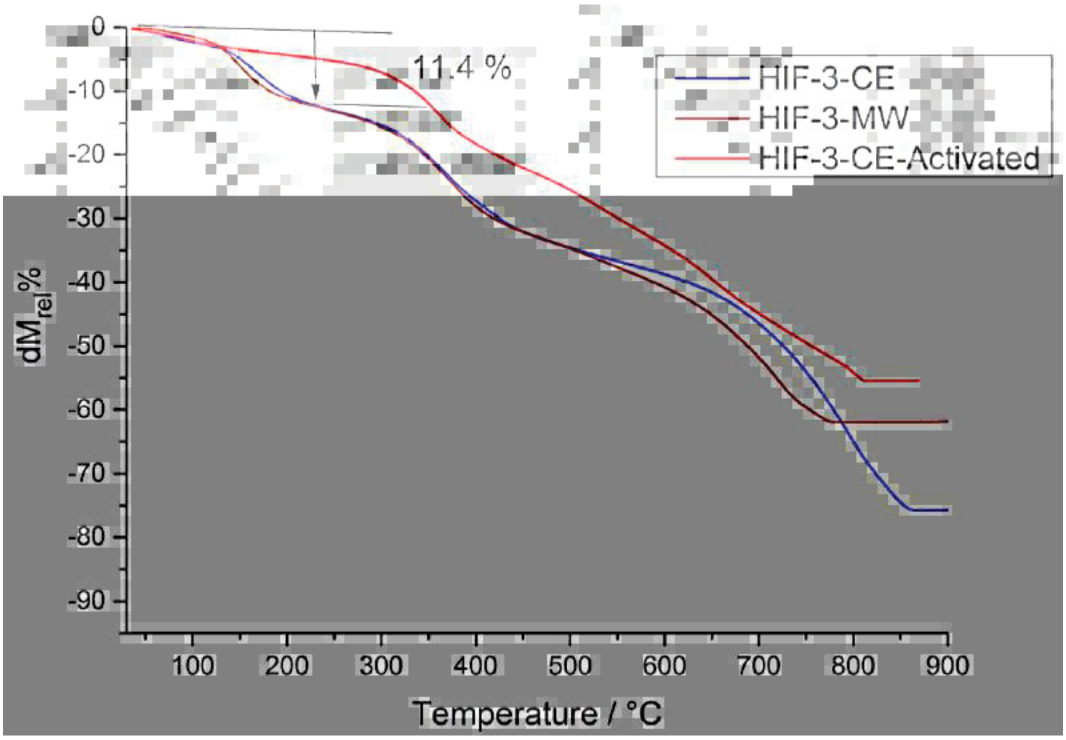

Figure S10. TGA curves for HIF-3.

8. Gas-sorption measurements

Sorption isotherms were measured using a Micromeritics ASAP 2020 automatic gas sorption analyzer equipped with oil-free vacuum pumps (ultimate vacuum <10^{-8} mbar) and valves, which guaranteed contamination free measurements. The sample was connected to the preparation port of the sorption analyzer and degassed under vacuum until the out gassing rate, i.e., the rate of pressure rise in the temporarily closed manifold with the connected sample tube, was less than 2 μTorr/min at the specified temperature 60 °C for 24 h. After weighing, the sample tube was then transferred to the analysis port of the sorption analyzer. All used gases (H_2, He, N_2, and CO_2) were of ultra high purity (UHP, grade 5.0, 99.999%) and the STP volumes are given according to the NIST standards (293.15 K, 101.325 kPa). Helium gas was used for the determination of the cold and warm free space of the sample tubes. H_2 and N_2 sorption isotherms were measured at 77 K (liquid nitrogen bath), whereas CO_2 sorption isotherms were measured at 273.15 K (ice/deionized water bath). N_2 sorption isotherms were obtained on a Quantachrome Nova 4000e at 77 K.

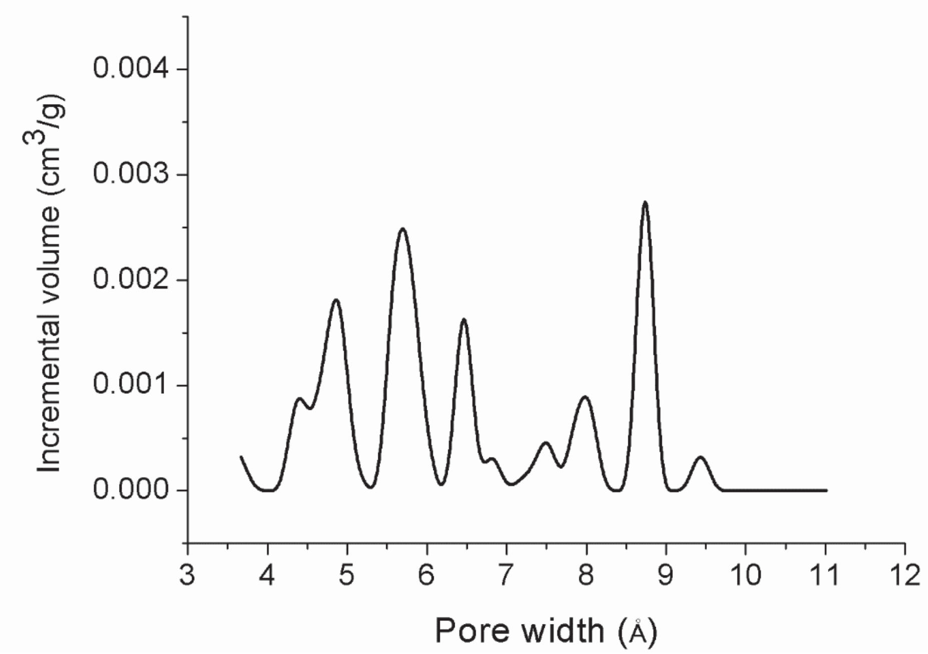

Figure S11. The pore size distribution from a CO2 adsorption isotherm at 273 K, calculated by the NL-DFT with a "CO2 on carbon based slit-pore" model at 273 K.

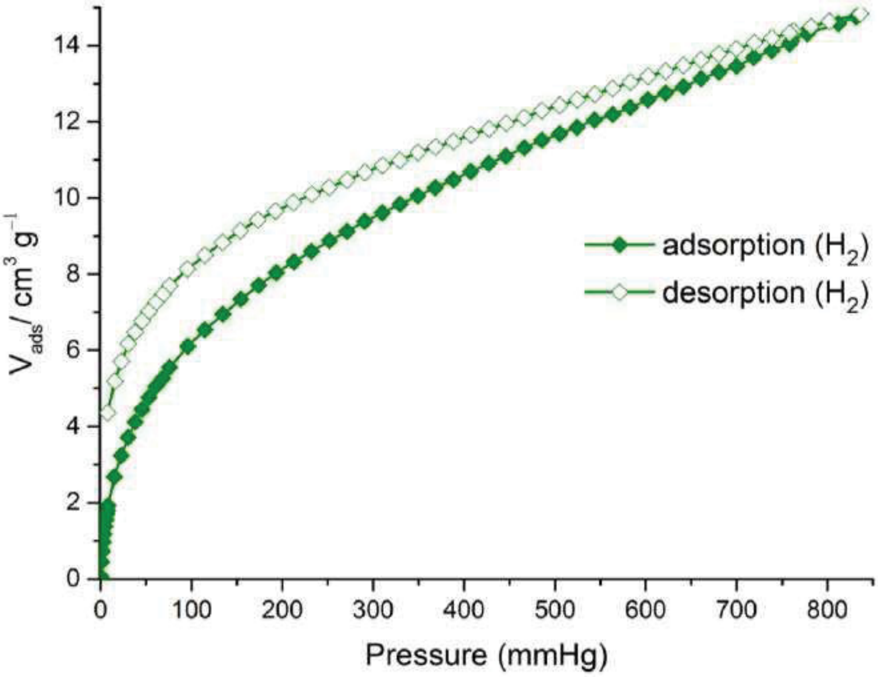

Figure S12. H_2 sorption isotherms of HIF-3-CE.

Table S6. CO_2 sorption data comparison.

Materials	$V(CO_2)$ cm^3 g^{-1}	Measured Conditions	Ref.
HIF-3-CE HIF-3- MW	18.2 14.4	273 K and 1 bar	This work
TBC[4]DHQ	35	35 atm	*Chem. Mater.* **2007**, *19*, 3354–3357
SOF-1a	16	296 K and 1 bar	*J. Am. Chem. Soc.* **2010**, *132*, 14457–14469
HOF-3a	21	296 K and 1 bar	*Chem. Commun*. **2014**, *50*, 13081–13084
HOF-7a	18	273 K and 1 bar	*Cryst. Growth Des*. **2015**, *15*, 2000–2004.
B2	15	298 K and 1 atm	*Angew. Chem. Int. Ed.* **2016**, *55*, 4523–4526
TPP	21	298 K and 1 atm	*Angew. Chem. Int. Ed.* **2005**, *44*, 1816–1820
HIF-1	56	273 K and 1 bar	*J. Am. Chem. Soc.* **2014**, *136*, 44–47.
HOF-1a	225	196 K and 1 bar	*J. Am. Chem. Soc.* **2011**, *133*, 14570–14573
CBDU	72	196 K, 1 bar at p/p_0 = 0.5.	*Chem. Mater.* **2006**, *18, 4855–4864.*

9. Positron Annihilation Lifetime Spectroscopy

Digital Positron Lifetime Spectrometer

The sample was measured at first in air at RT to see the activation effect on the pore size. The samples were annealed isothermally at 50 °C, 100 °C, 150 °C, and 200 °C for periods of 3, 6, 9, 12 hrs at each temperature then the measurements were performed at RT. All measurements were performed upon reaching RT after annealing. We used a 7 μCi 22-Na positron source. A pre and a turbo pumps used to evacuate the samples. A digital positron annihilation spectroscopy, with two Hamamatsu photomultiplier tubes with two plastic scintillator of ϕ40mm x22mm dimension and 240 ps resolution (fwhm), was used for these measurements. LT 10 program was used for the LT analysis. The pore size was calculated by using Excited Energy Levels and Various Shapes (EELViS) program,[8,9] and the program depends on the Extended Tao-Eldrup model with the following equation:[10]

$$\lambda_{RTE}(D,T)=\lambda_A-\frac{\lambda_S-\lambda_{3\gamma}}{4}\left[1-\frac{2\delta}{D}+\frac{\sum_{i=1}^{\infty}\frac{1}{i\pi}\sin\left(\frac{2i\pi\delta}{D}\right)e^{\left(\frac{-\beta i^2}{D^2kT}\right)}}{\sum_{i=1}^{\infty}e^{\left(\frac{-\beta i^2}{D^2kT}\right)}}\right]^3 \text{..........................1}$$

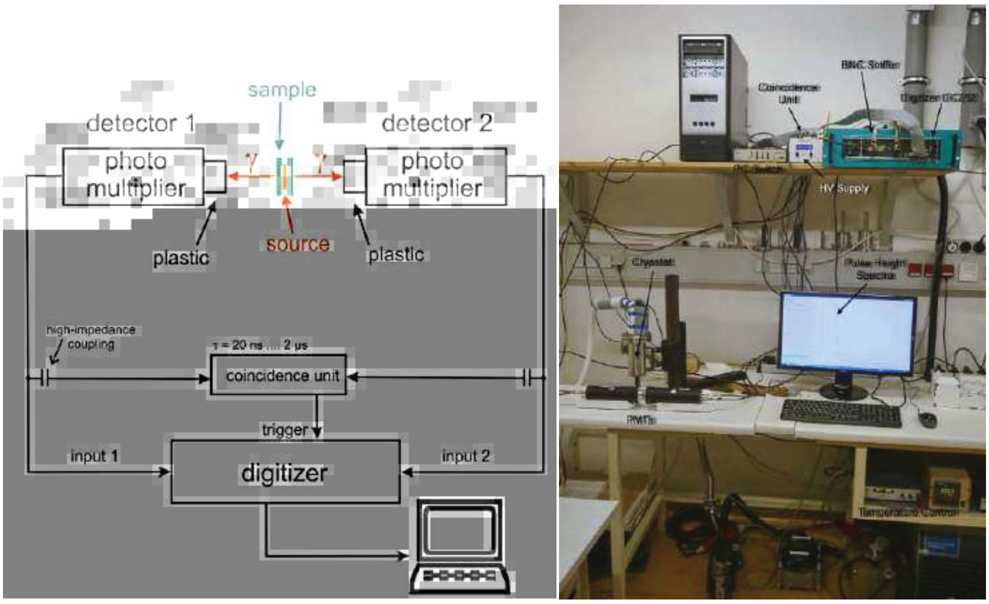

Figure S13. Instrumental set up of digital positron lifetime spectrometer. We used Na^{22} as a positron source and its activity is 7 μCi.

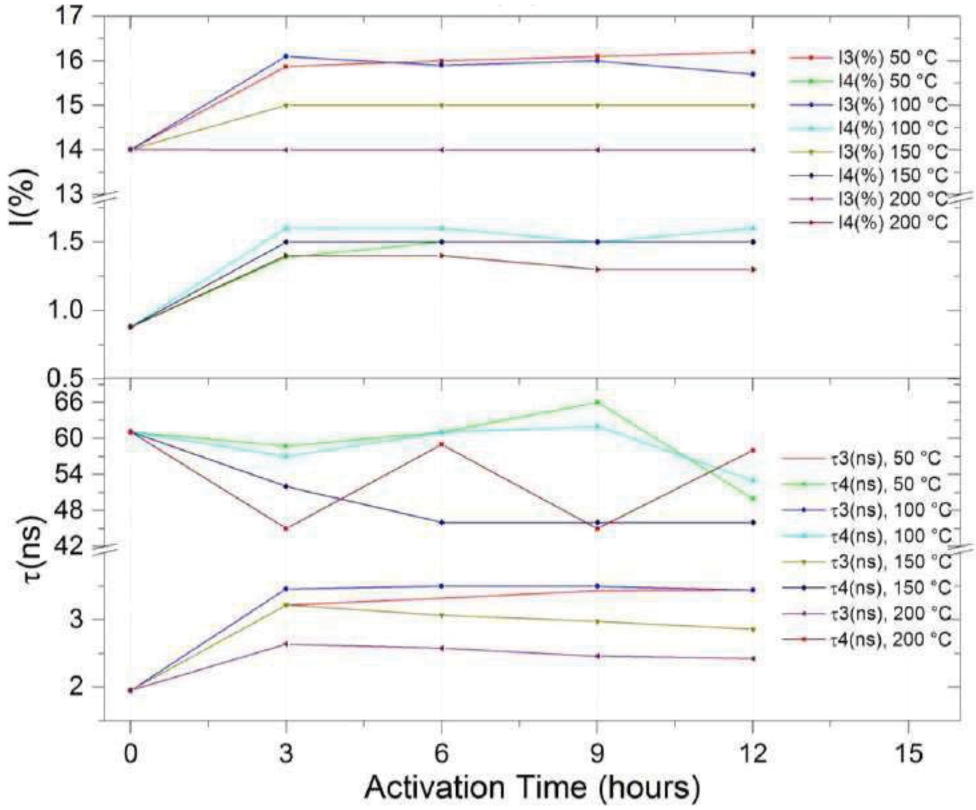

Figure S14. Positron lifetime of HIF-3-CE at different annealing temperatures as a function of annealing time.

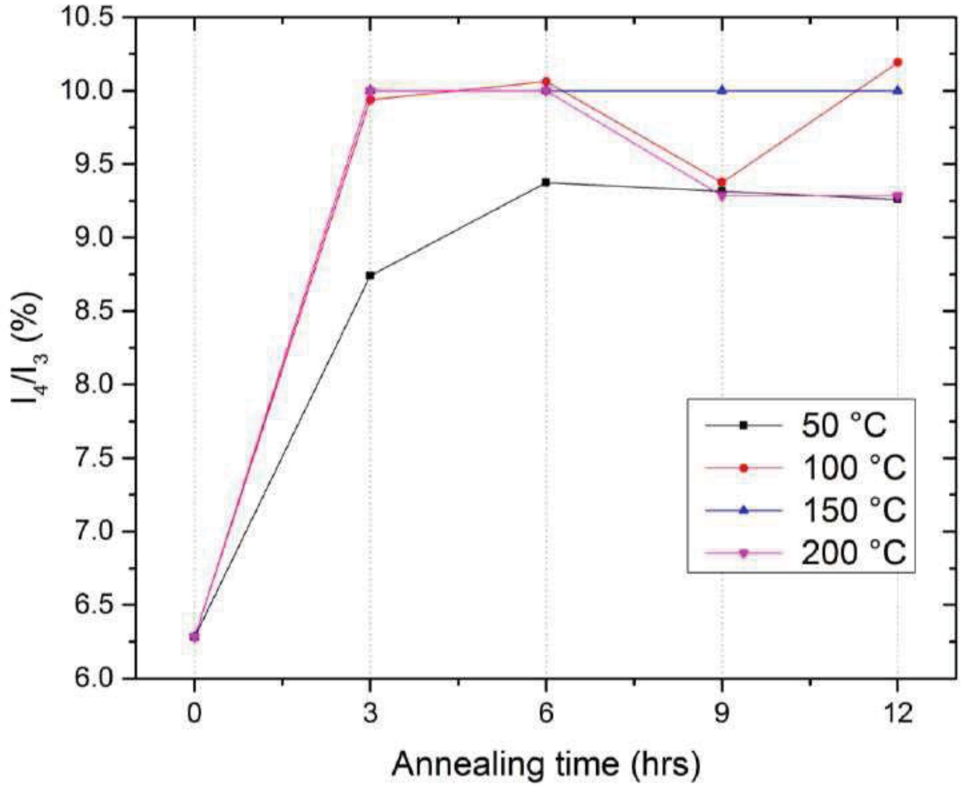

Figure S15. Intensity ratio of positron lifetime of HIF-3-CE at different annealing temperatures as a function of annealing time.

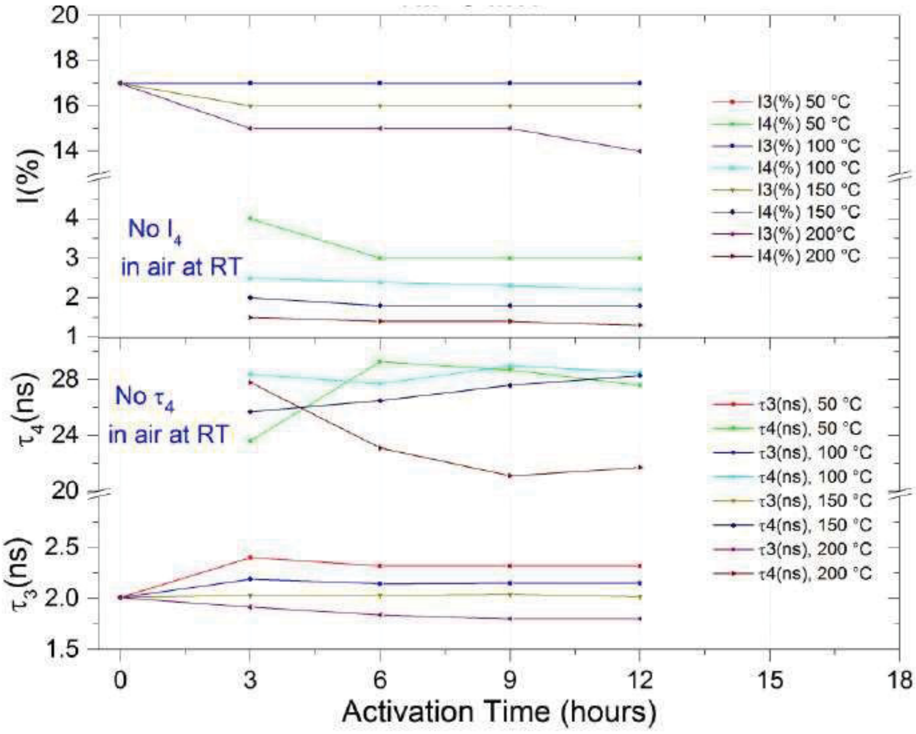

Figure S16. Positron lifetime of HIF-3-MW at different annealing temperatures as a function of annealing time.

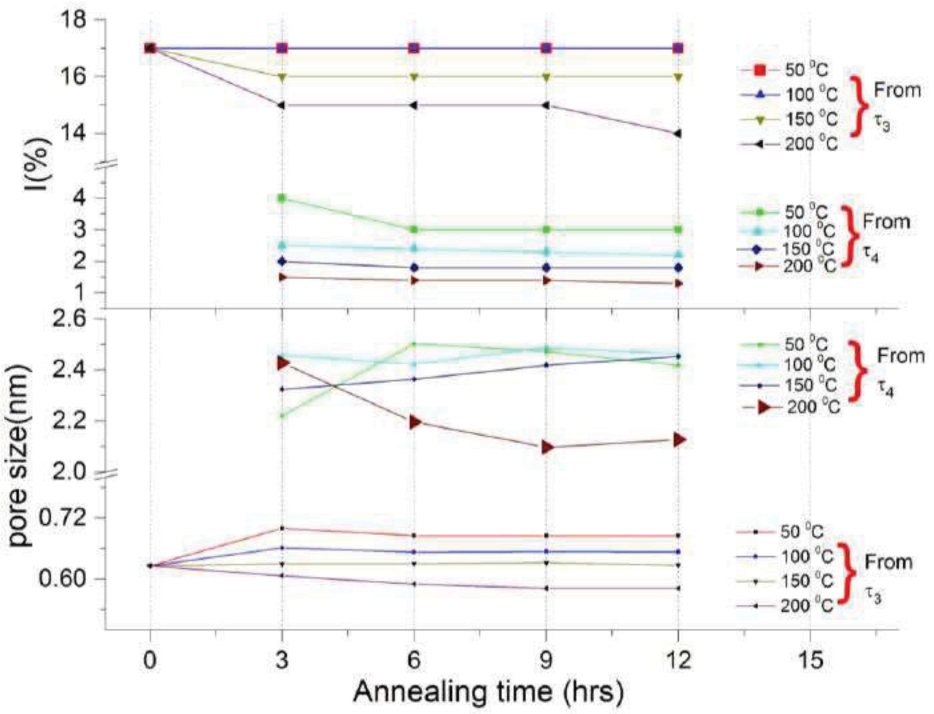

Figure S17. Spherical pore size of HIF-3-MW at different annealing temperatures as a function of annealing time.

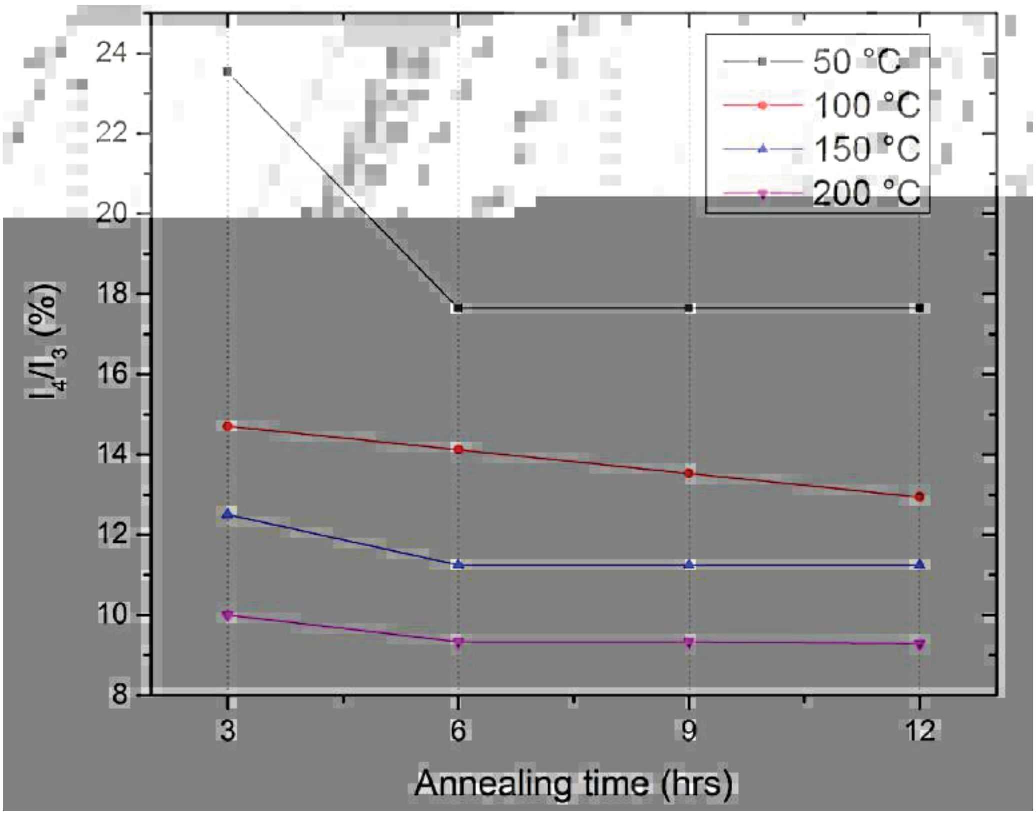

Figure S18. Intensity ratio of positron lifetime of HIF-3-MW at different annealing temperatures as a function of annealing time.

We draw each MBB looks like cubic (Figure 4 in the manuscript) because they are cubic shape. However, the defects pore size of the HIF-3 was calculated, assuming the spherical shape of the pore which is suitable fit than the cubical shape. MBB without peripheral amide groups seems to be spherical. The small pore diameter (0.87 nm), obtained from the pore size of annealing time (τ_3) is comparable with the pore size distribution of "CO_2 on carbon-based slit-pore model" (relative maximum at ~ 0.88 nm) and also close to X-ray structure (1.16 nm). The larger pore (~3.9 nm), obtained from τ_4, after 12 hours annealing time at the activation temperature at 100 °C has changed drastically during heating process and more dynamic behavior of the large pore is observed. Single X-ray crystal data only shows one type of pore which is comparable with the pore size, obtained form τ_3. The unit cell parameter, cell length ($a = b = 32.6744(11)$ Å) is consist of three MBBs are connected (view along c axis). If four MBBs connected together, forming a cube can be missing and created defects. The defect pore size could be comparable with the experimental data. However, there is slight deviation of pore size. The pore size of large pore suggests of the missing MBBs. Cubical pore sizes of HIF-3-CE (τ_3 and τ_4 are 0.22 and 0.89 nm, respectively, at 100 °C activation temperature after 6 h annealing time) and –MW (τ_3 and τ_4 are 0.14 and 0.60 nm, respectively, at 100 °C activation temperature after 6 h annealing time) at different annealing temperatures as a function of annealing time can not fit to the theoretical pore size. Therefore, experimental data suggests the defects pore size is spherical shape.

Table S7. Inductively coupled plasma optical emission spectrometry (ICP OES) result for HIF-3.

Material	Cd-content
HIF-3-CE	361.8 g/kg
HIF-3 MW	315.1 g/kg

10. References

[1] W. K. Anderson, D. Bhattacharjee, and D. M. Houston, *J. Med. Chem*. **1989**, *32*, 119–127.

[2] H. E. Gottlieb, V. Kotlyar, A. Nudelman, *J. Org. Chem.* **1997,** *62,* 7512–7515.

[3] a) W. Yang, B. Li, H. Wang, O. Alduhaish, K. Alfooty, M. Aldin Zayed, P. Li, H. D. Arman, B. Chen, *Cryst. Growth Des*. **2015**, *15*, 2000–2004; b) Y. He, S. Xiang, B. Chen, *J. Am. Chem. Soc.* **2011**, *133*, 14570–14573; c) P. Li, Y. He, H. D. Arman, R. Krishna, H. Wang, L. Weng, B. Chen, *Chem. Commun*. **2014**, *50*, 13081–13084; d) H. Wang, B. Li, H. Wu, T.-L. Hu, Z. Yao, W. Zhou, S. Xiang, B. Chen, *J. Am. Chem. Soc.* **2015**, *137*, 9963–9970; e) I. Hisaki, S. Nakagawa, N. Tohnai, M. Miyata, *Angew. Chem. Int. Ed.* **2015**, *54*, 3008–3012; *Angew. Chem.* **2015**, *127*, 3051–3055.

[4] G. M. Sheldrick, *SHELXS*-2013/1, Program for the Crystal Structure Solution, Universität Göttingen, Göttingen, Germany, **2013**.

[5] G. M. Sheldrick, *SHELXL*-2013/2, Program for the Crystal Structure Refinement, Universität Göttingen, Göttingen, Germany, **2013**.

[6] A. L. Spek, *PLATON*, Multipurpose Crystallographic Tool, Utrecht University, Utrecht, The Netherlands, **2008**.

[7] F. Debatin, A. Thomas, A. Kelling, N. Hedin, Z. Bacsik, I. Senkovska, S. Kaskel, M. Junginger, H. Müller, U. Schilde, C. Jäger, A. Friedrich, H.-J. Holdt, *Angew. Chem. Int. Ed.* **2010**, *49*, 1258–1262; *Angew. Chem.* **2010**, *122*, 1280–1284.

[8] R. Zaleski, J. Wawryszczuk, T. Goworek, *Radiat. Phys. Chem.* **2007**, 76, 243–247.

[9] http://sourceforge.net/projects/eelvis/

[10] D. W. Gidley, T. L. Dull, W. E. Frieze, J. N. Sun, A. F. Yee, *J. Phys. Chem.* B **2001**, *105,* 4657–4662.

4 Unpublished work

4.1 Synthesis and characterisation of CTF based mixed matrix membrane and their gas separation studies

Introduction

During last few decades membrane based separation technology is gaining major importance due to advantages like low operating cost, ease of operation, minimum energy requirement and environmental friendliness. Currently membrane based technology is used in chemical and petrochemical industry and for natural gas purification, hydrogen separation, nitrogen recovery, olefin/paraffin separation.[1,2,3,4] Polymeric membranes have been studied widely for their low cost, high processability and good intrinsic transport properties however face a trade-off relationship between permeability and selectivity.[5] In spite of having outstanding separation property, good thermal, mechanical and chemical stability, inorganic membranes suffer major issues like high production costs, lack of processability, large scale production, brittleness.[5] As an alternative to polymer and inorganic membrane, mixed matrix membranes (MMMs) have attracted major attention due to their low cost and high permeability and selectivity over the upper-bound limit.[5,6,7] A typical MMM contains a bulk continuous polymer phase and a dispersed inorganic particle phase. Polymers that are generally used to fabricate MMMs include polysulfone, polyarylates, polycarbonates, poly(arylethers), poly(arylketones) and polyimide.[7] Porous materials that are generally incorporated to fabricate MMMs are carbon molecular sieves, zeolite, mesoporous materials, activated carbons, carbon nanotubes and metal organic frameworks (MOFs).[8] In recent years porous aromatic frameworks (PAFs) or covalent organic frameworks (COFs) have also been explored to fabricate such membranes. Covalent triazine-based frameworks (CTFs) were developed by Kuhn and coworkers, are new class of porous material with excellent thermal and chemical stabilities with highly basic functionalities.[9] Up to now, only few examples of CTFs based MMMs are known. Recently Zhu *et al.* reported a triazine-framework-based porous membranes (TFMs) for CO_2 separation through super acid catalysed trimerization reaction of 4,4′-biphenyldicarbonitrile.[10] Zhong and co-workers developed a strategy for graphene oxide assisted restacking method to fabricate ultrathin CTF-1 membranes for gas separation.[11] Herein we reported CTF-1 baes MMMs for selective CO_2:N_2 gas separations by using polysulfone as polymeric matrix.

Synthesis and characterization of CTF-1

CTF-1 has been synthesized according to the following procedure[9]: a mixture of terephthalonitril (1.28 g, 10 mmol) and anhydrous $ZnCl_2$ (6.8 g, 50 mmol) were placed into a quartz ampoule under inert conditions. The ampoule was evacuated, sealed and heated for 48 h at 400 ºC followed by cooling to room temperature. The black product was collected and stirred with water for 72 h. Then the product was isolated by filtration and again stirred with 200 mL of 2 mol/L HCl for 24 h. The resulting black powder was further washed with water (3 × 75 mL), THF (3 × 75 mL), acetone (3 × 75 mL) and dried in vacuum. CTF-1 is characterized by spectroscopies techniques such as elemental analysis, IR, thermogravimetric analysis (TGA), powder XRD and scanning electron microscopy (SEM) images.

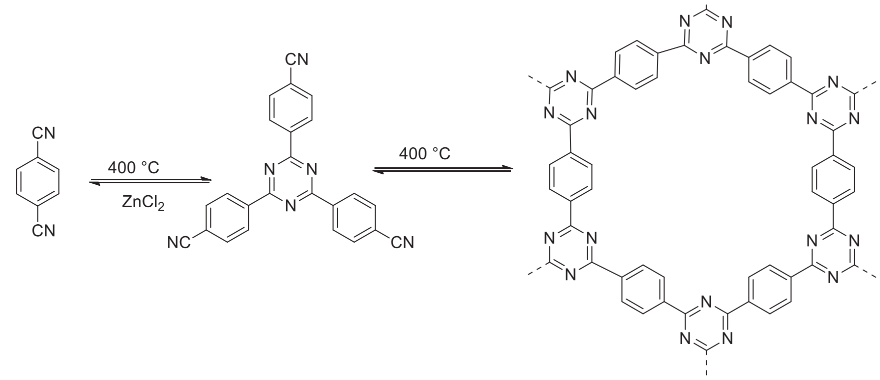

Scheme 1: Idealized structure of CTF-1 from the polymerization of terephthalonitrile.

The IR spectrum (Fig. 1) at 2225 cm^{-1} indicated the presence of unreacted nitrile groups in the polymer. The strong IR band around 1514 cm^{-1} is due to the C–N stretching mode of the triazine ring, whereas the band at 1352 cm^{-1} is due to inplane stretching vibrations of the triazine ring.[12] From TGA it is observed that the CTF-1 is stable up to around 450 °C. The PXRD pattern (Fig. 2) displayed the crystalline nature of the CTF with hexagonal packing of pores.[9] The SEM image (Fig. 3) showed that the material consisted particles of irregular shapes with an average particle size of about 10 μm. Elemental analysis of CTF-1 showed much lower nitrogen content which is due to nitrogen elimination during the high temperature polymerization reaction.[9]

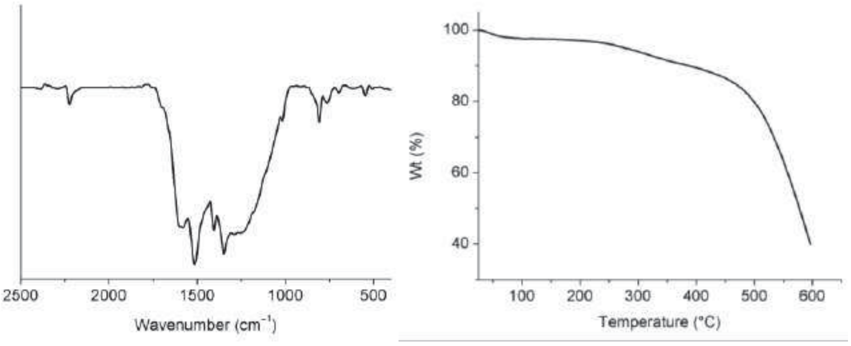

Fig. 1: FT-IR spectrum (left) and Thermogravimetric analysis (TGA) data (right) for CTF-1**.**

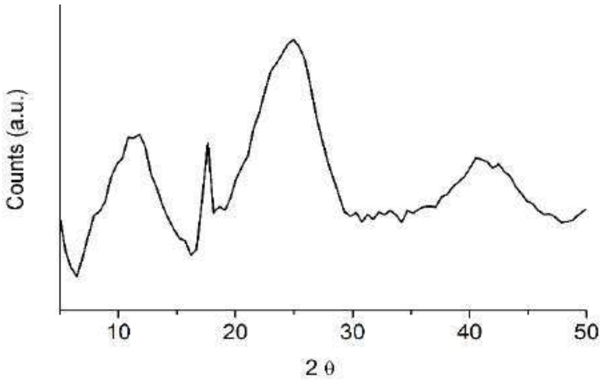

Fig. 2: Powder X-ray diffraction pattern of CTF-1.

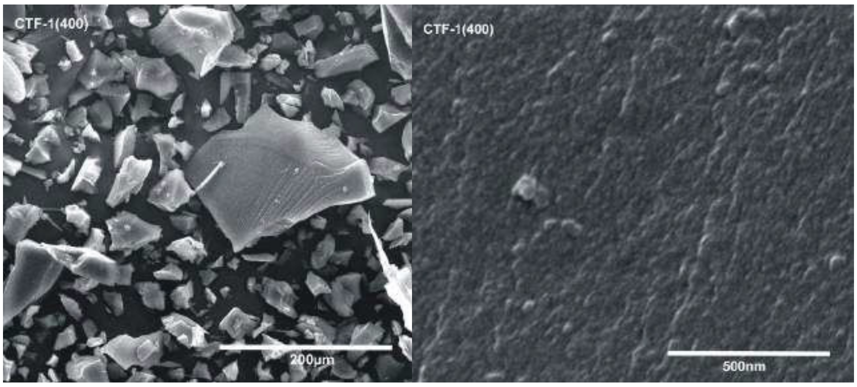

Fig. 3: SEM images for CTF-1.

Table 1: Elemental analysis.

Compound	Temperature (°C)	Calculated (wt%)					Found (wt%)				
		C	H	N	C/H	C/N	C	H	N	C/H	C/N
CTF-1	400	74.99	3.15	21.86	1.98	4.00	72.03	2.96	13.82	2.03	6.08

N_2 Sorption and pore size distribution

The porosity of the CTF-1 was characterized by N_2 sorption measurements as the accepted standard for surface area and pore size determination. The materials were activated by degassing at 200 °C for 24 h. The measured BET surface area for CTF-1 is 968 m^2/g. To understand the nature of porosity, non-local density functional theory (NLDFT) pore size distributions using a slit-pore model based on the N_2 adsorption isotherms were calculated. A narrow distribution of micropores centered mainly at 5, 6 and 12 Å were observed for CTF-1.

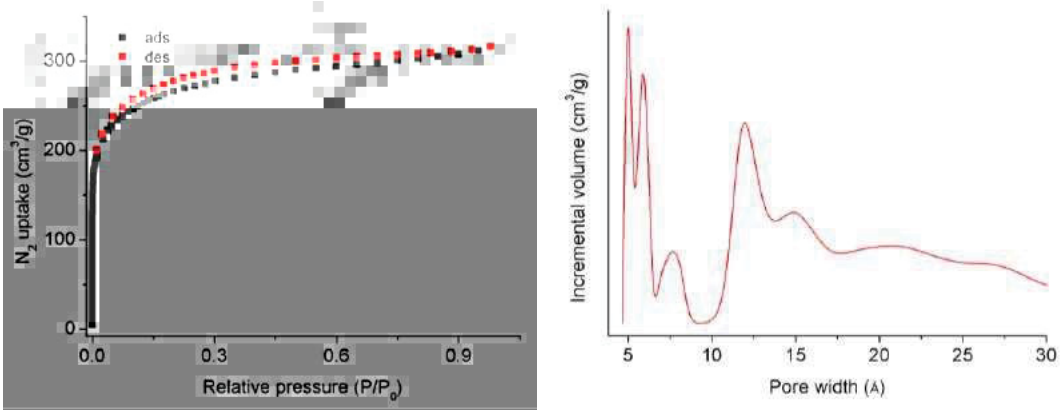

Fig. 4: Nitrogen adsorption-desorption isotherms for CTF-1 (left). NL-DFT pore size distribution curve of CTF-1 (right).

Table 2: Gas uptake of CTF-1.

Compound	S_{BET} $(m^2/g)^a$	S_{Lang} (m^2/g)	H_2 uptake at 77K $(cm^3/g)^b$	CO_2 uptake at 273K $(cm^3/g)^b$	CO_2 uptake at 293K $(cm^3/g)^b$
CTF-1	968	1181	136	72.35	49.2

[a]Calculated BET surface area over the pressure range 0.01–0.05 P/P_0. [b]Gas uptake at 1 bar.

We investigated the adsorption of other gases, such as H_2 and CO_2 at low pressure (Table 2). CTF-1 adsorbed 1.2 wt% (136 cm^3/g) H_2 at 77 K and 1 bar. The CO_2 uptake capacities of CTF-1 were measured at two different temperatures at 1 bar. The volume of CO_2 adsorption on CTF-1 at 273 K and 293 K were 72 and 49 cm^3/g, respectively.

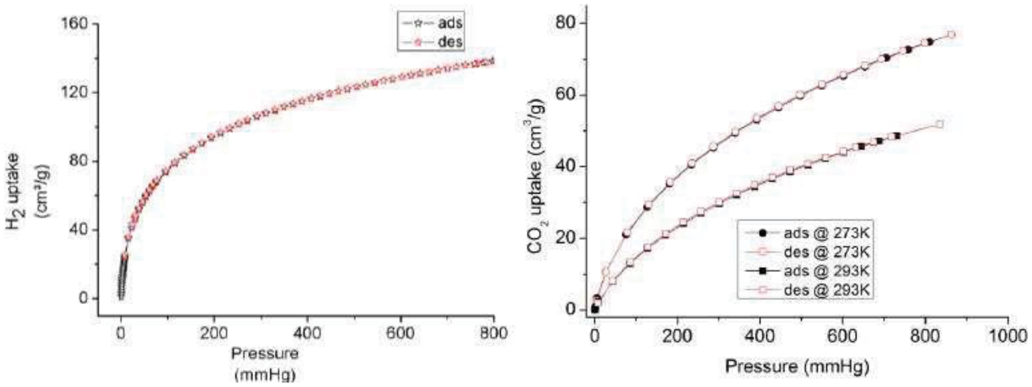

Fig. 7: H_2 sorption (left) and CO_2 sorption (right) for CTF-1

Fabrication of CTF-1/Polysulfone mixed matrix membranes

The polysulfone (PSF) polymer was dissolved in chloroform ($CHCl_3$) and CTF-1 was added to the polymer solution, and the obtained dispersion was stirred for one week. 8 wt% (0.034 g), 16 wt% (0.076 g), and 24 wt% (0.123 g) CTF-1 was added to the polymer. The casting solution was treated for 30 min in ultrasonic bath, afterwards it was stirred for 30 min again. This cycle was repeated three times. Before casting, the dispersion was kept under stirring for 30 more minutes. The dispersion was cast into metal rings placed on a flat glass surface. As soon as all solvent was evaporated, the membrane was removed from the metal ring. The membrane was finally dried in a vacuum oven at 120 °C overnight.

The SEM images of the membrane cross-sections of the pure polymer membrane and of the fabricated MMMs are depicted in Fig. 8. The images showed that the CTF-1 material present in the polymer matrix. Therefore, there was strong interfacial contact between PSF and CTF-1 materials.

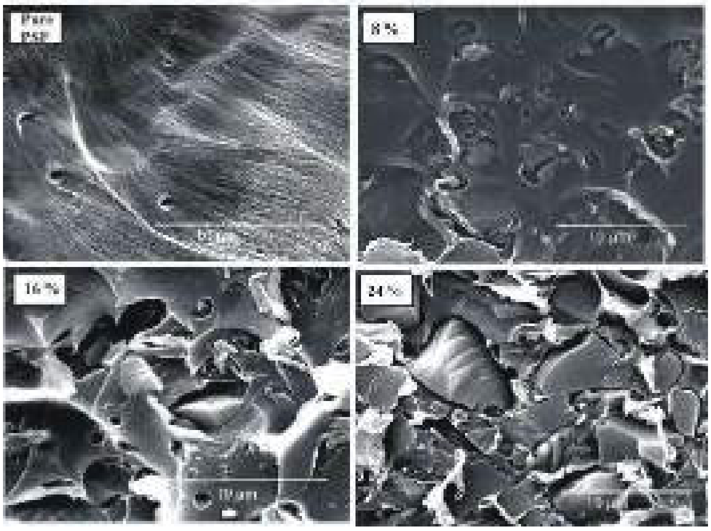

Fig. 8: SEM cross-sections of CTF-1-PSF membranes based on 400 mg of PSF with 0%, 8%, 16% 24% loadings.

Gas permeation experiments

The single-gas (O_2, N_2, CO_2 and CH_4) permeation and separation properties of PSF and PSF/CTF-1 MMMs is carried out at 25 °C and 3 bar (Table 3-4 and Fig. 9-10). The experiments showed that the permeability of all gases are increased with CTF-1 loading (Table 3, Fig. 9). For example, at 24 % loading, the permeability of the MMMs are 2.1, 0.39, 9.79 and 0.49 Barrer for O_2, N_2, CO_2 and CH_4, respectively. For CO_2, an increase in permeability from 7.29 (Pure PSF membrane) Barrer to 9.79 Barrer (24% CTF-1 MMMs) is achieved which is suggested that the CTF-1 is facilitated the gas transport (Table 2). Since the permiabilities of all gases are increased proportionally, the ideal selectivities are remained unchanged (Table 3). For CO_2/N_2 separation of pure PSF is 23.04 and, at 8% CTF-1 loading, the separation is 28.6 and at 16% CTF-1 loading, the separation is 26.27 (Table 4, Fig. 10). Therefore, at 8% the selectivity of CO_2/N_2 is favored.

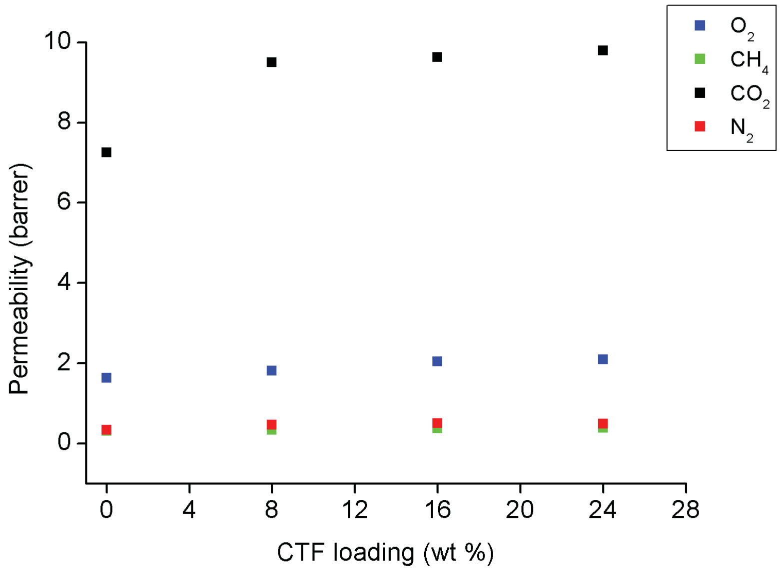

Fig. 9: Permeability performance of CTF-1 contain MMMs with different CTF-1 wt% loadings.

Table 3: Permeability of pure PSF and CTF-PSF MMMs

Polymer Amount (mg)	CTF loading (wt %)	P (O_2) [barrer]	P (N_2) [barrer]	P (CO_2) [barrer]	P (CH_4) [barrer]
400	0	1.6	0.3	7.3	0.3
400	8	1.8	0.3	9.5	0.5
400	16	2	0.4	9.6	0.5
400	24	2.1	0.4	9.8	0.5

Moreover, we also carried out the separation of O_2/N_2. The highest separation of O_2/N_2 is 5.57, which is observed at 16% CTF-1 loading. The O_2/N_2 separation is increased with increasing the CTF-1 loading up to 16%, and decreased with increasing the CTF-1 loading (Table 4, Fig. 10). On the other hand, the CO_2/CH_4 separations are changed bit from pure PSF to CTF-1 loading of MMMs with 8%, 16% and 24% (Table 4).

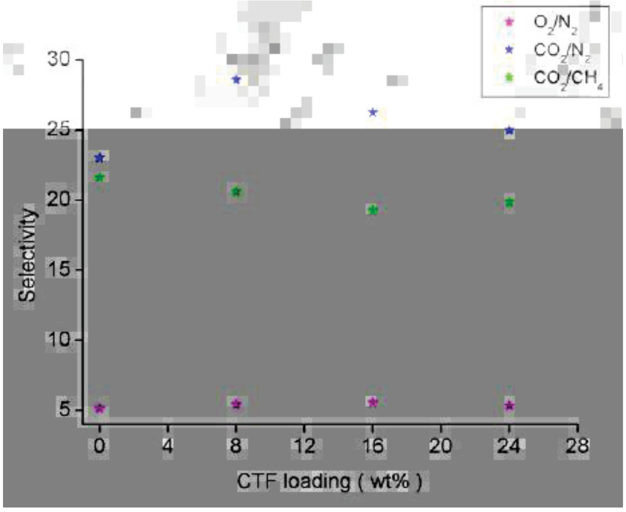

Fig. 10 Selectivity performance of CTF-1 contain MMMs with different CTF-1 wt% loadings.

Table 4: Selectivity of pure PSF and CTF-PSF MMMs

Polymer Amount (mg)	CTF loading (wt %)	S (CO_2/N_2)	S (O_2/N_2)	S (CO_2/CH_4)
400	0	23.0	5.1	21.6
400	8	28.6	5.45	20.62
400	16	26.27	5.57	19.28
400	24	25	5.35	19.87

Conclusion

In summary, we have successfully synthesized mixed matrix membranes containing thermally and chemically stable CTF-1. The fabricated membranes exhibited higher CO_2 permeability of 9.8 barrer than pure polysulfone membrane (7.3 barrer). For other gasses there are no significant improvement in the permeability. The MMMs showed higher CO_2/N_2 selectivity (28.6 for 8 wt% of CTF-1 loading) compared to pure polysulfone membrane (23), the selectivity decreases with increasing of CTF loading.

References

---

1. Y. Zhang, I. H. Musselman, J. P. Ferraris and K. J. Balkus Jr., *J. Membr. Sci.*, 2008, **313**, 170–181.

2. W. J. Koros and G. K. Fleming, *J. Membr. Sci.*, 1993, **83**, 1–80.

3. R. W. Baker, *Ind. Eng. Chem. Res.*, 2002, **41**, 1393–1411.

4. H. Strathmann, *AIChE J.*, 2001, **47**, 1077–1087.

5. B. Shimekit, H. Mukhtar and T. Murugesan, *J. Membr. Sci.*, 2011, **373**, 152-159.

6. G. Dong, H. Li and V. Chen, *J. Mater. Chem. A*, 2013, **1**, 4610-4630.

7. H. B. Tanh Jeazet, C. Staudt and C. Janiak, *Dalton Trans.*, 2012, **41**, 14003-14027.

8. M. J. C. Ordonez, K. J. Balkus Jr., J. P. Ferraris and I. H. Musselman, *J. Membr. Sci.*, 2010, **361**, 28–37.

9. P. Kuhn, M. Antonietti and A. Thomas, *Angew. Chem., Int. Ed.*, 2008, **47**, 3450–3453.

10. X. Zhu, C. Tian, S. M. Mahurin, S.-H. Chai, C. Wang, S. Brown, G. M. Veith, H. Luo, H. Liu and S. Dai, *J. Am. Chem. Soc.*, 2012, **134**, 10478–10484.

11. Y. Ying, D. Liu, J. Ma, M. Tong, W. Zhang, H. Huang, Q. Yang and C. Zhong, *J. Mater. Chem. A*, 2016, DOI: 10.1039/c6ta04579k.

12. S. Hug, M. B. Mesch, H. Oh, N. Popp, M. Hirscher, J. Senkerd and B. V. Lotsch, *J. Mater. Chem. A*, 2014, **2**, 5928-5936.

4.2 Amine supported covalent triazine-based frameworks (CTFs) for gas adsorption and separation

Introduction

Design and synthesis of porous materials have gained great attention over the last few years due to several applications including gas adsorption and separation especially as a selective carbon capture and storage (CCS) materials.[1,2,3,4] As a consequence of rapid economic growth, burning of fossil fuel and therefore emission of carbon dioxide in the atmosphere has become a crucial challenge to the environment. As a major greenhouse gases, emission of carbon dioxide causes global warming, sea level increasing and ocean acidification.[5,6] Three different technologies are currently use for CCS process[7]: (1) pre-combustion capture (2) post-combustion capture (3) oxyfuel coupling. For post combustion carbon dioxide capture from flue gas, the processes used are: (1) amine scrubbing, (2) membrane separation and (3) use of solid sorbents. Solid sorbents that generally used for low temperature (<200 °C) CO_2 capture included carbon[8], graphite/graphene[9], zeolite[10], silica[11], metal-organic frameworks (MOFs)[12] and microporous organic polymer[13,14] etc. Among them, porous organic frameworks (POPs) are found to be unique for their high surface area, light weight, structural modification and high thermal and chemical stability; and therefore gained enormous interest in applications like gas storage and separation, catalysis, optoelectronics and so on. Recently, synthesis of porous materials with functional groups including $–NO_2$, –OH, –COOH, $–SO_3H$, arylamines, and heterocyclic nitrogen atoms have gained attention as it show significant improvement of the properties like pore size modification and may affect the interaction with guest molecules which can favour the CO_2 adsorption through $O{=}C{=}O(\delta^-)–H(\delta^+)–O$ and $H_2N(\delta^-)–C(\delta^+)O_2$ interactions.[15] Functionality on porous networks could be achieved either by direct polymerisation of the functional monomers or by post synthetic modification of the existing frameworks.[16,17] Recent reports show that amine functionality into the porous frameworks could significantly improve the CO_2 uptake capacity. There are several reports on amine functionalization of MOFs[12,18] but functionalizations of POPs are relatively limited.

Herein we report a batch of CTFs networks with amine functionalities by bottom-up synthesis approach. Five networks AT-FL, AT-TPC, AT-TPB, AT-TPE, AT-TPS were synthesized by Friedel-Crafts reaction between 2-Amino-4,6-dichloro-1,3,5 triazine with fluorine (FL), 1,3,5-triphenylbenzene (TPB), triptycene (TPC), tetraphenylethelene (TPE) or tetraphenylsilane (TPS). The synthesized CTFs were tested for CO_2, N_2, H_2 and CH_4 adsorptions.

Experimental section

Materials

All chemicals were purchased from commercial suppliers (Sigma-Aldrich, Acros Organics, and Alfa Aesar chemical company) and used without further purification, unless stated otherwise. Dry dichloromethane (DCM) was collected from an MBraun solvent purification (drying) system under N_2 atmosphere and used for CTFs synthesis.

Instrumentation

Infrared (IR) spectra were obtained on a Bruker FT-IR Tensor 37 Spectrometer in the 4000-550 cm^{-1} region with 2 cm^{-1} resolution as KBr disks. ^1H and ^{13}C spectra were recorded on a Avance DRX-500 instruments. Elemental (CNH) analyses were carried out with a PerkinElmer 2400 series 2 elemental analyzer. Powder X-ray diffraction (PXRD) data was collected on a Bruker D2 Phaser diffractometer using a flat sample holder (also a flat silicon, low background sample holder) and Cu $K\alpha_1/\alpha_2$ radiation with $\lambda = 1.5418$ Å at 30 kV covering 2theta angles 5-80° over a time of 2 h, that is. 0.01°/sec. Diffractograms were obtained on flat layer sample holders where at low angle the beam spot is strongly broadened so that only a fraction of the reflected radiation reaches the detector which leads to low relative intensities measured at $2\theta < 7°$. For hygroscopic or air-sensitive samples, the sample holder can be sealed with a dome. Scanning electron microscopy (SEM) images were obtained using an ESEM Quanta 400 FEG SEM equipped with a secondary electron detector. Thermogravimetric analyses (TGA) were carried out at a ramp rate of 5 °C/min in a N_2 flow with a Netzsch Thermo-Microbalance Aparatus TG 209 F3 Tarsus.

Nitrogen (purity 99.9990 %) physisorption isotherms were carried out on a Nova 4000e from Quantachrome at 77 K. Carbon dioxide, methane, nitrogen and hydrogen sorption isotherms were measured using a Micromeritics ASAP 2020 automatic gas sorption analyzer equipped with oil-free vacuum pumps (ultimate vacuum $<10^{-8}$ mbar) and valves, which guaranteed contamination free measurements. The sample was connected to the preparation port of the sorption analyzer and degassed under vacuum until the outgassing rate, i.e., the rate of pressure rise in the temporarily closed manifold with the connected sample tube, was less than 2 μTorr/min at the specified temperature 130 °C. After weighing, the sample tube was then transferred to the analysis port of the sorption analyzer. All used gases (H_2, He, N_2, CO_2,

CH_4) were of ultra high purity (UHP, grade 5.0, 99.999%) and the STP volumes are given according to the NIST standards (293.15 K, 101.325 kPa). Helium gas was used for the determination of the cold and warm free space of the sample tubes. H_2 and N_2 sorption isotherms were measured at 77 K (liquid nitrogen bath), whereas CO_2 and CH_4 sorption isotherms were measured at 293±1 K (passive thermostating) and 273.15 K (ice/deionized water bath). The heat of adsorption values were calculated out using the ASAP 2020 v3.05 software and the DFT pore size distributions ('N_2 DFT slit pore' model) were calculated using NovaWin 11.03' software.

Synthesis of amine CTFs

AT-FL: In a typical synthesis, a mixture of fluorene (166 mg, 1.0 mmol), 2-amino-4,6-dichloro-1,3,5 triazine (165 mg, 1.0 mmol) and anhydrous $AlCl_3$ (400 mg, 3 mmol) was refluxed in 100 mL of DCM for 16 h. After cooling to room temperature, the orange-color product was isolated by filtration, and washed with 10 ml 1M NaOH, water (3 × 50 mL), MeOH (3 × 50 mL), THF (3 × 50 mL), acetone (3 × 50 mL), and dried in vacuum at 60 °C for 12 h. Yield: 190 mg. CHN (found%): C, 70.14; H, 4.0; N, 7.14

AT-TPC: The procedure for AT-FL was followed by using triptycene (170 mg, 0.67 mmol) and 2-amino-4,6-dichloro-1,3,5 triazine (165 mg, 1 mmol) and $AlCl_3$ (400 mg, 3 mmol). Yield: 230 mg. CHN (found%): C, 66.65; H, 4.86; N, 6.23.

AT-TPB: The procedure for AT-FL was followed by using triphenylbenzene (205 mg, 0.67 mmol) and 2-amino-4,6-dichloro-1,3,5 triazine (165 mg, 1 mmol) and $AlCl_3$ (400 mg, 3 mmol). Yield: 210 mg. CHN (found%): C, 68.19; H, 4.83; N, 7.9

AT-TPE: The procedure for AT-FL was followed by using tetraphenylethelene (166 mg, 0.5 mmol) and 2-amino-4,6-dichloro-1,3,5 triazine (165 mg, 1 mmol) and $AlCl_3$ (400 mg, 3 mmol). Yield: 200 mg. CHN (found%): C, 65.56; H, 4.83; N, 7.1

AT-TPS: The procedure for AT-FL was followed by using tetraphenylsilane (168 mg, 0.5 mmol) and 2-amino-4,6-dichloro-1,3,5 triazine (165 mg, 1 mmol) and $AlCl_3$ (400 mg, 3 mmol). Yield: 232 mg. CHN (found%): C, 66.43; H, 4.48; N, 7.9

Result and discussion

Synthesis and spectroscopic characterization

All the porous frameworks AT-FL, AT-TPB, AT-TPC, AT-TPE and AT-TPS were synthesized by Friedel-Crafts reactions between the "node" 2-amino-4,6-dichloro-1,3,5 triazine with fluorine (FL), 1,3,5-triphenylbenzene (TPB), triptycene (TPC), tetraphenylethelene (TPE) or tetraphenylsilane (TPS), respectively as “linker” in the presence of anhydrous $AlCl_3$ as catalyst in dichloromethane (Scheme 1). After purification, the insoluble color materials (Fig. 1) were reproducibly collected. The resulting frameworks were characterized by FT-IR and solid-state ^{13}C CP/MAS NMR spectroscopy. The FT-IR spectrum of all CTFs showed disappearance of the stretching band of C–Cl at 849 cm^{-1}, suggesting complete reaction between 2-amino-4,6-dichloro-1,3,5 triazine and monomers (Fig. 2).[19] Moreover, the characteristic absorption bands for triazine unit (1512 cm^{-1} and 1348 cm^{-1}) as well as for N–H bending at 1649 cm^{-1} in the 2-amino-4,6-dichloro-1,3,5 triazine were shifted for the materials[20]: (1) the triazine unit as well as N–H bending absorption bands for AT-FL were at 1543 and 1385 cm^{-1} as well as 1628 cm^{-1}, (2) the triazine unit as well as N-H bending absorption bands for AT-TPB were at 1543, 1366 cm^{-1} as well as 1618 cm^{-1}, (3) the triazine unit as well as N-H bending absorption bands for AT-TPC were at 1515 , 1385 cm^{-1} as well as 1600 cm^{-1}, (4) the triazine unit as well as N–H bending absorption bands for AT-TPE were at 1543, 1385 cm^{-1} as well as 1618 cm^{-1}, (5) the triazine unit as well as N–H bending absorption bands for AT-TPS were at 1553 and 1366 cm^{-1} as well as 1618 cm^{-1}, respectively.

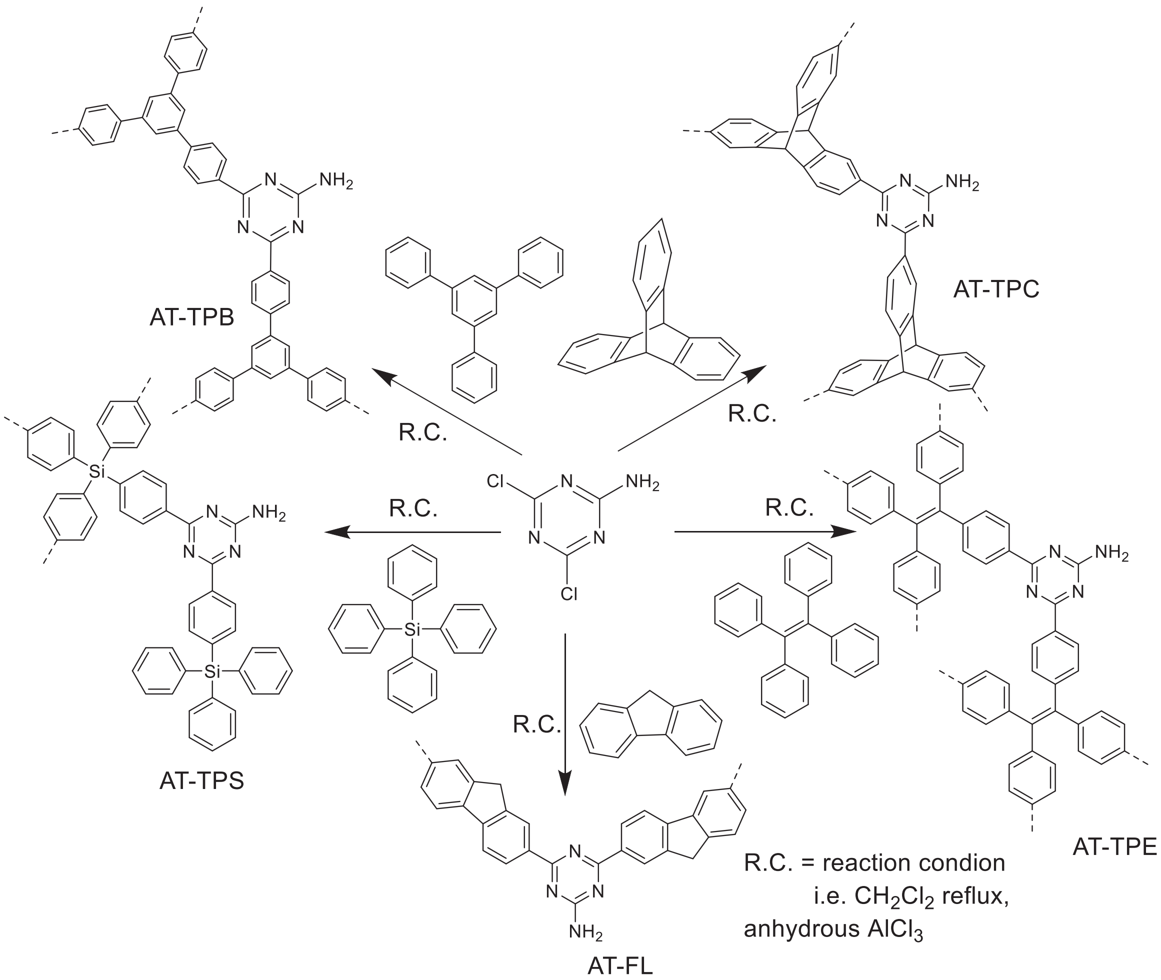

Scheme 1: Synthesis of amine CTFs AT-FL, AT-TPB, AT-TPC, AT-TPE and AT-TPS.

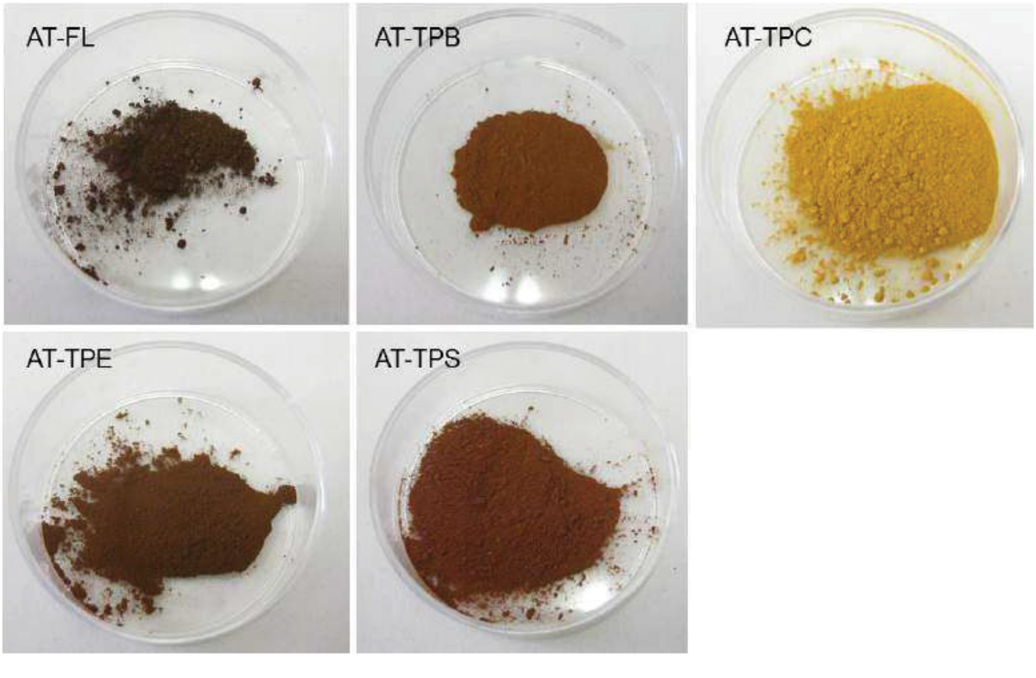

Fig. 1: Photograph of amine CTFs AT-FL, AT-TPB, AT-TPC, AT-TPE and AT-TPS.

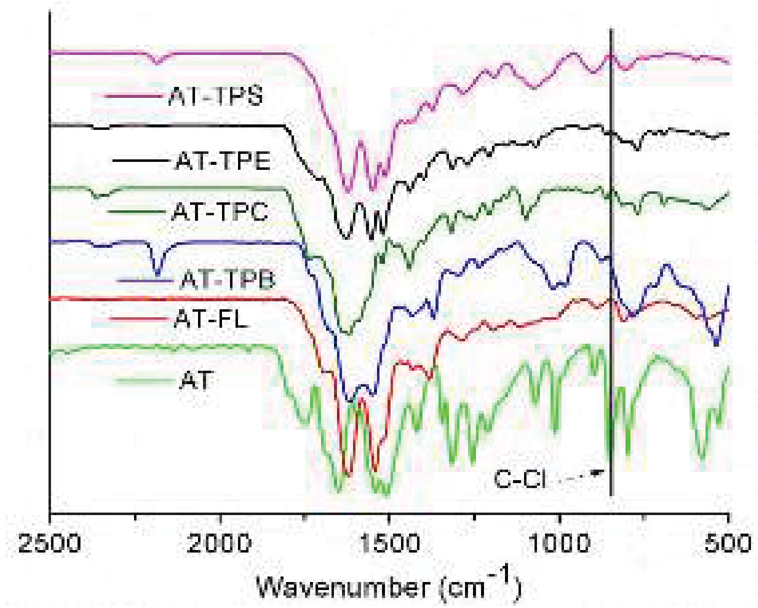

Fig. 2: FT-IR spectra of AT-FL to AT-TPS in comparison to that of 2-amino-4,6-dichloro-1,3,5 triazine.

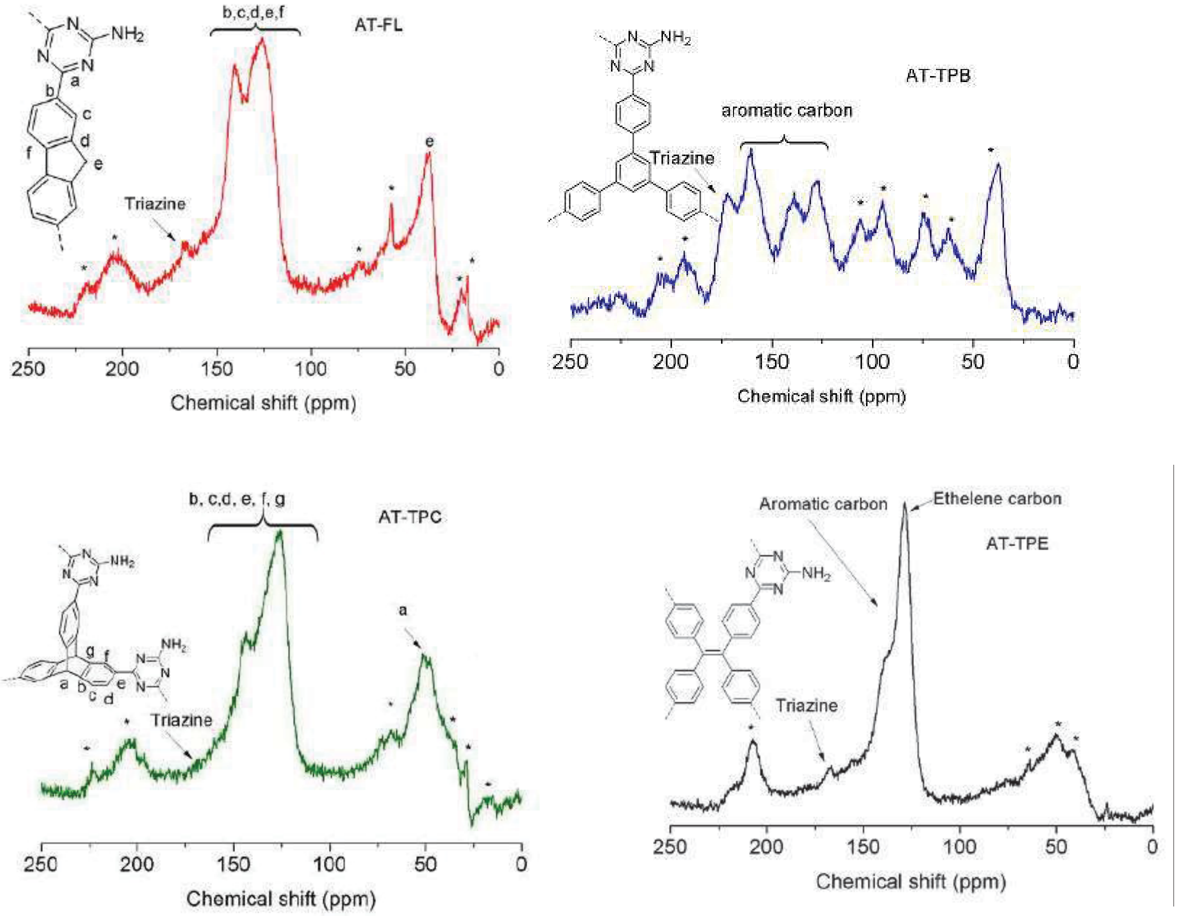

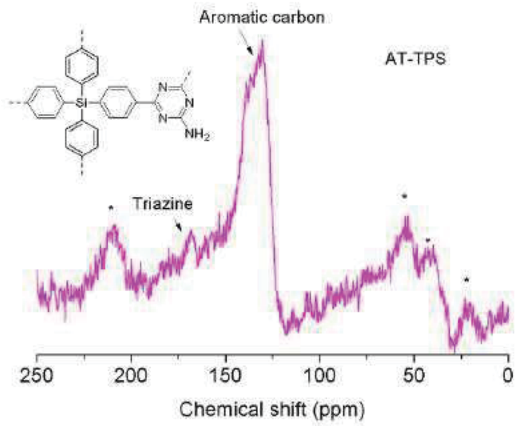

Fig. 3: solid state NMR of amine CTFs AT-FL, AT-TPB, AT-TPC, AT-TPE and AT-TPS. Asterisks represent the spinning sidebands.

Solid-state NMR of all amine CTFs AT-FL, AT-TPB, AT-TPC, AT-TPE and AT-TPS showed peaks at 167, 172, 167, 167 and 168 ppm corresponding to triazine units in the frameworks, respectively (Fig. 3).[21,22,23] On the other hand, these networks except AT-TPB showed only broad peaks in the range of 116-146 (AT-FL), 118-150 (AT-TPC), 122-145 (AT-TPE), 125-145 (AT-TPE) and 125-145 (AT-TPS) ppm, which can be assigned to the aromatic carbon atoms in the materials. For AT-TPB, three peaks at 127, 138 and 160 ppm were found. These evidences were confirming the successful incorporation of aromatic carbon atoms and triazine units in the polymer backbone. Powder X-ray diffraction indicates that the materials are amorphous in nature except AT-TPB (Fig. 4a). For the amorphous materials the diffractograms exhibit only three broad peaks around 18, 29 and 40° 2theta whereas for AT-TPB the presence of several peaks maxima in the diffractogram demonstrated the partial ordered nature of the framework. From thermogravimetric analysis (Fig. 4b), CTFs AT-FL to AT-TPS are stable up to in the range of 160 °C – 250 °C. All materials show an initial weight loss of 2.5-5.8 wt% in the temperature range 80-85 °C which is due to the hydrated or re-adsorbed water.

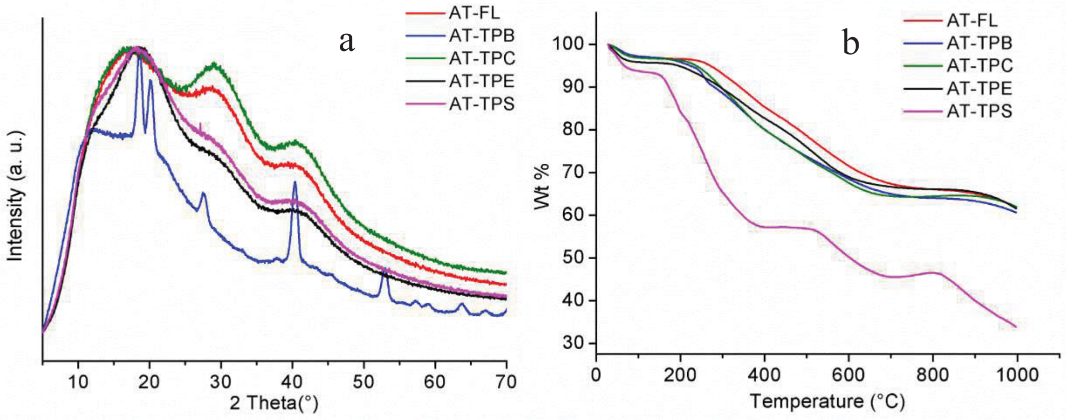

Fig. 4: (a) PXRD pattern for AT-FL to AT-TPS. (b) TGA plot for AT-FL to AT-TPS under N_2.

Particle morphology of the networks have been analysed by scanning electron microscopy method (Fig. 5) which suggested that the materials composed of spherical particles having diameter ranging from 0.2-3 µm. These particles were agglomerated to form bigger particles.

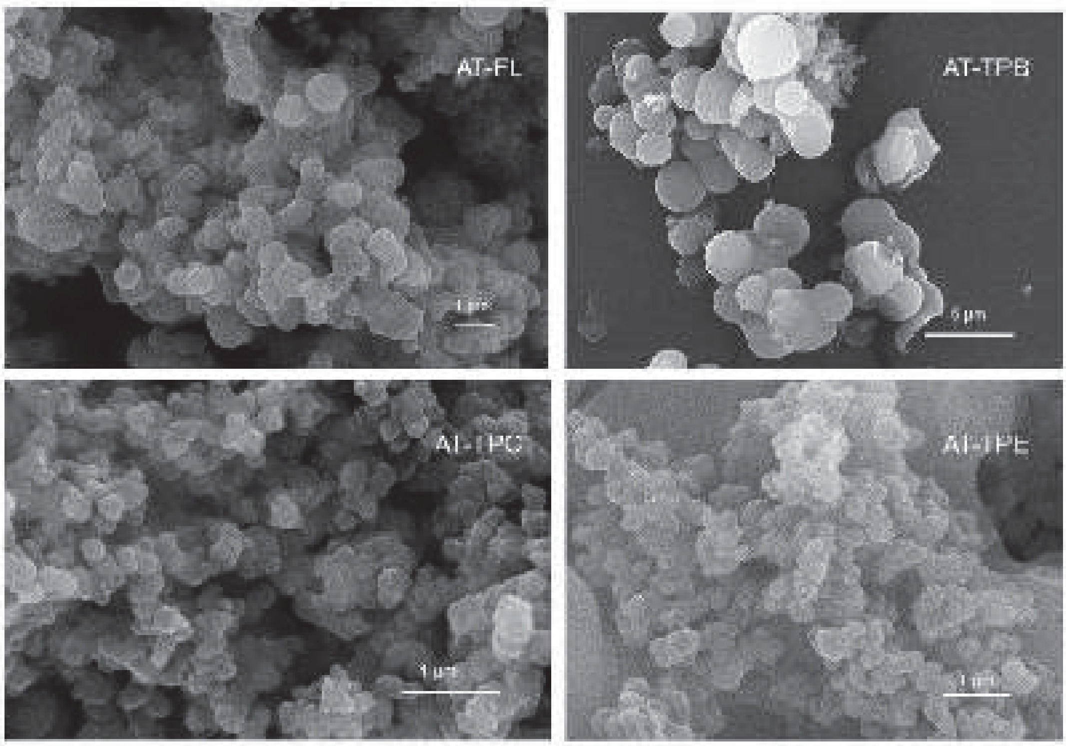

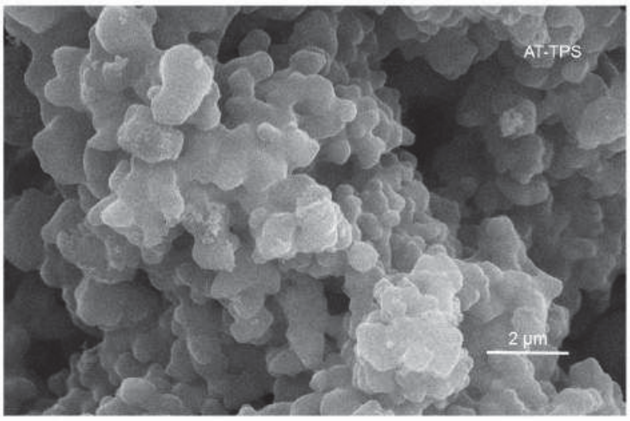

Fig. 5: Scanning electron microscopy images of AT-FL to AT-TPS.

Gas adsorption properties

The porosities of the five triazine frameworks were characterized by N_2 sorption measurements at 77 K as the accepted standard for surface area and pore size determination. All materials were activated by degassing at 130 °C for 12 h. The isotherms of AT-FL and AT-TPE can be classified as Type I isotherm whereas for AT-TPC, AT-TPE and AT-TPS the isotherms can be categorized as a combination of isotherms of Type I and Type IV (Fig. 6). Type I isotherms indicate microporosity, whereas Type IV associated with capillary condensation which takes place in the mesopores. All the isotherms associated with H4 type of hysteresis often observed for the materials with narrow slit like pores except AT-TPS which exhibit a H3 type of hysteresis loop.[24] Such type of isotherms and hysteresises are very common for CTFs materials.[22,23] However, the surface area was calculated by applying the Brunauer-Emmet-Teller (BET) model over the pressure range of P/P_0 = 0.01-0.05. The surface areas of AT-FL to AT-TPS were 572, 894, 1174, 594 and 451 m^2/g, respectively.

Pore size distribution were calculated by non local density functional theory (NLDFT) using the model of carbon as an adsorbent and slit pore (Fig. 7a). AT-FL and AT-TPE showed that most of the pores are in micropore region (up to 20Å). For AT-TPB, AT-TPC and AT-TPS micropores with a small fraction of mesopores have also been observed.

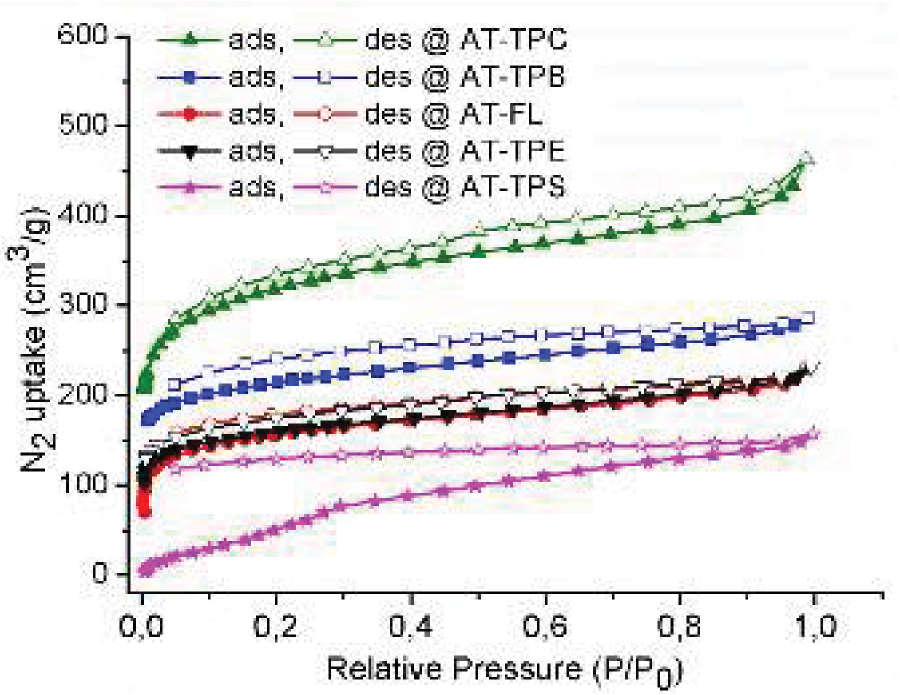

Fig. 6: N_2 sorption isotherm at 77 K for AT-FL to AT-TPS.

Ultramicropores were also calculated from CO_2 adsorption at 273 K for AT-FL to AT-TPS (Fig. 7b). From these measurements we observed all the materials have similar kind of micropore. The presence of ultramicropores was proved by CO_2 adsorption because of the diffusion of dinitrogen molecules at 77 K into ultramicropores (pores smaller than 7 Å) is quite slow.[25] At pore sizes close to the kinetic diameter of N_2 (~3.64 Å) and at 77 K the diffusion limitation can be alleviated by use of CO_2 as an adsorbate at 273 K. The saturation pressure of CO_2 at 0 °C is ~26141 Torr and low relative pressure measurements necessary for micropore analysis are achieved in the range of moderate absolute pressures (1–760 Torr).[26] CO_2 micropore analysis at 273 K versus N_2 analysis at 77 K ensures faster equilibration and slight extension of the range of analysis to pores of smaller sizes that are accessible to CO_2 molecules (kinetic diameter 3.30 Å), but not to N_2.[27]

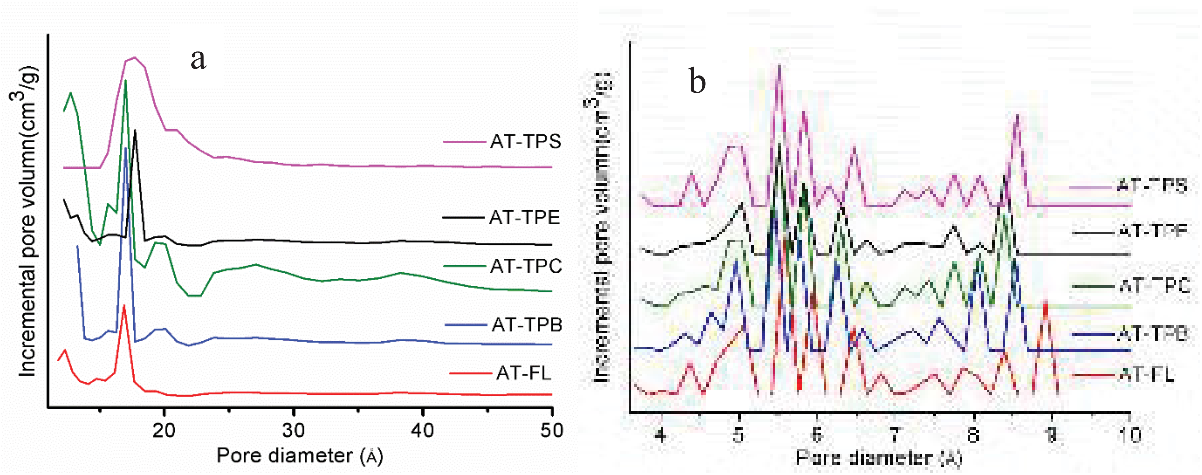

Fig.7: NLDFT pore size distribution (PSD) curves of AT-FL to AT-TPS from (a) N_2 adsorption (at 77 K) and (b) CO_2 adsorption (at 273 K) isotherms (N_2 DFT slit pore' model).

To understand the degree of microporosity of these materials the ratio of micropore volume to total pore volume were calculated from the N_2 sorption measurement at 77 K (Table 1). All frameworks (except AT-TPS) shows $V_{0.1}/V_{tot}$ values in the range of 0.66 to 0.74 which indicate the dominant microporous character of the networks, while for AT-TPS the $V_{0.1}/V_{tot}$ value is 0.2 proves the existence of mesopores.

Table 1: Porosity data for AT-FL to AT-TPS.

CTFs	S_{BET}^{a} (m^2/g)	$V_{0.1}$ ^{b} (cm^3/g)	V_{tot}^{c} (cm^3/g)	$V_{0.1}/V_{tot}$	$V_{micro}(CO_2)$ ^{d} (cm^3/g)
AT-FL	572	0.22	0.33	0.66	0.087
AT-TPB	804	0.31	0.42	0.74	0.109
AT-TPC	1174	0.45	0.65	0.7	0.079
AT-TPE	594	0.23	0.34	0.68	0.098
AT-TPS	451	0.045	0.22	0.20	0.086

[a] Calculated BET surface area over the pressure range 0.01–0.05 P/P_0. [b] Micropore volume calculated from N_2 sorption isotherm at $P/P_0 = 0.1$ for pores ≤2 nm (20 Å). [c] Total pore volume at $P/P_0 = 0.95$ for pores ≤20 nm. [d] Total pore volume for pores with diameters smaller than 1 nm (10 Å, cf. Fig. 7b) from the CO_2 NL-DFT model at 273 K.

With successful synthesis of five amine containing triazine frameworks, gas adsorption studies had been performed for H_2, CO_2, CH_4 and N_2 gasses at 1 bar. As shown in the Fig. 8, the H_2 uptakes at 77 K lie in the range of 0.9 to 1.3 wt%. AT-TPB shows the highest H_2

uptake (1.3 wt%) due to its higher micropore volume among the frameworks (Table 1). The H_2 uptake of AT-TPB is comparable with other CTFs.[22,23,28,29] Except AT-TPB, the AT-TPC showed almost equal H_2 uptakes in comparison to AT-FL, AT-TPC, AT-TPE and AT-TPS; although AT-TPC has almost double BET surface area than the AT-TPE. Volumetric CO_2 and CH_4 measurements were performed both at 273 K and 293 K up to 1 bar. The CH_4 uptake capacities of AT-FL to AT-TPS were in the range of 0.76-1.07 mmol/g (at 273 K) comparable with the values for PCTF-1 to -7 from our previous work as well as other CTFs.[27,29] The CO_2 adsorptions of AT-FL to AT-TPS were in the range of 2.29-3.38 mmol/g (at 273K) and show fully reversible adsorption desorption isotherms. Among all five frameworks, AT-TPB shows highest CO_2 adsorption of 3.38 mmol/g (at 273 K) and 2.15 mmol/g (at 293 K) at 1 bar. Such uptakes are highly comparable with other CTFs: fl-CTF (1.27-4.28 mmol/g)[30], *bipy* CTF300-400 (1.87-3.08 mmol/g)[31], CTF-1 (2.47-3.82 mmol/g)[32], CTF-Pl-P6 (1.88-3.39 mmol/g)[22], CTF-P1M-P6M (0.94-4.42 mmol/g)[22], MCTF300-500 (2.25-3.16 mmol/g)[33], PCTF-1-7 (1.85-3.26 mmol/g)[27,29], PCTF-8 (2.5 mmol/g)[21], CTF-FL (3.26 mmol/g)[23] and NOP-1-6 (1.31-2.51 mmol/g)[28].

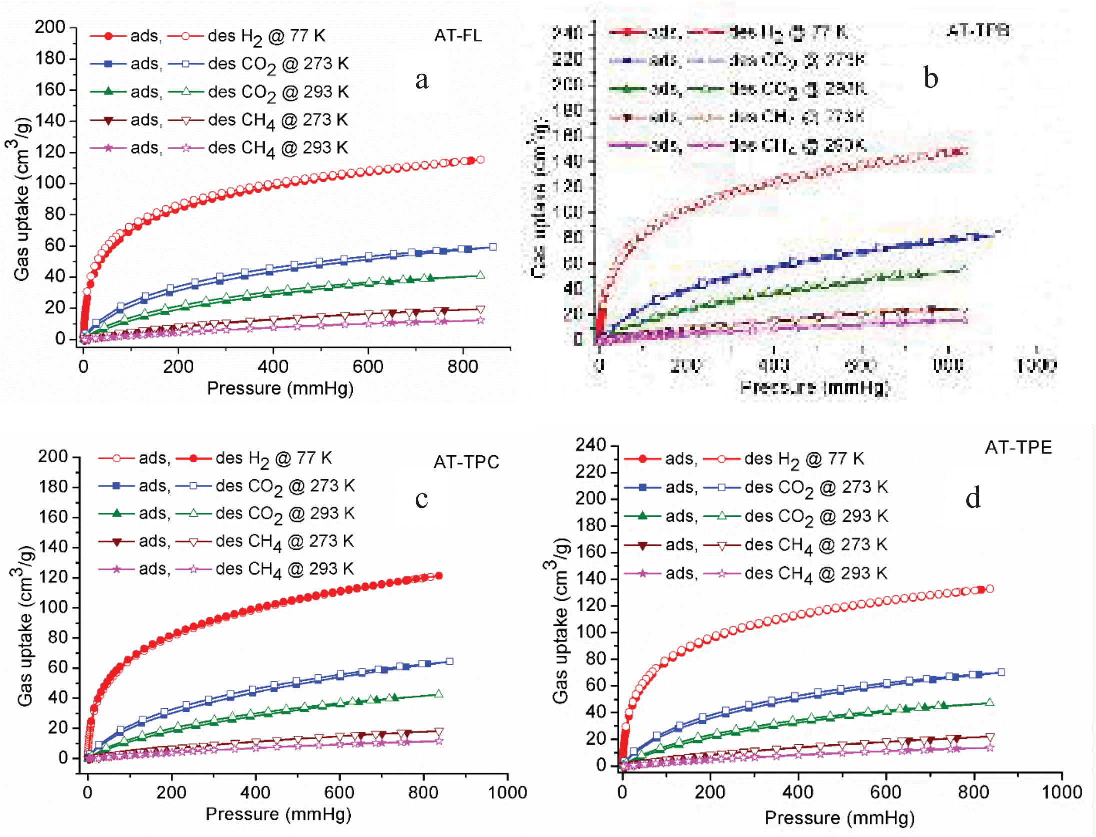

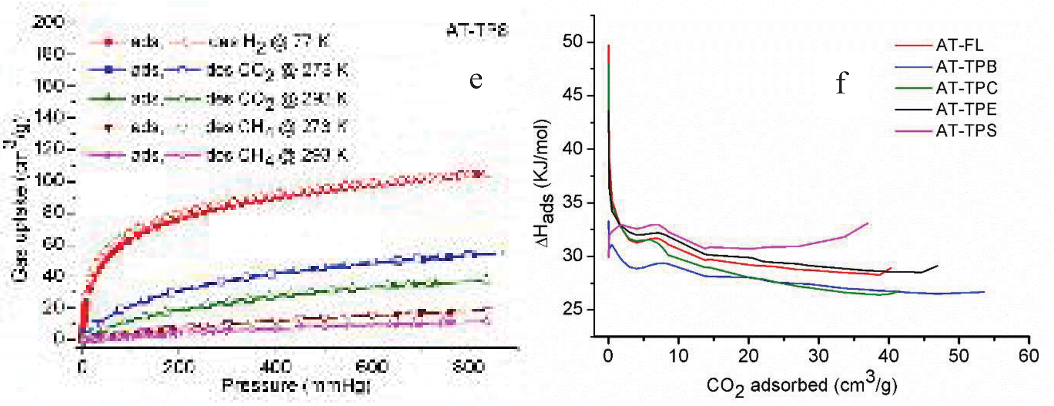

Fig. 8: Gas sorption isotherms (a-e) and heat of adsorption (f) of AT-FL, AT-TPB, AT-TPC, AT-TPE, AT-TPS (filled symbols for adsorption, empty symbols for desorption).

Table 2: H_2, CO_2, CH_4 and N_2 uptakes and heat of adsorption of AT-FL to AT-TPS.

Compound	H_2 (wt %)	CO_2 [a] (cm^3/g)	CO_2 [b] (cm^3/g)	Q^0_{ads} (CO_2) [c] (kJ/mol)	CH_4 [a] (cm^3/g)	CH_4 [b] (cm^3/g)	N_2 [a] (cm^3/g)
AT-FL	1.00	56.4	39.4	49	18.7	11.7	6.07
AT-TPB	1.3	76.7	52.5	33	24.2	14.9	6.7
AT-TPC	1.05	60.8	40.6	47	17.2	11	5.5
AT-TPE	1.16	66.7	45.3	43	20.9	13	6.4
AT-TPS	0.92	52.07	36.2	29	17.6	10.9	5.4

[a] Gas uptake at 273 K, 1 bar (750 mm Hg); [b] gas uptake at 293 K, 1 bar (760 mm Hg); [c] heat of adsorption for CO_2 at zero loading from adsorption isotherms acquired at 273 K and 293 K.

Table 3: Henry and IAST selectivity values for AT-FL to AT-TPS

Compound	CO_2:N_2 [a]	CO_2:N_2 [b]	CO_2:CH_4 [a]	CO_2:CH_4 [c]
	Selectivity			
AT-FL	21	19	5	5
AT-TPB	27	24	5	5
AT-TPC	26	29	5	5
AT-TPE	26	25	5	5
AT-TPS	25	23	5	6

[a] gas selectivity calculated at 273 K from the initial slopes in the Henry region; [b] IAST selectivity calculated at 273 K and 1 bar (In IAST model, the equilibrium partial pressure of 0.85 bar (N_2) and 0.15 bar (CO_2) in the bulk phase were consider); [c] selectivity calculated at 293 K from the initial slopes in the Henry region.

To identify the ideal CO_2 capture material, an absolute CO_2 uptake is not only the essential factor, but selectivity against other competing sorbates is also an important key. To test this hypothesis, we have used two different model to estimate the selectivity: (1) Henry's model:

The selectivity was estimated using the ratios of the Henry's law constant calculated from the initial slopes of the single-component gas adsorption isotherms at low pressure coverage (up to 0.1 bar); (2) ideal adsorbed solution theory (IAST): The selectivity, was predicted for CO_2 : N_2 (0.15 : 0.85) and CO_2 : CH_4 (0.05 : 0.95) mixtures, which has been used to predict binary gas mixture adsorption. As shown in the Table 3, the Henry selectivity of AT-FL to AT-TPS were in the range 21-27 (CO_2/N_2 at 273 K), 5 (CO_2/CH_4 at 273 K), 5-6 (CO_2/CH_4 at 293 K), whereas the IAST selectivity values were in the range of 19-29 (CO_2/N_2 at 273 K) (Fig. 9-10 and Table 3-4). These estimated selectivity values demonstrated that amine CTFs favoured the CO_2/N_2 selectivity with respect to CO_2/CH_4, and these selectivity values are highly comparable to reported CTFs materials. Moreover, the calculated IAST selectivities were almost similar than the values obtained from Henry's constant ratios (Table 3).

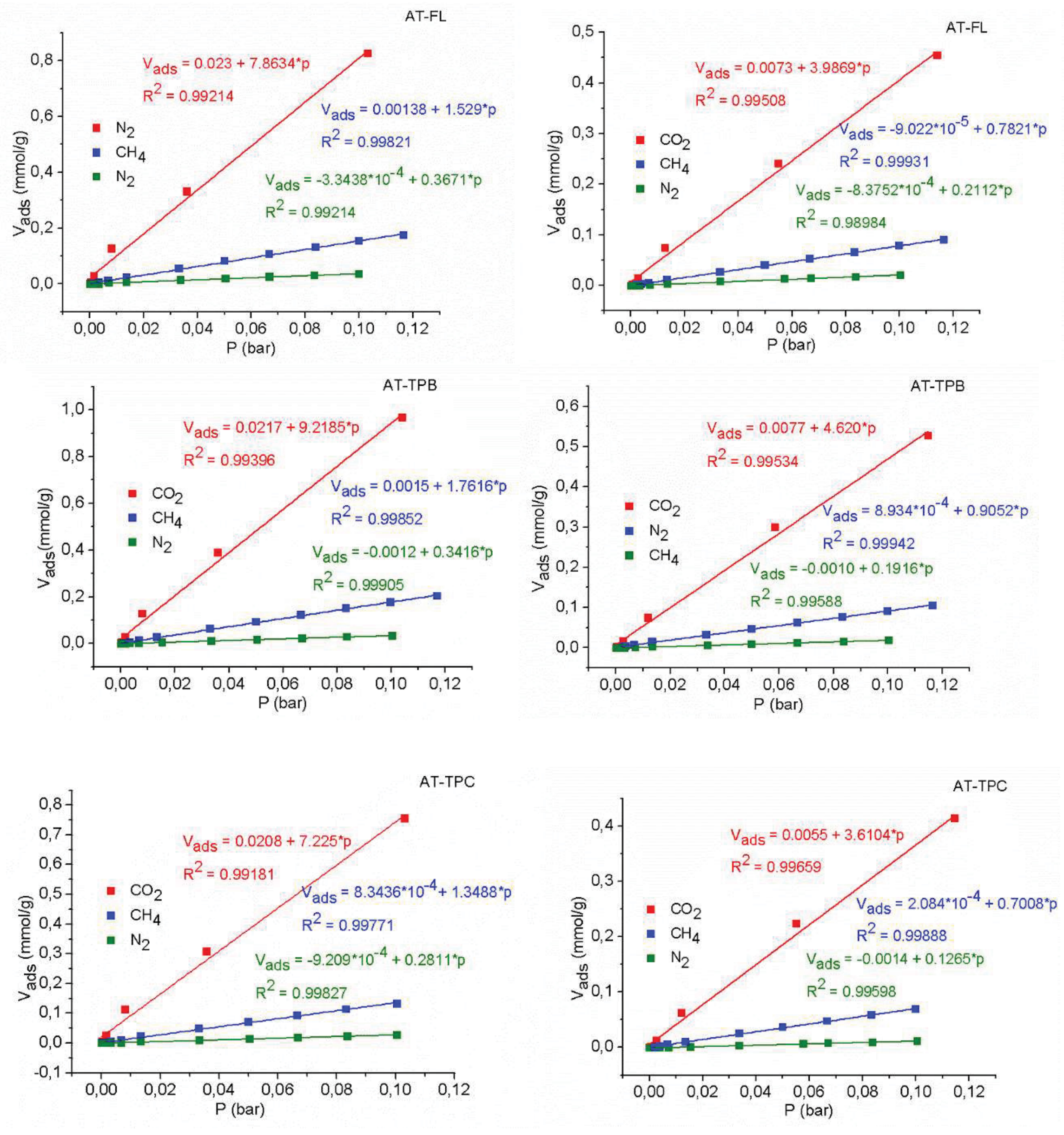

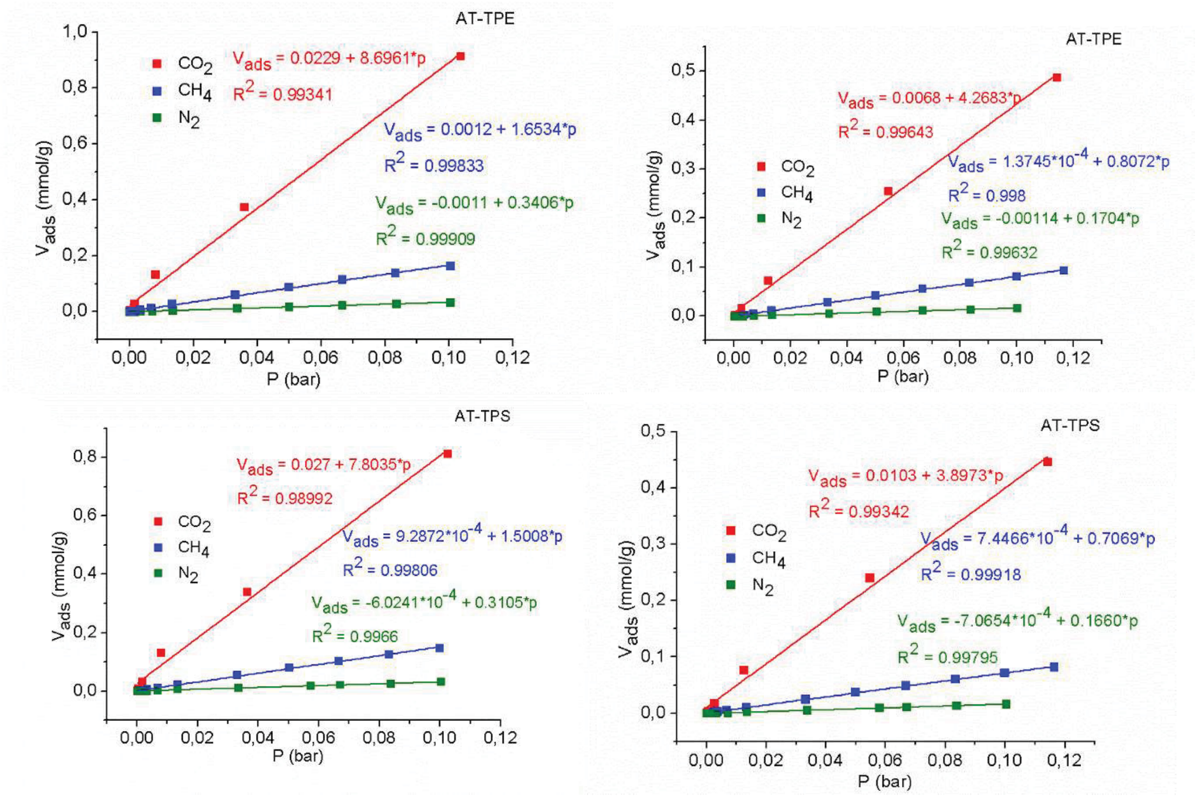

Fig. 9: The initial slopes in the Henry region of the adsorption isotherms for AT-FL to AT-TPS at 273 K (left) and 293 K (right).

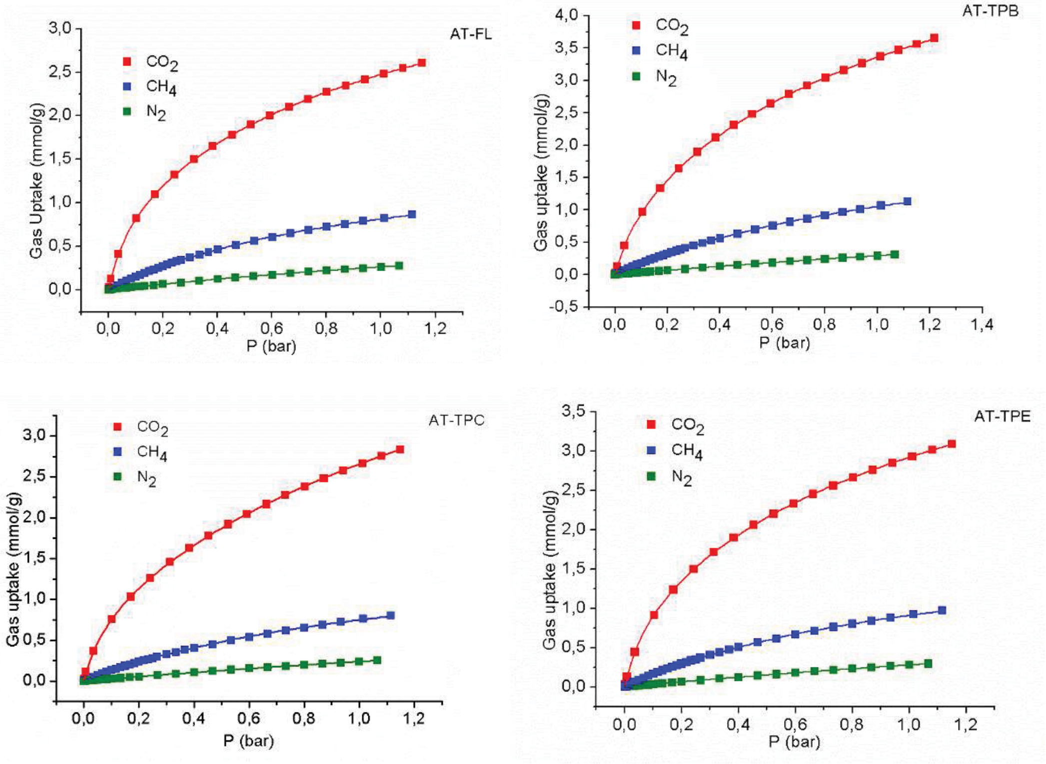

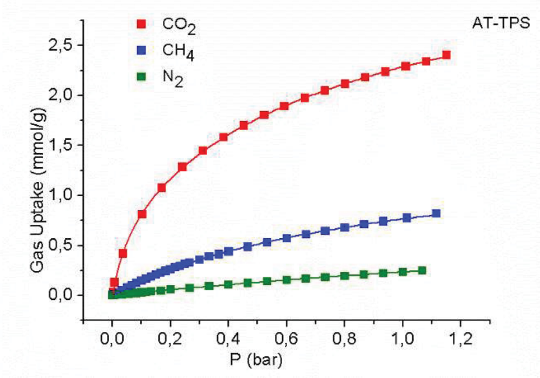

Fig. 10: DSL fitting for CO_2 adsorption and SSL fittings for CH_4 and N_2 adsorption at 273 K up to 1 bar for. AT-FL to AT-TPS.

Table 4: Langmuir fitting parameters of CO_2, CH_4, and N_2 adsorption for AT-FL to AT-TPS at 273 K and 1 bar.

AT-FL@273K	$q_{sat,A}$ (mmol/g)	b_A (bar^{-1})	$q_{sat,B}$ (mmol/g)	b_B (bar^{-1})	Adj. R^2
CO_2	0.96809	12.9955	3.4320	0.8479	0.99998
N_2	1.1011	0.31533	-		0.99987

AT-TBP@273K	$q_{sat,A}$ (mmol/g)	b_A (bar^{-1})	$q_{sat,B}$ (mmol/g)	b_B (bar^{-1})	Adj. R^2
CO_2	1.1559	9.99805	5.5041	0.7224	0.99999
N_2	2.0999	0.1611	-		0.99993

AT-TPC@273K	$q_{sat,A}$ (mmol/g)	b_A (bar^{-1})	$q_{sat,B}$ (mmol/g)	b_B (bar^{-1})	Adj. R^2
CO_2	0.8451	12.5428	5.1786	0.5661	0.99998
N_2	1.4565	0.1957			0.99991

AT-TPE@273K	$q_{sat,A}$ (mmol/g)	b_A (bar^{-1})	$q_{sat,B}$ (mmol/g)	b_B (bar^{-1})	Adj. R^2
CO_2	4.4050	0.7836	1.0695	11.8613	0.99998
N_2	1.6947	0.1967	-		0.99996

AT-TPS@273K	$q_{sat,A}$ (mmol/g)	b_A (bar^{-1})	$q_{sat,B}$ (mmol/g)	b_B (bar^{-1})	Adj. R^2
CO_2	2.7730	1.0717	0.91405	14.6925	0.99995
N_2	1.0716	0.2814	-		0.99981

Conclusions

We have demonstrated novel amine supported CTFs structures from fluorine, 1,3,5-triphenylbenzene, triptycene, tetraphenylethelene and tetraphenylsilane monomers by using $AlCl_3$ catalyzed Friedel-Crafts reaction. It has been found that the surface area, pore size and morphology of the resulting amine CTFs are diligently associated to the rigidity of building units. All CTFs displayed a permanent porosity and moderate surface areas in the range of 451-1174 m^2/g. Among all five frameworks, AT-TPB shows highest CO_2 adsorption of 76.7 cm^3/g (at 273 K and 1 bar) with good CO_2/N_2 selectivity (Henry: 27, IAST: 24).

References

---

1. A. H. Lu and S. Dai, *Porous Materials for Carbon Dioxide Capture*, Springer Berlin Heidelberg, 2014.

2. (a) Y. Liu, Z. U. Wang and H.-C. Zhou, *Greenhouse Gas Sci Technol.*, 2012, **2**, 239–259; (b) Y.-S. Bae and Randall Q. Snurr, *Angew. Chem. Int. Ed.*, 2011, **50**, 11586-11596; (c) K. Sumida, D. L. Rogow, J. A. Mason, T. M. McDonald, E. D. Bloch, Z. R. Herm, T.-H. Bae and J. R. Long, *Chem. Rev.*, 2012, **112**, 724–781.

3. Z. Xiang and D. Cao, *J. Mater. Chem. A*, 2013, **1**, 2691.

4. (a) Z. Chang, D.-S. Zhang, Q. Chen and X.-H. Bu, *Phys. Chem. Chem. Phys.*, 2013, **15**, 5430; (b) S.-Y. Ding and W. Wang, *Chem. Soc. Rev.*, 2013, **42**, 548– 568.

5. R. S. Haszeldine, *Science,* 2009, **325**, 1647.

6. H. He, W. Li, M. Zhong, D. Konkolewicz, D. Wu, K. Yaccato, T. Rappold, G. Sugar, N. E. David and K. Matyjaszewski, *Energy Environ. Sci.*, 2013, **6**, 488-493.

7. M. Z. Jacobson, *Energy Environ. Sci.*, 2009, **2**, 148–173; D. M. D'Alessandro, B. Smit and J. R. Long, *Angew. Chem. Int. Ed.*, 2010, **49**, 6058–6082.

8. L. Wang and R. T. Yang, *J. Phys. Chem. C*, 2012, **116**, 1099- 1106.

9. L. Y. Meng and S. J. Park, J. *Colloid Interface Sci.*, 2012, **386**, 285.

10. J. Zhang, P. A. Webley and P. Xiao, *Energy Convers. Manage.*, 2008, **49**, 346-356.

11. (a) G. Qi, Y. Wang, L. Estevez, X. Duan, N. Anako, A.-H. A. Park, W. Li, C. W. Jones and E. P. Giannelis, *Energy Environ. Sci.*, 2011, **4**, 444–452; (b) J. C. Hicks, J. H. Drese, D. J. Fauth, M. L. Gray, G. Qi and C. W. Jones, *J. Am. Chem. Soc.*, 2008, **130**, 2902–2903.

12. A. Khutia and C. Janiak, *Dalton Trans.*, 2014, **43**, 1338-1347.

13. V. Guillerm, L. J. Weselinski, M. Alkordi, M. I. H. Mohideen, Y. Belmabkhout, A. J. Cairns and M. Eddaoudi, *Chem. Commun.*, 2014, **50**, 1937-1940; (b) T. Islamoglu, M. Gulam Rabbani and H. M. El-Kaderi, *J. Mater.Chem. A*, 2013, **1**, 10259-10266.

14. R. Dawson, E. Stockel, J. R. Holst, D. J. Adams and A. I. Cooper, *Energy Environ. Sci.*, 2011, **4**, 4239.

15. S. Yang, J. Sun, A. J. Ramirez-Cuesta, S. K. Callear, W. I. F. David, D. P. Anderson, R. Newby, A. J. Blake, J. E. Parker, C. C. Tang and M. Schr¨oder, *Nat. Chem.*, 2012, **4**, 887.

16. R. Dawson, A. I. Cooper and D. J. Adams, *Polym. Int.*, 2013, **62**, 345.

17. H. Xu, J. Gao and D. Jiang, *Nat Chem.*, 2015, **7**, 905-912.

18. Y. Lin, C. Kong and Liang Chen, *RSC Adv.*, 2016, **6**, 32598-32614.

19. (a) P. Puthiaraj, S.-M. Cho, Y.-R. Lee and W.-S. Ahn, *J. Mater. Chem. A*, 2015, **3**, 6792; (b) P. Puthiaraj, S.-S. Kim and W.-S. Ahn, *Chem. Eng. J.*, 2016, **283**, 184-192.

20. W. E. Thompson, R. J. Warren, I. B. Eisdorfer and J. E. Zarembo, *Eur. J. Pharm. Sci.*, 1965, **54**, 1819-1821.

21. A. Bhunia, D. Esquivel, S. Dey, R. J. Fernandez-Teran, Y. Goto, S. Inagaki, P. Van Der Voort and C. Janiak, *J. Mater. Chem A*, 2016, **4**, 13450-13457.

22. S. Ren, M. J. Bojdys, R. Dawson, A. Laybourn, Y. Z. Khimyak, D. J. Adams and A. I. Cooper, *Adv. Mater.*, 2012, **24**, 2357– 2361.

23. S. Dey, A. Bhunia, M. D. Esquivel and C. Janiak, *J. Mater.Chem. A*, 2016, **4**, 6259-6263.

24. M. Thommes, K. Kaneko, A. V. Neimark, J. P. Olivier, F. Rodriguez-Reinoso, J. Rouquerol and K. S. W. Sing, *Pure Appl. Chem.*, 2015, **87**, 1051–1069.

25. F. Rodriguez-Reinoso and A. Linares-Solano, *in Chemistry and Physics of Carbon*, vol. **21** (P. A. Thrower, Ed.) Marcel Dekker, New York, 1988.

26. Quantachrome Instruments (1900 Corporate Drive, Boynton Beach, FL 33426 USA, www.quantachrome.com) Powder Tech Note 35.

27. A. Bhunia, I. Boldog, A. Möller and C. Janiak. *J. Mater. Chem. A*, 2013, **1**, 14990-14999.

28. S. Xiong, X. Fu, L. Xiang, G. Yu, J. Guan, Z. Wang, Y. Du, X. Xiong and C. Pan, *Polym. Chem.*, 2014, **5**, 3424–3431.

29. A. Bhunia, V. Vasylyeva and C. Janiak, *Chem. Commun.*, 2013, **49**, 3961–3963.

30. S. Hug, M. B. Mesch, H. Oh, N. Popp, M. Hirscher, J. Senker and B. V. Lotsch, *J.Mater. Chem. A*, 2014, **2**, 5928-5936.

31. S. Hug, L. Stegbauer, H. Oh, M. Hirscher and B. V. Lotsch, *Chem. Mater.*, 2015, **27**, 8001–8010.

32. Y. F. Zhao, K. X. Yao, B. Y. Teng, T. Zhang and Y. Han, *Energy Environ. Sci.*, 2013, **6**, 3684–3692.

33. X. Liu, H. Li, Y. Zhang, B. Xu, S. A, H. Xia and Y. Mu, *Polym. Chem.*, 2013, **4**, 2445-2448.

5 Experimental

5.1 General section

All chemicals were purchased from commercial suppliers (Sigma-Aldrich, Acros Organics, and Alfa Aesar chemical company) and used without further purification, unless stated otherwise. Dry dichloromethane (DCM) was collected from an MBraun solvent purification (drying) system under N_2 atmosphere and used for CTF synthesis ($AlCl_3$-catalyzed Friedel–Crafts reaction). Other solvents used for synthesis were obtained from chemical sources and were used as received without further purification. All reactions were carried out in aerobic conditions except ionothermal reactions (transferred $ZnCl_2$ into a pyrex ampule and evacuated, sealed under an inert atmosphere).

5.2 Analytical methods

5.2.1 Fourier transform infrared spectroscopy

Infrared (IR) spectra were obtained on a Bruker FT-IR Tensor 37 Spectrometer in the 4000-550 cm^{-1} region with 2 cm^{-1} resolution as KBr disks.

5.2.2 Powder X-ray diffraction

Powder X-ray diffraction (PXRD) data was collected on a Bruker D2 Phaser diffractometer using a flat sample holder (also a flat silicon, low background sample holder) and Cu Kα1/α2 radiation with $\lambda = 1.5418$ Å at 30 kV covering 2theta angles 5-80° over a time of 2 h, that is. 0.01°/sec. Diffractograms were obtained on flat layer sample holders where at low angle the beam spot is strongly broadened so that only a fraction of the reflected radiation reaches the detector, which leads to low relative intensities measured at $2\theta < 7°$.

5.2.3 Gas sorption analysis

Sorption isotherms were measured using a Nova 4000e from Quantachrome at 77 K and a Micromeritics ASAP 2020 automatic gas sorption analyzer equipped with oil-free vacuum pumps (ultimate vacuum < 10–8 mbar) and valves, which guaranteed contamination free measurements. The sample was connected to the preparation port of the sorption analyzer and degassed under vacuum until the outgassing rate, i.e., the rate of pressure rise in the temporarily closed manifold with the connected sample tube, was less than 2 S3 µTorr/min at the specified temperature 200 °C. After weighing, the sample tube was then transferred to the analysis port of the sorption analyzer. All used gases (H_2, He, N_2, CO_2, CH_4) were of ultra-high purity (UHP, grade 5.0, 99.999%) and the STP volumes are given according to the NIST standards (293.15 K, 101.325 kPa). Helium gas was used for the determination of the cold and warm free space of the sample tubes. H_2 and N_2 sorption isotherms were measured at 77 K (liquid nitrogen bath), whereas CO_2 and CH_4 sorption isotherms were measured at 293±1 K (passive thermostating) and 273.15 K (ice/deionized water bath). The heat of adsorption values and the DFT pore size distributions ('N2 DFT slit pore' model) were calculated out using the ASAP 2020 v3.05 software. Nitrogen sorption isotherms were also obtained on a Quantachrome Nova 4000e at 77 K.

5.2.4 Water sorption analysis

Water sorption isotherms at 20 °C were obtained volumetrically from a Quantachrome Autosorb iQ MP instrument equipped with an all-gas option. Prior to the sorption experiments, the compounds were degassed (130 °C, 2h) under dynamic vacuum.

5.2.5 Thermogravimetric analysis

Thermogravimetric analyses (TGA) were carried out at a ramp rate of 5 °C/min in a N_2 or O_2 flow with a Netzsch Thermo-Microbalance Aparatus TG 209 F3 Tarsus.

5.2.6 Scanning electron microscopy

Scanning electron microscopy (SEM) images were obtained using an ESEM Quanta 400 FEG SEM equipped with a secondary electron detector.

5.2.7 Elemental analysis

Elemental (CNH) analyses were carried out with a PerkinElmer 2400 series 2 elemental analyser.

5.2.8 Karl-Fischer titration

A coulometric Karl-Fischer titration (KFT) for the determination of the water content was carried out with a Karl-Fischer titration apparatus AQUA 40.00 with headspace module. The solid CTF sample was heated to 150 °C in the head space module and the liberated water transferred to the measurement cell.

5.3 Synthesis of materials

All the synthesis procedures during the course of study were place in the cumulative section (published work and unpublished work).

6 Overall summary

Design and synthesis of porous functional materials like metal organic frameworks (MOFs) and porous organic polymers (POPs) have gained tremendous interest among researchers and witnessed rapid growth over the last two decades. Due to their high surface areas and tuneable porosity, MOFs and POPs have been widely used for applications in gas storage and separation, catalysis, nanotechnology and as photofunctional materials. Covalent triazine frameworks (CTFs) are subclasses of POPs, which were first developed by Thomas *et al.* and coworkers via ionothermal synthesis. Cyclotrimerization of nitrile group leads to the formation of triazine framework in presence of $ZnCl_2$ which acts as a molten solvent, Lewis acid catalyst and porogen at high temperature (> 400 °C). CTFs can also be prepared using strong Brønsted acid (CF_3SO_3H) catalyst at room temperature, and under microwave assisted condition. Recently, anhydrous $AlCl_3$ catalysed Friedel-Craft reactions have also been used to synthesize CTFs materials.

CTFs have several advantages like cheap and readily available starting materials, easy synthesis, high thermal and chemical stability, conjugated planar structure and certain hydrophilicity which make them potential candidate for gas storage and separation, catalytic support for liquid phase reaction, as photocatalyst, for sensing application and electrode material in energy devices.

In this thesis, we have focused on the synthesis of new CTF materials following different synthetic procedures, and have explored the potential of these materials for liquid/gas/vapour adsorption and separation.

Section 3.1 describes synthesis of two-new CTFs namely, CTF-TPC and CTF-FL synthesized by Friedel-Craft alkylation reaction of cyanuric chloride with triptycene and fluorene linkers, respectively. The low temperature and one-step cost effective synthesis process was able to produce hydrolytically stable CTF materials with a thermal stability up to 400 °C. BET surface area of CTF-TPC and CTF-FL were measured to be 1668 m^2/g and 773 m^2/g, respectively. Low pressure gas adsorption measurements were carried out for CO_2, CH_4, H_2 and N_2 at different temperatures and the results were highly comparable to other reported triazine networks. At 273 K, CTF-TPC and CTF-FL exhibited CO_2 uptake of 4.24 mmol/g and 3.26 mmol/g which makes them promising candidate for CO_2 adsorbent. From IAST, the

CO_2/N_2 selectivity of CTF-TPC and CTF-FL were found to be 30 and 48, respectively.

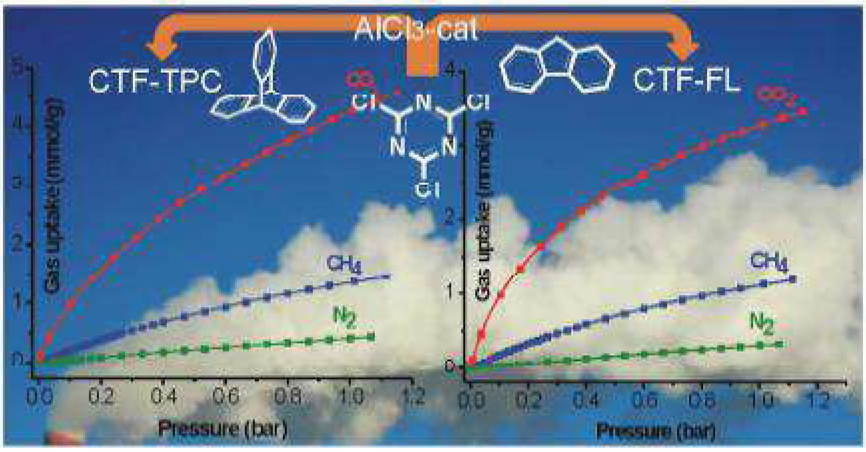

Another synthesis approach which has been adopted to fine tune the BET surface area and to enhance the CO_2 uptake capacity in CTFs is the $ZnCl_2$ mediated ionothermal synthesis using a mixed-linker (aromatic nitriles) strategy.

Section 3.2 presents four mixed-linker based CTFs synthesized by reacting tetrakis(4-cyanophenyl)ethylene (M) with terephthalonitrile (M1), tetrafluoroterephthalonitrile (M2), 4,4′-biphenyldicarbonitrile (M3) and 1,3,5-benzenetricarbonitrile (M4) at 400 °C for 48 h in the presence of $ZnCl_2$ catalyst to yield porous amorphous materials MM1, MM2, MM3 and MM4 respectively, with excellent thermal stability of > 400 °C, and an average particle size of 5-20 μm. The BET surface areas of MM1, MM2, MM3 and MM4 were 1800, 1360, 1884 and 1407 m^2/g, respectively. MM3 exhibited the highest surface area (1884 m^2/g) due to the presence of longer 4,4′-biphenyldicarbonitrile linker, while MM2 exhibited the lowest surface area (1360 m^2/g) due to the larger size of fluorine atoms as compared to the non-fluorinated analogue MM1 (1800 m^2/g). In order to explore the utility of the synthesized CTFs (MM1-MM4) as CCS materials, CO_2 sorption measurements were carried out at different temperatures (273 K and 298 K) and subsequently compared with their uptake capacity of other gases such as, CH_4, H_2 and N_2.

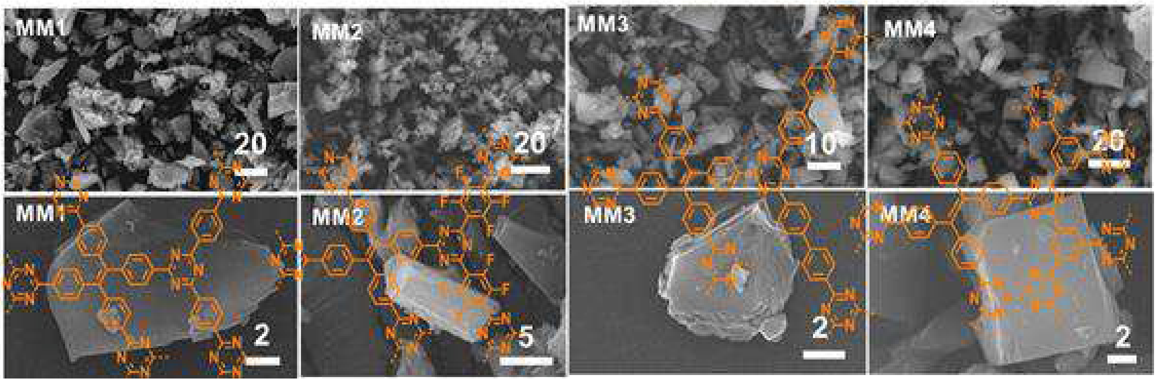

The CTFs MM1-MM4 exhibited CO_2 uptake in the range of 2.6-4.7 mmol/g. Highest CO_2 uptake of 4.7 mmol/g has been achieved with fluorinated CTF MM2 due to the possible electrostatic interactions between highly electronegative fluorine atoms and CO_2 molecules. Further, it has been observed that larger fluorine atoms in MM2 reduced the effective pore size of the material to < 0.5 nm, and thereby increasing the pore wall interaction and adsorption enthalpy of CO_2, as compared to the non-fluorinated CTFs MM1, MM3 and MM4. To evaluate the potentiality of the CTFs as CO_2 adsorbents from flue gas or natural gas, the selectivity of CO_2 over N_2 and CH_4 were calculated by using the Henry equation and the ideal adsorbed solution theory (IAST). The highest CO_2/N_2 selectivity was found for MM1 (Henry: 32, IAST: 130) at 273 K which is in close proximity of the high CO_2/N_2 selectivities of the reported CTFs. Water adsorption measurements have also been carried out with CTFs MM1-MM4, which demonstrated the hydrophobic nature of the materials displaying low water vapor uptake. Among these materials, MM2 exhibited higher water loading (0.035 g/g) at low relative pressure ($P/P_0 = 0.1$) compared to others which is possibly due to the hydrogen bonding interactions between water molecules and fluorine atoms of the triazine framework.

Similar mixed linker strategy (section 3.3) has also been applied to obtain several CTFs with an adamantane core and their gas sorption properties were studied. Nine CTF materials Ad2L1-Ad4L3 were synthesized by reacting 1,3-bis(4-cyanophenyl)adamantane (Ad2), 1,3,5-tries(4-cyanophenyl)adamantane (Ad3) and 1,3,5,7-tetrakis(4-cyanophenyl)adamantane (Ad4) with terepthalonitrile (L1), 4,4'- biphenyl dicarbonitrile (L2) and 1,3,5-benzenetricarbonitrile (L3) by ionothermal synthesis route ($ZnCl_2$, 400 °C, 48 h). The synthesized CTFs were found to be stable in the range of 460–530 °C and an average particle size of 6-20 μm. The BET surface areas calculated from the nitrogen sorption measurements at 77K were found in the range of 918–1885 m^2/g. The highest surface area of 1885 m^2/g was observed for Ad4L2 Gas adsorption studies were performed for different gasses (CO_2, CH_4 and N_2) at different temperature and selectivity studies were also carried out. The highest CO_2 uptake of 76.33 cm^3/g (at 273 K) was found for Ad4L1. The CH_4 uptake and N_2 uptake of Ad_2L_1–Ad_4L_3 at 273 K were found in the range of 14-26 cm^3/g and 5-9 cm^3/g, respectively.

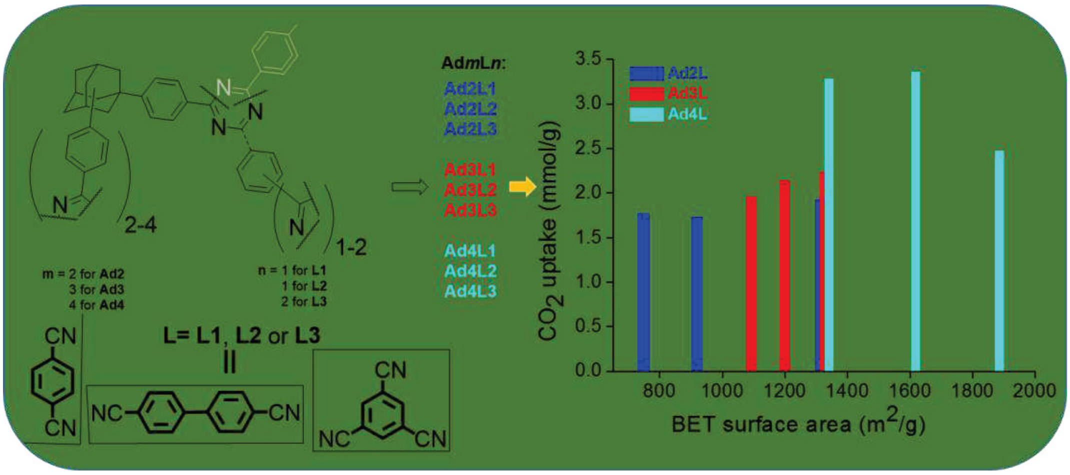

At 273 K, the Henry selectivities of CO_2/N_2 and CO_2/CH_4 were in the range of 13-20 and 4-5, respectively. Water adsorption studies were also performed for these CTFs. All these CTFs (Ad2L1-Ad4L3) were found to be hydrophobic in nature with a water uptake of 0.16-0.7 g/g at P/P_0 =0.9 at 20 °C which is due to capillary condensation in the available pore volume.

CTF-1 has also been used for surfactant adsorption for the first time (section 3.4). Two surfactants such as alkyl polyglycolether ($C_{12}EO_7$) and sodium dodecylsulfate (SDS) were tested. CTF-1(600) adsorbed 1.9 g/g and 4.9 g/g SDS and $C_{12}EO_7$, respectively which is much higher than carbon black (0.1 g/g and 0.2 g/g SDS and $C_{12}EO_7$, respectively) and it is due to CTF sheet exfoliation. Moreover, for the non-ionic $C_{12}EO_7$ surfactant the adsorbed amounts by weight (g/g) is higher because of the higher molecular mass of the non-ionic surfactant compared to the anionic surfactant.

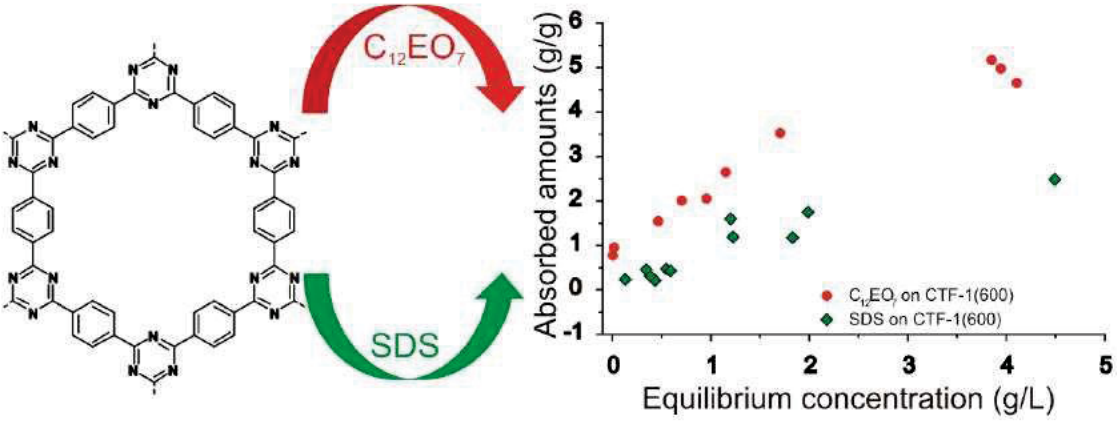

In collaboration with Prof. Dr. Holdt at the University Of Postdam, the gas adsorption measurements were carried out for two imidazole-based MOFs, Zn-MOF (IFP-9) and Co-MOF (IFP-10) (section 3.5). The BET surface areas of IFP-9 and IFP-10 were found to be 7 and 13 m^2/g, respectively. At 273 K, the IFP-9 exhibited CO_2 uptake of 5 cm^3/g, whereas IFP-10 exhibited CO_2 uptake of 39 cm^3/g with hysteresis in both the sorption isotherms, attributed to the flexible nature of the MOFs. At 273 K, CH_4 uptake values were 2.5 and 6 cm^3/g at 77 K, and H_2 uptake values were found to be 8.8 and 5.2 cm^3/g for IFP-9 and IFP-10, respectively.

In collaboration with Dr. H. P. Nayek at Indian School of Mines (ISM) Dhanbad, gas adsorptions studied were carried out for a La-MOF (section 3.6). BET surface area of La-MOF was found to be 1074 m^2/g with no hysteresis observed in the isotherm (Type-I) which indicated the stable and rigid nature of the framework. At 273 K, the CO_2 and CH_4 uptake values were 76.8 cm^3/g and 19.7 cm^3/g respectively. At 77 K, the H_2 uptake was found to be 158.4 cm^3/g.

In collaboration with Prof. Dr. van der Voort at the University of Ghent, the gas adsorption performances were executed for a homochiral vanadium-salen based Cd-MOF (section 3.7). The BET surface area of the framework was 574 m^2/g. The isotherm shows a steep slope at low P/P_0 values with a type-I isotherm, which is typical for microporous materials. Low pressure gas adsorption measurements were performed for CO_2, CH_4, and H_2 at different temperatures. The CO_2 adsorption capacities of the material were 51 cm^3/g and 32 cm^3/g at 273 K and 298 K, respectively. At 273 K, the CH_4 uptake was only 17 cm^3/g; and at 77 K the H_2 uptake was found to be 120 cm^3/g (1.05 wt%). The CO_2 and H_2 uptake values were highly comparable or even higher than the other reported chiral MOFs materials.

The low pressure gas adsorption of PCTF-8 (cooperation with Dr. Bhunia) were performed (section 3.8). The Brunauer–Emmett–Teller (BET) specific surface area of PCTF-8 is 625 m^2/g which is lower than the one obtained from synthesis under Lewis acid conditions ($ZnCl_2$). At 1 bar and 273 K, the PCTF-8 adsorbs significant amount of CO_2 (56 cm^3/g) and CH_4 (17 cm^3/g) which is highly comparable to nanoporous 1,3,5-triazine frameworks (NOP-1-6, 29-56 cm^3/g).

A microporous three-dimensional hydrogen-bonded metal organic framework HIF-3, ($[Cd_{14}(L)_{12}(O)(OH)_2(H_2O)_6(DMF)_2]$, where L = imidazolate-4,5-diamide-2-olate) showed good N_2, CO_2 and H_2 gas sorption in comparison with other porous H-bonded frameworks (in collaboration with Prof. Dr. Holdt at the University Of Postdam, section 3.9). The BET surface areas of HIF-3-CE and HIF-3-MW were found to be 127 and 43 m^2/g, respectively. The CO_2 adsorption capacities in activated HIF-3-CE and HIF-3-MW are 18 and 14 cm^3/g, respectively at 273 K, 1 bar. Moreover, HIF-3-CE and -MW adsorb 15 and 9 cm^3/g of H_2, respectively at 77 K and 1 bar.

In section 4.1, a CTF material (CTF-1) synthesized from 1,4-dicyanobenzene by ionothermal method has been studied for membrane based gas separation. Mixed matrix membranes (MMMs) were fabricated from polysulfone polymer with different wt% of CTF-1 loading. The resulted MMMs were extensively studied for single gases permeation and separation including O_2, N_2, CO_2 and CH_4. Highest CO_2/N_2 selectivity of 28.6 was found for the membrane with 8 wt% of CTF-1 loading whereas for pure polysulfone membrane the CO_2/N_2 selectivity value was 23.04. No significant changes were observed for the selectivities of O_2/N_2 and CO_2/CH_4 for single gas permeation. For mixed gas separation CO_2/CH_4 permeation also tested and the selectivity values increased from 31 (for pure polysulfone membrane) to 42.3 (for 16 wt% of CTF-1 loading).

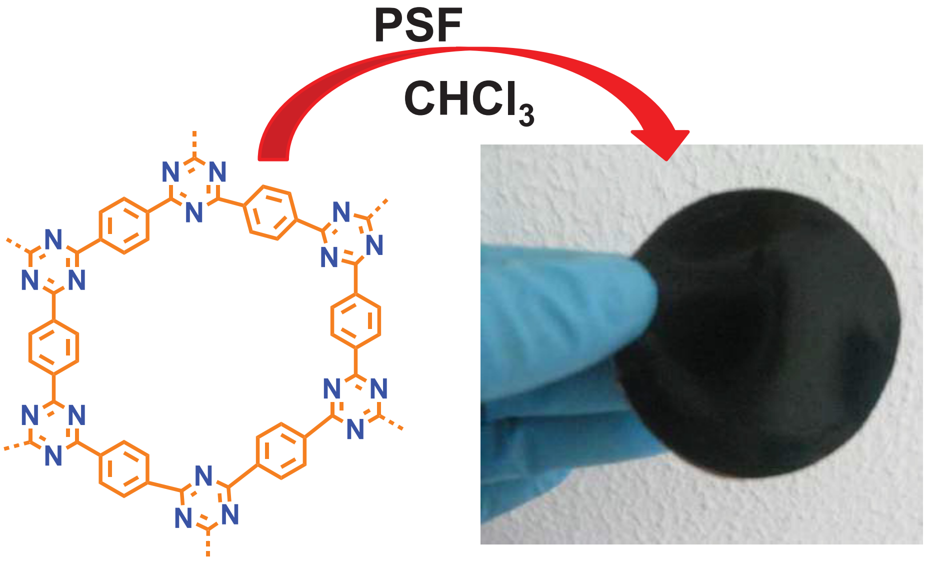

In section 4.2, Friedel-Craft alkylation reaction of 2-Amino-4,6-dichloro-1,3,5 triazine with some aromatic molecules were accomplished under mild conditions to isolate the amine-functionalized CTFs. Five porous CTFs namely AT-FL, AT-TPC, AT-TPB, AT-TPE, AT-TPS were synthesized using fluorene (FL), 1,3,5-triphenylbenzene (TPB), triptycene (TPC), tetraphenylethelene (TPE) and tetraphenyl silane (TPS) as aromatic building units. The synthesized CTFs were tested for CO_2, N_2, H_2 and CH_4 adsorptions. The BET surface areas of AT-TPC was found to be 1174 m^2/g and are in the order AT-TPC> AT-TBP>AT-TPE>AT-FL>AT-TPS. On the other hand, AT-TBP showed the highest CO_2 uptake (76.7 cm^3/g; 273 K and 1 bar) with respect to AT-TPE (66.7 cm^3/g), AT-TPC (60.8 cm^3/g), AT-FL (56.4 cm^3/g), AT-TPS (52 cm^3/g).

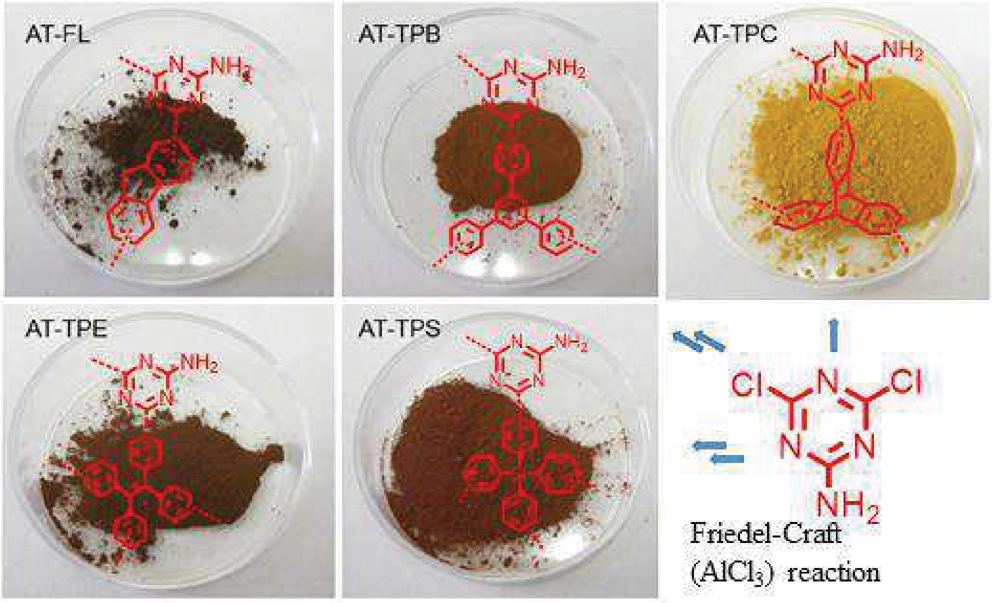
AT-FL
AT-TPB
AT-TPC
AT-TPE
AT-TPS
NH2
N
Cl
Friedel-Craft
(AlCl3) reaction

References

1.(a) S. M. Auerbach, K. A. Carrado and P. K. Dutta, *Handbook of Zeolite Science and Technology*, Marcel Dekker, Inc., New York, 2003; (b) R. Xu, W. Pang, J. Yu, Q. Huo and J. Chen, *Chemistry of Zeolites and Related Porous Materials Synthesis and Structure*, Wiley, Singapore, 2007; (c) D. W. Beck, *Zeolite Molecular Sieves*, John Wiley & Sons, New York, 1974.

2. (a) G. Férey, *Chem. Soc. Rev.*, 2008, **37**, 191-214; (b) K. Sumida, D. L. Rogow, J. A. Mason, T. M. McDonald, E. D. Bloch, Z. R. Herm, T.-H. Bae and J. R. Long, *Chem. Rev.*, 2012, **112**, 724-781; (c) F. Jeremias, D. Fröhlich, C. Janiak and S. K. Henninger, *New J. Chem.* 2014, **38**, 1846–1852; (d) J. R. Long and O. M. Yaghi, *Chem. Soc. Rev.*, 2009, **38**, 1213–1214. Editorial to the 2009 Metal–organic framework issue. (e) H.-C. Zhou and S. Kitagawa, *Chem. Soc. Rev.*, 2014, **43**, 5415-5418, Editorial to the 2014 Metal–organic framework issue.

3. (a) A. P. Coˆte´, A. I. Benin, N. W. Ockwig, M. O'Keeffe, A. J. Matzger and O. M. Yaghi, *Science*, 2005, 310, 1166–117; (b) J. R. Hunt, C. J. Doonan, J. D. LeVangie, A. P. Cote and O. M. Yaghi, *J. Am. Chem. Soc.*, 2008, 11872–11873; (c) A. P. Cote, H. M. El-Kaderi, H. Furukawa, J. R. Hunt and O. M. Yaghi, *J. Am. Chem. Soc.*, 2007, **129**, 12914–12915; (c) P. J. Waller, F. Gándara and O. M. Yaghi, *Acc. Chem. Res.*, 2015, **48**, 3053-3063.

4. (a) S.-Y. Ding and W. Wang, *Chem. Soc. Rev.*, 2013, **42**, 548-568; (b) Y. Xu, S. Jin, H. Xu, A. Nagai and D. Jiang, *Chem. Soc. Rev.*, 2013, **42**, 8012–8031; (c) N. B. Mckeown and P. M. Budd, *Chem. Soc. Rev.*, 2006, **35**, 675–683; (d) R. Dawson, A. I. Cooper and D. J. Adams, *Prog. Polym. Sci.*, 2012, **37**, 530–563; (e) A. I. Cooper, *CrystEngComm*, 2013, **15**, 1483-1483.

5 (a) L. B. McCusker, F. Liebau, G. Engelhardt, *Pure Appl. Chem.*, 2001, **73**, 381–394; (b) A. H. Ahmed, *Rev. Inorg. Chem.*, 2014, **34**, 135-175; (c) I. Petrov and T. Michalev, *НАУЧНИ ТРУДОВЕ НА РУСЕНСКИЯ УНИВЕРСИТЕТ*, 2012, том 51, серия 9.1, (c) J. Li, A. Corma, and J. Yu, *Chem. Soc. Rev.*, 2015, **44**, 7112; (d) O. Cheunga and N. Hedin, *RSC Adv.*, 2014, **4**, 14480-14494.

---

6. B. P. Biswal, S. Kandambeth, S. Chandra, D. B. Shinde, S. Bera, S. Karak, B. Garai, U. K. Kharulc and R. Banerjee, *J. Mater. Chem. A*, 2015, **3**, 23664-23669.

7. G. Das, D. B. Shinde, S. Kandambeth, B. P. Biswala and R. Banerjee, *Chem. Commun.*, 2014, **50**, 12615-12618.

8. C. R. DeBlase, K. E. Silberstein, T.-T. Truong, H. D. Abruña, and W. R. Dichtel, *J. Am. Chem. Soc.*, 2013, **135**, 16821–16824.

9. S. Dalapati, S. Jin, J. Gao, Y. Xu, A. Nagai, and D. Jiang, *J. Am. Chem. Soc.*, 2013, **135**, 17310–17313.

10. Q. Fang, Z. Zhuang, S. Gu, R. B. Kaspar, J. Zheng, J. Wang, S. Qiu and Y. Yan, *Nat. Commun.* 2014, **5**, 4503.

11. J. L. Segura, M. J. Mancheño and F. Zamora, *Chem. Soc. Rev.*, 2016, DOI: 10.1039/c5cs00878f.

12. (a) C. D. Wood, B. Tan, A. Trewin, H. Niu, D. Bradshaw, M. J. Rosseinsky, Y. Z. Khimyak, N. L. Campbell, R. Kirk, E. Stoeckel and A. I. Cooper, *Chem. Mater.*, 2007, **19**, 2034–2048; (b) M. P. Tsyurupa and V. A. Davankov, *React. Funct. Polym.*, 2006, **66**, 768–779; (c) J. Germain, J. Hradil, J. M. J. Fr´echet and F. Svec, *Chem. Mater.*, 2006, **18**, 4430–4435.

13. (a) T. Ben, H. Ren, S. Ma, D. Cao, J. Lan, X. Jing, W. Wang, J. Xu, F. Deng, J. M. Simmons, S. Qiu and G. Zhu, *Angew. Chem. Int. Ed.*, 2009, **48**, 9457-9460; (b) H. Zhao, Z. Jin, H. Su, J. Zhang, X. Yao, H. Zhao and G. Zhu, *Chem. Commun.*, 2013, **49**, 2780-2782; (c) A. Trewin and A. I. Cooper, *Angew. Chem., Int. Ed.*, 2010, **49**, 1533–1535.

14. (a) A. I. Cooper, *Adv. Mater.*, 2009, **21**, 1291–1295; (b) J.-X. Jiang, F. Su, A. Trewin, C. D. Wood, N. L. Campbell, H. Niu, C. Dickinson, A. Y. Ganin, M. J. Rosseinsky, Y. Z. Khimyak and A. I. Cooper, *Angew. Chem. Int. Ed.*, 2007, **46**, 8574-8578; (c) J. Weber and A. Thomas, *J. Am. Chem. Soc.*, 2008, **130**, 6334–6335.

15. (a) W. G. Lu, D. Q. Yuan, D. Zhao, C. I. Schilling, O. Plietzsch, T. Muller, S. Brase, J. Guenther, J. Blumel, R. Krishna, Z. Li and H. C. Zhou, *Chem. Mater.*, 2010, **22**, 5964–5972; (b) D. Q. Yuan, W. G. Lu, D. Zhao and H. C. Zhou, *Adv. Mater.*, 2011, **23**, 3723–3725; (c) W. Lu, D. Yuan, J. Sculley, D. Zhao, R. Krishna and H.-C. Zhou, *J. Am. Chem. Soc.*, 2011, **133**, 18126–18129; (d) W. Lu, J. P. Sculley, D. Yuan, R. Krishna, Z. Wei and H.-C. Zhou, *Angew. Chem., Int. Ed.*, 2012, **51**, 7480–7484.

---

16. (a) B. S. Ghanem, K. J. Msayib, N. B. McKeown, K. D. M. Harris, Z. Pan, P. M. Budd, A. Butler, J. Selbie, D. Book and A. Walton, *Chem. Commun.*, 2007, 67-69; (b) N. B. McKeown and P. M. Budd, *Chem. Soc. Rev.*, 2006, **35**, 675–683.

17. P. Kuhn, M. Antonietti and A. Thomas, *Angew. Chem., Int. Ed.*, 2008, **47**, 3450–3453.

18. P. Kuhn, A. l. Forget, D. Su, A. Thomas and M. Antonietti, *J. Am. Chem. Soc.*, 2008, **130**, 13333–13337.

19. M. J. Bojdys, J. Jeromenok, A. Thomas and M. Antonietti, *Adv. Mater.*, 2010, **22**, 2202-2205.

20. K. Sakaushi and M. Antonietti, *Acc. Chem. Res.*, 2015, **48**, 1591−1600.

21. S. Ren, M. J. Bojdys, R. Dawson, A. Laybourn, Y. Z. Khimyak, D. J. Adams and A. I. Cooper, *Adv. Mater.*, 2012, **24**, 2357–2361.

22 H. Ren, T. Ben, E. Wang, X. Jing, M. Xue, B. Liu, Y. Cui, S. Qiua and G. Zhu, *Chem. Commun.*, 2010, **46**, 291–293.

23. H. Lim, M. C. Cha and J. Y. Chang, *Macromole. Chem. Phys.* 2012, **213,** 1385-1390.

24. P. Puthiaraj, S.-M. Cho, Y.-R. Lee and W.-S. Ahn, *J. Mater. Chem. A,* 2015, **3**, 6792-6797.

25. C. Reece, D. J. Willock and A. Trewin, *Phys. Chem. Chem. Phys.*, 2015, **17**, 817-823.

26. Y. Liu, Z. U. Wang and H.-C. Zhou, *Greenhouse Gas Sci. Technol.*, 2012, **2**, 239–259.

27. Y. Zeng, R. Zou, Y. Zhao, *Adv. Mater.*, 2016, **28**, 2855–2873.

28. J. Wang, L. Huang, R. Yang, Z. Zhang, J. Wu, Y. Gao, Q. Wang, D. O'Hareb, Z. Zhong, *Energy Environ. Sci.*, 2014, **7**, 3478-3518.

29. Y. Zhao, K. X. Yao, B. Teng, T. Zhang and Y. Han, *Energy Environ. Sci.*, 2013, **6**, 3684-3692.

30. S. Xiong, X. Fu, L. Xiang, G. Yu, J. Guan, Z. Wang, Y. Du, X. Xiong and C. Pan, *Polym. Chem.*, 2014, **5**, 3424-3431.

31. S. Hug, M. B. Mesch, H. Oh, N. Popp, M. Hirscher, J. Senkerd, B. V. Lotsch, *J. Mater. Chem. A*, 2014, **2**, 5928-5936.

32 S. Hug, L. Stegbauer, H. Oh, M. Hirscher and B. V. Lotsch, *Chem. Mater.*, 2015, **27**, 8001−8010.

33. A. Bhunia, V. Vasylyeva and C. Janiak, *Chem. Commun.*, 2013, **49**, 3961–3963

34. (a) A. Bhunia, I. Boldog, A. Möller and C. Janiak, *J. Mater. Chem. A*, 2013, **1**, 14990–14999; (b) A. Bhunia, D. Esquivel, S. Dey, R. J. Fernández-Terán, Y. Goto, S. Inagaki, P. Van Der Voort and C. Janiak, *J. Mater. Chem A*, 2016, DOI: 10.1039/c6ta04623a.

---

35. P. Katekomol, J. Roeser, M. Bojdys, J. Weber, and A. Thomas, *Chem. Mater.*, 2013, **25**, 1542–1548.

36. H. A. Patel, F. Karadas,b A. Canlier, J. Park, E. Deniz, Y. Jung, M. Atilhan and C. T. Yavuz, *J. Mater. Chem.*, 2012, **22**, 8431-8437.

37. P. Puthiaraj, S.-S. Kim, and W-S. Ahn, *Chem. Eng. J.,* 2016, **283**, 184–192.

38 K. Wang, H. Huang, D. Liu, C. Wang, J. Li and C. Zhong, *Environ. Sci. Technol.*, 2016, **50**, 4869–4876.

39. X. Liu, He Li, Y. Zhang, B. Xu, S. A, H. Xi and Y. Mu, *Polym. Chem.*, 2013, **4**, 2445.

40. H. Furukawa and O. M. Yaghi, *J. Am. Chem. Soc.*, 2009, **131**, 8875–8883.

41. Y. He, W. Zhou, G. Qiand and B. Chen, *Chem. Soc. Rev.*, 2014, **43**, 5657-5678.

42. D. Zhao, D. Yuana and H-C. Zhou, *Energy Environ. Sci.*, 2008, **1**, 222-235.

43. L. Zhou, *Renewable Sustainable Energy Rev.*, 2005, **9**, 395–408.

44 Florida solar energy center: http://www.fsec.ucf.edu/en/consumer/hydrogen/basics/storage.htm

45. W. Zhang, C. Li, Y-P. Yuan, L-G. Qiu, A-J. Xie, Y-H. Shena and J-F. Zhu, *J. Mater. Chem.*, 2010, **20**, 6413-6415.

46. A. H. Chughtai, N. Ahmad, H. A. Younus, A. Laypkovc and F. Verpoort, *Chem. Soc. Rev.*, 2015, **44**, 6804.

47. R. Palkovits, M. Antonietti, P. Kuhn, A. Thomas and F. Schüth, *Angew. Chem. Int. Ed.*, 2009, **48**, 6909–6912.

48. C. E. Chan-Thaw, A. Villa, P. Katekomol, D. Su, A. Thomas and L. Prati*, Nano Lett.*, 2010, **10**, 537–541.

49. F. Chang, J. Guo, G. Wu, L. Liu, M. Zhang, T. He, P. Wang, P. Yu and P. Chen, *RSC Adv.*, 2015, **5**, 3605-3610.

50. J. Artz, S. Mallmann and R. Palkovits, *ChemSusChem*, 2015, **8**, 672–679.

51. A. V. Bavykina, M. G. Goesten, F. Kapteijn, M. Makkee and J. Gascon, *ChemSusChem*, 2015, **8**, 809–812.

52. K. Schwinghammer, S. Hug, M. B. Mesch, J. Senkerd, B. V. Lotsch, *Energy Environ. Sci.*, 2015, **8**, 3345-3353.

53 (a) K. Schwinghammer, B. Tuffy, M. B. Mesch, E. Wirnhier, C. Martineau, F. Taulelle,W. Schnick, J. Senker and B. V. Lotsch, *Angew. Chem., Int. Ed.*, 2013, **52**, 2435; (b) X. Wang, K.

Maeda, A. Thomas, K. Takanabe, G. Xin, J. M. Carlsson, K. Domen and M. Antonietti, *Nat. Mater.*, 2009, **8**, 76; (c) K. Schwinghammer, M. B. Mesch, V. Duppel, C. Ziegler, J. Senker and B. V. Lotsch, *J. Am. Chem. Soc.*, 2014, **136**, 1730; (d) M. K. Bhunia, K. Yamauchi and K. Takanabe, *Angew. Chem., Int. Ed.*, 2014, **53**, 11011; (e) X. Wang, K. Maeda, X. Chen, K. Takanabe, K. Domen, Y. Hou, X. Fu and M. Antonietti, *J. Am. Chem. Soc.*, 2009, *131*, 1680; (f) J. Liu, Y. Liu, N. Liu, Y. Han, X. Zhang, H. Huang, Y. Lifshitz, S.-T. Lee, J. Zhong and Z. Kang, *Science*, 2015, **347**, 970.

54. J. Bi , W. Fang , L. Li , J. Wang , S. Liang , Y. He , M. Liu , L. Wu, *Macromol. Rapid Commun.*, 2015, **36**, 1799−1805.

55. L. Chen, Y. Honsho, S. Seki and D. Jiang, *J. Am. Chem. Soc.*, 2010, **132**, 6742–6748.

56 A. Patra, J-M. Koenen and U. Scherf, *Chem. Commun.*, 2011, **47**, 9612–9614.

57 X. Liu, Y. Xu and D. Jiang, *J. Am. Chem. Soc.*, 2012, **134**, 8738−8741.

58 A. Patra and U. Scherf, *Chem. Eur. J.*, 2012, **18**, 10074–10080.

59. X. Wang, C. Zhang, Y. Zhao, S. Ren and J-X. Jiang, *Macromol. Rapid Commun.*, 2016, **37**, 323−329.

60. H. Strathmann, *Introduction to Membrane Science and Technology*, Wiley-VCH, 2011. Ch. 4.3.

61. Prof. C. Staudt Website in University Düsseldorf**:** http://www.chemie.uni-duesseldorf. de /Faecher/ Organische Chemie/OC2/ staudt/forschung/Membrantrennverfahren

62. (a) B. V. Bruggen, C. Vandecasteele, T. V. Gestel, W. Doyenb and R. Leysenb, *Envioronmental Progress*, 2003, **22**, 46; (b) V. Abetz, T. Brinkmann, M. Dijkstra, K. Ebert, D. Fritsch, K. Ohlrogge, D. Paul, K. V. Peinemann, S. Pereira-Nunes, N. Scharnagl, and M. Schossig, *Adv. Eng. Mater.,* 2006, **8**, 328.

63. E. D. Korn, *Science*, 1966, **153**, 1491.

64. W. Stoechenius and D. M. Engelman, *J. Cell Bioi.*, 1969, **42**, 613.

65. T.-S. Chung, L.Y. Jiang, Y. Li and S. Kulprathipanja, *Prog. Polym. Sci.*, 2007, **32**, 483.

66. A. Mersmann and B. Fill, R. Hartmann, S. Maurer, *Chem. Eng. Technol.*, 2000, **23**, 937.

67. D. Aaron and C. Tsouris, *Sep. Sci. Technol.*, 2005, **40**, 321.

68. W. J. Koros and G.K. Fleming, *J. Membr. Sci.*, 1993, **83**, 1.

69. L. M. Robeson, *J. Membr. Sci.*, 1991, **62**, 165.

---

70. L. M. Robeson, *J. Membr. Sci*., 2008, **320**, 390.

71. T. T. Moore and W. J. Koros, *J. Mol. Struct.*, 2005, **739**, 87.

72. R. Mahajan and W. J. Koros, *Polym. Eng. Sci.*, 2002, **42**, 1420

73. Y. Li, T.S. Chung, C. Cao and S. Kulprathipanja, *J. Membr. Sci.*,2005, **260**, 45.

74. Y. Y. Liu, Z. F. Ng, E. A. Khan, H. K. Jeong, C. B. Ching and Z. P.Lai, *Micropor. Mesopor. Mater.*, 2009, **118**, 296.

75. Y. Yoo, Z. Lai and H.-K.Jeong, *Micropor. Mesopor.Mater.*, 2009, **123**, 100.

76. H. L. Guo, G. S. Zhu, I. J. Hewitt and S. L. Qiu, *J. Am. Chem. Soc.*,2009, **131**, 1646.

77. R. Ranjan and M. Tsapatsis, *Chem. Mater.*, 2009, **21**, 4920.

78. R. D. Noble, *J. Membr. Sci*., 2011, **378**, 393.

79. D. Liu and C. Zhong, *J. Mater. Chem.*, 2010, **20**, 10308.

80. S. T. Meek, J. A. Greathouse and M. D. Allendorf, *Adv. Mater.*, 2011, **23**, 249.

81. T.-H. Bae, J. S. Lee, W. Qju, W. J. Koros, C. W. Jones and S. Nair, *Angew. Chem. Int. Ed.*, 2010, **49**, 9863.

82. X. Zhu, C. Tian, S. M. Mahurin, S-H. Chai, C. Wang, S. Brown, G. M. Veith, H. Luo‖, H. Liu and S. Dai, *J. Am. Chem. Soc.*, 2012, **134**, 10478–10484.

83. Y. P. Tang, H. Wang and T. S. Chung, *ChemSusChem*, 2015, **8**, 138–147.

84. Y. Wang, J. Li, Q. Yang and C. Zhong, *ACS Appl. Mater. Interfaces*, 2016, **8**, 8694–8701.

85. http://webspectra.chem.ucla.edu//irintro.html

86. http://chemistry.oregonstate.edu/courses/ch361-464/ch362/irinterp.htm

87. M. Reichenbächer and J. Popp, *Challenges in Molecular Structure Determination*, , Springer-Verlag Berlin Heidelberg 2012, DOI 10.1007/978-3-642-24390-5_2.

88 A. Bhunia, S. Dey, M. Bous, C. Zhang, W. von Rybinski, and C. Janiak, *Chem. Commun.*, 2015, **51**, 484-486.

89. https://www.sigmaaldrich.com/content/dam/sigma-aldrich/docs/Supelco/Posters/1/understanding-kf-090810.pdf

90. http://www.sigmaaldrich.com/technical-documents/articles/analytix/coulometric-water.html

91. http://www-f9.ijs.si/~krizan/sola/sempod/0607/rangus-seminar.pdf

92. S. Nandi, U. Werner-Zwanziger and R. Vaidhyanathan, *J. Mater. Chem. A*, 2015, **3**, 21116-21122.

---

93. G. Leofanti, M. Padovan, G. Tozzola and B. Venturelli, *Catalysis Today*, 1998, **41**, 207-219.

94. F. Rouquerol, J. Rouquerol and K. S. W. Sing, *Adsorption by Powders and Porous Solids*, Academic Press, 1999, 1-25.

95. (a) K. S. W. Sing, D. H. Everett, R. A. W. Haul, L. Moscou, R. A. Pierotti, J. Rouquerol and T. Siemieniewska, *Pure Appl. Chem.*, 1985. **57**, 603-619, (b) M. Thommes, K. Kaneko, A. V. Neimark, J. P. Olivier, F. Rodriguez-Reinoso, J. Rouquerol and K. S. W. Sing, *Pure Appl. Chem.*, 2015, **87**, 1051–1069.

96. C. X. Bezuidenhout, V. J. Smith, P. M. Bhatt, C. Esterhuysen and L. J. Barbour, *Angew. Chem. Int. Ed.*, 2015, **54**, 1-6.

97. A. Khutia, H. U. Rammelberg, T. Schmidt, S. Henninger and C. Janiak, *Chem. Mater.*, 2013, **25**, 790–798.

98. E.-P. Ng and S. Mintova, *Micropor. Mesopor. Mater.*, 2008, **114,** 1–26.

99. N. C. Burtch, H. Jasuja and K. S. Walton, *Chem. Rev.*, 2014, **114**, 10575–10612.

100. S. Dey, A. Bhunia, M. D. Esquivel and C. Janiak, *J. Mater. Chem. A*, 2016, **4**, 6259-6263.

101. S. Dey, A. Bhunia and C. Janiak, *J. Mater. Chem. A*, 2016, submitted.

102. S. Dey, A. Bhunia, I. Boldog and C. Janiak, *Micropor. Mesopor. Mater.*, 2016, submitted.

103. S. S. Mondal, S. Dey, I. A. Baburin, A. Kelling, U. Schilde, G. Seifert, C. Janiak and H-J Holdt, *CrystEngComm.*, 2013, **15**, 9394-9399.

104. S. Pal, A. Bhunia, P. P. Jana, S. Dey, J. Möllmer, C. Janiak, and H. P. Nayek, *Chem. Eur. J.*, 2015, **21**, 2789–2792.

105. A. Bhunia, S. Dey, J. M. Moreno, U. Diaz, P. Concepcion, K. Van Hecke, C. Janiak and P. Van Der Voort, *Chem. Commun.*, 2016, 52, 1401-1404.

106. S. S. Mondal, S. Dey, A. G. Attallah, A. Bhunia, A. Kelling, U. Schilde, R. Krause-Rehberg, C. Janiak, and H-J Holdt, *ChemistrySelect*, 2016, in revision.